Lecture Notes in Mechanical Engineering

B. N. Singh
Arnab Roy
Dipak Kumar Maiti *Editors*

Recent Advances in Theoretical, Applied, Computational and Experimental Mechanics

Proceedings of ICTACEM 2017

Springer

Lecture Notes in Mechanical Engineering

Lecture Notes in Mechanical Engineering (LNME) publishes the latest developments in Mechanical Engineering - quickly, informally and with high quality. Original research reported in proceedings and post-proceedings represents the core of LNME. Volumes published in LNME embrace all aspects, subfields and new challenges of mechanical engineering. Topics in the series include:

- Engineering Design
- Machinery and Machine Elements
- Mechanical Structures and Stress Analysis
- Automotive Engineering
- Engine Technology
- Aerospace Technology and Astronautics
- Nanotechnology and Microengineering
- Control, Robotics, Mechatronics
- MEMS
- Theoretical and Applied Mechanics
- Dynamical Systems, Control
- Fluid Mechanics
- Engineering Thermodynamics, Heat and Mass Transfer
- Manufacturing
- Precision Engineering, Instrumentation, Measurement
- Materials Engineering
- Tribology and Surface Technology

To submit a proposal or request further information, please contact the Springer Editor in your country:

China: Li Shen at li.shen@springer.com
India: Priya Vyas at priya.vyas@springer.com
Rest of Asia, Australia, New Zealand: Swati Meherishi at swati.meherishi@springer.com
All other countries: Dr. Leontina Di Cecco at Leontina.dicecco@springer.com

To submit a proposal for a monograph, please check our Springer Tracts in Mechanical Engineering at http://www.springer.com/series/11693 or contact Leontina.dicecco@springer.com

Indexed by SCOPUS. The books of the series are submitted for indexing to Web of Science.

More information about this series at http://www.springer.com/series/11236

B. N. Singh · Arnab Roy ·
Dipak Kumar Maiti
Editors

Recent Advances in Theoretical, Applied, Computational and Experimental Mechanics

Proceedings of ICTACEM 2017

Springer

Editors
B. N. Singh
Department of Aerospace Engineering
Indian Institute of Technology Kharagpur
Kharagpur, West Bengal, India

Arnab Roy
Department of Aerospace Engineering
Indian Institute of Technology Kharagpur
Kharagpur, West Bengal, India

Dipak Kumar Maiti
Department of Aerospace Engineering
Indian Institute of Technology Kharagpur
Kharagpur, West Bengal, India

ISSN 2195-4356 ISSN 2195-4364 (electronic)
Lecture Notes in Mechanical Engineering
ISBN 978-981-15-1188-2 ISBN 978-981-15-1189-9 (eBook)
https://doi.org/10.1007/978-981-15-1189-9

This Springer imprint is published by the registered company Springer Nature Singapore Pte Ltd.
The registered company address is: 152 Beach Road, #21-01/04 Gateway East, Singapore 189721, Singapore

Contents

About the Editors

B. N. Singh is a HAL Chair Professor and former Head of Aerospace Engineering Department and currently Dean (HR) and Registrar at the Indian Institute of Technology (IIT) Kharagpur, India. Prof. Singh has more than 25 years of teaching and research experience. His work focuses on aerospace composite structures and its uncertainty quantification and he has developed several stochastic and deterministic mathematical models and their applications in aerospace structural components made of smart composites. Prof. Singh has published more than 130 papers in reputed journals and more than 85 conference papers.

Arnab Roy is a Professor in the Department of Aerospace Engineering at IIT Kharagpur. His research areas include the development of high accuracy Navier Stokes solvers for LES and DNS for incompressible flows- studies on bluff bodies, jets and associated instabilities, reaction control system jets in supersonic cross flow, low Reynolds number airfoils for fixed wing UAV/ MAV applications and Particle Image Velocimetry for flapping wing aerodynamic studies. He has published 3 book chapters, 38 research papers in reputed journal and conferences.

Dipak Kumar Maiti is Professor and Former Head, Department of Aerospace Engineering at IIT Kharagpur, prior to which he has worked at ADA Bangalore and Department of Aerospace Engineering, IIT Bombay. His research interest include aeroelastic analysis of smart lifting surface, analysis of smart landing gear, structural health monitoring and FE analysis of smart multidirectional composites. He has authored over 80 international journal papers, over 70 conference papers and 50 technical reports related to various projects.

Multi-scale Simulation of Elastic Waves Containing Higher Harmonics

Ambuj Sharma, Sandeep Kumar and Amit Tyagi

Abstract Numerical simulation of wave propagation is essential to understand the physical phenomenon of the wide variety of practical problems. However, the requirement of minimum grid point density per wavelength limits the computational stability, convergence, and accuracy of simulation of engineering application by numerical method. The purpose of this paper is to provide an improved framework for simulation of linear and nonlinear elastic wave propagation and guided-wave-based damage identification techniques feasible in the context of online structural health monitoring (SHM). Nonstandard wavelet-based multi-scale operator developed by using finite element discretization is used to represent waves. The proposed masking eliminates the requirement of a very large number of nodes in finite element method necessary for the propagation of such waves. The method is also useful in the situation where higher harmonics of propagating waves are ignored due to very high computational cost. The wavelet-based finite element scheme achieves an excellent numerical simulation and expresses an applicability for the guided waves' study.

Keywords Nonstandard wavelet operator · Structural health monitoring · Multi-scale simulation · Higher harmonics · Lamb waves

1 Introduction

Wave propagation can be characterized by the localized region of the sharp gradient of field variable which changes its locations in space with time. This gives permission to recognize the unusual nature that could be suitable for ultrasonic nondestructive

A. Sharma (✉)
Mechanical Engineering Department, VIT-AP, Amaravati, India
e-mail: sharma.ambuj@vitap.ac.in

S. Kumar · A. Tyagi
Mechanical Engineering Department, IIT (BHU), Varanasi, India
e-mail: sandeep.mec@iitbhu.ac.in

A. Tyagi
e-mail: atyagi.mec@iitbhu.ac.in

B. N. Singh et al. (eds.), *Recent Advances in Theoretical, Applied, Computational and Experimental Mechanics*, Lecture Notes in Mechanical Engineering,
https://doi.org/10.1007/978-981-15-1189-9_1

testing techniques. Guided-wave-based nondestructive techniques offer to evaluate the integrity of critical structures and to find out damage position, shape, and size [1, 2]. Several numerical techniques have been proposed to analyze the wave equations. Due to their relatively simple mathematical expressions and the possibility to be applied to the very large class of engineering problems, finite difference [3], boundary element [4], and finite element [2] based methods have been used by many authors for the simulation of guided Lamb waves. Finite element method (FEM) [2, 5] is a widespread numerical method used to simulate elastic guided wave propagation problem. Finite difference method (FDM) has also been used for the study of wave simulation and damage interaction by several researchers. Although FDM schemes are well situated for wave propagation in homogeneous media, however, the major limitation of the FDM schemes is that stiffness jumps due to continuously changing physical properties cause stability problems [6]. Furthermore, boundaries as well as discontinuities between different types of media lead to fairly accurate solutions and can generate severe errors [7]. With this in mind, more recently, Delsanto et al. have proposed the local interaction simulation approach (LISA) in combination with the sharp interface model [7]. Recently, customized elements and geometric multiscale finite element method have been introduced to analyze various types of wave propagation problems [8]. The finite element method, which has been preferred for elastic wave propagation, is not suitable to simulate nonlinear waves or higher harmonics of propagating waves. A drastic increase of nodes for the simulation of nonlinear wave problems demands some necessary alteration in FEM which must be numerically efficient and straightforward.

In recent years, wavelet-based numerical methods gain much attention for solving partial differential equations. The major advantage of this approach allows one to examine a problem in different resolutions, simultaneously. In addition, wavelet-based schemes are efficient in problems comprising singularities and sharp transitions in solutions for limited zones of a computation domain. Initially, Beylkin et al. [9] employed the study of numerical computation based on wavelet. Several mathematicians and scientists have established the superiority of wavelet-based methods for solving elliptic partial differential equations [10, 11]. The adaptivity of wavelets is one of the leading advantages for the implementation of wavelets in numerical analysis [12, 13]. Liandrat and Tchamitchian have solved regularized 1D Burgers' equation by using spatial wavelet approximation [14]. Later, Beylkin and Keiser [15], Vasilyev and Bowman [16], and Kumar and Mehra [17] have developed different wavelets-based algorithms and tested on 1D Burgers' and advection–diffusion equations. Researchers have increased the usage of wavelets for solution of partial differential equations (PDEs) after the development of the lifting scheme by Swelden [17] and stable completion by Carnicer et al. [18]. A review of wavelet techniques for the solution of PDEs has been presented by Dahmen [19]. However, a very few researchers have applied the wavelet-based method for analyzing wave propagation problem. Hong and Kennett proposed wavelet-based method for the numerical modeling and simulation of elastic wave propagation in 2D media [20]. Chen and Yang et al. presented the wave motion analysis of short wave in one-dimensional structures [21]. Mitra and Gopalakrishnan proposed wavelet-based

spectral finite element method (WSFEM) for simulation of elastic wave propagation in one- and two-dimensional situations [22]. In the literature, some researchers have used wavelets as basis function to solve PDEs but most researchers have applied the wavelet-based adaptive technique in finite difference schemes. These papers have presented the adaptive method for propagation of a single wave, but there is a need for different algorithms for more than one waves propagating with different velocities. Generation of higher harmonics due to material nonlinearity is not addressed in these papers.

Multi-scale modeling is one possible solution for higher harmonics in wave propagation simulation. Wavelet-based multi-scale method leads to fast and locally adaptive algorithms. The compactly supported refinable basis functions are main potential advantage of the wavelet [10, 11]. However, these methods are unable to compete with conventional finite element method. In this paper, proposed technique is inspired by the interesting paper by Krysl et al. [23].

This paper presents multi-scale adaptive approach for solving the wave propagation problem. In the proposed wavelet-based technique, FEM is preferred due to its capability to handle complex boundary and loading conditions instead of any other methods. This multi-scale transformation hierarchically filters out the less significant frequencies and offers an operative framework to retain the necessary frequencies of the wave. In this procedure, the finest level of the coefficient matrix is calculated once for the whole domain while the adaptively compressed coefficient matrix, which is very small compared to complete coefficient matrix, is used in every marching step of the solution. This paper is presenting wavelet-based nonstandard operator to improve finite element simulation of linear and nonlinear wave propagation in a large structure. We use nonstandard operator because it is more efficient than standard operator [24]. This will not only be useful to the structural health monitoring, but it can also be used where waves with higher harmonics move at different group velocities. A simple description of the nonstandard operator along with necessary algorithm and mathematical comments is provided to remove an execution headache connected with adaptive grid techniques. The algorithm is applied to 2D plane strain problem, but it is general and independent of domain dimensions.

2 Mathematical Formulation

2.1 Lamb Waves

In an elastic medium, elastic waves are defined as propagating disturbances that transport energy without any material transfer. Elastic waves of plane strain that exist in free plates are called Lamb waves. For an orthotropic and symmetrical plate, particle motion is often outlined through the elemental elastodynamic differential equation of wave

$$\partial_l(C_{klmn}\partial_n w_m) = \rho\partial_t^2 w_k, \quad (k,l,m,n=1,2). \tag{1}$$

Substituting stress relation in governing equations and Lamb wave can be expressed as

$$C_L^2\frac{\partial^2 u}{\partial x^2} + (C_L^2 - C_T^2)\frac{\partial^2 v}{\partial x\partial y} + C_T^2\frac{\partial^2 u}{\partial y^2} + f_x = \frac{\partial^2 u}{\partial t^2}, \tag{2(a)}$$

$$C_L^2\frac{\partial^2 v}{\partial y^2} + (C_L^2 - C_T^2)\frac{\partial^2 u}{\partial x\partial y} + C_T^2\frac{\partial^2 v}{\partial x^2} + f_y = \frac{\partial^2 v}{\partial t^2}. \tag{2(b)}$$

$C_L^2 = \frac{\lambda+2\mu}{\rho}$ and $C_T^2 = \frac{\mu}{\rho}$ are longitudinal velocity and shear velocity, respectively, where $\lambda = \frac{E\nu}{(1+\nu)(1-2\nu)}$ and $\mu = \frac{E}{2(1+\nu)}$ are Lamé constants, E is Young's modulus, and ν is Poisson ratio. The 2D plane strain problem is discretized into the set of finite element equations as

$$[K][u] + [M][\ddot{u}] = 0, \tag{3}$$

where $[u]$ and $[\ddot{u}]$ are unknown coefficient vectors. $[K]$ and $[M]$ are global stiffness and mass matrix, respectively.

2.2 Multi-scaling Using Wavelets

The idea of multi-scale exploration is to interpolate an unknown field at a coarse level with the assistance of supposed scaling functions. Any enhancement to initial approximation is accomplished by adding "details" rendered by basis functions referred to as wavelets. A multi-scaling analysis forms a sequence of closed subspaces to satisfy certain self-similarity relations as well as completeness and regularity relations. The basis functions in W_j are called wavelet functions. Wavelet functions are symbolized by $\psi_{j,k}$. These scaling and wavelet functions are employed for wavelet-based multi-scaling. A function $f \in L^2(R)$ is approximated by its projection $P^j f$ onto the space V_j and the projection of f on W_j as $Q^j f$, we have

$$P^j f = P^{j-1} f + Q^{j-1} f. \tag{4}$$

If the coefficient vector of $P^j f$ (or coefficients of scaling functions) is $\mathbf{C}_j = \{C_{j,0}, \ldots, C_{j,v(j)}\}^{\mathrm{T}}$ and coefficient vector of $Q^j f$ (or coefficients of some wavelets) is $\mathbf{d}_j = \{d_{j,0}, \ldots, d_{j,w(j)}\}^{\mathrm{T}}$, then we can write wavelet transform as

$$\mathbf{C}_j = [T_j]\begin{bmatrix}\mathbf{C}_{j-1}\\ \mathbf{d}_{j-1}\end{bmatrix}. \tag{5}$$

The matrix $[T_j]$ is used to achieve next higher level by transforming scaling and detail coefficients of V_{j-1} and W_{j-1} spaces, respectively. In this paper, B-spline wavelet and Daubechies (D4) wavelet [25] are used for wave propagation.

2.3 Nonstandard Multi-scale Decomposition of Finite Element Matrix

Two observations can be made while solving some PDEs using the wavelet bases: (i) In theoretical terms, most of the available wavelet methods have stable Riesz basis and better condition number than FEM or FDM. (ii) But in practical applications, wavelet methods are not yet ready to compete with the traditional FEM approach. One important reason is while the FEM can always produce a sparse matrix with more regular sparsity patterns, use of wavelet bases does not produce such sparse matrices. But the combination of wavelets with other methods, such as FDM, FEM, and recently SEM [22], show good results. Here, we have used FEM discretization to derive a sparse matrix, as the FEM remains the most versatile tool to solve PDEs.

Let us consider a continuous wave field $u(x, y)$ and $v(x, y)$ for a source of excitation over 2D homogeneous medium. The approximation of the continuous wave field on the discrete domain is denoted by u^j and v^j. It represents the discrete wave field that is obtained with a classic time–space finite element method for a sufficiently fine discretization of $V_j \subset R^2$. The 2D wavelet transform cascades projections of the discrete wave field over different approximation grids $V_1, V_2, V_3, \ldots, V_j$ of increasing resolution.

In this multi-scale algorithm, we used NS operator proposed by Beylkin [26]. To the best of authors' knowledge, no one researcher has used NS operator in wavelet–FEM coupling or wavelet–FDM coupling. It has been proved by Beylkin [26, 27] that NS operator is more efficient than the standard form of operator used by most of the researchers. In this paper, we have used NS operator in two-dimensional wavelet–finite element coupling technique. The finite element equations for the transient problem, Eq. 3, can be expressed in the expanded form as

$$\begin{bmatrix} \begin{bmatrix} k_{uu}^j \\ k_{vu}^j \end{bmatrix} \begin{bmatrix} k_{uv}^j \\ k_{vv}^j \end{bmatrix} \end{bmatrix} \begin{bmatrix} u^j \\ v^j \end{bmatrix} = \begin{bmatrix} \begin{bmatrix} f_u^j \\ f_v^j \end{bmatrix} \end{bmatrix}. \tag{6}$$

We can apply the wavelet transformation on the field variables of both the directions:

$$\begin{bmatrix} [T^{\mathrm{T}}] & [0] \\ [0] & [T^{\mathrm{T}}] \end{bmatrix} \begin{bmatrix} \begin{bmatrix} k_{uu}^{j} \\ k_{vu}^{j} \end{bmatrix} & \begin{bmatrix} k_{uv}^{j} \\ k_{vv}^{j} \end{bmatrix} \end{bmatrix} \begin{bmatrix} [T] & [0] \\ [0] & [T] \end{bmatrix} \begin{bmatrix} \begin{bmatrix} d^{1} \\ u^{1} \\ e^{1} \\ v^{1} \end{bmatrix} \end{bmatrix} = \begin{bmatrix} [T^{\mathrm{T}}] & [0] \\ [0] & [T^{\mathrm{T}}] \end{bmatrix} \begin{bmatrix} \begin{bmatrix} f_{u}^{j} \\ f_{v}^{j} \end{bmatrix} \end{bmatrix}. \tag{7}$$

The organization of the matrix after three-level transform of nonstandard form can be extended and expressed in the new notations as [24]

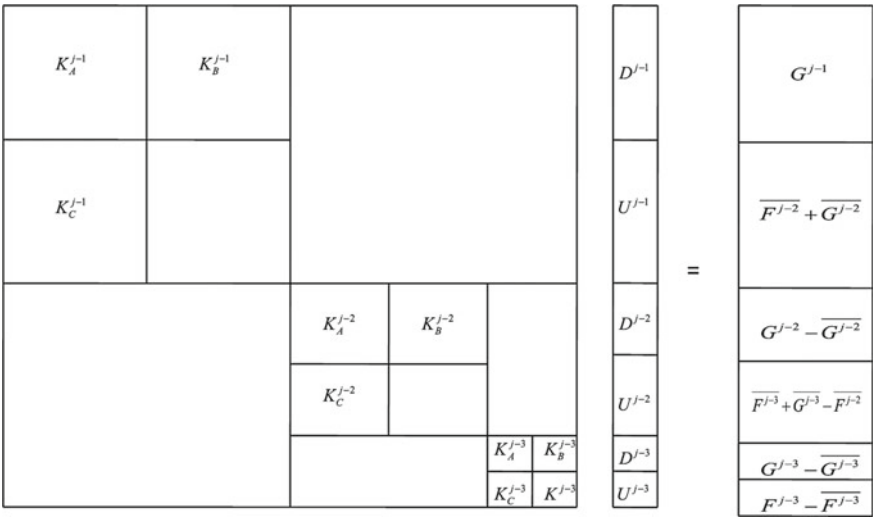

(8)

In order to solve it, Gines et al. [24] proposed nonstandard LU decomposition.

3 Results and Discussion

Elastic waves have been employed for identification of damage in the thin wall structures such as plates and pipes [5]. Guided Lamb waves are excited in the structures through narrowband burst signals. In order to evaluate the performance of wavelet-based multi-scale method. We considered an example in which a 50 × 50 mm^2 homogeneous, isotropic aluminum plate with a density of 2700 kg/m^3. The simulation of Lamb wave in this plate with 400 kHz central frequency is presented in Fig. 1. Contour plots of the displacement in the x-direction at three different time instants are well depicted in this figure.

Nonlinear Lamb wave is more sensitive to small-scale damage identification. However, the investigations of the higher harmonics in propagating Lamb waves

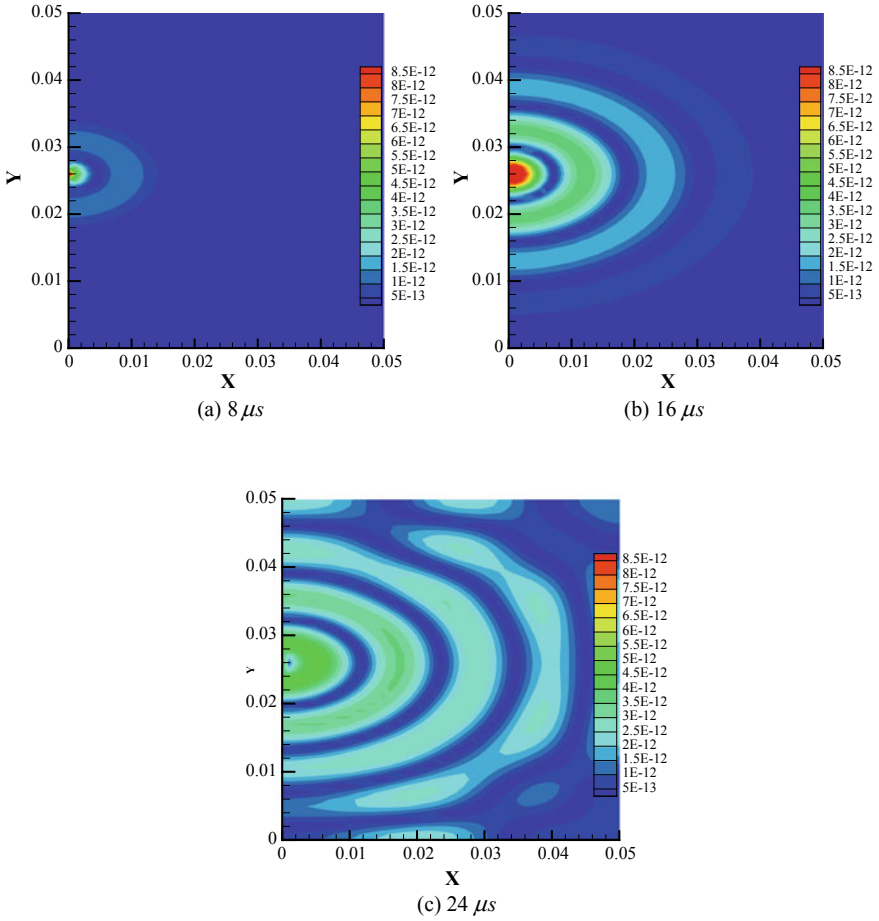

(a) 8 μs (b) 16 μs

(c) 24 μs

Fig. 1 Contour plots of the displacement in the x-direction at three different time frames for isotropic plate

were ignored due to high computational cost. To see the efficiency of the wavelet-based method, higher harmonics are added in the Lamb wave and propagation of waves is observed. This study uses the following actuation function with 400 kHz central frequency:

$$E(t) = \begin{cases} f_o \sin(\Omega t) * (\sin(0.1\Omega t))^2 + 0.1 f_o \sin(2 * 5\Omega t) * (\sin(\Omega t))^2, & t < 10\pi / \Omega \\ 0, & \text{otherwise,} \end{cases}$$

where Ω is the frequency of excitation and E_o is the maximum amplitude. The excitation signal on a plate with a higher harmonics is shown in Fig. 2. An aluminum plate of 200 mm length and 2 mm thickness is used in the analysis. Poisson's ratio =

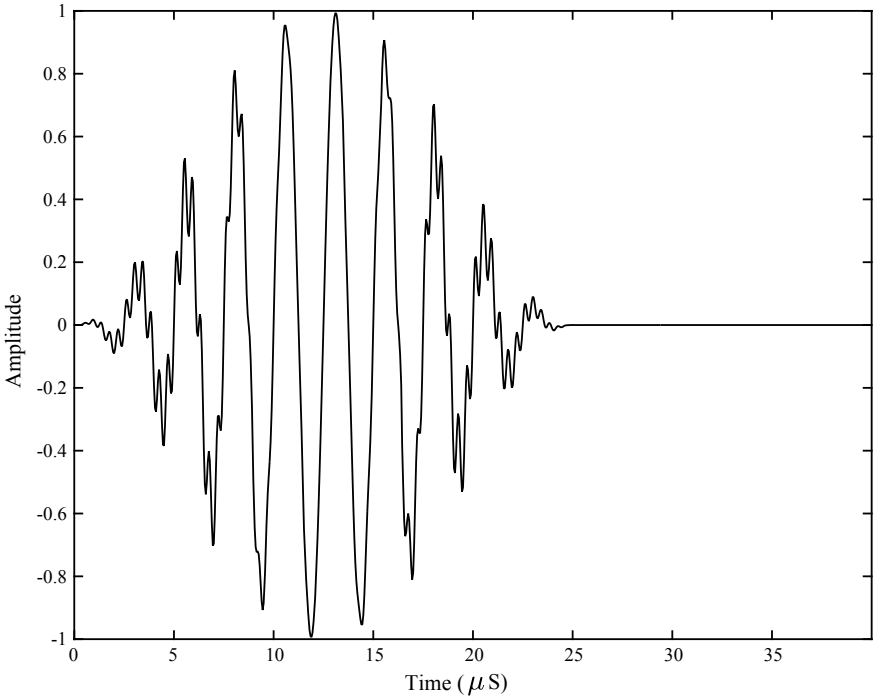

Fig. 2 Excitation signal for Lamb wave with higher harmonics

0.3, density = 2700 kg/m^3, and Young's modulus $E = 69$ GPa are assumed as material properties. The Lamb wave in this material has longitudinal velocity $C_{\mathrm{L}} = 5299$ m/s and transverse velocity $C_{\mathrm{T}} = 3135$ m/s. The waves are actuated by employing pin forces applied to the left boundary of the plate. The excitation forces are parallel to the longitudinal (propagating) direction. In-phase pin forces are applied to the top and bottom edge nodes of the plate for excitation of fundamental symmetric (S_0) modes, and the antisymmetric modes are propagated by imposing out-of-phase pin forces. In this paper, we considered the cases in which the pure S_0 mode is excited. Ten cycles Hanning-window actuation is given through excitation function to deliver a limited cycle sinusoidal tone burst.

Higher frequency wave propagation problems demand enormous computer resources because of very large number of time integration steps and highly dense mesh. Generally, in the case of Lamb wave, 20 elements per wavelength are required but this is not sufficient for higher harmonic simulation. Figure 3 depicts the measured nodal displacement response of time-domain signals obtained using FEM simulation of the plate with 40, 80, and 120 elements per wavelength. It can be observed that higher harmonics are not properly visible in the response of the plate with 40 elements per wavelet. On the other hand, as shown in the same figure, higher harmonics are visible for 80 elements per wavelength.

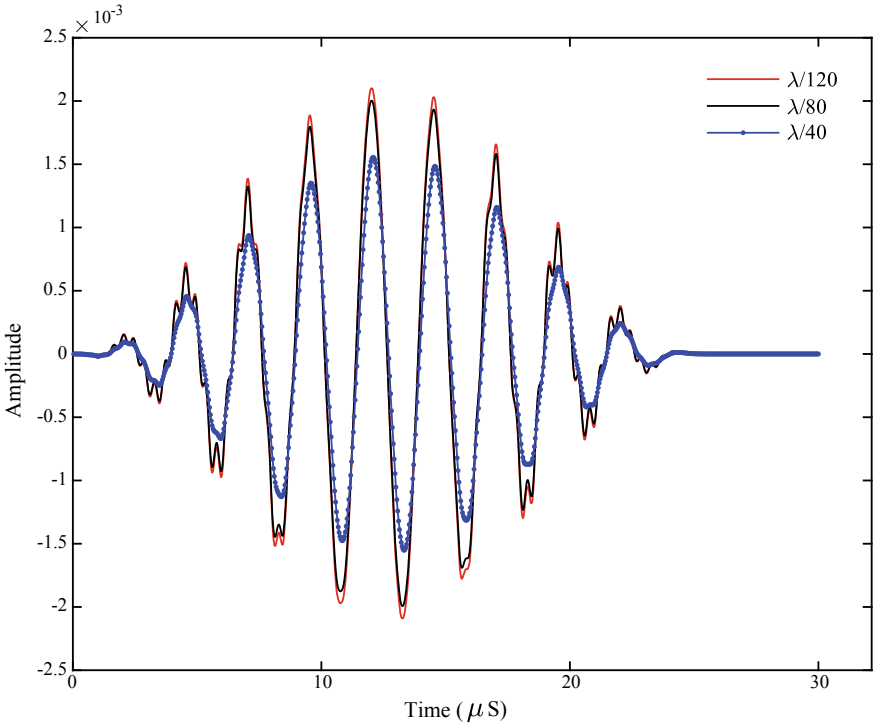

Fig. 3 Comparison of response of plate for 40, 80, and 120 elements per wavelength

In the present analysis, B-spline and Daubechies (D4) wavelet are used to establish robustness and sensitivity of wavelet-based wave propagation method. To capture higher harmonics in the plates, FEM uses 17,080 uniformly distributed nodes while half of the FEM nodes are required after application of one level of wavelet transform. Nodal displacement response of plate received from B-spline and D4 wavelet transform at level 1 along with FEM results is demonstrated in Fig. 4. It establishes good agreement between conventional finite element and proposed wavelet-based method. It can be observed that B-spline wavelet produces response close to FEM results, while there is some deviation in the results of D4 wavelet. Further, we examined wavelet-based method at various levels of wavelet transform to find the level up to which this method can work efficiently. These results show some attenuation but wavelets are not eliminating higher frequency components of waves which are important in many analyses.

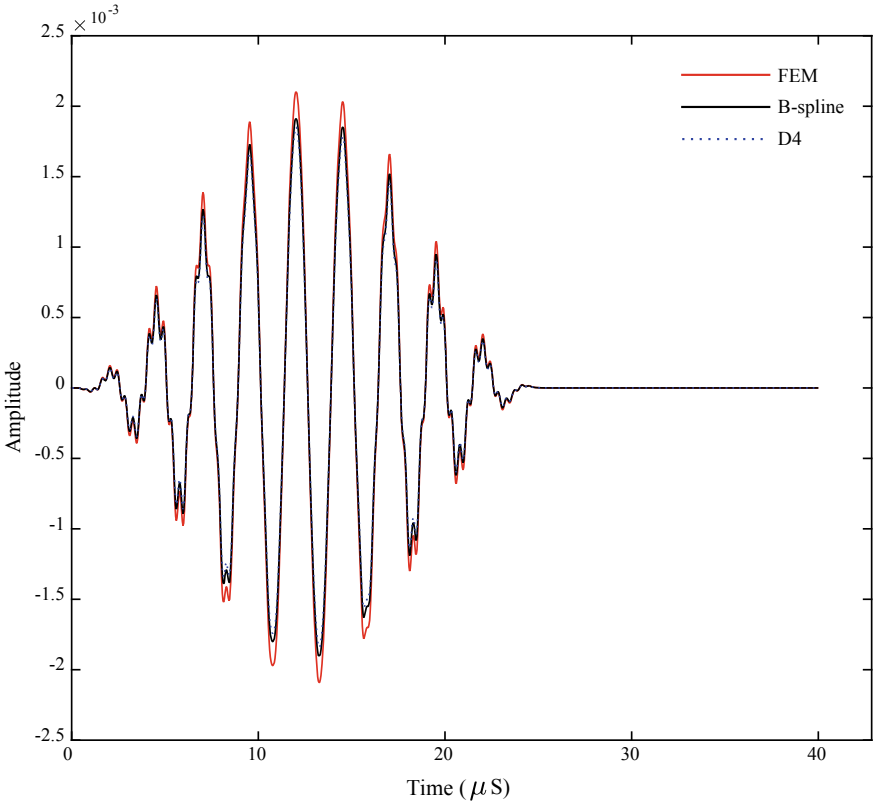

Fig. 4 Comparison of higher harmonic Lamb waves plates response at wavelet transform level 1

4 Conclusion

The spatial derivative operators in the wave equations are handled using multi-resolution transforms in a physical domain. We presented a wavelet-based framework to reduce the size of global stiffness matrix of finite element analysis which is becoming too large in the case of nonlinear wave propagation problem. Wavelet-based method is not only to develop the compressed stiffness matrix, but also to propagate higher harmonics of waves using least number of nodes and able to reduce the computational cost significantly. Without disturbing the programming advantages of FE regarding the implementation of boundary conditions and efficient numerical integration of interpolation functions, wavelet-based methods are able to reduce the size of matrix as much as one by a sixteenth of original FE matrix. These fundamental characteristics show that the wavelet-based method can be utilized for more complex wave propagation problems.

References

1. Hassan W, Veronesi W (2003) Finite element analysis of Rayleigh wave interaction with finite-size, surface-breaking cracks. Ultrasonics 41:41–52
2. Ham S, Bathe KJ (2012) A finite element method enriched for wave propagation problems. Comput Struct 94–95:1–12
3. Per W, Bertil G (2005) High-order difference methods for waves in discontinuous media. J Comput Appl Math 192(1):142–147
4. Tadeu A, Godinhoa L, Antónioa J, Mendesa PA (2007) Wave propagation in cracked elastic slabs and half-space domains—TBEM and MFS approaches. Eng Anal Bound Elements 31(7):819–835
5. Nieuwenhuis JH, Neumann JJ, Greve DM, Oppenheim IJ (2005) Generation and detection of guided waves using PZT wafer transducers. IEEE Trans Ultrason Ferroelectr Freq Control 52(11):2103–2111
6. Delsanto PP, Whitcombe T, Chaskelis HH, Mignogna RB (1992) Connection machine simulation of ultrasonic wave propagation in materials. I: the one-dimensional case. Wave Motion 16:65–80
7. Delsanto PP, Schechter RS, Migogna RB (1997) Connection machine simulation of ultrasonic wave propagation in materials. III: the three-dimensional case. Wave Motion 26(4):329–339
8. Casadei F (2012) Multiscale analysis of wave propagation in heterogeneous structures. Dissertation, School of Aerospace Engineering, Georgia Institute of Technology
9. Beylkin G, Coifman R, Rokhlin V (1991) Fast wavelet transforms and numerical algorithms I. Commun Pure Appl Math XLIV:141–183
10. Amaratunga K, Williams JR (1993) Wavelet based Green's function approach to 2D PDEs. Eng Comput 10(4):349–367
11. Qian S, Weiss JJ (1993) Wavelets and the numerical solution of partial differential equations. J Comput Phys 106:155–175
12. Holmstrom M (1999) Solving hyperbolic PDEs using interpolating wavelets. SIAM J Sci Comput 21(2):405–420
13. Lippert RA, Arias TA, Edelman A (1998) Multiscale computation with interpolating wavelets. J Comput Phys 140:278–310
14. Liandrat J, Tchamitchian PH (1990) Resolution of the 1D regularized burgers equation using a spatial wavelet approximation. Report NASA Langley Research Centre, Report No: NASA CR – 187480, Hampton VA
15. Vasilyev OV, Bowman C (2000) Second generation wavelet collocation method for the solution of partial differential equations. J Comput Phys 165:660–693
16. Rathish Kumar BV, Mehra M (2005) Wavelet-Taylor Galerkin method for the burgers equation. BIT Numer Math 45:543–560
17. Swelden W (1998) The lifting scheme: a construction of second generation wavelets. SIAM J Math Anal 29(2):511–546
18. Carnicer JM, Dahmen W, Peña JM (1996) Local decomposition of refinable spaces and wavelets. Appl Comput Harmon Anal 3:127–153
19. Dahmen W, Stevenson R, Siam S (2015) Element-by-element construction of wavelets satisfying stability and moment conditions. SIAM Numer Anal 37:319–352
20. Hong T-K, Kennett BLN (2002) A wavelet-based method for simulation of 2-D elastic wave propagation. Geophys J Int 150(3):610–638
21. Chen XF, Yang ZB, Zhang XW, He ZJ (2012) Modeling of wave propagation in one-dimension structures using B-spline wavelet on interval finite element. Finite Elements Anal Des 51:1–9
22. Mitra M, Gopalakrishnan S (2006) Wavelet based 2-D spectral finite element formulation for wave propagation analysis in isotropic plates. Comput Model Eng Sci 15(1):49–67
23. Krysl P, Grinspun E, Schroder P (2002) Natural hierarchical refinement for finite element methods. Int J Numer Methods Eng 56(8):1109–1124
24. Gines D, Beylkin G, Dunn J (1998) LU Factorization of non-standard forms and direct multiresolution solvers. Appl Comput Harmon Anal 5:156–201

25. Stollnitz EJ, Derose TD, Salesin DH (1996) Wavelets for computer graphics. Morgan Kaufmann Publishers Inc., California
26. Beylkin G (1992) On the representation of operator in bases of compactly supported wavelets. SIAM J Numer Anal 6(6):1716–1740
27. Beylkin G, Keiser JM (1997) On the adaptive numerical solution of nonlinear partial differential equations in wavelet bases. J Comput Phys 132:233–259

Effect of Skewness on Random Frequency Responses of Sandwich Plates

R. R. Kumar, Vaishali, K. M. Pandey and S. Dey

Abstract This study presents the effect of skewness in natural frequency responses of sandwich plates. The free vibration analysis is carried out by using higher order zigzag theory (HOZT) considering random input parameters. It satisfies the transverse shear stress continuity condition and the transverse flexibility effect. The in-plane displacement throughout the thickness is assumed to vary cubically while transverse displacement is considered to vary quadratically within the core and constant at top and bottom plates. An efficient C_0 stochastic finite element approach is developed for the implementation of proposed plate theory in the random variable surrounding. Compound stochastic effect of all input parameters is presented for the different degrees of skewness in sandwich plates. Intensive Monte Carlo simulation (MCS) is employed for solving the stochastic-free vibration equations and statistical analysis is conducted for illustration of the results. The present algorithm for sandwich plate is validated with previous literatures and it is found to be in good agreement.

Keywords Monte Carlo simulation · Sandwich plate · Natural frequency · Higher order zigzag theory · Skewness

1 Introduction

A sandwich plate is a multilayered plate having two face sheets and a core embedded in between them through adhesive. The face sheets are relatively thin but of high strength and stiffness material, whereas the core is made up of relatively thick and lower density material. The high specific strength and stiffness of sandwich structures make them suitable for crucial engineering applications like automobile, civil construction, aerospace, and marine industries. Sandwich plates are widely used in design and construction of aerospace craft. In such application, these materials are subjected to wide environmental changes such as pressure, temperature, density, and

R. R. Kumar · Vaishali (✉) · K. M. Pandey · S. Dey
Department of Mechanical Engineering, National Institute of Technology, Silchar, Silchar, India
e-mail: vaishali765@gmail.com

B. N. Singh et al. (eds.), *Recent Advances in Theoretical, Applied, Computational and Experimental Mechanics*, Lecture Notes in Mechanical Engineering,
https://doi.org/10.1007/978-981-15-1189-9_2

humidity. This inevitable change in surrounding affects the vibrational response of the structure. Therefore, it is essential to include the actual operating condition in order to get the changes in vibration characteristic of sandwich plate. The vibration response of the aerospace craft is usually carried out in atmospheric condition rather than actual unevenly varying condition for the cause of convenience. Thus, it is essential to consider the material and geometric uncertainty in order to accommodate above-mentioned environmental changes as well as other inaccuracies occurring during design and fabrication of the sandwich plate. The cost-effective sandwich panel requires sandwich core of low-cost material which exhibits better weight sensitiveness as well. The development and automation in production processes make possible the production of low-cost sandwich panel. The sandwich panel is not considered for low-cost application due to insufficient knowledge about their cost-saving potential. The manufacturing of such sandwich structure always experiences spatial variability due to manufacturing imperfections and other inaccuracies. Moreover, dynamic behavior of sandwich structure possesses high statistical variation due to unavoidable skewness occurring during complex fabrication processes. Various interdependent parameters influencing the properties are core thickness, number of face sheet layer, face sheet and core material properties, and topology of core. Because of these parameters, uncertain responses can be seen and the system properties become inevitably random in nature. So to have a safe and realistic design, we must not neglect these inherent uncertainties. This cannot be obtained through usual deterministic approach. So, to incorporate the source uncertainties in design and analysis of the mechanical system, it is required to quantify the present uncertainties.

Recently, Grover et al. [1] worked on sandwich plate and studied the parametric uncertainties influencing the deflection statics and after that they also ensured the validity by comparing it with that of Monte Carlo simulation having finite element solution. Earlier, Aguib et al. [2] worked on magnetorheological elastomer core sandwich beam. The proposed structure was directly applied to civil engineering. Nayak et al. [3] studied the free vibration response on sandwich plates in damped random environment. Jin et al. [4] studied the natural frequency response by considering a viscoelastic core sandwich beam. For honeycomb sandwich beams, Debruyne et al. [5] analyzed the design parameters' variability. The compressibility effect in transverse direction is studied using laminate mechanics by Plagianakos and Papadopoulos [6] and Liu [7] carried out the analytical study on sensitivity analysis for natural frequencies and their mode shapes. SFEM was furthermore studied by Gadade et al. [8]. The vibration characteristic was studied by Scarpa and Tomlinson [9] on regular hexagonal honeycomb cells and re-entrant auxetic honeycomb cells. Later, spectral finite element method was used by Ruzzene [10]. By using this method, we can accurately evaluate the acoustic properties of honeycomb. An optimized study of truss-core sandwich panel was done by Denli and Sun [11]. A similar study was also presented by Franco et al. [12]. With recent advancement in finite element software, for example, ABAQUS and ANSYS, the efficiency and accuracy have greatly increased. The study of stochastic natural frequency including the effect of noise was done by Dey

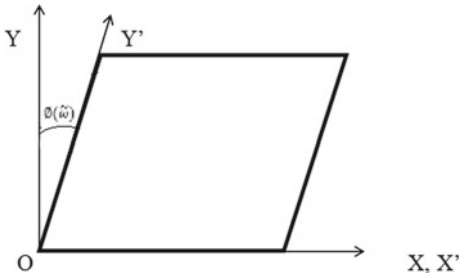

Fig. 1 Skewed plate

et al. [13]. Recently, stochastic analysis is carried out by Kumar et al. [14–19], Karsh et al. [20–26], and Mukhopadhyay et al. [27, 28]. Most of the research is carried out by using deterministic approach, whereas few researchers focused on stochastic approach.

Here, the effect of skewness (Fig. 1) on natural frequency response, having taken into consideration the compound variation of all input parameters, is studied. Thereafter, this paper is presented as: Theoretical formulation is described in Sect. 2, result and discussion are illustrated in Sect. 3, whereas conclusion and future scope are presented in Sect. 4.

2 Theoretical Formulation

The strain–displacement equation [29] can be shown as

$$\{\bar{\varepsilon}(\varpi)\} = \left[\frac{\partial u(\varpi)}{\partial x}\frac{\partial v(\varpi)}{\partial y}\frac{\partial w(\varpi)}{\partial z}\frac{\partial u(\varpi)}{\partial x} + \frac{\partial v(\varpi)}{\partial y}\frac{\partial u(\varpi)}{\partial z} + \frac{\partial w(\varpi)}{\partial x}\frac{\partial v(\varpi)}{\partial z} + \frac{\partial w(\varpi)}{\partial x}\right], \quad (1)$$

$$\text{i.e., } \{\psi(\varpi)\} = [a(\varpi)]\{\psi(\varpi)\},$$

where $[a]$ is unit step function. The equation for generalized displacement vector is given as

$$\{s(\varpi)\} = \sum_{k=1}^{n} \zeta_i(\varpi) s_i(\varpi), \quad (2)$$

where $\{s\} = \{U_0 V_0 W_0 \theta_x \theta_y U_u V_u W_u U_l V_l W_l\}^{\mathrm{T}}$. Equation (1) is used to give strain vector equation

$$\{\psi(\varpi)\} = [a(\varpi)]\{s(\varpi)\}. \quad (3)$$

The strain–displacement matrix can be represented as $[a]$. The dynamic equilibrium equation for natural frequency analysis is written by using Hamilton's principle as

$$[r(\varpi)]\{\bar{s}\} = \lambda^2[m(\varpi)]\{\bar{s}\}, \tag{4}$$

where $[r(\varpi)]$ is the random natural frequency. The global mass matrix $[m(\varpi)]$ is

$$[m(\varpi)] = \sum_{k=1}^{n_u+n_l} \iiint \rho_k(\varpi)[n]^{\mathrm{T}}[j]^{\mathrm{T}}[n][j]\mathrm{d}x\mathrm{d}y\mathrm{d}z = \iint [n]^{\mathrm{T}}[k(\varpi)][n]\mathrm{d}x\mathrm{d}y, \tag{5}$$

where$\rho_k(\varpi)$ is stochastic mass density of kth order, $[j]$ is of the order of 3X11, and $[n]$ is the shape function matrix. The equation for stiffness matrix $[k(\varpi)]$ is given as

$$[k(\varpi)] = \sum_{k_l}^{n_u+n_l} \rho_k(\varpi)[j]^{\mathrm{T}}[j]\mathrm{d}z. \tag{6}$$

For storing the global stiffness in one array, we have used the skyline technique. For getting static solution, Gaussian decomposition scheme is used and for free vibration analysis simultaneous iteration technique is used.

3 Results and Discussion

Here, HOZT is applied to a sandwich plate (simply supported boundary condition) of length $(l) = 10$ cm, width $(b) = 10$ cm, and thickness $(t) = 1$ cm to demonstrate the proposed finite element (FE) model. The present model is having eight-layer symmetric cross-ply laminate having core thickness of 0.8 and face sheet thickness of 0.1 with equal layers on both sides of core. Here, the first, second, and third natural frequencies without any skewness are compared with 15°, 30°, 45°, and 60° skewed plates. The material properties considered for the present analysis are shown in Table 1.

Based on the present model, the natural frequencies for the first mode obtained for 30° and 45° skew angles and the results of Wang et al. [30] and Kulkarni and Kapuria [31] are tabulated in Table 2. Such a small deviation between various results obtained for natural frequencies is shown in Table 2, which can justify the accuracy and applicability of HOZT.

It is evident from Fig. 2 that with increase in skew angle, fundamental and third natural frequencies initially increase for $(\phi) = 15°$ and 30°, decrease for $(\phi) = 45°$, and then again increase up to maximum for $(\phi) = 60°$, whereas second natural frequency initially increases for $(\phi) = 15°$ and 30° and decreases for $(\phi) = 45°$ and 60°. The mean value of second natural frequency for $(\phi) = 45°$ and 60° remains

Table 1 Material properties

	Core	Face sheet
E_1 (GPa)	0.5	38.6
$E_2 = E_3$ (GPa)	0.5	8.27
$G_{12} = G_{13}$ (GPa)	0.4	4.14
G_{23} (GPa)	0.2	1.656
$\upsilon_{12} = \upsilon_{13} = \upsilon_{23} = \upsilon_{32}$	0.27	0.26
$\upsilon_{21} = \upsilon_{31}$	0.006	0.006
P (kg/m^3)	1000	2600

Table 2 Natural frequency of (0°/90°/0°/90°) sandwich plate

Skew angle (ϕ) (°)	Present study	Wang et al. [30]	Kulkarni and Kapuria [31]
30	1.8889	1.9410	1.9209
45	2.5806	2.6652	2.6391

almost same which lies in between $\phi = 15°$ and $\phi = 30°$. This corroborates the fact obtained vide probability density function (PDF) plots.

4 Conclusions

Based on higher order zigzag theory (HOZT), the accuracy and applicability of the proposed finite element model for free vibration analysis of sandwich plates are studied. The novelty of the present study includes the skewness effect on free vibration of sandwich plates. The natural frequency of sandwich plate is compared with that of skewed sandwich plate by means of probability density function (PDF) plots. The first, second, and third natural frequencies of unskewed sandwich plates are compared with plates having skewness of 15°, 30°, 45°, and 60°. It is observed that the unavoidable source uncertainties cause significant deviation of natural frequency from the mean deterministic value. Therefore, it is of utmost importance to consider the effect of skewness and source uncertainty in design and analysis of sandwich plate and other complex structures for safe and realistic design. Based on these observations, the present work can be extended to deal with more complex structures.

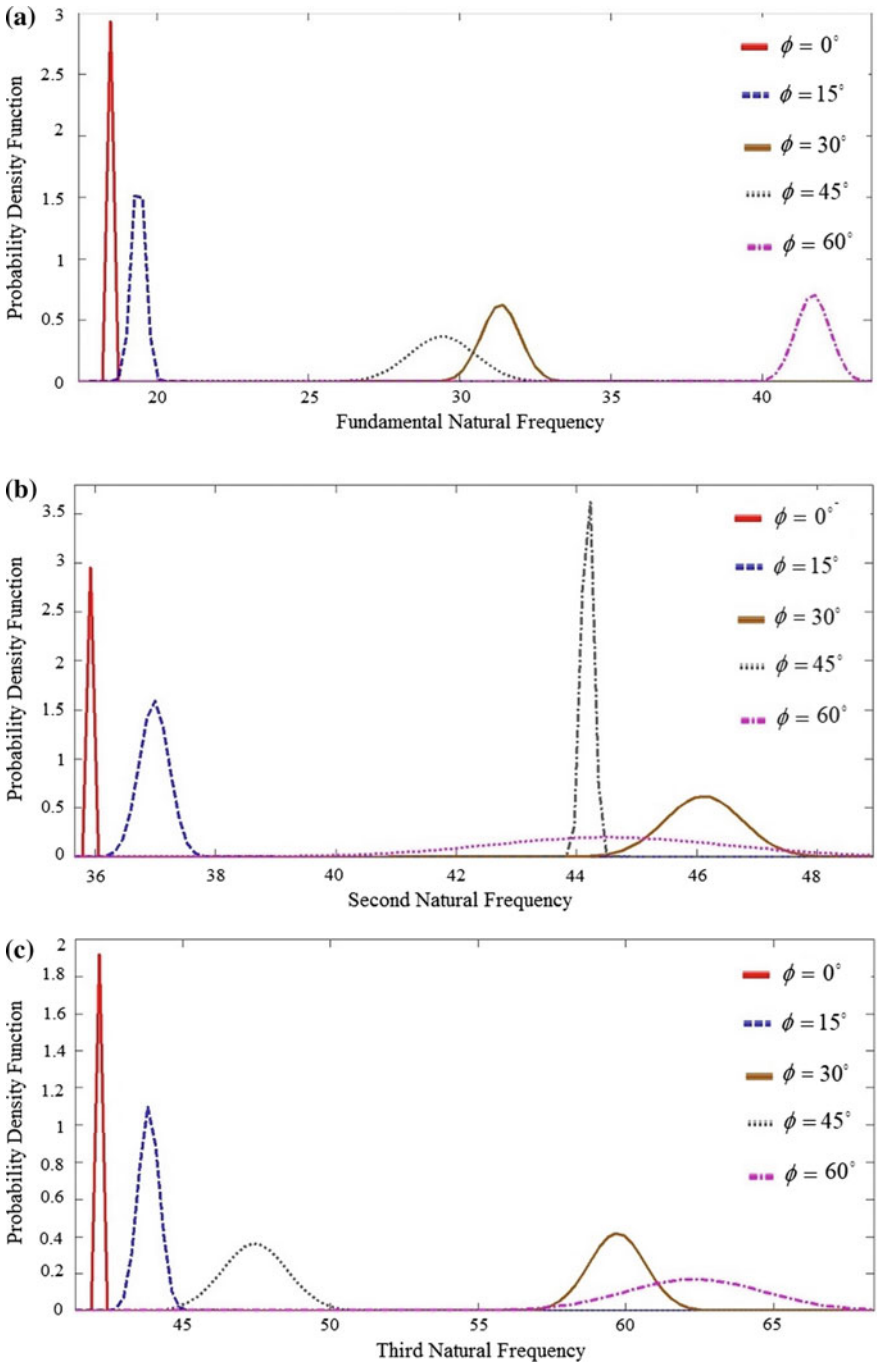

Fig. 2 Random natural frequency (rad/s) of sandwich plates for **a** first, **b** second, and **c** third natural frequencies with skew angle, (φ) = 0°, 15°, 30°, 45°, and 60°

Acknowledgements The first and second authors would like to acknowledge the financial support received from MHRD GOI during this research work.

References

1. Grover N, Sahoo R, Singh BN, Maiti DK (2017) Influence of parametric uncertainties on the deflection statistics of general laminated composite and sandwich plates. Compos Struct 171:158–169
2. Aguib S, Nour A, Benkoussas B, Tawfiq I, Djedid T, Chikh N (2016) Numerical simulation of the nonlinear static behavior of composite sandwich beams with a magnetorheological elastomer core. Compos Struct 139:111–119
3. Nayak AK, Satapathy AK (2016) Stochastic damped free vibration analysis of composite sandwich plates. Procedia Eng 144:1315–1324
4. Jin G, Yang C, Liu Z (2016) Vibration and damping analysis of sandwich viscoelastic-core beam using Reddy's higher-order theory. Compos Struct 140:390–409
5. Debruyne S, Vandepitte D, Moens D (2015) Identification of design parameter variability of honeycomb sandwich beams from a study of limited available experimental dynamic structural response data. Comput Struct 146:197–213
6. Plagianakos TS, Papadopoulos EG (2015) Higher-order 2-D/3-D layerwise mechanics and finite elements for composite and sandwich composite plates with piezoelectric layers. Aerosp Sci Technol 40:150–163
7. Liu Q (2015) Analytical sensitivity analysis of frequencies and modes for composite laminated structures. Int J Mech Sci 90:258–277
8. Gadade AM, Lal A, Singh BN (2016) Accurate stochastic initial and final failure of laminated plates subjected to hygro-thermo-mechanical loadings using Puck's failure criteria. Int J Mech Sci 114:177–206
9. Scarpa F, Tomlinson G (2000) Theoretical characteristics of the vibration of sandwich plates with in-plane negative Poisson's ratio values. J Sound Vib 230(1):45–67
10. Ruzzene M (2003) Vibration and sound radiation of sandwich beams with honeycomb truss core. In: ASME 2003 international mechanical engineering congress and exposition. American Society of Mechanical Engineers
11. Denli H, Sun JQ (2007) Structural-acoustic optimization of sandwich structures with cellular cores for minimum sound radiation. J Sound Vib 301(1-2):93–105
12. Franco F, Cunefare KA, Ruzzene M (2007) Structural-acoustic optimization of sandwich panels. J Vib Acoust 129(3):330–340
13. Dey S, Mukhopadhyay T, Sahu SK, Adhikari S (2016) Effect of cutout on stochastic natural frequency of composite curved panels. Compos B 105:188–202
14. Kumar RR, Mukhopadhyay T, Pandey KM, Dey S (2018) Stochastic buckling analysis of sandwich plates: the importance of higher order modes. Int J Mech Sci 152:630–643
15. Kumar RR, Pandey KM, Dey S (2019) Probabilistic assessment on buckling behavior of sandwich panel: a radial basis function approach. Struct Eng Mech 71(2):197–210
16. Kumar RR, Karsh PK, Pandey KM, Dey S (2019) Stochastic natural frequency analysis of skewed sandwich plates. Eng Comput
17. Kumar RR, Mukhopadhyay T, Naskar S, Pandey KM, Dey S (2019) Stochastic low-velocity impact analysis of sandwich plates including the effects of obliqueness and twist. Thin-Walled Structures 145:106411
18. Kumar RR, Mukhopadhya T, Pandey KM, Dey S (2020) Prediction capability of polynomial neural network for uncertain buckling behavior of sandwich plates. In: Handbook of Probabilistic Models. Butterworth-Heinemann, pp 131–140

19. Kumar RR, Pandey KM, Dey S (2020) Stochastic free vibration analysis of sandwich plates: a radial basis function approach. In: Reliability, Safety and Hazard Assessment for Risk-Based Technologies. Springer, Singapore, pp 449–458
20. Karsh PK, Mukhopadhyay T, Dey S (2018) Spatial vulnerability analysis for the first ply failure strength of composite laminates including effect of delamination. Compos Struct 15(184):554–567
21. Karsh PK, Mukhopadhyay T, Dey S (2018) Stochastic dynamic analysis of twisted functionally graded plates. Compos B Eng 15(147):259–278
22. Karsh PK, Mukhopadhyay T, Dey S (2019) Stochastic low-velocity impact on functionally graded plates: probabilistic and non-probabilistic uncertainty quantification. Compos B Eng 15(159):461–480
23. Karsh PK, Mukhopadhyay T, Dey S (2018) Stochastic investigation of natural frequency for functionally graded plates. In: IOP conference series: materials science and engineering 2018 Mar, vol 326, no 1. IOP Publishing, p 012003
24. Karsh PK, Kumar RR, Dey S (2019) Stochastic impact responses analysis of functionally graded plates. J Braz Soc Mech Sci Eng 41(11):501
25. Karsh PK, Kumar RR, Dey S (2019) Radial basis function based stochastic natural frequencies anaysis of functionally graded plates. Int J Comput Methods
26. Karsh PK, Mukhopadhyay T, Chakraborty S, Naskar S, Dey S (2019) A hybrid stochastic sensitivity analysis for low-frequency vibration and low-velocity impact of functionally graded plates. Compos B Eng 176:107221
27. Mukhopadhyay T, Naskar S, Karsh PK, Dey S, You Z (2018) Effect of delamination on the stochastic natural frequencies of composite laminates. Compos B Eng 1(154):242–256
28. Mukhopadhyay T, Naskar S, Karsh PK, Dey S, You Z (2018) Effect of delamination on the stochastic natural frequencies of composite laminates. Compos B Eng 154:242–256
29. Dey S, Mukhopadhyay T, Naskar S, Dey TK, Chalak HD, Adhikari S (2017) Probabilistic characterisation for dynamics and stability of laminated soft core sandwich plates. J Sandw Struct Mater 1–32
30. Wang CM, Ang KK, Yang L (2000) Free vibration of skew sandwich plates with laminated facings. J Sound Vib 235:317–340
31. Kulkarni SD, Kapuria S (2008) Free vibration analysis of composite and sandwich plates using an improved discrete Kirchhoff quadrilateral element based on third order zigzag theory. Comput Mech 42:803–824

Design and Simulation of 3-DoF Strain Gauge Force Transducer

Ankur Jaiswal, H. P. Jawale and Kshitij Shrivastava

Abstract Force transducers are capable of determining the magnitude of force applied by measuring strain deformations. The strain induced on the transducer is measured using strain gauges. Usually, the force transducers, being unidirectional, are able to sense only axial force or torque. This paper presents an innovative force transducer for sensing triaxial loads and moments pertaining to its unique shape which allows strategic placement of strain gauges. The transducer is designed in a frame-like structure by stacking three cantilever beams one in each orthogonal axis. Each frame is sensitive to the load applied in the corresponding orthogonal direction. This configuration provides advantage of uniform sensitivity in triaxial loading applications with negligible cross sensitivity. The transducer is having a proportional force and moment conversion due to its single body structure and isotropic material properties. A new design for the transducer is also proposed and the comparative behavior of both, for uniaxial and triaxial loading, is presented. The two designs are analyzed by FE analysis in ABAQUS for principle and shear strain with varying loading conditions.

Keywords Force transducers · FE analysis · Strain gauges

A. Jaiswal (✉)
Department of Mechatronics Engineering, Manipal Institute of Technology, Manipal Academy of Higher education (MAHE), Manipal 576104, Karnataka, India
e-mail: ankurmech13@gmail.com

H. P. Jawale
Department of Mechanical Engineering, Visvesvaraya National Institute of Technology, Nagpur 440010, Maharashtra, India
e-mail: j.hemanth@rediffmail.com

K. Shrivastava
Department of Ocean Engineering and Naval Architecture, Indian Institute of Technology, Kharagpur, India
e-mail: krshrivastava@gmail.com

B. N. Singh et al. (eds.), *Recent Advances in Theoretical, Applied, Computational and Experimental Mechanics*, Lecture Notes in Mechanical Engineering,
https://doi.org/10.1007/978-981-15-1189-9_3

1 Introduction

Force transducers are extensively used to measure the applied force on structural members. It generally consists of an elastic load-bearing element which undergoes strain deformation upon application of force or torque. This deformation could be measured using strain gauges, thus converting the applied force into a proportional electric signal.

Traditionally, force transducers are uniaxial and multiple such transducers could be used to contrive multiaxial transducers. For instance, Kaneko [1] demonstrated that a combination of two similar three-axis force sensors could form one six-axis force sensor and developed a characteristic matrix, connecting the load and sensor output vectors. Svinin and Uchiyama [2] proposed a generalized theoretical model for multidimensional force sensor designed using elastic components connected in parallel.

Kim et al. [3] and Kim [4] described a design and development procedure of a six-component force and moment sensor. They derived equations for calculating rated strains on the components of the sensor and performed a finite element (FEM) analysis for confirming the strains obtained from the theoretical analysis. Liu and Tzo [5] proposed identical T-shaped bar-type six-axis force sensor. They calculated the sensitivity of force-sensing member with respect to design parameters using finite element analysis in conjunction with a design optimization. Liu et al. [6] designed a six-dimensional piezoelectric heavy force sensor based on load-sharing principle. They performed a finite element analysis using ANSYS software for calculating the static and dynamic response of the designed sensor under heavy loading. The experiments on the fabricated sensor demonstrated very less nonlinearity errors and verified the numerical results. Liang et al. [7] and Sunand et al. [8] derived the equations of force and moment for the six-component force sensor and determined the theoretical value of strains. This result was validated using finite element method (FEM) and optimization method by trial and error, employing the response surface methodology (RSM).

Bayo and Stubbe [9] proposed a frame/truss-type six-axis sensor for robotic applications. They employed the axial deformation behavior of the six-axis sensor to eliminate disadvantages of the crossbar and obtained better measure of isotropy and decoupling. They also compared the performance parameters (condition number, overall static and dynamic stiffness, strain gauge sensitivity) and found significant improvement over the earlier design of six-axis wrist force sensor. Chao and Chen [10] applied penalty method to optimize the geometrical design parameters of a wrist-type elastic force sensor. They used calibration matrix along with strain gauge sensitivity as a performance index for design optimization. Based on these design criteria they devised a novel decoupled wrist force sensor with enhanced force sensitivity and minimum stiffness.

Kang [11] formulated closed-form solution of forward kinematics for 6-DoF Stewart platform based force transducer using linearization approach. Later, Dwarakanath

et al. [12] performed design parameter sensitivity analysis for optimal size of Stewart platform based force transducer and fabricated a prototype of the sensor.

Present study is an extension to the work done by Deshpande et al. [13]. They did a mathematical analysis of a novel three-axis force transducer and validated the analytical results with experimental results. This paper incorporates finite element analysis to study the behavior of the initial design of force transducer (FT1) and determines the optimal locations for mounting the strain gauges. A modified design of the force transducer (FT2) is also proposed in order to enhance the performance of the cantilever-beam-type force-sensing elements. In the new design, the principal stress and shear stress are also analyzed using finite element analysis for various loading conditions. The comparison of analysis results is presented herewith. This sensor could find its application in robotic manipulators and multiaxial load cells.

2 Force Sensing in Strain Gauges

Force transducers are deployed for knowing the numerical value of the applied force and torque on the body, which is ideally equal to the true value of the applied load. The output of the transducer depends on the characterized relationship between the output value and the property under measurement. Force transducers are designed so as to have elastic member for loading elements in any of the six loading axes. The input loading creates deflection in the elastic member which in turn creates proportional elongation also known as strain. The strain is measured as a quantifiable change in resistance of the coiled conductor in the strain gauge. Thus, strain gauges proportionally convert the strain developed into change in the electric current at output terminals [14].

There are various methods used to determine torque and force applied on any elastic member among which the most common method is using strain gauges. The strain gauge can be configured to distinguish tensile and compressive strains, to give conversions in the form of positive or negative signals, thus making it possible to distinguish expansion as well as contractions of the members having strain gauges on it. The gauge factor is fundamental term correlating the sensitivity of the strain gauge. It is defined as the ratio of change in electrical resistance (R) to the mechanical strain ε captured by gauge conductor coil, and expressed as

$$R = \frac{\rho L}{A} \tag{1}$$

$$\mathrm{GF} = \frac{\Delta R/R}{\Delta L/L} = \frac{\Delta R/R}{\varepsilon} \tag{2}$$

where

ρ = Resistivity/conductivity constant,
L = Length of the sensor,

A = Cross-sectional area of sensor,
R = Electrical resistance of sensor,
ε = Mechanical strain, and
GF = Gauge factor.

Strain gauge rosettes are geometric combination of strain gauges which could be mounted on elastic transducer element to capture strains in desired loading axes. The strain induced due to loading is reliant on the shape and geometric configuration as well as the elastic modulus of that element. Every strain gauge in a rosette captures the local strain at that location, and through combination of these individual strain gauges, proportional force is estimated [15].

Usually, forces in real-life scenarios are multidirectional, dynamic, and fluctuating in nature. This makes it difficult for single-axis sensor to completely perceive the applied load. Multi-axis force transducers are well suited for such situations, which transfer input signals at elastic members due to applied force and torque to proportional voltage and estimates the proportional output with respect to external force/torque applied as input. The important applications are found in force and torque sensors including robotic control and manipulation, aerospace and industries [16].

3 Design of the Transducer

This paper presents an innovative design for a force transducer capable of sensing triaxial loads and moments. The transducer is designed in a frame-like structure by stacking three cantilever beams upon each as depicted in Fig. 1. Each frame carries its individual strain rosettes which are sensitive to a specific orthogonal loading direction. Stacking all three frames into a single structure produces a 3-DoF force-sensing transducer.

This paper also discusses variations to the original design of the transducer in order to enhance its sensing capabilities. The alterations were proposed to attain uniform stress distribution and better strain dispersion among the structural members. Figure 2a depicts the original and Fig. 2b depicts modified designs of the force transducer. The two designs are further evaluated for stress distribution patterns using FE analysis. For the sake of simplicity, the original design of the transducer will be denoted as FT1 and the modified new design would be denoted as FT2, further along this paper.

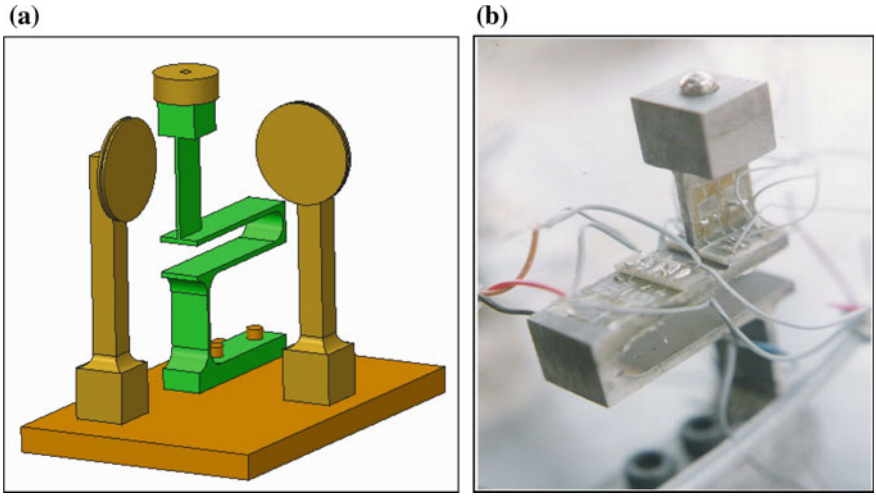

Fig. 1 **a** CAD model depicting the force transducer (green) also schematics of pulleys and deadweight for loading (brown). **b** Experimental setup [14]

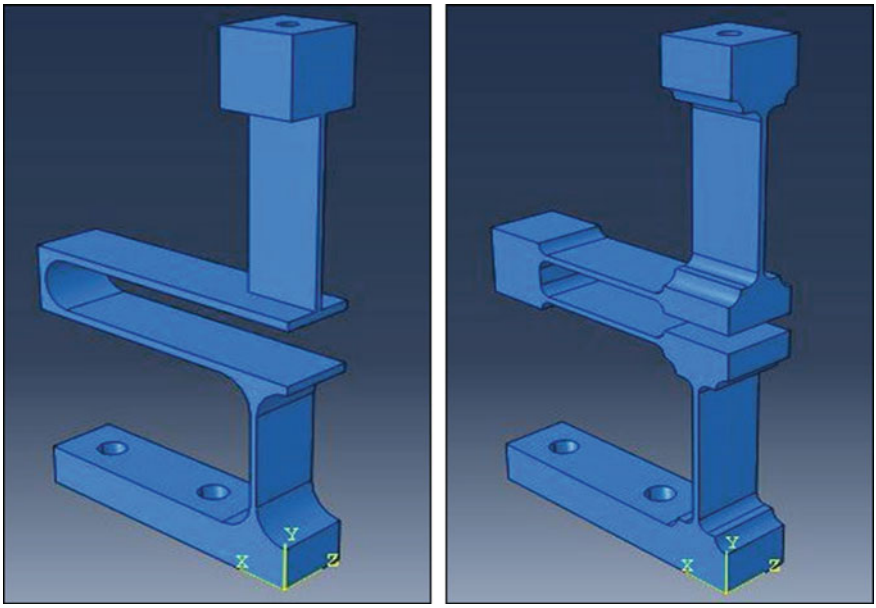

(a) FT1 (b) FT2

Fig. 2 CAD model depicting transducer designs **a** FT1 (original design) and **b** FT2 (modified design)

4 Transducer Analysis Using FEA

Finite element analysis is a numerical approach to determine the behavior of a structure under static or dynamic loading conditions. In FEM, a mathematical model compatible with the geometric and material properties of the structure is discretized into small, multiple finite elements. The change in field quantity over the entire domain of the structure is derived by analyzing these discrete finite elements. The FE model analysis was limited to static loading conditions. There are various commercial packages available for FE analysis. ABACUS was chosen for performing the static FE analysis on both the transducer designs.

4.1 Material Properties

The material used for constructing the transducer was considered to be isotropic and homogeneous. Standard structural steel properties were assumed as shown in Table 1.

4.2 FE Mesh Properties

The meshing for FE analysis was performed in ABAQUS using a ten-noded quadratic tetrahedron element (C3D10). Size of the mesh was program controlled. Figure 3 illustrates the meshing pattern for FT1 and FT2 transducer designs.

4.3 Boundary Conditions

The transducer was constrained in all directions at its base to depict a fixed–fixed boundary condition. This was done to replicate a real-life scenario when the transducer is firmly placed on a solid surface. The load was applied on the topmost surface of the transducer. The load was applied for uniaxial and triaxial loading conditions, with varying magnitudes, in order to achieve a detailed analysis. The boundary conditions and loading patterns were kept identical for FT1 and FT2 transducers as shown in Fig. 4.

Table 1 Transducer material properties

Young's modulus	200 GPa
Poisson's ratio	0.3
Density	7850 kg/m^3

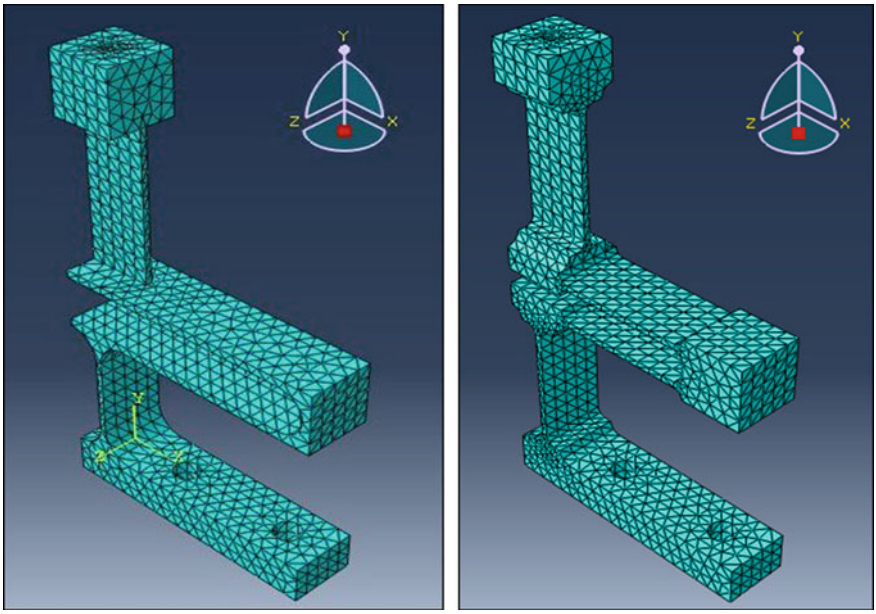

(a) FT1 (b) FT2

Fig. 3 Meshed FE model of force transducer **a** FT1 (original design) and **b** FT2 (modified design)

4.4 Loading Parameters

The static analysis was performed by applying various discrete load levels having uniform increment from 0.2 to 2 N. Loads were applied in all three uniaxial directions (x, y, and z) independently. A triaxial loading was also applied for the same load levels. The load was applied on the cube-shaped block at the top of the transducer.

5 Results and Discussion

5.1 Principal Strain Analysis

Maximum principal strain contour on different elements of transducers FT1 and FT2 at 0.2 N, 1 N, and 2 N loads is depicted in Fig. 5a, c, e and Fig. 5b, d, f, respectively. Table 2 enumerates the maximum principal strain for different magnitudes of load in FT1 and FT2.

Figure 6 represents the linear relationship between magnitude of load and induced strain exhibited by the FT1 and FT2 transducers. It is observed that maximum

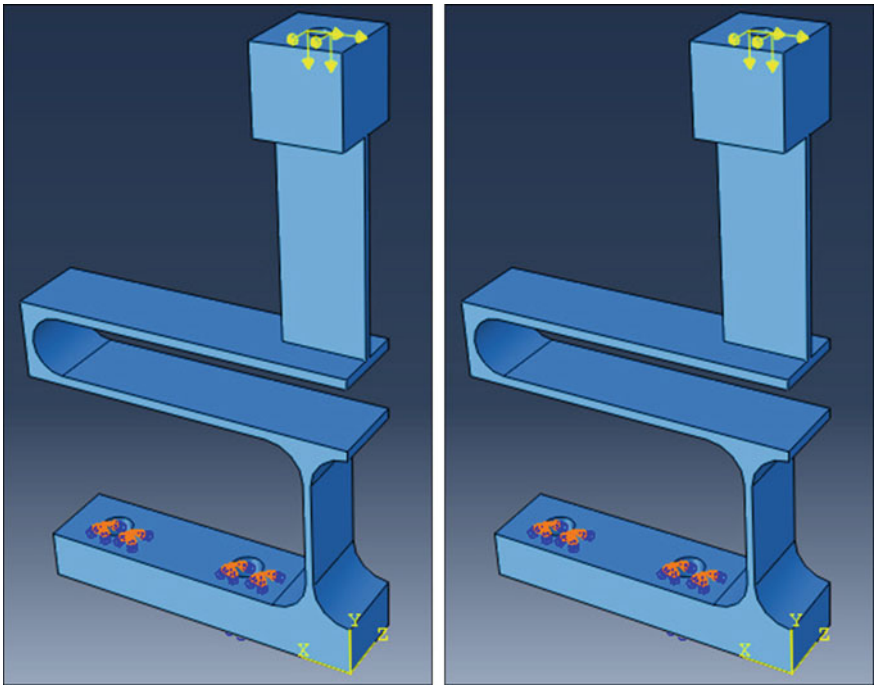

(a) FT1 (b) FT2

Fig. 4 Boundary conditions and loading patterns for **a** FT1 and **b** FT2

strain occurs on the element which is sensitive to the direction of applied force. The experimental results of FT1 transducer [14] confirm this linear relationship.

Figure 7 shows the strain difference between FT1- and FT2-type transducers when the applied load is same. It is observed that the strain difference also increases linearly with load.

The modified design, FT2, has additional blocks at the end of each sensing element, which provide rigidity to the cantilever-sensing element. It is observed that in single loading conditions, the induced strain values in FT2 transducers are higher than FT1 transducers. It is also observed that in triaxial loading conditions, the strain difference between FT1 and FT2 is higher compared to single loading conditions. This infers that the modified design is more sensitive to smaller variations in the load. The advantage of the modified design is that it detects the strain when the applied load is very small and when there is a small variation in the applied load.

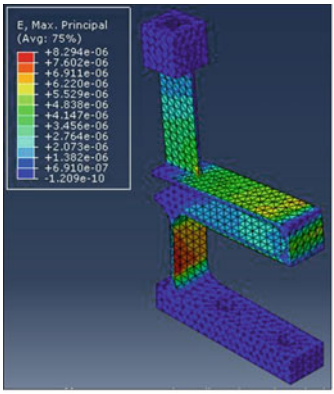

(a) FT1 at 0.2N

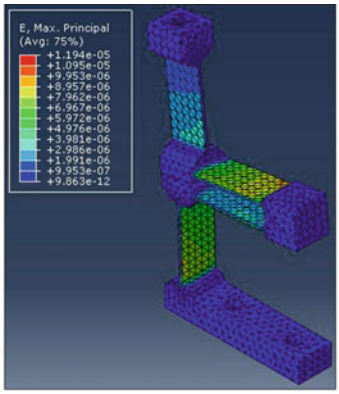

(b) FT2 at 0.2N

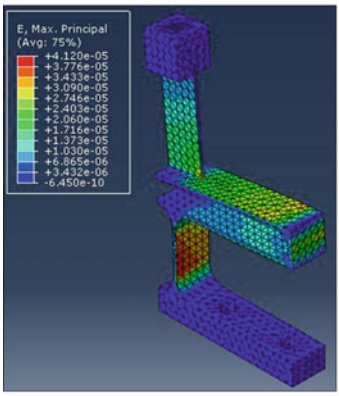

(c) FT1 at 1N

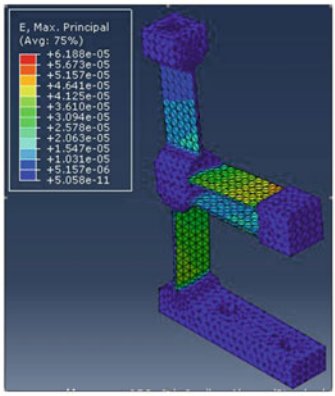

(d) FT2 at 1N

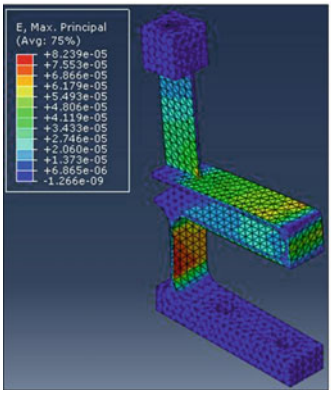

(e) FT1 at 2N

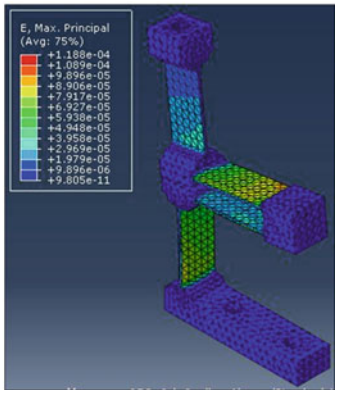

(f) FT2 at 2N

Fig. 5 **a–f** Principal strain distribution for FT1 and FT2

Table 2 Value of strain obtained from ABAQUS for maximum principal elastic strain in FT1 and FT2

FT1					FT2				
Load (N)	Maximum principal strain (* e^{-5})				Load (N)	Maximum principal strain (* e^{-5})			
	x	*y*	*z*	*xyz*		*x*	*y*	*z*	*xyz*
0.2	1.513	0.459	0.594	0.829	0.2	1.551	0.59	0.619	1.194
0.4	3.026	0.918	1.189	1.645	0.4	3.101	1.181	1.238	2.371
0.6	4.551	1.381	1.788	2.474	0.6	4.664	1.777	1.862	3.565
0.8	6.068	1.844	2.38	3.29	0.8	6.215	2.368	2.481	4.745
1	7.587	2.32	2.983	4.113	1	7.766	2.958	3.1	5.93
1.2	9.106	2.767	3.584	4.954	1.2	9.316	3.549	3.719	7.121
1.4	10.625	3.229	4.171	5.755	1.4	10.87	4.14	4.338	8.299
1.6	12.144	3.681	4.77	6.569	1.6	12.43	4.735	4.962	9.485
1.8	13.663	4.143	5.366	7.41	1.8	13.98	5.326	5.581	10.6
2	15.182	4.61	5.959	8.218	2	15.53	5.917	6.2	11.84

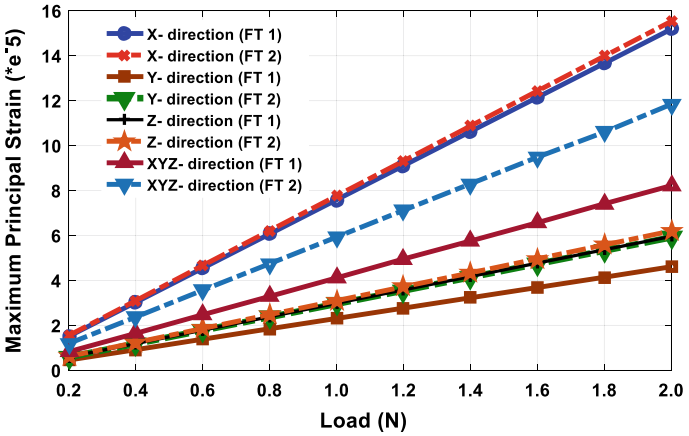

Fig. 6 Change in maximum principal strain at various load magnitudes

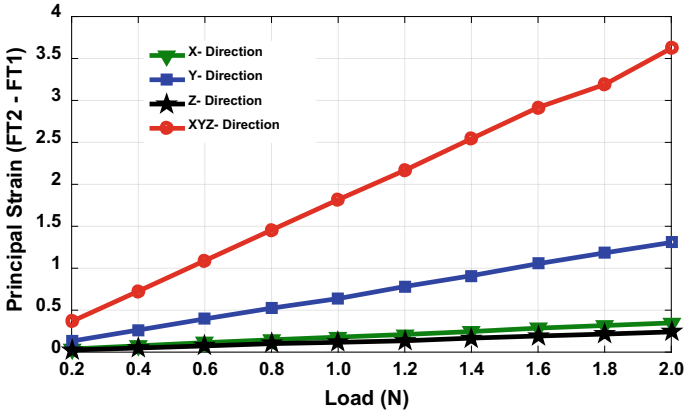

Fig. 7 Principal strain difference curve between FT1 and FT2

5.2 Shear Strain Analysis

The transducer FE model was analyzed for shear strain by applying biaxial combinational loading of varying magnitude. The load increment was similar to that used in principal strain analysis. The moment generated in the sensing element of the transducer was neglected in this analysis. The strain gauge deployed for direct strain estimation measures both the normal and shear components of the strains. The analysis carried out gives a better visualization of shear patterns as shown in Fig. 8a, c, e for FT1 and Fig. 8b, d, f for FT2. The maximum shear elastic strain in FT1 and FT2 is given in Table 3.

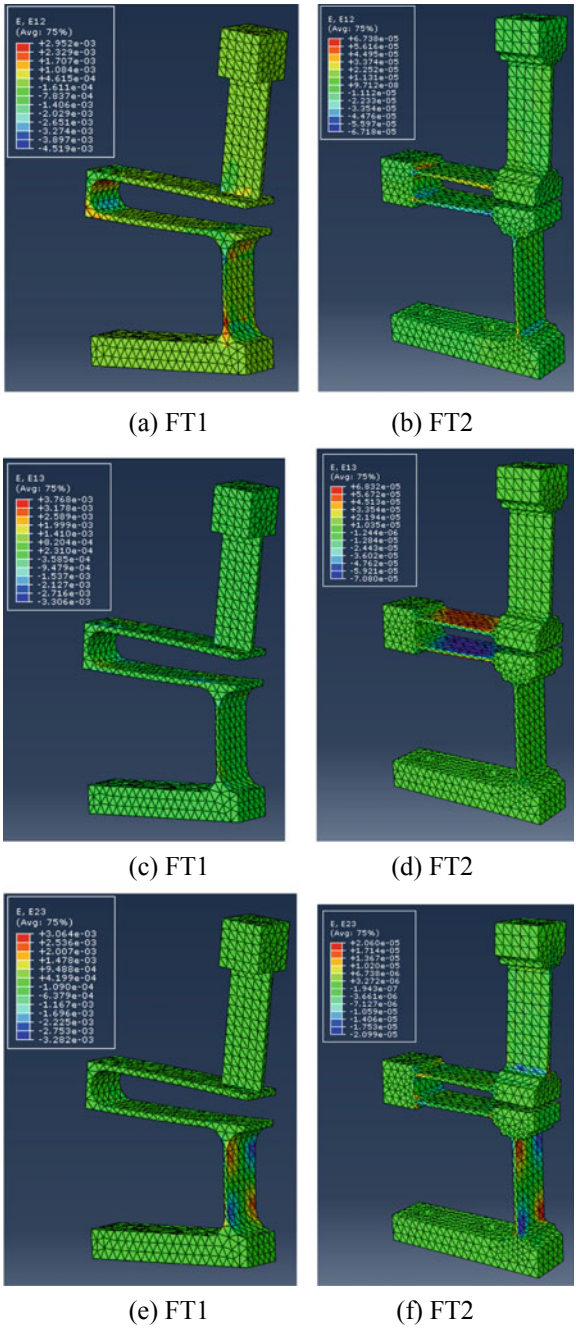

(a) FT1 (b) FT2

(c) FT1 (d) FT2

(e) FT1 (f) FT2

Fig. 8 **a–f** Maximum shear elastic strain in FT1 and FT2

Table 3 Value of strain obtained from ABAQUS for maximum shear elastic strain in FT1 and FT2

FT1				FT2			
Load (N)	Maximum shear strain (* e^{-5})			Load (N)	Maximum shear strain (* e^{-5})		
	x-y	*y-z*	*z-x*		*x-y*	*y-z*	*z-x*
0.2	4.977	2.274	4.586	0.2	6.757	2.113	7.126
0.4	9.937	4.541	9.157	0.4	13.41	4.191	14.14
0.6	14.95	6.83	13.77	0.6	20.17	6.304	21.26
0.8	19.88	9.084	18.32	0.8	26.85	8.383	28.28
1	24.89	11.37	22.93	1	33.6	10.5	35.4
1.2	29.89	13.66	27.55	1.2	40.34	12.61	42.53
1.4	34.82	15.91	32.09	1.4	47.02	14.69	49.54
1.6	39.83	18.2	36.71	1.6	53.77	16.8	56.67
1.8	44.76	20.46	41.25	1.8	60.43	18.88	63.68
2	49.77	22.74	45.86	2	67.18	20.99	70.8

The variation in maximum shear strain with respect to applied load is represented in Fig. 9. The transducer exhibits linear relationship between load and induced shear strain in both FT1- and FT2-type transducers. The FT2 transducer exhibits higher strain values in *x-y* and *z-x* loading directions, whereas FT1 has higher strain magnitude in *y–z* direction. Figure 10 represents the shear strain difference between FT1- and FT2-type transducers when the applied load is same.

It is evident from the data enumerated in Tables 2 and 3 that FT2 shows enhanced stress concentration levels for similar loading conditions as FT1 for majority of the cases. This leads to more localized strain and provides an advantage of better stress sensitivity. One exception to the case could be noted in *Y–Z* principal shear

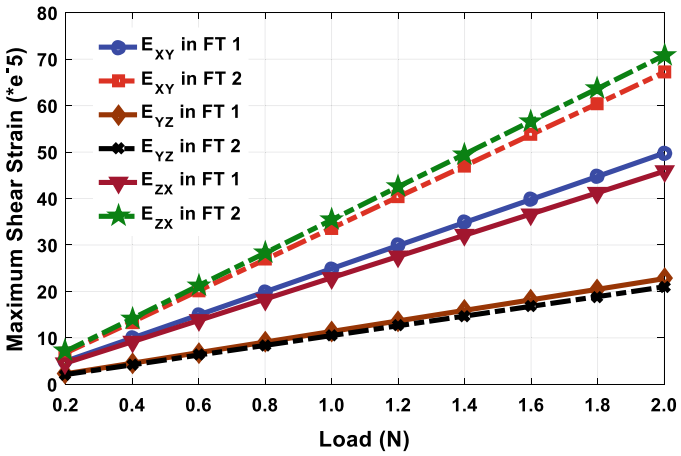

Fig. 9 Change in maximum shear strain at various load magnitudes

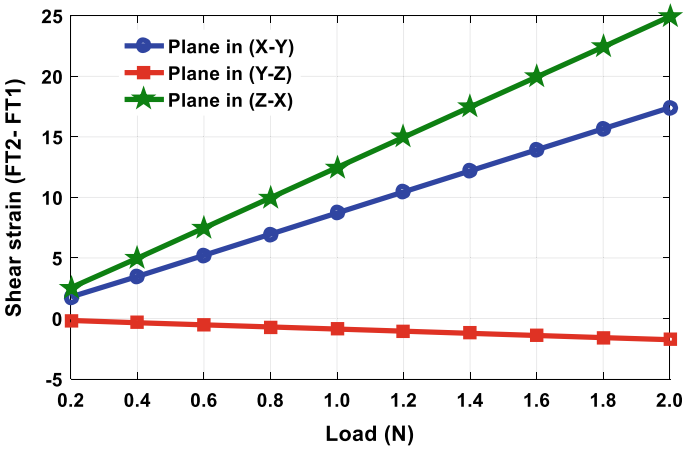

Fig. 10 Shear strain difference curve between FT1 and FT2

stress loading, where FT2 shows the reduced sensitivity than its predecessor. It is also observed that change in maximum principal strain is least in *X*-direction. The member most sensitive to the *X*-directional loading is at the bottom and attached to the base. The rigidity provided by the fixed–fixed boundary condition and increased mass in the modified design could be attributed for this deficit. It warrants further research and possible alterations to the design of FT2 in order to rectify this problem.

6 Conclusions

This paper describes a detailed analysis of strain estimation in a triaxial force transducer which has engineering applications in platform-type sensor. The experimental observations reflect that the strain concentration at specific locations modifies the characteristics of the transducer. A comparative study of the strain estimation for two different transducer designs is also presented, which is necessary for the safe design and manufacturing of the transducers. The analysis of the strain patterns helps in determining the location of maximum stress concentration, which provides an estimate location to mount the strain gauges. Some of the notable observations from the FE analysis are summarized below:

1. The experimental results for transducer FT1 show that a linear increase in load causes a linear increase in strain on the sensing element [13]. The transducer FT1 has been tested and validated in simulation environment.
2. The estimation of strain for FT2 has been done by simulation and results suggest that the strain in the sensing elements increases linearly with the applied load, as in the case of FT1.

3. In transducer FT2, the blocks added at the end of each sensing element confine the principal strain to a smaller region as compared to FT1. The advantage of the modified design is that it detects the strain when the applied load or the variation in the applied load is very small.

The strain-sensing capability of the proposed design (FT2) is better than that of the FT1 transducer. This kind of transducer finds applications in serial- and spatial-type parallel manipulators used for payload sensing.

References

1. Kaneko M (1993) A new design of six-axis force sensors. In: Proceedings of the IEEE international conference on robotics and automation, pp 961–967
2. Svinin MM, Uchiyama M (1995) Optimal geometric structures of force/torque sensors. Int J Robot Res 14:560–573
3. Kim GS, Kang DI, Rhee SH (1999) Design and fabrication of a six-component force/moment sensor. Sens Actuators A 77:209–220
4. Kim GS (2001) The design of a six-component force/moment sensor and evaluation of its uncertainty. Meas Sci Technol 12:1445
5. Liu SA, Tzo HL (2002) A novel six-component force sensor of good measurement isotropy and sensitivities. Sens Actuators A 100:223–230
6. Liu W, Li Y et al (2011) Research on parallel load sharing principle of piezoelectric six-dimensional heavy force/torque sensor. Mech Syst Signal Process 25:331–343
7. Liang Q, Zhang D et al (2013) Design and analysis of a novel six-component F/T sensor based on CPM for passive compliant assembly. Meas Sci Rev 13:253–264
8. Sunand Y, Liu Y et al (2015) Design and optimization of a novel six-axis force/torque sensor for space robot. Measurement 65:135–148
9. Bayo E, Stubbe J (1989) Six-axis force sensor evaluation and a new type of optimal frame truss design for robotic applications. J Field Robot 6:191–208
10. Chao LP, Chen KT (1997) Shape optimal design and force sensitivity evaluation of six-axis force sensors. Sens Actuators A Phys 63:105–112
11. Kang CG (2001) Closed-form force sensing of a 6-axis force transducer based on the Stewart platform. Sens Actuators A 90:31–37
12. Dwarakanath T, Dasgupta B, Mruthyunjaya T (2001) Design and development of a Stewart platform based force–torque sensor. Mechatronics 11:793–809
13. Deshpande M, Jawale HP, Thorat HT (2016) Development, calibration and testing of three axis force sensor. In: 2016 7th international conference on mechanical and aerospace engineering (ICMAE), IEEE, pp 285–289
14. Stefanescu DM (2011) Handbook of force transducers: principles and components. Springer Science & Business Media
15. Yurish S (2014) Modern sensors, transducers and sensor networks. Lulu.com
16. Chen D, Song A, Li A (2015) Design and calibration of a six-axis force/torque sensor with large measurement range used for the space manipulator. Procedia Eng 99:1164–1170

A Micromechanical Study of Fibre-Reinforced Composites with Uncertainty Quantification and Statically Equivalent Random Fibre Distribution

S. Koley, P. M. Mohite and C. S. Upadhyay

Abstract The effects of manufacturing defects creates uncertainty on the mechanical response of unidirectional fibre-reinforced composites. These are studied through modelling of three-dimensional Representative Volume Element (RVE). In this study, an algorithm is developed to generate the microstructure of unidirectional fibre reinforced composite with both regular and random fibre distribution and then analyzed using mathematical theory of homogenization to estimate the homogenized or effective material properties. Here, the RVEs are modelled with random fibre distribution but increasing the number of fibres gradually and also randomly varying their positions. This variation in the randomness of the fibre distribution affects the effective properties. Also, the effect of different loading conditions is investigated. The significance of this structural distribution of heterogeneities on the overall effective behaviour is discussed for random structures and uncertainties that occur in composite materials. The variations in the predicted elastic properties for the given volume fraction of the above mentioned scenarios are compared with the experimental values and good agreement is achieved. There is a significant percentage change in transverse shear moduli, G_{23} and ν_{23}, which are 21.87 and 35.20% with respect to the experimental results.

Keywords Composite materials · Microstructure · Randomness · Effective properties

1 Introduction

Composite materials have become an advisable choice in aerospace and other industries due to their high strength to weight ratio and high modulus [1]. In fibre reinforced composites, fibres are the main load-carrying members. Therefore, fibre

S. Koley (✉) · P. M. Mohite · C. S. Upadhyay
Structural Analysis Lab, Department of Aerospace Engineering IIT, Kanpur, India
e-mail: skoley@iitk.ac.in

B. N. Singh et al. (eds.), *Recent Advances in Theoretical, Applied, Computational and Experimental Mechanics*, Lecture Notes in Mechanical Engineering,
https://doi.org/10.1007/978-981-15-1189-9_4

volume fraction and fibre distribution morphology have a crucial influence on the strength and stiffness properties of composite material. To study these effects, many researchers addressed micromechanics of composite material. The issue concerning the micromechanical study is the generation of RVE with the desired dimensions and spatial distribution of reinforcements in RVE, which highly depends upon the manufacturing process. Many methods have been developed for the generation of RVE model with a random distribution of fibres using Poisson point distribution [2]. In this microscopic scale approach, the constituents are employed in conjunction with homogenization to predict the composite behaviour. Here, the average mechanical characteristics of a lamina have to be estimated from the known characteristics of the fibre and matrix materials taking into account the fibre volume fraction and fibre packing arrangement. The current study in micromechanics is to estimate the effective elastic properties of the RVE of the material with an equivalent random distribution of fibres [3, 4]. Effective elastic properties of composite material depend on the shape, properties and spatial distribution of the fibre. Among the various uncertainties present, the following uncertainties have been considered for the analysis: (a) effects of volume fraction (b) effect of the randomness in the fibre arrangements (c) effect of the uncertainty in the geometry of the fibre cross section.

In the current study, a micromechanical study [5] is proposed to calculate mechanical properties of composite material with regular fibre array and random fibre arrangement in a unit cell model [6]. In this case, an image of the cross section of a certain unidirectional ply is taken and transformed into a computer recognizable format by using binary image processing technique. From the binary image, RVEs are generated with single fibre and random fibre distribution by defining different scatter conditions and also to incorporate randomness in the RVE. The evaluation of the effect of fibre arrangements on the mechanical properties should be both qualitative and quantitative [7]. To achieve this goal, a comprehensive study is carried out with RVEs having 1, 12, 20 and 50 fibres. The overall properties are calculated as an average over the respective volumes of the constituents. Mathematical theory of homogenization [8] is used to obtain a suitable constitutive model at the macroscopic level. In the next study, we considered the RVEs with fibres randomly distributed in a periodic unit cell but with different fibre cross sections, i.e. circular, distorted and elliptical cross sections. Then, we studied how these different fibre cross sections affect the mechanical properties.

2 Characterization of Uncertainties in Composites

Due to the complex manufacturing process, the composite renders randomness in the material parameters. The instability in properties such as elastic modulus, fibre distribution and volume fraction measurements result in variability in the response of composite materials. Uncertainty can be addressed by means of material, geometric and structural considerations [2].

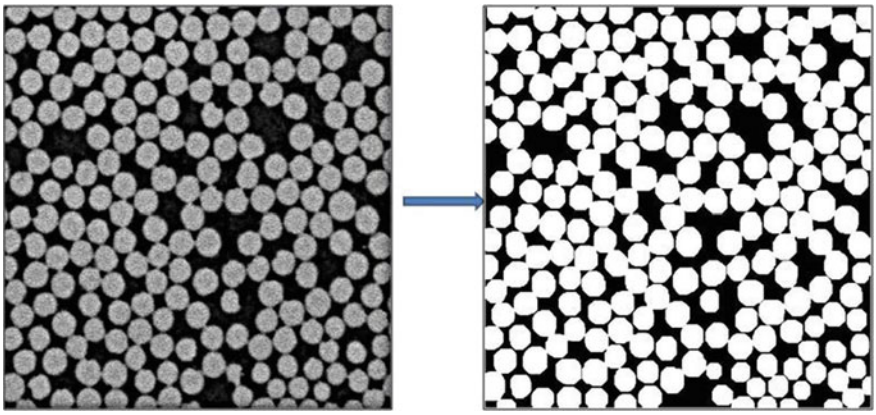

Fig. 1 Greyscale image to binary image

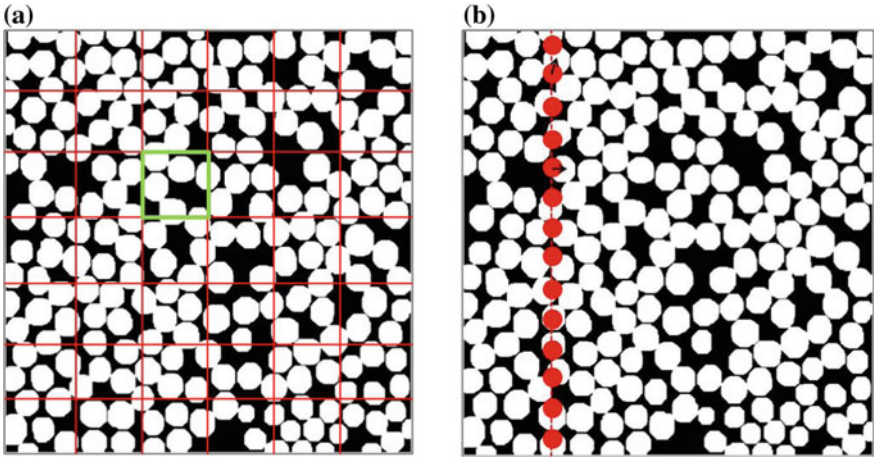

Fig. 2 Random fibre distribution. **a** Moving window technique used to calculate RVE, **b** Deviation of fibre from their ideal distribution

Initially, scatter has been estimated in the fibre distribution from digital image analysis. Using these data, information about the location of centre of the fibres, distribution of fibre radius and distance between neighbouring fibres are obtained. Then, the obtained statistical parameters are utilized to construct a statistically equivalent RVE based on certain numerical algorithms [9]. Figure 1 is a micrograph image of composite microstructure of size 706×678 pixels (Fig. 2).

From the image, for an ideal distribution of fibre, four random fibres are chosen along the breadth. Then, ideal positions are calculated from the deviation of centre of fibres in the original micrograph. Figure 3 also shows centres of ideal fibre distribution. After extracting the actual coordinates of the fibre centres, we estimate the

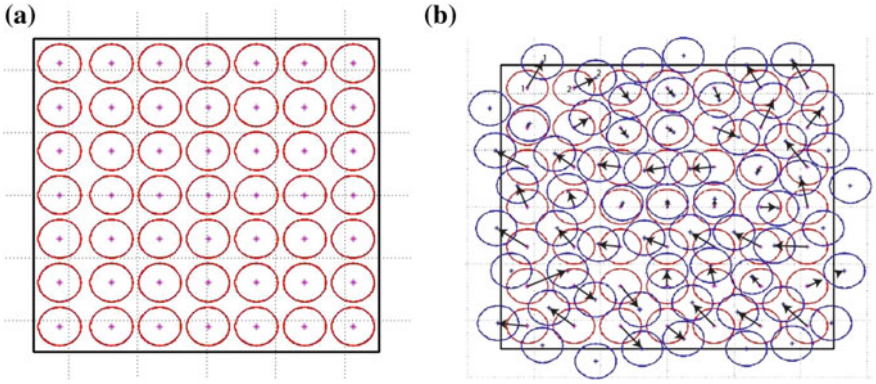

Fig. 3 RVE with regular and random fibre distribution. **a** Regular fibre arrangements in a square domain, **b** Modelling of RVE with random fibre distribution

ideal coordinates and then, the deviation from the real to the ideal coordinates are calculated. By doing this process, scatter has been estimated and with reference to this, an RVE is modelled with the random distribution of fibres.

3 Generation of RVE

In the estimation of effective properties of composite materials, the generation of RVE plays a vital role. A new algorithm has been proposed to generate the RVE achieving fibre volume fraction nearly 60% and the fibres are evenly distributed throughout the RVE. According to Hill [10] and Kanit et al. [11], representative volume should have two main properties: Its structure is "entirely typical" for the composite and it should contain a "sufficient number" of microstructure elements so that boundary conditions at the surface do not affect its effective properties.

Considering the above characteristics of generating the RVE, it has been generated with a random arrangement of fibres with reference to the scatter from the above micrograph. The RVEs with ideal/regular arrangements of fibres are shown in Fig. 3 by maintaining the fibre volume fraction of 0.6.

Figure 3 shows the scatter of the fibres from the original position to the random position but maintaining the minimum distance so that the fibres do not intersect each other. In Fig. 3, the fibres are displaced randomly both in x and y directions and maintaining the periodicity at the edges. The RVE possesses very similar microstructural features as in the original micrograph, such as fibre aggregation zones and also maintaining the geometric periodicity, i.e. periodicity across faces, edges and corners.

4 Mathematical Theory of Homogenization

This theory establishes mathematical relations between micro and macro-fields [8], using a multi-scale perturbation method, the effective properties emerge as a consequence of these relations. The local displacement field in the cell is given as

$$u(x; y) = u_0(x) + \varepsilon u_1(y) \tag{1}$$

where x is the actual coordinate, y is the scaled unit cell coordinate, $u_0(x)$ is the macro response and $u_1(y)$ is the periodic micro correction, ε denotes the ration of the RVE size to the global structural dimension. $u_1(y)$ can be obtained from each of the six fundamental macro-strains e_x^{ij}, by solving the periodic cell problem with applied unit macro strain.

$$-\frac{\partial}{\partial y_j}(C_{ijkl}^{\varepsilon} e_{kl}^{y}(\chi^{rs})) = \frac{\partial}{\partial y_j}\left(C_{ijrs}(y)\right) \tag{2}$$

where χ^{rs} is y periodic. From the periodic solution, the total strain $e_{ij}(u) \approx e_{ij}^{x}(u_0) + e_{ij}^{y}(u_1) \approx (1 + M_{ijkl})e_{kl}^{x}(u_0)$, where M_{ijkl} are the pointwise influence functions and they depend on v_f at the level of the cell.

5 Results and Discussion

In the present study, an in-house finite element code is developed to determine the homogenized properties of composite materials using the mathematical theory of homogenization. Polymeric matrix such as 3501-6 epoxy and AS4 carbon fibre material is considered in this study. These properties are given in Soden et al. [12]. The focus of the analysis is to study both the longitudinal, transverse and shear behaviour of the material at the microscale.

5.1 Prediction of the Elastic Constants of RVE with Single Fibre (Circular Cross Section)

RVE is modelled with single fibre keeping the fibre volume fraction 0.6. The RVE model is meshed with three-dimensional four-node tetrahedral elements. Effective properties for this RVE are estimated and the results are tabulated in Table 1.

Mechanical properties for the composite laminae were considered from experiment studies carried out in Soden et al. [12].

Predicted effective elastic constants are given in Table 1, which are close to the experimental results (see Table 2). The typical percentage differences of the effective

Table 1 Effective properties of RVE model with single fibre

V_f	E_1 (GPa)	E_2 (GPa)	E_3 (GPa)	G_{12} (GPa)	G_{13} (GPa)	G_{23} (GPa)	ν_{12}	ν_{13}	ν_{23}
0.60	139.58	9.55	9.55	4.70	4.70	3.06	0.25	0.25	0.26

Table 2 Effective properties of T-300/3501-6 epoxy composite (experimental results) [12]

V_f	E_1 (GPa)	E_2 (GPa)	G_{12} (GPa)	G_{23} (GPa)	ν_{12}	ν_{23}
0.60	138	11.00	5.50	3.93	0.28	0.40

elastic constants are –1.14% for E_1, 13.21% for E_2 and E_3, 14.45% for G_{12} and G_{13} and 21.87% for G_{23} with respect to the experimental results.

5.2 Prediction of the Elastic Constants of RVE with 12, 20 and 50 Fibres

RVEs are generated with 12, 20 and 50 fibres maintaining the volume fraction of 0.6. Here, the fibres are randomly distributed as shown in Fig. 4. Three cases are considered: Case 1: RVE with 12 fibres, Case 2: RVE with 20 fibres and Case 3: RVE with 50 fibres. For Case 1, three RVE models are generated, for Case 2, four RVE models are generated and for Case 3, eight RVE models are generated. In Fig. 4, sample RVEs of each case are shown but the results are given for all the models.

Observations are made for the prediction of the effective elastic constants of the RVEs with randomly distributed fibres (Table 3).

Case 1: Three RVE models are considered, i.e. RVE 1, RVE 2 and RVE 3. Axial modulus, E_1 predicted for all the three RVEs with different fibre arrangements has percentage difference less than 1% with respect to the effective properties of RVE

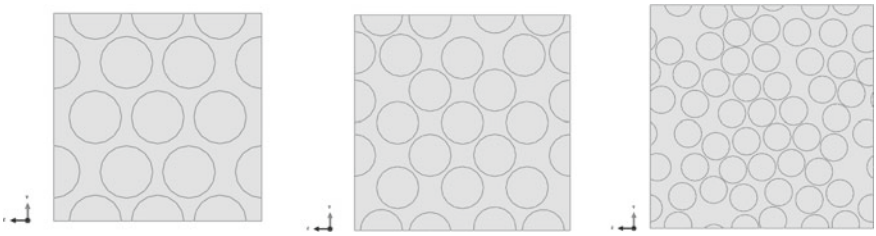

(a) Case 1 (b) Case 2 (c) Case 3

Fig. 4 Micrograph of RVEs with 12, 20 and 50 fibres

Table 3 Effective properties of RVE model with 12 fibres

Model	E_1 (GPa)	E_2 (GPa)	E_3 (GPa)	G_{12} (GPa)	G_{13} (GPa)	G_{23} (GPa)	ν_{12}	ν_{13}	ν_{23}
RVE 1	138.19	8.77	8.88	4.51	4.81	3.57	0.25	0.25	0.26
RVE 2	138.70	8.96	8.88	4.91	4.67	3.52	0.25	0.25	0.31
RVE 3	138.54	9.06	9.01	5.06	4.86	3.50	0.25	0.25	0.30
Average	138.48	8.93	8.93	4.83	4.78	3.53	0.25	0.25	0.29
SD	0.26	0.15	0.07	0.28	0.10	0.03	0.00	0.00	0.03
% error	0.19	1.68	0.78	5.80	2.09	0.85	0.00	0.00	10.34

Table 4 Percentage change in the effective properties of RVEs with 12 fibres with respect to RVE model with single fibre

Model	E_1	E_2	E_3	G_{12}	G_{13}	G_{23}	ν_{12}	ν_{13}	ν_{23}
RVE 1	0.98	8.13	6.95	4.01	–2.28	–16.36	–1.31	0.67	–19.91
RVE 2	0.62	6.11	6.88	–4.44	0.72	–14.74	0.52	–0.71	–18.71
RVE 3	0.74	5.06	5.59	–7.71	–3.46	–14.24	0.44	–0.40	–15.51

Table 5 Effective properties of RVE model with 20 fibre

Model	E_1 (GPa)	E_2 (GPa)	E_3 (GPa)	G_{12} (GPa)	G_{13} (GPa)	G_{23} (GPa)	ν_{12}	ν_{13}	ν_{23}
RVE 1	139.23	8.83	8.84	5.02	5.10	3.69	0.25	0.25	0.32
RVE 2	139.42	9.13	9.21	4.97	5.22	3.52	0.25	0.25	0.29
RVE 3	139.45	9.08	9.12	4.94	5.04	3.54	0.25	0.25	0.29
RVE 4	139.45	9.11	9.23	4.90	5.20	3.51	0.25	0.25	0.29
Average	139.39	9.04	9.11	4.96	5.17	3.57	0.25	0.25	0.30
SD	0.11	0.14	0.18	0.05	0.11	0.09	0.00	0.00	0.01
% error	0.08	1.55	1.98	1.01	2.13	2.52	0.00	0.00	3.33

with single fibre given in Table 4. The standard deviation for all the properties is less than 1 but the percentage error is more for G_{12} and ν_{23}, i.e. 5.8% and 10.34%, respectively and for the other properties, it is less than 2%.

But for the transverse shear modulus, G_{23} the percentage difference is much higher compared to axial shear modulus G_{12} and G_{13} and it is about 15%.

Case 2: Four RVE models are considered and observations are made for the predicted effective elastic constants. Axial modulus, E_1 for all the four RVEs are very close to the RVE with single fibre and also with the experimental value. The standard deviation for all the properties is less than 1 (Table 5).

Axial modulus, E_1 predicted for all the four RVEs with different fibre arrangements has a percentage difference less than 1% as given in Table 6. But for RVE 1,

Table 6 Percentage change in the effective properties of RVEs with 20 fibres with respect to RVE model with single fibre

Model	E_1	E_2	E_3	G_{12}	G_{13}	G_{23}	ν_{12}	ν_{13}	ν_{23}
RVE 1	0.25	7.49	7.32	–6.74	–8.54	–20.39	0.40	0.63	–21.57
RVE 2	0.12	4.28	3.47	–5.68	–11.07	–14.74	–0.32	0.91	–11.30
RVE 3	0.09	4.86	4.38	–5.16	–7.27	–15.49	–0.16	0.59	–13.43
RVE 4	0.09	4.47	3.29	–4.34	–12.26	–14.39	–0.63	1.19	–11.11

Table 7 Effective properties of RVE model with 50 fibre (circular cross section)

Model	E_1 (GPa)	E_2 (GPa)	E_3 (GPa)	G_{12} (GPa)	G_{13} (GPa)	G_{23} (GPa)	ν_{12}	ν_{13}	ν_{23}
RVE 1	136.19	9.20	9.28	4.93	5.20	3.53	0.25	0.25	0.28
RVE 2	136.01	9.10	9.14	5.01	5.16	3.61	0.25	0.25	0.29
RVE 3	136.04	9.20	9.24	4.24	5.05	3.57	0.25	0.25	0.28
RVE 4	136.73	9.27	9.26	5.45	5.41	3.60	0.25	0.25	0.28
RVE 5	136.64	9.25	9.28	5.41	5.44	3.59	0.25	0.25	0.28
RVE 6	136.47	9.22	9.21	5.43	5.40	3.59	0.25	0.25	0.29
RVE 7	136.44	9.21	9.16	5.36	5.29	3.60	0.25	0.25	0.29
RVE 8	136.60	9.31	9.26	5.45	5.29	3.56	0.25	0.25	0.28
Average	136.39	9.22	9.23	5.17	5.28	3.59	0.25	0.25	0.28
SD	0.28	0.06	0.05	0.43	0.14	0.02	0.00	0.00	0.01
% error	0.21	0.65	0.54	8.32	2.65	0.56	0.00	0.00	3.52

the percentage difference is more compared to the other three RVE models. This is because the number of fibres at the edges of this RVE is more.

The percentage difference for transverse shear modulus, G_{23} is much more for RVE 1, i.e 20% compared to other three RVE models. It is observed that the average values of the elastic properties of RVE models with 20 fibres is higher comparable to RVE with 12 fibres.

Case 3: Eight RVE models are considered, i.e. RVE 1 to RVE 8 and it is observed that there is a reduction in effective axial modulus E_1 compared with the RVEs with 12 and 20 fibres. The standard deviation is less than 1 for all the properties but the percentage error is also less than 1% except for G_{12}, G_{13} and ν_{23}. The percentage error for G_{12}, G_{13} and ν_{23} are 8, 2 and 3%, respectively. But if we notice the percentage change with respect to RVE with single fibre, for the shear, i.e the axial shear modulus G_{13} and transverse shear modulus G_{23} are more than 9% (Tables 7,8).

In the next study, RVEs with uncertainty in fibre cross section are considered. Here, three cases are considered, Case 1: RVE with circular cross section, Case 2: RVE with a distorted cross section and Case 3: RVE with an elliptical cross section. For all the three cases, eight RVE models are generated.

Table 8 Percentage change in the effective properties of RVEs with 50 fibres with respect to RVE model with single fibre

Model	E_1	E_2	E_3	G_{12}	G_{13}	G_{23}	ν_{12}	ν_{13}	ν_{23}
RVE 1	2.42	3.60	2.77	–4.93	–10.52	–15.34	–0.44	0.79	–9.03
RVE 2	2.56	4.66	4.22	–6.68	–9.66	–17.75	–0.16	0.52	–12.81
RVE 3	2.53	3.60	3.16	9.78	–7.46	–16.58	–0.16	0.52	–9.76
RVE 4	2.04	2.86	2.93	–16.01	–15.03	–17.46	0.52	0.39	–8.76
RVE 5	2.10	3.02	2.74	–15.10	–15.78	–17.19	0.36	0.52	–8.45
RVE 6	2.22	3.32	3.43	–15.57	–14.79	–17.03	0.44	0.28	–10.19
RVE 7	2.25	3.51	4.01	–14.03	–12.43	–17.31	0.59	–0.04	–11.11
RVE 8	2.13	2.40	2.96	–16.01	–12.49	–16.02	0.91	–0.24	–8.37

Table 9 Effective properties of RVE model with 50 fibre (distorted cross section)

Model	E_1 (GPa)	E_2 (GPa)	E_3 (GPa)	G_{12} (GPa)	G_{13} (GPa)	G_{23} (GPa)	ν_{12}	ν_{13}	ν_{23}
RVE 1	132.18	9.12	9.07	5.41	5.28	3.50	0.25	0.25	0.29
RVE 2	131.63	8.96	8.89	5.24	5.11	3.53	0.25	0.26	0.30
RVE 3	131.48	8.97	9.00	5.02	5.07	3.47	0.25	0.25	0.29
RVE 4	130.91	8.99	8.98	5.22	5.17	3.46	0.25	0.25	0.29
RVE 5	130.11	8.95	8.95	5.21	5.15	3.43	0.25	0.26	0.29
RVE 6	131.48	8.99	8.99	5.33	5.33	3.47	0.25	0.25	0.29
RVE 7	130.65	8.95	8.91	5.30	5.21	3.47	0.25	0.26	0.30
RVE 8	131.79	9.13	9.08	5.55	5.41	3.49	0.25	0.25	0.29
Average	131.28	9.01	8.99	5.29	5.22	3.48	0.25	0.25	0.29
SD	0.68	0.07	0.07	0.16	0.12	0.03	0.00	0.00	0.00
% error	0.52	0.78	0.78	3.02	2.30	0.86	0.00	0.00	0.00

RVE with circular fibre cross section has been discussed in the previous section. Now, RVE with distorted fibre cross section are considered. Observations are made for the distorted fibre cross section, where the effective properties for all the models are much less than the values compared with the RVE with single fibre. This is mainly due to reduction of fibre volume fraction (Table 9).

The standard deviation is less than 1 for all the properties but the percentage error is also less than 1% except for G_{12} and G_{13} (Table 10).

From these tables, it can be seen that the values of E_1, E_2 and E_3 show about 7% change. Similarly, this change for G_{12} is about 18% and for G_{13} and G_{23} is 15% when compared to that of RVE with single fibre. Further, there is a change in fibre volume fraction for each RVE as they contain fibres with distorted cross section. This distortion also affects the percentage change in the effective properties.

For the last case, RVEs are modelled with elliptical fibre cross section with + 0.5% of the radius of the circular fibre cross section as major axis and –0.5%

Table 10 Percentage change in the effective properties of RVEs with 50 fibres with respect to RVE model with single fibre

Model	E_1	E_2	E_3	G_{12}	G_{13}	G_{23}	ν_{12}	ν_{13}	ν_{23}
RVE 1	5.29	4.44	4.96	–15.06	–12.37	–14.09	–0.08	–0.83	–11.19
RVE 2	5.69	6.14	6.79	–11.47	–8.77	–15.27	–0.24	–1.07	–15.93
RVE 3	5.79	5.97	5.70	–6.75	–7.89	–13.38	–1.03	–0.67	–13.12
RVE 4	6.21	5.79	5.91	–10.99	–9.94	–13.03	–0.87	–0.99	–13.19
RVE 5	6.78	6.18	6.21	–10.85	–9.55	–12.06	–0.99	–1.19	–13.54
RVE 6	5.79	5.76	5.82	–13.44	–13.29	–13.26	–0.87	–0.87	–13.62
RVE 7	6.39	6.23	6.65	–12.77	–10.84	–13.33	–0.67	–1.35	–15.01
RVE 8	5.58	4.35	4.83	–18.08	–15.12	–13.86	0.12	–0.91	–11.19

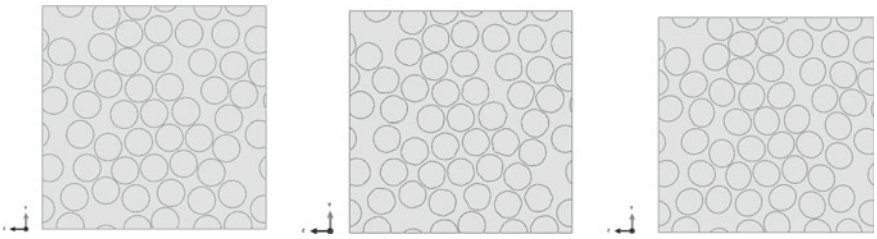

(a) Case 1 (b) Case 2 (c) Case 3

Fig. 5 Micrograph of RVE with different fibre cross sections

of the circular fibre cross section as minor axis as shown in Fig. 5. The fibres are distributed throughout the window with random orientations, i.e. the major axis of the elliptical fibre cross section is placed randomly in the y–z plane.

The effective properties are shown in Table 11. The effective properties for E_1, E_2 and E_3 are less than the experimental values but the shear values are almost the same or more than the experimental values. The standard deviation for all the properties are less than 1 but the percentage change is greater than 1 for G_{12} and G_{13} (Table 12).

Observations are obtained for the fibres with elliptical fibre cross section, the percentage change for effective axial modulus E_1 is about 3% whereas for E_2 and E_3 it is about 5%. The percentage change for shear moduli is more than 18%.

6 Conclusion

In the present study, a statistical representation of unidirectional fibre composite with random fibre distribution at microscale has been developed. A numerical tool developed using MATLAB generates the RVE for a volume fraction of 60%. Geometric periodicity is implemented while developing the RVE to ensure the continuity of the

Table 11 Effective properties of RVE model with 50 fibres (elliptical cross section)

Model	E_1 (GPa)	E_2 (GPa)	E_3 (GPa)	G_{12} (GPa)	G_{13} (GPa)	G_{23} (GPa)	ν_{12}	ν_{13}	ν_{23}
RVE 1	135.94	9.26	9.19	5.52	5.31	3.57	0.25	0.25	0.28
RVE 2	135.94	9.15	9.09	5.48	5.29	3.62	0.25	0.25	0.29
RVE 3	136.31	9.21	9.23	5.27	5.23	3.58	0.25	0.25	0.28
RVE 4	136.39	9.26	9.22	5.50	5.29	3.59	0.25	0.25	0.28
RVE 5	136.48	9.27	9.27	5.41	5.34	3.58	0.25	0.25	0.28
RVE 6	135.91	9.16	9.19	5.27	5.42	3.58	0.25	0.25	0.29
RVE 7	135.93	9.18	9.28	5.12	5.58	3.55	0.25	0.25	0.28
RVE 8	135.93	9.26	9.25	5.35	5.31	3.54	0.25	0.25	0.28
Average	136.11	9.22	9.22	5.37	5.35	3.58	0.25	0.25	0.28
SD	0.24	0.05	0.06	0.14	0.11	0.03	0.00	0.00	0.00
% error	0.18	0.54	0.65	2.61	2.06	0.84	0.00	0.00	0.00

Table 12 Percentage change in the effective properties of RVEs with 50 fibres with respect to RVE model with single fibre

Model	E_1	E_2	E_3	G_{12}	G_{13}	G_{23}	ν_{12}	ν_{13}	ν_{23}
RVE 1	2.60	2.91	3.69	–17.45	–12.88	–16.41	0.83	–0.48	–9.72
RVE 2	2.60	4.13	4.74	–16.59	–12.62	–18.13	0.63	–0.20	–12.92
RVE 3	2.33	3.46	3.26	–12.13	–11.17	–16.90	0.28	0.28	–9.57
RVE 4	2.28	2.89	3.41	–17.04	–12.51	–17.25	0.75	–0.04	–9.57
RVE 5	2.21	2.81	2.87	–15.11	–13.60	–16.77	0.52	0.28	–8.64
RVE 6	2.62	4.02	3.63	–12.15	–15.27	–16.86	–0.12	0.48	–10.73
RVE 7	2.61	3.79	2.78	–8.87	–18.69	–15.69	–0.59	0.99	–8.68
RVE 8	2.61	2.97	3.07	–13.72	–12.84	–15.49	0.36	–0.08	–8.60

fibres across the neighbouring RVEs. Mathematical theory of homogenization has been materialized for the prediction of effective stiffness. Eight RVEs are modelled for circular, distorted and elliptical fibre cross sections with random fibre distribution and studied how these uncertainties affect the effective properties.

The key conclusions that can be made from this study are listed as

1. For RVE with 12 fibres, the percentage error is more for G_{12} and ν_{23}, i.e. 5.80% and 10.34%, respectively and for the other properties, it is less than 2%.
2. In particular, the percentage change of predicated transverse shear moduli G_{23} from UD composites with fibre distributed at random over transverse cross section has higher values comparable to the experimental data. For the RVE with single fibre, the percentage change is 21.87% with respect to experimental result and for the other RVEs with more number of fibres, not only the transverse shear moduli

has higher value but there is also increase in percentage change values for axial shear between 6–17%.

3. The percentage change with respect to single fibre RVE, E_1 is about 2% for circular and elliptical fibre cross section whereas for distorted fibre cross section, it is about (5–6)%. The uncertainty of fibre cross section is studied and the effective properties are estimated. It is observed that E_1 is about 136 GPa for the models with circular fibre cross section but it is reduced to (130–131) GPa for distorted fibre cross section which is mainly due to reduction in fibre volume fraction.

References

1. Daniel IM, Isaac O (1994) Engineering mechanics of composite materials, USA: Oxford University Press
2. Pyrz R (1994) Quantitative description of the microstructure of composites, part i: morphology of unidirectional composite systems. Compos Sci Technol 50(2):197–208
3. Pyrz R (1994) Correlation of microstructure variability and local stress field in two-phase materials. Mater. Sci. Eng.: A 177(1–2):253–259
4. Ghosh S, Nowak Z, Lee K (1997) Quantitative characterization and modeling of composite microstructures by voronoi cells. Acta Mater 45(6):2215–2234
5. Ju J, Zhang X (1998) Micromechanics and effective transverse elastic moduli of composites with randomly located aligned circular fibers. Int J Solids Struct 35(9–10):941–960
6. Tyrus J, Gosz M, DeSantiago E (2007) A local finite element implementation for imposing periodic boundary conditions on composite micromechanical models. Int J Solids Struct 44(9):2972–2989
7. Huang Y, Jin KK, Ha SK (2008) Effects of fiber arrangement on mechanical behavior of unidirectional composites. J Compos Mater
8. Terada K, Hori M, Kyoya T, Kikuchi N (2000) Simulation of the multi-scale convergence in computational homogenization approaches. Int J Solids Struct 37(16):2285–2311
9. Aboudi J (2013) Mechanics of composite materials: a unified micromechanical approach, vol 29, Elsevier
10. Hill R (1964) Theory of mechanical properties of fibre-strengthened materials: I. elastic behaviour. J Mech Phys Solids 12(4):199–212
11. Kanit T, Forest S, Galliet I, Mounoury V, Jeulin D (2003) Determination of the size of the representative volume element for random composites: statistical and numerical approach. Int J Solids Struct 40(13):3647–3679
12. Soden P, Hinton M, Kaddour A (1998) Lamina properties, lay-up configurations and loading conditions for a range of fibre-reinforced composite laminates. Compos Sci Technol 58(7):1011–1022

Free Vibration Analysis of Laminated Composite Plates and Shells Subjected to Concentrated Mass at the Centre

Arpita Mandal, Chaitali Ray and Salil Haldar

Abstract In this present paper, we deal with free vibration analysis of laminated composite plates and shell panels with concentrated mass at the centre of the shell. Two types of mass lumping schemes (RWOERI and RWERI) have been proposed in the present study. In one of the mass lumping schemes, effect of rotary inertia has been included. First-order shear deformation theory has been incorporated in the formulation. The entire finite element programme has been written using FORTRAN language. A nine-noded isoparametric shallow shell element has been used. Cylindrical composite shell panels having different boundary conditions with various concentrated masses at the centre have been analysed.

Keywords Cylindrical composite shell · Mass lumping scheme · Rotary inertia · Concentrated load

1 Introduction

Due to the curved configuration, shell structures offer better performance in carrying load and moment for the combined bending and membrane action. The multilayered laminated composite material contributes extra advantage due to lightweight and tailorable properties. The analysis of laminated composite structures has attracted several researchers since few decades. A significant number of literature are available on free vibration of normal shell panels. However, investigation on shell panels with

A. Mandal
Narula Institute of Technology, Kolkata, India
e-mail: mandal.arpita6@gmail.com

C. Ray (✉)
Department of Civil Engineering, IIEST, Shibpur, India
e-mail: chaitali@civil.iiests.ac.in

S. Haldar
Department of Aerospace Engineering & Applied Mechanics, IIEST, Shibpur, India
e-mail: salilhaldar@gmail.com

B. N. Singh et al. (eds.), *Recent Advances in Theoretical, Applied, Computational and Experimental Mechanics*, Lecture Notes in Mechanical Engineering,
https://doi.org/10.1007/978-981-15-1189-9_5

concentrated mass is very rare. Very few studies on free vibration of composite plates with concentrated mass are reported in the available literature till date.

Bhimaraddi [1] worked on free vibration analysis of doubly curved shallow shell panels on rectangular planform using three-dimensional elasticity theory. Boay [2] made a study on natural frequencies of plates without and with a concentrated mass using Rayleigh-energy method. Low et al. [3] made a comparative study of frequencies for plates carrying concentrated mass. A free vibration analysis of rectangular isotropic plate carrying a concentrated mass at different positions is analysed and presented by Boay [4]. Low et al. [5] made a comparison between the analytical and experimental results in terms of the frequencies for plates carrying concentrated mass. Sheikh et al. [6] carried out a study on vibration of plates in different situations using a high-precision shear deformable element.

It is found from the extensive literature review that most of the researchers have paid attention towards the numerical analysis of isotropic plates with concentrated mass mostly. The literature review also reveals that the study on free vibration response of shell panels with concentrated mass and, in particular, studies on laminated composite shell panels with concentrated mass are very rare. Therefore, the present investigation has attempted to conduct a numerical modal analysis on composite plates and shell panels with concentrated mass to obtain natural frequencies.

2 Mathematical Formulation

2.1 Finite Element Model for Modal Analysis

The finite element model has been developed in the present study and a computer code is prepared using FORTRAN. The nine-noded laminated shell element with five degrees of freedom (u, v, w, θ_x and θ_y) at each node has been considered for the present formulation.

The nodal displacement components at any node 'r' of the element can be written as

$$\{\delta_r\}^{\mathrm{T}} = \left\{ u_r \;\; v_r \;\; w_r \;\; \theta_{xr} \;\; \theta_{xr} \right\} \tag{1}$$

where

$$u = \sum_{r=1}^{9} N_r u_r, \; v = \sum_{r=1}^{9} N_r v_r, \; w = \sum_{r=1}^{9} N_r w_r, \; \theta_x = \sum_{r=1}^{9} N_r \theta_{xr}, \; \theta_y = \sum_{r=1}^{9} N_r \theta_{yr}$$

and u, v and w are the translational displacements and θ_x and θ_y are the rotations about y- and x-axis, respectively. The shape functions N_r are developed by applying

Lagrangian interpolation function. The effect of shear deformation can be expressed as the following, where the bending rotations are independent field variables.

$$\begin{Bmatrix} \varnothing_x \\ \varnothing_y \end{Bmatrix} = \begin{bmatrix} \theta_x - \frac{\partial w}{\partial x} \\ \theta_y - \frac{\partial w}{\partial y} \end{bmatrix} \tag{2}$$

and $\emptyset_x$ and $\emptyset_y$ are the average shear rotation throughout the thickness of laminated shell as shown in Fig. 1.

The constitutive relationship with respect to its reference plane may be expressed as

$$\{\sigma\} = [D]\{\varepsilon\} \tag{3}$$

where σ is the stress resultants vector and can be expressed as

$$\{\sigma\}^{\mathrm{T}} = \left[N_x \; N_y \; N_{xy} \; M_x \; M_y \; M_{xy} \; Q_x \; Q_y \right] \tag{4}$$

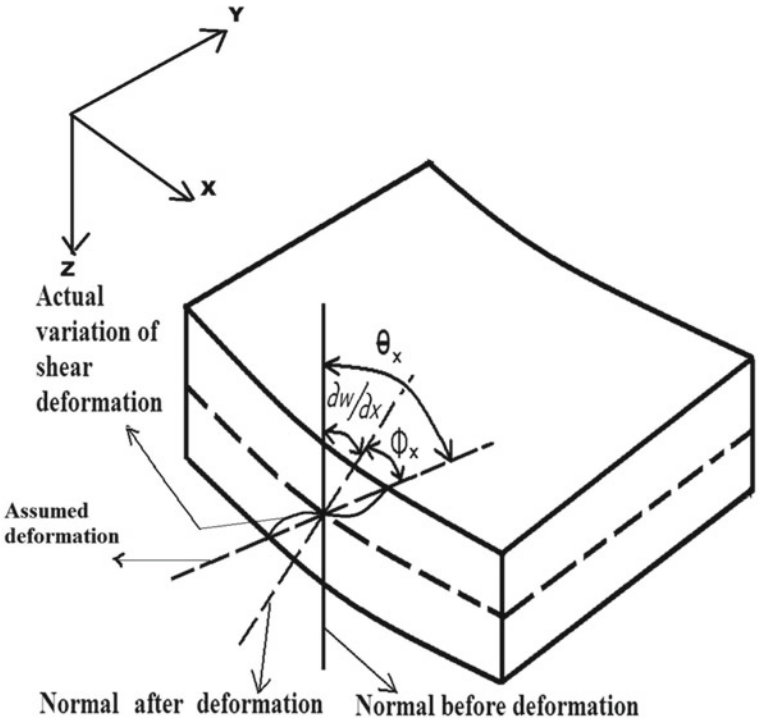

Fig. 1 Deformation of the shell panel

$$\{\varepsilon\}^{\mathrm{T}} = \left[\left(\frac{\partial u}{\partial x} + \frac{w}{R}\right)\left(\frac{\partial v}{\partial y}\right)\left(\frac{\partial u}{\partial y} + \frac{\partial v}{\partial x}\right) - \frac{\partial \theta_x}{\partial x} - \frac{\partial \theta_y}{\partial y} - \left(\frac{\partial \theta_x}{\partial y} + \frac{\partial \theta_y}{\partial x}\right) - \varnothing_x - \varnothing_y\right] \tag{5}$$

where $[D]$ is the rigidity matrix of laminated shell and written as

$$[D] = \begin{bmatrix} \left[A_{ij}\right]_{3\times 3} & \left[B_{ij}\right]_{3\times 3} & [0]_{3\times 2} \\ \left[B_{ij}\right]_{3\times 3} & \left[D_{ij}\right]_{3\times 3} & [0]_{3\times 2} \\ [0]_{2\times 3} & [0]_{2\times 3} & [A_{lk}]_{2\times 2} \end{bmatrix} \tag{6}$$

where (A_{ij}), (B_{ij}), (D_{ij}) and (A_{lk}) are extensional, extension–bending coupling, bending and transverse shear stiffness matrices, respectively, and defined as

$$A_{ij} = \sum_{k=1}^{n}\left(Q_{ij}\right)(z_k - z_{k-1}), \quad B_{ij} = \sum_{k=1}^{n}\left(Q_{ij}\right)\left(z_k^2 - z_{k-1}^2\right)$$
$$D_{ij} = \sum_{k=1}^{n}\left(Q_{ij}\right)\left(z_k^3 - Z_{k-1}^3\right), \quad A_{lk} = \sum_{k=1}^{n} K_S(Q_{lk})(z_k - z_{k-1})$$

where $K_S = \frac{5}{6}$ and z_k is the distance of kth layer from the reference plane.

The stiffness matrix $[K]_e$ of an element derived from the concept of virtual work method may be written as

$$[K]_e = \int_{-1}^{+1}\int_{-1}^{+1} [B]^{\mathrm{T}}\,[D][B]|J|\mathrm{d}\varepsilon\mathrm{d}\eta \tag{7}$$

where $[B]$ is the strain–displacement matrix and $|J|$ is the determinant of Jacobian matrix. Applying the idea of consistent mass matrix, a lumped mass matrix has been developed as follows:

$$[M] = \rho h \int_{-1}^{+1}\int_{-1}^{+1}\Big[[N_u]^{\mathrm{T}}[N_u] + [N_v]^{\mathrm{T}}[N_v] + [N_w]^{\mathrm{T}}[N_w] + \frac{h^2}{12}\left[N_{\theta_x}\right]^{\mathrm{T}}\left[N_{\theta_x}\right] + \frac{h^2}{12}\left[N_{\theta_y}\right]^{\mathrm{T}}\left[N_{\theta_y}\right]\Big]|J|\mathrm{d}\varepsilon\mathrm{d}\eta \tag{8}$$

where

$$[N_u] = [[N_r][N_0][N_0][N_0][N_0]] \quad [N_v] = [[N_0][N_r][N_0][N_0][N_0]]$$
$$[N_w] = [[N_0][N_0][N_r][N_0][N_0]] \quad \left[N_{\theta_x}\right] = [[N_0][N_0][N_0][N_r][N_0]]$$
$$\left[N_{\theta_y}\right] = [[N_0][N_0][N_0][N_0][N_r]]$$

where ρ is the density of the material, N_r is the corresponding interpolation function, $[N_0]$ is a null matrix and h is the thickness of the laminate.

The rotary inertia in the mass matrix has significant contribution to the dynamic behaviour of thicker laminates. However, the rotary inertia cannot be included in the consistent mass matrix formulation. The lumped model of mass matrix has been derived to include rotary inertia and expressed in the last two terms in Eq. (8). The in-plane movement of mass is defined by first two terms in the mass matrix given in Eq. (8). Transverse movement of mass contributes the major inertia and defined by the third term. The effect of rotary inertia has been examined by developing two types of proportionate mass lumping schemes. The effect of in-plane and transverse movements of mass has been considered in the first lumping schemes. This lumping scheme has been defined as RWOERI (mass lumping without rotary inertia) and may be expressed as

$$m_{ii}^{wl} = \frac{m_{ii}}{\sum m_{ii}} m_{\mathrm{e}} \quad (i = 1, 2, 3, 6, 7, 8, 11, 12, 13, 16, 17, 18, 21, 22, 23, 26, 27, 28, 31, 32, 33, 36, 37, 38, 41, 42, 43) \tag{9}$$

where m_{ii}^{wl} are the ith diagonal elements corresponding to u, v and w in the proposed model of lumped mass matrix, m_{ii} is the ith diagonal element of the consistent mass matrix and m_{e} is the actual mass of element.

The mass lumping scheme considering the effect of rotary inertia (RWERI) along with in-plane and transverse movement is expressed as

$$m_{ii}^{wl} = \frac{m_{ii}}{\sum m_{ii}} m_{\mathrm{e}} \quad (i = 1, 2, 3, 6, 7, 8, 11, 12, 13, 16, 17, 18, 21, 22, 23, 26, 27, 28, 31, 32, 33, 36, 37, 38, 41, 42, 43) \tag{10}$$

$$m_{ii}^{\theta xl} = \frac{h^2}{12} \frac{m_{ii}}{\sum m_{ii}} m_{\mathrm{e}} \; (i = 4, 9, 14, 19, 24, 29, 34, 39, 44) \tag{11}$$

$$m_{ii}^{\theta xl} = \frac{h^2}{12} \frac{m_{ii}}{\sum m_{ii}} m_{\mathrm{e}} \; (i = 5, 10, 15, 20, 25, 30, 35, 40, 45) \tag{12}$$

The element stiffness and the mass matrices have been generated and assembled together to form the global stiffness matrix $[K_0]$ and the global mass matrix $[M_0]$. The equation of motion for the free vibration analysis is expressed as

$$[K_0]\{\delta\} = \omega^2 [M_0]\{\delta\} \tag{13}$$

Equation (13) is solved by using the simultaneous iterative technique following Ref. [7] to compute the natural frequencies.

The present finite element formulation has been validated by solving several numerical problems and comparing the results with published literature. The effect

of rotary inertia in mass matrix has been studied (RWERI) and the convergence has also been verified.

3 Results and Discussions

3.1 Simply Supported Cross-ply Laminated Shell

Non-dimensional fundamental frequency of simply supported cross-ply [0°/90°] laminated shell panel with thickness ratio of $a/h = 10$ has been evaluated using the present formulation with different mesh divisions. Both mass lumping schemes have been applied in the present study. The relative material properties are $E_1/E_2 = 25$, $G_{12} =$

Table 1 Non-dimensional fundamental frequency of laminated cross-ply [0°/90°] cylindrical shell, $\lambda = (\omega a^2/h)\sqrt{(\rho/E_2)}$ $(a = b,\ a/h = 10, Rx = R,\ Ry = \text{inf})$

R/a	Bhimaraddi [1]			Present results		
	3-D	FSDT	HSDT	Mass lumping Schemes	Mesh division	Results
2	9.3627	9.3653	9.5664	RWOERI[b]	6 × 6[a]	9.551
					8 × 8	9.552
					12 × 12	9.553
					16 × 16	9.553
				RWERI[c]	6 × 6	9.496
					8 × 8	9.498
					12 × 12	9.498
3	9.1442	9.0563	9.2642	RWOERI	6 × 6	9.315
					8 × 8	9.317
					12 × 12	9.317
				RWERI	6 × 6	9.262
					8 × 8	9.263
					12 × 12	9.263
4	9.0613	8.9403	9.1506	RWOERI	6 × 6	9.234
					8 × 8	9.235
					12 × 12	9.236
					16 × 16	9.236
				RWERI	6 × 6	9.180
					8 × 8	9.182
					12 × 12	9.182

[a]Mesh divisions, [b]result without effect of rotary inertia, [c]result with effect of rotary inertia

Table 2 Fundamental frequency ($\lambda = \frac{\omega}{2\pi}$) (in Hz) of a rectangular plate having a concentrated mass at the plate centre

Concentrated mass (kg)	Present result (RWERI)	Boay [4]	Sheikh et al. [6]
3	18.053	18.03	17.93
4	15.703	15.73	15.65
5	14.082	14.12	14.04

$G_{13} = 0.5E_2$, $G_{23} = 0.2E_2$, $\gamma_{12} = \gamma_{13} = \gamma_{23} = 0.25$. Non-dimensional fundamental frequency $\lambda = wa^2\sqrt{(\rho/E_2)}/h$ obtained from the present formulation is shown in Table 1 and compared with those obtained from closed-form solution. Bhimaraddi [1] has used the three-dimensional theory of elasticity to obtain exact solution. It is observed from Table 1 that the present results are in very good agreement with published results and also converge with mesh refinement. From Table 1, it is clear that the results obtained using RWERI (considering rotary inertia) show a better agreement with published literature than RWOERI (without rotary inertia). Here, a and b are the curve length of the edges of the shell panels and $a = b$.

3.2 Rectangular Plate Having Lumped Mass at the Centre

The fundamental frequency of an isotropic rectangular plate (0.71 m long, 0.42 m wide, and 2.0 mm thick) having concentrated mass at the centre with the self mass has been studied. The plate is simply supported at two opposite smaller sides and clamped along the other two longer sides. Fundamental frequency ($\lambda = \frac{\omega}{2\pi}$) obtained from the present formulation for varying mass is shown in Table 1 and compared with those obtained from closed-form solution [4] (using Ritz Method). Sheikh et al. [6] have presented the same results using FSDT. The relative material properties are $E = 70.0$ Gpa, $G = 26.92$ Gpa, $\gamma = 0.3$, $\rho = 1770$ kg/m^3 (Table 2).

3.3 Cross-ply Laminated Cylindrical Shallow Shell Having Lumped Mass at the Centre

A cross-ply [0°/90°] laminated shell panel having lumped mass at the centre with thickness ratio of $a/h = 10$ and different boundary conditions has been analysed using the present formulation. The relative material properties are $E_1/E_2 = 25$, $G_{12} = G_{13} = 0.5E_2$, $G_{23} = 0.2E_2$, $\gamma_{12} = \gamma_{13} = \gamma_{23} = 0.25$. First three natural frequencies obtained from the present formulation are shown in Table 3. Here, a and b are the curve length of the edges of the shell panels and $a = b$.

Table 3 Fundamental frequency of laminated cross-ply [0°/90°] cylindrical shell, $\lambda = (\omega a^2/h)\sqrt{(\rho/E_2)}$ $(a = b,\ a/h = 10, Rx = R,\ Ry = \text{inf})$

R/a	Boundary condition	Concentrated mass (kg)	Present result (RWERI)		
			Mode1	Mode2	Mode3
3	Four edges simply supported	0	9.263	21.655	22.118
		3	6.165	13.136	21.655
		4	5.341	13.132	21.654
		5	4.778	13.130	21.655
	Four edges clamped	0	18.999	27.199	29.420
		3	7.680	21.985	27.200
		4	6.651	21.984	27.199
		5	5.949	21.983	27.199
4	Four edges simply supported	0	9.1820	21.691	21.980
		3	6.124	13.101	21.691
		4	5.305	13.098	21.691
		5	4.746	13.096	21.691
	Four edges clamped	0	17.683	27.246	28.566
		3	7.538	20.817	27.247
		4	6.529	20.816	27.246
		5	5.840	20.815	27.246

4 Conclusions

It is found from the present numerical analysis that there is a significant effect of rotary inertia on the free vibration of laminated plates and shell panels. It is recommended that the mass lumping scheme with rotary inertia is more suitable for both plates and shell panels. In this present investigation, both simply supported and fixed shell panels with different *R/a* ratio have been taken under consideration. For all the cases, results show the same pattern with the increasing value of applied lumped mass. The present study reveals that the fundamental frequency of plates and shell panels with lumped mass at the centre decreases with the increment of the applied lumped mass value. Another observation from this study is that with the increment of lumped mass value, the rate of change of the frequency increases the clamped shells.

References

1. Bhimaraddi A (1991) Free vibration analysis of doubly curved shallow shells on rectangular planform using three-dimensional elasticity theory. Int J Solids Struct 27(7):897–913
2. Boay CG (1993) Free vibration on rectangular isotropic plates with and without a concentrated mass. Comput Struct 48:529–533

3. Low KH, Ng CK, Ong YK (1993) Comparative study of frequencies for plates carrying concentrated mass. J Eng Mech 119:917
4. Boay CG (1995) Frequency analysis of rectangular isotropic plates carrying a concentrated mass. Comput Struct 56(1):39–48
5. Low KH, Chai GB, TanA GS (1997) comparative study of vibrating loaded plates between the Rayleigh-Ritz and experimental methods. J Sound Vib 199(2):285–297
6. Sheikh AH, Haldar S, Sengupta D (2002) Vibration of plates in different situations using a high-precision shear deformable element. J Sound Vib 253(2):329–345
7. Corr RB, Jennings A (1976) A simultaneous iteration algorithm for symmetric Eigen value problems. Int J Numer Eng 10:647–663

Buckling Analysis of Thick Isotropic Shear Deformable Beams

Kedar S. Pakhare, Rameshchandra P. Shimpi and P. J. Guruprasad

Abstract This paper presents buckling analysis of thick isotropic shear deformable beams using single variable new first-order shear deformation theory (*SVNFSDT*) for beams. As in the case of Timoshenko beam theory, *SVNFSDT* is a displacement-based first-order shear deformation beam theory and assumes constant transverse shear strain through the thickness of the beam. *SVNFSDT* has only one unknown function and has striking resemblance to that of Bernoulli–Euler beam theory as far as expressions for governing differential equation, moment, and shear force are concerned. Hence, efforts involved in obtaining buckling solutions using *SVNFSDT* are only marginally higher as compared to those involved in the case of Bernoulli–Euler beam theory. Numerical results are presented for rectangular isotropic beams with several values of beam thickness-to-length ratio and with physically meaningful boundary conditions. To demonstrate the efficacy of numerical results of buckling analysis obtained using *SVNFSDT*, these results are compared with corresponding results available in the literature.

Keywords Shear deformation beam theory · Single variable beam theory

1 Introduction

Bernoulli–Euler beam theory (*BEBT*) is the simplest and an extremely important beam theory. It is being utilized widely for preliminary analysis of beam-like structures. However, *BEBT* neglects the effects of transverse shear deformation present through the thickness of the beam. It should be noted that for beams with higher thickness-to-length ratio, effects of shear in beam deformation become significant. Therefore, *BEBT* can provide reasonably accurate results only for slender beams wherein effects of shear in beam deformation do not play an important role. For thick

K. S. Pakhare (✉) · R. P. Shimpi · P. J. Guruprasad
Aerospace Engineering Department, IIT Bombay, Mumbai, India
e-mail: kedar188200@gmail.com

R. P. Shimpi
e-mail: rpshimpi@aero.iitb.ac.in

B. N. Singh et al. (eds.), *Recent Advances in Theoretical, Applied, Computational and Experimental Mechanics*, Lecture Notes in Mechanical Engineering,
https://doi.org/10.1007/978-981-15-1189-9_6

beams in which shear deformation effects are significant, the use of *BEBT* overestimates the buckling loads. Hence, it is necessary to have beam theories which account for effects of transverse shear strain which are prominent in case of thick beams. The beam transverse shear strain is assumed to have a constant value through the beam thickness in the case of first-order shear deformation beam theories (*FSDT*). In order to approximately satisfy the constitutive relation between the beam transverse shear stress and the beam transverse shear strain, *FSDT* utilize a shear correction coefficient. Timoshenko beam theory (*TBT*) is the first *FSDT* and has two unknown functions. On the other hand, the beam transverse shear strain is assumed to have a polynomial variation through the beam thickness in the case of higher-order shear deformation beam theories (*HSDT*). Although *FSDT* and *HSDT* are adequate for analyzing shear deformable beams, they generally have coupled governing differential equations, increased number of independent unknowns, and require specification of increased number of beam boundary conditions. More details regarding *FSDT* and *HSDT* are presented in Ghugal and Shimpi [1]. Higher accuracy offered by *HSDT* comes with a price of longer computation time and effort [2]. Pakhare et al. [3] have developed single variable new first-order shear deformation theory (*SVNFSDT*) for isotropic beams based on new first-order shear deformation theories (*NFSDT*) by Shimpi et al. [4]. Unlike *TBT*, *SVNFSDT* has single governing differential equation involving single unknown function and requires specification of only two physically meaningful boundary conditions at each end of the beam.

Buckling of beam is a functional failure phenomenon wherein beam loses its ability to carry lateral loads when compressive force acting along the beam length reaches a critical value. Beam thickness-to-length ratio and hence shear deformation effects have direct implications on critical buckling loads wherein increase in beam thickness-to-length ratio causes reduction in non-dimensional critical buckling load. Thai [5] has performed stability analysis of nanobeams using nonlocal shear deformation beam theory. Shimpi et al. [6] have utilized single variable *HSDT* to perform stability analysis of thick beams.

In this paper, *SVNFSDT* is used to perform buckling analysis of thick isotropic shear deformable beams. Numerical results obtained using *SVNFSDT* are compared with existing results in order to demonstrate the effectiveness of the presented method.

2 Theoretical Formulation

In accordance with the recent work by Pakhare et al. [3] and Shimpi et al. [4] on *NFSDT*, single valued displacement fields are assumed for the beam, which are on similar lines to the displacement fields given by Shimpi el al. [4]. Lateral displacement "w" is split into a bending component "w_b" and a shearing component "w_s". These two components of lateral displacement are functions of longitudinal coordinate "x" alone. Longitudinal displacement "u" is a function of longitudinal coordinate "x" and lateral coordinate "z". Assumed displacement field is given below:

$$u(x, z) = -z\frac{dw_b}{dx} \tag{1}$$

$$w = w_b(x) + w_s(x) \tag{2}$$

Using assumed displacement field and linear strain-displacement relations, expressions for strains are obtained. These strains are then used in stress–strain relations pertaining to linear elastic isotropic material so as to get expressions for stresses. Shear correction coefficient "k" is incorporated in stress–strain relations. By using value of shear correction coefficient equal to 5/6 which is typically utilized in *TBT* for the beam with rectangular cross section, bending moment "M_x" of the proposed theory is given below:

$$M_x = -EI\frac{d^2w_b}{dx^2} \tag{3}$$

whereas shear force "Q_x" of the proposed theory is given below:

$$Q_x = -EI\frac{d^3w_b}{dx^3} \tag{4}$$

As stated by Shimpi et al. [6], conditions of gross equilibrium for the beam acted upon by an axial tensile load "N_x" are given below:

$$N_x\frac{dw}{dx} + \frac{dM_x}{dx} - Q_x = 0 \tag{5}$$

$$\frac{dQ_x}{dx} = 0 \tag{6}$$

Beam gross equilibrium equations are utilized to obtain the relation between w_b and w_s. Equations (3), (5), (6) along with the relation between w_b and w_s are utilized to derive governing differential equation of *SVNFSDT* for beam under the influence of an axial compressive load which is given below:

$$\left[EI - \frac{h^2(1+\mu)N_o}{5}\right]\frac{d^4w_b}{dx^4} + N_o\frac{d^2w_b}{dx^2} = 0 \tag{7}$$

In Eq. (7), "μ" is Poisson's ratio and "E" is modulus of elasticity of the beam material, "h" is the beam thickness, "I" is the beam cross-sectional area moment of inertia, and "N_o" is axial compressive load acting on the beam.

General solution of Eq. (7) can be given as below:

$$w_b = C_1 + C_2x + C_3\cos(\beta x) + C_4\sin(\beta x) \tag{8}$$

where C_1, C_2, C_3, and C_4 are arbitrary integration constants whose values can be found out by using boundary conditions imposed on the beam and

$$\beta^2 = \frac{N_0}{\left[EI - \frac{h^2(1+\mu)N_0}{5}\right]} \tag{9}$$

Depending upon the type of end supports, physically meaningful boundary conditions, viz, free, clamped, and simply-supported boundary conditions can be prescribed at each end of the beam in terms of the displacements. Furthermore, as in Timoshenko and Goodier [7], it is possible to represent two distinct beam clamped boundary conditions, viz, "clamp type 1" and "clamp type 2" in the present beam theory.

Four linear algebraic equations in C_1, C_2, C_3, and C_4 can be obtained by substituting general solution given by Eq. (8) in four boundary conditions imposed on the beam, two at each beam end. Then, critical buckling load for the beam can be obtained by performing eigenvalue buckling analysis on these four linear algebraic equations.

3 Numerical Results and Comparison

In this section, numerical results obtained by utilizing *SVNFSDT* pertaining to buckling of rectangular isotropic simply-supported shear deformable beams for various values of beam thickness-to-length ratio are presented. *SVNFSDT* is then utilized to present variation of buckling loads with beam thickness-to-length ratio for beams with different fixity conditions. *SVNFSDT* is also utilized to present effects of two distinct beam clamped boundary conditions of the theory on buckling loads of clamped-simply-supported beam.

Table 1 compares non-dimensional critical buckling loads ($N_{cr} = (N_o L^2)/(EI)$) obtained using *SVNFSDT* with corresponding results available in the literature for simply-supported beam (*SS* beam).

Maximum percentage difference between critical buckling load obtained using *RBT* and *SVNFSDT* is 0.011% with respect to *RBT* for a beam thickness-to-length ratio of 0.20. Comparison presented in Table 1 confirms the accuracy of the buckling analysis carried out using *SVNFSDT* for thin as well as thick rectangular isotropic beams.

Figure 1 depicts the variation of N_{cr} obtained using *SVNFSDT* with respect to beam thickness-to-length ratio for clamped-clamped beam (*CC* beam) with "clamp type 1" boundary conditions, clamped-simply-supported beam (*CS* beam) with "clamp type 1" boundary conditions and *SS* beam.

For a given beam thickness-to-length ratio, critical buckling load increases as fixity conditions on ends of the beam changes from simply-supported to clamped

Table 1 Comparison of non-dimensional critical buckling loads ($N_{cr} = (N_o L^2)/(EI)$) for *SS* beam obtained by various theories ($\mu = 0.3$)

Beam thickness-to-length ratio	Non-dimensional critical buckling loads (N_{cr})				
	BEBT [5]	*TBT* [5]	Reddy's beam theory (*RBT*) [5]	Simple single variable beam theory [6]	*SVNFSDT*
0.01	9.8696	9.8671	9.8671	9.8671	9.8671
0.02	9.8696*	–	–	9.8595	9.8595
0.05	9.8696	9.8067	9.8067	9.8067	9.8067
0.10	9.8696	9.6227	9.6228	9.6227	9.6227
0.15	9.8696*	–	–	9.3309	9.3309
0.20	9.8696	8.9509	8.9519	8.9509	8.9509
0.25	9.8696*	–	–	8.5055	8.5055
0.30	9.8696*	–	–	8.0179	8.0179
0.35	9.8696*	–	–	7.5091	7.5091
0.40	9.8696*	–	–	6.9969	6.9969

Results with * are calculated by the present authors

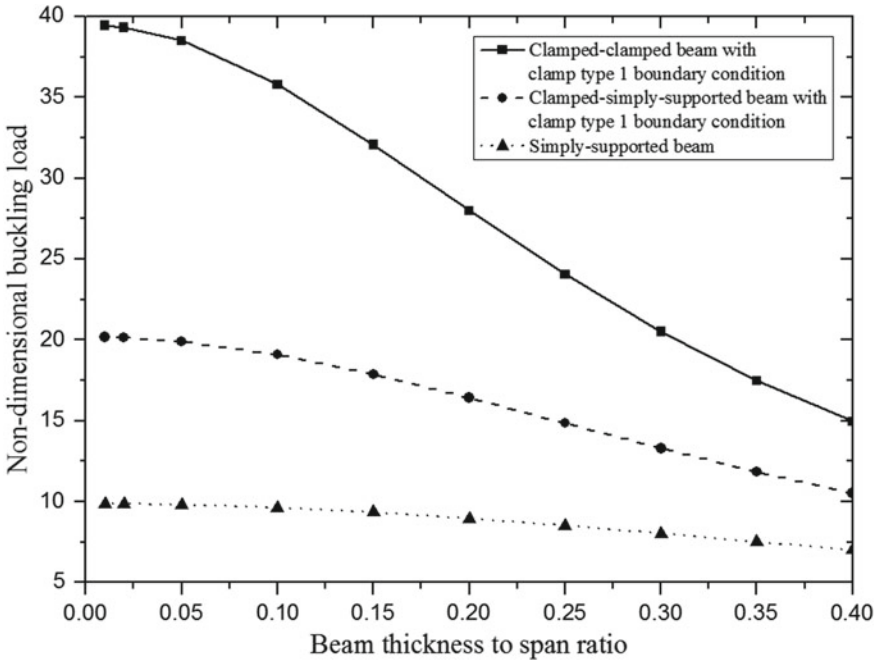

Fig. 1 Variation of non-dimensional critical buckling loads ($N_{cr} = (N_o L^2)/(EI)$) with respect to beam thickness-to-length ratio

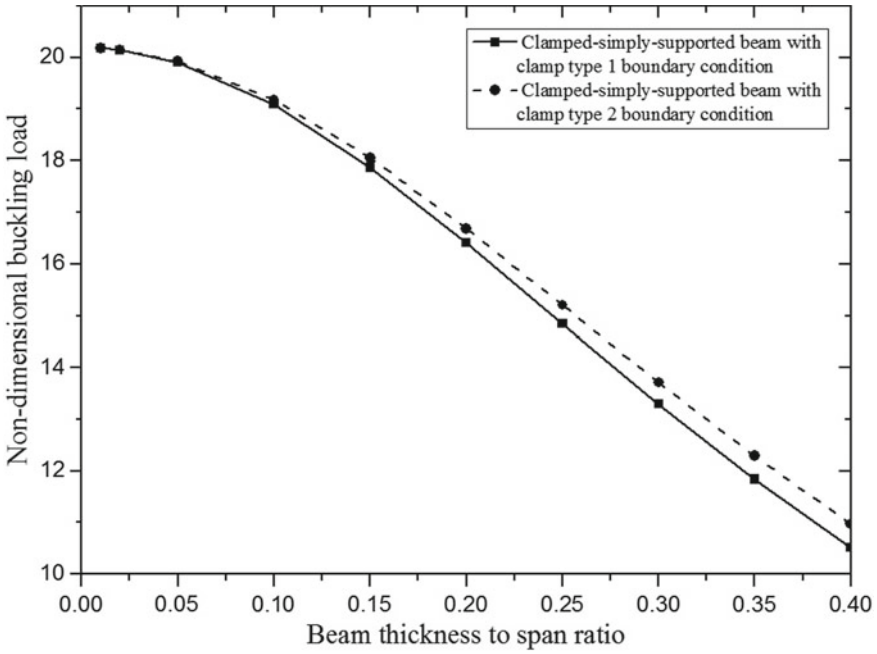

Fig. 2 Effects of "clamp type 1" and "clamp type 2" conditions on the variation of non-dimensional critical buckling loads ($N_{cr} = (N_o L^2)/(EI)$) with respect to beam thickness-to-length ratio for *CS* beam

(Fig. 1). Also for any beam fixity conditions, increase in beam thickness-to-length ratio causes N_{cr} to decrease.

Figure 2 depicts the effects of "clamp type 1" and "clamp type 2" conditions on the variation of N_{cr} obtained using *SVNFSDT* with respect to beam thickness-to-length ratio for *CS* beam.

For *CS* beam, N_{cr} is higher for the beam with "clamp type 2" boundary conditions as compared to the beam with "clamp type 1" boundary conditions for a given beam thickness-to-length ratio (Fig. 2). Hence "clamp type 2" boundary conditions make the beam stiffer as compared to "clamp type 1" boundary conditions. With reduction in beam thickness-to-length ratio, effects of clamping conditions attenuate.

4 Concluding Remarks

In this paper, buckling analysis of thick isotropic shear deformable beams is performed by using single variable new first-order shear deformation beam theory. For thick isotropic rectangular beams with various beam fixity conditions, influence of

shear deformation on critical buckling loads is presented. To demonstrate the effectiveness of the presented method, obtained results are compared with corresponding results available in the literature. For clamped-simply-supported beam, effect of two distinct clamp boundary conditions on non-dimensional critical buckling loads is also presented. These results and comparisons prove that the buckling analysis of thick isotropic shear deformable beams carried out with easy to use *SVNFSDT* is reliable for a range of beam fixity conditions as well as beam thickness-to-length ratio.

References

1. Ghugal YM, Shimpi RP (2001) A review of refined shear deformation theories for isotropic and anisotropic laminated beams. J Reinf Plast Compos 20(3):255–272
2. Lee KH, Lim GT, Wang CM (2002) Thick Lévy plates re-visited. Int J Solids Struct 39:127–144
3. Pakhare KS, Mitra M, Shimpi RP (2016) Development of single variable new first-order shear deformation theories for plates and beams. Master of Technology Dissertation, Department of Aerospace Engineering, Indian Institute of Technology Bombay
4. Shimpi RP, Patel HG, Arya H (2007) New first-order shear deformation plate theories. ASME J Appl Mech 74:523–533
5. Thai HT (2012) A nonlocal beam theory for bending, buckling, and vibration of nanobeams. Int J Eng Sci 52:56–64
6. Shimpi RP, Shetty RA, Guha A (2017) A simple single variable shear deformation theory for a rectangular beam. J Mech Eng Sci 231:4576–4591
7. Timoshenko SP, Goodier JN (1951) Theory of elasticity. McGraw-Hill Book Company, New York, pp 35–39

Spectral Finite Element for Dynamic Analysis of Piezoelectric Laminated Composite Beams

Namita Nanda

Abstract In this paper, a frequency-domain spectral finite element model (SFEM) is developed for dynamic analysis of piezoelectric laminated composite beams. The displacement field of the beam is represented by the first-order shear deformation theory (FSDT). The electric potential for the piezoelectric layer is expressed in two ways: (i) distributed linearly through the thickness and (ii) layerwise through thickness distribution consistent with the FSDT. The governing differential equation of motion for piezoelectric laminated composite beam is obtained using Hamilton's principle. These time-domain equations are transformed to frequency domain using the Fourier transformation. The spectral element is derived from the exact solution of the frequency domain governing equations of motion. The formulation is validated by comparing the results of the natural frequencies with the published finite element method (FEM) results. The developed element is used to perform dispersion, free vibration analysis, and elastic wave propagation in laminated composite beam fully or partially covered with surface-bonded piezoelectric layer.

Keywords Spectral element · Piezoelectric · Dynamic analysis · Composite · Beam

1 Introduction

Recently, the study of piezoelectric materials in structures has received significant attention due to the increasing demands of high structural performance requirements. The piezoelectric materials tend to produce an electric potential when mechanical stress is applied (direct piezoelectric effect). Conversely, applying electric potential, mechanical deformation is produced (converse piezoelectric effect). Therefore, piezoelectric materials are used both as sensors and actuators. Numerous analytical models have been developed for smart composite structures, including piezoelectric

N. Nanda (✉)
Department of Applied Mechanics, Indian Institute of Technology Delhi, New Delhi 110 016, India
e-mail: namita_nanda@rediffmail.com

B. N. Singh et al. (eds.), *Recent Advances in Theoretical, Applied, Computational and Experimental Mechanics*, Lecture Notes in Mechanical Engineering,
https://doi.org/10.1007/978-981-15-1189-9_7

laminated composite beams. Many researchers used the conventional finite element method to study the dynamic behavior of structures. However, the conventional FEM requires very fine mesh to obtain reliable dynamic solutions of such structures. This creates very large problem size which costs more computational effort and time [1]. A more efficient method is the frequency-domain spectral finite element method [2]. In this method, the discretization of the time-domain solution to frequency domain in terms of spectral amplitudes (Fourier coefficients) is done using the fast Fourier transform (FFT). The fundamental difference between FEM and SFEM is that the spectral element stiffness matrix is exact and frequency dependent. The governing equations are solved in the frequency domain, which are transformed from time-domain equations using the discrete Fourier transform. These responses are then transformed back to the time domain using the inverse FFT. Due to the exact formulation of the system, only one spectral element is sufficient for solution in most cases where thousands of finite elements are required.

The frequency-domain SFEM considered in the present study is different from the time-domain SFEM proposed by Patera [3]. In time-domain SFEM, Legendre polynomials or Chebyshev polynomials are used as shape functions to formulate the finite element matrices in the time domain. The element mass matrix formulated is diagonal hence the computational cost is less expensive than conventional FEM. This method has been used for wave propagation analysis in laminated composite beams, plates, and panels [4–7]. Though the method is more robust and has high accuracy, the problem size remains large. The time-domain SFEM analysis is inadequate to furnish most of the useful frequency domain properties such as wave dispersion and nature of each wave modes.

The frequency-domain SFEM proposed by Doyle [2] has been widely used by researchers to study wave propagation in structures. Wave propagation analysis in isotropic beams has been studied [8–11] using this frequency-domain SFEM. Lee et al. [11] presented a brief review of the spectral element method in structural dynamics. Spectral element models for wave propagation and dynamic analysis of composite beams have been developed [12–15]. A spectral finite element based on an efficient layerwise theory has been developed by Nanda et al. [16] for wave propagation analysis of anisotropic beams. Wavelet spectral finite element method has also been used to study wave propagation in laminated composite plates with transverse cracks [17].

Many theories and models have been developed for analyzing piezoelectric laminated composite structures [18–21] with different displacement field and electric potential approximations. However, the studies on smart piezoelectric composite structures using SFEM are limited [22, 23] and have not been well addressed. Moreover, these spectral element formulations used linear variation of the electric potential through the thickness. However, the electric potential distribution is actually nonlinear due to the induced potential effects. In the present work, a spectral finite element model in the frequency domain is presented for the free vibration and high-frequency wave propagation analyses of piezoelectric laminated composite beams. The displacement field of the beam is represented by first-order shear deformation theory

with both linear and layerwise through thickness distribution of electric potential [21] in the piezoelectric layer.

2 Theory and Formulation

The constitutive relations for the piezoelectric smart beam are

$$\sigma_x = \hat{Q}_{11}\varepsilon_x - \hat{e}_{31}E_z,\ \tau_{zx} = \hat{Q}_{55}\gamma_{zx},\ D_z = \hat{e}_{31}\varepsilon_x + \eta_{33}E_z \tag{1}$$

where σ_x, τ_{zx}, ε_x, γ_{zx}, D_z, and E_z denote the axial stress, shear stress, normal strain, shear strain, electric displacement, and electric field, respectively. $\hat{Q}_{11}$, $\hat{Q}_{55}$, $\hat{e}_{31}$, and η_{33} are the reduced elastic, piezoelectric, and dielectric coefficients. The displacement field of the beam is represented by the first-order shear deformation theory. The in-plane and transverse displacements u and w are represented as

$$u(x,z,t) = u_0(x,t) + z\psi_0(x,t),\ w(x,z,t) = w_0(x,t) \tag{2}$$

where u_0, w_0, and ψ_0 denote the in-plane displacement, the transverse displacement, and the rotation of the mid-surface, respectively.

The strain–displacement relation is given as

$$\varepsilon_x = \frac{\partial u}{\partial x},\quad \gamma_{zx} = \frac{\partial u}{\partial z} + \frac{\partial w}{\partial x} \tag{3}$$

The electric potential (ϕ) for the piezoelectric layer (Fig. 1) is expressed in two ways:

(i) Linear distribution through the thickness.

The electric potential and the electric field of the ith piezoelectric layer is expressed as

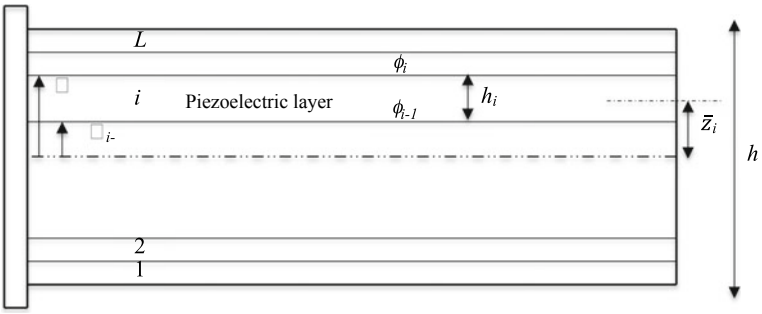

Fig. 1 Geometry of a multilayered piezoelectric smart beam

$$\phi_i(x,z) = (z - z_{i-1})\phi_{0i}(x)/h_i,\ E_z^i = -\partial\phi_i/\partial z = -\phi_{0i}/h_i \tag{4}$$

where h_i is the thickness of the ith piezoelectric layer.

(ii) Through thickness distribution consistent with FSDT [21].

The electric potential of the ith piezoelectric layer is

$$\phi_i(x,z) = \bar{\phi}_i(x) + (\tilde{\phi}_i(x)(z - \bar{z}_i)/h_i) - (\hat{e}_{31}h_i^2(1 - 4(z - \bar{z}_i)^2/h_i^2)\psi_0^{'}/8\eta_{33}) \tag{5a}$$

where $\bar{\phi}_i = (\phi_i + \phi_{i-1})/2$, $\tilde{\phi}_i = \phi_i - \phi_{i-1}, \cdots \bar{z}_i = (z_i + z_{i-1})/2$ and ϕ_i, ϕ_{i-1} are the electric potential at the top and bottom faces of the ith piezoelectric layer and $\psi_0^{'}$ is the first derivative of ψ_0. From Eq. (5a), it is observed that the electric potential is quadratic in thickness direction. The first two terms describe the conventional linear part. The quadratic term represents the bending deformation contribution to the potential.

The resulting electric field is

$$E_z^i = -\partial\phi_i/\partial z = -(\tilde{\phi}_i(x)/h_i) - (\hat{e}_{31}(z - \bar{z}_i)\psi_0^{'}/\eta_{33}) \tag{5b}$$

The spectral elements developed using the above representations for ϕ using Eqs. (4) and (5a, 5b) are denoted as FSDT-A and FSDT-M, respectively.

The equations of motion and the corresponding variationally consistent boundary conditions for the beam with piezoelectric layers are derived from Hamilton's principle, which states that

$$\int_{t_1}^{t_2} (\delta T - \delta U + \delta W)\mathrm{d}t = 0 \tag{6}$$

where t_1 and t_2 are the starting and finish time, respectively; δT and δU are the first-order variations of total kinetic and total strain energies of the piezoelectric composite beam, respectively, and δW denotes the total virtual work done by the external mechanical and electrical forces. These variations are obtained as

$$\delta T = \int_z \rho(\dot{u}\delta\dot{u} + \dot{w}\delta\dot{w})b\mathrm{d}z \tag{7}$$

$$\delta U = \int_z (\sigma_x\partial\varepsilon_x + \tau_{zx}\partial\gamma_{zx} - D_z\partial E_z)b\mathrm{d}z \tag{8}$$

The variation of the virtual work done by external surface force q and the applied surface charge density q_0 is expressed as

$$\delta W = \int q \partial w_0 b \mathrm{d}x - \int q_0 \partial \phi b \mathrm{d}x \tag{9}$$

Substituting Eqs. (7–9) into Eq. (6) and using Eqs. (1–3), the governing differential equations of the smart composite beams are expressed as

$$\partial u_0 : \quad I_0 \ddot{u}_0 + I_1 \ddot{\psi}_0 - N_{x,x} = 0 \tag{10a}$$

$$\partial w_0 : \quad I_0 \ddot{w}_0 - Q_{x,x} - F_2 = 0 \tag{10b}$$

$$\partial \psi_0 : \quad I_1 \ddot{u}_0 + I_2 \ddot{\psi}_0 - M_{x,x} + Q_x = 0 \tag{10c}$$

$$\partial \phi : \quad G_z^k + q_0 = 0 \tag{10d}$$

where F_2 is the applied distributed force along the z-direction and $G_z^k = \sum_{k=1}^{L} D_z \frac{1}{h_p} \mathrm{d}z$. The coefficient G_z^k is obtained for FSDT-A and FSDT-M using the expressions for D_z and E_z from Eqs. (1), (4), and (5a, 5b), and subsequently the electric-field potential function in terms of primary displacement variables is found out from Eq. (10d).

The stress resultants are defined as

$$N_x = \sum_{k=1}^{L} \int_{z_{k-1}}^{z_k} \sigma_x \mathrm{d}z\,, \quad M_x = \sum_{k=1}^{L} \int_{z_{k-1}}^{z_k} \sigma_x z \mathrm{d}z\,, \quad Q_x = \sum_{k=1}^{L} \int_{z_{k-1}}^{z_k} \tau_{zx} \mathrm{d}z \tag{11}$$

Thus,

$$\begin{Bmatrix} N_x \\ M_x \\ Q_x \end{Bmatrix} = \begin{bmatrix} A_{11} & B_{11} & 0 \\ B_{11} & D_{11} & 0 \\ 0 & 0 & A_{55} \end{bmatrix} \begin{Bmatrix} \partial u_0/\partial x \\ \partial \psi_0/\partial x \\ \psi_0 + \partial w_0/\partial x \end{Bmatrix} - \begin{Bmatrix} N_x^p \\ M_x^p \\ 0 \end{Bmatrix} \tag{12}$$

where $\left\{N_x^p, M_x^p\right\} = \int_{z_{k-1}}^{z_k} \hat{e}_{31} E_z(1, z) \mathrm{d}z$

Equation (9) is subjected to the boundary conditions at $x = 0$, and $x = l$ as given below:

$$\begin{aligned} u_0 &= u_0^*, \text{ or } N_x = N_x^* \\ w_0 &= w_0^*, \text{ or } Q_x = Q_x^* \\ \psi_0 &= \psi_0^*, \text{ or } M_x = M_x^* \end{aligned} \tag{13}$$

The general solution of the homogeneous form of Eqs. (10a, 10b, 10c, 10d) is written in the spectral form as

$$u_0(x,t) = \sum_{n=1}^{N} \hat{u}(x,\omega_n)e^{i\omega_n t} = \sum_{n=1}^{N} (\tilde{u}_j e^{-ik_j x})e^{i\omega_n t}$$
$$w_0(x,t) = \sum_{n=1}^{N} \hat{w}(x,\omega_n)e^{i\omega_n t} = \sum_{n=1}^{N} (\tilde{w}_j e^{-ik_j x})e^{i\omega_n t}$$
$$\psi_0(x,t) = \sum_{n=1}^{N} \hat{\psi}(x,\omega_n)e^{i\omega_n t} = \sum_{n=1}^{N} (\tilde{\psi}_j e^{-ik_j x})e^{i\omega_n t} \tag{14}$$

where $\hat{u}$, $\hat{w}$, and $\hat{\psi}$ are the Fourier coefficients (or spectral components) of the axial, flexural, and shear deformations, respectively, $\tilde{u}_j$, $\tilde{w}_j$, and $\tilde{\psi}_j$ are the wave amplitudes, which are evaluated from the essential and natural boundary conditions, ω_n is the discrete frequency at the nth sampling point, and k_j is the wavenumber. The summation is performed up to the Nyquist frequency in FFT ω_N, where N is the number of samples.

Substituting Eq. (14) into the governing differential Eqs. (10a, 10b, 10c, 10d), we get

$$\begin{bmatrix} (\tilde{A}_{11}k^2 - I_0\omega_n^2) & 0 & (\tilde{B}_{11}k^2 - I_1\omega_n^2) \\ 0 & (\tilde{A}_{55}k^2 - I_0\omega_n^2) & ikA_{55} \\ (\tilde{B}_{11}k^2 - I_1\omega_n^2) & -ikA_{55} & (\tilde{D}_{11}k^2 + A_{55} - I_2\omega_n^2) \end{bmatrix} \begin{Bmatrix} \tilde{u}_j \\ \tilde{w}_j \\ \tilde{\psi}_j \end{Bmatrix} = 0 \tag{15}$$

where $\tilde{A}_{11}$, $\tilde{B}_{11}$, and $\tilde{D}_{11}$ are the modified stiffness coefficients due to $\hat{e}_{31}$ and η_{33} terms. Equation (15) will have a nontrivial solution by setting the determinant of the coefficient matrix of $\tilde{u}_j$, $\tilde{w}_j$, and $\tilde{\psi}_j$ to zero. This gives a sixth-order characteristic equation in terms of the wavenumber k_j,

$$a_w k_j^6 + b_w k_j^4 + c_w k_j^2 + d_w = 0 \tag{16}$$

The coefficients a_w, b_w, c_w, and d_w are not listed here due to their lengthy appearance. Since Eq. (16) is a cubic equation in k_j^2, there are three pairs of wavenumbers, $\pm k_1$, $\pm k_2$, and $\pm k_3$: three for forward modes and three for backward modes. These three modes constitute the axial mode (mode 1), flexural mode (mode 2), and the shear mode (mode 3).

The solution for the spectral components of the displacement field (Eq. 14) is obtained as

$$\begin{Bmatrix} \hat{u}(x,\omega_n) \\ \hat{w}(x,\omega_n) \\ \hat{\psi}(x,\omega_n) \end{Bmatrix} = \begin{bmatrix} R_{11} & R_{12} & R_{13} & R_{14} & R_{15} & R_{16} \\ R_{21} & R_{22} & R_{23} & R_{24} & R_{25} & R_{26} \\ R_{31} & R_{32} & R_{33} & R_{34} & R_{35} & R_{36} \end{bmatrix} \begin{Bmatrix} \tilde{u}_1 e^{-ik_1 x} \\ \tilde{u}_2 e^{-ik_1(l-x)} \\ \tilde{u}_3 e^{-ik_2 x} \\ \tilde{u}_4 e^{-ik_2(l-x)} \\ \tilde{u}_5 e^{-ik_3 x} \\ \tilde{u}_6 e^{-ik_3(l-x)} \end{Bmatrix} \tag{17}$$

where R_{1j}, R_{2j}, and R_{3j} are the amplitude ratios for the three modes of propagation. At nodes 1 ($x = 0$) and 2 ($x = l$), the spectral amplitudes of the nodal displacements $\hat{u}_1 = \hat{u}(0, \omega_n)$, $\hat{w}_1 = \hat{w}(0, \omega_n)$, $\hat{\psi}_1 = \hat{\psi}(0, \omega_n)$, $\hat{u}_2 = \hat{u}(l, \omega_n)$, $\hat{w}_2 = \hat{w}(l, \omega_n)$, and $\hat{\psi}_2 = \hat{\psi}(l, \omega_n)$ of the element of length l are expressed as

$$\hat{\mathbf{u}}_e(\omega_n) = \mathbf{T}_1(\omega_n)\tilde{\mathbf{u}} \tag{18}$$

where

$$\hat{\mathbf{u}}_e = \begin{bmatrix} \hat{u}_1 & \hat{w}_1 & \hat{\psi}_1 & \hat{u}_2 & \hat{w}_2 & \hat{\psi}_2 \end{bmatrix}^T \text{ and } \tilde{\mathbf{u}} = \begin{bmatrix} \tilde{u}_1 & \tilde{u}_2 & \tilde{u}_3 & \tilde{u}_4 & \tilde{u}_5 & \tilde{u}_6 \end{bmatrix}^T.$$

The elements of the matrix $\mathbf{T}_1$ for $j = (1, \ldots 6)$ are given by

$$\begin{aligned} &\mathbf{T}_1(1, j) = R_{1j}\Lambda(0), \mathbf{T}_1(2, j) = R_{2j}\Lambda(0), \mathbf{T}_1(3, j) = R_{3j}\Lambda(0), \\ &\mathbf{T}_1(4, j) = R_{1j}\Lambda(l), \mathbf{T}_1(5, j) = R_{2j}\Lambda(l), \mathbf{T}_1(6, j) = R_{3j}\Lambda(l) \end{aligned} \tag{19}$$

where R_{ij} is the eigenvector matrix [16] and $\Lambda(x)$ is a diagonal matrix containing the exponential terms, $\Lambda(x) = \text{diag}(e^{-ik_1 x}, e^{-ik_1(l-x)}, e^{-ik_2 x}, e^{-ik_2(l-x)}, e^{-ik_3 x}, e^{-ik_3(l-x)})$.

The nodal stress resultants $\left(\hat{N}_1, \hat{Q}_1, \hat{M}_1, \hat{N}_2, \hat{Q}, \hat{M}_2\right)$ corresponding to the natural boundary conditions in Eq. (13) is

$$\hat{\mathbf{F}}_e(\omega_n) = \mathbf{T}_2(\omega_n)\tilde{\mathbf{u}} = \mathbf{T}_2\mathbf{T}_1^{-1}\hat{\mathbf{u}} = \hat{\mathbf{K}}(\omega_n)\hat{\mathbf{u}} \tag{20}$$

where $\hat{\mathbf{F}}_e = \begin{bmatrix} \hat{N}_1 & \hat{Q}_1 & \hat{M}_1 & \hat{N}_2 & \hat{Q}_2 & \hat{M}_2 \end{bmatrix}^T$

The elements of the matrix $\mathbf{T}_2$ for $j = (1, \ldots 6)$ are given by

$$\begin{aligned} &\mathbf{T}_2(1, j) = (\tilde{A}_{11}R_{1j} + \tilde{B}_{11}R_{3j})\Lambda'(0), \quad \mathbf{T}_2(2, j) = A_{55}[R_{2j}\Lambda'(0) + R_{3j}\Lambda(0)], \\ &\mathbf{T}_2(3, j) = (\tilde{B}_{11}R_{1j} + \tilde{D}_{11}R_{3j})\Lambda'(0), \quad \mathbf{T}_2(4, j) = -(\tilde{A}_{11}R_{1j} + \tilde{B}_{11}R_{3j})\Lambda'(l), \\ &\mathbf{T}_2(5, j) = -A_{55}[R_{2j}\Lambda'(l) + R_{3j}\Lambda(l)], \quad (6, j) = -(\tilde{B}_{11}R_{1j} + \tilde{D}_{11}R_{3j})\Lambda'(l) \end{aligned} \tag{21}$$

Here $\hat{\mathbf{K}}(\omega_n)$ is the exact dynamic stiffness matrix of the piezoelectric laminated beam.

3 Results and Discussion

The SFEM developed using Eqs. (4) and (5a, 5b) for ϕ (FSDT-A and FSDT-M, respectively) are employed to perform dispersion, free vibration, and wave propagation analyses of smart composite beams. The results for natural frequencies of a piezoelectric cantilever beam using the present SFEM are compared with the FEM

results [21]. The beam has length $L = 100$ mm and thickness $h = 5$ mm. The material properties are for steel: $E_1 = E_2 = E_3 = 210$ GPa, $G_{12} = G_{23} = G_{13} = 80.77$ GPa, $\nu_{12} = \nu_{13} = \nu_{23} = 0.3$, $\rho = 7850$ kg/m^3 and for PZT G1195 N: $E_1 = E_2 = E_3 = 63$ GPa, $G_{12} = G_{23} = G_{13} = 24.2$ GPa, $\nu_{12} = \nu_{13} = \nu_{23} = 0.3$, $d_{31} = d_{32} = 254\times 10^{-12}$ m/V, $\eta_{11} = \eta_{22} = 1.53 \times 10^{-8}$, $\eta_{33} = 1.5 \times 10^{-8}$ F/m, $\rho = 7600$ kg/m^3. The performance of both the FSDT-based spectral elements is evaluated over a wide range of thickness ratios (h_p/h), which is the ratio of the thickness of the piezoelectric layer to the total beam thickness. Tables 1 and 2 present the natural frequencies in Hertz for different thickness ratios for both open and closed-circuit electrical boundary conditions. The closed-circuit condition is obtained by grounding both the lower and upper surfaces of piezoelectric layer. In open-circuit condition, only the lower surface of the piezoelectric layer is grounded. The comparison shows good agreement with the published results. The free vibration results reveal that the natural frequencies predicted by the conventional FSDT-A show significant deviation from those of the coupled FSDT-M when the thickness ratio is more. This may be because of the predominant induced potential effect. The accuracy of the coupled FSDT-M based SFEM is established from the close agreement of the results with the ANSYS 2D solutions.

To study the effect of material properties of PZT layers, a cantilever composite beam ($L = 600$ mm, $h = 30$ mm) with a surface-bonded piezoelectric layer of PZT 5A and G1195 N is considered (Fig. 2). The material properties of graphite–epoxy composite [0/90/90/0] and piezoelectric layers are

Composite: $E_1 = 181$ GPa, $E_2 = E_3 = 10.3$ GPa, $G_{12} = G_{13} = 7.17$ GPa, $G_{23} = 2.87$ GPa, $\nu_{12} = \nu_{13} = 0.28$, $\nu_{23} = 0.33$, $\rho = 1578$ kg/m^3.

PZT 5A : $E_1 = E_2 = 61$ GPa, $E_3 = 53.2$ GPa, $G_{12} = 22.6$ GPa, $G_{23} = G_{13} = 21.1$ GPa, $\nu_{12} = 0.35$, $\nu_{13} = \nu_{23} = 0.38$, $d_{31} = d_{32} = -171\times 10^{-12}$ m/V, $d_{33} = 374\times 10^{-12}$

Table 1 Comparison of natural frequencies (Hz) of a piezoelectric cantilever beam in open-circuit condition

Thickness ratio (h_p/h)	FSDT-M (present)	FSDT-M [21]	ANSYS 2D [21]	FSDT-A (present)	FSDT-A [21]
0.05	398.87	398.93	399.07	398.87	398.93
0.1	382.69	382.67	382.81	382.69	382.66
0.2	355.84	356.03	356.16	355.84	355.87
0.3	337.52	337.45	337.57	336.91	336.89
0.4	326.54	326.57	326.64	325.01	325.17
0.5	321.96	322.03	322.02	319.21	319.24
0.6	321.35	321.48	321.37	316.47	316.61
0.7	321.35	321.54	321.37	313.72	313.76
0.8	317.69	317.58	317.72	305.79	305.71
0.9	302.43	302.41	302.33	284.42	284.40
1.0	261.54	261.62	261.63	232.24	232.14

Table 2 Comparison of natural frequencies (Hz) of piezoelectric cantilever beam in closed-circuit condition

Thickness ratio	FSDT-M (present)	FSDT-M [21]	ANSYS 2D [21]	FSDT-A (present)	FSDT-A [21]
0.05	396.42	396.36	396.50	396.12	396.36
0.1	377.72	377.49	377.63	377.50	377.47
0.2	345.74	345.71	345.86	345.46	345.55
0.3	322.73	322.65	322.79	321.96	322.06
0.4	308.66	308.62	308.73	307.01	307.13
0.5	302.81	302.86	302.91	299.68	299.88
0.6	303.23	303.30	303.27	298.16	298.13
0.7	306.45	306.53	306.43	298.46	298.35
0.8	307.69	307.59	307.46	295.41	295.31
0.9	298.48	298.43	298.35	280.15	280.17
1.0	261.64	261.62	261.63	232.24	232.14

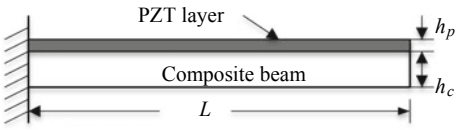

Fig. 2 Cantilever composite beam with a PZT layer at the top

m/V, $d_{15} = d_{24} = 584 \times 10^{-12}$ m/V, $\eta_{11} = \eta_{22} = 1.53 \times 10^{-8}$ F/m, $\eta_{33} = 1.5 \times 10^{-8}$ F/m, $\rho = 7600$ kg/m$^{3.}$

Table 3 compares the first four natural frequencies of cantilever composite beam ($h_p/h = 0.1, 0.5, 1.0$) with two different piezoelectric layers, viz., PZT-5A and G1195 N at the top using both FSDT-A- and FSDT-M-based SFEM. The study of natural frequencies in Table 3 shows that, with increase of thickness ratio, FSDT-A results deviate significantly from those of the coupled FSDT-M for both PZT-5A and G1195 N. These deviations become more significant in case of a beam with PZT G1195 N layer than those for the beam with PZT-5A layer at higher thickness ratios, i.e., 0.5 and 1.0. This is because the modulus induced in PZT G1195 N is more than PZT-5A. At higher modes, the differences in frequencies obtained using FSDT-M and FSDT-A spectral elements are noteworthy. Coupled FSDT-M-based SFEM is used to study free vibration, dispersion, and wave propagation analysis of cantilever composite beams. A four-layered cantilever composite beam with two PZT-5A patches at the top as shown in Fig. 3 is considered. The geometric properties of the beam are $L_1 = 200$ mm, $L_2 = 150$ mm, $L_3 = 200$ mm, $L_\mathrm{p} = 25$ mm, $h_c = 10$ mm, and $h_\mathrm{p} = 1$ mm. Table 4 compares the first four natural frequencies of the beam for three lamination sequences $[0]_4$, [0/90/90/0] and [0/90/0/90].

Next, the dispersion relation, i.e., the variations of the nondimensional wavenumber ($k_i h$) with the frequency is studied. For this, a cantilever steel beam with a piezoelectric layer of G1195 N at the top is considered. The material and geometric

Table 3 Comparison of the first four natural frequencies (Hz) of cantilever composite beam [0/90/90/0] with a piezoelectric layer at the top

Thickness ratio	Mode no.	PZT-5A		PZT G1195 N	
		FSDT-A	FSDT-M	FSDT-A	FSDT-M
0.1	1	104.37	104.37	106.20	106.20
	2	614.62	614.62	623.78	623.78
	3	1577.1	1577.1	1603.4	1603.4
	4	2706.3	2706.3	2729.5	2729.5
0.5	1	57.983	58.594	60.425	61.035
	2	355.84	357.67	370.48	374.76
	3	963.75	966.80	1004.6	1015.0
	4	1738.3	1738.9	1813.9	1815.8
1.0	1	37.842	39.673	38.452	43.335
	2	236.21	245.36	239.87	269.77
	3	649.41	674.44	661.62	741.58
	4	1242.7	1289.1	1267.7	1416.0

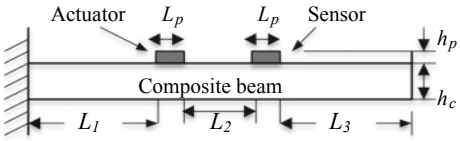

Fig. 3 Cantilever composite beam covered with two PZT patches at the top

Table 4 Comparison of the first four natural frequencies (Hz) of cantilever composite beam with two PZT-5A patches at the top

Mode no.	$[0]_4$	[0/90/90/0]	[0/90/0/90]
1	47.607	44.556	31.738
2	292.36	274.05	198.36
3	801.39	748.29	548.71
4	1574.7	1463.0	1073.0

properties are the same as described in the previous problem. Figure 4 shows the dispersion relations for the asymmetric beam with and without a surface-bonded PZT layer using the FSDT-M. It is noticed that the wavenumbers corresponding to axial (k_1h), flexural (k_2h), and shear rotation (k_3h) modes with piezoelectric layer being more than that of the beam without the piezoelectric layer. Moreover, the wavenumbers of all these modes increase with the increase of thickness of the piezoelectric layer. The cutoff frequency, i.e., the frequency at which the evanescent wave mode (imaginary wavenumbers) changes to propagating wave mode (real wavenumbers), decreases with an increase of thickness ratio.

The FSDT-M-based spectral element is then used for wave propagation in a smart composite beam subjected to modulated tone burst excitations. A graphite–epoxy

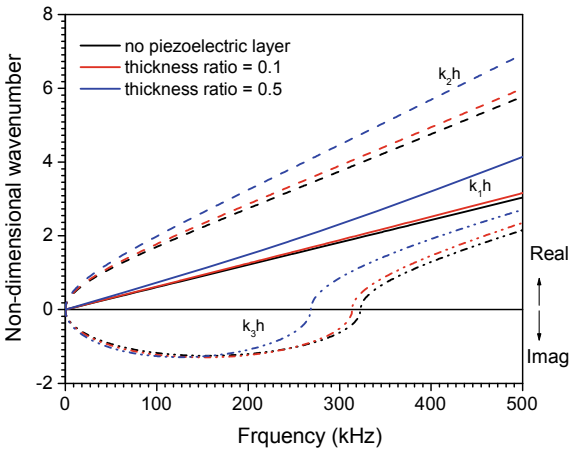

Fig. 4 Dispersion relations with and without PZT layer at the top

composite [0/90/90/0] beam with PZT-5A actuator and sensor (Fig. 3) is considered. The Lamb wave is generated using five-cycle sinusoidal tone burst modulated by Hanning window with center frequency of 100 kHz (Fig. 5). The wave signal of 100 kHz frequency with peak voltage of 200 is applied to the PZT actuator and the response measured at the PZT sensor is shown in Fig. 6. The geometric properties of the beam for this example are $L_1 = 300$ mm, $L_2 = 200$ mm, $L_3 = 300$ mm, $L_p = 5$ mm, $h_c = 5$ mm, and $h_p = 0.5$ mm. The first peak in Fig. 6 is the symmetric S_0 mode and the second peak is the antisymmetric A_0 mode. Symmetric modes are described as extensional or axial modes whereas the antisymmetric modes are described as the flexural modes. The group speed ($C_g = \text{Re}\,[\text{d}\omega_n/\text{d}k_j]$) for the S_0 and A_0 modes at 100 kHz frequency are obtained as 7785.5 m/s and 1702 m/s. The time of arrival of the S_0 and A_0 modes at the sensor found from group speed relation (L_2/C_g) are 26 μs and 118 μs, respectively, which are in good agreement with the times of flight of S_0 and A_0 modes in the wave propagation response (Fig. 6).

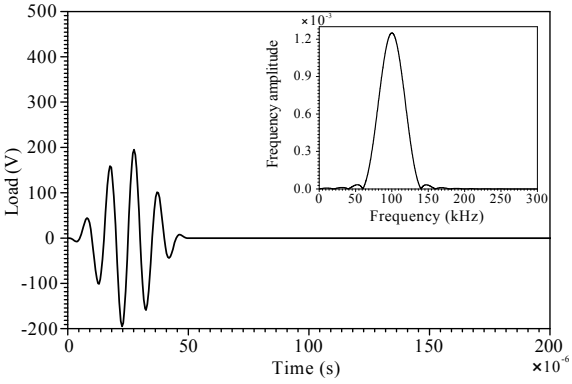

Fig. 5 Tone burst excitation with 100 kHz center frequency (frequency spectrum at the inset)

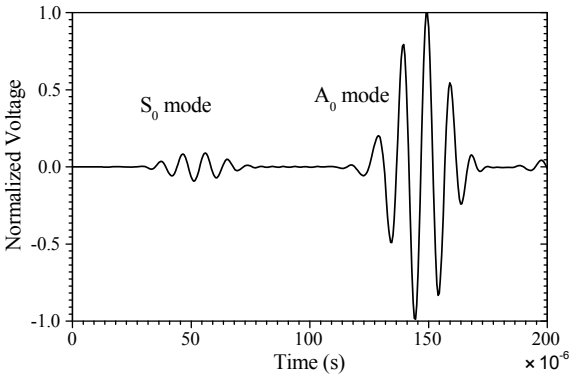

Fig. 6 S_0 and A_0 mode response measured at the PZT sensor

The axial and flexural velocity responses of the same symmetric cross-ply [0/90/90/0] cantilever beam (Fig. 3) due to axial and transverse excitation of 100 kHz frequency with a peak voltage of 200 applied to the PZT actuator are investigated. The beam has $L_1 = 300$ mm, $L_2 = 200$ mm, $L_3 = 500$ mm, $L_p = 5$ mm, $h_c = 5$ mm, and $h_p = 0.5$ mm. The response at a distance of 200 mm from the actuator is plotted. Figures 7 and 8 are the axial and flexural velocity response of the cantilever beam obtained using the developed FSDT-M-based SFEM. The group speed C_g for the axial and flexural modes at 100 kHz frequency are obtained as 7785.5 m/s and 1682 m/s, respectively. The time of arrival of the first peak of the excitation corresponding to axial mode from group speed relation is 26 μs (= 0.2/7785.5). The second and third peaks correspond to the reflection from the left and right boundaries and the time of arrival is obtained as 103 μs and 155 μs, respectively. These values of the time of arrival of axial mode are in perfect agreement with the times of flight in the wave propagation response (Fig. 7). Similarly, the time of flight of the flexural mode in the wave propagation response in Fig. 8 is matching well with the time of arrival obtained from group speed (= 0.2/1682).

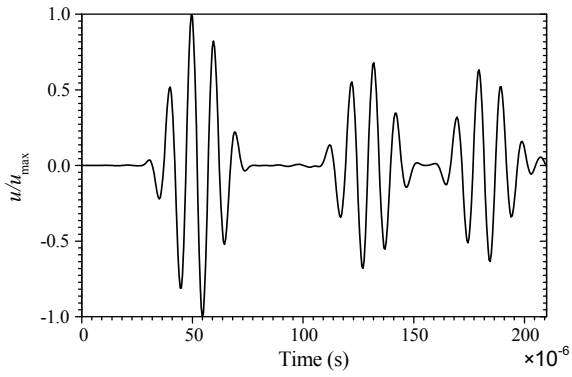

Fig. 7 Axial velocity response due to axial load at the PZT actuator

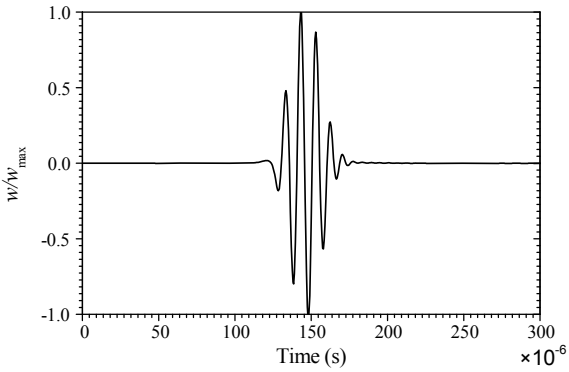

Fig. 8 Transverse velocity response due to transverse load at the PZT actuator

4 Conclusions

This paper presents the frequency-domain spectral finite element method for dispersion, free vibration, and wave propagation analyses of piezoelectric composite beams based on the first-order shear deformation theory. The electric potential distribution through the thickness of the piezoelectric layer is expressed in two ways, i.e., linear and coupled layerwise through thickness potential distribution consistent with the FSDT. The results for natural frequencies for a piezoelectric cantilever beam using the SFEM developed here are compared with the FEM results. The SFEM results using FSDT-A and FSDT-M show large deviation from each other when the piezoelectric layer thickness is increased. This shows the predominant induced potential effect when the thickness ratio is increased. The comparison proved the superiority of the spectral finite element formulation based on coupled layerwise through thickness potential distribution over the conventional linear potential distribution in the piezoelectric layer. Furthermore, the developed spectral element has been used to study the free vibration in composite beams fully and partially covered with PZT layer at the top. The dispersion studies show that at a given frequency, the wavenumbers corresponding to axial, flexural, and shear rotation modes with piezoelectric layer are more than that of the beam without the piezoelectric layer. The cutoff frequency decreases with the increase of thickness ratio. A detailed analysis of wave propagation of composite beams with PZT actuator and sensors is also provided. The times of flight of axial and flexural modes in the wave propagation response are corroborated from the group speeds.

Acknowledgements The author gratefully acknowledges the financial assistance by the Science and Engineering Research Board, Department of Science and Technology, New Delhi, under Start-up grant for Young Scientists.

References

1. Gopalakrishnan S, Chakraborty A, Mahapatra DR (2007) Spectral finite element method. Springer, London
2. Doyle JF (1997) Wave propagation in Structures. Springer, New York
3. Patera AT (1984) Spectral element method for fluid dynamics: laminar flow in a channel expansion. J Comput Phys 54:468–488
4. Peng H, Ye L, Meng G, Mustapha S, Li F (2010) Concise analysis of wave propagation using the spectral element method and identification of delamination in CF/EP composite beams. Smart Mater Struct 19:085018
5. Li F, Peng H, Sun X, Wamg J, Meng G (2012) Wave propagation analysis in composite laminates containing a delamination using a three-dimensional; spectral element method. Math Prob Eng 1:1–19
6. Kudela P, Zak A, Krawczuk M, Ostachowicz W (2007) Modelling of wave propagation in composite plates using the time domain spectral element method. J Sound Vib 302:728–745
7. Zak A, Krawczuk M, Ostachowicz W (2006) Propagation of in-plane elastic waves in a composite panel. Finite Elem Anal Design 43:145–154
8. Doyle JF (1988) A spectrally formulated finite element for longitudinal wave propagation. Int J Anal Exp Modal Anal 3:1–5
9. Doyle JF, Farris TN (1990) A spectrally formulated finite element for flexural wave propagation in beams. Int J Anal Exp Modal Anal 5:13–23
10. Gopalakrishnan S, Martin M, Doyle JF (1992) A matrix methodology for spectral analysis of wave propagation in multiple connected Timoshenko beams. J Sound Vib 158:11–24
11. Lee U, Kim J, Leung AYT (2000) The spectral element method in structural dynamics. The Shock Vib Digest 32:451–465
12. Mahapatra DR, Gopalakrishnan S, Shankar TS (2000) Spectral element based solution for wave propagation analysis of multiply connected unsymmetric laminated composite beams. J Sound Vib 237:819–836
13. Ruotolo R (2004) A spectral element for laminated composite beams: theory and application to pyroshock analysis. J Sound Vib 270:149–169
14. Mitra M, Gopalakrishnan S (2005) Spectrally formulated wavelet finite element for wave propagation and impact force identification in connected 1D waveguides. Int J Solids Struct 42:4695–4721
15. Lee U, Jang I (2010) Spectral element model for axially loaded bending-shear-torsion coupled composite Timoshenko beams. Compos Struct 92:2860–2870
16. Nanda N, Kapuria S, Gopalakrishnan S (2014) Spectral finite element based on an efficient layerwise theory for wave propagation analysis of composite and sandwich beams. J Sound Vib 333:3120–3137
17. Smaratunga D, Jha R, Gopalakrishnan S (2014) Wave propagation analysis in laminated composite plates with transverse cracks using the wavelet spectral finite element method. Finite Elem Anal Des 89:19–32
18. Lee HJ, Saravanos DA (1996) Coupled layerwise analysis of thermopiezoelectric composite beams. AIAA J 34:1231–1237
19. Kapuria S, Alam N (2006) Efficient layerwise finite element model for dynamic analysis of laminated piezoelectric beams. Comput Methods Appl Mech Eng 195:2742–2760
20. Bendary IM, Elshafei MA, Riad AM (2010) Finite element model of smart beams with distributed piezoelectric actuators. J Intell Mater Syst Struct 21:747–758
21. Sulbhewar LN, Raveendranath P (2016) A Timoshenko piezoelectric beam finite element with consistent performance irrespective of geometric and material configurations. Lat Am J Solids Struct 13:992–1015
22. Lee U, Kim D, Park I (2013) Dynamic modeling and analysis of the PZT-bonded composite Timoshenko beams: Spectral element method. J Sound Vib 332:1585–1609
23. Song Y, Kim S, Park I, Lee U (2015) Dynamics of two layer smart composite Timoshenko beams: Frequency domain spectral element analysis. Thin-Walled Struct 89:84–92

Determination of Interlaminar Stress Components in a Pretwisted Composite Strip by VAM

Santosh B. Salunkhe and P. J. Guruprasad

Abstract The interlaminar stress components can cause delamination (separation of laminae), resulting in the failure of material before its elastic limit. Thus, the accurate prediction of the stress components in the composite laminates is vital for the prediction of onset and progress of delamination. Our aim is to analytically arrive at a close approximation solution for interlaminar stress components using recovery relations through 1-D analyses. In this study, the development of an efficient analytical approach to obtain the 3-D elasticity solutions by using recovery relations is achieved. In order to get these stress components accurately, a procedure combining VAM-based framework with approximation method is developed. The approximate method is based upon the stress distribution from more appropriate, sophisticated, and simple polynomials on the equilibrium equation of elasticity. The resulting solution satisfies all the boundary conditions and the compatibility. A parametric study is carried out to understand the nature of 3-D stress components along the thickness of various symmetric, quasi-isotropic, and antisymmetric stacking sequences by this approach. The effectiveness of our approach is demonstrated by comparing the results for interlaminar normal and shear stress components along the interface and through the thickness near free edge under axial strain with those of the available in literature and 3-D FEM for the symmetric, antisymmetric, angle-ply, and cross-ply laminates. This newly described approach shows a good agreement and the computational efficiency. This approach effectively predicts the 3-D stress components with great time-saving.

Keywords Composite beam · Delamination · Interlaminar stresses · Finite element method · Variational asymptotic method

S. B. Salunkhe (✉) · P. J. Guruprasad
Department of Aerospace Engineering, Indian Institute of Technology Bombay, Mumbai 400076, India
e-mail: santosh@aero.iitb.ac.in

P. J. Guruprasad
e-mail: pjguru@aero.iitb.ac.in

B. N. Singh et al. (eds.), *Recent Advances in Theoretical, Applied, Computational and Experimental Mechanics*, Lecture Notes in Mechanical Engineering,
https://doi.org/10.1007/978-981-15-1189-9_8

1 Introduction

The fiber-reinforced laminated composites are widely used in a variety of weight-conscious and high-performance applications, i.e., military, aerospace structures, and much more. The composite provides an added advantage of tailoring the material properties along with good specific strength. The tailoring capabilities of composite material properties can be used to manipulate the structure with required coupling characteristics. However, fiber-reinforced composite laminate show failure modes classified as follows:

1. In-plane fiber fracture and
2. Out of plane
   (a) delamination failure,
   (b) matrix failure, and
   (c) fiber-matrix debonding or fiber splitting.

Usually, these failure initiates at fiber–matrix interface and progresses into delamination process and eventually leads to complete failure. The interlaminar stress components are responsible for delamination resulting in the failure of material before reaching its elastic limit. Therefore, the detailed study of interlaminar stress components for accurate prediction of the structural behavior and the progressive delamination under the influence of continued loading is mandatory.

In case of analytical, semi-analytical and numerical studies, over the last few decades, researchers have practiced many techniques to estimate the stress components at free edges. The complete review is available in the review articles by Kant et al. [1], Wang et al. [2], Sen et al. [3] and Mittelstaedt et al. [4]. In particular, the methods can be divided into the following: perturbation method by Hsu et al. [5], boundary layer theory by Tang et al. [6], higher order plate theory by Pagano [7], and Whitney et al. [8], layerwise theory by Noiser et al. [9], interlaminar shear stress continuity theory by Liu [10], variational approach by Yin [11], global local model by Pagano [7] and Whitney et al. [8], Galerkin's method by Wang et al. [12], and approximate elasticity solution by Kim et al. [13] and Puppo et al. [14].

Hayashi [15] was the first researcher who estimated the interlaminar stress components in angle-ply laminates under axial tension by the analytical approach. Further, a similar type of analysis on $[45/-45]_s$ glass–epoxy laminates has been done by Puppo et al. [14]. The pioneering work at the numerical level has done by Pipes et al. [16] in 1970. Further, significant scientific work has been done by R. B. Pipes and his co-worker in the modeling and analyses of the free edge effects correctly and their many papers concerning to the free edge effect are available.

Pipes et al. [17] have used finite difference method in order to solve a coupled second-order partial differential equilibrium equation for a laminate with tensile loading and traction free boundary conditions. During his study, he observed that the interlaminar shear stress grows rapidly near the free edge which is "approxi-

mately one laminate thickness from the free edge of width". It is often known as the "boundary layer effect" or "free edge effect". It was also showed that the mismatch of shear coupling coefficients between the two adjacent plies is responsible for soaring in an interlaminar shear stress in the angle-ply laminate. Later, several researchers have used these results as a reference result for validation. Further, Pagano [18] solved for cross-ply $[0/90]_s$ laminate by using the analytical solution. He showed that the interlaminar normal stress σ_{33} is increasing near the free edge and it can cause delamination for cross-ply laminate. Similarly, Wang et al. [2] also used to solve cross-ply $[0/90]_s$ and $[90/0]_s$ laminates by using finite element method. In the same paper, they used $[90/0/45/-45]_s$ laminate which is a combination of angle-ply and cross-ply laminate for understanding the behavior of σ_{33} near free edges. For same geometric and material properties, they observed that the stacking sequence $[45/-45/0/90]_s$ and $[90/0/45/-45]_s$ gives tension and compression through the thickness, respectively, for the axial extension. Further, through the experiments, they observed that the laminate $[45/-45/0/90]_s$ stacking sequence undergoes delamination in the midplane, while laminate $[90/0/45/-45]_s$ stacking sequence did not delaminate. Next, Makeev et al. [19] developed an iterative method for the one-term approximate solution of partial differential equations. This approach can be applied to several boundary value problems.

From literature, it is observed that some of the researchers solved angle-ply laminate ($[45/-45]_s$), some of them used cross-ply laminate ($[90/0]_s$ or $[0/90]_s$), and some of them solved quasi-isotropic ($[90/0/45/-45]_s$) laminate. Further, some of the researchers used analytical solution and some of them used finite element method while some of them used finite difference method. However, which method is a best fit for the assessment of a given mechanical problem including free edge effects in the laminate structures cannot be answered universally and priorly. It further appears through literature that the results obtained from various approaches have shown some of the similarity, but in some cases, discrepancies were also observed. These discrepancies do exist in sign as well as in the magnitude of the interlaminar stresses. As a requirement, an analysis method should be in good agreement between the possible correctness and computational expense. There are very few methods available which gives closed-form solution by using recovery relation to get interlaminar stress components and satisfy the above requirements. Nonetheless, there are challenging opportunities, for predicting the interlaminar stress components accurately and efficiently.

Following the above motive, a new analytical methodology is used by the author. The present method gives a closed-form solution by using recovery relation. The proposed approach is a combination of the VAM and the approximation method. We know that VAM is the powerful mathematical tool to address the linear as well as nonlinear challenges in beam modeling. Berdichevskii [20] was the first researcher who used VAM for modeling shell structure, by simplifying the original 3-D problem to a 1-D problem by sustaining strain energy. The final results from this approach

include linear as well as nonlinear stiffness terms. Further, this theory was developed and much work has been done by Hodges and his co-workers [21–24]. Next, the approximation approach used in this paper is based on an assumed stress distribution derived from more sophisticated solution and on the equilibrium equations of elasticity. This method involves the use of polynomial, and it is an extension of Pagano and Pipes approach. Further, the precision of the method is examined by correlating the present results, wherever possible, with the data available in the literature and the 3-D FEM. Finally, the method is used to study the thickness-wise 3-D stress behavior of pretwisted, antisymmetric, symmetric, quasi-isotropic, and crossed ply laminated strip. In particular, the proposed approach can provide a correct 3-D elasticity solution for any laminated composite strip through 1-D analysis in a computationally efficient manner.

2 Mathematical Formulation

In the first part of this section, VAM is employed to develop reduced-order 1D strip-like model. In the latter part of the section, the approximation method is employed to obtain out of plane stresses.

2.1 Strip Kinematics and Formulation

A three-dimensional structural problem can be reduced to a 1D problem by considering the relative ratios of their three dimensions. Regarding this, the VAM is a unique synergy to bring the traditional asymptotic and variational formulations without any ad hoc assumption. An asymptotic formulation is based on the existence of small parameters. In the strip, thickness-to-width and width-to-length ratios are minimal. The correct 3D energy of the strip can be found by asymptotically expanding these small parameters. Further, the variational method is adopted. Here, one should note that the terms of the energy functional are dropped off at an energy level, not at the strain displacement relation level. The detailed procedure and formulation can be found in [24–28]. This exercise is shortly explained here for completeness and also gives some insight into the VAM theoretical foundation. The geometry of the strip is shown in Fig. 1. Here and throughout the paper, Greek indices assume values 2 and 3, and Latin indices assume 1, 2, and 3. Repeated indices are summed over their range except where explicitly indicated. From the general formulas, one can write the nonlinear three-dimensional strain field for delaminated strip as

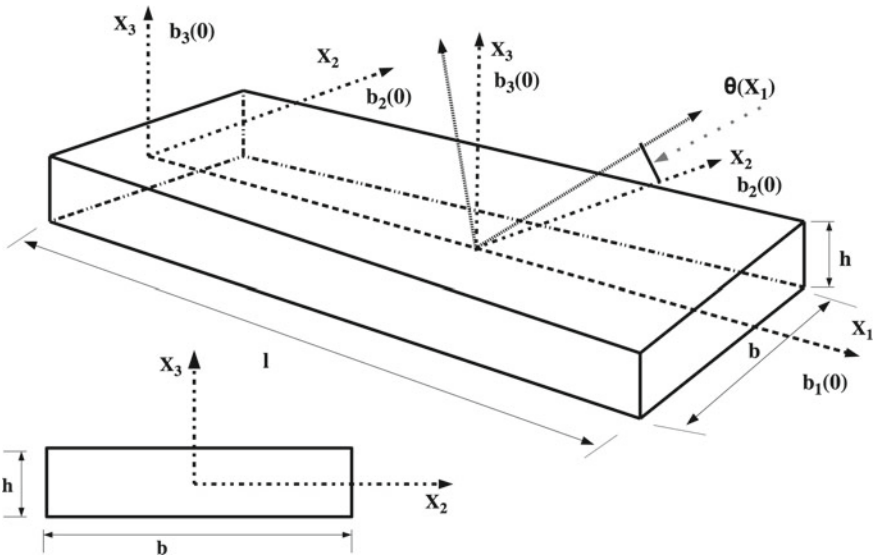

Fig. 1 Pretwisted strip configuration

$$
\begin{aligned}
\Gamma_{11} &= \underbrace{\gamma_{11} - x_2\kappa_3 + x_3\kappa_2}_{O(\epsilon)} + \overbrace{k_1 x_2^2 \kappa_1}^{O\left(\frac{\epsilon\delta_t}{\delta_h}\right)} + \underbrace{\frac{x_2^2\kappa_1^2}{2} + w_3^{(1)}\kappa_2}_{O\left(\frac{\epsilon^2}{\delta_h^2}\right)} + O\left(\epsilon\delta_b, \epsilon\delta_t, \frac{\epsilon^2}{\delta_h}\right) \\
\Gamma_{22} &= \underbrace{w_{2,2}^{(1)} - x_3 w_{3,22}^{(1)}}_{O(\epsilon)} + \overbrace{\frac{1}{2} w_{3,2}^{(1)^2}}^{O\left(\frac{\epsilon^2}{\delta_h^2}\right)} + O(\epsilon\delta_h) \\
2\Gamma_{12} &= \underbrace{w_1^{(1)} - 2x_3\kappa_1}_{O(\epsilon)} + \overbrace{k_1\left(x_2 w_{3,2}^{(1)} - w_3^{(1)}\right)}^{O\left(\frac{\epsilon\delta_t}{\delta_h}\right)} + \underbrace{\kappa_1\left(x_2 w_{3,2}^{(1)} - w_3^{(1)}\right)}_{O\left(\frac{\epsilon^2}{\delta_h^2}\right)} \\
&\quad + O\left(\epsilon\delta_b, \epsilon\delta_h, \epsilon\delta_t, \frac{\epsilon^2}{\delta_h}\right)
\end{aligned}
\tag{1}
$$

The 2D strain measures can be extracted from the 3D strain measures by using the relation $\Gamma_{\alpha\beta} = \epsilon_{\alpha\beta} + x_3\rho_{\alpha\beta}$, where $\epsilon_{\alpha\beta}$ are the middle surface membrane strains and $\rho_{\alpha\beta}$ are the middle surface. The expressions for membrane strains, which are obtained by inspection of Eq. (1) are bending curvatures.

$$\begin{aligned}
\epsilon_{11} &\approx \gamma_{11} - x_2\kappa_3 + k_1 x_2^2 \kappa_1 + \underline{\frac{x_2^2\kappa_1^2}{2}} + \underline{w_3\kappa_2} \\
\epsilon_{22} &\approx w_{2,2} + \underline{\tfrac{1}{2}{w_{3,2}}^2} \\
2\,\epsilon_{12} &\approx w_{1,2} + \underline{k_1\left(x_2 w_{3,2} - w_3\right)} + \underline{\kappa_1\left(x_2 w_{3,2} - w_3\right)}
\end{aligned}$$

while 2-D curvatures are:

$$\begin{aligned}
\rho_{11} &\approx \kappa_2 \\
\rho_{22} &\approx -w_{3,22} \\
2\,\rho_{12} &\approx -2\kappa_1
\end{aligned} \tag{2}$$

To receive the zeroth-order 2D strain energy density through VAM, use the non-underlined terms from the above equation in energy functional and integrate over the thickness. Thus, one can get zeroth-order approximation. Similarly, to get first-order approximation consider the complete above equation, i.e., admit underlined term. The 2D strain energy density can be expressed as

$$U_{2D} = \frac{1}{2}\left\{\,\epsilon_{11}\ \epsilon_{22}\ 2\epsilon_{12}\ \rho_{11}\ \rho_{22}\ 2\rho_{12}\,\right\} \cdot \begin{bmatrix} A & B \\ B & D \end{bmatrix} \cdot \begin{Bmatrix} \epsilon_{11} \\ \epsilon_{22} \\ 2\epsilon_{12} \\ \rho_{11} \\ \rho_{22} \\ 2\rho_{12} \end{Bmatrix} \tag{3}$$

where the A, B, and D terms in the strain energy represents membrane, bending and coupling stiffness matrices, respectively. Following the procedure of minimization by using variational minimization principle and after integrating U_{2D} along the width direction, the 1-D strain energy, U_{1D}, can be expressed in terms of the linear and nonlinear 1-D strain measures as,

$$U_{1D} = \frac{1}{2}\epsilon_L^T[S_L]\epsilon_L + \epsilon_L^T[S_{LN}]\epsilon_N + \frac{1}{2}\epsilon_N^T[S_N]\epsilon_N \tag{4}$$

where $[S_L]$ is linear, $[S_{LN}]$ linear–nonlinear, and $[S_N]$ nonlinear stiffness matrix. The terms of these stiffnesses are given in Appendices and ϵ_L is linear and ϵ_N nonlinear strain measures which are defined as follows:

$$\begin{aligned}
\epsilon_L &= \{\gamma_{11}, \kappa_1, \kappa_2, \kappa_3\}^T \\
\epsilon_N &= \{\kappa_1^2, \kappa_2^2, \kappa_2\gamma_{11}, \kappa_2\kappa_3, \kappa_2\kappa_1\}^T
\end{aligned}$$

and the matrices $[S_L]$, $[S_{LN}]$, and $[S_N]$ can be thought of as partitions of a 9×9 matrix [S]. The terms of the linear and nonlinear stiffness matrices are presented in [27]. The term γ_1, κ_1, κ_2 and κ_3 represents the one-dimensional generalized strains associated with extension, torsion, and bending.

2.2 Recovery of 3-D Stress Components

VAM is used to develop reduced-order 1-D strip-like model. Further, based on the theory, a finite element formulation is generated for the structural analysis, where the linear and nonlinear cross-sectional stiffnesses derived from VAM serves as the input. After solving the differential equations by finite element method, we have a solution for 1-D displacement. From this, one can obtain the 1-D generalized strain measures through the nonlinear beam constitutive law. Knowing the 1-D strains and curvatures from which one can obtain the warping solutions. Further, 2-D strain field can be obtained using the already established kinematics. Now, the plane stress field can be obtained using the plane stress reduced transformed stiffness matrix which depends on the ply orientation. Expressions for the in-plane stress components are given below:

$$\begin{aligned}
\sigma_{11} &= \mathrm{Q}_{11}\Gamma_{11} + \mathrm{Q}_{12}\Gamma_{22} + \mathrm{Q}_{13}2\Gamma_{12};\\
\sigma_{22} &= \mathrm{Q}_{12}\Gamma_{11} + \mathrm{Q}_{22}\Gamma_{22} + \mathrm{Q}_{23}2\Gamma_{12};\\
\tau_{12} &= \mathrm{Q}_{13}\Gamma_{11} + \mathrm{Q}_{23}\Gamma_{22} + \mathrm{Q}_{33}2\Gamma_{12}
\end{aligned} \tag{5}$$

The $\Gamma_{\alpha\beta}$ are related to 3-D strain measures which can be simplified in 2-D strain measures by $\Gamma_{\alpha\beta} = \epsilon_{\alpha\beta} + x_3\rho_{\alpha\beta}$. The $Q_{\alpha\beta}$ represents transformed reduced stiffness matrix. Here and throughout the paper, Latin indices run from 1 to 3 while Greek indices run from 1 to 2; repeated indices are summed up over their ranges. This expression can be simplified for zeroth order is as

$$\begin{aligned}
\sigma_{11} &= \mathrm{Q}_{11}\Big(\gamma_{11} + \kappa_1 k_1 x_2^2 + \kappa_2 x_3 - \kappa_3 x_2\Big) + \mathrm{Q}_{12}\Big(w^0_{2,2} - w^0_{3,22}x_3\Big)\\
&\quad + \mathrm{Q}_{13}\Big(k_1(w^0_{3,2}x_2 - w^0_3) + w^0_{1,2} - 2\kappa_1 x_3\Big);\\
\sigma_{22} &= \mathrm{Q}_{12}\Big(\gamma_{11} + \kappa_1 k_1 x_2^2 + \kappa_2 x_3 - \kappa_3 x_2\Big) + \mathrm{Q}_{22}\Big(w^0_{2,2} - w^0_{3,22}x_3\Big)\\
&\quad + \mathrm{Q}_{23}\Big(k_1(w^0_{3,2}y - w^0_3) + w^0_{1,2} - 2\kappa_1 x_3\Big);\\
\tau_{12} &= \mathrm{Q}_{13}\Big(\gamma_{11} + \kappa_1 k_1 x_2^2 + \kappa_2 x_3 - \kappa_3 x_2\Big) + \mathrm{Q}_{23}\Big(w^0_{2,2} - w^0_{3,22}x_3\Big)\\
&\quad + \mathrm{Q}_{33}\Big(k_1(w^0_{3,2}y - w^0_3) + w^0_{1,2} - 2\kappa_1 x_3\Big)
\end{aligned} \tag{6}$$

Similarly, the expressions for the first-order stress are given below:

$$\sigma_{11} = \mathrm{Q}_{11}\left(\gamma_{11} + \kappa_1 k_1 x_2^2 + \kappa_2 w_3^I + \kappa_2 x_3 + \frac{1}{2}\kappa_1^2 x_2^2 - \kappa_3 x_2\right) + \mathrm{Q}_{12}\left(w_{2,2}^I + 0.5(w_{3,2}^I)^2 - w_{3,22}^I x_3\right) + \mathrm{Q}_{13}\left(k_1(w_{32}^I x_2 - w_3^I) + w_{12}^I + \kappa_1(w_{3,2}^I x_2 - w_3^I) - 2\kappa_1 x_3\right);$$

$$\sigma_{22} = \mathrm{Q}_{12}\left(\gamma_{11} + \kappa_1 k_1 x_2^2 + \kappa_2 w_3^I + \kappa_2 x_3 + \frac{1}{2}\kappa_1^2 x_2^2 - \kappa_3 x_2\right) + \mathrm{Q}_{22}\left(w_{2,2}^I + 0.5(w_{3,2}^I)^2 - w_{3,22}^I x_3\right) + \mathrm{Q}_{23}\left(k_1(w_{32}^I x_2 - w_3^I) + w_{12}^I + \kappa_1(w_{3,2}^I x_2 - w_3^I) - 2\kappa_1 x_3\right);$$

$$\tau_{12} = \mathrm{Q}_{13}\left(\gamma_{11} + \kappa_1 k_1 x_2^2 + \kappa_2 w_3^I + \kappa_2 x_3 + \frac{1}{2}\kappa_1^2 x_2^2 - \kappa_3 x_2\right) + \mathrm{Q}_{23}\left(w_{2,2}^I + 0.5(w_{3,2}^I)^2 - w_{3,22}^I x_3\right) + \mathrm{Q}_{33}\left(k_1(w_{32}^I x_2 - w_3^I) + w_{12}^I + \kappa_1(w_{3,2}^I x_2 - w_3^I) - 2\kappa_1 x_3\right) \tag{7}$$

The warping terms w_i, $w_{i,2}$, $w_{3,22}$ used above are for healthy case available in paper of [24]. The superscript 0 and I above the warping terms represents the zeroth and the first-order approximation, respectively. For a case of in-plane loading, however, the present theory produces only in-plane stress components. These values from the variational asymptotic method are shown in Fig. 2. Results are compared with the 3-D finite element result. It shows that results are accurate for interior regions removed from free edges. However, discrepancies at the free edge are due to the following issues:

- In strain energy, the strain terms are restricted to the zeroth and the first-order approximation.
- Procedure of the dimensional reduction adopted in this work is based on the 2-D strain energy functional as a starting point. It will be reduced to 1-D strain energy functional through VAM. It makes ad hoc assumption of the line originally normal to the midplane remains normal even after deformation.

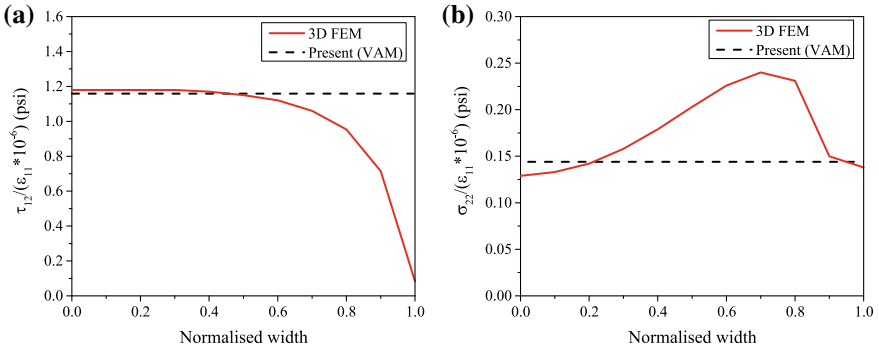

Fig. 2 **a** Variation of (**a**) τ_{12} and **b** σ_{22} in the interface along the width of laminate and comparison between the results of present approach by using VAM and the 3-D finite element method

These issues can be resolved by considering the 3-D strain energy functional as a starting point and through asymptotically correct dimensional reduction procedure using VAM. By this process, a 3-D problem is reduced to a 1-D beam problem and the constitutive law associated with the warping fields is obtained. For primary study, the goal was set to develop an analytical solution based on 1-D, which can produce accurate 3-D elasticity solution with less computational time. By using present VAM approach, it is not possible to get interlaminar shear stress components. To estimate these components near the free edges, approximation method which is based on global 3-D equilibrium equations is used, which is mentioned in next subsection.

2.3 The Approximation Method

This method is based on assumed stress distribution from more sophisticated solutions and equilibrium equation of elasticity, and it is an extension of the approach of Pagano and Pipes [29]. In this method involve the use of polynomial for one laminate thickness from free edge, and constants of the polynomials are determined from interface continuity or by traction free conditions. A midplane coordinate system is considered at the free edge. Due to symmetry and antisymmetry of the stress components, only half portion of the width of laminate is considered. Now, we assume [29] the shear stress τ_{12} has following distribution along the width:

$$\begin{aligned} \tau_{12}^k &= \left(A_1 x_2 + A_2 x_2^2\right) \sigma_0 Q_0^k, \; 0 \le x_2 \le h \\ \tau_{12}^k &= \sigma_0 Q_0^k, \qquad\qquad\qquad\quad h \le x_2 \le b \end{aligned} \tag{8}$$

In Eq. 8, $\sigma_0 Q_0^k$ denotes the value of τ_{12} in the kth ply as determined from the VAM-based 1-D theory. Here, k represents the layer number; A_1 and A_2 represent constants. To solve the stress components in free edge boundary layer, we use the equilibrium equation without considering the body forces.

$$\frac{\partial \sigma_{11}^k}{\partial x_1} + \frac{\partial \tau_{12}^k}{\partial x_2} + \frac{\partial \tau_{13}^k}{\partial x_3} = 0 \tag{9}$$

For uniaxial loading, the axial stress is independent of x_1, then equilibrium equation becomes

$$\frac{\partial \tau_{12}^k}{\partial x_2} + \frac{\partial \tau_{13}^k}{\partial x_3} = 0 \tag{10}$$

substituting Eq. 8 into Eq. 10

$$\frac{\partial \tau_{13}^k}{\partial x_3} = -\sigma_0 \left(A_1 + 2A_2 x_2\right) Q_0^k \tag{11}$$

After integration

$$\tau_{13}^{k} = -\sigma_0 \left(A_1 + 2A_2 x_2\right) \left(h Q_1^k + x_3 Q_0^k\right) \tag{12}$$

since τ_{12} is constant within each ply. The value of hQ_1^k is determined by the requirement that τ_{13} vanish on the top or bottom of the surface. By following the boundary conditions, the value of constants A_1 and A_2 are determined.

$$\begin{aligned} \tau_{12}^{k}(h, x_3) &= \sigma_0 Q_0^k \\ \tau_{13}^{k}(h, x_3) &= 0 \end{aligned} \tag{13}$$

The value of constants are $A_1 = 2/h$ and $A_2 = -1/h^2$. Now the complete equation can be written is as

$$\begin{aligned} \tau_{12}^{k} &= \frac{x_2}{h}\left(2 - \frac{x_2}{h}\right)\sigma_0 Q_0^k, && 0 \le x_2 \le h \\ \tau_{12}^{k} &= \sigma_0 Q_0^k, && h \le x_2 \le b \end{aligned} \tag{14}$$

$$\begin{aligned} \tau_{13}^{k} &= \left(\frac{x_2}{h} - 1\right)\Gamma_{13}^{k}, && 0 \le x_2 \le h \\ \tau_{13}^{k} &= 0, && h \le x_2 \le b \end{aligned} \tag{15}$$

In the above equation

$$\Gamma_{13}^{k} = 2\sigma_0 \left(\frac{x_3 Q_0^k}{h} + Q_1^k\right) \tag{16}$$

Similarly, for σ_{22} following distribution has been assumed:

$$\begin{aligned} \sigma_{22}^{k} &= \sigma_0 P_0^k F(x_2), && 0 \le x_2 \le h \\ \sigma_{22}^{k} &= \sigma_0 P_0^k, && h \le x_2 \le b \end{aligned} \tag{17}$$

where $\sigma_0 P_0^k$ is determined from the VAM-based 1-D theory, and F is variable along the free edge. To solve these stresses in the free edge boundary layer, we use the second equilibrium equation.

$$\frac{\partial \tau_{12}^{k}}{\partial x_1} + \frac{\partial \sigma_{22}^{k}}{\partial x_2} + \frac{\partial \tau_{23}^{k}}{\partial x_3} = 0 \tag{18}$$

As we know, τ_{12} is independent of x_1. Then Eq. 18 become

$$\frac{\partial \sigma_{22}^{k}}{\partial x_2} + \frac{\partial \tau_{23}^{k}}{\partial x_3} = 0 \tag{19}$$

Substituting Eq. 17 into Eq. 19

$$\frac{\partial \tau_{23}^{k}}{\partial x_3} = -\sigma_0 P_0^k \frac{dF}{dx_2} \tag{20}$$

Integrating along the thickness (x_3),

$$\tau_{23}^k = -\sigma_0 \left(P_1^k h + x_3 P_0^k\right) \frac{dF}{dx_2} \tag{21}$$

In Eq. 21, value of $P_1^k h$ is determined by interface continuity conditions or the requirement that τ_{23} vanish on the laminate surface.

The third equilibrium equation is as

$$\frac{\partial \tau_{13}^k}{\partial x_1} + \frac{\partial \tau_{23}^k}{\partial x_2} + \frac{\partial \sigma_{33}^k}{\partial x_3} = 0 \tag{22}$$

With τ_{13} being independent along the length, Eq. 22 becomes

$$\frac{\partial \tau_{23}^k}{\partial x_2} + \frac{\partial \sigma_{33}^k}{\partial x_3} = 0 \tag{23}$$

Differentiating Eq. 21 with respect to x_2 and substituting

$$\frac{\partial \sigma_{33}^k}{\partial x_3} = \sigma_0 (P_1^k h + x_3 P_0^k) \frac{d^2 F}{dx_2^2} \tag{24}$$

Integrating the above equation

$$\sigma_{33}^k = \sigma_0 \left(P_2^k h^2 + P_1^k h x_3 + \frac{P_0^k}{2} x_3^2\right) \frac{d^2 F}{dx_2^2} \tag{25}$$

The value of $P_2^k h^2$ is determined by the requirements that σ_{33} vanish on the top or bottom of the surfaces. Similarly, we can find σ_{33}

$$\begin{aligned} \sigma_{33}^k &= \left[1 - 3(1+C)\frac{x_2}{h}\right] \tilde{\sigma}_{33}^k, && 0 \le x_2 \le \frac{h}{3} \\ \sigma_{33}^k &= -C\tilde{\sigma}_{33}^k, && \frac{h}{3} \le x_2 \le h \\ \sigma_{33}^k &= 0, && h \le x_2 \le b \end{aligned} \tag{26}$$

In the above equation

$$\tilde{\sigma}_{33}^k = K\sigma_0 \left(P_2^k + P_1^k \frac{x_3}{h} + P_0^k \frac{x_3^2}{2h^2}\right) \tag{27}$$

and C and K are constants. The σ_{33} produces the moment and the stress distribution of Eq. 26 must be self-equilibrating,

$$\int_0^h \sigma_{33}^k \, dx_2 = 0 \tag{28}$$

Substituting Eq. 26 into this integral yields and performing this integration gives the value of $C = \frac{1}{5}$ and Eq. 26 becomes

$$\begin{aligned}
\sigma_{33}^k &= \frac{1}{5}\left(5 - 18\frac{x_2}{h}\right)\tilde{\sigma}_{33}^k, && 0 \le x_2 \le \frac{h}{3} \\
\sigma_{33}^k &= \frac{\tilde{\sigma}_{33}^k}{5}, && \frac{h}{3} \le x_2 \le h \\
\sigma_{33}^k &= 0, && h \le x_2 \le b
\end{aligned} \tag{29}$$

Comparing Eq. 25 with Eq. 29 it is easily seen that

$$\begin{aligned}
\frac{d^2F}{dx_2^2} &= \frac{K}{5h^2}\left(5 - 18\frac{x_2}{h}\right) && 0 \le x_2 \le \frac{h}{3} \\
\frac{d^2F}{dx_2^2} &= \frac{-K}{5h^2} && \frac{h}{3} \le x_2 \le h
\end{aligned} \tag{30}$$

Integration yields

$$\begin{aligned}
\frac{dF}{dx_2} &= \frac{Kx_2}{5h^2}\left(5 - 9\frac{x_2}{h}\right) + Ka_0 && 0 \le x_2 \le \frac{h}{3} \\
\frac{dF}{dx_2} &= \frac{-Kx_2}{5h^2} + Ka_1 && \frac{h}{3} \le x_2 \le h
\end{aligned} \tag{31}$$

Substituting for in Eq. 21, we get

$$\begin{aligned}
\tau_{23}^k &= \frac{-K\sigma_0}{h}\left(P_1^k h + P_0^k x_3\right)\left[\frac{x_2}{5h}\left(5 - 9\frac{x_2}{h}\right) + a_0 h\right], && 0 \le x_2 \le \frac{h}{3} \\
\tau_{23}^k &= \frac{K\sigma_0}{h}\left(P_1^k h + P_0^k x_3\right)\left(\frac{x_2}{5h} - a_1 h\right), && \frac{h}{3} \le x_2 \le h \\
\tau_{23}^k &= 0, && h \le x_2 \le b
\end{aligned} \tag{32}$$

Since τ_{23}^k is a free edge stress, it must vanish at $x_2 = 0$. Thus, $a_0 = 0$. The constant a_1 is determined from continuity at $x_2 = h/3$, with the result $a_1 = \frac{1}{5h}$ and Eq. 32 becomes

$$\begin{aligned}
\tau_{23}^k &= \frac{36}{25}\left(5 - \frac{9x_2}{h}\right)\Gamma_{23}^k\frac{x_2}{h}, && 0 \le x_2 \le \frac{h}{3} \\
\tau_{23}^k &= \frac{36}{25}\left(1 - \frac{x_2}{h}\right)\Gamma_{23}^k, && \frac{h}{3} \le x_2 \le h \\
\tau_{23}^k &= 0, && h \le x_2 \le b
\end{aligned} \tag{33}$$

In the above equation

$$\Gamma_{23}^{k} = -\frac{5}{36}\sigma_0 K\left(P_1^k + \frac{x_3}{h}P_1^k\right) \tag{34}$$

Integrating Eq. 31, we get

$$\begin{aligned} F &= K\left(\frac{x_2^2}{2h^2} - \frac{3x_2^3}{5h^3} + b_0\right) \qquad 0 \le x_2 \le \frac{h}{3} \\ F &= K\left(\frac{x_2}{5h} - \frac{x_2^2}{10h^2} + b_1\right) \qquad \frac{h}{3} \le x_2 \le h \end{aligned} \tag{35}$$

Substituting these results in Eq. 19

$$\begin{aligned} \sigma_{22}^{k} &= K\sigma_0 P_0^k\left[\frac{x_2^2}{h^2}\left(\frac{1}{2} - \frac{3x_2}{5h}\right) + b_0\right] \qquad 0 \le x_2 \le \frac{h}{3} \\ \sigma_{22}^{k} &= K\sigma_0 P_0^k\left[\frac{x_2}{h}\left(\frac{1}{5} - \frac{x_2}{10h}\right) + b_1\right] \qquad \frac{h}{3} \le x_2 \le h \\ \sigma_{22}^{k} &= \sigma_0 P_0^k, \qquad h \le x_2 \le b \end{aligned} \tag{36}$$

Since σ_{22}^{k} is a free edge stress, it must vanish at $x_2 = 0$. Thus, $b_0 = 0$. The constants b_1 is determined from continuity condition at $y = \frac{h}{3}$, with the result

$$b_1 = \frac{1}{45} \tag{37}$$

Now, K is determined from continuity condition at $y = h$, with the result

$$K = \frac{90}{7} \tag{38}$$

Now, Eq. 19 becomes

$$\begin{aligned} \sigma_{22}^{k} &= \frac{9}{7}\left(5 - 6\frac{x_2}{h}\right)P_0^k\frac{x_2^2}{h^2}, & 0 \le x_2 \le \frac{h}{3} \\ \sigma_{22}^{k} &= -\frac{1}{7}\left(9\frac{x_2^2}{h^2} - 18\frac{x_2}{h} + 2\right)\sigma_0 P_0^k, & \frac{h}{3} \le x_2 \le h \\ \sigma_{22}^{k} &= \sigma_0 P_0^k, & h \le x_2 \le b \end{aligned} \tag{39}$$

By keeping value of K, Eqs. 27 and 34 become

$$\tilde{\sigma}_{33}^{k} = \frac{90}{7}\sigma_0 \left(P_2^k + P_1^k \frac{x_3}{h} + P_0^k \frac{x_3^2}{2h^2} \right) \tag{40}$$

$$\Gamma_{23}^{k} = -\frac{25}{14} \left(P_1^k + \frac{x_3}{h} P_0^k \right) \sigma_0 \tag{41}$$

3 Results and Discussion

This section begins with the validation of the proposed modeling approach for interlaminar stress components. The geometric and material properties corresponding to each case against which the present method has been compared are given in Table 1. The geometric representation of laminate structure has been shown in Fig. 3. The method is then extended for the pretwisted, antisymmetric, or symmetric laminated composite strip of solid cross section. All the results are for thin laminated composite strip subjected to uniform axial extension. Moreover, these results are an average

Table 1 Aterial and geometric properties

Materials	E_{11} (GPa)	E_{22} (GPa)	G_{12} (GPa)	G_{23} (GPa)	ν_{12}	$\rho\ (kg/m^3)$	l (m)	b (m)	T/ply (m)
Graphite–epoxy [16]	137.9	14.48	5.86	5.86	0.21	1520	2	0.04	0.0025
Glass–epoxy [30]	44.1	12.4	4.46	3.40	0.29	1520	0.254	0.026	0.000075
Graphite–epoxy [9]	132	10.8	5.65	4.40	0.24	1520	2	0.08	0.0013

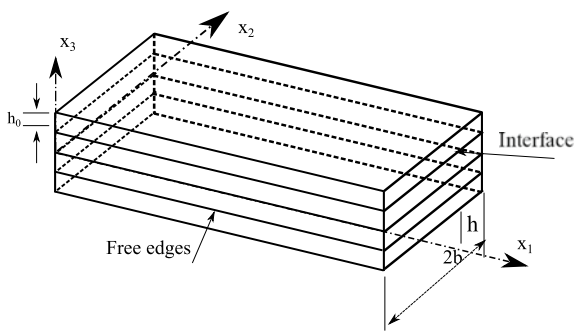

Fig. 3 The geometry and nomenclature of 3-D laminate

value calculated from the gauss points located near to the interface. The discussion is for all the stress components through the thickness of few laminates. At the end of section, the results are summarized.

3.1 Verification and Validation

In this section, many interlaminar stress components and in-plane stress components results have been compared with the literature to evaluate the performance of the present method. The results are for through the thickness near to the free edge and at the interface of the composite laminate. Specifically, the results are compared with Pipes et al. [16] for the symmetric angle-ply laminate, Wang et al. [2] for cross-ply and quasi-isotropic laminate under the axial extension.

In Fig. 4a, the behavior of all 3-D stress components along the width at interface between 45° and −45° for a graphite–epoxy laminate are shown. The material and geometric properties are given in the first row of Table 1. These geometrical and material properties are same as that of Ref. [16]. It is observed from the figure that the values and the trend of stress components of the present approach are almost the same with the corresponding results. Though small differences observed are due to the difference in the finite difference method used by Pipes et al. [16] and the finite element method used in the current work. Furthermore, in the present case all 3-D stress components has been predicted from the 1-D approach. However, in the reference all 3-D stress components results are predicted from the 2-D approach. It can be observed from Fig. 4a that the values of stress components start to decrease or increase near the free edge, i.e., at $x_2/b = 0.8$. This portion of the width of the free edge is a function of geometry, ply orientation and the properties of the laminate. However, a simple thumb rule proposed by Pipes et al. [16] is that the width of the boundary layer is equal to the laminate thickness. In Fig. 4a, the value of τ_{13} increases

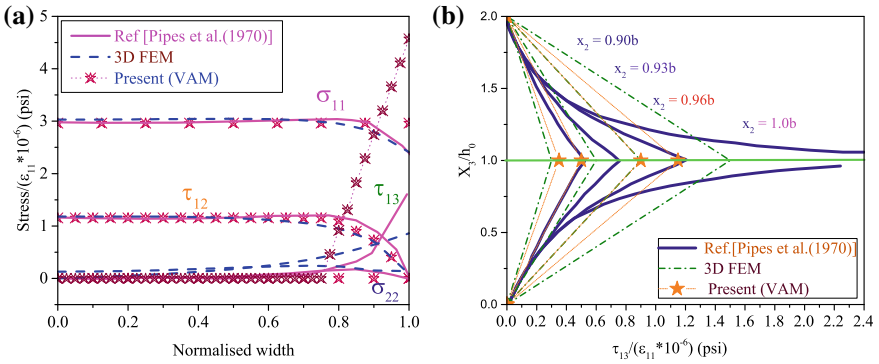

Fig. 4 **a** Result of stress components in the interface between the +45° and −45° under axial extension along the width. **b** Interlaminar shear stress τ_{13} distribution through the laminate thickness

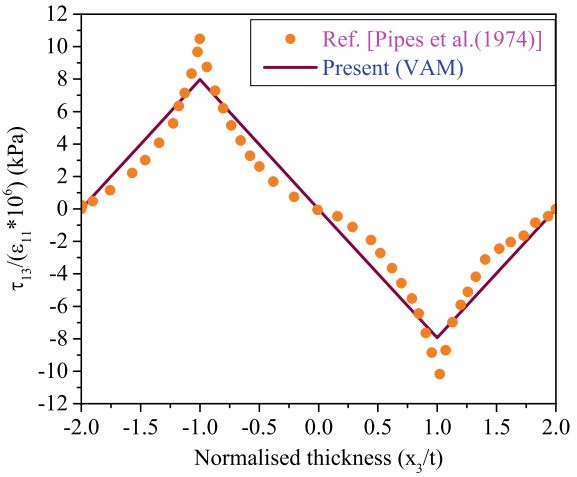

Fig. 5 Variation of the interlaminar stress τ_{13} along the thickness at the free edge of a $[45°/-45°]_s$ laminate and its comparison between the present and the reference results

and becomes high near the free edge and at the same time σ_{11}, τ_{12} decreases. This can be explained by the interlaminar stress transfer for the angle-ply laminate which occurs due to the mismatch in the shear coupling coefficient between θ and $-\theta$ layers. The mechanism of interlaminar stress transfer for angle-ply laminate is also called as the first mode mechanism. The interlaminar shear stress can be one of the reasons for delamination at the free edge in case of angle-ply laminates. The interlaminar normal stress σ_{33} disappears at all interfaces as well as on free edge. It can be understood that this stress may not do any damage to the angle-ply laminate. The present method is further extended to evaluate the performance of through the thickness of the laminate. In Fig. 4b shows the distribution of interlaminar shear stress τ_{13} across the laminate thickness at the free edge. It is witnessed from the figure that shear stress τ_{13} vanishes at free surface and laminate midplane, while it attains the maximum value in the interface between the 45° and −45° layers. Figure 5 shows the distribution of τ_{13} stress along thickness for $[45°/-45°]_s$ laminate. Stress distribution through the thickness, distribution of stress component near to the free edge region is compared with Pipes et al. [16]. All the above results and their comparison with Pipes et al. [16] result shows that there is not much variation in the two results.

In Fig. 6, the comparison has been made between the present and Ref. [2] results for $[90°/0°]s$ and $[0°/90°]_s$ laminate. The result shows a good correlation at the free edge. However, the results are inaccurate at the interior regions removed from free edge. This is because they found out the results of interior regions by using CLT and the present results are by using VAM. It is noted that when the cross-ply lamina is subjected to tensile loading in one direction; it shrinks in the other direction perpendicular to the applied load. If the laminae with different Poisson's ratios are bonded together, then the interlaminar stress is being produced to force all laminae to deform uniformly at the interfaces. This mechanism of interlaminar stress transfer due to mismatch of Poisson's ratio between cross-ply laminate is termed the second mode mechanism. In such a situation, the values of σ_{11} and τ_{12} are same for

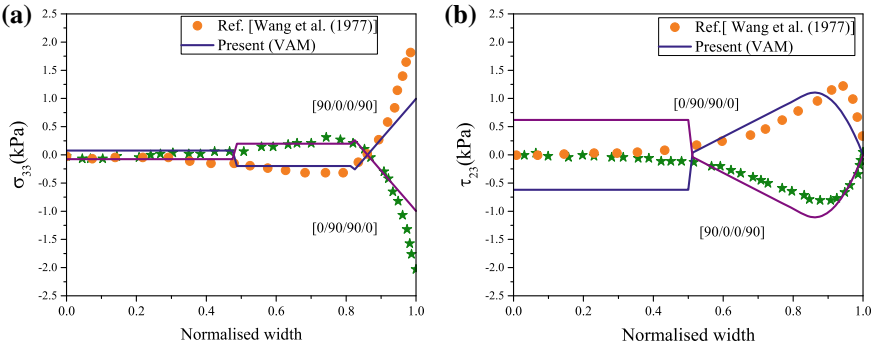

Fig. 6 **a** Variation of interlaminar normal stress σ_{33} in the interface of a [90°/0°] and [0°/90°] laminate along the normalized width and its comparison between the reference and present result. **b** Interlaminar shear stress τ_{23} result at interface (along the normalized width) of [90°/0°] and [0°/90°] in a $[90°/0°]_s$ and $[0°/90°]_s$ graphite/epoxy laminate, respectively, and its comparison between the present and the reference result

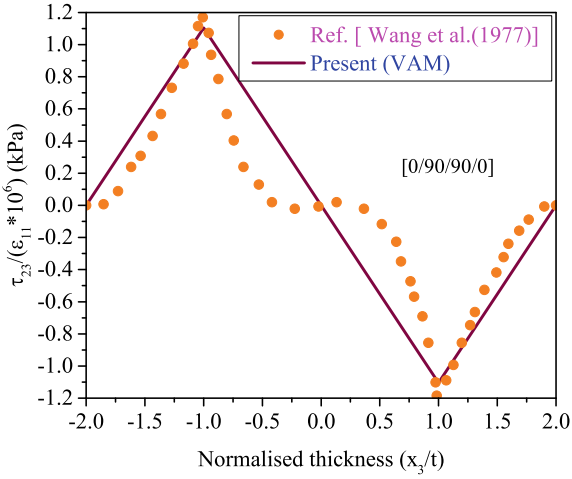

Fig. 7 Variation of interlaminar stress τ_{23} along the thickness at free edge of $[90°/0°]_s$ laminate and its comparison between present and reference results

all over width. However, the values of interlaminar normal stress σ_{33} for $[0°/90°]_s$ layup drastically increases from negative to positive. Whereas in $[90°/0°]_s$ laminate, contrary behavior has been observed. From this one can predict that the interlaminar normal stress σ_{33} is responsible for delamination in the case of cross-ply laminate. Further, it can be observed that the interlaminar shear stress τ_{23} value starts from zero and increases but near the end of an interface ($x_2 = 0.99$*h), it tends to become zero. From this, it can be concluded that the τ_{23} could not be responsible for delamination in the case of cross-ply laminate. Similarly, through the thickness at $x_2 = h/3$, results of interlaminar shear stress τ_{23} is presented in Fig. 7. The results are compared with the most favorable literature results. Again, it demonstrates a good agreement. From the above studies, a hostile behavior in angle-ply and cross-ply laminates is noticed.

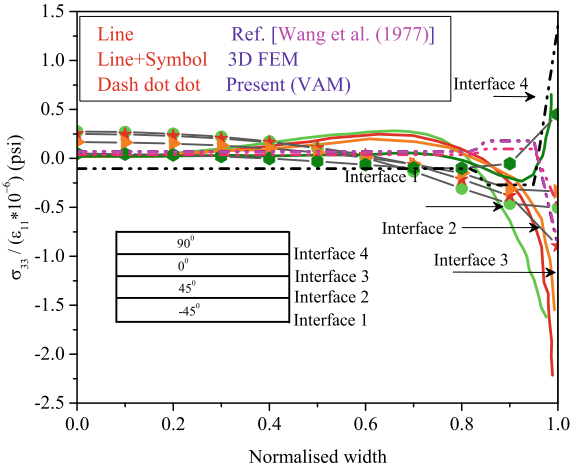

Fig. 8 Variation of interlaminar normal stress σ_{33} in the interface of a $[90°/0°/45°/-45°]$ laminate along the width and its comparison of present, 3-D FEM and reference result

To evaluate the performance of the present method, the quasi-isotropic laminate is considered for the study. In Fig. 8, the value of σ_{33} has been shown at different interfaces for the $[90°/0°/45°/-45°]_s$. Here, the values of σ_{33} are starting from almost zero for all the interfaces. However, when they reach near $x_2/b = 0.7$, the value of σ_{33} for all the interfaces start decreasing except for the interface four which is the interface of 90° and 0°. A similar trend of σ_{33} for $[90°/0°]_s$ laminate has been seen in Fig. 8. The results are correlated with the result of Wang et al. [2] and 3-D FEM and it shows a good agreement. Further, Fig. 9 shows the comparison between the present and the reference [2] thickness-wise result for the interlaminar normal stress at the free edge for the two quasi-isotropic ($[90°/0°/45°/-45°]_s$ and $[45°/-45°/0°/90°]_s$) laminate under the uniform axial extension. It is observed that the $[45°/-45°/0°/90°]_s$ laminate produces tension through the entire thickness of the free edge, while the $[90°/0°/45°/-45°]_s$ laminate produces compression through the thickness. The results are in a good agreement with the literature for these two cases. This investigation shows that the stacking sequence has an intense impact on the laminate strength. Therefore, it is essential to know all the stress components during the initial design phase.

In an another analysis, the interlaminar shear stress results have been compared with the results of Rose et al. [31] for $[10°_2/-10°_2]_s$ laminated composite beam. The material and the geometric properties are given in the third row of Table 1. Figure 10 shows a good correlation between the present and the literature result for interlaminar shear stress τ_{13}. Same explanation regarding angle-ply is applicable in this case also.

Further, the interlaminar shear stress results are compared with the results of Noiser et al. [9]. The material and the geometric properties have been given in the third row of Table 1. The variation of the interlaminar shear stress at the free edge for $[0°/45°/90°]_s$ symmetric laminate is displayed in Fig. 11. The result shows a fair agreement. The discrepancy may be due to the inability of the present method to handle a thick laminated composite beam.

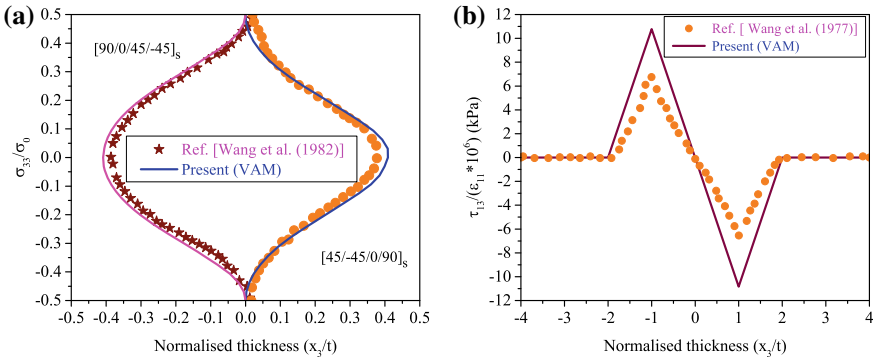

Fig. 9 **a** The effect of stacking sequence on interlaminar normal stress in quasi-isotropic graphite/epoxy laminate and its comparison between the present and reference result. **b** Variation of interlaminar stress τ_{13} along the thickness at the free edge of a $[90°/0°/45°/-45°]_s$ laminate of graphite/epoxy material and its comparison between the present and the reference results

Fig. 10 Variation of interlaminar stress τ_{13} along the thickness at free edge of a $[10^\circ_2/-10^\circ_2]_s$ laminate and its comparison between present and reference results

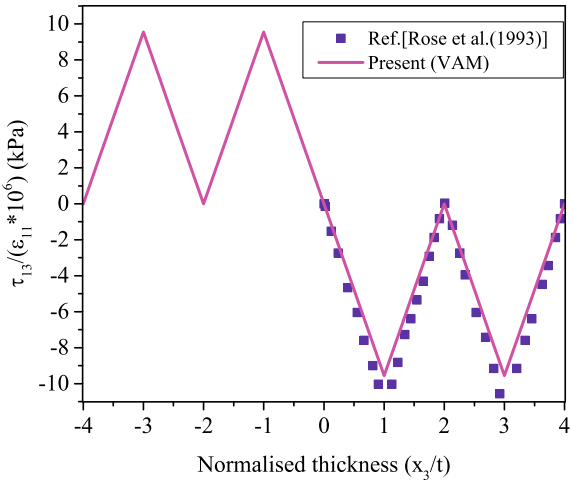

It can be concluded that the trend and the magnitude of the interlaminar stress components along the thickness and width matches well within the limits of error. Thus, this approach has been proved to deliver results efficiently. In the next section, all the six stress components behavior along the thickness of the different ply stacking sequences have been computed and plotted.

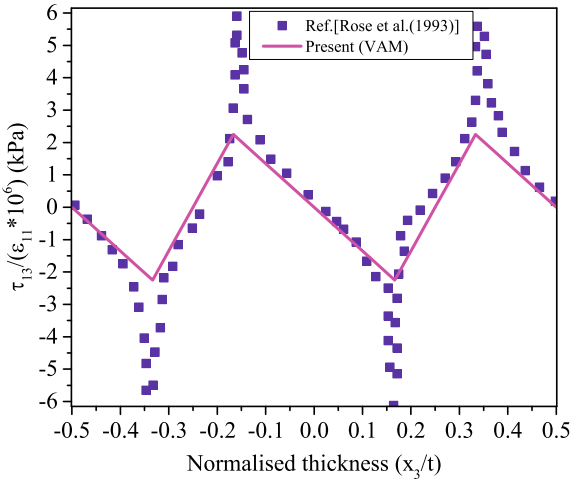

Fig. 11 Variation of the interlaminar stress τ_{13} along the thickness at the free edge of a $[0°/45°/90°]_s$ laminate and its comparison between the present and the reference results

3.2 Discussion on Through the Thickness Stress Components Near the Free Edge

In this section, the approach is applied to the additional laminates to check the utility of the method. In addition to this, it will be helpful to check the effect of out of plane deformation on interlaminar stress components between the asymmetric and the symmetric laminates. This section gives the behavior of the stress components through the thickness for the different layup orientations. The 3-D FEM simulation are run for the present case of the cantilevered beam. In the simulation, a strategy was formed such that the top and the bottom surface yield traction. However, in real practice, the top and the bottom surfaces are traction free. For simplicity, these conditions are relaxed in the present case. Excluding the top and the bottom surface of geometry, all the results between the proposed scheme and the 3-D FEM are showing a good agreement. These discussions are restricted to the transverse stress-related studies. These stress results are shown for symmetric or asymmetric, cross-ply, angle-ply and quasi-isotropic laminate subjected to an axial loading of 1000N. For the stress analyses, the following boundary conditions have been enforced:

1. The stress boundary conditions on the top and bottom surfaces are given by

$$\begin{aligned} \sigma_{33}(x_1, x_2, \pm\frac{h}{2}) &= 0 \\ \tau_{13}(x_1, x_2, \pm\frac{h}{2}) &= 0 \\ \tau_{23}(x_1, x_2, \pm\frac{h}{2}) &= 0 \end{aligned} \tag{42}$$

2. The interface boundary conditions are given by

$$\begin{aligned} \sigma_{33}(x_1, x_2) &= \sigma_{33}(x_1, x_2) \\ \tau_{13}(x_1, x_2) &= \tau_{13}(x_1, x_2) \\ \tau_{23}(x_1, x_2) &= \tau_{23}(x_1, x_2) \end{aligned} \tag{43}$$

The parametric study has been are carried out due to the following things:

1. The interlaminar stress components changes due to the stacking sequence under a uniform axial load.
2. It will help to understand the behavior of stress components along the thickness.
3. To check the computational efficiency and the accuracy of the present method.

The implementation of the developed approach is demonstrated first for the Winckler's type ($[\alpha_2/(90^\circ - \alpha)_4/\alpha_2/\alpha_2/(\alpha - 90^\circ)_4/\alpha_2]_T$) antisymmetric laminate. This layup exhibits a strong nonlinear extensional-twist coupling. This coupling is nonlinear in nature, and generally, it is called as trapeze effect. Before the 3-D stress analyses, the author validated static, dynamic, and the stability results by using the present approach for the same laminate. The static validation for healthy and damaged laminate is provided in the author's paper [27]. Therefore, from the previous study, it is observed that the method is capable of capturing nonlinearity. For this analysis also, the cantilevered strips made of graphite/cyanate and glass/epoxy are considered with Winckler's type layup corresponding to $\alpha = 20^\circ$. The material and the geometrical properties corresponding to AS4/3501-6 are shown in the second row of Table 1.

The distribution of the stress components through the laminate thickness is shown in Fig. 12. Similarly, the results are also validated for the symmetric layup with all the geometric and the material properties remain the same to the antisymmetric layup orientation. The 3-D stress components results for the symmetric Winckler's type layup are shown in Fig. 13. The in-plane stress results are exactly matching with the 3-D elasticity solution. Hence, by using the present formulation (which makes no ad hoc kinematic assumption) the 3-D analyses (capturing nonlinearity) can be carried out without depending on the computationally expensive 3-D FE analyses. These two figures show that the thickness-wise stress distribution for the same physical condition. By comparing these two figures following salient observation can be noted:

- Axial stress σ_{11} of the symmetric layup is more as compared to the antisymmetric and less fluctuation along the thickness is observed. In both cases, the stress pattern is symmetric about its midplane of the laminate.
- Both the transverse shear stresses and the normal transverse stresses are found to be more in the antisymmetric layup.
- Smooth transitions are observed and are represented by least quadratic functions for σ_{33} for both cases between the plies. The linear variations of τ_{13} and τ_{23} near the free edge get influenced due to the alternating stacking sequence of angle-ply laminates. This resulted in sharp transitions for τ_{13} and τ_{23} between the plies.
- These significant variations of interlaminar stress components may be due to constraining of the axial twist of general laminates under extension. It is to be noted

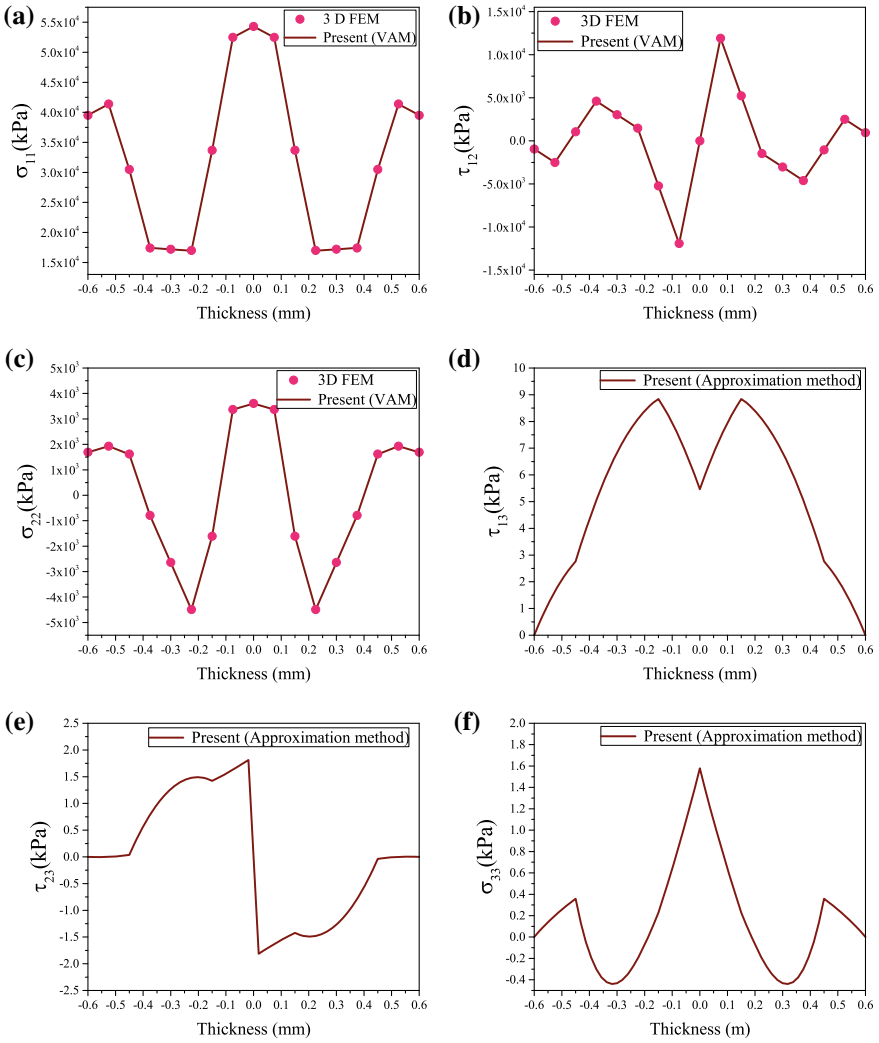

Fig. 12 Stress distribution through the thickness of the antisymmetric Winckler's type of laminate at the free edge due to the axial loading when $\alpha = 20°$

that the same physical layers are used in the two laminates. It is clearly seen that by changing the stacking sequences in the laminate (from symmetric to Antisymmetric), the numerical values of both stress components are considerably increased, almost throughout the entire thickness of the laminate. Thus, it is envisioned here that by changing the fiber orientations from symmetric to antisymmetric, the state of interlaminar stresses can be significantly changed. One can easily see the variation of the plot between in these two type of layup in Figs. 12 and 13.

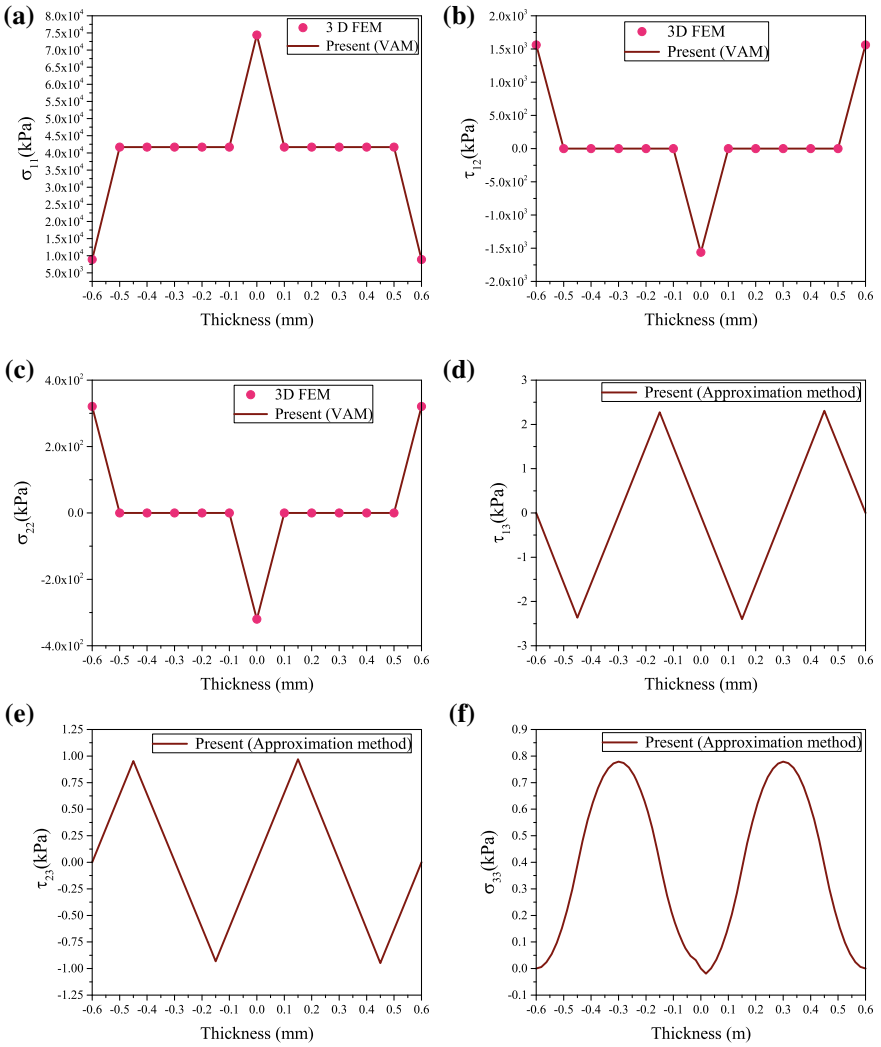

Fig. 13 Stress distribution through the thickness of the symmetric Winckler's type of laminate at the free edge due to axial loading when $\alpha = 20°$

- Maximum positive value of σ_{33} takes place at midplane of the antisymmetric laminate whereas at the same position, the value is zero in the symmetric laminate.
- Similarly, the values of interlaminar shear stress variation at the midplane are drastic in the antisymmetric laminate whereas at same position value is zero in the symmetric laminate.

- The nonlinear analyses of the same antisymmetric layup were carried out. The comparison for the magnitudes of the stress components shows more difference between them.
- By altering the stacking sequences of the individual layers and the fiber orientations, the interlaminar stress components can be controlled to avoid the free edge effect.

A comparison is further extended for the layup orientation $[45°/0°/45°/0°/45°/0°]_s$. The material and the geometric properties have been given in the first row of Table 1. The stress results for the angle-ply laminate under the extensional loading are given in Fig. 14. The comparisons are shown for through the thickness profile in the figure, and a good agreement between them can be observed.

To understand the effect of stacking sequence, the quasi-isotropic laminate with ply properties shown in the first row of Table 1 under the uniform axial extension has been considered. A good correlation can be observed for the stress distribution across the thickness with 3-D FEM results in Fig. 15. Some deviations observed are due to the higher thickness to width ratio of the laminate. This drawback can be overcome by using the higher order terms in asymptotic series. All the interlaminar stress components approaches zero near the top and the bottom surface of the laminate. As shown in Fig. 15, the interlaminar shear is symmetric concerning the midplane interface. The maximum interlaminar shear and the normal stress occur at the midplane of laminates.

In all the above cases, in the composite structure under the mechanical load, the results achieved from the present 1-D formulation matched almost with its corresponding elasticity and the 3-D FE solutions. The present results in Table 2 show that the 1-D VAM and the approximation method-based formulation reduces the computational time without much dishonor to the exactness. Such a simplified and a computationally efficient approach is most useful in the analyses of laboratory coupon type specimens to minimize the free edge effects.

4 Conclusion

The key feature of any successful structural design is to predict the structural response at a given condition accurately. By keeping this thing in mind, here in the work, our goal was set to develop an analytical solution based on 1-D, which can produce accurate 3-D elasticity solution with less computational time. To achieve the goal, the 1-D analytical approach based on the variational asymptotic method and the approximate method were used to recover an accurate 3-D elasticity solution. This approach also satisfies the interlaminar displacement continuity and the transverse equilibrium requirements as demanded by the exact 3-D formulation. Based on the derived theory, the numerical codes were developed in-house. The 3-D displacements, interlaminar normal, and the shear stress distributions were obtained. To check the correctness of it, results were compared to the available literature for the different layup orienta-

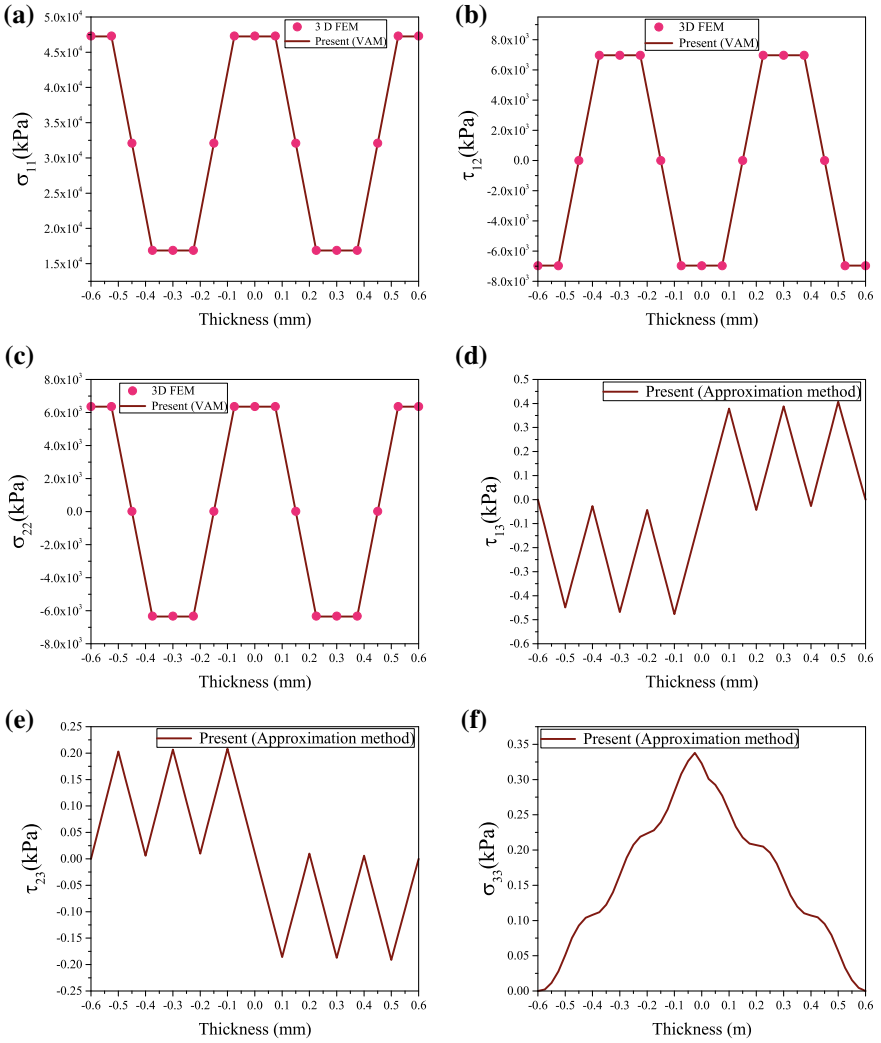

Fig. 14 Stress distribution through the thickness of $[45/0/45/0/45/0]_s$ laminate at free edge due to axial loading

tions. They show a good agreement especially with the numerical solution of Pipes [16, 17], Pagano [7, 18, 29], Sen [3], and Wang [32, 33]. Further, the deviation in the results was less than 1% when compared to the commercial 3-D finite element packages. Subsequent to the analyses results obtained from the recovery relation, the following things are confirmed and noted:

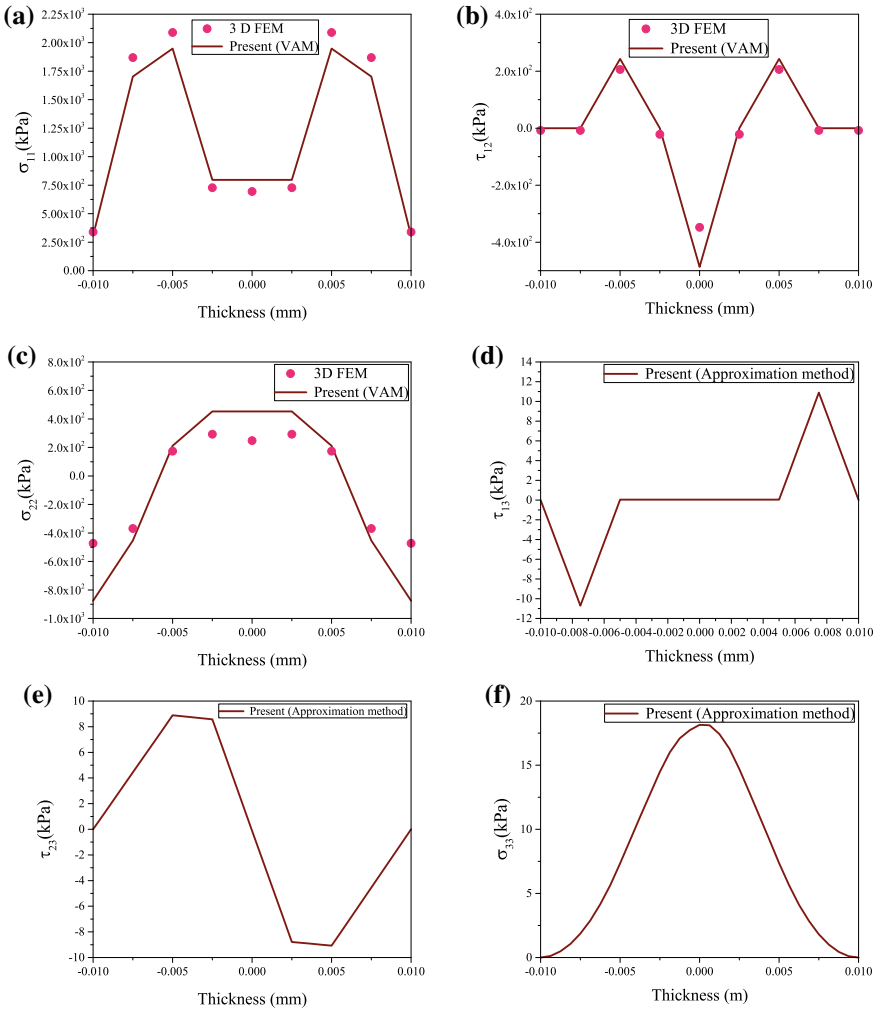

Fig. 15 Stress distribution through the thickness of $[90/0/45/-45]_s$ laminate at free edge due to axial loading

- Mechanism of the free edge effect in angle-ply laminates is due to the mismatch in the shear coupling coefficients between the adjacent layers.
- In-plane shear stress components vanish at the free edge in angle-ply laminates.
- In cross-ply laminates, the interlaminar normal stress appears to be singular at the free edge.
- In cross-ply laminates, the mechanism of the free edge effect is due to the mismatch in Poisson's ratio between 0° and 90° plies.

Table 2 Comparison between ANSYS® and present (VAM) simulation time

Sr. No.	Model	Computing time (hh:mm:ss)	
		ANSYS®	Present
I	Linear		
1	$\left[20_2^\circ/-70_4^\circ/20_2^\circ/-20_2^\circ/70_4^\circ/-20_2^\circ\right]_T$	2:44:20	00:00:30
2	$\left[20_2^\circ/-70_4^\circ/20_2^\circ/20_2^\circ/-70_4^\circ/20_2^\circ\right]_T$	02:33:00	00:00:35
3	$[0^\circ/45^\circ/90^\circ]_s$	01:00:00	00:00:20
II	Nonlinear		
1	$\left[20_2^\circ/-70_4^\circ/20_2^\circ/-20_2^\circ/70_4^\circ/-20_2^\circ\right]_T$	06:30:00	00:00:35

- In quasi-isotropic laminate, the stacking sequence plays a vital role in the development of interlaminar stresses.
- The effect of interlaminar stress was found to be restricted near the laminate free edge.
- The approach presented in this paper is possibly the simplest and the efficient of all the currently available methods.
- It is attractive and can be extended during the design phase in order to study the free edge stress components and their effect under the static and the fatigue loading.
- The computational time in this case is also very less as compared to the 3-D finite element solver, i.e., ANSYS®.
- The development of an analytical solution for the interlaminar 3-D stress components by using 1-D approach is important from the point of saving the time as well as can be built into machine intelligence.

References

1. Kant T, Swaminathan K (2000) Estimation of transverse/interlaminar stresses in laminated composites - a selective review and survey of current developments. Compos Struct 49(1):65–75
2. Wang ASD, Crossman FW (1977) Some new results on edge effect in symmetric composite laminates. J Compos Mater 11(1):92–106
3. Sen JK, Fish JC (1995) Fracture of glass-epoxy laminates under torsion and combined tension-torsion loads. In: ASTM Special Technical Publication, pp 440–466
4. Mittelstedt C, Becker W (2007) Free - edge effects in composite laminates. Appl Mech Rev 60(1–6):217–245
5. Hsu PW, Herakovich CT (1977) Edge effects in angle - ply composite laminates. J Compos Mater 11(4):422–428
6. Tang S, Levy A (1975) A boundary layer theory - part II: extension of laminated finite strip. J Compos Mater 9(1):42–52
7. Pagano NJ (1978) Stress fields in composite laminates. Int J Solids Struct 14(5):385–400
8. Whitney JM, Sun CT (1973) A higher order theory for extensional motion of laminated composites. J Sound Vib 30(1):85–97

9. Nosier A, Bahrami A (2007) Interlaminar stresses in antisymmetric angle-ply laminates. Compos Struct 78(1):18–33
10. Lu X, Liu D (1992) Interlayer shear slip theory for cross-ply laminates with nonrigid interfaces. AIAA J 30(4):1063–1073
11. Yin WL (1994) Free-edge effects in anisotropic laminates under extension bending and twisting, part I; a stress-function-based variational approach. J Appl Mech Trans ASME 61(2):410–415
12. Wang SS, Yuan FG (1983) A singular hybrid finite element analysis of boundary-layer stress in composite laminates. Int J Solid Struct 19(9):825
13. Kim T, Atluri SN (1994) Interlaminar stresses in composite laminates under out-of-plane shear/bending. AIAA J 32(8):1700–1708
14. Puppo AH, Evensen H (1970) Intertamlnar shear in laminated composites under generalized plane stress. J Compos Mater 4(1):204
15. Hayashi T (1968) Analytical study of interlaminar shear stresses in laminated composite plate. In: Space technology and science, p 279
16. Pipes RB, Pagano NJ (1970) Interlaminar stresses in composite laminates under uniform axial extension. J Compos Mater 4(4):538–548
17. Pipes RB, Pagano NJ (1974) Inter-laminar stress in composite laminates - an approximate elasticity solution. J Appl Mech 41(1):668
18. Pagano NJ (1974) On the calculation of interlaminar normal stress in composite laminate. J Compos Mater 8(1):65–81
19. Makeev A, Armanios EA (2000) An iterative method for solving elasticity problems for composite laminates. J Appl Mech Trans ASME 67(1):96–104
20. Berdichevskii VL (1979) Variational-asymptotic method of constructing a theory of shells. J Appl Math Mech 43(4):711–736
21. Hodges DH (2003) Geometrically exact, intrinsic theory for dynamics of curved and twisted anisotropic beams. AIAA J 41(6):1131–1137
22. Hodges DH, Atilgan AR, Fulton MV, Rehfield LW (1991) Free vibration analysis of composite beams. J Am Helicopter Soc 36(3):36–47
23. Hodges DH, Lee BW, Atilgan AR (1993) Application of the variational asymptotical method to laminated composite plates. AIAA J 31(9):1674–1683
24. Hodges DH, Harursampath D, Volovoi VV, Cesnik CES (1999) Non-classical effects in nonlinear analysis of pretwisted anisotropic strips. Int J Non-Linear Mech 34(2):259–277
25. Harursampath D, Hodges DH (1999) Asymptotic analysis of the non - linear behavior of long anisotropic tubes. Int J Non-Linear Mech 34(6):1003–1018
26. Guruprasad PJ, Thejasvi M, Harursampath D (2014) Nonlinear analysis of a thin pre-twisted and delaminated anisotropic strip. Acta Mech 225(10):2815–2832
27. Salunkhe SB, Singh CV, Guruprasad PJ (2017) Effect of matrix cracks and delamination on extension-twist coupling of thin pretwisted composite strips. Compos Struct 180:234–250
28. Salunkhe SB, Guruprasad PJ (2019) Free vibration analysis of a rotating thin pretwisted and delaminated composite strip. AIAA J pp 1–14
29. Pagano NJ, Pipes RB (1973) Some observations on the interlaminar strength of composite laminates. Int J Mech Sci 15(8):679IN1687–686IN2688
30. Armanios EA, Makeev A, Hooke D (1996) Finite-displacement analysis of laminated composite strips with extension-twist coupling. J Aerosp Eng 9(3):80–91
31. Rose CT, Herakovich CA (1993) An approximate solution for interlaminar stresses in composite laminates. Compos Eng 3(3):271–285
32. Wang ASD, Crossman FW (1980) Initiation and growth of transverse cracks and edge delamination in composite laminates part I. an energy method part II. experimental correlation. J Compos Mater 14(1):71
33. Wang JTS, Liu YY, Gibby JA (1982) Vibrations of split beams. J Sound Vib 84(4):491–502

A Study on Wrinkling Characteristics of NBR Material

Vaibhav S. Pawar, Rajkumar S. Pant and P. J. Guruprasad

Abstract This work details wrinkling for hyperelastic materials with the Ogden material model. First, generalized expressions are derived for stresses and tangent stiffness terms. Material constants obtained through testing work have been used to determine stiffness terms as well as second Piola–Kirchhoff's stress for a range of stretch ratios. This is then followed with a new model based upon modified deformation gradient tensor and hence Green tensor. Wrinkling parameter is monitored with material constants and stretch ratios. Analytically performance of material has been accessed for different conditions of uniaxial tension, equi-biaxial loading and plane strain condition. It has been observed that over a range of stretches; uniaxial condition and plane strain condition results in a situation which is consistent in the context of wrinkling, i.e. possibility of wrinkling gets boosted. On the other hand, when equi-biaxial loading or stretch ratio approaches unity for a region, chances of wrinkling being triggered reduce substantially. Developed numerical models are validated against tested work on planar hyperelastic structures for the cases of uniaxial, biaxial as well as shear loading. It has been observed that numerical results obtained hint possible scenarios of wrinkling.

Keywords Cauchy's stress · Ogden model · Wrinkling · Hyperelastic material

1 Introduction

Nitrile rubber (NBR) is a synthetic rubber consisting of the phase of acrylonitrile and butadiene, popularly known as acrylonitrile-butadiene rubber [1]. Traces of other metallic inclusions are generally used during the manufacturing of NBR. This includes Sulphur, Zinc oxide, TDP oil, etc. This type of material finds its uses in

V. S. Pawar (✉) · R. S. Pant · P. J. Guruprasad
Department of Aerospace Engineering, Indian Institute of Technology Bombay, Mumbai, Maharashtra, India
e-mail: pawar@aero.iitb.ac.in

P. J. Guruprasad
e-mail: pjguru@aero.iitb.ac.in

B. N. Singh et al. (eds.), *Recent Advances in Theoretical, Applied, Computational and Experimental Mechanics*, Lecture Notes in Mechanical Engineering,
https://doi.org/10.1007/978-981-15-1189-9_9

hydraulic hoses, seals, gaskets, tank liners, aircraft applications. One of the dominant application is in the medical section. Doctors use to have NBR gloves for surgical procedures. Such gloves are susceptible to wrinkling. The wrinkle is fold or bifurcation or generation of the wavy surface due to the inability of material to resist compressive loads. This class of problem has been tackled in the literature by two approaches. First being tension field theory, in which secondary principal stresses are assumed to be zero and analytical formulations are built [2–4]. But it is not easy to determine the wrinkling details such as wavelength and amplitude from this approach. The second approach is based on the bifurcation theory. This treats the problem on the lines of buckling of plates. Wrinkling of NBR is considered in this paper. The material under study is incompressible hyperelastic. Further, Ogden's constitutive rule is representing the characteristics of the same. The formulation accounts for wrinkling features by introducing a wrinkling tensor and modified stretches in the kinematics. Material constants are obtained from experiments with the in-house developed test rig. Test prototype has been developed to take care of large deformations with large strains under uniaxial, biaxial as well as shear conditions. It also generates stress relaxation data. Wrinkling measurements are done using non-contact method with a brand new technique using the Arduino controller.

2 Methodology

2.1 Wrinkling Criteria

There are three different criteria, which determine the existence of wrinkling in a membrane, rubber or soft tissue.

1. Principal stress criterion,
2. Principal strain criterion, and
3. Combined criterion, including both principal stresses and principal strains.

For the wrinkling criterion based on principal stresses/strains, the membrane is said to be in a taut condition when both the principal stresses/strains are positive. If both principal stresses/strains are zero, then the slack condition of membrane results. Obviously, wrinkling will not be there for the taut and slack states. Thus, wrinkling occurs in the membrane when the minor principal stress/ strain is zero and the major principal stress/strain is tensile. Tension field theory is depending upon fictitious wrinkled surface and everything is required to be derived based upon following or similar geometry as shown in Fig. 1. As shown, in a direction perpendicular to uniaxial stress direction, the material is not able to resist compression as compressive stiffness or bending stiffness of the material is very small. Based upon the deformed configuration of the figure, wrinkling strain is defined as

$$\text{Wrinkling strain} = \frac{\beta - 1}{\beta} \tag{1}$$

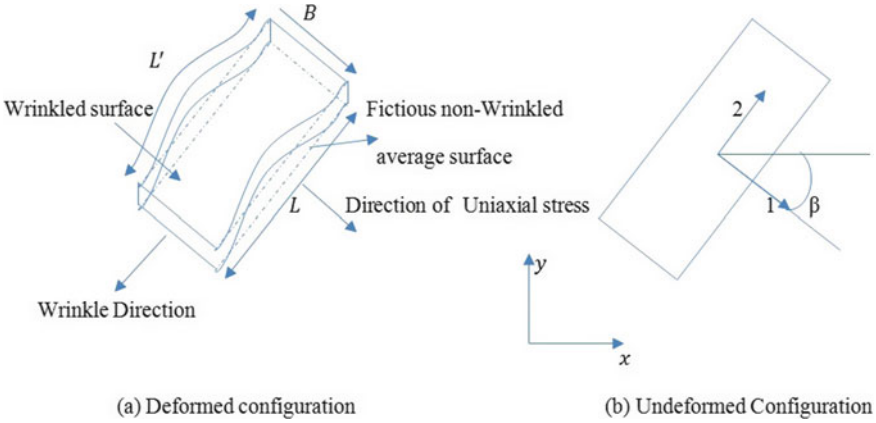

Fig. 1 Wrinkling configuration details

where β is wrinkling parameter, which decides the amount of wrinkling and defined with respect to pseudo-deformed surface or fictitious non-wrinkled average surface. Deformed length is $L' = \beta * L$

For wrinkling based on the combined criterion, the membrane is in a taut condition when the minor principal stress is positive and is in the slack condition when the major principal stress is zero. When the minor principal stress is negative and the maximum principal strain is positive, the membrane gets wrinkled. Here, σ_1 and σ_2 are the major and minor principal stresses, respectively, e_1 and e_2 are major and minor strains, respectively, ν is Poisson's ratio.

The wrinkling criteria are summarized below:

a. Principal stress criterion

   i. $\sigma_1 > 0$ and $\sigma_2 > 0$ taut
   ii. $\sigma_2 \leq 0$ and $\sigma_1 > 0$ wrinkled
   iii. $\sigma_2 \leq 0$ and $\sigma_1 \leq 0$ slack

b. Principal strain criterion

   i. $e_1 > 0$ and $e_2 > -\nu e_1$ taut
   ii. $e_2 \leq -\nu e_1$ and $e_1 > 0$ wrinkled
   iii. $e_2 \leq 0$ and $e_1 \leq 0$ slack

c. Combined criterion

   i. $\sigma_1 > 0$ and $\sigma_2 > 0$ taut
   ii. $\sigma_2 \leq 0$ and $e_1 > 0$ wrinkled
   iii. $\sigma_1 \leq 0$ and $e_1 \leq 0$ slack

Principle strain criterion is used in user subroutine developed for predicting the occurrence of wrinkling. The procedure used in this subroutine for finite element implementation of wrinkling is summarized in Fig. 2. At the start of every increment,

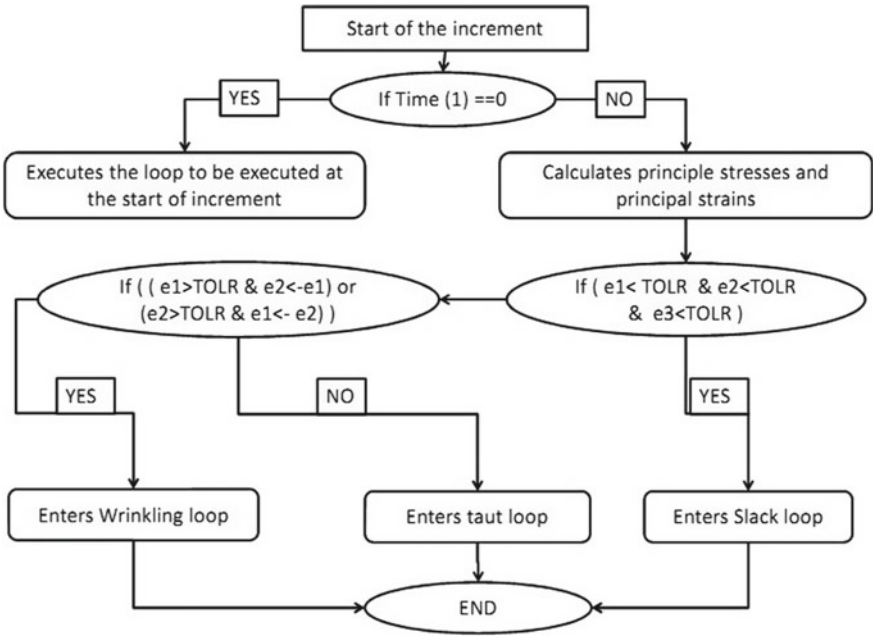

Fig. 2 Implemented wrinkling scheme

ABAQUS calls the subroutine with trial strain increment and trial strain obtained from the previous increment except for the first increment. At the start of the first increment, strain increment executed based on tangent stiffness owing to linear elasticity is obtained. At each increment, strain increment is rotated in the principal direction within the framework. Based upon the framework used in the implementation, the state of the membrane is accessed. Accordingly, the scheme picks suitable tangent stiffness available and updates stress at the end of increment. Next trial increment is evaluated based upon stress updates of the previous increment. This loop continues until the convergence criteria get satisfied. Tolerance (TOLR) is set of the order of 10^{-12}. Since the problem is of large deformation, Jaumann's rate of Kirchoff's stress is used for tangent stiffness updates. This being incompressible material, Jaumann's rate of Kirchoff's stress is the same as Jaumann's rate of Cauchy's stress.

NBR is tested for uniaxial testing and is calibrated. It has been observed that the Ogden model, reduced-order model of order 2 are best for representing the material and both the models are found to be stable.

2.2 Material Model

The stored energy function for rubber-like material is given by Ogden [2] in terms of principal stretches as

$$\emptyset(\lambda_1, \lambda_2, \lambda_3) = \sum_{p=1}^{N} \frac{\mu_p}{\alpha_p}(\lambda_1^{\alpha_p} + \lambda_2^{\alpha_p} + \lambda_3^{\alpha_p} - 3) \tag{2}$$

where N, μ_p and α_p are material constants. Under the assumption of incompressibility, one can rewrite it as

$$\emptyset(\lambda_1, \lambda_2, \lambda_3) = \sum_{p=1}^{N} \frac{\mu_p}{\alpha_p}(\lambda_1^{\alpha_p} + \lambda_2^{\alpha_p} + \lambda_1^{-\alpha_p}\lambda_2^{-\alpha_p} - 3) \tag{3}$$

In general shear modulus results from

$$2\mu = \sum_{p=1}^{N} \mu_p \alpha_p \tag{4}$$

With N = 3 and by fitting the material parameters, the material behaviour of rubbers can be described very accurately. For particular values of material constants, the Ogden model will reduce to either the Neo-Hookean solid (N = 1, $\alpha = 2$) or Mooney–Rivlin material ($N = 2, \alpha_1 = 2, \alpha_2 = -2$, with the constraint condition of $\lambda_1\lambda_2\lambda_3 = 1$).

Using the Ogden material model, the three principal values of the Cauchy stresses can now be computed as

$$\sigma_j = p + \lambda_j \frac{d\phi}{d\lambda_j} \tag{5}$$

where $\sigma_j = \lambda_j P_j$

Now considering an incompressible material under uniaxial tension, with the stretch ratio given as $\lambda = \frac{l}{l_0}$, the principal stresses are given by

$$\sigma_j = p + \sum_{p=1}^{N} \mu_p \lambda_j^{\alpha_p} \tag{6}$$

The pressure p is determined from incompressibility and boundary condition.

$$\sigma_2 = \sigma_3 = 0, \text{ yielding}$$

$$\sigma_j = \sum_{p=1}^{N} (\mu_p \lambda_j^{\alpha_p} - \mu_p \lambda_j^{-\frac{1}{2}\alpha_p}) \tag{7}$$

It can be rightly said that, for rubber and biological materials, more sophisticated models are necessary. Such materials may exhibit non-linear stress–strain behaviour at modest strains, or are elastic up to large strains. These non-linear stress–strain behaviours need to be accommodated using specifically tailored strain-energy density functions.

3 Result and Discussion

Typical wrinkling configuration and parameters involved in the model are highlighted in Fig. 1. Ogden model captured material response for both cases of with wrinkling parameter and without wrinkling parameter. On the onset of wrinkling, when secondary principal stress is approaching zero, the maximum principal stress determined are shown in Fig. 3. In realtime conditions, situations result such that uniaxial tension condition may prevail which forces other two stretches to be equal or sometime plane strain assumptions may sustain while it may be possible that equi-biaxial stretch involves in some of the applications. Second Piola–Kirchhoff's stress is used as a stress measure. Incompressibility condition is accommodated by imposing constraints. The associated multiplying parameter is obtained to ensure the plane stress problem. Wrinkling depth, orientation and associated loads are captured experimentally.

Figure 4 evaluates the performance of NBR under the conditions of uniaxial, equi-biaxial and plane strain conditions analytically. Since the grip of the test rig developed is such that samples can be fixed over a wide range of width, uniaxial and plane strain situations can be immediately achieved. Since the prototype is developed by keeping a wide range of stretch ratios in mind, equi-biaxial condition can be maintained as well. Secondary principle stress variations with almost all possibilities are shown in Fig. 4. All the cases are depicted in terms of true stresses as the problem is of large deformation. The developed framework has considered Jaumann rate of Kirchoff's stress as already mentioned for quick convergence. As the material is incompressible, it can be termed as Jaumann's rate of Cauchy's stress as well, which is required in the Eulerian description. Over a range of stretch, it is possible to have negative compressive stress for plane strain and for uniaxial condition it is zero. As opposed to this, if equi-biaxial case is to be dealt with, most zones are turning out to be wrinkle free. For unequal stretch ratios, the intermediate scenario appears as shown in Fig. 4.

Figure 5 depicts maximum Cauchy's principal stresses against corresponding true strain over a range for which material was tested. No significant difference resulted in stress for the different cases that have been considered in this study. The behaviour has been captured perfectly through the Ogden model, reduced-order polynomial

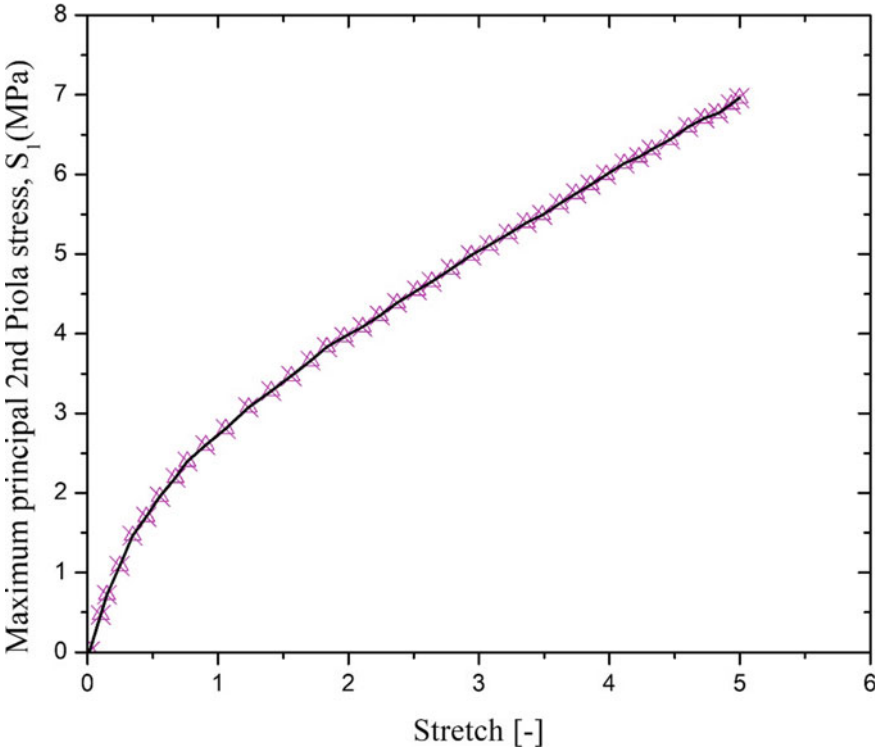

Fig. 3 Maximum principal stress at the onset of wrinkling using Ogden material model

model of order 2 and order 3. Most of the applications such as large shear, pure shear and biaxial loading conditions can be approximated as plane strain problem. For wide grip of the specimen with comparable width, this case is different from the uniaxial loading case; and it follows the plane strain assumptions. With a slight stretch in the perpendicular direction to loading as is the case of typical NBR tubes or gloves, secondary principal true stress is approximately zero. Hence such NBR gloves or tubes wrinkle. This is illustrated in Fig. 5 for low true strains. For low strength NBR, these effects get more pronounced.

In general, the use of tension field theory captured wrinkling but only orientation can be obtained with this theory. Implicit solution schemes for user subroutines in the finite element package require the calculation of the tangent stiffness matrix. Primarily this is done by resolving the stiffness matrix in principal directions and then back into the original coordinate system; thus rendering FE program to have co-rotational part to be dealt in subroutine through transformation tensor R. There is an additional shear stiffness that gets developed due to changes in the shear stress which will change the direction of the principal stresses. These are related to the current principal stresses and stretches (Cauchy's stresses and stretches).

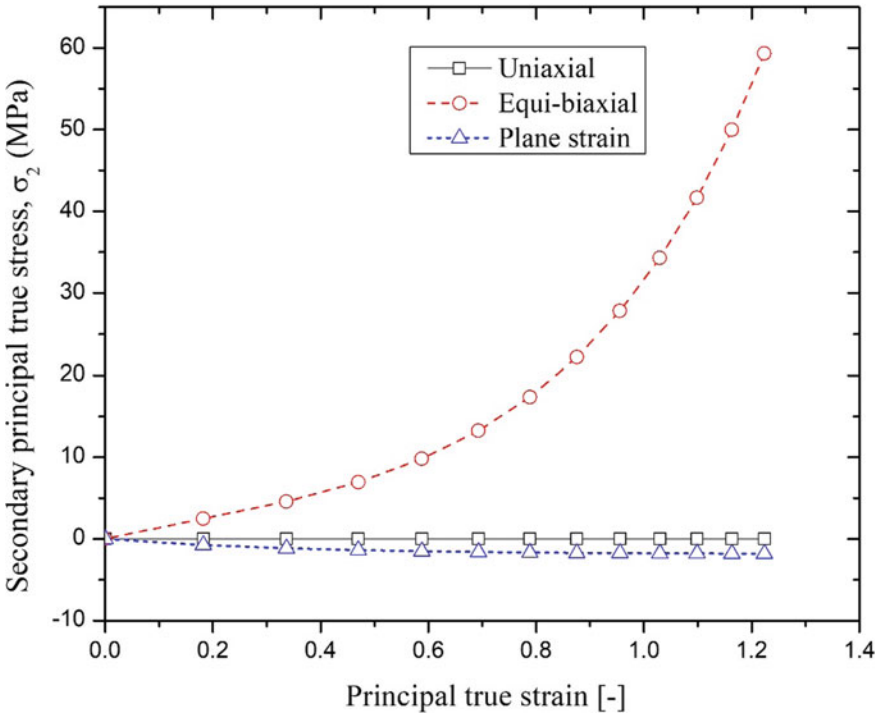

Fig. 4 Secondary principal stress against true strain for different cases of NBR

4 Summary

This work presents the analytical development of wrinkling using the Ogden model and the same has been numerically treated using user subroutines. NBR of moderate strength has been considered for the analysis and the developed framework is applied to it. Merits and demerits of the type of test used in the context of the developed prototypes have been discussed. Conditions for wrinkling have been elaborated and possible situations are addressed. For small strains, it can be concluded that as the strength of NBR gets reduced with the reduction in polymer percentage, chances of wrinkling get triggered. This is true for larger stretch ratios for biaxial loading and in general for plane strain and uniaxial conditions where the width of such structure is small compared to length.

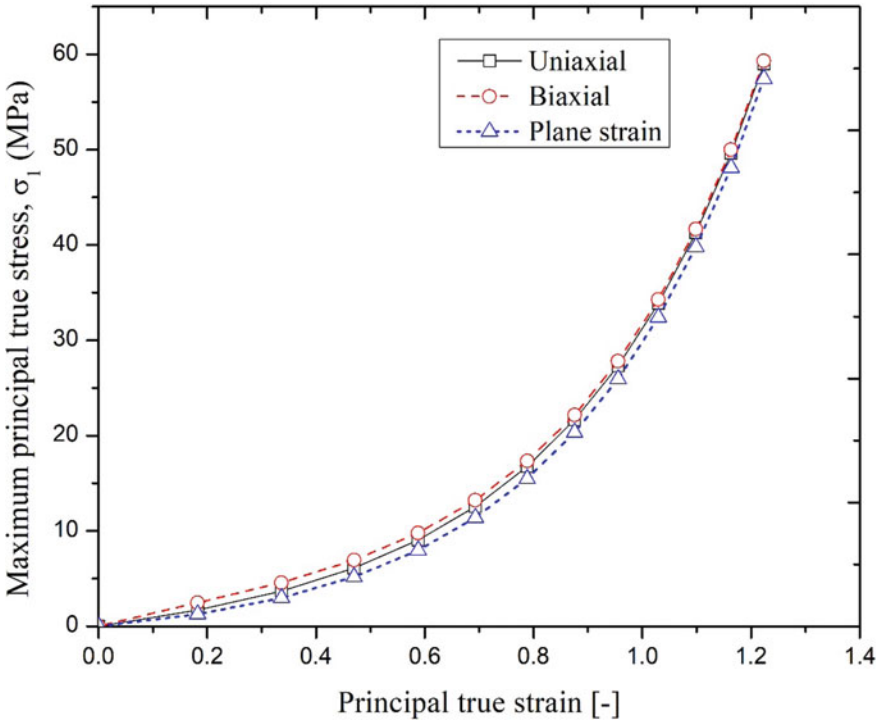

Fig. 5 Maximum principal true stress against true strain for different cases of NBR

References

1. Khan AS, Farrokh B (2006) Thermo-mechanical response of nylon 101 under uniaxial and multi-axial loadings: part I, experimental results over wide ranges of temperatures and strain rates. Int J Plasticity 1506–1529
2. Ogden RW (1972) Large deformation isotropic elasticity—on the correlation of theory and experiment for incompressible rubberlike solids. Proc R Soc London Ser A, Math Phys Sci 326(1567):565–584
3. Steigmann DJ, Pipkin AC (1989) Finite deformation of wrinkled membranes. Q J Mech Appl Math 42(3):427–440
4. Deng X, Pellegrino S (2012) Wrinkling of orthotropic viscoelastic membranes. AIAA J 50:668–681

First Ply Failure Study of Laminated Composite Conoidal Shells Using Geometrically Nonlinear Formulation

Kaustav Bakshi and Dipankar Chakravorty

Abstract The literature clearly indicates that the failure of laminated composite plates have been studied in detail while composite shell structures have received limited attention. Though few recent papers reported first ply failure of conoidal shells in order to apply these shell forms confidently in industrial applications, the failure investigations need to be continued for different parametric variations keeping the industrial requirements in mind. This study attempts to fill the lacuna. An isoparametric finite element code considering geometrically nonlinear strains and constant shear deformation along the thickness direction of the shell is proposed to study failure initiation in uniformly loaded laminated conoidal shell roofs having two adjacent boundaries simply supported and other two adjacent edges clamped. Moreover, failure locations and modes or tendencies of failure are also reported. The results are studied for varying stacking orders and laminations. This study recommends that the practicing engineers must adopt 30°/−30°/30° laminate to maximize load-carrying capacity of the shell for the edge condition taken up here.

Keywords First ply failure · Laminated conoidal shell · Geometrically nonlinear finite elements · Constant shear deformation

1 Introduction

The conoidal shells are stiffer and easy to cast compared to singly curved cylindrical and doubly curved spherical shell surfaces. Additionally, the conoidal shell form allows natural ventilation and entry of diffused sunlight from both ends which is preferred in medicinal and chemical plants. Thus the practicing civil engineers choose

K. Bakshi (✉)
Indian Institute of Technology Indore, Indore, India
e-mail: Bakshi.kaustav@gmail.com; kaustav.bakshi@iiti.ac.in

Discipline of Civil Engineering, Khandwa Road, Simrol, Madhya Pradesh 453552, India

D. Chakravorty
Jadavpur University, Kolkata, India
e-mail: prof.dipankar@gmail.com

B. N. Singh et al. (eds.), *Recent Advances in Theoretical, Applied, Computational and Experimental Mechanics*, Lecture Notes in Mechanical Engineering,
https://doi.org/10.1007/978-981-15-1189-9_10

conoidal shells as roofs to cover large unsupported areas one finds in aircraft hangers, stadiums and shopping malls. The high specific strength/stiffness of the laminated composites render lesser foundation force and seismic force compared to conventional reinforced cement concrete shell roofs. Moreover, the material offers designer flexibility, where the relatively stronger direction of a lamina can be oriented along the major direction of load transfer. Keeping these advantages in mind the practicing civil engineers prefer the laminated conoids over the isotropic ones. A group of researchers started working on bending and dynamic responses of laminated conoids. Dey et al. [1] studied static bending responses of laminated composite conoids. Ghosh and Bandyopadhyay [2] applied an isoparametric finite element formulation to study static responses of isotropic conoidal shells with cut-outs. Dynamic analysis of stiffened conoids was conducted by Nayak and Bandyopadhyay [3] using eight noded doubly curved elements. Das and Chakravorty [4] studied the free vibration of laminated conoids for complicated edge conditions. Bending responses of delaminated conoids were reported by Kumari and Chakravorty [5]. But the authors did not study the damage initiation and propagation in the composite material. Dynamic instability of laminated conoids was reported by Pradyumna and Bandyopadhyay [6].

A shell roof can be confidently used in practical applications when the allowable load before failure is known to the practicing engineers. The failure of the laminated composite is progressive as indicated by Singh and Kumar [7]. The failure initiates at the weakest ply in the laminate. The failure initiation is termed as the first ply failure. If the latent damage remains undetected and unprotected then the cracks propagate within the laminate and culminate to total collapse under service condition. Such a sudden catastrophe can be avoided by studying failure initiation in composite shell roofs. The failure of composite plates was studied by many researchers in detail. Reddy and Reddy [8] reported the failure of composite plates using geometrically linear and nonlinear strains. Kam et al. [9] conducted an experiment to study failure initiation and propagation in laminated plates. Sathish Kumar and Srivastava [10] worked on the failure of stiffened plates. The failure study of composite plates was continued by Lal et al. [11] and Coelho et al. [12] where the authors studied progressive failure of the composite material using geometrically nonlinear formulation. The research reports on laminated composite shells are really scanty compared to the study carried out on composite plates. Prusty et al. [13] and Adali and Cagdas [14] worked on the failure of singly curved and doubly curved shell panels using geometrically linear strains. The present authors worked on failure initiation in laminated conoids using geometrically linear [15] and nonlinear strains [16]. The failure initiation in clamped conoids [15] and a conoid with a set of parallel edges clamped and other edges free [16] were studied by the present authors. The failure study on composite conoidal shells still requires attention from the researchers for industrially important parametric variations to apply these shell form confidently in industrial applications. Thus the present study focuses on failure initiation in conoids with two adjacent boundaries simply supported and other two adjacent edges clamped. This paper also reports the failure location on the shell surface and modes of failure.

2 Mathematical Formulation

A conoidal shell having radii of curvatures R_{yy} and R_{xy} is taken up here where the total laminate thickness 'h' is consisting of thin arbitrarily oriented layers ($h = h_1 + h_2 + \ldots$) (see Fig. 1). The reference axes (x and y) are taken up at the shell mid-surface. The 'z' axis is oriented along the thickness direction of the shell.

The displacement at any arbitrary point is expressed in Eq. (1) assuming a constant shear deformation acting along the z-axis.

$$u = u_0 + z\alpha, v = v_0 + z\beta, w = w_0 \tag{1}$$

u, v, w, α, β are shown in Fig. 1. u_0, v_0, and w_0 are the degrees of freedom at the mid-surface.

$$\{\varepsilon\} = \{\varepsilon\}^L + \{\varepsilon\}^{NL} \tag{2}$$

$\{\varepsilon\}^L$ and $\{\varepsilon\}^{NL}$ are linear and nonlinear mid-surface strains, respectively. The linear strains are adopted from Kumari and Chakravorty [5] for an undamaged shell. The nonlinear strains are the same as those were reported in [16]. The laminate constitutive relationship is given as the following:

$$\{F\} = [D]\{\varepsilon\} \tag{3}$$

The stress resultants $\{F\}$ and laminate stiffness matrix $[D]$ are adopted from Kumari and Chakravorty [5] for an undamaged shell.

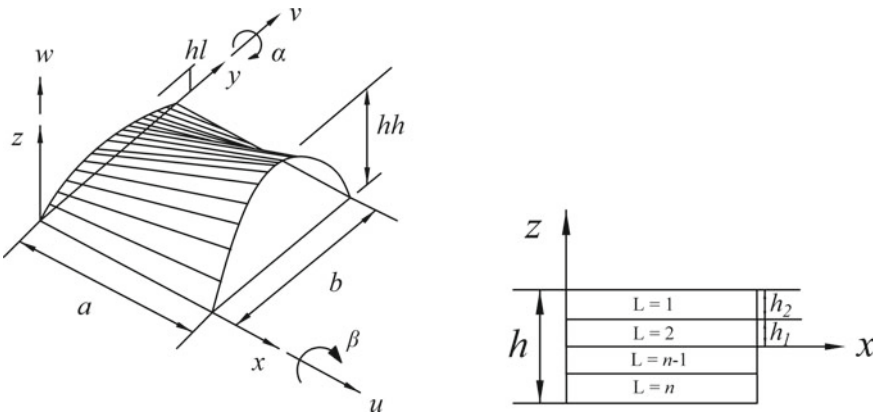

Fig. 1 The conoidal shell with global reference axes and degrees of freedom

2.1 Finite Element Formulation

The isoparametric finite element code is generated using the same element reported by Bakshi and Chakravorty [15]. The strain–displacement relation is expressed in Eq. (4).

$$\{\varepsilon\} = ([B]^L + \frac{1}{2}[B]^{NL})\{u_i\} \tag{4}$$

$[B]^L$ is taken up from Kumari and Chakravorty [5] for an undamaged shell. The nonlinear matrix $[B]^{NL}$ is the same as it was reported in [16].

2.2 Governing Differential Equation

The total potential energy (π) of the conoid [refer to Eq. (5)] is minimized with respect to its displacements to derive the governing equation of shell bending.

$$\pi = \frac{1}{2}\iint_A \{\varepsilon\}^T[D]\{\varepsilon\}dA - \iint_A \{u\}^T\{q\}dA \tag{5}$$

The external load intensity on the shell is $\{q\}$, shell displacements are $\{u\}$, and laminate strains are $\{\varepsilon\}$.

The governing equation is given as the following:

$$\frac{\partial \pi}{\partial \{u\}} = \psi \tag{6}$$

For geometrically linear analysis, $\Psi = 0$. For the nonlinear analysis, it is expressed as the following:

$$\sum_{i=1}^{ne} \psi_i = \sum_{i=1}^{ne} \left(\iint_A \frac{\partial \{\varepsilon\}^T}{\partial \{u\}}[D]\{\varepsilon\}dxdy - \sum_{i=1}^{8} \iint_A \{N_i\}^T\{q\}dxdy \right)_i \tag{7}$$

ne = number of elements. A = Area of the shell. $\{N_i\}$ = Shape functions [5].

The residual load $\{\psi\}$ = Internal load $\{P\}$ − external load $\{R\}$

where $P = \sum_{i=1}^{ne} \left(\iint_A \frac{\partial \{\varepsilon\}^T}{\partial \{u\}}[D]\{\varepsilon\}dxdy \right)_i = \sum_{i=1}^{ne} \left(\iint_A \left[\bar{B}\right]^T[D]\{\varepsilon\}dxdy - \{Q\} \right)_i$

$\left[\bar{B}\right] = [B]^L + [B]^{NL}$, $\{R\} = \sum_{i=1}^{8} \iint_A [N_i]^T\{q\}dxdy$

The governing differential equation is solved following the Newton–Raphson iterative approach (Fig. 2).

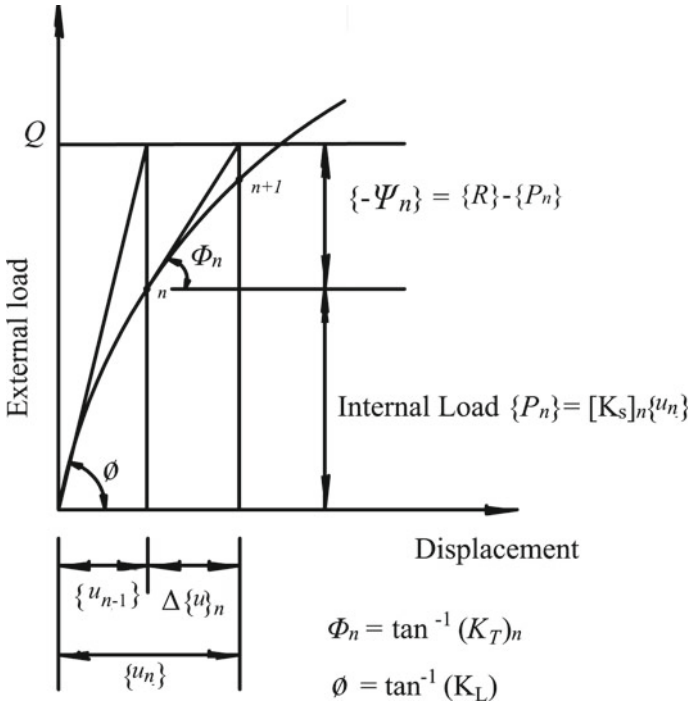

Fig. 2 The Newton–Raphson method

Displacement of the shell for the *n*th iteration is calculated following Fig. 2.

$$\Delta\{u\}_n = [K_T]\{-\psi_n\} \tag{8}$$

The total displacement after '*n*' iterations is $\{u_n\} = \{u_{n-1}\} + \Delta\{u\}_n$

The stiffness matrices ($[K_T]$ and $[K_s]$) are the same as reported in [16]. The element stiffness matrices and load vectors are computed using 2×2 Gauss quadrature rule. The iterative approach converges following the criterion reported by Chattopadhyay et al. [17]. The converged displacements of the conoid are used to calculate the stresses and strains for each lamina following the procedure elaborated in [15]. The stresses and strains for a given lamina are applied to failure theories like maximum stress, maximum strain, Tsai–Wu, Tsai–Hill, and Hoffman failure criterion [8] to identify failure initiation in the composite shell. The failure modes are identified following the steps given in [15].

Table 1 Nondimensional central displacements ($\hat{w} \times 10^3$) of simply supported composite spherical shell under uniformly distributed load

Lamination	0°/90°	0°/90°/0°	0°/90°/90°/0°
Reddy [18]	16.980	6.697	6.833
Present FEM	17.009	6.707	6.835

$a/b = 1$, $a/h = 100$, $E_{11} = 25E_{22}$, $G_{12} = G_{13} = 0.5E_{22}$, $G_{23} = 0.2E_{22}$, $\nu = 0.25$, $E_{22} = 10^6$ N/cm^2, $R/a = 10^{30}$

3 Numerical Problems

Accuracy of the proposed code is confirmed by the solution of benchmark problems. The first benchmark problem compares the nondimensional static displacements of a spherical shell obtained from the proposed code with the closed-form results reported by Reddy [18]. The comparison is furnished in Table 1, where the elastic constants and geometric dimensions of the shell are also presented. A uniform 8 × 8 mesh is adopted by the proposed code to obtain the results furnished in Table 1. The nondimensional form of displacement adopted in this study is the same as it was reported by Reddy [18].

The second benchmark problem shows a comparison of static deflections of an isotropic conoidal shell calculated using the proposed code and the values reported by Hadid [19]. Figure 3 shows the comparison. The dimensions, elastic constants, and Poisson's ratio of the isotropic shell are furnished in that figure.

The third problem compares the load values corresponding to failure initiation in a laminated composite clamped plate calculated using the proposed code with the results previously published by Kam et al. [9]. The authors obtained the failure load values through the experiment and by using an isoparametric finite element formulation. Both the results are compared with the present outcome to confirm the accuracies of the geometrically nonlinear formulation and first ply failure formulation of the proposed code. Table 2 shows the comparison where the dimensions of the plate are also reported. The material properties adopted by Kam et al. [9] is reported in Table 3.

Apart from the benchmark problems, the proposed code is also used to investigate failure initiation in uniformly loaded conoids. The shell is simply supported along $x = 0$ and $y = b$ and clamped along $x = a$ and $y = 0$. The material constants are reported in Table 3. The failure loads of the shell are studied using eight number of divisions along each of its plan directions.

4 Results and Discussion

Table 1 confirms accuracy of the proposed static formulation as the central displacements of the spherical shell obtained using the proposed finite element code are in a close match with the results reported by Reddy [18]. Figure 3 confirms that the

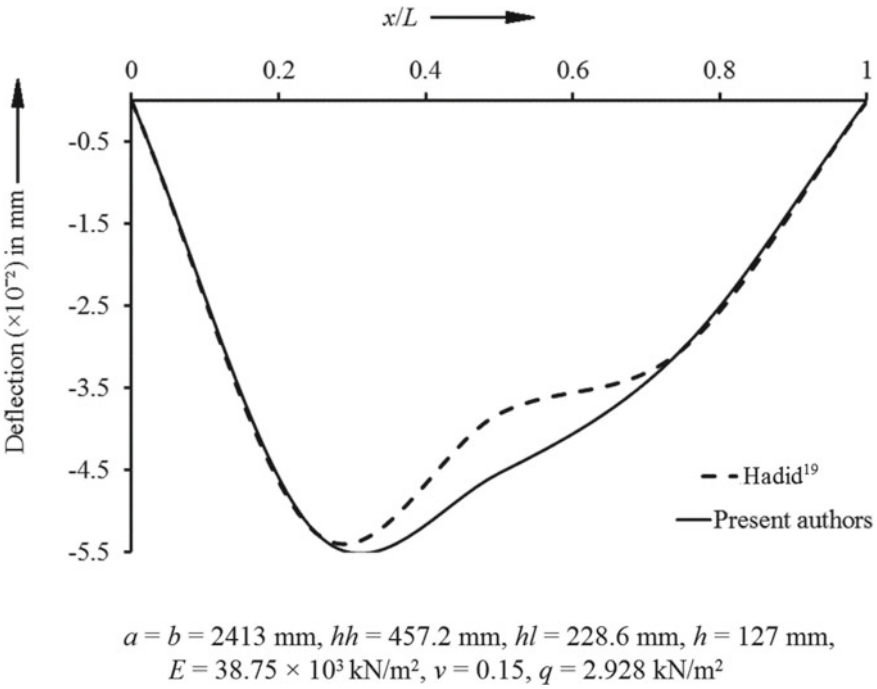

Fig. 3 The comparison of static deflections of an isotropic conoidal shell

Table 2 Nonlinear first ply failure loads in Newton for a $(0_2^\circ/90^\circ)_s$ plate

Failure theories	Side/thickness	Failure loads [9]	Experimental failure load [9]	Failure loads (proposed code)
Maximum stress	105.26	147.61	157.34	135.94
Maximum strain		185.31		218.10
Hoffman		143.15		133.21
Tsai–Wu		144.42		134.50
Tsai–Hill		157.58		134.91

Length = 100 mm, ply thickness = 0.155 mm

proposed code accurately formulated the conoidal shell geometry as good agreement is noted between the proposed results with the data reported by Hadid [19]. The first ply failure and geometrically nonlinear formulations are correctly formulated in the proposed code as it is found in Table 2 that the experimental and numerical failure loads reported by Kam et al. [9] show a close match with present results.

The additional problems concentrate on failure initiation in uniformly loaded conoidal shells. The failure initiation is studied for three different fiber orientations. The fibers run along 0°, 45°, and 90° with global x-axis of the shell. These

Table 3 Elastic constants, permissible stresses and strains Q-1115 composite

Elastic constants	Permissible stresses (MPa)	Permissible strains
$E_{11} = 142.5$ GPa	$X_T = 2193.50$	$X_{\varepsilon t} = 0.01539$
$E_{22} = 9.79$ GPa	$X_C = 2457.0$	$X_{\varepsilon c} = 0.01724$
$E_{33} = 9.79$ GPa	$Y_T = Z_T = 41.30$	$Y_{\varepsilon t} = Z_{\varepsilon t} = 0.00412$
$G_{12} = G_{13} = 4.72$ GPa	$Y_C = Z_C = 206.80$	$Y_{\varepsilon c} = Z_{\varepsilon c} = 0.02112$
$G_{23} = 1.192$ GPa	$R = 61.28$	$R_{\varepsilon} = 0.05141$
$\nu_{12} = \nu_{13} = 0.27$	$S = 78.78$	$S_{\varepsilon} = 0.01669$
$\nu_{23} = 0.25$	$T = 78.78$	$T_{\varepsilon} = 0.01669$

laminations are stacked in symmetric and antisymmetric orders to form two- and three-layered laminates by keeping the total material thickness as fixed. The nondimensional first ply failure loads of the shell for different laminations and stacking orders are reported in Table 4. The dimensions of the shell are furnished with the table. The nondimensional failure pressure (NFL) is obtained by using the expression, NFL $= (F/E_{22})(a/h)^4$, where 'F' is the failure load in MPa. Apart from the failure pressure, failure initiation location on the shell surface, first failed ply number and failure modes or tendencies are also reported in that table. The first lamina is the topmost one (see Fig. 1). The highest number is assigned to the bottommost lamina. It is obvious that the working load of a laminate can be obtained by assigning the factor of safety to the minimum failure pressure for a given laminate.

An in-depth study of Table 4 shows that the practicing civil engineers must adopt the angle-ply laminates for the conoids as the nondimensional failure pressure values are greater in magnitude for angle-ply laminations than the cross-ply ones. The minimum failure pressure is yielded by Hoffman failure theory for the cross-ply laminations and by maximum strain theory for the angle-ply ones. It is important to note from Table 4 that all the cross and angle-ply laminates taken up here fail through transverse tension acting perpendicular to the fiber and they fail at points lying on the simply supported boundaries of the conoid. It can be concluded from these observations that diagonal tension caused by a shear force acting at the simply supported edges of the shell is the cause of failure for all the laminates considered in Table 4.

In cross-ply laminates, the fibers run along the beam direction of the conoid in 0° lamina and along the arch direction in 90° lamina. The elastic modulus of a lamina is relatively higher along its fiber direction. It is noted from Table 4 that the 90° lamina fails first for both the 0°/90° and 0°/90°/0° laminates. The diagonal tension has almost equal components along x and y directions of the shell. The arch direction of the conoid is stiffer than the beam direction by virtue of the curved geometry of the shell. The 90° fiber, being aligned along the arch direction of the conoid makes the beam direction a relatively weaker side of the shell. Thus, for both the 0°/90° and 0°/90°/0° laminates, the component of diagonal tension acting along the arch

Table 4 Nondimensional first ply failure pressure, failed ply number, failure location, and failure modes/tendencies of laminated conoid

Lamination	Failure criteria	Nondimensional failure pressure (NFL)	Failed ply	Failure location (x, y) (m, m)	Failure mode/failure tendency
0°/90°	Maximum stress theory	1510.73	2	(0, 0.75)	2
	Maximum strain theory	1502.55	1	(0.25, 1)	2
	Hoffman failure theory	1496.42^{L}	2	(0, 0.75)	2
	Tsai–Hill failure theory	1500.51	2	(0, 0.75)	2
	Tsai–Wu failure theory	1497.45	2	(0, 0.75)	2
0°/90°/0°	Maximum stress theory	1927.48	2	(0, 0.75)	2
	Maximum strain theory	1922.37	2	(0, 0.75)	2
	Hoffman failure theory	1865.17^{L}	2	(0, 0.75)	2
	Tsai–Hill failure theory	1891.73	2	(0, 0.75)	2
	Tsai–Wu failure theory	1866.19	2	(0, 0.75)	2
45°/−45°	Maximum stress theory	1991.83	2	(0, 0.88)	2
	Maximum strain theory	1621.04^{L}	2	(0, 1)	2
	Hoffman failure theory	1971.40	2	(0, 0.88)	2
	Tsai–Hill failure theory	1979.57	2	(0, 0.88)	2
	Tsai–Wu failure theory	1973.44	2	(0, 0.88)	2

(continued)

Table 4 (continued)

Lamination	Failure criteria	Nondimensional failure pressure (NFL)	Failed ply	Failure location (x, y) (m, m)	Failure mode/failure tendency
45°/−45°/45°	Maximum stress theory	3266.60	3	(0, 0.13)	2
	Maximum strain theory	2939.73^{L}	3	(0, 0.13)	2
	Hoffman failure theory	3250.26	3	(0, 0.13)	2
	Tsai–Hill failure theory	3245.15	3	(0, 0.13)	2
	Tsai–Wu failure theory	3161.39	3	(0, 0.13)	2

Note 1 Failure mode/tendencies as 2 indicates tensile matrix cracking [15]
Note 2 $a/b = 1$, $a = 1000$ mm, $h = 10$ mm, $hh = 200$ mm, $hl = 50$ mm
Note 3 'L' indicates minimum failure pressure

direction of the conoid is appropriately encountered by a higher permissible limit of normal stress (2193.5 MPa). But the component along beam direction acts directly to the matrix which is weaker in normal strength (41.3 MPa) and cracks in transverse tension. For 45°/−45° and 45°/−45°/45° ones, the fibers are oriented along the diagonal direction of the shell. Naturally, in the case of angle-ply laminates, the lamina is relatively stronger along the major direction of load transfer. This is why the failure pressures yielded by the angle-ply laminates are higher than their cross-ply counterparts. The angle-ply shells do not fail through shear at all and they finally fail when the transverse tension exceeds the permissible limit. The symmetric stacking sequences of the cross and angle-ply laminates offer greater failure to pressure the antisymmetric ones. Among the laminations considered in Table 4, the 45°/−45°/45° shows the highest load-carrying capacity.

The study so far reveals that the three-layered symmetric angle-ply laminate (45°/−45°/45°) yields maximum nondimensional failure pressure for given material consumption. The failure study of the conoidal shell is further extended to explore how the first ply failure pressure varies with different fiber orientation ($\theta°$) in a $\theta°/-\theta°/\theta°$ laminate. The $\theta°/-\theta°/\theta°$ shells are studied for varying $\theta°$ ranging from 0° to 90° and the result is reported in Fig. 4.

The figure clearly indicates that the nondimensional failure pressure does not follow a monotonous pattern with $\theta°$ in case of $\theta°/-\theta°/\theta°$ laminate. The curve initially increases with increasing $\theta°$ and attains the peak (3590.4) for $\theta = 30°$. The failure pressure of the 30°/−30°/30° laminate is 18% more than the failure pressure obtained for the conventional 45°/−45°/45° one. The 30°/−30°/30° laminate fails

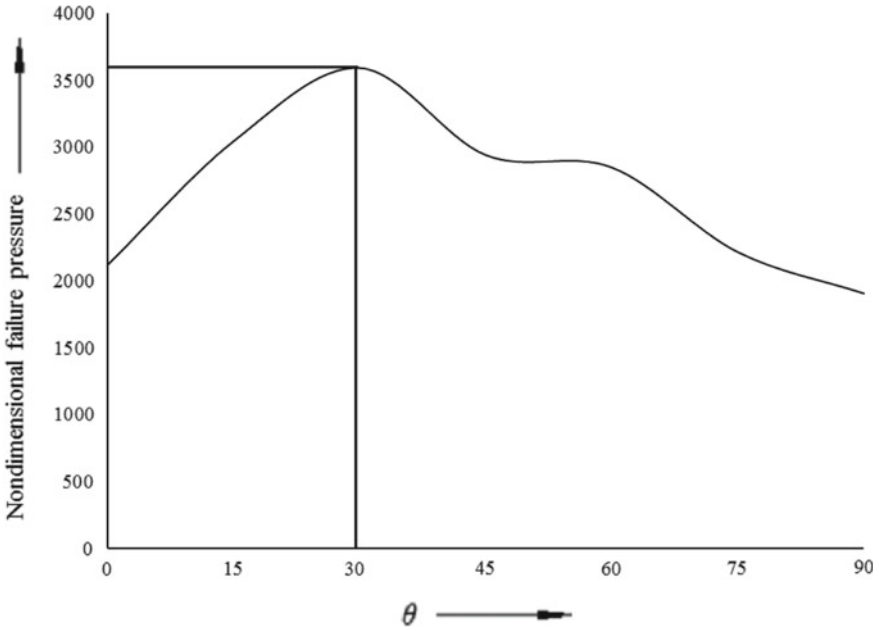

Fig. 4 Nondimensional first ply failure pressure for varying '$\theta°$' in $\theta°/-\theta°/\theta°$ laminate

at the bottommost lamina and on the simply supported boundary ($x = 0.38$ m, $y = 1.0$ m). The top and bottom layers contribute to the bending rigidity of the shell and the middle layer contributes significantly to resist the shear stress. Thus, a proper balance of bending and shear rigidities is attained and this is why the failure pressure is maximum for the $30°/-30°/30°$ laminate.

5 Conclusion

The present study leads to the following conclusions,

(1) The proposed code is capable of adequately predicting the failure initiation in laminated conoidal shells as it is noted from the solution of the benchmark problems.
(2) Two- and three-layered laminates of the cross and angle-ply laminations are taken up to form different conoidal shell options which are studied in this paper. Among the laminates considered here, the angle-ply ones are recommended for use in practical engineering applications as they show higher nondimensional failure pressures compared to the cross-ply laminates.

(3) The symmetric stacking orders found to fail in higher magnitudes of externally superimposed pressure compared to the antisymmetric orders. Thus, the practicing civil engineers must adopt the three-layered symmetric angle-ply laminate to fabricate the conoidal shell option studied here.
(4) Among the angle-ply laminations studied in this paper, it is found that for a constant quantity of material use, the 30°/−30°/30° laminate shows the highest failure pressure. Thus the 30°/−30°/30° laminate is recommended for practical use. The bottommost lamina of the 30°/−30°/30° laminate fails first. The failure initiates from a point lying on the simply supported boundary of the 30°/−30°/30° shell.

References

1. Dey A, Bandyopadhyay JN, Sinha PK (1992) Finite element analysis of laminated composite conoidal shell structures. Comput Struct 43:469–476
2. Ghosh B, Bandyopadhyay JN (1994) Bending analysis of conoidal shells with cut-outs. Comput Struct 53:9–18
3. Nayak AN, Bandyopadhyay JN (2006) Dynamic response analysis of stiffened conoidal shells. J Sound Vib 291:1288–1297
4. Das HS, Chakravorty D (2008) Natural frequencies and mode shapes of composite conoids with complicated boundary conditions. J Reinf Plast Compos 27:1397–1415
5. Kumari S, Chakravorty D (2010) On the bending characteristics of damaged composite conoidal shells—a finite element approach. J Reinf Plast Compos 29:3287–3296
6. Pradyumna S, Bandyopadhyay JN (2011) Dynamic instability behavior of laminated hypar and conoid shells using a higher-order shear deformation theory. Thin Walled Struct 49:77–84
7. Singh SB, Kumar A (1998) Postbuckling response and failure of symmetric laminates under in-plane shear. Compos Sci Technol 58:1949–1960
8. Reddy YSN, Reddy JN (1992) Linear and nonlinear failure analysis of composite laminates with transverse shear. Compos Sci Technol 44:227–255
9. Kam TY, Sher HF, Chao TN, Chang RR (1996) Predictions of deflection and first-ply failure load of thin laminated composite plates via the finite element approach. Int J Solids Struct 33:375–398
10. Satish Kumar YV, Srivastava A (2003) First ply failure analysis of laminated stiffened plates. Compos Struct 60:307–315
11. Lal A, Singh BN, Patel D (2012) Stochastic nonlinear failure analysis of laminated composite plates under compressive transverse loading. Compos Struct 94:1211–1223
12. Coelho AMG, Mottram JT, Harries KA (2015) Finite element guidelines for simulation of fiber-tension dominated failures in composite materials validated by case studies. Compos Struct 126:299–313
13. Prusty BG, Ray C, Satsangi SK (2001) First ply failure analysis of stiffened panels—a finite element approach. Compos Struct 51:73–81
14. Adali S, Cagdas IU (2011) Failure analysis of curved composite panels based on first-ply and buckling failures. Procedia Eng 10:1591–1596
15. Bakshi K, Chakravorty D (2013) First ply failure study of composite conoidal shells used as roofing units in civil engineering. J Fail Anal Prev 13:624–633
16. Bakshi K, Chakravorty D (2017) Geometrically nonlinear first ply failure loads of laminated composite conoidal shells. Procedia Eng 173:1619–1626

17. Chattopadhyay B, Sinha PK, Mukhopadhyay M (1995) Geometrically nonlinear analysis of composite stiffened plates using finite elements. Compos Struct 31:107–118
18. Reddy JN (1984) Exact solutions of moderately thick laminated shells. J Eng Mech 110:794–809
19. Hadid HA (1964) An analytical and experimental investigation into the bending theory of elastic conoidal shells. Doctoral dissertation, University of Southampton

Analysis of Transformed Sixth-Order Polynomial for the Contraction Wall Profile by Using OpenFOAM

R. Lakshman and Ranjan Basak

Abstract While designing the wind tunnel components, extreme care is taken for the designing of the contraction wall profile. Contraction plays an important role in flow uniformity and turbulence reduction inside the test section. Due to this, researchers are having a greater interest in the designing of a contraction wall profile. The sixth-order polynomial curve proposed by Sargison et al. is a well-acknowledged design for the contraction wall profile. Almost all design criteria were considered for the designing of the sixth-order polynomial curve except the proportionality criteria of inlet and outlet radii. According to the design criteria, the inlet radius must be larger compared to the outer radius of the contraction but in the sixth-order polynomial design, both the radii are almost similar. A transformed polynomial design was proposed by Daniel Brassard to meet this design criterion by changing the value of polynomial according to a proposed variable α. In this paper, the open-source CFD tool OpenFOAM was used to analyse the transformed sixth-order polynomial. The adverse pressure gradient, uniformity of flow, and turbulence intensity inside the test section as well as at the contraction outlet was taken into account for the analysis. The comparative results from the analysis show that the transformed polynomial model is giving better outcomes than the conventional sixth-order polynomial model.

Keywords Design · Wind tunnel · Contraction · Transformation · Turbulence · CFD · OpenFOAM

R. Lakshman (✉) · R. Basak
Department of Mechanical Engineering, National Institute of Technology Sikkim, Sikkim, India
e-mail: lakshmanr03@gmail.com

R. Basak
e-mail: basakranjan@nitsikkim.ac.in

B. N. Singh et al. (eds.), *Recent Advances in Theoretical, Applied, Computational and Experimental Mechanics*, Lecture Notes in Mechanical Engineering,
https://doi.org/10.1007/978-981-15-1189-9_11

1 Introduction

A wind tunnel is an aerodynamic tool that can simulate the fluid flow around a body as well as the forces produced at the fluid–body interface. Wind tunnels are basically categorized with respect to the tunnel geometry (open-circuit wind tunnel or closed-circuit wind tunnel) or by the wind speed in the test section relative to the speed of sound [1]. With the help of instrumentation measurement of local as well as the total velocity along with the temperature and pressure can be done using a wind tunnel. Flow visualization can also be done inside the test section by using smoke generators. The main parts of a conventional wind tunnel are the settling chamber, contraction, diffuser, test section and drive section [2]. Due to the wide real-world applications, plenty of efforts has been done in designing wind tunnel [3, 4]. Lots of researches are going on in the field of optimized designing of wind tunnel components. The creation of uniform flow inside the test section is the key objective of wind tunnel design.

The contraction plays a crucial role in producing a uniform flow with minimal turbulence inside the test section. Many research works have been done on the wind tunnel contraction design [5–11]. The prime objectives for the design of contraction are to improve the uniformity of flow, minimization of turbulence inside the working section, minimization of the boundary layer thickness at the entry of the test section and to evade boundary layer separation inside the contraction. The design of the contraction wall profile using a higher order polynomial equation got more significance in due time. The present work investigates the transformed sixth-order polynomial profile for the contraction wall profile of the wind tunnel.

2 Sixth-Order Contraction Profile

Flow uniformity inside the test section of a wind tunnel is directly affected by the contraction design. The criteria that should be satisfied with the design of the contraction wall profile ensures uniform flow at the contraction outlet. So that the velocity or pressure gradients should not create a progression of boundary layer thickness or generation of boundary layer separation. Sargison et al. proposed a sixth-order polynomial curve that fits in with all the following seven conditions that define the contraction profile [12].

$$\begin{gathered} y(x=0)=H; \quad y'(x=0)=0; \quad y''(x=0)=0; \\ y(x=l)=h; \quad y'(x=l)=0; \quad y''(x=l)=0; \quad y''(x=i)=0; \end{gathered} \tag{1}$$

where 'i' is the position of inversion point from the inlet, l refers to the total length of contraction, H and h represent height at the inlet and the outlet of the contraction, respectively. The location of the inversion point has been found to be one of the main factors in the optimization of the design. For finding the optimal position of

inversion point, the degree of curvature at contraction inlet is varied. In their paper, 0.6 was found to be the optimal position of inversion point. Solving the following matrix equation provides the values of unknown coefficients.

$$\mathrm{Aw} = \mathrm{B}; \tag{2}$$

where

$$\mathrm{A} = \begin{bmatrix} 30i^4 & 20i^3 & 12i^2 & 6i \\ l^6 & l^5 & l^4 & l^3 \\ 6l^5 & 5l^4 & 4l & 3l^2 \\ 30l^4 & 20l^3 & 12l^2 & 6l \end{bmatrix}, \quad \mathrm{B} = \begin{bmatrix} 0 \\ -h \\ 0 \\ 0 \end{bmatrix}, \quad \mathrm{w} = \begin{bmatrix} a \\ b \\ c \\ d \end{bmatrix} \tag{3}$$

3 Transformation of Contraction Design

The design for the contraction must ensure a larger radius at inlet compared to the outlet radius of the contraction profile. But in most of the higher order polynomial designs, both inlet and outlet radii of the profiles are nearly similar. For providing better results, transformed polynomial curves were proposed by Daniel Brassard by making the inlet and outlet radius of the contraction proportional to their area [13]. The transformed polynomial profiles were obtained by varying the value of polynomial according to a proposed variable 'α'. An analysis of transformed fifth-order polynomial profile showed better results compared to untransformed polynomial curve design [14]. In this paper, the analysis of transformed sixth-order polynomial is evaluated by providing various values for 'α' in the following equation:

$$y = \left(\eta\left(H_i^{\frac{1}{\alpha}} - H_e^{\frac{1}{\alpha}}\right) + H_e^{\frac{1}{\alpha}}\right)^{\alpha} \tag{4}$$

where, η is the sixth-order polynomial designed by Sargison et al. for the contraction; 'α' is some function of ζ (where $\zeta = x/l$); ζ is the dimensionless distance from the contraction inlet, with $\zeta = 1$ at the contraction outlet and $\zeta = 0$ at the inlet of the contraction.

By judicious selection of 'α' (either as a constant or as a function of ζ), the radius at the inlet and radius ant the outlet of the profile can be made proportional to their area. The values of α considered for the present analysis are 2, 1.5, 0.9, 0.7, 0.5, sine function of ζ, the quadratic function of ζ. Figure 1 shows the profiles generated by giving different values of 'α'.

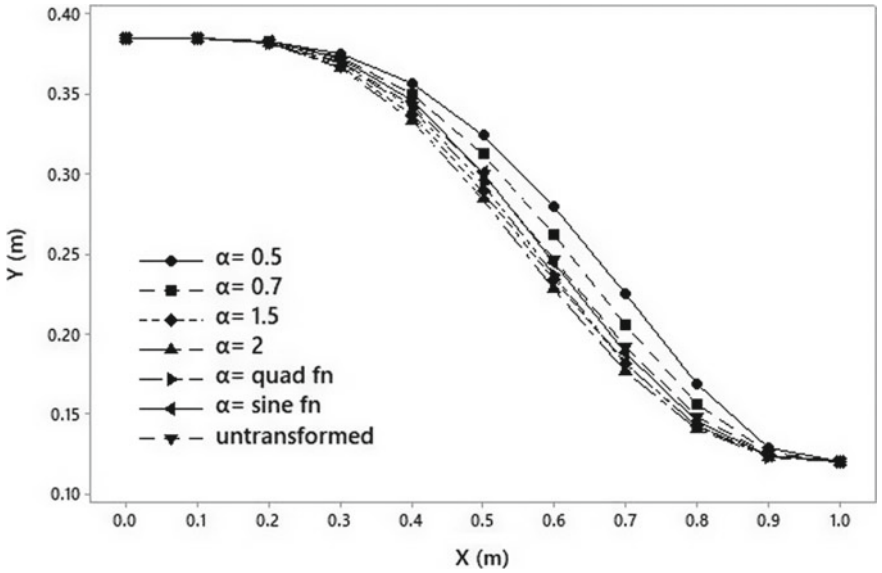

Fig. 1 Various profiles obtained by using different values of α

4 Numerical Setup

For solving the incompressible, steady-state, Reynolds-averaged Navier–Stokes equations, a segregated method for the velocity–pressure coupling was used in the computations. The OpenFOAM-provided solver SimpleFOAM [15] is employed for obtaining the solution. SimpleFOAM utilizes the SIMPLE algorithm to yield distinct pressure and velocity equations. The K-ε model is selected for computing Turbulence properties. The mass and momentum steady-state equations in a stationary frame can be written as follows [16].

$$\frac{\delta u}{\delta x} + \frac{\delta v}{\delta y} = 0 \tag{5}$$

$$u\frac{\delta u}{\delta x} + v\frac{\delta u}{\delta y} = -\frac{\delta P}{\delta x} + \mu\nabla^2 u + \frac{\delta}{\delta x}\left(-\rho\overline{u'^2}\right) + \frac{\delta}{\delta y}(-\rho\overline{u'v'}) \tag{6}$$

$$u\frac{\delta v}{\delta x} + v\frac{\delta v}{\delta y} = -\frac{\delta P}{\delta x} + \mu\nabla^2 v + \frac{\delta}{\delta x}(-\rho\overline{v'^2}) + \frac{\delta}{\delta y}(-\rho\overline{u'v'}) \tag{7}$$

After creating structural grids for the geometry, areas adjacent to the walls are provided with very fine grids. SnappyHexMesh utility in OpenFOAM is used for meshing the models. The model has meshed into hex-dominant meshes having 202,140 elements with 100,483 nodes (Fig. 2). A grid convergence study was also conducted to eliminate spatial error.

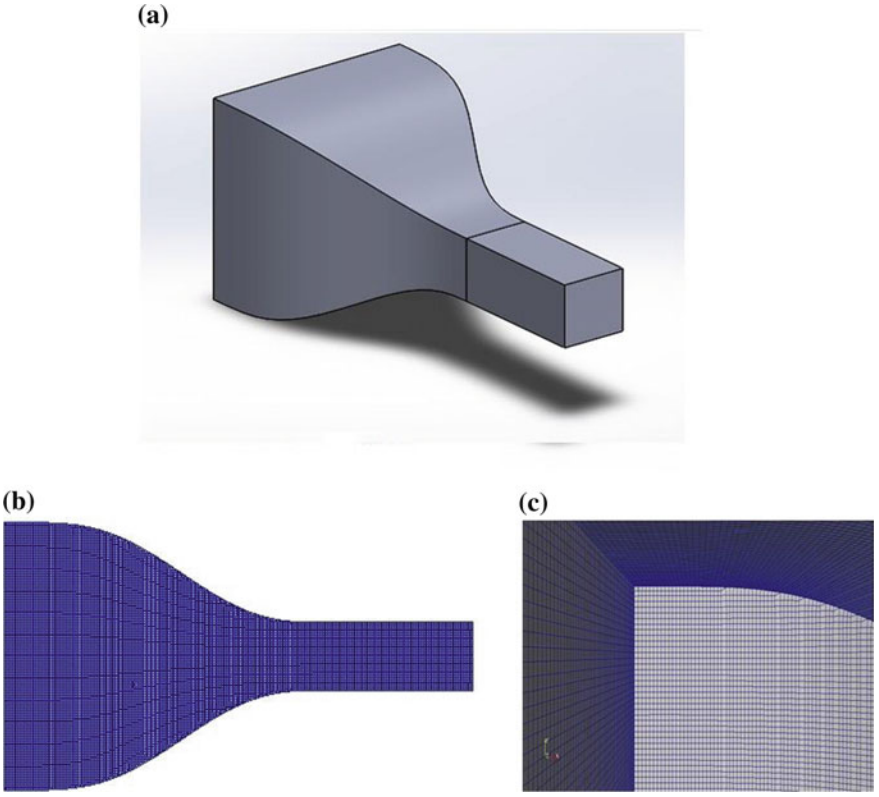

Fig. 2 **a** Geometrical model of wind tunnel contraction along with the test section. **b** Hex-dominant mesh created using SnappyHexMesh utility. **c** Detailed mesh view along the corner of the geometry

4.1 Geometry and Grid

The geometrical model involves the three-dimensional contraction along with the test section of 0.52 length. The dimension details of the geometry are given in Table 1.

The extension of the geometrical model up to the test section improves the stability of the computation as well as enhances the flow uniformity. Figure 2 shows the structure and the mesh grid generated for the geometrical model. The minimum y+

Table 1 Details of the geometry

Element	Dimension (m)
Inlet of contraction	0.75 × 0.75
Outlet of contraction	0.2 × 0.2
Length of contraction	1.0
Test section length	0.52

Table 2 Details of the grids selected for the grid convergence study

Grid Type	Refinement level	No of cells	No of faces	No of points
Coarse	1	20,034	61,980	22,038
Medium	2	51,091	168,516	66,459
Fine	3	202,140	676,034	272,040
Very fine	4	700,077	2,393,935	995,022

value for the geometry created for the computation was below 5. The pressure at the outlet and velocity at the inlet are used as boundary conditions. For the numerical simulation, the residual value of 10^{-5} was taken as the convergence criterion. A grid independence study was done to estimate discretization errors and to finalize the satisfactory mesh size. With the help of SnappyHexMesh utility in OpenFOAM, four sets of grids were generated for the grid independence study.

4.2 Grid Convergence

Four grid levels were selected (coarse, medium, fine, and very fine) for the grid convergence study. The grid level was changed using SnappyHexMesh utility available on OpenFOAM by changing the refinement level from 1 to 4. The details about the number of cells, faces, and points in each refined grids are shown in Table 2. Velocity $U = (2.1, 0, 0)$ m/s, the turbulent length scale $l = 1$ mm and the turbulence intensity $I = 2\%$ was given at the domain inlet as the boundary condition. A constant zero-pressure condition is given as the outlet boundary condition. Non-slip wall conditions ($|U| = 0$ m/s and $\delta P/\delta n = 0$) is given to the side and upper walls. The spatial error can be eliminated by selecting the grid with the least difference in result compared to the subsequent level. By doing so the solution will be depending on the physics and boundary condition but not on the type of grid applied [16].

In this study, the velocity (U) and the coefficient of the pressure value (CP) along the contraction were selected as the criterion for the study. The results obtained were plotted and was shown in Figs. 3 and 4.

From the result, it was found out that the difference in results between very fine and fine grids is much inferior compared to the difference in results between medium and the fine grid. Therefore, the fine grid with 202,140 cells is selected for the numerical simulation in the current study.

4.3 Validation of SimpleFOAM Solver

SimpleFOAM solver available in OpenFOAM was selected for the simulation of the present study. The data obtained from the wind tunnel test conducted at the

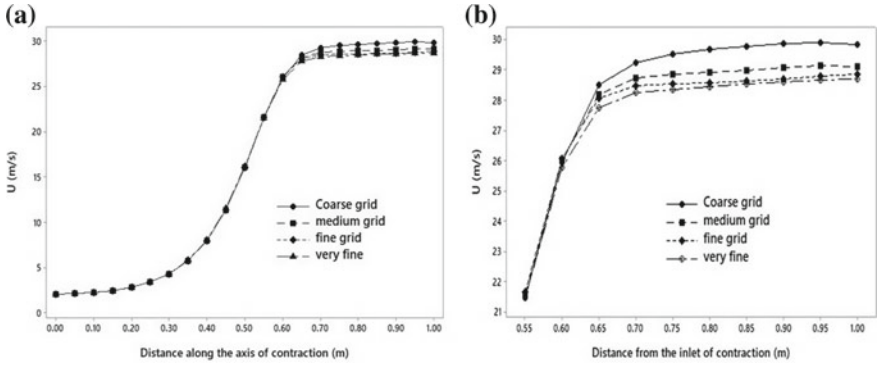

Fig. 3 **a** Velocity variation along the axis of contraction for various grids selected. **b** Velocity variation along the outlet zone of contraction

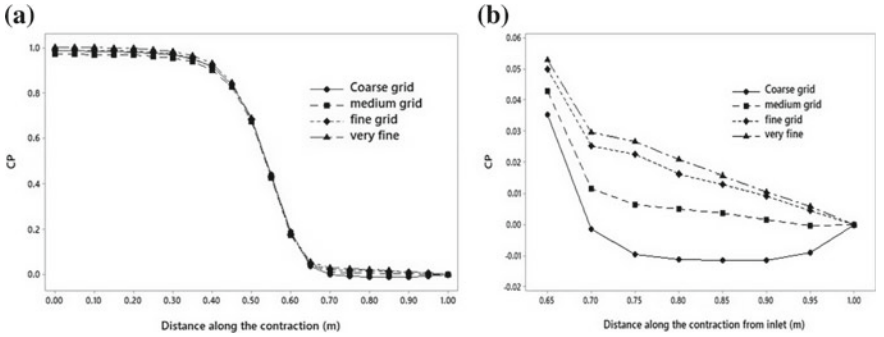

Fig. 4 **a** Coefficient of pressure variation along the axis of contraction for various grids selected. **b** Coefficient of pressure variation along the outlet zone of contraction

College of Engineering, Adoor is used for the validation of SimpleFOAM solver. The contraction cone of the wind tunnel has a length of 1 m with an inlet cross section of 0.75 m × 0.75 m and an outlet cross section of 0.2 m × 0.2 m, followed by a test section of 0.52 m length. The velocity profile was plotted using the data obtained from the Pitot-static tube placed at a distance of 0.5 m from the test section inlet. The same dimension of wind tunnel set up is used for the simulation. The open-source geometry tool SALOME was used for creating geometry. Figure 2 shows the details of the mesh created for the geometry. The kinematic viscosity of air is taken at 30 °C ($\upsilon = 1.6036 \times 10^{-5}$ m^2/s). Inlet velocity, U is taken as 2.1 m/s and a constant pressure $p = 0$ Pa was given at the domain exit. The velocity profile at a distance of 0.5 m from the inlet of the test section was taken for the comparison between the simulation and the one obtained experimentally. As displayed in Fig. 5, the comparative result between the experimental value and the simulation result shows good agreement with each other.

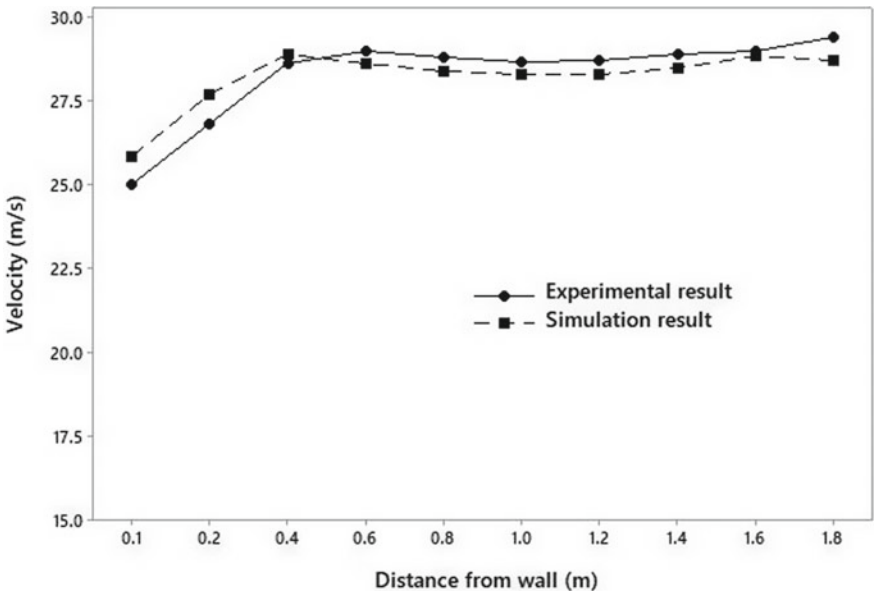

Fig. 5 Comparison of the velocity profile obtained at $x = 0.5$ m from the test section inlet

In this paper, the dimensions of contraction and test section used for the validation is taken for the computation. In order to obtain steady condition flow, contraction along with the test section was considered for the geometry. The SnappyHexMesh utility is used for meshing the geometry. Figure 2 shows the mesh grid generated. The same boundary condition which is used for validation is applied for the analysis (velocity at inlet = 2.1 m/s and outlet pressure is equated to atmospheric pressure).

5 Results and Discussion

The boundary layer separation can occur if there is a reversal in flow direction by the section of the boundary layer nearer to the wall causes. Wall shear stress is an important parameter to find the presence of separation. The points where the value of wall shear stress becomes zero or negative suggests a possibility of separation at that point. Shear stress distribution along the wall was plotted for each profile and found that none of them are subjected to separation. The wall shear stress distribution for all the contraction profiles is shown in Fig. 6. It is found that all the models are having a positive value for wall shear stress which proves the absence of separation.

The wall pressure coefficients along the contraction for all the transformed and untransformed profiles are shown in Fig. 7. This dimensionless parameter coefficient of pressure, C was used to normalize the data. There is a risk of separation if the pressure gradient is high enough. If there is a constant pressure region on the CP

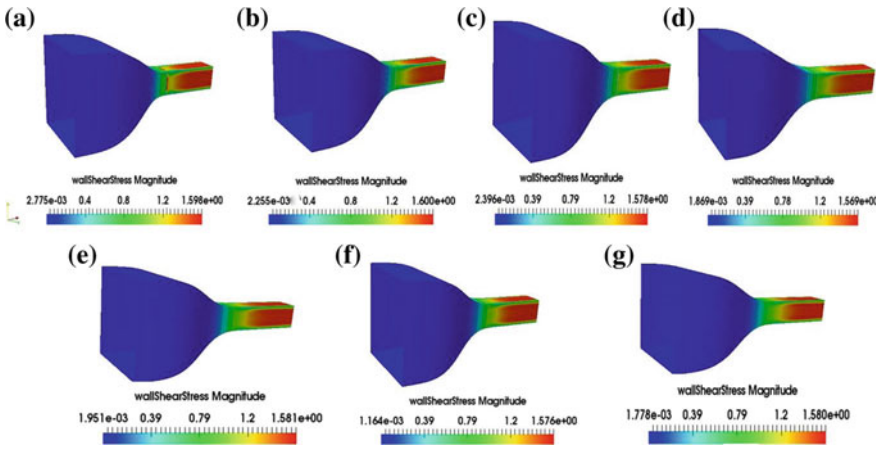

Fig. 6 Wall shear stress contour plot for the profiles when **a** $\alpha = 0.5$, **b** $\alpha = 0.7$, **c** $\alpha = 1.5$, **d** $\alpha = 2$, **e** $\alpha =$ quadratic function of ζ, **f** $\alpha =$ sine function of ζ, **g** untransformed

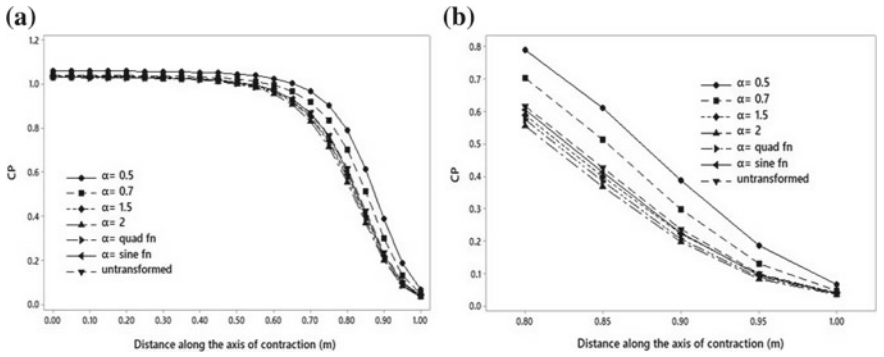

Fig. 7 **a** Pressure coefficient along the contraction, **b** magnified view at the outlet of contraction

graph in this adverse pressure gradient region, it indicates the presence of separation. The expression for finding Cp is as shown below.

$$\text{Cp} = \frac{(P - P_\infty)}{0.5\rho U^2}$$

where P is the static pressure measured along the wall, P_∞ is the static pressure at the outlet of contraction and U is the mean value of the velocity measured at the contraction outlet.

From the figure, the adverse pressure gradient is found at the inlet and outlet portion of the contraction. The outlet adverse pressure gradient is found to be more significant compared to the inlet. From the comparison, it is clear that the adverse pressure is more when the alpha value is less and a lesser adverse pressure gradient

is seen for the profile having higher alpha value ($\alpha = 1.5$ and $\alpha = 2$). On comparing Quadratic function and sine function, the quadratic function is having superior results.

The prime objective of the design of contraction is to improve the uniformity of flow inside the test section. Figure 8 shows the velocity profile at the mid vertical plane of the working section. The same graph was used to analyse the flow uniformity along the test section. Due to the growth in turbulence intensity, flow uniformity is found to be disturbed adjacent to the walls. It is seen that the flow uniformity is getting better with the increase in the value of 'α'. It is also detected that the contraction with '$\alpha =$ quadratic function of ζ' hold better uniformity than other contraction profiles.

Figure 9 shows the turbulence intensity profile for the various profiles (both transformed and untransformed). The turbulence intensity value is very much depended on the contraction profile and contraction ratio. If the turbulence intensity in the test section is very high, it may generate unfavorable conditions and measurements. So the value of turbulence intensity inside the test section must be kept as low as possible. From the figure, it is clear that the value of turbulence is falling with an increase

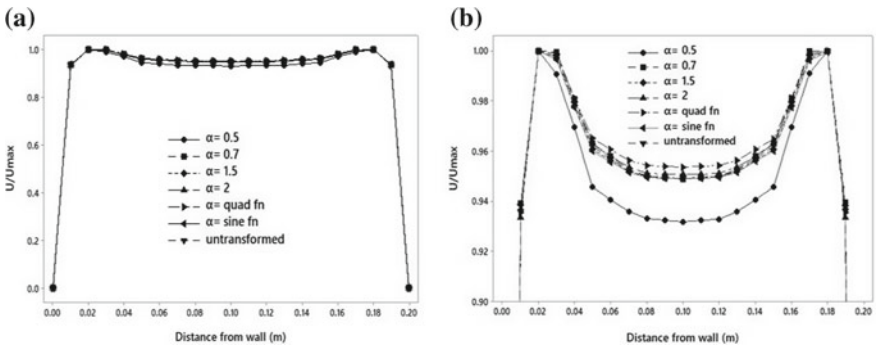

Fig. 8 **a** Velocity profile at the contraction outlet along the vertical plane, **b** magnified the view of the velocity profile at the contraction outlet along the vertical plane

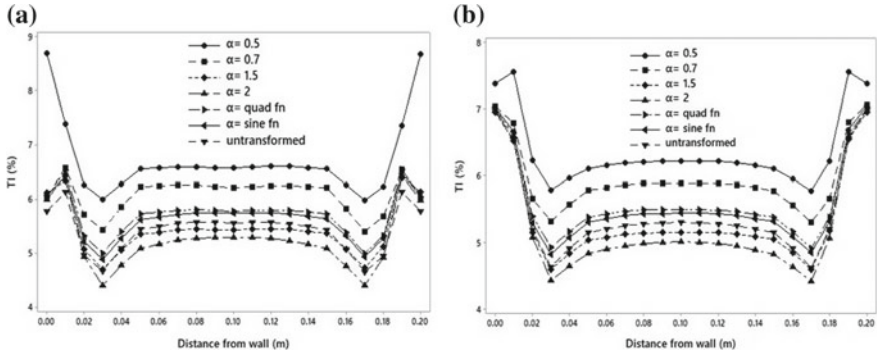

Fig. 9 **a** Turbulence intensity at the contraction outlet. **b** Turbulence intensity at the mid-vertical plane of the test section

Table 3 The average turbulence intensities and uniformity at the outlet of contraction and test section midplane for various values of α

Value of α	Average turbulence intensity (%)		Flow uniformity (%)	
	At contraction outlet	At test section midplane	At contraction outlet	At test section midplane
0.5	6.735	6.368	86.210	88.403
0.7	6.077	5.958	87.332	88.555
1.5	5.441	5.352	87.224	88.246
2	5.255	5.225	87.287	88.163
The quadratic function of ζ	5.716	5.628	87.454	88.428
Sine function of ζ	5.652	5.580	87.177	88.321
Untransformed	5.426	5.439	87.227	88.254

in the value of α. The profile with $\alpha = 2$ shows better performance compared to others. Among the quadratic function of ζ and sine function of ζ, it is seen that better results are obtained for the quadratic function of ζ compared to the sine function. It is also found that the value of turbulence intensity is increasing at lower values of α. Table 3 shows the average turbulence intensities and average uniformity calculated at the contraction outlet, as well as at the midplane of the test section.

6 Conclusion

The proportionality of inlet and outlet radius with respect to their cross-sectional area is one of the key design criteria for the contraction of the wind tunnel. While analysing the sixth-order polynomial contraction proposed by Sargison et al., it was found that the inlet radius and outlet radius are not having much difference. This can be resolved by using a transformed polynomial curve using the Eq. (2). Both the normal and transformed curves were analysed based on uniformity of flow, turbulence intensity, and adverse pressure gradient by using open source CFD tool OpenFOAM. Experimental data were taken for validation of results. The results show the transformed contraction is having better results compared to the untransformed polynomial profile. As the value of alpha is increasing it was found that the uniformity and turbulence intensity is getting better. This analytical study thus proves the significance of using transformed curves for the design of the contraction of the wind tunnel.

Although this analysis (using the k-ε model turbulence model) found that the transformed polynomial curves are performing better compared to untransformed

curves, further studies can be conducted by using different turbulence models to make it certain.

References

1. Mehta RD, Bradshaw P (1979) Design rules for small low speed wind tunnels. Aeronaut J 83(827):443–453
2. Dolan DS, Zepeda D, Taufik T (2011) Development of wind tunnel for laboratory wind turbine testing. In: North American power symposium (NAPS), pp 1–5. IEEE
3. Panda MK, Samanta AK (2016) Design of low cost open circuit wind tunnel—a case study. Indian J Sci Technol 9(30)
4. Cattafesta L, Bahr C, Mathew J (2010) Fundamentals of wind-tunnel design. Encycl Aerosp Eng
5. Rouse H, Hassan MM (1949) Cavitation-free inlets and contractions. Mech Eng 71(3):213–216
6. Bell JH, Mehta RD (1988) Contraction design for small low-speed wind tunnels
7. Mikhail MN (1979) Optimum design of wind tunnel contractions. AIAA J 17(5):471–477
8. Wolf T (1995) Design of a variable contraction for a full-scale automotive wind tunnel. J Wind Eng Ind Aerodyn 56(1):1–21
9. Lastra MR, Oro JMF, Vega MG, Marigorta EB, Morros CS (2013) Novel design and experimental validation of a contraction nozzle for aerodynamic measurements in a subsonic wind tunnel. J Wind Eng Ind Aerodyn 118:35–43
10. Hoghooghi H, Ahmadabadi MN, Manshadi MD (2016) Optimization of a subsonic wind tunnel nozzle with low contraction ratio via ball-spine inverse design method. J Mech Sci Technol 30(5):2059–2067
11. Abdelhamed AS, Yassen YES, ElSakka MM (2015) Design optimization of three dimensional geometry of wind tunnel contraction. Ain Shams Eng J 6(1):281–288
12. Sargison JE, Walker GJ, Rossi R (2004) Design and calibration of a wind tunnel with a two dimensional contraction. In: Australasian fluid mechanics conference, The University of Sydney, Australia
13. Brassard D, Ferchichi M (2005) Transformation of a polynomial for a contraction wall profile. Trans ASME I J Fluids Eng 127(1):183–185
14. Lakshman R, Basak R (2018) Analysis of transformed fifth order polynomial curve for the contraction of wind tunnel by using OpenFOAM. In: IOP conference series: materials science and engineering, vol 377, no 1, p 012048. IOP Publishing
15. OpenFOAM (2015) The open source CFD toolbox, User guide, Version 3.0.1
16. Anderson JD, Wendt J (1995) Computational fluid dynamics, vol 206. McGraw-Hill, New York

Fatigue Life Assessment of an Existing Railway Bridge in India Incorporating Uncertainty

Mrinal Chanda, Kishore Chandra Misra and Soumya Bhattacharjya

Abstract Fatigue Life Assessment of an existing railway steel truss bridge near Dumdum, Kolkata is presented. The deterministic approach using the Palmgren–Miner rule and probabilistic approach by (i) available probabilistic formulations and (ii) direct Monte Carlo Simulation (MCS) have been adopted in the study. The bridge is unique of its type since the movement of traffic is transverse to the main span of the truss. The truss bridge is modeled in STAADPro.V8i SS5 with a moving load of (i) coal rakes, (ii) Passenger rakes, and (iii) EMU cars. The train running schedule, composition of train and loading is obtained from the Indian Railway. After analysis, the stress range time spectra is obtained and the reservoir method is applied to evaluate the damage. Also, the probability of fatigue failure of the bridge is estimated which indicates a risk of 77% damage of the critical members after 80 years. It is observed that fatigue failure is supposed to occur in between 80 and 90 years of service. The probabilistic approach with direct MCS yields the most conservative prediction.

Keywords Fatigue life · Monte Carlo simulation · Steel bridge · Palmgren–Miner rule

1 Introduction

The Indian Railway (IR) in its vast network is having over one lakh bridges and most of them are steel bridges. The assessment of fatigue life of such existing bridges is a major issue in the perspective of ever-increasing traffic load (e.g., fatigue failure of Jubilee bridge in Bandel, West Bengal). There have been lots of studies on the assessment of fatigue life in deterministic [1] and probabilistic format [2] in the past few decades. Solimon et al. [3] predicted the life of existing fatigue prone steel bridges by integrating Structural Health Monitoring (SHM) data by probabilistic bilinear S-N approach. The effect of changing the value slope of AASTHO S-N lines below the constant amplitude fatigue threshold on the fatigue life is investigated through a

M. Chanda · K. C. Misra · S. Bhattacharjya (✉)
Department of Civil Engineering, IIEST Shibpur, Shibpur, West Bengal, India
e-mail: soumyaiiests@gmail.com

B. N. Singh et al. (eds.), *Recent Advances in Theoretical, Applied, Computational and Experimental Mechanics*, Lecture Notes in Mechanical Engineering,
https://doi.org/10.1007/978-981-15-1189-9_12

parametric study. Krejsa [4] described methods for probabilistic assessment of the reliability of steel structures and bridges that are exposed to cyclic loads taking into account the propagation of fatigue cracks from surface. Ye et al. [5] presented a critical review of the fatigue life assessment of railway bridges. Lee and Cho [6] presented a new approach for probabilistic fatigue life prediction for bridges using finite element model updating based on SHM data. Ding and Chen [7] evaluated fatigue damage using closed-form spectral methods considering narrowband and Gaussian response characteristics. After a thorough literature survey, scarcity is noted regarding the fatigue life assessment of existing railway bridges in India. Thus, in this study, the fatigue life assessment of an existing railway trussed bridge near Dumdum, Kolkata is accomplished by (i) deterministic approach using Palmgren-Miner rule [8] using IS:800-2007 [9] (Approach I), (ii) Monte Carlo Simulation (MCS) on Approach I to incorporate uncertainty in load and parameters (Approach II), (iii) Probabilistic approach as per formulation of Crandall and Mark [10] (Approach III), and (iv) Probabilistic approach as per Wirscheng [2]. The bridge is unique of its type since the movement of traffic is transverse to the main span of the truss. The truss bridge is modeled in STAAD.Pro.v8iSS5 [11] with moving load of (i) coal rakes, (ii) Passenger rakes, and (iii) EMU cars. The train running schedule, composition of train and loading is obtained from the IR. After analysis, the stress range time spectra is obtained and the reservoir method is applied to evaluate damage by approach I. The uncertainty in loading and strength parameters are incorporated by the MCS in approach II. In approach III, the expectation of damage is estimated through zero-crossing rate of random stress assuming Rayleigh distribution for stress range history. In approach IV the probabilistic fatigue life is assessed assuming the stress range history to be lognormal. Also, the probability of failure of the bridge is evaluated following [12] (approach V) considering the endurance strength of the material. In Sect. 2, these four approaches are presented in brief followed by the modeling of the bridge in Sect. 3 and results and discussion in Sect. 4.

2 Fatigue Life Assessment Approaches

As mentioned, Approach I is a deterministic approach and approaches II to V are probabilistic approaches. A brief formulation of these approaches is presented in the following subsections.

2.1 Approach I

This approach is based on the Palmgren–Miner's rule and uses the S-N curve of IS: 800-2007 [9]. The calculation of the remaining fatigue life is generally manifested through the calculation of the damage accumulation. The task is to find the year of operation when Damage (D) exceeds unity. This method, based on the S-N approach,

Table 1 Yearly number of the run of trains in the IR in 2017

Types of train	Goods train	Passenger train	EMU train
Yearly number of cycle	1600	4380	7300

is called the linear Palmgren–Miner's rule for damage accumulation and is expressed by the form

$$D = \sum \frac{n_i}{N_i} \tag{1}$$

where n_i is the number of cycles occurring at the stress range spectrum for ith type train. N_i is the number of cycles corresponding to a particular fatigue strength for the induced stress range magnitude, $\Delta\sigma_i$ by the ith type train and obtained from the S-N curve. The standard S-N curve can be expressed in the form of Basquin equation as

$$NS^b = C \tag{2}$$

where N is the number of stress cycles to failure at a constant amplitude stress range S, and C and b are the material parameters, termed as the fatigue strength coefficient and the fatigue strength exponent, respectively. The n_i is obtained from the stress range spectrum using Reservoir method following the approach of Lee and Noori [13]. The traffic flow data as in 2017 through the IR is obtained as in Table 1. The extrapolated cumulative number of train run in upcoming years is presented in Fig. 1, which is based on the trend and perspective of growth in the IR in the past few years.

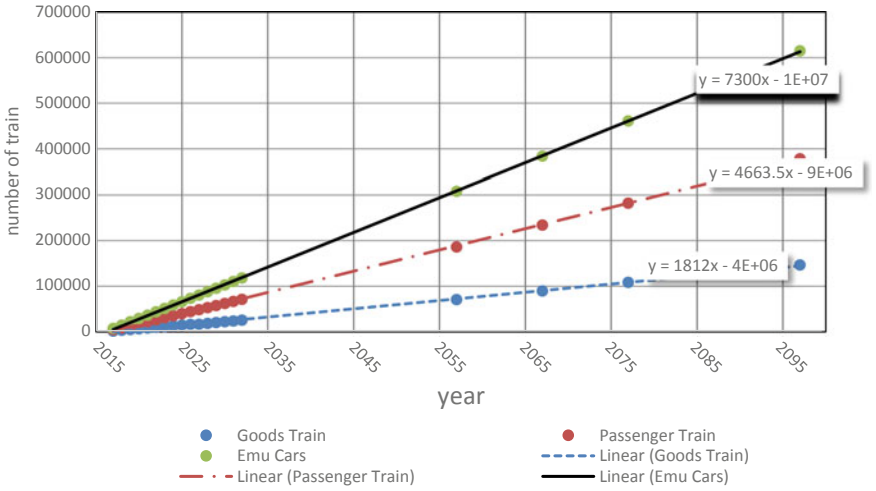

Fig. 1 Cumulative train flow data

2.2 Approach II

In this approach, the involved parameters, viz. wheel loading of different trains, yearly number of trains, dynamic magnification factor, S-N curve parameters b and C are assumed to be uncertain with the lognormal distribution. The Coefficient of Variation (COV) for wheel load for goods, passenger, and EMU train are assumed as 36%, 30% and 25% based on statistical analysis. The COV for the number of trains, dynamic magnification factor, b and C are taken as 15%, 10%, 10%, and 10%, respectively. The uncertainty is incorporated through a direct Monte Carlo Simulation (MCS). The MCS converges at around 1.2 lakhs simulation.

2.3 Approach III

Based on Crandall and Marks [10] approach, if the stress history follows the normal distribution, the peak follows Rayleigh's distribution as

$$f(S) = \frac{S}{\sigma_s^2} \exp\left(-\frac{S^2}{2\sigma_s^2}\right) \tag{3}$$

where σ_s is the standard deviation of random stress range, S. Then, it is possible to derive the expected damage $E(D)$ in the probabilistic sense [10] as

$$E(D) = \frac{\omega T}{2\pi C}\left(\sqrt{2}\sigma_S\right)^{\alpha} \Gamma\left(1 + \frac{b}{2}\right) \tag{4}$$

where ω the frequency of load is cycle variation and T is expected fatigue damage time.

2.4 Approach IV

This approach [2] is similar to approach I. But, in place of the MCS, second-moment reliability method is used. The approach assumes that the involved parameters are lognormal. This approach attempts to find after how many years of operation the fatigue reliability (or probability of failure) becomes less than the acceptable limit (or more than the safety threshold). The probability of failure is estimated by $p_f = \phi(-\beta)$, where, ϕ is the CDF of the standard normal distribution function and β is safety index. Then, following [2]

$$\beta = \frac{\ln\left(\tilde{N} \Big/ Ns\right)}{\sigma_{\ln N}} \tag{5}$$

where *Ns* is the intended service life and the tilde denote median values.

$$\tilde{N} = \frac{\tilde{C}D}{\widetilde{B^b}S_e^b} \quad \sigma_{\ln N} = \sqrt{\ln\left[\left(1+V_C^2\right)\left(1+V_D^2\right)\left(1+V_B^2\right)\right]} \tag{6}$$

The *V*'s denotes the coefficient of variation, *B* is the blanket random variable denoting uncertainty in stress range [2].

2.5 *Approach V*

If the induced repeated stress is below the endurance strength of the material, theoretically the component will not fail no matter how many cycles are repeated. In this approach, the endurance strength of a material in fatigue is estimated following Mischke [12]. The endurance strength is given by S_e as

$$S_e = K_a K_b K_c K_d K_e K_f \emptyset \overline{S_{ut}} \tag{7}$$

where K_a, K_b, K_c, K_d, K_e, K_f, $\emptyset$ *and* $\overline{S_{ut}}$ are Surface modification factor, Size modification factor, Loading modification factor, Temperature modification factor, Stress concentration, and notch sensitivity modification factor, Fatigue strength factor, empirical random proportionality factor and the mean ultimate tensile strength of the material, respectively. These are assumed to be random normal whose mean values are obtained from Mischke [12] and COV is assumed to be 10%. Then, the reliability that the endurance strength is not exceeded is estimated by the first-order second-moment method.

3 Model of the Bridge

The present study focuses on the fatigue life assessment of the Dumdum bridge in Kolkata. The plan view of the bridge is shown in Fig. 2. The length of the bridge along train movement is 6 m and the bridge span is 30 m. The height of the truss from the deck is 6 m. The direction of the traffic is transverse to the bridge span direction. One typical bridge is considered for analysis and is modeled in STAADPro Select Series 6. The moving load as per the IR specification of the train configuration is applied on the bridge (Fig. 3). The load data of three kinds of railway goods rakes is considered to act as a moving load over the span of the bridge. The specification of a load of each rake are as follows:

(i) Taken over coal rakes (Composition − engine + 55 BOXN, Rake Length = 624.15 m, Total Weight = 5140 t);

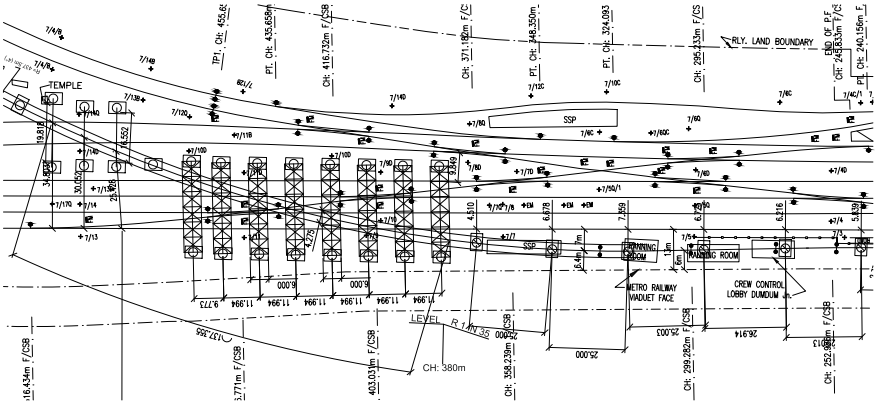

Fig. 2 Layout plan of the trussed bridge

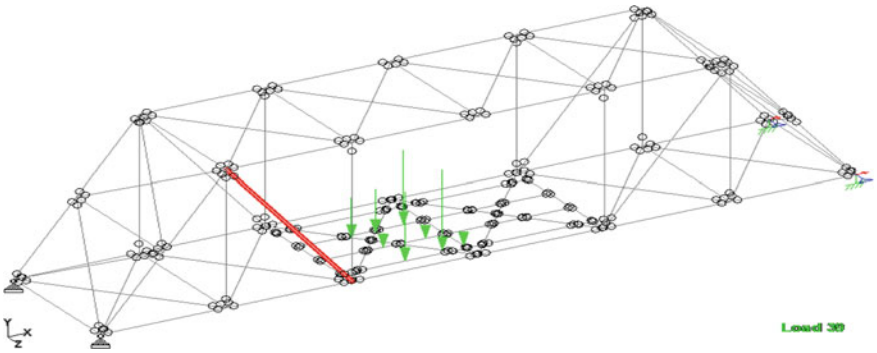

Fig. 3 STAAD model of the bridge

(ii) Passenger rakes (Composition − engine + 15 coaches, Rake Length = 373 m, Total Weight = 2175 t.);
(iii) EMU cars (Composition − 2 engine cum bogie + 7 coaches = 153 m, total weight = 1195.2 t).

Apart from the bearings, the most critical member of the truss where maximum stress range occurs is also shown in Fig. 3 in red.

4 Results and Discussion

A typical stress spectrum obtained after the STAADPro analysis is shown in Fig. 4. It will provide n_i by the reservoir method. The maximum axial stress in the truss member, effective stress (including dynamic magnification factor) and the number

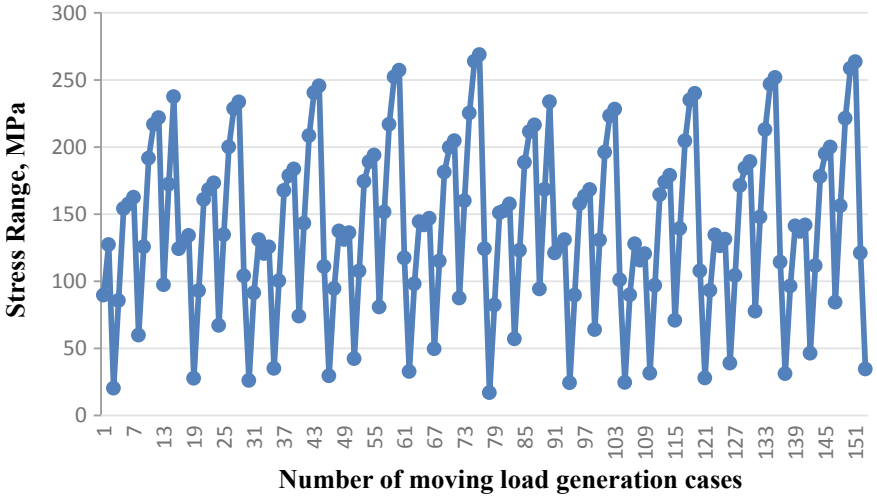

Fig. 4 Stress range spectra for passenger train

Table 2 Maximum axial stress and N for various type of rakes

	Goods train	Passenger train	EMU cars
Maximum axial stress range in N/mm^2	277	266	186
Effective stress range in N/mm^2	340	327	229
Number of cycles to fatigue failure	488,500	549,108	1,598,802

of cycles to failure for each category of train (N_i) is shown in Table 2. Then, by using Eqs. (1) and (2) the fatigue life estimated through Approach I, deterministically. The bridge is in operation from the year 2017. It is observed that the fatigue life of the bridge is 85 years.

Now, the uncertainty information on the involved parameters (see Sect. 2.2) is incorporated by the direct MCS and the probabilistic fatigue life is estimated as 80 years by Approach II. In approach III, assuming S-N curve parameters as of approach I, σ_S as of approach II the probabilistic fatigue life is estimated by Eq. (4) as 90 years. The trend of accumulated damage over operation year by approach III is shown in Fig. 5. Since the extrapolated growth rate model of the train is considered as linear in Fig. 1, the trend of accumulated damage over the operation year is also linear. The probabilistic fatigue life is further assessed following Approach IV. The variation of Probability of failure by Eqs. (5) and (6) over the operation year is presented in Fig. 6. It can be observed that the truss attains 77% failure after 80 years of operation.

The endurance strength of the member material is estimated in Approach V by Eq. (7). The mean values of the parameters are $K_a = 0.09106$, $K_b = 1$, $K_c = 0.774\,(1, 0.163)$, $K_d = 1$, $K_e = 0.5722$, $K_f = 1.0$, $\emptyset = 0.505\,(1, 0.146)$

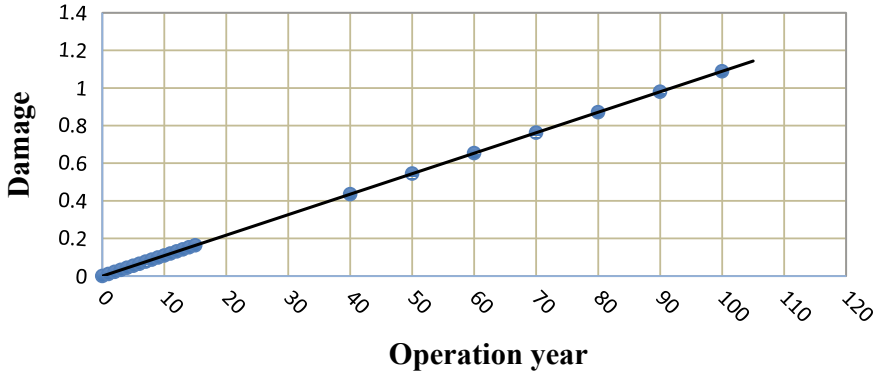

Fig. 5 Accumulated damage over operation year by Approach III

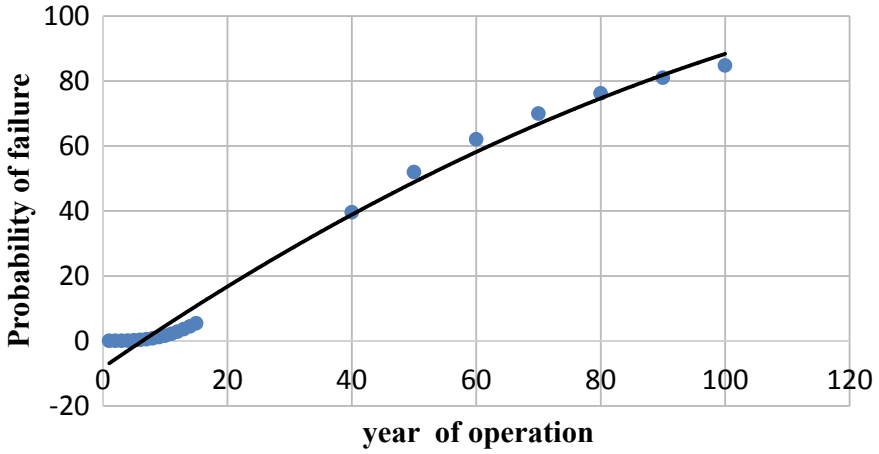

Fig. 6 Probability of failure by Approach IV

following equations mentioned in Mischke [12] and based on the fabrication of the considered bridge. The uncertainty is incorporated in the parameters as mentioned in Sect. 2.5 by the direct MCS. The MCS converges at 10,000 iterations yielding a probability of failure of most critical as 13%. In a nutshell, the fatigue life obtained by various approaches is presented in Table 3. It may be observed that the MCS based probabilistic fatigue life approach yields the most conservative result. However, predictions by all the approaches are in close conformity yielding the range of 80–90 years, which further indicate acceptability of all the approaches and accuracy of the assumptions. In the most conservative sense the bridge is expected to exhaust its fatigue life in the year 2097 (Approach II) and in optimistic sense the same is in the year 2107 (Approach III).

Table 3 Fatigue life by various approaches

Sl no	Approaches	Expected fatigue life (years)
1	Approach I	85
2	Approach II	80
3	Approach III	90
4	Approach IV	88

However, the main limitation of the study is its assumed linear extrapolated traffic growth rate data, which is supposed to vary in the future. Though uncertainty on this extrapolated data is duly incorporated in the study, there is always a chance of higher deviation than the assumed COV.

5 Conclusions

Fatigue Life Assessment of an existing railway bridge of India, viz. Dumdum bridge, Kolkata is presented. The fatigue Life is investigated both by the deterministic and probabilistic approaches. The bridge is modeled in STAAD Pro and analyzed for moving load. Uncertainty in various parameters is considered through available probability formulation and by the direct MCS. All the approaches yield similar results, with approach II (by the MCS) predicting the most conservative assessment. The expected fatigue life of the trussed bridge is in between 80 and 90 years. As per approach II, the fatigue life of the bridge is supposed to be exhausted in 2097. It is observed from the Figure that there is a 77% chance of fatigue failure of the critical members at 80 years. The approach V estimates a 13% probability of failure of the most critical member in consideration to the endurance strength.

Acknowledgements The authors gratefully acknowledge the Indian Railway for sharing the information on the considered bridge, loading on the bridge, train schedule, and other uncertainty information.

References

1. Wang X, Sayed AM, Wu Z (2015) Modeling of the flexural fatigue capacity of RC beams strengthened with FRP sheets based on finite-element simulation. J Struct Eng ASCE 141(8):04014189-1-14
2. Wirsching PH (2006) Application of reliability methods to fatigue analysis and design. In: Halder A (ed) Recent developments in reliability based civil engineering. World Scientific, USA, pp 125–139
3. Solimon M, Frangpool DM, Kown K (2013) Fatigue assessment and service life prediction of existing steel bridges by integrating SHM into a probabilistic bilinear *S-N* approach. ASCE J Struc Eng 139(10):1728–1740

4. Krejsa N (2014) Probabilistic reliability assessment of steel structures exposed to fatigue VSB, Technical University Ostrava, Czech Republic
5. Ye XW, Su YH, Han JP (2014) A state-of-the-art review on fatigue life assessment of steel bridges. Math Problems Eng. Article iD 956473
6. Lee YJ, Cho S (2015) Probabilistic fatigue life prediction for bridges using system reliability analysis and SHM-based finite element model updating. In: 12th international conference on applications of statistics and probability in civil engineering, ICASP12 Vancouver, Canada, 12–15 July 2015
7. Ding J, Chen X (2015) Fatigue damage evaluation of broad-band Gaussian and non-Gaussian wind load effects by a spectral method. Probab Eng Mech 41:139–154
8. Ciaverella M, Antuono PD, Demelio GP (2017) A simple finding on variable amplitude (Gassner) fatigue SN curves obtained using Miner's rule for unnotched or notched specimen. Eng Fract Mech 176:178–185
9. IS: 800-2007. Indian Standard. General Construction In. Steel—code of practice (Third Revision), BIS, India
10. Crandall SH, Mark WD (1963) Random vibrations in mechanical systems. Elsevier
11. STAAD.Pro, Select Series 6. Bentley Inc
12. Mishke CR (1987) Prediction of stochastic endurance strength. ASME J Vib Acous Stress Rel Des 109:113–122
13. Lee NW, Noori M (2016) A framework for fatigue reliability assessment of orthotropic bridge decks under stochastic fatigue truck loads. In: Wang HW, Li J, Zhang J, Chen JB (eds) 6th Asian-Pacific symposium on structural reliability and its applications (APSSRA 2016), 28–30 May 2016, Shanghai, China

Numerical Simulation of Acoustic Emission Waveforms Generated by Tension and Shear Cracks in RCC Beams

Arun Roy, Paresh Mirgal and Sauvik Banerjee

Abstract The objective of this paper is to model acoustic emission (AE) sources and examine the propagation characteristics of AE waveforms generated by these sources in—concrete structures using finite element (FE) simulation. In order to model AE sources in the form of tensile and shear cracks, a new simulation technique is developed, where the sudden release of nodes is introduced at the crack face on a stressed concrete FE model. In this context, two different concrete models are used for the study, namely the concrete half-space model and the concrete beam model. The resulting AE waveforms are analysed using the wave speed and scalogram to classify various types of AE sources. It is shown that due to a tensile crack at the surface, S-waves and surface (or Rayleigh) waves are formed, whereas, a shear crack at the surface, predominantly produces S-waves. On the other hand, body waves (P- and S- waves) are predominantly formed for internal tensile as well as shear cracks. The developed simulation technique and signal processing tools are expected to be helpful for the direct correlation of AE waveforms with the recorded signal and identification of various AE sources in an experiment.

Keywords Acoustic emission · Crack classification · Half-space model · Scalogram

A. Roy · P. Mirgal (✉) · S. Banerjee
Department of Civil Engineering, Indian Institute of Technology Bombay, Powai, Mumbai 400076, India
e-mail: parsh49@gmail.com

A. Roy
e-mail: arunroy993@gmail.com

S. Banerjee
e-mail: sauvik@civil.iitb.ac.in

B. N. Singh et al. (eds.), *Recent Advances in Theoretical, Applied, Computational and Experimental Mechanics*, Lecture Notes in Mechanical Engineering,
https://doi.org/10.1007/978-981-15-1189-9_13

1 Introduction

Heavy cracking, excessive deflections, corrosion in civil engineering structures are considered as major threats as they prevent the structure from performing its intended use or reduces its service life considerably. Depending upon its importance, structures are needed to be monitored and evaluated for the material condition in order to maintain their stability and serviceability performance. Assessment of structural characteristics like residual strength of concrete, corrosion, crack surface, etc., are used to identify current situation and future durability problem of structure which demands continuous monitoring of a structure. AE had been developed in the early 1980s, which then evolve as a standardized health monitoring technique for in-service structures. In simple words, AE is the propagation of elastic waves due to the release of internal energy, which is generated due to the irreversible structural change of material. An AE sensor records the elastic motion that follows crack initiation and propagation events within the material and transforms them into electric waveforms, which can help in understanding the nature of damage and deterioration level.

The AE events can be analysed qualitatively or quantitatively. Qualitative analysis methods make use of basic parameters of recorded signals, which are directly or indirectly used to assess the condition of the structure or identify the nature of the source event. A relatively small amount of parameter data, which requires less amount of time and storage space make this an economical approach. This is also considered as a limitation, as a complicated signal recorded with few parameters might be a misleading interpretation. Quantitative analysis provides a recording of signals in terms of waveforms, which allows for more comprehensive but time-consuming analysis [1].

Although a lot of other techniques for crack closure are available including surface measurements by displacement gauges, enlarged photographs of surface displacement, strain gauges placed across the crack surface, ultrasonic methods, photo-elastic techniques, and surface replicas, the results obtained from these were often contradictory [2]. According to available literature, the acoustic emission technique began in the 1950s with the research work on metal carried out by J. Kaiser, although acoustic emission on the rock was known in mining technology. Terminology wise the use of 'AE' was initiated by B. H. Schofield in the U.S. in 1954. The recent application of AE to concrete engineering started in the late 1970s [3]. In the present scenario, AE is a commonly used NDE technique for structural health monitoring of concrete structures. Its major objectives include localizing the damage, quantifying the severity of damage and characterizing the nature of the source. Basically, there are two approaches by which AE data can be analysed: Parametric approach and Waveform approach [1]. In the parametric approach, the parameters are extracted from the AE data without saving the waveforms. The parameters like hit, amplitude, count, rise time, duration are recorded to monitor the AE activities [4], and also to evaluate the extent as well as the nature of the damage. This approach tends to be more feasible if a huge amount of AE activity occurs during a short period of time. In waveform approach, the signals are recorded and are post-processed at a later stage.

This method demands the ability to record and store as many signals as possible along their waveform so that they can be converted from analog to digital (A/D) signals. These requirements can be easily met by newly developed high capability sensors as well as multichannel acquisition systems. With the advent of increased computational power and greater availability of software based on finite element methods, several studies have been done on this area, which proves that finite element (FE) modeling has a major role in simulating elastic wave propagation associated with structural vibrations, acoustic phenomena and ultrasound problems [5]. FEM has been used to generate elastic waves from fatigue cracks in a large isotropic plate-like structure to produce the quantitative analysis. The simulations on the two-dimensional (2D) model showed that fatigue cracks can be introduced in plates in a realistic way by the sudden release of nodes in finite element mesh [6]. However, there are limited literature presenting quantitative results for materials like concrete [7, 8].

In this study, the AE sources are modelled in the form of tensile and shear cracks, with the sudden release of nodes at the crack face on a stressed concrete FE model in an effort to examine the propagation characteristics of the waveforms generated by these sources in the concrete structures using finite element (FE) simulation. The aim is to develop a direct correlation of AE waveforms with the recorded signal and the identification of various AE sources in an experiment conducted. Towards this, two different concrete models are used for the study, namely concrete half-space model and concrete beam model. The resulting AE waveforms are analysed using the wave speed and scalogram to classify various types of AE sources.

2 Methodology

An innovative modelling technique is developed by applying the principle of superposition in fracture mechanics problems. By this approach, we can separate a complex problem into two simple problems, thus reducing computational resources and time. The principle of superposition can be applied to identical geometries for linearly elastic bodies. Since we are dealing with linearly elastic bodies, this principle can be exploited to solve fracture mechanics problems.

Consider a centrally cracked plate with two different loads, σ as far-field stress and line loads σ_c at the cracked face as shown in Fig. 1. Invoking the principle of superposition, stress at any point in the vicinity of the crack tip is given by the sum of stresses of configuration m and n,

$$\sigma = \sigma_m + \sigma_n$$

For a crack that occurs suddenly, configuration m is a static problem while configuration n is a dynamic one as shown in Fig. 1. Since we are interested in the events after the formation of a crack, configuration n is our main concern. So we could use a coarser mesh for the static part (configuration m) and finer mesh for the dynamic part (configuration n). This method is also effective for studying different modes

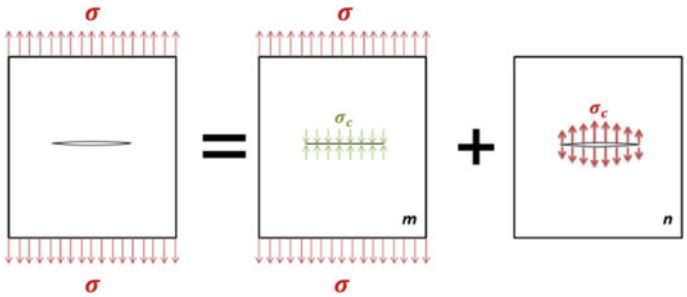

Fig. 1 Principle of superposition [9]

of fracture separately, by applying the required stress at the crack face as shown in configuration *n*.

This method can be easily adapted for modelling different modes of fracture. In this study, two modes of fracture are modelled using this technique. Mode-I (Tensile) and Mode-II (Shear). In Mode-I, pure tensile stress is applied at the surface, and for Mode-II, pure shear is applied. For tensile crack, the approximate flexural strength of concrete (IS 456) is applied at the crack surface.

$$\sigma_c = 0.7\sqrt{f_{ck}}$$

For shear crack, the maximum shear strength for M20 concrete (IS 456) was applied at the crack face.

$$\sigma_c = 2.8\,\mathrm{N/mm^2}$$

3 FE Analysis

Finite element modelling is carried out using commercially available FE package ABAQUS. Two types of models, a concrete half-space model and concrete beam model are considered for this study as shown in Fig. 2.

All these models are prepared with geometric and material properties as mentioned in Table 1. Each model is created as two parts and joined using tie constraint, which ties two separate surfaces together so that there is no relative motion between them. CPS4R, a 4-node bilinear plane stress quadrilateral element is assigned from the ABAQUS/Standard element library. The geometric order of the element is assigned as linear. Mesh size is different for each model according to its size. Quadratic structured mesh with minimized mesh transitions is used for an aluminium plate with mesh size as 0.375 mm. In the case of the semi-infinite model, since the model is very large, fine meshing requires enormous time and memory for analysis. Also,

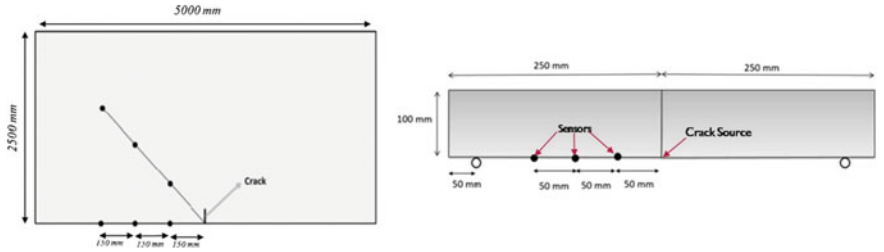

Fig. 2 Schematic representation of concrete half-space model and concrete beam model with sensor positions and crack source

Table 1 Material properties of various models considered

Material property	Value
Material	Concrete
Modulus of elasticity	22,360 MPa
Poisson's ratio	0.15
Density	2400 kg/cm^3
Element property	
Element	CPS4R, 4-noded quadrilateral
Geometric order	Linear
Structure	Quadratic
Step property	
Time increment	1e(−8) s
Time period	0.004 s

the area of concern is near to the crack, so a different type of meshing was adopted which provides a transition from fine to coarse mesh as we move away from the centre. It also has a minimal effect of reflection caused by mesh transitions. Fine mesh is having a mesh size of 0.5 mm and coarse mesh 10 mm. For concrete beam model, the same quadratic structured mesh with minimized mesh transitions is used. Loading and support conditions are also varied for every model. Concrete beam model is created as per the experimental setup. The size and loading conditions are identical to the flexural strength test specified in IS 516 (1959) [10].

For M20 grade of concrete, static Young's modulus (E) is 22.36 GPa, Poisson ratio (υ) is 0.15 and density (ρ) is 2400 kg/m^3. The longitudinal wave velocity is 3136.4 m/s, whereas the transverse wave velocity is 2012.6 m/s.

$$V_L = \sqrt{\frac{E(1-\upsilon)}{\rho(1+\upsilon)(1-2\upsilon)}}$$

$$V_T = \sqrt{\frac{E}{2\rho(1+\upsilon)}}$$

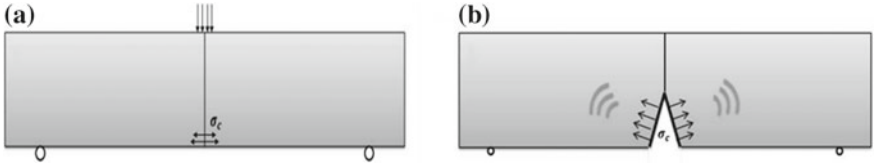

Fig. 3 **a** Static analysis, **b** dynamic analysis

Static analysis is done in ABAQUS/Standard with a time period of 1 s. Dynamic analysis is done in ABAQUS/Explicit with a time period of 0.0004 s. The time increment is fixed with a user-defined time increment of 10^{-8} s. This value is set manually to get the results at the same interval, which will be easier for the post-processing of the signal. The stress state of the ABAQUS/Standard model is imported to ABAQUS/Explicit model using predefined fields command.

For the static part of the analysis, the model is statically loaded in ABAQUS/Standard and the stresses at the crack face are recorded as σ_c. The exact model is created in the ABAQUS/Explicit platform for dynamic analysis as shown in Fig. 3. In the latter case, a fine mesh is generated considering the time increment and frequency of the stress wave.

The previously recorded stresses (σ_c) are applied at the crack face in opposite directions. Since these stresses are instantaneously applied to the model, the elastic wave propagates from the crack face. The displacement time history is recorded at the relevant nodes (these nodes correspond to the sensor position in an experimental setup). The output signal is imported to the MATLAB platform for post-processing. The signal is frequency filtered for the range of interest and the results are analysed.

4 Result and Discussion

4.1 Comparison of Lead Break Source and Crack in Simulation

Pencil-Lead breaks are widely used as a reproducible source for test signals in acoustic emission applications. This type of source is also referred to as Hsu–Nielsen source, based on the works of Hsu and Nielsen. A lead pencil is used to apply pressure on the surface under investigation until the lead breaks. The sudden release of pressure, at the point of breakage, creates a microscopic displacement and an acoustic wave associated with that. This is one of the most common artificial sources because of its simplicity in implementation, in the laboratory as well as the field. The lead break source was modelled in ABAQUS using the Eqs. 1 and 2 given in [5] and applied to the half-space model.

$$F(x_1; x_2; t) = f(t)\delta(x_1)\delta(x_2) \tag{1}$$

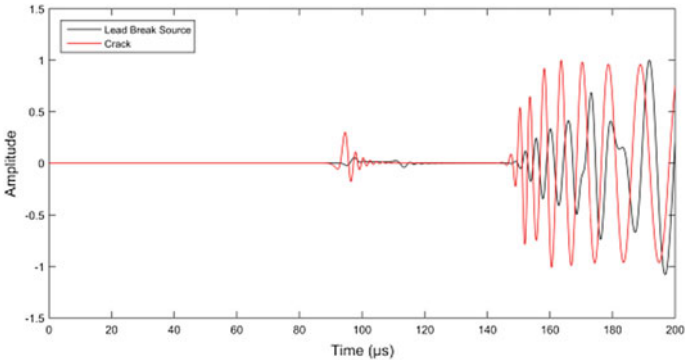

Fig. 4 Comparison of crack versus lead break source (filtered signal)

where

$$f(x) = \begin{cases} \frac{t(t-\tau)}{\tau^2}, & 0 < t < \tau \\ 1 - e^{-2.1(t-\tau)}, & t \geq \tau \end{cases} \tag{2}$$

From Fig. 4, it is clear that the response from the lead break source is not able to simulate an actual crack. The amplitude of the lead break signal is having large variations when compared with that of crack.

Though the pattern is almost the same, it cannot reproduce the higher frequency components. These are justifiable considering the fact that these waveforms vary significantly with respect to the type of crack, crack length, thickness, the total length of plate etc., which can't be included in a single lead break source. There are several functions that can resemble a lead break source. In order to obtain the most appropriate function resembling the crack, we have to adopt a trial and error procedure, which is not considered in the present work.

4.2 Concrete Half-Space Model

To avoid reflections from the edges of a beam, a semi-infinite half-space model is considered in this study. The material properties and modelling methodology are similar to that of the beam model except for the size of the model. In this case, sensors are also placed along 45° as shown in Fig. 5.

4.2.1 Tensile Crack

The time history of y-displacement (vertical) of nodes located at three different locations are recorded under tensile and shear cracks. Figure 6 shows the recorded

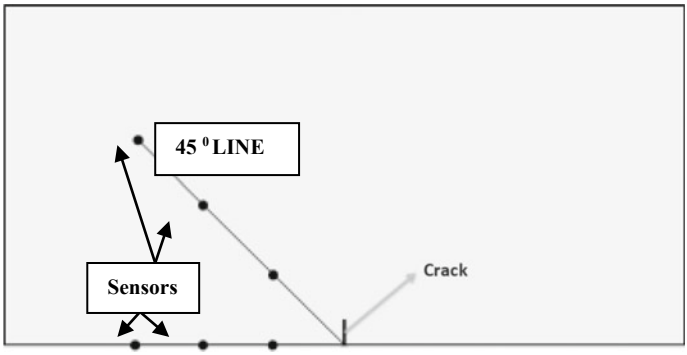

Fig. 5 Schematic representation of crack in the concrete half-space

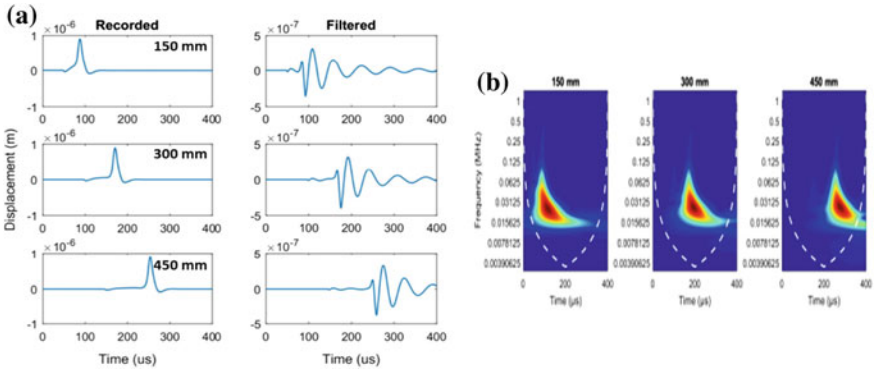

Fig. 6 **a** Recorded and filtered signal at output nodes, **b** magnitude scalogram for a tensile crack received at a distance of 150, 300, 450 mm at 0° angle with the bottom edge of the half-space

and frequency filtered signal along with the respective scalogram at the output node located at 0° with the bottom edge at 150, 300 and 450 mm due to a tensile crack. From the scalogram shown in Fig. 6b, it is clear that the major frequency content of the signal occurs at the time of around 84.5 μs for the sensor located at a distance of 150 mm from the crack and the velocity is found out to be 1776 m/s. This can be due to an S-Wave or Rayleigh (R) Wave because they both have almost similar theoretical velocity. S-Wave has a velocity of 1820 m/s and R-wave has a velocity of 1779 m/s. The corresponding frequency content is 40 kHz.

Figure 7 shows the variation of recorded and frequency filtered signals, and the corresponding scalogram for a tensile crack at the output node located at 45° with the bottom edge at 150, 300 and 450 mm.

As shown in Fig. 7, two distinct peaks are observed in signals. Better resolution of these peak signals is observed with an increase in distance between crack and the sensor. In the filtered signal for the first plot, we can notice that the first peak occurs at 71 μs. Since the crack is located at a distance of 150 mm, the velocity

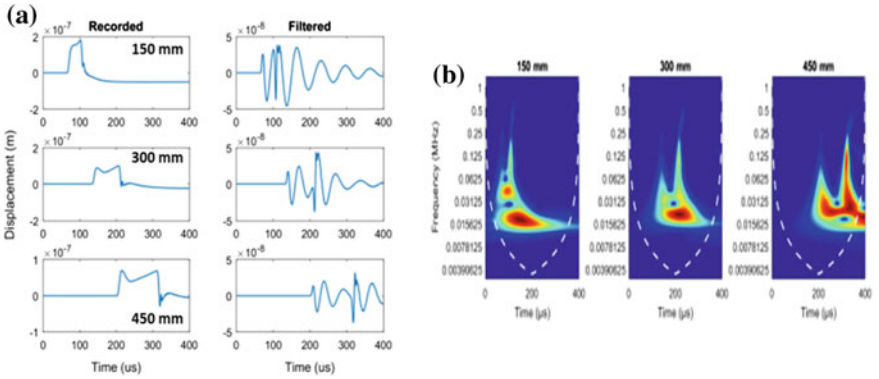

Fig. 7 **a** Recorded and filtered signal at output nodes, **b** magnitude scalogram for a tensile crack received at a distance of 150, 300, 450 mm at 45° angle with the bottom edge of the half-space

equals to 2987 m/s. The theoretical velocity of the P wave is 3116 m/s. The second peak occurs at a time of 117 μs, which corresponds to a velocity of 1928 m/s. The respected frequency contents are 58 kHz for the first peak and 25 kHz for the second peak. The scalogram of the above waveforms presented in Fig. 7b shows that the separation of peaks is visible as the distance of the sensors increases. So the first peak corresponds to P-Wave and the second peak corresponds to S or R-Waves.

4.2.2 Shear Crack

Figure 8 shows the variation of recorded and filtered signals for a shear crack for sensor position of 150 mm, 300 mm and 450 mm, respectively at 0° angle with the

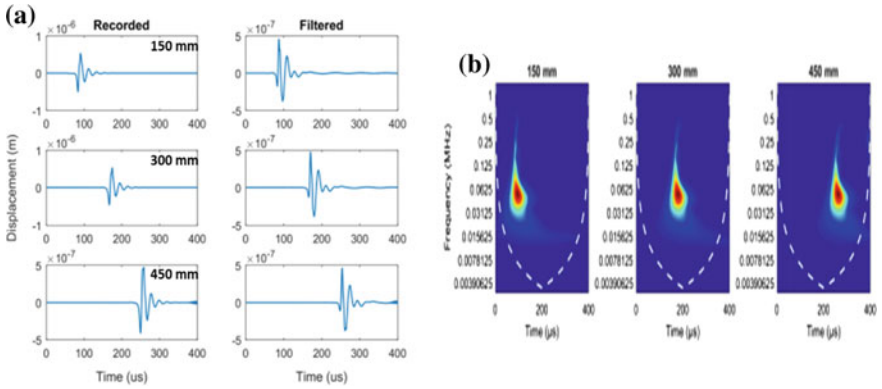

Fig. 8 **a** Recorded and filtered signal at output nodes, **b** magnitude scalogram for a shear crack received at a distance of 150, 300, 450 mm at 0° angle with the bottom edge of the half-space

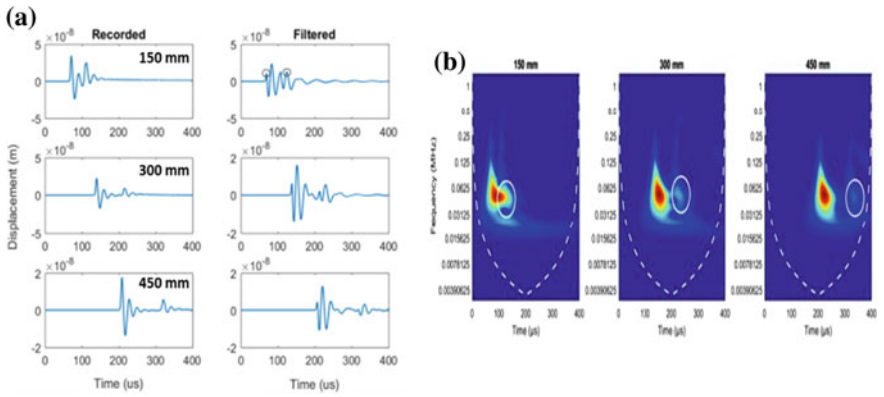

Fig. 9 **a** Recorded and filtered signal at output nodes, **b** magnitude scalogram for a shear crack received at a distance of 150, 300, 450 mm at 45° angle with the bottom edge of the half-space

bottom edge of the half-space along with magnitude scalogram. From Fig. 8a, we can observe that the first peak occurs at a time of 82.72 μs at a 150 mm sensor, with a velocity of 1813 m/s. The theoretical surface (R) wave velocities in concrete are around 1800 m/s. So the first peak corresponds to an S-Wave.

From the scalogram shown in Fig. 8b, it is clear that the maximum value of frequency is 50 kHz. So from the frequency content its evident that the wave is S-Wave because Rayleigh wave will have less frequency.

Figure 9a shows the recorded and filtered signals at the output node located at 45° with the bottom edge at 150, 300 and 450 mm due to a shear crack. The corresponding scalogram is also presented in Fig. 9a. In the filtered signal, 2 different peaks are noticeable, which occurs at a time of 69 μs and 123 μs, respectively. Corresponding velocities are 3074 and 1710 m/s. So we can deduce that the first peak is that of a P-Wave. We can also notice the separation of peaks as the distance of sensors increase.

From Fig. 9b, we can see that for the first plot the major frequency content lies around 65 kHz, which occurs at 90 μs. It is evident that in all the three figures the maximum frequency value is around 50–65 kHz. So we can infer that for a shear crack measured at the same surface it will have predominantly S-Wave. But for the second and third plot we can see a separation of frequencies, which is represented by a circle. So by comparing waveforms and the scalogram from Fig. 9, we can deduce that it is the shear wave that is separating from the P-Wave. So, in this case, S-Wave and P-Wave are having comparable frequencies.

From the above results for half-space model for tensile and shear crack, we can conclude the following:

1. Waves received at sensors places at 0° angle with the bottom edge, shows that surface waves are predominant for both tensile and shear cracks.

2. For Surface cracks, waves received at sensors placed at 45° angle with the bottom edge, both P- and S-waves are obtained with distinct frequency peaks separated as longer sensor distance.

4.3 Concrete Beam

The displacement time history of nodes at six different locations are recorded under tensile and shear cracks. The nodes are located at a distance of 50, 100 and 150 mm from the middle of the beam. Three of them are at the bottom and the other three at the top. Similar to half-space two different modes of cracks are modelled: tensile and shear.

4.3.1 Tensile Crack

Figure 10 shows the recorded signal for a surface tensile crack received at the bottom sensor located at a distance of 100 mm from the middle of the beam. The recorded signal is similar to that of the half-space in the initial portion, and later on, the reflections from boundaries affect the signal. Hence only the first 100 μs of the recorded signals are considered in each case. Recorded signals are filtered with an elliptical high pass filter above 20 kHz. The waveform is similar to that of half-space with tensile crack signals received at sensors placed at 0° angle with the bottom edge. The high-frequency peak at 60 μs with a velocity of 1666 m/s with the major frequency contents at 40 kHz, indicates that the signal contains predominantly S-Wave and R-Wave.

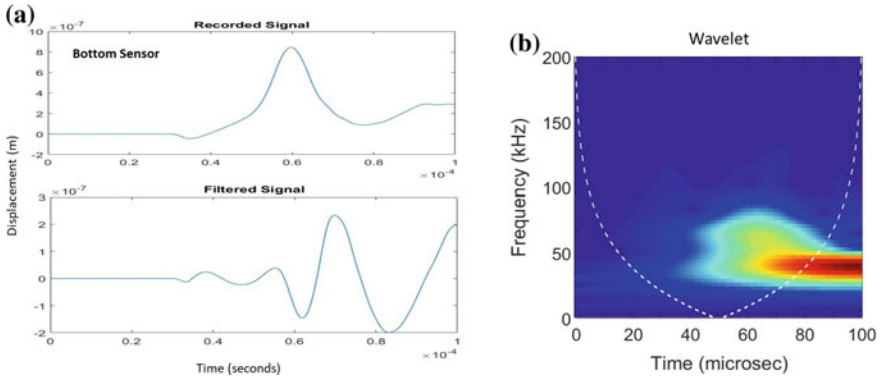

Fig. 10 **a** Recorded and filtered signal at a bottom output node located at a distance of 100 m from a surface tensile crack, **b** magnitude scalogram of the signal

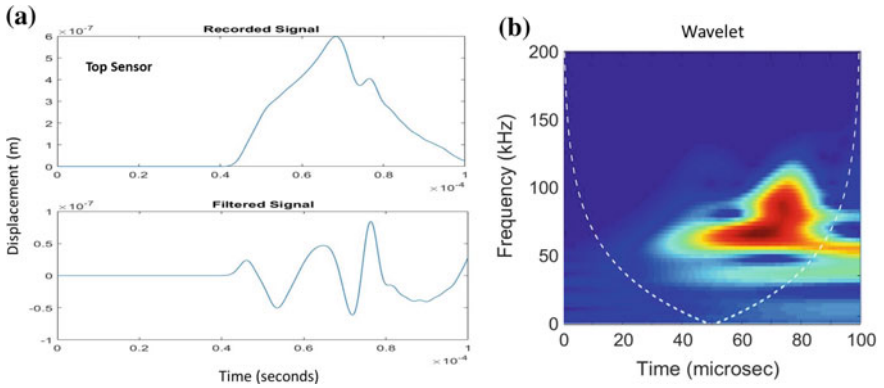

Fig. 11 **a** Recorded and filtered signal at a top output node located at a distance of 100 m from a surface tensile crack, **b** magnitude scalogram of the signal

Figure 11 shows the recorded signal for a surface tensile crack received at the top sensor located at a distance of 100 mm from the middle of the beam. The recorded waveform received at the top sensor, placed at 141.42 mm from crack has 2 peaks, which are similar to the recorded waveform for tensile crack signals, received at the sensors placed at 45° angle with the bottom edge in half-space. The initial peak occurs at 44 μs, corresponding to a velocity of 3214 m/s and 2nd peak at 60 μs with a velocity of 2357 m/s with the frequency content of 120 kHz and 60 kHz respectively. From the scalogram, the Higher frequency content of nearly 120 kHz corresponding to the first peak is observed along with a lower frequency content of 60 kHz corresponding to the later part of the waveform. So we can infer that the first peak corresponds to P-Wave and the second peak can be that of an S-Wave or surface wave.

4.3.2 Shear Crack

Figure 12 shows the recorded signal for a surface shear crack received at the bottom sensor located at a distance of 100 mm from the middle of the beam. The high-frequency peak at 59 μs with a velocity of 1694 m/s with major frequency content at 50 kHz indicates that the signal contains predominantly S-Wave and R-Wave.

Figure 13 shows the recorded signal for surface shear crack received at a distance 100 mm from the middle of the beam. Similar to the recorded signal obtained in half-space, it has 2 peaks. The higher frequency corresponding to the first peak and lower frequency for the later part of the waveform is observed. The initial peak occurs at 45 μs, corresponding to a velocity of 3142 m/s and 2nd peak at 60 μs with a velocity of 2357 m/s with the frequency content of 110 kHz and 70–90 kHz respectively. So we can infer that the first peak corresponds to P-Wave and second can be S-Wave or surface wave.

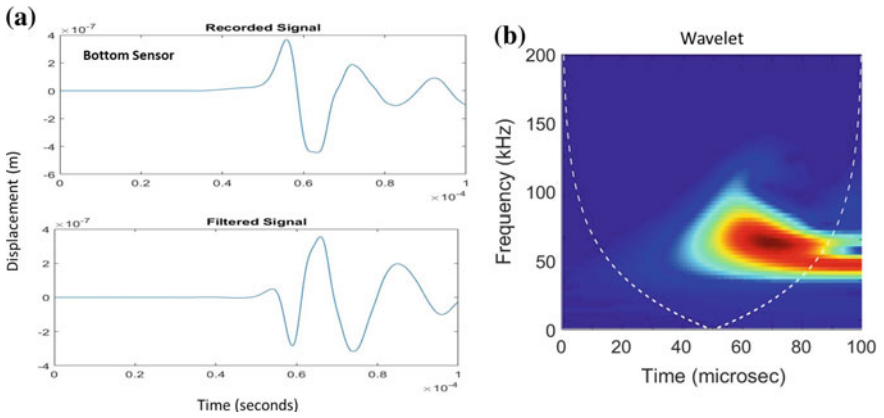

Fig. 12 **a** Recorded and filtered signal at the bottom output node located at a distance of 100 m from a surface shear crack, **b** magnitude scalogram of the signal

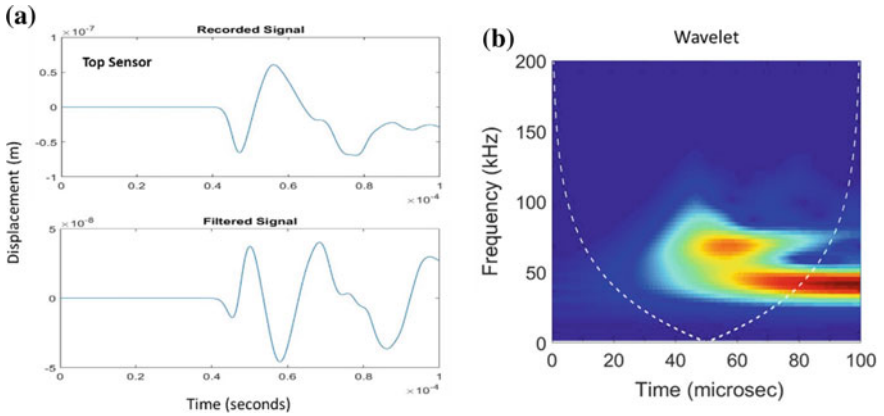

Fig. 13 **a** Recorded and filtered signal at the top output node located at a distance of 100 m from a surface shear crack, **b** magnitude scalogram of the signal

4.4 Crack Inside the Beam

Internal crack is also modelled in ABAQUS. The crack with a length of 10 mm, placed in the middle of the beam as shown in Fig. 14. The nodes above and below the crack surface are given symmetric boundary conditions (horizontal symmetry). The sensor is at the same location as that of surface cracks as shown in Fig. 14.

Figure 15 shows the recorded signal of internal tensile crack at the bottom sensor located at a distance of 100 mm from the middle of the beam. Two distinct peaks are observed with high-frequency contents. For sensor placed at 111.8 mm, the initial peak occurs at 37 μs, corresponding to a velocity of 3021 m/s and 2nd peak at 80 μs

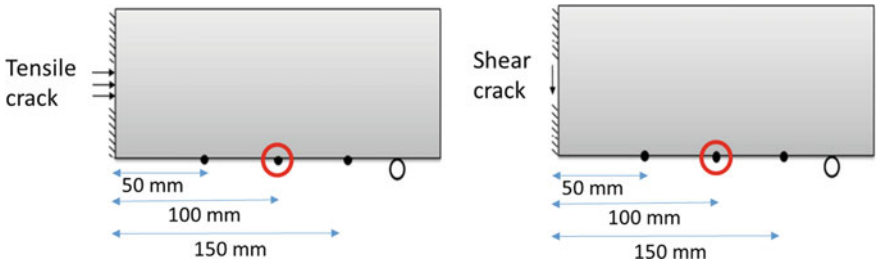

Fig. 14 Schematic representation of internal tensile and shear crack

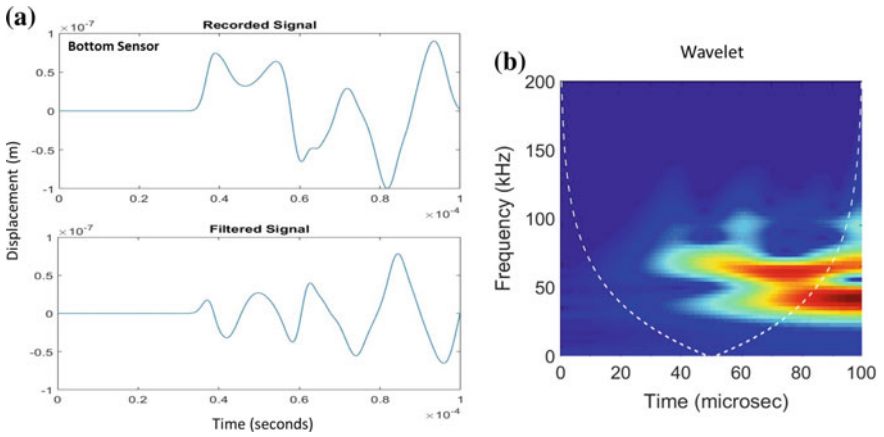

Fig. 15 **a** Recorded and filtered signal at the bottom output node located at a distance of 100 m from an internal tensile crack, **b** magnitude scalogram of the signal

with a velocity of 1863 m/s with the frequency content of 110 kHz and 80 kHz respectively. So we can infer that the first peak corresponds to P-Wave and second can be S-Wave or surface wave.

Similar behaviour of the waves is observed in case of internal shear cracks. It also shows a similar pattern as the half-space shear crack signal recorded at internal sensors. Figure 16 shows the recorded signal of internal shear crack at the bottom sensor located at a distance of 100 mm from the middle of the beam.

Two distinct peaks are observed with high-frequency contents. The initial peak occurs at 38 μs, corresponding to a velocity of 2942.19 m/s and second peak at 62 μs with a velocity of 1803 m/s with the frequency content of 100 kHz and 80 kHz respectively. So we can infer that in this case also, the first peak corresponds to P-Wave and second can be S-Wave or surface wave.

From the above results for 2D concrete beam model for tensile and shear crack, we can conclude the following,

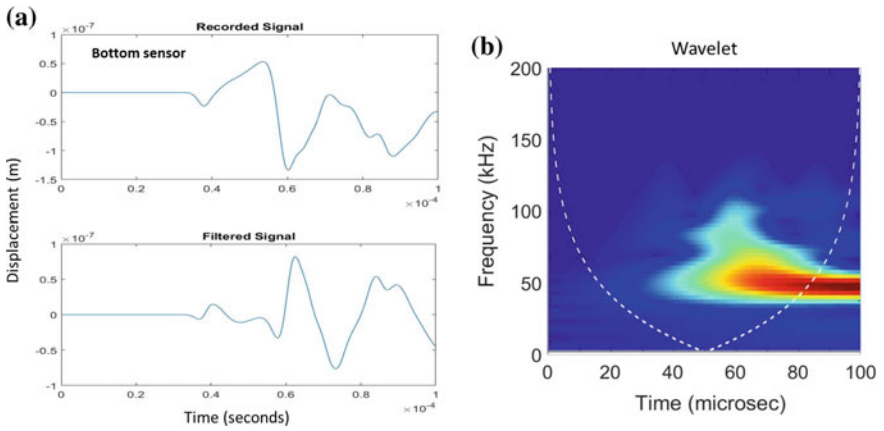

Fig. 16 **a** Recorded and filtered signal at the bottom output node located at a distance of 100 m from an internal shear crack, **b** magnitude scalogram of the signal

1. For surface cracks, surface waves are dominated if the signals are recorded on the same surface. For these surface waves, the frequency content of 60–90 kHz was observed.
2. For surface cracks, P-waves become prominent with higher frequency content 100–120 kHz for the signals received on the other surface of the beam.
3. For Internal cracks, both P-waves and S/R-waves are seen for recorded signals on the surface.

5 Conclusion

Two different models were used for the study, concrete half-space model and beam model. The major conclusions gathered from the study are explained below.

1. Due to a tensile crack at the surface, P-Waves, S-Waves, and surface (R) waves are formed in the beam and half-space. P-Wave is having less amplitude when compared to S-Waves so they are not clearly visible in the scalogram. Since the S-Waves and surface waves are having almost the same velocity they can't be distinguished in the unfiltered signal.
2. Shear crack at surface predominantly produces S-Waves. Surface waves and P-Waves are not generated.
3. Body waves (P and S waves) are predominantly formed for internal tensile as well as shear crack. But the interaction of body waves with the surface causes the formation of surface waves. Body waves also have significant amplitude and energy when compared to surface waves.

The study has to be extended by analysing different models and conducting several experimental studies. The model has to be analysed three dimensionally in order to include the effect of side reflections also.

Acknowledgements The authors want to acknowledge the funding received from the Board of Research in Nuclear Sciences, Department of Atomic Energy, Government of India, with grant number 36(2)/15/05/2016-BRNS/36058 (16BRNS0003) with NRFCC, BRNS, for carrying out the research work presented in this paper.

References

1. Behnia A, Chai HK, Shiotani T (2014) Advanced structural health monitoring of concrete structures with the aid of acoustic emission. Constr Build Mater 65:282–302
2. Berkovits A, Fang D (1995) Study of fatigue crack characteristics by acoustic emission. Eng Fracture Mech 51(3):401–416
3. Ohtsu M (1996) The history and development of acoustic emission in concrete engineering. Mag Concr Res 48(177):321–330
4. Ohno K, Ohtsu M (2010) Crack classification in concrete based on acoustic emission. Constr Build Mater 24(12):2339–2346
5. Hill R, Forsyth S, Macey P (2004) Finite element modelling of ultrasound, with reference to transducers and AE waves. Ultrasonics 42(19):253–258
6. Lee C, Drinkwater B, Friswell M, Scholey J, Wilcox P, Wisnom M (2006) Acoustic emission during fatigue crack growth in aluminium plates. In: 9th European conference on NDT, ECNDT 2006, Berlin
7. Sause M (2011) Investigation of pencil-lead breaks as acoustic emission sources. J Acoust Emiss 29:184–196
8. Banerjee S, Mal AK (2005) Acoustic emission waveform simulation in multilayered composites. J Strain Anal Eng Des 40(1):25–32
9. Kumar P (2009) Elements of fracture mechanics. McGraw Hill Education (India) Pvt. Ltd
10. Indian Standard. Method of tests for strength of concrete. IS 516: 1959, Edition 1.2 (07-1991)

Applicability of Tricycle Modelling in the Simulation of Aircraft Steering System

S. Sathish, L. Suryanarayanan, J. Jaidev Vyas and G. Balamurugan

Abstract Aircraft nose wheel steering system is simulated on MATLAB–Simulink platform to understand the influence of tyre–ground interaction and aircraft ground dynamics on the steering behaviour of the aircraft. The aircraft steering system model generally includes the Nose Landing gear model, Aircraft Dynamics model and Tyre model. In most of the literature, bicycle modelling method is adapted with two main gears lumped together and a nose landing gear, whereas tricycle modelling method with all the three gears is more appropriate and accurate way of predicting the aircraft steering response. In the present work, the mathematical formulation for the tricycle model is developed and it is observed that the resultant equations are non-linear and coupled, whereas the bicycle model is represented with linear and coupled equations. For the same inputs parameters, both tricycle and bicycle models are simulated. Results obtained from both the models are within 5% difference with the introduction of additional non-linearity in the tricycle modelling. Hence for aircraft with nose wheel steering, bicycle method is sufficient for predicting steering response but for the all-wheel steering system (steering on both nose and main landing gear), it is more appropriate to use the tricycle modelling method to predict the accurate steering response.

Keywords Aircraft steering system · Aircraft-on-ground dynamics · Landing gear · Bicycle and tricycle modelling method

Nomenclature

Symbol	**Definition** (Units)
WOW	Weight on Wheels (kgf)
MW	Main Wheel
NW	Nose Wheel

S. Sathish (✉) · L. Suryanarayanan · J. Jaidev Vyas · G. Balamurugan
CSIR-National Aerospace Laboratories, Bangalore, India
e-mail: sathishs@nal.res.in

B. N. Singh et al. (eds.), *Recent Advances in Theoretical, Applied, Computational and Experimental Mechanics*, Lecture Notes in Mechanical Engineering,
https://doi.org/10.1007/978-981-15-1189-9_14

MLG	Main Landing Gear
NLG	Nose Landing Gear
L_{NW}	Distance between Nose wheel and centre of gravity (m)
L_{MW}	Distance between Main wheel and centre of gravity (m)
L	Wheel Base (m)
β_{MW}	Sideslip at Main Wheel (rad)
β_{NW}	Sideslip at Nose Wheel (rad)
F_{YMW}	Lateral Force in Main Wheel (N)
F_{YNW}	Lateral Force in Nose Wheel (N)
M_z	Yawing Moment (N-m)
C.G	Centre of Gravity
β	Slip of Aircraft (rad)
V	Aircraft Resultant Velocity (m/s)
V_x	Longitudinal Velocity (m/s)
V_y	Lateral Velocity (m/s)
r	Yaw rate (rad/s)
$M_{A/C}$	Mass of Aircraft (kg)
I_{zz}	Moment of inertia of the aircraft about C.G (kg-m^2)
δ_f	Steering Angle (rad)
b	Wheel Track (m)
β_{MWL}	Sideslip at Left Main Wheel (rad)
β_{MWR}	Sideslip at Right Main Wheel (rad)
F_{YMWL}	Lateral Force in Left Main Wheel (N)
F_{YMWR}	Lateral Force in Right Main Wheel (N)
CS_{NW}	Cornering stiffness of Nose wheel tyre (N/rad)
CS_{MW}	Cornering stiffness of Main wheel tyre (N/rad)
CS_{MWL}	Cornering stiffness of Left Main wheel tyre (N/rad)
CS_{MWR}	Cornering stiffness of Right Main wheel tyre (N/rad)
J_e	Equivalent inertia of NLG (kg-m^2)
B_e	Equivalent damping constant of the NLG (N-m/rad/s)
k	Load stiffness coefficient (N m/rad)
T_{net}	Net Torque (N-m)
T_a	Applied Torque on Steering Actuator (N-m)
T_r	Resistive Torque from Tyre-Ground Interaction (N-m)
L_L	Reference radius of steering pinion (m)
P_L	Hydraulic Pressure (N/m^2)
A	Piston area of steering actuator (m^2)
SAS_{NW}	Self-Aligning Stiffness of Nose Wheel (N/rad)
e	Caster length (m)

1 Introduction

Landing gear systems are used in aircraft for energy absorption during landing and for aircraft ground manoeuvring. Tricycle arrangement of landing gear is commonly used in most of the aircraft because of its stability and less expensive design. Steering system is one of the major subsystems associated with the aircraft landing gear systems for steering operation on the ground using landing gear along with the rudder steering. The rudder steering is used at higher speeds and landing gear steering is used during taxiing or any other manoeuvring at lower speeds when the aircraft is on the ground. Aircraft Steering is done by using Nose Wheel Steering (Nose Gear) in most of the aircrafts. All-wheel steering (Nose + Main Gear) is used in large aircraft during sharp turns. In this paper, simulation studies are carried out using the different ground dynamic models to understand the steering response of the aircraft steering system for the given pilot inputs.

2 Literature Survey

In the available literature [1–6], more emphasis is given on bicycle modelling for the aircraft ground dynamics model. Biannic et al. [1] developed a simplified Linear Fractional Transformation Model for predicting the aircraft-on-ground forces to be used for the development of robust ground control systems. Pouly [2], Pouly et al. [3] used bicycle methodology to simulate aircraft steering system. Ross et al. [4] developed high-fidelity non-linear model for lateral control of aircraft-on-ground using bicycle methodology. Chen et al. [5] proposed a non-linear control model with kinematic constraints of nose wheel cornering and the tyre side-slip effects, to predict the steering response of the aircraft. Pavan et al. [6] predicted the steering response of the given aircraft using bicycle methodology and analysed the hydraulic system based on the torque output from the aircraft steering simulations.

Though the tricycle modelling is more accurate, very few authors have reported this method [7, 8]. Duprez et al. [7] developed a feedback linearizing control model using tricycle method to predict the yaw rate control during aircraft on ground. Chen et al. [8] developed a dynamical adaptive backstepping controller to address the path following the control problem of the aircraft on ground. Also, the comparison and applicability of these modelling methods have not been discussed in the available literature.

In this paper, mathematical models for tricycle modelling are formulated and their mathematical relationships are compared with the bicycle model formulations. Steering response results are obtained from both the models and are compared in detail for similar inputs.

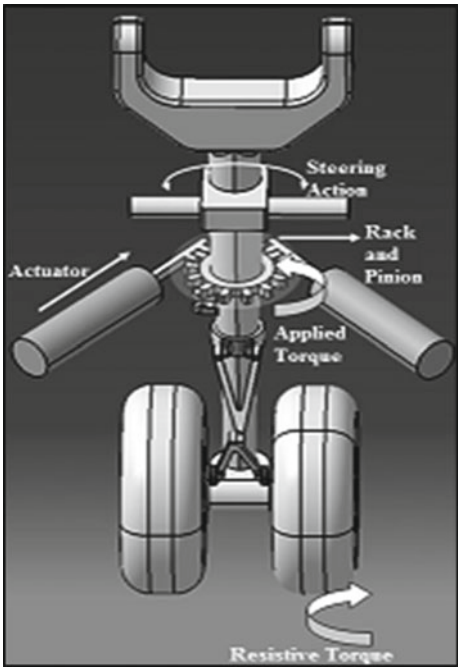

Fig. 1 Aircraft landing gear with steering arrangement [6]

3 Aircraft Steering System

Typical Modern Aircraft Steering System consists of a mechanical arrangement for wheel rotation, steer control unit, hydraulic valves and actuators as shown in Fig. 1. Mechanical arrangements such as rack and pinion, planetary gears, Bell crank mechanism, push–pull rods, etc., can be used for steering operation on ground.

Pilot mechanical input on the pedals or tiller is converted to electrical signals through potentiometers [6]. Steer Control Unit regulates the flow on the hydraulic valves based on the input signals which enables the motion of actuators attached to the mechanical arrangement. This arrangement ensures in acquiring the desired steering response of aircraft with the help of the steer control unit.

Typical architecture of the aircraft steering system [6] is shown in Fig. 2.

4 Aircraft Bicycle Model

Aircraft nose wheel steering system includes Nose Landing gear (NLG) model, Aircraft Ground Dynamics model and Tyre model. Aircraft ground dynamics model is commonly modelled as bicycle/single-track model as shown in Fig. 3. This two degree of freedom model simplifies the aircraft model to study the effects of steering

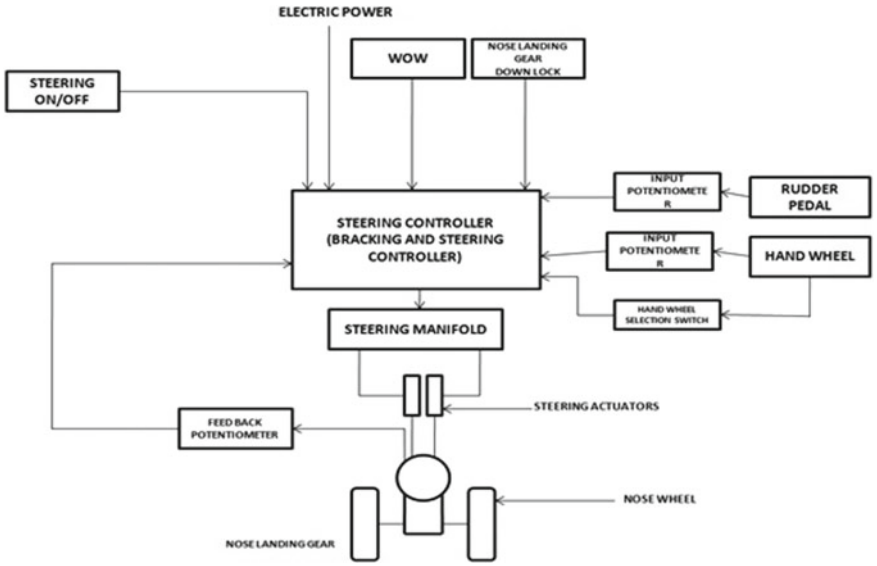

Fig. 2 Typical aircraft steering system architecture [6]

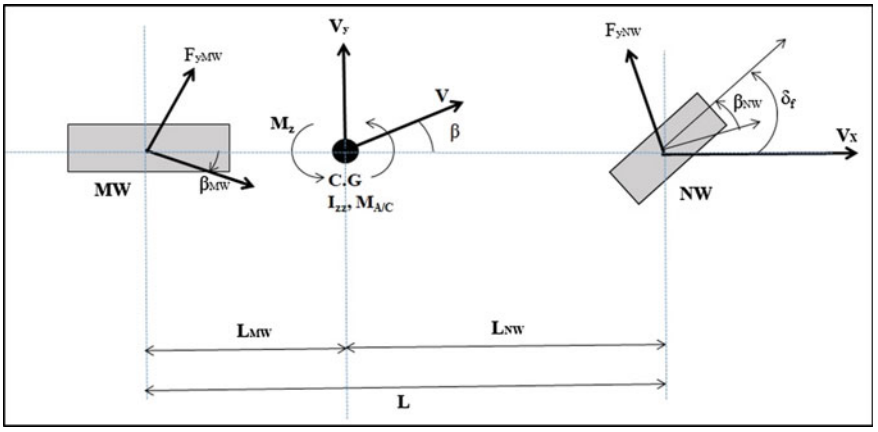

Fig. 3 Single track/bicycle representation of aircraft model

input on the attitude and path of the aircraft. Major assumptions are rigid landing gear, low slip angles for linearization of tyre model, constant low aircraft velocity and no roll or pitch movement on the ground. In the bicycle model, both the main landing gears are assumed as single gear with four tyres (for twin wheel arrangement) and one nose gear with two tyres.

From Fig. 3, Force balance along the lateral direction and Moment balance about C.G of aircraft results in equations of motion as [6],

$$\dot{V_y} = \left[\frac{-1}{M_{a/c}} \times \left(CS_{NW} \times \frac{V_y + r \times L_{NW}}{V_x} + 2 \times CS_{MW} \times \frac{V_y - r \times L_{MW}}{V_x}\right)\right] + \left[\frac{CS_{NW} \times \delta_f}{M_{a/c}}\right] - [r \times V_x] \quad (1)$$

$$\dot{r} = \left[\frac{-1}{I_{zz}} \times \begin{pmatrix} CS_{NW} \times L_{NW} \times \dfrac{V_y + r \times L_{NW}}{V_x} \\ -2 \times CS_{MW} \times L_{MW} \times \dfrac{V_y - r \times L_{MW}}{V_x} \end{pmatrix}\right] + \left[\frac{CS_{NW} \times L_{NW} \times \delta_f}{I_{zz}}\right]. \quad (2)$$

Equations (1) and (2) are solved to get lateral velocity (v_y) and yaw rate (r) to predict the lateral resisting force and sideslip on the tyres which are given by

$$F_{YNW} = CS_{NW} * \beta_{NW} \quad (3)$$

$$F_{YMW} = CS_{MW} * \beta_{MW} \quad (4)$$

$$\beta_{NW} = \delta_f - \left(\frac{V_y + r \times L_{NW}}{V_x}\right) \quad (5)$$

$$\beta_{MW} = -\left(\frac{V_y - r \times L_{MW}}{V_x}\right) \quad (6)$$

These are linear and coupled equations that can be solved using state-space methods in MATLAB–Simulink for the unknowns, lateral velocity, V_y and yaw rate, r. V_y and r are used in calculating side slip using Eqs. (5) and (6). Using sideslip, resistive torque is calculated as shown in Eq. (20).

5 Aircraft Tricycle Model

Tricycle modelling of aircraft steering system as shown in Fig. 4 is more appropriate as aircraft contains generally one nose gear and two main gears. Two main gears are located at the semi track distance from CG and hence steering response on the two gears could be different. Assumptions are the same as considered in the bicycle model except that both the main gears are modelled separately.

From Fig. 4, Force balance along the lateral direction and moment balance about CG of aircraft results in equations of motion for tricycle aircraft model as

$$M_{a/c}\left(\dot{V_y} + rV_x\right) = F_{YNW} + F_{YMWL} + F_{YMWR} \quad (7)$$

$$I_{zz}\dot{r} = F_{YNW}\, L_{NW} - F_{YMWL}\, L_{MW} - F_{YMWR}\, L_{MW} \quad (8)$$

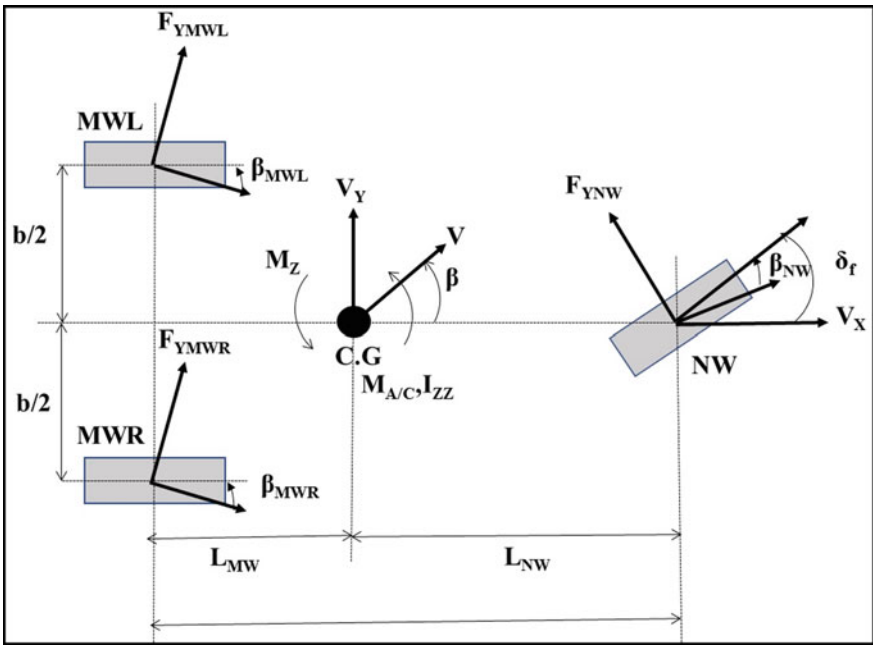

Fig. 4 Tricycle representation of aircraft model

Sideslip on the nose and main wheel are given as

$$\beta_{\mathrm{NW}} = \delta_{\mathrm{f}} - \left(\frac{\mathrm{V_y} + \mathrm{r} \times \mathrm{L_{NW}}}{\mathrm{V_x}}\right) \tag{9}$$

$$\beta_{\mathrm{MWL}} = -\left(\frac{\mathrm{V_y} - \mathrm{r} \times \mathrm{L_{MW}}}{\mathrm{V_x} + r\left(\frac{b}{2}\right)}\right) \tag{10}$$

$$\beta_{\mathrm{MWR}} = -\left(\frac{\mathrm{V_y} - \mathrm{r} \times \mathrm{L_{MW}}}{\mathrm{V_x} - r\left(\frac{b}{2}\right)}\right) \tag{11}$$

From the assumption of linear tyre model,

$$\mathrm{F_{YNW}} = \mathrm{CS_{NW}}\beta_{\mathrm{NW}} = \mathrm{CS_{NW}} \times \left[\delta_{\mathrm{f}} - \left(\frac{\mathrm{V_y} + \mathrm{r} \times \mathrm{L_{NW}}}{\mathrm{V_x}}\right)\right] \tag{12}$$

$$\mathrm{F_{YMWL}} = \mathrm{CS_{MWL}}\beta_{\mathrm{MWL}} = \mathrm{CS_{MWL}} \times \left[-\left(\frac{\mathrm{V_y} - \mathrm{r} \times \mathrm{L_{MW}}}{\mathrm{V_x} + r\left(\frac{b}{2}\right)}\right)\right] \tag{13}$$

$$\mathrm{F_{YMWR}} = \mathrm{CS_{MWR}}\beta_{\mathrm{MWR}} = \mathrm{CS_{MWR}} \times \left[-\left(\frac{\mathrm{V_y} - \mathrm{r} \times \mathrm{L_{MW}}}{\mathrm{V_x} - r\left(\frac{b}{2}\right)}\right)\right] \tag{14}$$

Substituting Eqs. (9) to (14) above on Eqs. (7) and (8) and defined in terms of unknowns as

$$\dot{V_y} = \left[\frac{-1}{M_{a/c}} \times \left(\begin{array}{l} CS_{NW} \times \dfrac{V_y + r \times L_{NW}}{V_x} + CS_{MWL} \times \dfrac{V_y - r \times L_{MW}}{V_x + r \times \left(\frac{b}{2}\right)} \\ + CS_{MWR} \times \dfrac{V_y - r \times L_{MW}}{V_x - r \times \left(\frac{b}{2}\right)} \end{array}\right)\right] + \left[\frac{CS_{NW} \times \delta_f}{M_{a/c}}\right] - [r \times V_x] \tag{15}$$

$$\dot{r} = \left[\frac{-1}{I_{zz}} \times \left(\begin{array}{l} CS_{NW} \times L_{NW} \times \dfrac{V_y + r \times L_{NW}}{V_x} - CS_{MWL} \times L_{MW} \\ \times \dfrac{V_y - r \times L_{MW}}{V_x + r \times \left(\frac{b}{2}\right)} - CS_{MWR} \times L_{MW} \times \dfrac{V_y - r \times L_{MW}}{V_x - r \times \left(\frac{b}{2}\right)} \end{array}\right)\right] + \left[\frac{CS_{NW} \times L_{NW} \times \delta_f}{I_{zz}}\right] \tag{16}$$

As seen above, Eqs. (15) and (16) are coupled, non-linear and hence they cannot be solved using linear state-space methods. Non-linearity arises because of the presence of unknown term, r in the denominator of sideslip terms. The function block approach in MATLAB-Simulink is first applied to the bicycle model to validate the approach with state-space methods and the same is applied to tricycle model.

6 Landing Gear and Resistive Torque Model

Torque balance equation [6] of Landing Gear with reference to Fig. 1 is given as

$$J_e \ddot{\delta}_f + B_e \dot{\delta}_f + k\delta_f = T_{net} \tag{17}$$

$$T_{net} = T_a - T_r \tag{18}$$

$$T_a = A P_L L_L \tag{19}$$

Tyre Resistive Torque Equation [6] is given as,

$$T_r = 2SAS_{NW}\beta_{NW} - 2eCS_{NW}\beta_{NW} \tag{20}$$

As seen from Eq. (20), resistive torque model is depending only on nose wheel parameters as steering operation in most of the aircraft are done using nose wheel alone. Hence the controller system is going to depend on this resistive torque model apart from bicycle or tricycle method for aircraft ground dynamics model.

7 Simulations

Aircraft steering system is modelled in MATLAB-Simulink and it is shown in Fig. 5. The error between pilot input and steering response output is fed to the controller unit which controls the hydraulic system. Based on the steering response, hydraulic flow parameters are changed by the controller which changes the applied torque. This is a closed-loop feedback system where the hydraulic flow is changed until the desired steering response is obtained.

Input Steering Profile is considered as shown in Fig. 6.

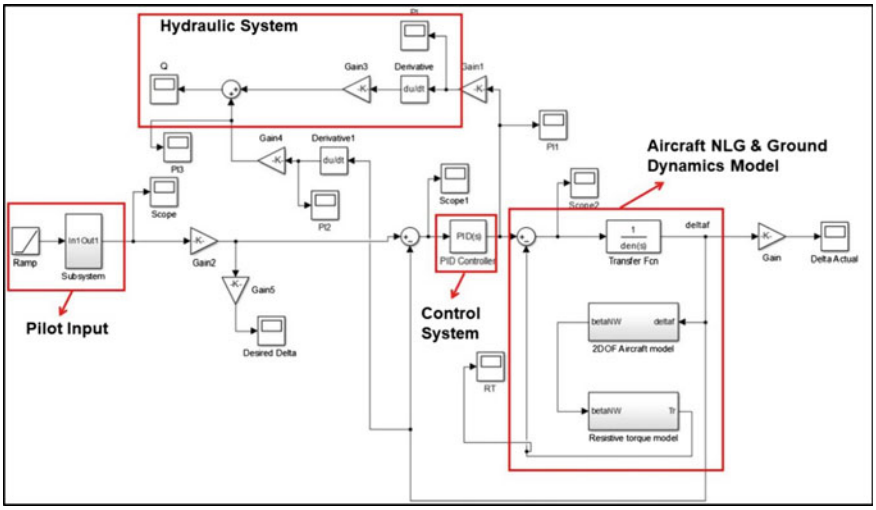

Fig. 5 Simulink model of the aircraft steering system

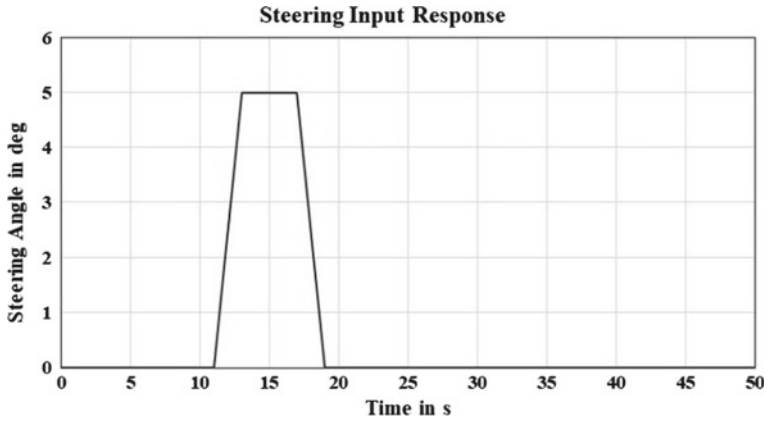

Fig. 6 Input steering profile

Aircraft data [6] is given in Table 1.

2DOF Aircraft Model contains the function blocks to solve for lateral velocity and yaw rate as shown in Fig. 7.

Table 1 Aircraft input data

Parameter	Value	Units
Mass of aircraft	17,690	kg
Moment of inertia of the aircraft about C.G	189,740	kg-m^2
Distance between nose wheel and centre of gravity	3.81	m
Distance between main wheel and centre of gravity	0.58	m
Longitudinal velocity	6	m/s
Cornering stiffness of nose wheel tyre	33,015	N/rad
Cornering stiffness of main wheel tyre	48,287	N/rad
Effective bulk modulus of fluid	8 * 10^8	N/m^2
Total volume of actuator chamber	0.0014	m^3
Piston area of the steering actuator	0.0053	m^2
Reference radius of steering pinion	0.1	m
Equivalent damping constant of the NLG	10	N-m/rad/s
Load stiffness coefficient	100,000	N m/rad
Equivalent inertia of NLG	1.0	kg-m^2
Caster length	0.1	m
Self-aligning stiffness	38,000	N/rad

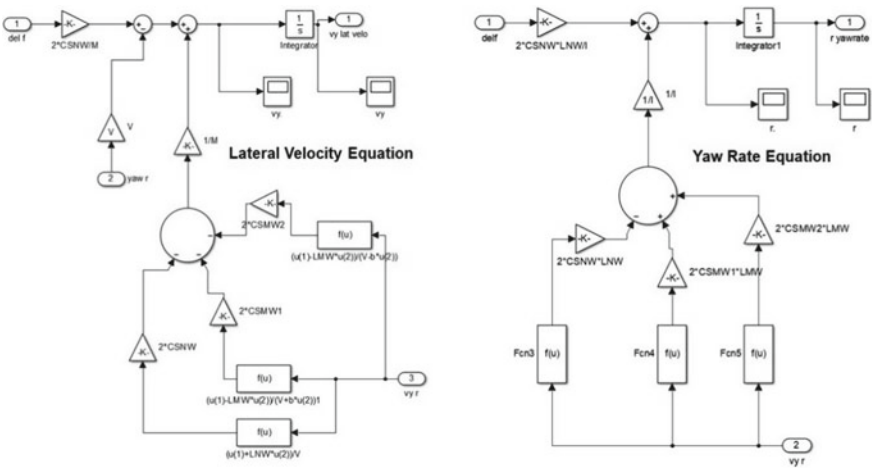

Fig. 7 Simulink function blocks method to solve aircraft ground dynamics model

8 Results and Discussions

Both the bicycle and tricycle models are simulated with typical aircraft data [6] with the longitudinal velocity of 6 m/s for a typical input steering profile. Comparison of various parameters between the bicycle and tricycle model is shown in Table 2. As expected, there is no difference in nose wheel parameters because of the same equations prevail for both the models. There is an increase of 5% in slip angle on the main wheel because of the additional track parameter in the tricycle equations. In addition, it is found that there is a difference of 3% in lateral force on the main wheel between the models.

Variation of for lateral force and sideslip on main gear for bicycle and tricycle modelling method is shown in Fig. 8.

In the sensitivity study 1, both the models are simulated with different steer rates to understand its influence on the modelling methods as shown in Table 3. Parameters such as slip angle, lateral force, yaw rate, etc., increase slightly with an increase in the steering rate of aircraft. For 50% increase in steering rate, the slip angle and lateral force at the nose wheel increase by 12%.

In the sensitivity study 2, both the models are simulated with different longitudinal velocities of aircraft to understand its influence on the modelling methods as shown in Table 3. Also, it is observed that with an increase in the linear velocity, slip angles

Table 2 Comparison between bicycle and tricycle model

Parameters	Bicycle model	Tricycle model
Max yaw rate (rad/s)	0.168	0.168
Max lateral velocity (m/s)	0.390	0.390
Slip angle at MWL (deg)	4.60	4.39
Max lateral force at MWL (N)	3872	3700
Max slip angle at MWR (deg)	NA	4.82
Max lateral force at MWR (N)	NA	4000

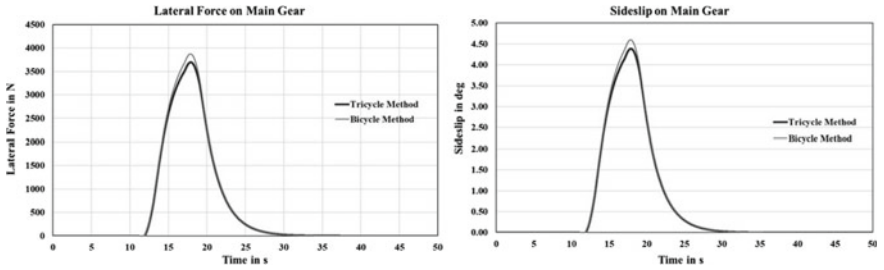

Fig. 8 Comparison of lateral force and sideslip between tricycle and bicycle method on MLG

Table 3 Comparison between Bicycle and tricycle model for different steering rate (Study 1)

Parameters	Bicycle model	Tricycle model	Bicycle model	Tricycle model
Steering rate (deg/s)	2.5		5	
Max yaw rate (rad/s)	0.1685	0.1685	0.1775	0.1775
Max lateral velocity (m/s)	−0.39	−0.39	−0.42	−0.42
Slip angle at MWL (deg)	4.6	4.3	4.9	4.7
Max lateral force at MWL (N)	3872	3700	4137	3948
Max slip angle at MWR (deg)	NA	4.8	NA	5.1
Max lateral force at MWR (N)	NA	4000	NA	4319

become more than 5 deg and hence the linear tyre model considered in the simulations is not applicable. For a 33.3% increase in longitudinal velocity, a 32% increase in slip angle and lateral force is observed (Table 4).

Table 4 Comparison between bicycle and tricycle model for different longitudinal velocity (Study 2)

Parameters	Bicycle model	Tricycle model	Bicycle model	Tricycle model	Bicycle model	Tricycle model	Bicycle model	Tricycle model
Longitudinal velocity (m/s)	4		6		8		10	
Max yaw rate (rad/s)	0.094	0.094	0.168	0.168	0.275	0.275	0.442	0.442
Max lateral velocity (m/s)	−0.078	−0.078	−0.390	−0.390	−1.22	−1.22	−3.18	−3.18
Slip angle at MWL (deg)	1.80	1.72	4.60	4.39	9.85	9.28	20.00	18.35
Max lateral force at MWL (N)	1503	1450	3872	3700	8380	7820	18,000	15,400
Max slip angle at MWR (deg)	NA	1.85	NA	4.82	NA	10.35	NA	21.25
Max lateral force at MWR (N)	NA	1560	NA	4000	NA	8720	NA	17,900

9 Conclusions

In the above study, the lateral forces and slip angles on the main wheel are predicted from bicycle and tricycle modelling methods. It is observed that the bicycle modelling methodology is 5% less accurate when compared to tricycle method. The steering actuator response is based on the resistive torque generated on the tyres. When the nose wheel steering is used, resistive torque is calculated using lateral forces and slip angles from the nose gear alone. Hence, the bicycle or tricycle modelling method will not change the steering actuator response. But in tri-wheel steering, resistive torque is calculated using lateral forces and slip angles from both the gears. If the bicycle model is considered in the all-wheel steering system, the predicted steering actuator response will be different from actual because of the difference in the lateral forces and slip angles of the main gear. Hence, it is concluded that the bicycle model is sufficient in the simulation of the nose wheel steering system as in many aircraft but tricycle modelling is required in the simulation of the tri-wheel steering system as in some wide-body aircraft to predict the right steering response.

Acknowledgements The authors would like to thank "Council of Scientific and Industrial Research (CSIR)", Government of India for funding this project under the 12th Five Year Plan. The authors also like to thank Director, CSIR-National Aerospace Laboratories (NAL), India and Head, Structural Technologies Division, CSIR-NAL, for their kind support.

References

1. Biannic J-M, Marcos A, Jeanneau M, Roos C (2006) Nonlinear simplified LFT modelling of an aircraft on ground. In: Proceedings of the 2006 IEEE international conference on control applications, Munich, pp 2213–2218
2. Pouly G (2009) Analysis and synthesis of advanced control laws for vehicle ground guidance. PhD thesis, University de Haute Alsace
3. Pouly G, Lauffenburger J-P, Basset M (2009) Reduced order H_∞ control design of a nose landing gear steering system. In: Proceedings of the 12th IFAC symposium on transportation systems, pp 478–483
4. Roos C, Biannic J-M, Tarbouriech S, Prieur C, Jeanneau M (2010) On-ground aircraft control design using a parameter-varying anti-windup approach. Aerosp Sci Technol 14:459–471
5. Chen B, Jiao Z, Ge SS (2011) Nonlinear control of aircraft on ground runway keeping. IEEE Xplore, pp 576–581
6. Pavan MS, Jaidev Vyas J, Balamurugan G (2016) Modelling and simulation of aircraft nose wheel steering system. IEEE Xplore
7. Duprez J, Mora-Camino F, Villaume F (2004) Control of the aircraft-on-ground lateral motion during low speed roll and manoeuvers. In: IEEE aerospace conference proceedings, pp 2656–2666
8. Chen B, Jiao Z, Ge SS (2013) Aircraft-on-ground path following control by dynamical adaptive backstepping. Chinese Journal of Aeronautics, 26:668–675

Free Vibration and Stress Analysis of Laminated Box Beam with and Without Cut-Off

Raj B. Bharati, Prashanta K. Mahato, E. Carrera, M. Filippi and A. Pagani

Abstract This paper presents the free vibration and static analysis of composite box beam using refined beam theory. The structural model based on one-dimensional (1D) is derived in the Carrera Unified Formulation (CUF) framework. The principle of virtual displacement has been used along with CUF to formulate the finite element arrays in the terms of fundamental nuclei, which either do not depend on the expansion order or on the class of the beam model. In the present study, the various composite box beam models with and without cut-off model using different aspect ratio has been analyzed the free vibration and static analysis. The results of free vibration analysis are compared to published literature. The present study indicates the high-level accuracy reached by refined beam models with lower computational costs than 3D solid elements.

Keywords Free vibration · Static analysis · Refine one-dimensional model · Box beam · Composite beams · Carrera unified formulation

1 Introduction

In modern times, laminated composite beams, plates, and shells are extensively used in high-speed aircraft, rocket, launch vehicle, aerospace, or civil structures due to their high specific strength and stiffness, excellent fatigue and corrosion resistance. In engineering application, many structures are required stiffness-to-weight ratio,

R. B. Bharati (✉) · P. K. Mahato (✉)
Department of Mechanical Engineering, Indian Institute of Technology (ISM), Dhanbad, Dhanbad 826004, Jharkhand, India
e-mail: rajiitism@gmail.com

P. K. Mahato
e-mail: pkmahato@gmail.com

R. B. Bharati · E. Carrera · M. Filippi · A. Pagani
Department of Mechanical and Aerospace Engineering, Politecnico di Torino, Corso Duca degli Abruzzi 24, 10129 Turin, Italy

B. N. Singh et al. (eds.), *Recent Advances in Theoretical, Applied, Computational and Experimental Mechanics*, Lecture Notes in Mechanical Engineering,
https://doi.org/10.1007/978-981-15-1189-9_15

thus the structure made of laminated composite materials represents efficient constructive solutions. To analyze the mechanical behavior of such type of structures are extremely complex process. Although a considerable number of analytical and numerical methods have been proposed over the years. To analyze the structural behavior of this type of structure, the beam theories are extensively used. In the case of modeling of weight-sensitive structures, the one-dimensional (1D) approach is more significant due to its simplicity and low computational cost and more efficient than two-dimensional (2D) (plate and shell) and three-dimensional (3D) (solid) elements. The classical theories that are most employed are proposed by Euler–Bernoulli [1] and Timoshenko [2], which are also known as first-order shear deformation theories (FSDTs).

For modeling the composite structure these theories are inadequate. Several higher order shear deformation theories (HSDTs) are purposed for the composite structure, which can be classified into two main categories: equivalent single layer (ESL) and layer-wise (LW) theories. The ESL enables to produce piecewise continuous displacement and transverse stress in the thickness direction of the laminate structures [3, 4]. In this approach, the number of unknowns is independent of the number of layers, for example, first-and second-order shear deformation theories [5, 6]. Third-order shear deformation theories were purposed for the analysis of beams [7] and plates [8]. Arya et al. [9] presented a HSDT for the static analysis of laminated composite beams. Later, Li et al. [10] extended this refined model to study the free vibration of angle-ply laminated beams. And recently, Sahoo and Singh [11] studied new inverse zig-zag shear deformation theories for the static analysis of sandwich laminated plates. Carrera [12] compared different 2D theories to investigate the effects of the curvature and shear deformation on the buckling and vibrations of cross-ply laminated shells. Although ESL exhibits many applications in static and dynamic analysis of composite beams, it results in efficient theories for laminate structures. The main drawback of the ESL approach is that the continuity of transverse shear and normal stresses is not always assured. In the domain of LW, a continuous displacement assumption is considered in each separate layer. In LW approach, the number of degrees of freedom (DOFs) depends directly on the number of layers. In the LW approach the required computational cost is more than the ESL approach. Robin and Reddy [13] used LW theory to develop modeling of thick composites. Shimpi and Ainapure [14] presented a trigonometric shear deformation theory to develop modeling of two-layered cross-ply beams. Later, the same theory extended and utilized [15] for free vibration analysis of cross-ply laminated beams.

The present work has focused on refined theories with generalized displacement variables for the free vibration and stress analysis of the laminated box beam. For preliminaries model, the Carrera unified formulations (CUF) are used. CUF formulation has been developed over the last decade for plate/shell models [12, 16–18] and it has recently been extended for beam modeling [19]. In this study the cross section of laminated box beam made of orthotropic material with discretized with 16 nine-node elements (16L9). Two types of cross-sectional distribution 16L9 (a) and 16L9 (b) are used for the analysis as shown in Fig. 2. A combination of orthotropic fiber composite layers is used to be a construction of walls. The objective of this

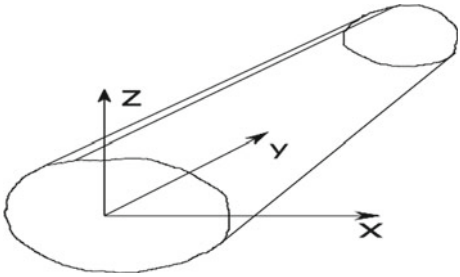

Fig. 1 Coordinate frame work of the beam model

study is to develop a laminated box beam model with cut-off and without cut-off and this model is used for analysis in the form of free vibrations, displacements, and stresses with the help of refined one-dimensional beam theories. For finite element formulation, CUF framework is used to prepare a model, which is a hierarchical formulation leading to very accurate and computationally efficient finite element (FE) models. The laminated box made of two orthotropic layers with same thickness. In order to demonstrate the effectiveness of the proposed refined elements, the results in terms of natural frequencies, and displacements, are computed and compared with the available research literature.

2 The Structural Model: Carrera Unified Formulation

According to the Carrera Unified Formulation the displacement fields $u^T(x, y, z, t) = \{u_x u_y u_z\}^T$, for the displacement vector, $u_\tau(y)$ with expansion of generic functions, $F_\tau(x, z)$

$$u(x, y, z, t) = F_\tau(x, z)u_\tau(y) \quad \tau = 1, 2, \ldots, T \tag{1}$$

where T stands for the terms in expansion, in Einstein's generalized notation it stands for summation, u_τ is the displacement vector, and F_τ represents expansion function to approximate the behavior of the cross section of box beam.

In this work Eq. (1) consists of Lagrange polynomials, which are used to build the 1D higher order models. In this paper, the nine points (L9) cross-sectional polynomial (Fig. 2) set was adopted and the interpolation functions are given as:

$$\begin{aligned}
F_\tau &= \frac{1}{4}\left(r^2 + rr_\tau\right)\left(s^2 + ss_\tau\right), \quad \tau = 1, 3, 5, 7 \\
F_\tau &= \frac{1}{2}s_\tau^2\left(s^2 - ss_\tau\right)\left(1 - r^2\right) + \frac{1}{2}r_\tau^2\left(r^2 + rr_\tau\right)\left(1 - s^2\right), \quad \tau = 2, 4, 6, 8 \\
F_\tau &= \left(1 - r^2\right)\left(1 - s^2\right), \quad \tau = 9
\end{aligned} \tag{2}$$

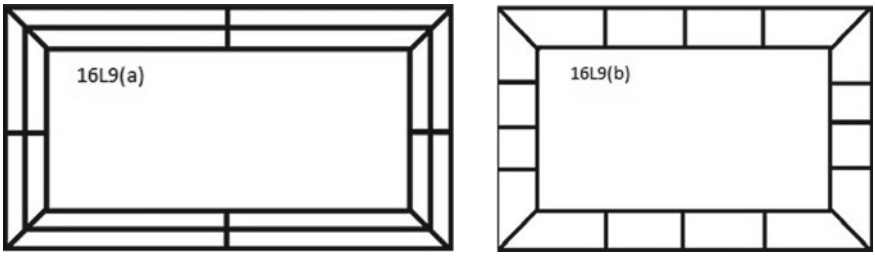

Fig. 2 Cross-sectional distribution of L9 elements of laminated box beam

where r and s vary from -1 to $+1$, whereas r_τ and s_τ are the coordinates of the nine points whose locations in the natural coordinate frame. The displacement of a L9 element therefore

$$\begin{aligned} u_x &= F_1 u_{x_1} + F_2 u_{x_2} + F_3 u_{x_3} + \cdots + F_9 u_{x_9} \\ u_y &= F_1 u_{y_1} + F_2 u_{y_2} + F_3 u_{y_3} + \cdots + F_9 u_{y_9} \\ u_z &= F_1 u_{z_1} + F_2 u_{z_2} + F_3 u_{z_3} + \cdots + F_9 u_{z_9} \end{aligned} \tag{3}$$

where $u_{x_1} \ldots u_{x_9}$ represents the displacement field of the components x of the L9 element.

The stress and strains are

$$\begin{aligned} \sigma_p &= \{\sigma_{zz}\sigma_{xx}\sigma_{xz}\}^T, \varepsilon_p = \{\varepsilon_{zz}\varepsilon_{xx}\varepsilon_{xz}\}^T \\ \sigma_n &= \left\{\sigma_{zy}\sigma_{xy}\sigma_{yy}\right\}^T, \varepsilon_n = \left\{\varepsilon_{zy}\varepsilon_{xy}\varepsilon_{yy}\right\}^T \end{aligned} \tag{4}$$

where the subscripts p and n stands for the terms lying cross section and planes, respectively.

Hooke's law and strain–displacement relations are, respectively,

$$\begin{aligned} \sigma_p &= \widetilde{C}_{pp}\varepsilon_p + \widetilde{C}_{np}\varepsilon_n \\ \sigma_n &= \widetilde{C}_{np}\varepsilon_p + \widetilde{C}_{nn}\varepsilon_n \\ \varepsilon_p &= D_p u \\ \varepsilon_n &= \left(D_{ny} + D_{np}\right) \end{aligned} \tag{5}$$

where

$$D_p = \begin{bmatrix} 0 & 0 & \frac{\partial}{\partial z} \\ \frac{\partial}{\partial x} & 0 & 0 \\ \frac{\partial}{\partial z} & 0 & \frac{\partial}{\partial x} \end{bmatrix}, \quad D_{nA} = \begin{bmatrix} 0 & \frac{\partial}{\partial z} & 0 \\ 0 & \frac{\partial}{\partial x} & 0 \\ 0 & 0 & 0 \end{bmatrix}, \quad D_{ny} = \begin{bmatrix} 0 & 0 & \frac{\partial}{\partial y} \\ \frac{\partial}{\partial y} & 0 & 0 \\ 0 & \frac{\partial}{\partial y} & 0 \end{bmatrix} \tag{6}$$

Box beam is a complex laminated structure, for such type of structure can be considered constituted by a certain number of straight orthotropic layers, material coordinate system (1; 2; 3) generally do not coincide with the physical coordinate system (x; y; z) as shown in Fig. 1. The matrices of the material coefficient of the generic material k based on the above approach are

$$\widetilde{C}_{pp}^{k} = \begin{bmatrix} \widetilde{C}_{11}^{k} & \widetilde{C}_{12}^{k} & \widetilde{C}_{14}^{k} \\ \widetilde{C}_{12}^{k} & \widetilde{C}_{22}^{k} & \widetilde{C}_{24}^{k} \\ \widetilde{C}_{14}^{k} & \widetilde{C}_{24}^{k} & \widetilde{C}_{44}^{k} \end{bmatrix}, \quad \widetilde{C}_{pn}^{k} = \begin{bmatrix} \widetilde{C}_{15}^{k} & \widetilde{C}_{16}^{k} & \widetilde{C}_{13}^{k} \\ \widetilde{C}_{25}^{k} & \widetilde{C}_{26}^{k} & \widetilde{C}_{23}^{k} \\ \widetilde{C}_{45}^{k} & \widetilde{C}_{46}^{k} & \widetilde{C}_{43}^{k} \end{bmatrix}, \quad \widetilde{C}_{nn}^{k} = \begin{bmatrix} \widetilde{C}_{55}^{k} & \widetilde{C}_{56}^{k} & \widetilde{C}_{35}^{k} \\ \widetilde{C}_{56}^{k} & \widetilde{C}_{66}^{k} & \widetilde{C}_{36}^{k} \\ \widetilde{C}_{35}^{k} & \widetilde{C}_{36}^{k} & \widetilde{C}_{33}^{k} \end{bmatrix} \tag{7}$$

For the sake of brevity, shape function and explicit form of the coefficients are shown in [12]. To handle for arbitrary shaped cross section, classical finite element technique is adopted here and generalized displacement vector becomes

$$u_{\tau}(y) = N_i(y) q_{\tau i} \tag{8}$$

where $N_i(y)$ is the shape function and $q_{\tau i}$ is the nodal displacement vector:

$$q_{\tau i} = \left\{ q_{u_{x_{\tau i}}} q_{u_{y_{\tau i}}} q_{u_{z_{\tau i}}} \right\}^{T} \tag{9}$$

3 The Equation of Motion in the CUF Framework

The equation of motion can be directly derived from the Principle of Virtual Displacement (PVD), which states

$$\delta L_{\text{int}} = \delta L_{\text{ext}} + \delta L_{\text{ine}} \tag{10}$$

where δL_{int}, δL_{ext}, δL_{ine}, and δ stands for internal work, external work, inertial work, and virtual variation, respectively.

With the help of Eqs. (1), (3), (4), and (5), the virtual variation can be written as

$$\delta L_{\text{int}} = \delta q_{\tau i}^{T} K^{ij\tau s} q_{si} \tag{11}$$

where $K^{ij\tau s}$ is in the form of a fundamental nucleus for the stiffness matrix and can be written as follows:

$$\begin{aligned} K^{ij\tau s} = I_l^{ij} \int \Big\{ & D_{np}^{T}(F_\tau I)\big[\widetilde{C}_{np}^{k} D_p(F_s I) + \widetilde{C}_{nn}^{k} D_{np}(F_s I)\big] \\ & + D_p^{T}(F_\tau I)\big[\widetilde{C}_{pp}^{k} D_p(F_s I) + \widetilde{C}_{pn}^{k} D_{np}(F_s I)\big] \Big\} \mathrm{d}A \\ & + + I_l^{ij,y} \int \big[D_{np}^{T}(F_\tau I) + D_p^{T}(F_\tau I) \widetilde{C}_{pn}^{k} \big] F_s \mathrm{d}A + I_{Ay} \end{aligned}$$

$$+ I_l^{i,yj} I_{Ay}^T \int F_\tau \left[\widetilde{C}_{np}^k D_p(F_s I) + \widetilde{C}_{nn}^k D_{np}(F_s I)\right] \mathrm{d}A$$
$$+ I_l^{i,yj,y} I_{Ay}^T I_{Ay} \int F_\tau \widetilde{C}_{nn}^k F_s \mathrm{d}A \tag{12}$$

where apex k denotes the layer and

$$I_{Ay} = \begin{bmatrix} 0 & 1 & 0 \\ 1 & 0 & 0 \\ 0 & 0 & 1 \end{bmatrix} \tag{13}$$

$$\left(I_l^{ij}, I_l^{ij,y}, I_l^{i,yj}, I_l^{i,yj,y}\right) = \int_l \left(N_i N_j, N_i N_{j,y}, N_{i,y} N_j, N_{i,y} N_{j,y}\right) \mathrm{d}y \tag{14}$$

Similarly for the inertial loads

$$\delta L_{\text{ine}} = \delta q_{\tau i}^T M^{ij\tau s} \ddot{q}_{sj} \mathrm{d}y \tag{15}$$

where $\ddot{q}$ stands for nodal acceleration and $M^{ij\tau s}$ stands for mass matrix in the form of fundamental nucleus:

$$M^{ij\tau s} = I_l^{ij} \int \left(F_\tau \rho^k I F_\tau\right) \mathrm{d}A \tag{16}$$

Similarly for the external loads

$$\delta L_{\text{ext}} = P \delta u^T \tag{17}$$

$$\delta L_{\text{ext}} = F_\tau N_i P \delta q_{\tau i}^T \tag{18}$$

$$P = \left\{P_{u_x} \; P_{u_y} \; P_{u_z}\right\}^T \tag{19}$$

After assembly of global FE matrices, the undamped dynamic problem as follows:

$$M\ddot{q} + Kq = 0 \tag{20}$$

Introducing harmonic solution, it is possible to compute the natural frequencies, ω_k by solving a classical eigenvalue problem,

$$\left(-\omega_k^2 M + K\right) q_k = 0 \tag{21}$$

Table 1 The different lamination sequences of the layered box beam

Layup	Flanges		Webs	
	Top	Bottom	Left	Right
Case 1	θ	θ	θ	θ
Case 2	θ	θ	0	0
Case 3	0	0	θ	θ
Case 4	θ	k_1 θ	k_1 k_2 θ	k_1 k_2 k_3 θ
Note $k_1 = -1, k_2 = 2, k_3 = -1$				

4 Analysis of Composite Box Beam

4.1 Free Vibration Analysis

In this section, the free vibration analysis of composite box beam is discussed. The cantilever box beam is prismatic with length $L = 762$ mm, width $b = 24{:}21$ mm, and height $h = 13{:}46$ mm. Each wall of the box beam has a total thickness equal to $t = 0.762$ mm was consider in the first numerical example. The length to height ratio, *L/h* is assumed equal to 10 and each layer of the structure is made of an orthotropic material, whose density and mechanical properties along the fiber (L) and transverse (T) directions are $\rho = 1601$ kg/m^3, $E_L = 142$ GPa, $E_T = 9.8$ GPa, $G_{LT} = 6$ GPa, $G_{TT} = 4.83$ GPa, $\nu = 0.5$. The box beam made of single and double layers and lamination schemes are reported in Table 1. The Lagrange Element (LE) consists of 9 four-noded (9B4) beam elements along the longitudinal axis and various approximations of the cross-sectional kinematics are assumed shows in Fig. 2 where each rectangle represents one L9 (Fig. 3) polynomial set. The two 16L9 models are considered for the free vibration analysis. Natural frequencies of the box beam reported in Table 2 and the computed results were compared with the finite element solution provided by [16]. The compared results have good agreement with references. The natural frequencies related to the mode number for the various aspect ratio and stacking sequences of 16L9(a) and 16L9(b) models were shown in Fig. 4 and Fig. 5 respectively. From the results given, it should be clear that aspect ratio and stacking sequences can significantly influence the natural frequencies of the model.

4.2 Static Analysis

In this section the static analysis of a composite box beam has been discussed, the box beam was clamped at the one end while a point load applied at the other end. The magnitude of the applied load was $F = -5000$ N. The geometrical data of the structure were as the previous and length to height ratio was equal to the 10. 9B4 elements were used to describe the box beam and the number of beam elements was

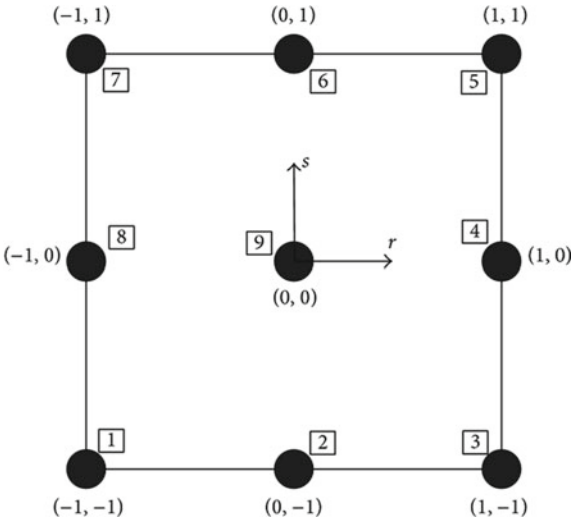

Fig. 3 L9 element in the natural coordinate system

Table 2 Comparison of natural frequencies for Case 1 and 3 with $\theta = 45°$

	Present		Ref. [16]		
	16L9(a)	16L9(b)	16L9(a)	16L9(b)	MSC-Nastran
Case 1	231.79	231.47	232.02	233.28	232.38
Case 3	610.56	605.58	610.78	605.73	604.52

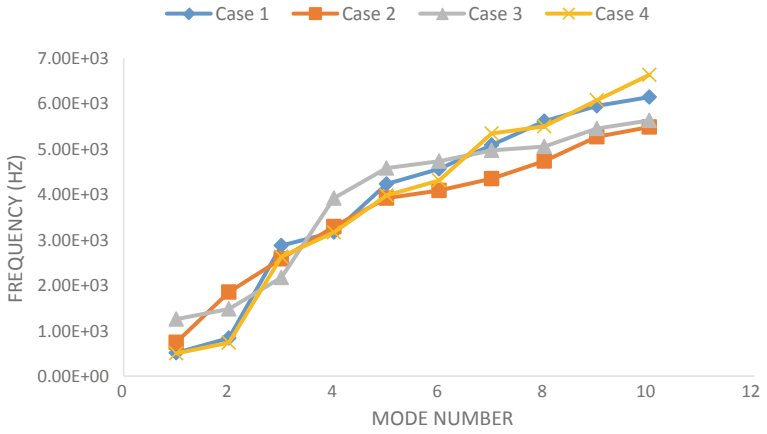

Fig. 4 Natural frequencies for 16L9(a) model of box beam

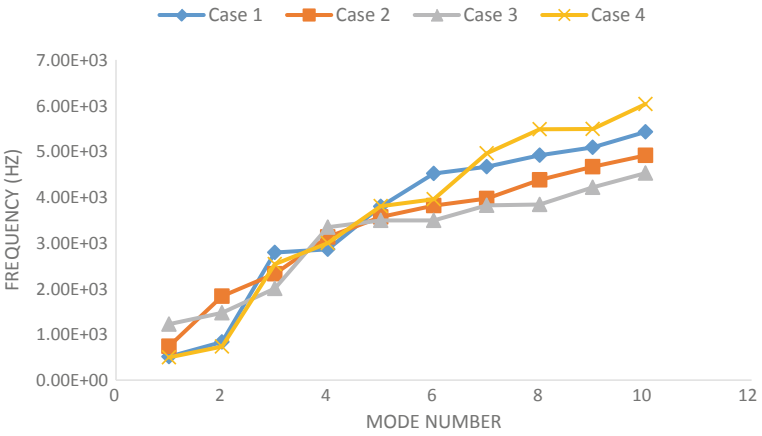

Fig. 5 Natural frequencies for 16L9(b) model of box beam

derived from the convergence analysis. The vertical displacement reported in Table 3 for the various cases and computed results were compared with shell element of the commercial software. The vertical displacement was computed at two points '*a*' and '*b*' those projected on the middle of top and bottom surface at the free end of the beam. The computed results were compared with commercial software and have a

Table 3 Vertical displacement of box beam with and without cut-off model

		Without cut-off			With cut-off		
		CUF model		Shell element	CUF model		Shell element
		16L9(a)	16L9(b)		16L9(a)	16L9(b)	
Case 1	W_a [m * 10^{-1}]	−2.02	−2.39	−2.58	−2.32	−2.57	−2.73
	W_b [m * 10^{-1}]	−1.52	−1.51	−1.56	−1.82	−1.69	−1.69
Case 2	W_a [m * 10^{-1}]	−1.34	−1.71	−1.94	−1.39	−1.74	−2.02
	W_b [m * 10^{-1}]	−0.63	−0.63	−0.66	−0.67	−0.66	−0.68
Case 3	W_a [m * 10^{-1}]	−0.63	−1.29	−1.64	−0.77	−1.33	−1.63
	W_b [m * 10^{-1}]	−0.14	−0.17	−0.19	−0.28	−0.21	−0.22
Case 4	W_a [m * 10^{-1}]	−1.95	−2.33	−2.51	−2.31	−2.53	−2.77
	W_b [m * 10^{-1}]	−1.67	−1.71	−1.74	−2.03	−1.91	−1.95

Table 4 Natural frequencies (Hz) of box beam with and without cut-off model

	Without cut-off			With cut-off		
	CUF model		Shell element	CUF model		Shell element
	16L9(a)	16L9(b)		16L9(a)	16L9(b)	
Case 1	514.70	513.56	510.64	489.52	501.55	503.42
Case 2	741.72	738.7	735.26	737.78	741.33	737.25
Case 3	1251.73	1222.93	1193.36	1067.37	1169.48	1167.86
Case 4	518.87	498.84	495.61	498.19	485.67	482.38

good agreement. The study shows that the different stacking sequence can influence the vertical displacement of the box beam.

4.3 Effects of Cut-Offs

In this section, the static and free vibration analysis of a composite box beam with cut-off has been discussed. The cut-off located on the center of the bottom surface of the box beam, the dimension of the cut-off was width (b_c) = 11:343 and length (l_c) = 44:866 mm. The vertical displacement and natural frequencies of box beam ($L/h = 10$) without and with cut-off have been reported in Table 3 and Table 4 respectively. The computed results are in good agreement with shell elements model of commercial software. For the static analysis, the magnitude of the applied force was $F = -5000$ N. Vertical displacement and natural frequencies have been analyzed for various cases. The computed results show that the cut-off model was more displaced than the without cut-off model for static analysis and natural frequencies of cut-off model were lower than the without cut-off model for free vibration analysis. The natural frequencies related to the mode number for case 1 and case 3 of 16L9(b) models have been shown in Figs. 6 and 7. The graph shows that the low variation trends of frequencies at lower modes and higher modes but more variation in between lower and higher modes.

5 Conclusion

In this present work, free vibration and static analyses of composite box beam have been carried out. The analyses were performed by means of a refined beam model based on the Lagrange Expansion (LE). The principle of virtual displacement has been used along with CUF to formulate the finite element arrays in the terms of fundamental nuclei, which neither depend on the expansion order nor the class of the beam model. The present methodology can deal with full material anisotropy and the cut-off also can be easily implemented in the box structure. Various composite box

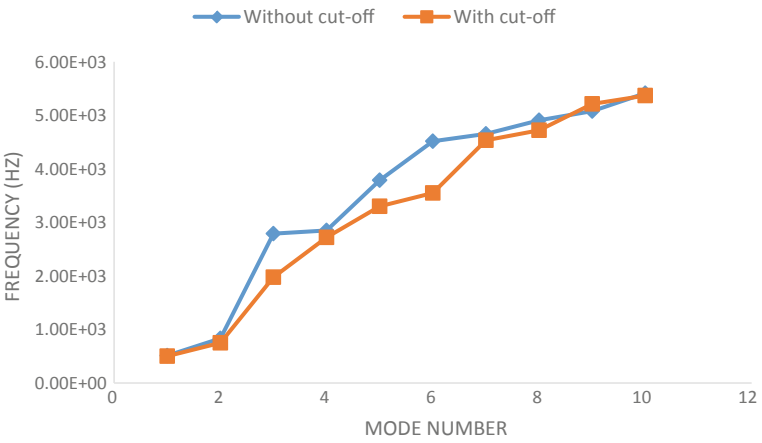

Fig. 6 Natural frequencies for 16L9(b) model of box beam for case 1

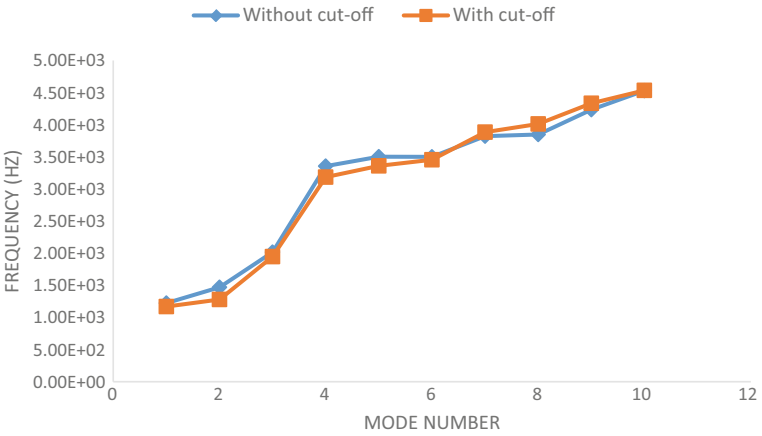

Fig. 7 Natural frequencies for 16L9(b) model of box beam for case 3

beams have been analyzed and in the domain to focus on the parametric studies have been performed to see the effects of cut-off versus free vibration and static analysis. The computed results show that the different stacking sequence and aspect ratio can influence the results of both free vibration and static analysis. The results were compared with published literature obtained in LE expansion of CUF models. The provided comparison shows that with lower computation cost, the 1D-CUF approach yields eventually the same results of the 3D solid element solution.

Acknowledgements The authors are grateful to the Director of Indian Institute of Technology (Indian School of Mines), Dhanbad, India and Politecnico di Torino, Italy, for research collaboration and facilities.

References

1. Euler L (1744) De curvis elastics. Bousquet, Lausanne and Geneva
2. Timoshenko SP (1922) On the transverse vibration of bars of uniform cross section. Philos Mag 43:125–131
3. Pagano NJ (1969) Exact solution for composite laminates in cylindrical bending. J Compos Mater 3:398–411
4. Carrera E (2002) Historical review of zig-zag theories for multilayered plates and shells. Appl Mech Rev 9(2):287–308
5. Yang PC, Norrish CH, Stavsky Y (1996) Elastic wave propagation in heterogeneous plates. Int J Solids Struct 2(4):665–684
6. Whitney JM, Sun CT (1973) A higher order theory of extension motion of laminated composite. J Sound Vib 30(1):85–97
7. Reddy JN, Wang CM, Lee KH (1997) Relationship between bending solution of classical and shear deformation beam theories. Int J Solids Struct 34(26):3373–3384
8. Shi G (2007) A new simple third order shear deformation theory of plates. Int J Solids Struct 44:4394–4417
9. Arya H, Shimpi RP, Naik NK (2002) A zig-zag model for laminated composite beams. Compos Struct 56(1):21–24
10. Li J, Hua HX (2009) Dynamic stiffness analysis of laminated composite beams using trigonometric shear deformation theory. Compos Struct 89(3):433–442
11. Sahoo R, Singh BN (2013) A new inverse hyperbolic zigzag theory for the static analysis of laminated composite and sandwich plates. Compos Struct 105:385–397
12. Carrera E (1991) The effects of shear deformation and curvature on buckling and vibration of cross-ply laminated composite shells. J Sound Vib 150(3):405–433
13. Robbin DH, Reddy JN (1993) Modelling of thick composites using a layerwise laminate theory. Int J Numer Meth Eng 36(4):655–677
14. Shimpi RP, Ghugal YM (2001) A new layerwise trigonometric shear deformation theory for two-layered cross-ply beams. Compos Sci Technol 61(9):1271–1283
15. Shimpi RP, Ainapure AV (2002) Free vibration analysis of two layered cross-ply laminated beams using layer-wise trigonometric shear deformation theory. J Reinf Plast Compos 21(16):1477–1492
16. Carrera E (2002) Theories and finite elements for multilayered, anisotropic, composite plates and shells. Arch Comput Methods Eng 9:87–140
17. Carrera E (2003) Theories and finite elements for multilayered plates and shells: a unified compact formulation with numerical assessment and benchmarking. Arch Comput Methods Eng 10(3):216–296
18. Carrera E, Brischetto S, Robaldo A (2008) Variable kinematic model for the analysis of functionally graded material plates. AIAA J 46(1):194–203
19. Carrera E, Giunta G, Petrolo M (2011) Beam structures: classical and advanced theories. Wiley. https://doi.org/10.1002/9781119978565

Free Vibration Analysis of the Functionally Graded Porous Circular Arches in the Thermal Environment

Mohammad Amir and Mohammad Talha

Abstract In the present study, free vibration analysis of porous functionally graded material (FGM) circular arches has been performed using finite element methodology. The present mathematical model is formed on the higher-order shear deformation theory (HSDT). The mechanical properties of the functionally graded material arches are varying along the thickness direction. The effective mechanical properties of FGM are defined by a modified power law in terms of volume fractions of its constituents. Two distributions of porosity are considered, viz., even and uneven porosity distributions. Convergence and a comparative study have been executed to verify the present formulation. The effect of various influencing parameters, viz., volume fraction index, temperature change, porosity index, and thickness to length ratio, with both distributions of porosity (even and uneven porosity distributions), on the frequency parameter of the arch have been studied.

Keywords Circular arch · FGM · Thermal environment · Vibration analysis · Porosity

1 Introduction

The functionally graded materials (FGMs) are advanced composite materials in which mechanical properties are varying continuously and uniformly from one face to the other. The material gradation can be in the radial direction or along the length of the arch. Due to the smooth alteration of the mechanical properties, stress concentration, and residual stresses can be avoided, unlike traditional composites. Typically, the FGM materials are the graded mixture of metal and ceramic, where the metallic constitute provides superior fracture toughness and the ceramic constitute provides admirable corrosion and thermal resistance competence [1]. Because of exceptional

M. Amir · M. Talha (✉)
School of Engineering, Indian Institute of Technology Mandi, Kamand 175005, Himachal Pradesh, India
e-mail: talha@iitmandi.ac.in

B. N. Singh et al. (eds.), *Recent Advances in Theoretical, Applied, Computational and Experimental Mechanics*, Lecture Notes in Mechanical Engineering,
https://doi.org/10.1007/978-981-15-1189-9_16

properties of FGM, like high specific strength, ability to withstand ultrahigh temperature gradients and high specific stiffness, their use in spacecraft, nuclear reactors, and space structures has been increased [2]. The curved beams and circular arches are being widely used as structural members in various engineering applications such as in civil, mechanical and aerospace industries [3]. Therefore, it is important to analyze and find out the vibrational behavior of these structures in order to avoid catastrophic failure.

The FGMs are difficult to manufacture, microstructural voids, or porosities may arise in the FGMs because of the substantial difference in the solidification temperature of the material constituents, during the process of sintering [4, 5]. The porosity also affects the response of the FGM structure, for example, Ebrahimi et al. [6] scrutinized the vibration response of the FGM porous beam subjected to different types of thermal loadings using the semi-analytical method. Ebrahimi and Jafari [7] obtained Navier solution for the analysis of thermomechanical vibrations of the porous FGM beams under the various thermal loading conditions, viz., uniform, the linear, sinusoidal temperature rises, and nonlinear. They modified power law to calculate the mechanical properties of the FGM with the even and uneven porosity distributions. Gupta and Talha [8] examined the effect of the porosity on the vibration characteristics of the FGM plates and found that the porosity noticeably affected the vibration response of a thin plate. Sometimes the porous FGMs can be very useful in biomaterial applications, such as bone replacements and dental implants [9].

The FGM structures like arches are frequently used in various engineering applications. Malekzadeh [10] scrutinized the vibration analysis of the FG thick arches under thermal environment condition. He found that the material properties dependent on temperature have a notable effect on the natural frequency. The in-plane thermomechanical vibrations of FGM circular beams using beam theory approach have been studied by Eroglu [11]. Filipich and Piovan [12] discussed the analytical solution for dynamics of the thick FGM curved beams using the power series method. They also implemented the neutral axis shifting concept to minimize the algebraic calculations. Lim et al. [13] scrutinized the free vibration response of functionally gradient arches under the thermal environment condition analytically, using state-space method.

It is carrying out from the literature that the thermos-elastic vibration analysis of the FGM porous circular arches has not been proclaimed to the best of authors' knowledge. So in this paper, the effect of porosity on frequency parameters of FGM arches under the thermal environment is analyzed. It is assumed that mechanical properties are temperature dependent and varying along with the thickness. To incorporate even and uneven porosity distributions in the formulation the modified power laws have been chosen. To obtain the final governing equation of the vibrations for the arch, a C^0 continuous finite element method has been used. The validation and convergence studies have been executed to establish the efficacy of the current finite element model. The effect of various influencing parameter, viz., porosity index (α), temperature change (ΔT), porosity distribution type, volume fraction index (n), and the thickness to length ratio (h/L) on the natural frequency of the arches have been investigated.

2 Theory and Formulation

Consider an FGM circular arch with the thickness h, length of the arch (along A-A') $L = R\theta_0$, and the mid-surface radius of the arch R as displayed in Fig. 1. The curvilinear coordinate axes (ξ, z) are used to obtain the present formulation, where $\xi = r\theta$ and $z = r - R$.

2.1 Power Law Distribution for Porous FGM Circular Arch

The circular arch made of porous FGM and having continuously varying mechanical properties along the thickness is considered. The bottom surface of FGM circular arch ($z = -h/2$) is metal-rich, while the top surface ($z = h/2$) is assumed to be ceramic-rich. In this paper, even and uneven distributions of the porosity throughout the thickness of FG circular arches have been considered. In the even distribution, the porosity disseminated uniformly over the cross section, whereas in uneven distribution, the porosity occurred frequently in the neighboring of the middle region of the cross section as displayed in Fig. 2.

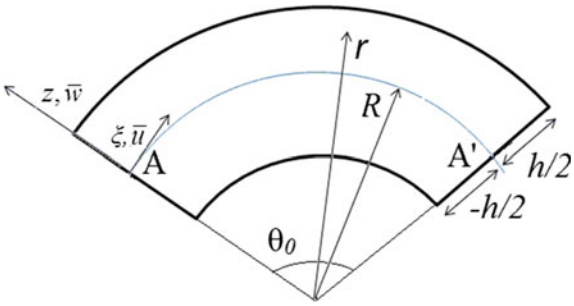

Fig. 1 The geometry and the coordinates of the FGM arch

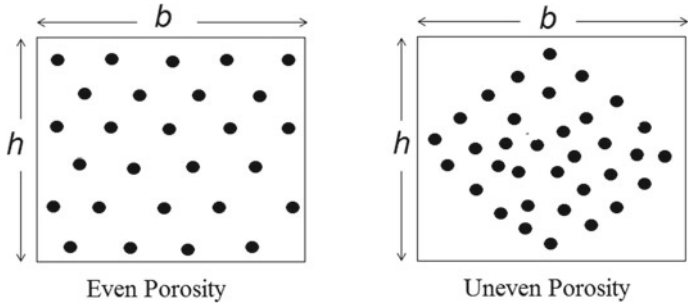

Fig. 2 Cross section of the FGM arch with the even and uneven porosity distributions

For the even distribution, the effective mechanical properties are obtained by a power law as

$$H(z) = (H_c - H_m)\left(0.5 + \frac{z}{h}\right)^n + H_m - \alpha(H_c + H_m) \tag{1}$$

The effective mechanical properties of the FGM circular arch for the uneven porosity distribution can be declared as in [7]:

$$H(z) = (H_c - H_m)\left(0.5 + \frac{z}{h}\right)^n + H_m - \frac{\alpha}{2}(H_c + H_m)\left(1 - \frac{2|z|}{h}\right) \tag{2}$$

Figure 3a, b shows the alteration of effective mechanical properties of porous FGM with *z/h* for the even and uneven porosity distributions. The effective property $E(z)$ is calculated for even (Eq. 1) and uneven (Eq. 2) porosity distributions of the FGM at $E_c = 390$ Gpa, $E_m = 214$ Gpa, and $\alpha = 0.1$. The effective elastic constant for the even porosity distribution at the porosity index ($\alpha = 0.1$) reduces throughout the thickness as shown in Fig. 3a. But for the uneven porosity distribution, the effective elastic constant reduces utmost at $z/h = 0$ as given in Fig. 3b, because, at the middle plane the porosity concentration is maximum. While in case of even distribution the pores are spread uniformly throughout the thickness.

Where α is the porosity index, H_c and H_m are the mechanical properties of the ceramics and metal, respectively. The mechanical properties of the FGM are considered as temperature dependent and declared as a function of temperature:

$$H = H_0(H_{-1}T^{-1} + 1 + H_1T + H_2T^2 + H_3T^3) \tag{3}$$

where H_{-1}, H_0, H_1, H_2, and H_3 are the temperature-dependent coefficients as given in Table 1 and T is the temperature [5, 6, 9, 10].

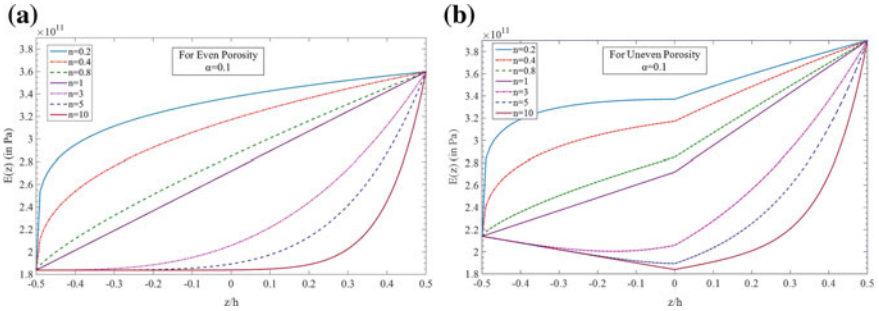

Fig. 3 The variation of the effective elastic modulus of porous FGM with *z/h* at $\alpha = 0.1$ for the various *n*; **a** even porosity **b** uneven porosity

Table 1 The coefficients of the temperature-dependent mechanical properties of the FGMs

Materials	Properties	H_0	H_{-1}	H_1	H_2	H_3
Si_3N_4 [7]	E (Pa)	348.43×10^9	0	-3.070×10^{-4}	2.160×10^{-7}	-8.946×10^{-11}
	α_{exp} (K^{-1})	5.8723×10^{-6}	0	9.095×10^{-4}	0	0
	ν	0.24	0	0	0	0
	ρ (kg/m^3)	2370	0	0	0	0
SUS304 [7]	E (Pa)	201.04×10^9	0	3.079×10^{-4}	-6.534×10^{-7}	0
	α_{exp} (K^{-1})	12.33×10^{-6}	0	8.086×10^{-4}	0	0
	ν	0.3262	0	-2.002×10^{-4}	3.797×10^{-7}	0
	ρ (kg/m^3)	8166	0	0	0	0
Ti–6Al–4V [10, 11]	E (Pa)	122.9×10^9	0	-4.605×10^{-4}	0	0
	α_{exp} (K^{-1})	$7.43e \times 10^{-6}$	0	7.483×10^{-4}	-3.621×10^{-7}	0
	ν	0.2888	0	1.108×10^{-4}	0	0
	ρ (kg/m^3)	4420	0	0	0	0
ZrO_2 [10, 11]	E (Pa)	132.2×10^9	0	-3.805×10^{-4}	-6.12×10^{-8}	0
	α_{exp} (K^{-1})	13.3×10^{-6}	0	-1.421×10^{-3}	9.549×10^{-7}	0
	ν	0.3330	0	0	0	0
	ρ (kg/m^3)	3657	0	0	0	0

2.2 *Kinematic Relations and Displacement Field*

Using the curvilinear coordinate axes (ξ, z) the displacement field is defined in the terms of midplane displacements and the higher-order rotation terms. By incorporation of the traction-free conditions on the top and the bottom surface of the arch and accommodating C^0 continuity the modified displacement field becomes

$$\begin{aligned} \bar{u}(\xi, z) &= u(\xi) + z\phi_\xi(\xi) - \frac{4z^3}{3h^2}\big(\phi_\xi(\xi) + \beta_\xi(\xi)\big) \\ \bar{w}(\xi, z) &= w(\xi) \end{aligned} \tag{4}$$

where $\beta_\xi = \frac{\partial w}{\partial \xi}$; The primary field variables are represented as

$$\{\Lambda\} = \left\{u, w, \phi_\xi, \beta_\xi\right\} \tag{5}$$

The compressed or matrix form representation of the displacement as

$$\begin{Bmatrix} \bar{u}(\xi, z, t) \\ \bar{w}(\xi, z, t) \end{Bmatrix} = \left\{\bar{U}\right\} = \left[\bar{N}\right]\{\Lambda\}, \quad \text{where } \bar{N} = \begin{bmatrix} 1 & 0 & (z - 4z^3/3h^2) & -4z^3/3h^2 \\ 0 & 1 & 0 & 0 \end{bmatrix} \tag{6}$$

The strain terms for the circular arch are linearly defined as [14, 15]

$$\begin{aligned} \varepsilon_{\xi\xi} &= \frac{1}{(1 + z/R)}\left(\frac{\partial \bar{u}}{\partial \xi} + \frac{\bar{w}}{R}\right) \\ \gamma_{\xi z} &= \frac{1}{(1 + z/R)}\left(\frac{\partial \bar{w}}{\partial \xi} - \frac{\bar{u}}{R}\right) + \frac{\partial \bar{u}}{\partial z} \end{aligned} \tag{7}$$

The strain vector is given as

$$\{\varepsilon\} = \begin{Bmatrix} \varepsilon_{\xi\xi} \\ \gamma_{\xi z} \end{Bmatrix} \tag{8}$$

The linear stress–strain relations of the FGM circular arch under thermal environment conditions are defined as

$$\begin{Bmatrix} \sigma_{\xi\xi} \\ \tau_{\xi z} \end{Bmatrix} = \begin{bmatrix} \mathbb{Q}_{11} & 0 \\ 0 & \mathbb{Q}_{55} \end{bmatrix}\left(\begin{Bmatrix} \varepsilon_{\xi\xi} \\ \gamma_{\xi z} \end{Bmatrix} - \begin{Bmatrix} \delta \\ 0 \end{Bmatrix}\Delta T\right) \tag{9}$$

where $\mathbb{Q}_{ij}$ and δ are the material elastic coefficients and thermal expansion coefficient, respectively. ΔT is a change in the temperature.

2.3 Finite Element Methodology

A C^0 continuous finite element formulation is applied with 2 noded elements and 4 dof at each node. The generalized displacement and strain vectors are expressed as

$$\{\Lambda\} = [N]\{\Lambda\}^e \quad \text{and } \{\varepsilon\} = [B]\{\Lambda\}^e \tag{10}$$

The strain energy and the kinetic energy of the FGM circular arch are given as

$$U_s = \frac{1}{2}\int_V \{\varepsilon\}^T\{\sigma\}\mathrm{d}V = \frac{1}{2}b\int_0^L \left\{\Lambda^e\right\}^T[B]^T[D][B]\left\{\Lambda^e\right\}\mathrm{d}\xi$$

$$= \frac{1}{2}\{\Lambda^e\}^T[K^e]\{\Lambda^e\} \tag{11}$$

$$T_k = \frac{1}{2}\int_V \rho\left\{\dot{\bar{U}}\right\}^T\left\{\dot{\bar{U}}\right\}\mathrm{d}V = \frac{1}{2}b\int_0^L \rho\{\dot{\Lambda}\}^{eT}[N]^T[N]\{\dot{\Lambda}\}^e\mathrm{d}\xi$$

$$= \frac{1}{2}\{\dot{\Lambda}\}^{eT}[M]\{\dot{\Lambda}\}^e \tag{12}$$

The variational principle can be used to derive the governing equation for the free vibration of the FGM circular arch, which is a generalized principle of virtual displacement. The equilibrium equation for free vibration analysis can be obtained as

$$[M]\{\ddot{\Lambda}\} + [K]\{\Lambda\} = 0 \tag{13}$$

or

$$[K]\{\Lambda\} = \lambda[M]\{\Lambda\} \tag{14}$$

where λ is the eigenvalue, which can be obtained by incorporating the end conditions of the arch.

3 Numerical Results

To determine the efficacy and precision of the present finite element model, convergence and validation studies are carried out. The validation is performed for free vibration analysis of straight FGM beam with even and uneven porosity distributions. The simply supported (S-S) straight beam made of FGM (SUS304/Si_3N_4) is considered whose mechanical properties are assumed to be temperature dependent and are given in Table 1. The frequency parameters of the FGM straight beam are evaluated at $\Delta T = 20\,\mathrm{K}$ and also compared with those results presented by Ebrahimi and Jafari [7]. It is seen from Table 2 that the present results are in reasonable agreement with those results presented by Ebrahimi and Jafari [7].

Table 3 shows the first three frequency parameters of the FGM circular arch for the $h/L = 0.2$ are compared with those results given by Malekzadeh [10] and Eroglu [11]. The mechanical properties of FGM (Ti–6Al–4V/ZrO_2) are considered as temperature dependent as provided in Table 1. The frequency parameters of FGM circular arch have been obtained for clamped–clamped boundary conditions with temperature change $\Delta T = 400$ K, $\theta_0 = 60°$, and $n = 2$. It is noticeable that the current results are in the excellent agreement with those results presented by Eroglu [11] and Malekzadeh [10]. It is also evident from this study that performance and rate of convergence of the present model are very good in terms of solution accuracy.

Table 2 Comparison of the frequency parameters $\bar{\lambda}$ of S-S FGM straight beam with the porosity at $L/h = 20$ and $\Delta T = 20$K

n		Even porosity			Uneven porosity		
		$\alpha = 0$	$\alpha = 0.1$	$\alpha = 0.2$	$\alpha = 0$	$\alpha = 0.1$	$\alpha = 0.2$
0	Present	6.38672	6.94562	7.84147	6.38672	6.70292	7.0885
	Ref. [7]	6.30389	6.88939	7.82479	6.30389	6.64111	7.04845
0.5	Present	4.41545	4.48376	4.57254	4.41545	4.50182	4.59810
	Ref. [7]	4.27875	4.36908	4.47876	4.27875	4.38047	4.49154
1	Present	3.88201	3.88076	3.87884	3.88201	3.93159	3.98587
	Ref. [7]	3.72764	3.74463	3.75865	3.72764	3.79112	3.85843
2	Present	3.49029	3.45061	3.40190	3.49029	3.51835	3.54861
	Ref. [7]	3.33104	3.30844	3.27411	3.33104	3.37261	3.41549
5	Present	3.16545	3.10088	3.02325	3.16545	3.17928	3.19398
	Ref. [7]	3.01417	2.96886	2.90872	3.01417	3.04242	3.0708

Table 3 Comparison and convergence study of the frequency parameter $\bar{\lambda}$ of the FGM circular arch at $n = 2$, $h/L = 0.2$ and $\Delta T = 400$ K with the C-C boundary condition

No of elements	$\bar{\lambda}_1$	$\bar{\lambda}_2$	$\bar{\lambda}_3$
5	5.8553	10.4816	13.5889
10	5.2831	9.0384	12.7836
20	5.1324	8.6054	12.6305
30	5.1041	8.5229	12.6034
40	5.0942	8.4938	12.5940
50	5.0896	8.4803	12.5897
Ref. [10]	5.069 (0.406%)	8.401 (0.943%)	12.606 (−0.129%)
Ref. [11]	5.064 (0.505%)	8.299 (2.184%)	12.652 (−0.492%)

The dimensionless frequency parameter is defined as $\bar{\lambda} = \lambda L^2/h\sqrt{\rho_m/E_m}$, where $L = R\theta$.

Table 4 displays the frequency parameter of the FGM (Ti–6Al–4V/ZrO_2) porous circular arch for different values of h/L ($h/L = 0.2, 0.1, 0.05$), gradient indices ($n = 0, 1, 2, 5$), porosity indices ($\alpha = 0, 0.1, 0.2$) for both even and uneven distributions at ΔT = 400 K and $\theta_0 = 60°$. On observing Table 4, it is concluded that the frequency parameter ($\bar{\lambda}$) reduces with the increase in the value of n. This is because of the metallic content in FGM increases with an increase in the value of n, consequently stiffness decreases and hence frequency decreases. In case of even distribution of porosity, on increasing the value of α, the frequency parameter increases up to $n < 1$ but decreases after $n \geq 1$. In case of uneven distribution of porosity the frequency parameter ever increases with increasing in α. This is due to the modulus term in the expression for the uneven distribution of porosity. The influence of thickness to

Table 4 Influence of porosity on the frequency parameter of the fully clamped FG circular arch with the volume fraction indices (n) at $\Delta T = 400$ K, and $\theta_0 = 60°$

h/L	*n*	Even porosity			Uneven porosity		
		$\alpha = 0$	$\alpha = 0.1$	$\alpha = 0.2$	$\alpha = 0$	$\alpha = 0.1$	$\alpha = 0.2$
0.2	0	5.6522	5.7033	5.7681	5.6522	5.7006	5.7536
	1	5.2119	5. 2108	5.2091	5.2119	5.2356	5.2609
	2	5.0896	5.0752	5.0570	5.0896	5.1067	5.1245
	5	4.9740	4.9476	4.9147	4.9740	4.9850	4.9961
0.1	0	8.7536	8.8330	8.9335	8.7536	8.8215	8.8965
	1	8.0799	8.0793	8.0781	8.0799	8.1096	8.1418
	2	7.8869	7.8653	7.8382	7.8869	7.9063	7.9272
	5	7.7030	7.6624	7.6118	7.7030	7.7131	7.7236
0.05	0	14.0980	14.2256	14.3873	14.0980	14.3027	14.5276
	1	13.0111	13.0092	13.0061	13.0111	13.1518	13.3045
	2	12.7284	12.6958	12.6546	12.7284	12.8528	12.9873
	5	12.4553	12.3948	12.3192	12.4553	12.5649	12.6829

length ratio (*h/L*) is noticed that the frequency parameter increases with a decrease in the value of *h/L*.

Table 5 presents the dimensionless frequency parameter of the porous FGM (Ti–6Al–4V/ZrO_2) circular arch. In this table, the effect of temperature rise on the frequency parameter of the porous circular arch with the porosity is studied. The frequency parameter ($\bar{\lambda}$) of the FGM porous circular arch have been determined for the various values of the porosity index ($\alpha = 0, 0.1, 0.2$) and volume fraction index ($n = 0, 1, 2, 5$) at $\Delta T = 0, 100, 200, 300$ K, h/L $= 0.2$ and $\theta_0 = 60°$ for the both even and uneven distributions of porosity as given in Table 5. It is noticed that for the both even and uneven distributions of porosity, the frequency parameters start declining with the rise in the temperature. This is because of the value of elastic moduli reduces with rising in the temperature.

4 Conclusions

A C^0 finite element method has been adopted to scrutinize the frequency response of the porous FGM circular arch with clamped–clamped boundary conditions in the thermal environment. The effect of porosity (microstructural defects) on the free vibrations of the FGM circular arch is examined. It is concluded that the frequency parameters reduce with the rise in the temperature for both even and uneven porosity distributions. The frequency parameters reduce with the increase in the volume fraction index. It is also observed that the frequency parameters always increase by decreasing the value of thickness to length ratio.

Table 5 The change in the frequency parameter of the C–C FGM circular arch with distinct values of n, α, and ΔT, at $\theta_0 = 60°$, and $h/L = 0.2$

ΔT (K)	n	Even porosity			Uneven porosity		
		$\alpha = 0$	$\alpha = 0.1$	$\alpha = 0.2$	$\alpha = 0$	$\alpha = 0.1$	$\alpha = 0.2$
0	0	6.3288	6.3826	6.4510	6.3288	6.3817	6.4396
	1	5.8625	5.8607	5.8584	5.8625	5.8890	5.9172
	2	5.7322	5.7162	5.6963	5.7322	5.7515	5.7717
	5	5.6089	5.5801	5.5445	5.6089	5.6217	5.6347
100	0	6.1727	6.2263	6.2943	6.1727	6.2247	6.2817
	1	5.7095	5.7078	5.7056	5.7095	5.7353	5.7628
	2	5.5802	5.5645	5.5449	5.5802	5.5989	5.6186
	5	5.4580	5.4296	5.3944	5.4580	5.4703	5.4828
200	0	6.0086	6.0616	6.1289	6.0086	6.0596	6.1154
	1	5.5505	5.5489	5.5469	5.5505	5.5756	5.6024
	2	5.4228	5.4075	5.3882	5.4228	5.4410	5.4600
	5	5.3022	5.2743	5.2397	5.3022	5.3140	5.3260
300	0	5.8354	5.8877	5.9539	5.8354	5.8852	5.9397
	1	5.3848	5.3835	5.3816	5.3848	5.4093	5.4353
	2	5.2595	5.2445	5.2258	5.2595	5.2771	5.2955
	5	5.1410	5.1138	5.0800	5.1410	5.1524	5.1639

Acknowledgements The authors would like to acknowledge the financial support provided by the Science and Engineering Research Board, Department of Science and Technology (**SERB-DST**), Government of India to carry out this research. Project number-**YSS/2015/001290**, Dated-**09th NOV 2015**.

References

1. Gupta A, Talha M, Singh BN (2016) Vibration characteristics of functionally graded material plate with various boundary constraints using higher order shear deformation theory. Compos Part B: Eng 94:64–74
2. Gupta A, Talha M, Singh BN (2017) Large amplitude free flexural vibration analysis of finite element modeled FGM plates using new hyperbolic shear and normal deformation theory. Aerosp Sci Technol 67:287–308
3. Amir M, Talha M (2018) Thermoelastic vibration of shear deformable functionally graded curved beams with microstructural defects. Int J Struct Stab Dyn 18:1850135 (24 pp)
4. Zhu J, Lai Z, Yin Z, Jeon J, Lee S (2001) Fabrication of ZrO_2–NiCr functionally graded material by powder metallurgy. Mater Chem Phys 68:130–135
5. Gupta A, Talha M (2015) Recent development in modeling and analysis of functionally graded materials and structures. Prog Aerosp Sci 79:1–14
6. Ebrahimi F, Ghasemi F, Salari Er (2016) Investigating thermal effects on vibration behavior of temperature-dependent compositionally graded Euler beams with porosities. Meccanica 51:223–249

7. Ebrahimi F, Jafari A (2016) A higher-order thermomechanical vibration analysis of temperature-dependent FGM beams with porosities. J Eng 2016:1–20
8. Gupta A, Talha M (2018) Influence of porosity on the flexural and free vibration responses of functionally graded plates in thermal environment. Int J Struct Stab Dyn 18(1):1850013 (31 pp)
9. Ebrahimi F, Mokhtari M (2015) Transverse vibration analysis of rotating porous beam with functionally graded microstructure using the differential transform method. J Braz Soc Mech Sci Eng 37:1435–1444
10. Malekzadeh P (2009) Two-dimensional in-plane free vibrations of functionally graded circular arches with temperature-dependent properties. Compos Struct 91:38–47
11. Eroglu U (2015) In-plane free vibrations of circular beams made of functionally graded material in thermal environment: beam theory approach. Compos Struct 122:217–228
12. Filipich CP, Piovan MT (2010) The dynamics of thick curved beams constructed with functionally graded materials. Mech Res Commun 37:565–570
13. Lim CW, Yang Q, Lü CF, Xu R (2009) Two-dimensional elasticity solutions for temperature-dependent in-plane vibration of FGM circular arches. Compos Struct 90(3):323–390
14. Su Z, Jin G, Ye T (2016) Vibration analysis and transient response of a functionally graded piezoelectric curved beam with general boundary conditions. Smart Mater Struct 25(6):065003 (14 pp)
15. Qatu MS (2004). Vibration of laminated shells and plates. Elsevier, Amsterdam, pp 82–88

Vibration Response of Shear Deformable Gradient Plate with Geometric Imperfection

Ankit Gupta and Mohammad Talha

Abstract The vibration analysis of the geometrically imperfect functionally gradient (FGM) plate has been performed using hybrid higher order deformation theory. The present theory contains the nonlinear variation of thickness coordinate in in-plane and transverse displacement. The equation of motion for FGM plates are obtained through variational principle. The solution has been performed using a finite element method by employing C^0 continuous isoparametric formulation with 72 DOF/element. The parametric study has been done to examine the influence of geometric configurations, volume fraction index and various modes of geometric imperfection on the vibration characteristics of the FGM plate.

Keywords Geometric imperfection · Vibration · Thickness stretching effect · Functionally graded plate

1 Introduction

Functionally gradient materials (FGMs) are advanced materials having the progressive variation of their constituent materials along the predetermined direction [1]. Since the past three decades, these materials have proven their worth in numerous applications such as aerospace, civil, biomechanical, and mechanical industries [2]. The ability to retain the structural integrity under extreme thermal–mechanical loading makes theses material suitable for structural application as well.

Considerable investigations have been perpetrated to inspect the vibrational attributes of gradient structures. Early research efforts for dynamic analysis of FGM plate have been presented by Praveen and Reddy [3] in which nonlinear time-dependent thermoelastic examination of FGM plate has been studied using a finite

A. Gupta (✉)
School of Engineering, Shiv Nadar University, Noida, UP, India
e-mail: ankit.gupta1@snu.edu.in

M. Talha
School of Engineering, I.I.T Mandi, Mandi, India
e-mail: talha@iitmandi.ac.in

B. N. Singh et al. (eds.), *Recent Advances in Theoretical, Applied, Computational and Experimental Mechanics*, Lecture Notes in Mechanical Engineering,
https://doi.org/10.1007/978-981-15-1189-9_17

element method. The buckling and vibration response of the FGM polygonal plate using TSDT has been studied by Cheng and Batra [4]. Ferreira et al. [5] employed FSDT and TSDT with the global collocation method to examine the vibration behavior of gradient plates. Neves et al. [6] explored the structural characteristics of sandwich gradient plates using a meshless technique and HSDT. Talha and Singh [7] employed a modified displacement field with thirteen DOFs/node to demonstrate the displacement and vibration attributes of a gradient plate. Gupta and Talha [8, 9] developed non-polynomial HOSNT to analyze the flexural and vibration response of the gradient plate.

In this article, the vibration behavior of the gradient plate with initial geometric imperfection has been investigated using non-polynomial HOSNT. The effective material properties of the gradient plate have been computed using sigmoid rule. Initial geometric imperfection in the plate has been incorporated using a generic function that is capable to model various imperfection modes such as sine, global, and local. Comparative studies are provided to illustrate the correctness of the present formulation.

2 Mathematical Idealization

2.1 Problem Formulation

In the present study, a gradient plate with a cross section ($a \times b \times h$) is considered for the vibration analysis as shown in Fig. 1.

2.2 Displacement Model

A hybrid HOSNT developed by the authors [10] is used in this study for the vibration analysis of the gradient plate.

$$\begin{aligned} U &= u - z\left[A_x + \left(\frac{\Phi \mathrm{H}}{h}\right)B_x\right] + \mathrm{N}\sinh^{-1}\left(\frac{\Phi z}{h}\right)B_x \\ V &= v - z\left[A_y + \left(\frac{\Phi \mathrm{H}}{h}\right)B_y\right] + \mathrm{N}\sinh^{-1}\left(\frac{\Phi z}{h}\right)B_y \\ W &= w + \Phi\cosh^2\left(\frac{\Phi z}{h}\right)B_z \end{aligned} \tag{1}$$

where $\mathrm{H} = -\frac{h\cosh^2(\Phi/2)}{\sqrt{\left(1+\Phi^2/4\right)^{-1}-1}}$, and the value of the shape parameter "κ" is 3.4. The associated field variables are

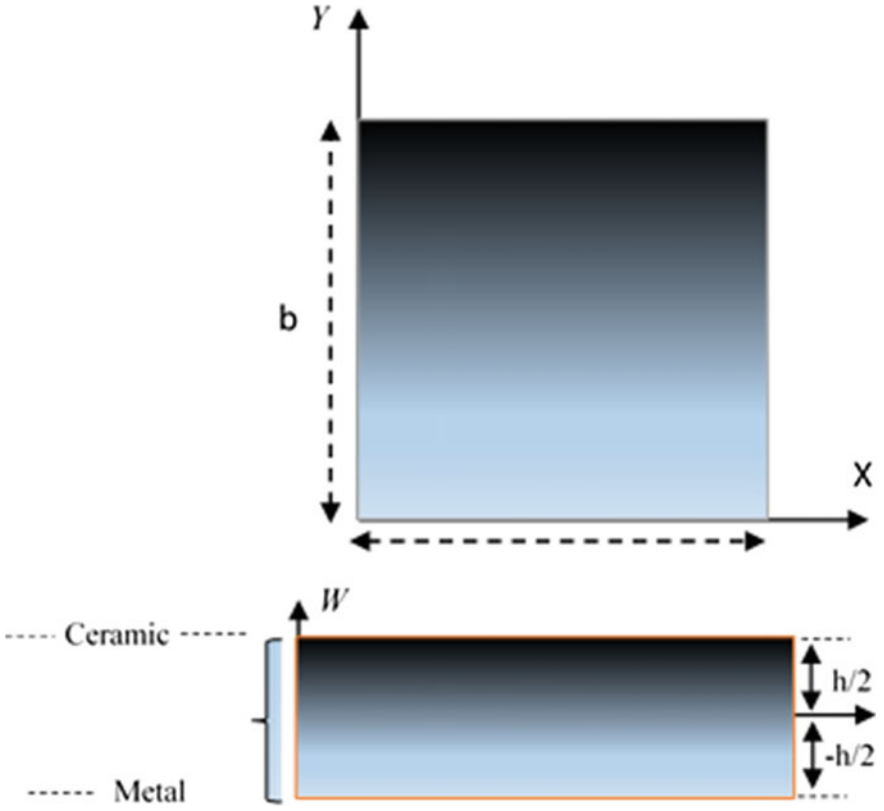

Fig. 1 Pictorial representation of gradient plate

$$\{\Re\} = \left\{ u \; v \; w \; A_x \; A_y \; B_x \; B_y \; B_z \right\}^T. \tag{2}$$

The expression for strains developed can be given as

$$\begin{aligned} &\varepsilon_{xx} = \partial U/\partial x; \varepsilon_{yy} = \partial V/\partial y; \varepsilon_{zz} = \partial W/\partial z \\ &\gamma_{xy} = \partial U/\partial x + \partial V/\partial y; \gamma_{xz} = \partial U/\partial z + \partial W/\partial x; \gamma_{yz} = \partial V/\partial z + \partial W/\partial y \end{aligned} \tag{3}$$

The Stress–Strain relations of the gradient plate is written as [11]:

$$\{\sigma\}_{6x1} = Q_{ij}\{\varepsilon\}_{6x1} \tag{4}$$

$$\begin{Bmatrix} \sigma_{xx} \\ \sigma_{yy} \\ \sigma_{zz} \\ \sigma_{xy} \\ \sigma_{yz} \\ \sigma_{xz} \end{Bmatrix} = \begin{bmatrix} Q_{11} & Q_{12} & Q_{13} & 0 & 0 & 0 \\ Q_{21} & Q_{22} & Q_{23} & 0 & 0 & 0 \\ Q_{31} & Q_{32} & Q_{33} & 0 & 0 & 0 \\ 0 & 0 & 0 & Q_{44} & 0 & 0 \\ 0 & 0 & 0 & 0 & Q_{55} & 0 \\ 0 & 0 & 0 & 0 & 0 & Q_{66} \end{bmatrix} \begin{Bmatrix} \varepsilon_{xx} \\ \varepsilon_{yy} \\ \varepsilon_{zz} \\ \varepsilon_{xy} \\ \varepsilon_{yz} \\ \varepsilon_{xz} \end{Bmatrix}$$

$$Q_{11} = Q_{22} = Q_{33} = \frac{E(z)\left(1-\upsilon^2\right)}{1-2\upsilon^2-2\upsilon^3}$$

$$Q_{12} = Q_{21} = Q_{13} = Q_{31} = Q_{23} = Q_{32} = \frac{E(z)\upsilon(1+\upsilon)}{1-2\upsilon^2-2\upsilon^3}$$

$$Q_{44} = Q_{55} = Q_{66} = \frac{E(z)}{2(1+\upsilon)}$$

2.3 Various Material Properties of Gradient Material

In this study, the Sigmoid law has been employed to compute the effective Young's modulus and density of the gradient plate and is written as

$$\left\{Vol^1_{fr}(z)\right\} = 1 - 0.5(1 - 2z/\mathrm{t})^n$$
$$\left\{Vol^2_{fr}(z)\right\} = 0.5(1 + 2z/\mathrm{t})^n$$

Employing the rule of mixture, the effective Young's modulus and density of the gradient material can be computed by

$$\begin{Bmatrix} \mathrm{E}(z) \\ \rho(z) \end{Bmatrix} = \begin{Bmatrix} \mathrm{E}_c \\ \rho_c \end{Bmatrix} Vol^1_{fr}(z) + \begin{Bmatrix} \mathrm{E}_m \\ \rho_m \end{Bmatrix}\left(1 - Vol^1_{fr}(z)\right) \quad \text{for } 0 \le z \le t/2$$

$$\begin{Bmatrix} \mathrm{E}(z) \\ \rho(z) \end{Bmatrix} = \begin{Bmatrix} \mathrm{E}_c \\ \rho_c \end{Bmatrix} Vol^2_{fr}(z) + \begin{Bmatrix} \mathrm{E}_m \\ \rho_m \end{Bmatrix}\left(1 - Vol^2_{fr}(z)\right) \quad \text{for } -t/2 \le z < 0$$

2.4 Characteristics Equation

The characteristics equation for the Eigenvalue problem is given as

$$[K]\{\Lambda\} = \lambda[M]\{\Lambda\} \tag{5}$$

with $\lambda = \omega^2$, where is the frequency of vibrated plate.

3 Results and Discussion

In this section, first validation examination has been accomplished to exhibit the exactness of the present solution, then after some new results have been shown for geometrically imperfect FGM plate. The Young's modulus and density of metal (Ti–6AL–4V) is $E_m = 105.7 \times 10^9$ Pa and $\rho_m = 4429$ kg/m^3 and for ceramic (Si_3N_4) is $E_c = 322.27 \times 10^9$ Pa and $\rho_m = 2370$ kg/m^3, respectively. The generic imperfection function is employed to generate various geometric imperfection models as shown in Eq. (6) [12].

$$\bar{\zeta} = h\varsigma \cos\left[\beta_1\pi\left(\frac{x}{a} - \chi_1\right)\right] / \cosh\left[\alpha_1\left(\frac{x}{a} - \chi_1\right)\right] \times \cos\left[\beta_2\pi\left(\frac{y}{b} - \chi_2\right) / \cosh\left[\alpha_2\left(\frac{x}{b} - \chi_2\right)\right]\right] \quad (6)$$

where "ς" is the Imperfection parameter. Various modes of imperfection can be obtained using different parameters as presented in Fig. 2 and Table 1.

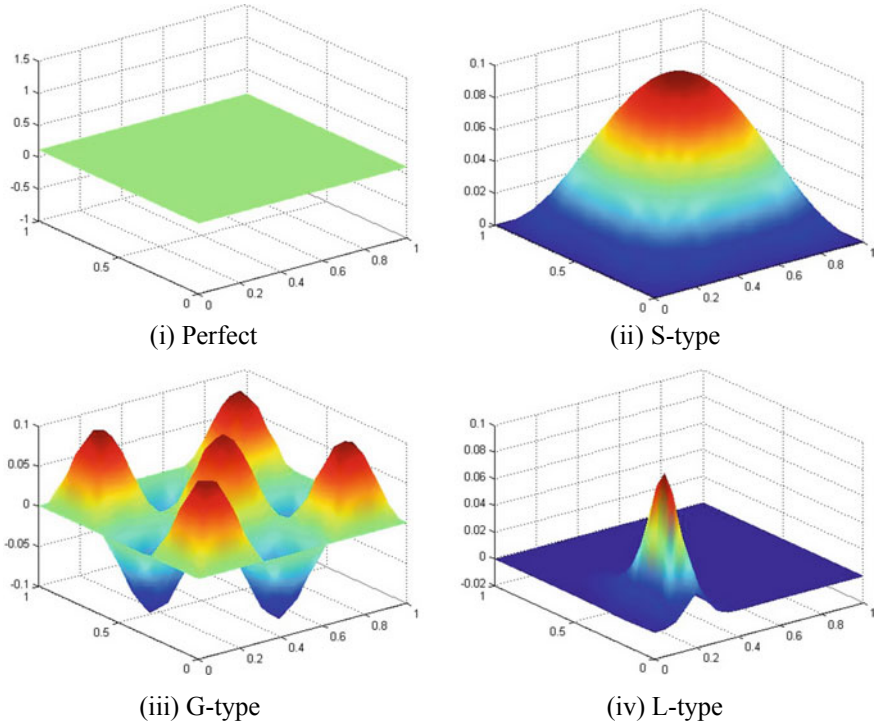

Fig. 2 Modes of geometric imperfection

Table 1 Geometric imperfection models

Type	α_2	α_2	β_1	β_2	χ_1	χ_2
Perfect plate	0	0	0	0	0	0
Sine-type	0	0	1	1	0.5	0.5
Global-type	0	0	1	1	0.5	0.5
Local-type	20	10	3	1	0.2	0.2

Table 2 Validation of frequency parameter of (SSSS) Al/ZrO_2 gradient plate

Mesh size	n				
	0	0.25	1	5	100
2×2	0.0941	0.0912	0.0874	0.0876	0.0823
3×3	0.0939	0.0911	0.0873	0.0873	0.0821
4×4	0.0922	0.0893	0.0856	0.0859	0.0806
5×5	0.0915	0.0886	0.0849	0.0854	0.0801
6×6	0.0914	0.0885	0.0848	0.0852	0.0799
Akavci [13]	0.09203	0.08895	0.08489	0.08576	0.0790

3.1 Validation Analysis

Example 1 To verify the authenticity of the present method, an Al/ZrO_2 gradient plate has been considered in this example. The calculated results are compared with the referred results given by Akavci [13]. The nondimensional frequency is assumed as $\left(\bar{\omega} = \omega h\sqrt{(\rho_c/\pi E_c)}\right)$. Akavci [13] used non-polynomial HSDT to perform the vibration analysis of FGM plate. Table 2 presents the comparative study of the frequency of SSSS gradient plate. The results reflect the reasonable agreement with the referred results.

3.2 Numerical Study

3.2.1 Influence of Geometric Imperfection and Geometric Configurations

Tables 3 and 4 present the nondimensional frequency of Ti–6Al–4V/Si_3N_4 gradient plate having different *a/h* and geometric imperfection with simply supported and fully fixed boundary constraints. The "*n*" and *b/a* is considered as 1. It is noticed that the frequency parameter increases with *a/h* ratio. It is also observed that the G-type imperfection has a noteworthy influence on the frequency of the gradient plate, whereas the influence of L-type imperfection is least. The maximum change between

Table 3 Change in frequency of (SSSS) gradient plate with *a/h* and geometric imperfection ($n = 1$, $b/a = 1$)

Modes	*a/h*				
	5	10	20	50	100
Perfect	1.0308	1.2046	1.2420	1.2561	1.2587
Sine-type	1.0221	1.2424	1.2697	1.2803	1.2824
% difference*	0.8440	3.1380	2.2303	1.9266	1.8829
Global-type	1.0094	2.0394	2.6731	2.5640	2.5442
% difference	2.0760	69.301	115.225	104.124	102.129
Local-type	1.0259	1.2051	1.2472	1.5283	1.7239
% difference	0.4754	0.0415	0.4187	21.6702	36.9588

*$\%\ difference = 100 * (Perfect\ plate\ frequency - Im\ perfect\ plate\ frequency / Perfect\ plate\ frequency)$

Table 4 Change in frequency of (CCCC) gradient plate with *a/h* and geometric imperfection ($n = 1$, $b/a = 1$)

Modes	*a/h*				
	5	10	20	50	100
Perfect	1.7039	2.1089	2.2920	2.3947	2.4199
Sine-type	1.7409	2.1381	2.3102	2.4088	2.4333
% difference	2.1715	1.3846	0.7941	0.5888	0.5537
Global-type	1.8577	3.3921	3.4341	3.3444	3.3330
% difference	9.0264	60.8469	49.8298	39.6584	37.7330
Local-type	1.7230	2.1094	2.2952	2.5619	3.3570
% difference	1.1210	0.0237	0.1396	6.9821	38.7247

the results obtained from the perfect plate and the imperfect plate is 3.1380, 102.129 and 36% for S-type, G–type and L-type imperfection, respectively, for CCCC boundary condition. It is noteworthy that the influence of imperfection is more in thin plates. The consistent behavior is observed for SSSS boundary constraint as shown in Table 4.

Tables 5 and 6 depict the change of frequency of gradient plate with *b/a* and geometric imperfection for SSSS and CCCC boundary constraints, respectively. It is found that the nondimensional frequency increases with *b/a*. Again the same observation is perceived as outlined in the previous discussion that G-type imperfection has a substantial impact on the frequency. It is also evident that the change in nondimensional frequency is more in the case of a rectangular plate compared to the square plate.

Table 5 Change in nondimensional frequency of (CCCC) gradient plate with *b/a* and geometric imperfection ($n = 1$, a/$h = 10$)

Modes	*b/a*				
	1	1.5	2	2.5	3
Perfect	2.1089	2.4278	2.9625	3.5697	4.2066
Sine-type	2.1381	2.4785	3.0322	3.6574	4.3118
% difference	1.3846	2.0883	2.3527	2.4568	2.5008
Global-type	3.3921	4.2595	5.1168	5.9837	6.8742
% difference	60.8469	75.4469	72.7190	67.6247	63.4146
Local-type	2.1094	2.4287	2.9637	3.5712	4.2084
% difference	0.0237	0.0371	0.0405	0.0420	0.0428

Table 6 Change in nondimensional frequency of (SSSS) FGM plate with *b/a* and geometric imperfection ($n = 1$, a/$h = 10$)

Modes	*b/a*				
	1	1.5	2	2.5	3
Perfect	1.2046	1.3192	1.5289	1.7777	2.0460
Sine-type	1.2424	1.3896	1.6320	1.9128	2.2126
% difference	3.1380	5.3366	6.7434	7.5997	8.1427
Global-type	2.0394	2.9937	3.8567	4.1483	4.1438
% difference	69.3010	126.9330	152.2533	133.3521	102.5318
Local-type	1.2051	1.3203	1.5306	1.7800	2.0489
% difference	0.0415	0.0834	0.1112	0.1294	0.1417

3.2.2 Influence of Geometric Imperfection and "n"

The change in frequency with "*n*" and geometric imperfection with fully fixed and simply supported boundary constraints is given in Table 7 and 8. It is clear that the frequency decreases as "*n*" increases. This is because that as "*n*" increases, the metallic fraction in the gradient plate increases, therefore the stiffness decreases. It is noteworthy that the effect of imperfection is more in gradient plate having more metallic contents.

3.2.3 Effect of Geometric Imperfection and Boundary Constraints

The consequence of the presence of geometric imperfections and various boundary constraints on the frequency of the gradient plate is given in Table 9. It is clear that the fewer constraints imposed on the boundary leads in a decrement in the frequency. It is obvious because less constraint at the boundary of the plate results in the decrement

Table 7 Variation of frequency of (CCCC) gradient plate with "*n*" and geometric imperfection ($b/a = 1$, $a/h = 10$)

Modes	"*n*"					
	0	1	2	5	10	100
Perfect	2.1916	2.1089	2.0606	2.0181	2.0053	1.9992
Sine-type	2.2217	2.1381	2.0895	2.0467	2.0338	2.0277
% difference	1.3734	1.3846	1.4025	1.4172	1.4212	1.4256
Global-type	3.6804	3.3921	3.2877	3.2074	3.1847	3.1742
% difference	67.9321	60.8469	59.5506	58.9317	58.8141	58.7735
Local-type	2.1921	2.1094	2.0611	2.0186	2.0058	1.9997
% difference	0.0228	0.0237	0.0243	0.0248	0.0249	0.0250

Table 8 Variation of frequency of (SSSS) gradient plate with "*n*" and geometric imperfection ($b/a = 1$, $a/h = 10$)

Modes	"*n*"					
	0	1	2	5	10	100
Perfect	1.2571	1.2046	1.1738	1.1467	1.1385	1.1345
Sine-type	1.2951	1.2424	1.2117	1.1846	1.1764	1.1725
% difference	3.0228	3.1379	3.2288	3.3051	3.3289	3.3494
Global-type	2.1332	2.0394	2.0138	1.9954	1.9906	1.9885
% difference	69.6921	69.301	71.5624	74.0124	74.8441	75.2755
Local-type	1.2576	1.2051	1.1744	1.1472	1.1390	1.1351
% difference	0.0397	0.0415	0.0511	0.0436	0.0439	0.0528

in the stiffness. It is notable that the impact of imperfection is maximum in the case of FFFF whereas least in CCCC boundary constraint.

4 Conclusions

In this article, the vibration behavior of the geometrically imperfect gradient plate has been investigated using hybrid HOSNT. It is concluded that the geometric imperfection has a prominent effect on thin plates. The L-type and G-type imperfection have minimum and maximum effect on the frequency parameter of the FGM plate. It is also concluded that the influence of geometric imperfection decreases as the constraint at the boundaries of the gradient plate increases.

Table 9 Change in nondimensional frequency of gradient plate with various boundary constraints and geometric imperfection ($b/a = 1$, $a/h = 10$)

Model	n	Boundary conditions				
		CCCC	CFCF	SSSS	CFSF	FFFF
Perfect	0	2.1916	1.3983	1.2571	0.9784	0.8806
	5	2.0181	1.2835	1.1467	0.8928	0.8007
	10	2.0053	1.2750	1.1385	0.8865	0.7950
Sine-type	0	2.2217	1.4214	1.2951	1.0673	0.1930
	% difference	1.3734	1.6520	3.0228	9.0862	78.0831
	5	2.0467	1.3060	1.1846	0.9764	0.1922
	% difference	1.4171	1.7530	3.3051	9.3638	75.9960
	10	2.0338	1.2975	1.1764	0.9697	0.1921
	% difference	1.42123	1.76471	3.32894	9.38522	75.8364
Global-type	0	3.6804	2.5870	2.1332	1.7695	1.9474
	% difference	67.9321	85.0104	69.6921	80.8565	121.145
	5	3.2074	2.3013	1.9954	1.6683	1.8548
	% difference	58.9317	79.2988	74.0124	86.8616	131.647
	10	3.1847	2.2852	1.9906	1.6654	1.8483
	% difference	58.8141	79.2314	74.8441	87.8624	132.491
Local-type	0	2.1921	1.3988	1.2576	0.9874	0.0254
	% difference	0.02281	0.03576	0.03977	0.91987	97.1156
	5	2.0186	1.2839	1.1472	0.9011	0.0253
	% difference	0.0247	0.0311	0.0436	0.9296	96.8402
	10	2.0058	1.2754	1.1390	0.8947	0.0253
	% difference	0.0249	0.0313	0.0439	0.9249	96.8176

References

1. Koizumi M (1997) FGM activities in Japan. Compos Part B Eng 28:1–4
2. Gupta A, Talha M (2015) Recent development in modeling and analysis of functionally graded materials and structures. Prog Aerosp Sci 79:1–14
3. Praveen GN, Reddy JN (1998) Nonlinear transient thermoelastic analysis of functionally graded ceramic-metal plates. Int J Solids Struct 35:4457–4476
4. Cheng Z-Q, Batra RC (2000) Exact correspondence between eigenvalues of membranes and functionally graded simply supported polygonal plates. J Sound Vib 229:879–895
5. Ferreira AJM, Batra RC, Roque CMC, Qian LF, Jorge RMN (2006) Natural frequencies of functionally graded plates by a meshless method. Compos Struct 75:593–600
6. Neves AMA, Ferreira AJM, Carrera E, Cinefra M, Roque CMC, Jorge RMN, Soares CMM (2013) Static, free vibration and buckling analysis of isotropic and sandwich functionally graded plates using a quasi-3D higher-order shear deformation theory and a meshless technique. Compos Part B Eng 44:657–674
7. Talha M, Singh BN (2010) Static response and free vibration analysis of FGM plates using higher order shear deformation theory. Appl Math Model 34:3991–4011

8. Gupta A, Talha M (2016) An assessment of a non-polynomial based higher order shear and normal deformation theory for vibration response of gradient plates with initial geometric imperfections. Compos Part B 107:141–161
9. Gupta A, Talha M (2017) Large amplitude free flexural vibration analysis of finite element modeled FGM plates using new hyperbolic shear and normal deformation theory 287–308
10. Gupta A, Talha M (2017) Influence of porosity on the flexural and vibration response of gradient plate using nonpolynomial higher-order shear and normal deformation theory. Int J Mech Mater Des
11. Gupta A, Talha M, Singh BN (2016) Vibration characteristics of functionally graded material plate with various boundary constraints using higher order shear deformation theory. Compos Part B Eng 94:64–74
12. Yang J, Huang X-L (2007) Nonlinear transient response of functionally graded plates with general imperfections in thermal environments. Comput Methods Appl Mech Eng 196:2619–2630
13. Akavci SS (2014) An efficient shear deformation theory for free vibration of functionally graded thick rectangular plates on elastic foundation. Compos Struct 108:667–676

Characterization of 2D Nanomaterials for Energy Storage

Akarsh Verma and Avinash Parashar

Abstract Objective of this article is to explore the influence of hydrogenation on the mechanical and fracture properties of two-dimensional nanomaterials mainly graphene and hexagonal boron nitride (h-BN) nanosheets. Classical mechanics-based molecular dynamics approach was used in conjunction with AIREBO and ReaxFF interatomic potentials to capture the realistic behavior of graphene and h-BN, respectively. It was predicted from the simulations that full as well as partial (50%) hydrogenation has deteriorating effect on the properties of graphene; but, in contrast has a favorable influence on the fracture properties of h-BN. Out-of-plane displacement in the hydrogenated nanosheets has a significant impact on the overall properties of these 2D nanomaterials. This study gives important design guidelines to fabricate nanomaterials for the hydrogen energy storage.

Keywords Graphene · Hexagonal boron nitride · Molecular dynamics · Fracture · Hydrogen

1 Introduction

During the last couple of decades, graphene, and h-BN have emerged as the most promising and fascinating two-dimensional (2D) nanomaterials [1, 2]. Their exceptional mechanical and thermal properties are attributed to its space frame honeycomb lattice structure and quantum confinement. Researchers are exploring diversifying areas of applications that include microelectronics, biomedical, reinforcing nanocomposites, desalination membrane, clean energy devices, and solar cells for utilizing these aforementioned 2D nanomaterials [3].

Hydrogen chemical group is a highly combustible and potential futuristic energy source for an uncontaminated and sustainable economy; but, its room temperature storage has raised a few questions to the materials scientific community. Ozturk et al. [4] proposed a 3D carbon-based nanoporous material (containing fullerene

A. Verma (✉) · A. Parashar
Indian Institute of Technology Roorkee, Roorkee, Uttarakhand, India
e-mail: akarshverma007@gmail.com

B. N. Singh et al. (eds.), *Recent Advances in Theoretical, Applied, Computational and Experimental Mechanics*, Lecture Notes in Mechanical Engineering,
https://doi.org/10.1007/978-981-15-1189-9_18

compound sandwiched between graphene sheets) for the hydrogen storage application. In addition to the hydrogen storage dilemma, water desalination, and separation of ions also make these 2D nanomaterials prone to hydrogenation effect [5, 6].

In the present scrutiny, molecular models were designed in the background of molecular dynamics (MD) based simulations technique. Accomplishment of MD computational study depends on the interatomic chemical potential that is mainly used for perceiving the bonded and nonbonded atomistic interaction. Herein, the adaptive intermolecular reactive empirical bond order (AIREBO) potential is employed in all the simulations for calculating and analyzing atomistic interactions between carbon–hydrogen chemical systems in graphene [7]; whereas, reactive force field (ReaxFF) is utilized for graphene, h-BN and hydrogen chemical systems [8, 9]. For the per atom stress tensor, virial stresses [10, 11] were predicted using the mathematical formula (refer Eq. 1):

$$\sigma_{ij}^{\alpha} = \frac{1}{\varphi^{\alpha}} \left(\frac{1}{2} m^{\alpha} v_i^{\alpha} v_j^{\alpha} + \sum_{\beta=1,n} r_{\alpha\beta}^{j} f_{\alpha\beta}^{i} \right) \tag{1}$$

The brittle behavior of graphene and h-BN leads to characterizing them from the fracture point of view, that is quantified by the fracture toughness/critical stress intensity factor (K_{IC}) as described in the Eq. 2:

$$K_{\mathrm{IC}} = Y \sigma \sqrt{\pi a} \tag{2}$$

here, Y is the dimensionless geometry parameter ($Y \approx 1$), σ is the normal virial stress value at the first bond rupture instant and a is half of the central crack length present in graphene and h-BN sheet. To avoid thermal disturbances and maintain a realistic room temperature, all the computations were executed at room temperature (300 K) under NPT ensemble [12]. Open source code software large-scale Atomic/Molecular Massively Parallel Simulator (LAMMPS) was employed for this simulations [13, 14]; whereas, open visualization tool OVITO was executed for post handling of dump files produced by LAMMPS [15, 16]. The authors have taken an integration time step of 0.5 fs and the nanomaterials were subjected to a tensile deformation (strain rate being equal to 0.0005 ps^{-1}). The nanosheet size was taken to be 270 Å (in length and breadth) and the periodic boundary conditions were taken.

2 Results and Discussion

Preliminary computations were carried out to validate the AIREBO and ReaxFF potential factors for graphene and h-BN, respectively. After validation, tensile test was conducted for predicting the mechanical behavior of these nanomaterials, as shown in Figs. 1 and 2. It was concluded from Fig. 1 that failure stress and strain considerably reduced for the fully and partially hydrogenated graphene sheets as

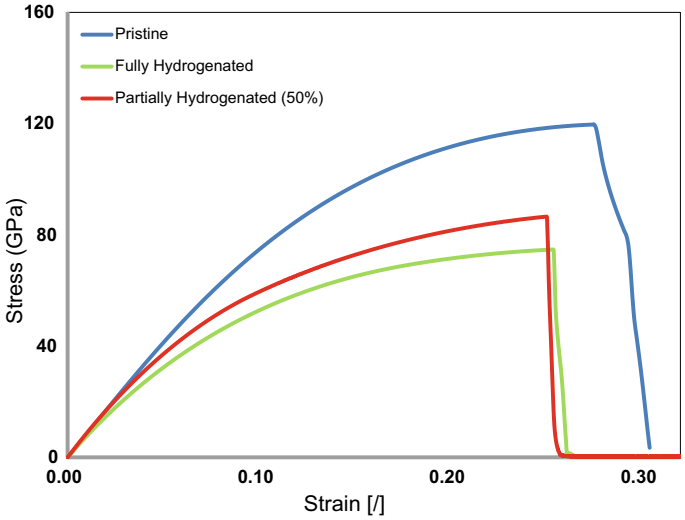

Fig. 1 Stress–strain response of pristine, fully and partially hydrogenated sheets of graphene at 300 K

Fig. 2 Stress–strain response of pristine, fully (H-BN) and partially (H-BN) hydrogenated h-BN nanosheets at 300 K

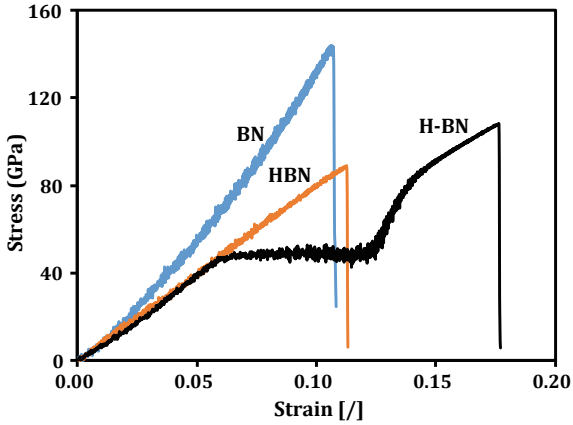

compared to pristine one. Moreover, the partially hydrogenated graphene (with 50% coverage) has comparatively higher fracture strength than the fully hydrogenated one. Out-of-plane displacement in the hydrogenated graphene and the change in its hybridization state from sp^2 to sp^3 were attributed as the main reasons behind diluting the properties of graphene (see Fig. 3). The out-of-plane displacement leads to an increase in carbon–carbon bond length, thus, decreasing its bond strength. Besides this, decrement in contribution of *s*-orbital and increment of *p*-orbital (directional dependent) lead to bond strength deterioration in the in-plane direction. Hence, we observed an overall deteriorating tensile strength for the hydrogenated graphene

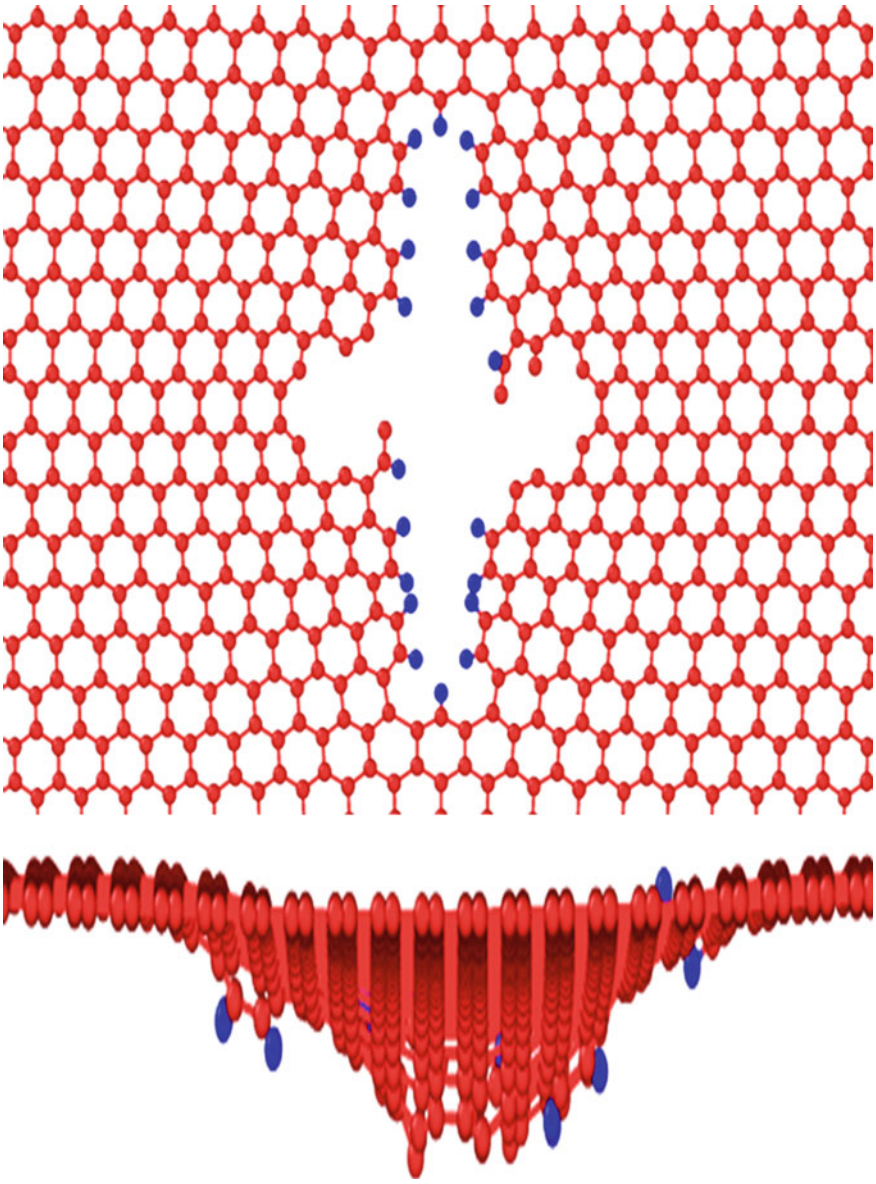

Fig. 3 Out-of-plane displacement in hydrogenated graphene

Table 1 Fracture toughness of pristine and hydrogen passivated crack edges for graphene

Material	Configuration	K_{IC} (MPa $m^{-1/2}$)	
		ZZ	AC
Graphene	Pristine	3.54	2.65
	Fully hydrogenated	2.77	2.40
	Partially hydrogenated (50%)	2.85	2.43
h-BN	Pristine	4.35	4.17
	Fully hydrogenated	5.13	5.13
	Partially hydrogenated (H-BN)	4.49	5.03

structure. Similar kind of declining effect was predicted for hydrogenated h-BN as shown in Fig. 2. Despite the reduction in fracture stress of fully hydrogenated (100% coverage) as well as partially hydrogenated (50% coverage with H atom attached only to B atoms) h-BN nanosheets, a noteworthy enlargement in fracture toughness of H-BN (partially hydrogenated) was detected. The improvement in fracture toughness of H-BN was accredited to shifting of the polarization charge state of hydrogen with increase in the strain values and also to the crack tip blunting phenomenon. Similar kind of effort was implemented to witness the influence of hydrogen passivation of crack tip atoms on the fracture toughness of aforementioned 2D nanosheets. The fracture toughness in terms of stress intensity factor (K_{IC}) was estimated and has been showcased in Table 1. It may be predicted from this table that the hydrogenation has deteriorating effect on K_{IC} of graphene, but it helps in improving the K_{IC} of h-BN nanosheets. This enhanced fracture toughness would enable these 2D nanomaterials to soak large energy erstwhile to failure and augmented toughness too, leading to amended energy storage and structural applications.

Thus, we have shown that the molecular dynamics-based simulation helps in predicting positive as well as negative impact of hydrogenation on h-BN and graphene nanosheets, respectively.

3 Conclusion

Molecular dynamics-based simulations have been conducted to analyze the effect of hydrogen adatoms on the mechanical and fracture properties of 2D nanomaterials (graphene and hexagonal boron nitride (h-BN) nanosheets in particular). AIREBO and ReaxFF interatomic potentials were used to capture the realistic behavior of graphene and h-BN, respectively. It was predicted from the simulations that full as well as partial hydrogenation has deteriorating effect on the properties of graphene because of the transition in hybridization state and significant out-of-plane displacement; but, in contrast has a favorable influence on the fracture properties of h-BN. This work gives significant design guidelines to fabricate 2D nanomaterials for the hydrogen energy storage application.

Acknowledgements Monetary funding from the Nano mission unit of Government of India is appreciatively recognized (Project number: DST-952-MID).

References

1. Novoselov KS, Fal'ko VI, Colombo L, Gellert PR, Schwab MG, Kim K (2012) A roadmap for graphene. Nature 490(7419):192–200
2. Rajasekaran G, Narayanan P, Parashar A (2016) Effect of point and line defects on mechanical and thermal properties of graphene: a review. Crit Rev Solid State Mater Sci 41(1):47–71
3. Verma A, Parashar A, Packirisamy M (2018) Atomistic modeling of graphene/hexagonal boron nitride polymer nanocomposites: a review. Wiley Interdiscip Rev: Comput Mol Sci 8(3):e1346
4. Ozturk Z, Baykasoglu C, Kirca M (2016) Sandwiched graphene-fullerene composite: a novel 3-D nanostructured material for hydrogen storage. Int J Hydrog Energy 41(15):6403–6411
5. Verma A, Parashar A (2017) The effect of STW defects on the mechanical properties and fracture toughness of pristine and hydrogenated graphene. Phys Chem Chem Phys 19:16023–16037
6. Kumar R, Parashar A (2017) Fracture toughness enhancement of h-BN monolayers via hydrogen passivation of a crack edge. Nanotechnology 28(16):165702
7. Rajasekaran G, Parashar A (2017) Enhancement of fracture toughness of graphene via crack bridging with stone-thrower-wales defects. Diam Relat Mater 74:90–99
8. Verma A, Parashar A (2018) Reactive force field based atomistic simulations to study fracture toughness of bicrystalline graphene functionalised with oxide groups. Diam Relat Mater 88:193–203
9. Verma A, Parashar A (2018) Molecular dynamics based simulations to study the fracture strength of monolayer graphene oxide. Nanotechnology 29(11):115706
10. Zhou M (2003) A new look at the atomic level virial stress: on continuum-molecular system equivalence. Proc R Soc Lond A: Math Phys Eng Sci 459(2037):2347–2392
11. Verma A, Parashar A (2018) Molecular dynamics based simulations to study failure morphology of hydroxyl and epoxide functionalised graphene. Comput Mater Sci 143:15–26
12. Hoover WG (1985) Canonical dynamics: equilibrium phase-space distributions. Phys Rev A 31(3):1695
13. Plimpton S (1995) Fast parallel algorithms for short-range molecular dynamics. J Comput Phys 117(1):1–19
14. Verma A, Parashar A (2018) Structural and chemical insights into thermal transport for strained functionalised graphene: a molecular dynamics study. Mater Res Express 5(11):115605
15. Stukowski A (2009) Visualization and analysis of atomistic simulation data with OVITO—the open visualization tool. Modell Simul Mater Sci Eng 18(1):015012
16. Verma A, Parashar A, Packirisamy M (2018) Tailoring the failure morphology of 2D bicrystalline graphene oxide. J Appl Phys 124(1):015102

Cold Expansion of Elongated Hole: A Realistic Finite Element Simulation

S. Anil Kumar and N. C. Mahendra Babu

Abstract Elongated holes are found in many aerospace structural components and are prone to fatigue failure due to the stress concentration effect at the edge of the hole. Different approaches like shape reworking, shape optimization, and cold expansion combined with interference fitting are currently used as a repair/life extension option, to overcome fatigue cracking problems around elongated holes. In practice, these approaches lead to either addition of material or modification of geometry. A novel and economical method derived from renowned hole cold expansion process is proposed in the literature to enhance the fatigue life of elongated hole without adding material and modifying hole geometries. Benefit of implementing proposed novel cold expansion method for elongated hole is investigated in this work through a simplified three-dimensional nonlinear Finite Element simulation. Distributions of induced beneficial residual stress around and along the thickness direction of elongated hole are predicted from the FE simulation. The results indicate introduction of significant beneficial residual stresses throughout the thickness surface of elongated hole. These beneficial residual stresses are responsible for fatigue life extension and can be further used to quantify the achieved fatigue life enhancement.

Keywords Elongated hole · Cold expansion · Beneficial residual stresses · Fatigue life enhancement

1 Introduction

Aircraft industries are continuously facing challenges in developing the lightweight structures with increased durability and damage tolerance. One such example is the frequent in-service fatigue cracking problems around fuel flow vent holes of

S. Anil Kumar (✉) · N. C. Mahendra Babu
Department of Mechanical and Manufacturing Engineering, M. S. Ramaiah University of Applied Sciences, Bengaluru 560058, India
e-mail: anilpassion86@gmail.com

N. C. Mahendra Babu
e-mail: ncmbabu@gmail.com

B. N. Singh et al. (eds.), *Recent Advances in Theoretical, Applied, Computational and Experimental Mechanics*, Lecture Notes in Mechanical Engineering,
https://doi.org/10.1007/978-981-15-1189-9_19

wing pivot fittings in F-111 aircarfts [1–3]. These fuel flow vent holes are machined elongated holes with semi-circular ends (i.e., noncircular holes) in wing pivot fitting components for the purpose of allowing fuel flow in the wings. Among several such functional elongated holes in wing pivot fittings, some of the elongated holes are extremely vulnerable for premature fatigue cracking owing to flight operational loads [4–6]. To repair the fatigue-damaged elongated holes, different life extension approaches, viz., shape reworking, shape optimization, and cold expansion combined with interference fitting approaches are used in practice [1–6].

In shape reworking approach, the material layers on the elongated hole boundaries are progressively machined to slightly higher sizes so that the material layers containing fatigue cracks are completely eliminated [1, 4]. Although shape reworking eliminates fatigue cracking problem during repair stage, it is not possible to avoid fatigue cracking problems which arise during later stages of service life of the component. The shape optimization approach involves optimizing fatigue-damaged elongated hole shapes with an objective of minimizing stress concentrations and maximizing fatigue life/damage tolerance by employing optimization algorithms [1, 6]. Although optimization of elongated hole shapes significantly reduces the peak stresses at stress concentration locations, the production of optimized hole shapes often poses difficulties due to complexities in hole geometries. Hence, to overcome the limitations of shape reworking and shape optimization approaches, cold expansion combined with interference fitting approach is developed. In this approach, a specially designed oversized mandrel/sleeve combination made of hardened material is permanently inserted into elongated hole opening causing cold expansion combined with interference fitting. As a result, compressive residual stresses are developed around damaged elongated hole impeding the fatigue crack initiation/propagation under in-service operational loads [1–6]. Though the cold expansion combined with interference fitting approach is found to be capable of enhancing the fatigue life of elongated holes to larger extents, it leads to addition of extra material on the wing pivot fitting assemblies. Application of proceeding approaches in repairing fatigue-damaged elongated holes lead to either shape modification or material addition thereby posing a difficulty in meeting one of the mandatory air force durability and damage tolerance certification requirements. This requirement insists to prevent or repair fatigue-damaged structural holes without adding extra material and imposing costly structural replacements [7, 8].

To overcome the aforementioned limitations of different life extension approaches, a novel cold expansion method which is derived from the renowned hole cold expansion process is proposed in Ref. [9] for enhancing the fatigue life of elongated holes. Although the novel method of cold expansion for elongated holes is proposed, none of the researchers have previously attempted to investigate the method in detail and quantify resulting fatigue life enhancement benefits. Hence, an attempt is made in the present work to realistically simulate the novel cold expansion method for typical elongated hole in Al 7075-T651 plate and adequately predict the cold expansion-induced beneficial residual around the elongated hole and its thickness directions by developing a simplified FE framework.

2 A Novel Cold Expansion Method for Elongated Hole

The proposed novel cold expansion method can be implemented on fatigue-damaged or aged elongated hole in two steps as schematically illustrated in Fig. 1. In the first step, a specially designed hard metal insert is tightly fitted into elongated hole opening in such a way that circular hole region is obtained at one of the ends as shown in Fig. 1. Further, a hardened and tapered mandrel of size greater than the diameter of hole region is gradually forced into hole region from one (entry) side and subsequently removed from the other (exit) side. As an effect, the material surrounding semi-circular end region of the elongated hole is cold expanded similar to regular cold expansion process [9–11].

In the second step, the hard insert is reversed and again fitted into elongated hole opening so as to obtain circular hole region at other end of the elongated hole. The obtained circular hole region is further cold expanded by gradually passing the oversized mandrel and the operation is completed by removing the insert. This novel method of cold expansion process can be applied to critical elongated holes either during manufacturing stage or repair stage. As a result of cold expansion, permanent compressive residual stresses are induced around stress concentration locations such as semi-circular ends of elongated hole. The extent of compressive residual stresses induced around semi-circular ends of elongated hole depends on the diametrical interference between maximum diameter of the mandrel and diameter of the circular hole region. Although the compressive residual stresses are induced in all three-dimensions such as radial, tangential, and transverse (thickness) directions, the residual stresses induced in tangential directions are effective in preventing fatigue crack initiations/propagations. Hence, these tangential residual stresses (σ_θ) are termed as beneficial residual stresses which actually lead to fatigue life enhancement of cold expanded elongated holes.

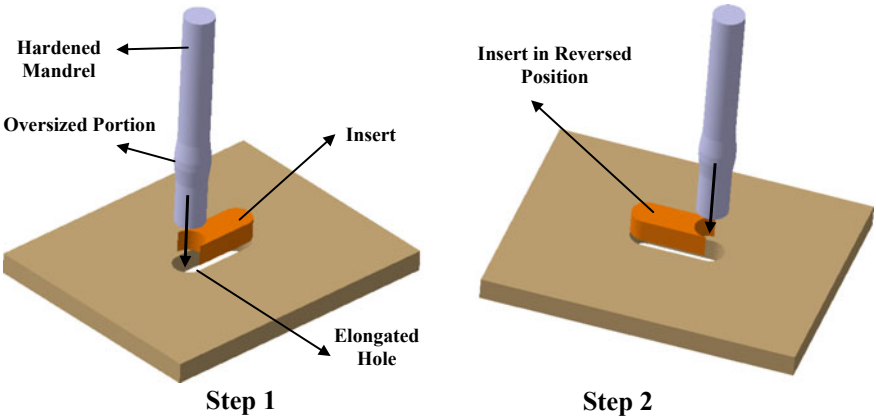

Fig. 1 Schematic of steps involved in cold expansion of elongated hole

3 Three-Dimensional Finite Element Simulation of Cold Expansion of Elongated Hole

To investigate the benefit of implementing proposed cold expansion method to elongated hole, a three-dimensional nonlinear FE simulation is carried out. For the purpose of simulation, a typical elongated hole configuration made of aircraft grade Al 7075-T651 material as shown in Fig. 2 is considered. Owing to the symmetry of the geometry considered (Fig. 2), only quarter symmetry FE model is created in FEA tool (ANSYS) as shown in Fig. 3. In this model, 9,568 numbers of 8-noded solid 185 element types are used after ensuring mesh convergence through the number of trial runs. The material properties for present FE simulation are obtained from the true stress–strain curve reported in Ref. [12]. These properties include elastic modulus = 72 GPa, Poison's ratio = 0.3 and yield strength (σ_y) = 506 MPa. The

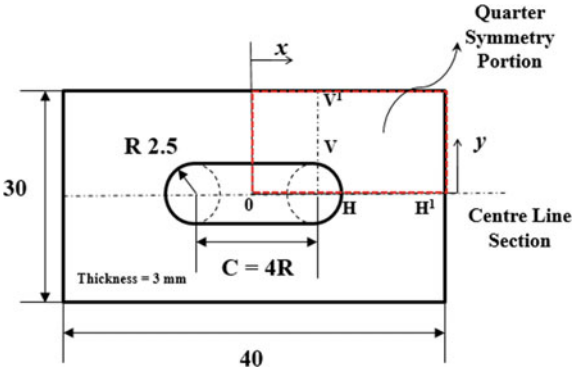

Fig. 2 Dimensions (mm) of the plate with elongated hole (*R*—radius of the semi-circular end, *C*—spacing between semi-circular ends)

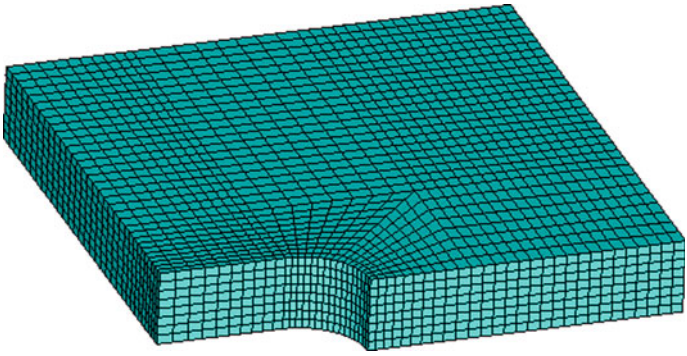

Fig. 3 Quarter symmetry FE model of the plate with elongated hole

nonlinear material behavior is modeled using tangent modulus of 1000 MPa under Mises plasticity option with isotropic hardening rule.

The situation of implementing proposed cold expansion method to elongated holes can be considered as equivalent to sequential cold expansion of two closely spaced adjacent circular holes (Fig. 1). Taking this consideration into account, the mechanics of cold expansion process around closely spaced adjacent holes have been reviewed from the published literature [12–16]. It is identified that either simultaneous or sequential cold expansion of closely spaced adjacent holes (hole center-to-center spacing is equal to two times the hole diameter) induces approximately same level of compressive residual stresses around the holes. Hence, during simulation of cold expansion for elongated hole, it can be considered that both circular hole regions (at either semi-circular ends) are simultaneously cold expanded for the purpose of simplifying FE modeling and reducing computational time.

The complete cold expansion method for elongated hole is simulated in two stages, viz., gradual expansion of the material layer by layer on semi-circular end during first stage and release of expanded material layer by layer in the same sequence during second stage. For accounting the effects of layer by layer material expansion and relaxation, the total thickness (3 mm) of the plate is divided into 8 equal elemental divisions as shown in Fig. 3. These eight divisions are further grouped as three layers having three elemental divisions in each layer. This grouping of layers is only for the purpose of studying through-thickness effects, whereas, in the actual plate, the material along the thickness is continuous. In the first stage of simulation, each layer along the thickness direction is sequentially expanded one after the other starting from mandrel entry side (top plane) and moving towards the exit side (bottom plane) of the plate. The expansion of each layer is simulated by applying the displacements that cause circular hole region to expand by 2% of its diameter (expansion level). This indicates the gradual engagement of mandrel into circular hole region from the entry side (top plane), expansion of material along hole thickness direction and removal of mandrel from the exit side (bottom plane).

In the second stage of simulation, all the displacements which are applied in the first stage of simulation are successively removed layer by layer starting from mandrel entry side towards the exit side of the plate. This indicates the gradual elastic-plastic recovery (spring-back) of expanded material on the circular hole region starting from mandrel entry side to exit side. Throughout the simulation, the effect of insert in elongated hole slot is considered by constraining the displacements on straight edge portion of elongated hole boundary. Whereas, in actual cold expansion situations, after cold expansion of circular hole regions at either end of elongated hole, the insert is permanently ejected-out thereby leaving the semi-circular ends in cold expanded state. Thus, after the complete FE simulation, the semi-circular ends of elongated hole are in cold expanded state.

4 Results and Discussions

4.1 Validation of Finite Element Simulation Framework

To validate the FE simulation framework developed for simulating the cold expansion of elongated hole in the present work, either experimental or numerical results are not available in literature. Hence, for validating the present FE simulation framework, the case of two adjacent circular holes whose radius equal to end radii of elongated hole is considered in the configuration identical to elongated hole configuration shown in Fig. 2. For this case having two adjacent circular holes in the plate of dimensions shown in Fig. 2, the results of sequential cold expansion process are available [16]. Therefore, for the purpose of validation, a separate half-symmetry FE model having two adjacent circular holes is developed as shown in Fig. 4 using 14,896 numbers of 8-noded solid 185 element type after testing mesh convergence.

To capture through-thickness variation effects, the thickness (3 mm) of the plate is discretized into 8 equal elemental divisions as shown in Fig. 4. The complete simulation of cold expansion around adjacent circular holes is carried out through several loading steps by following the FE simulation framework employed for elongated hole. From the FE simulation on cold expansion of adjacent circular holes for 2% expansion level, the beneficial residual stress distribution is predicted and presented in Fig. 5. It is evident from Fig. 5 that cold expansion-induced beneficial residual stresses vary throughout the thickness of holes starting from a minimum magnitude of 228 MPa (compressive) to maximum magnitude of 606 MPa (compressive). Also, the beneficial residual stress variations on top and bottom planes of two adjacent holes are predicted and validated with published results [16] as shown in Fig. 6. This validation study shows that present simplified FE simulation framework is

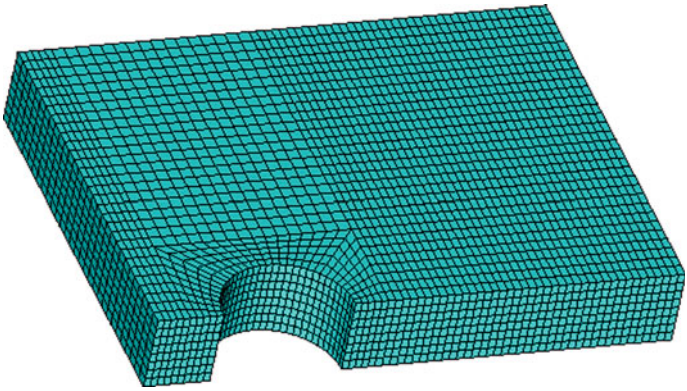

Fig. 4 Quarter symmetry FE model of the plate with two adjacent circular holes

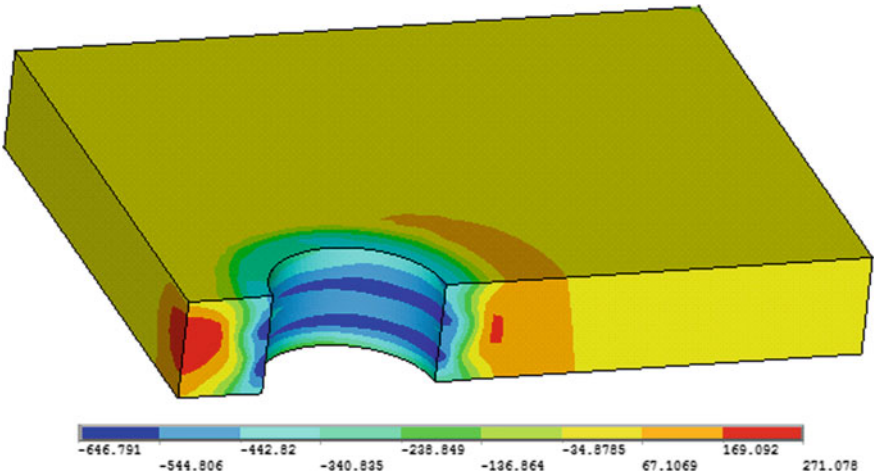

Fig. 5 Beneficial residual stress distribution around adjacent circular holes

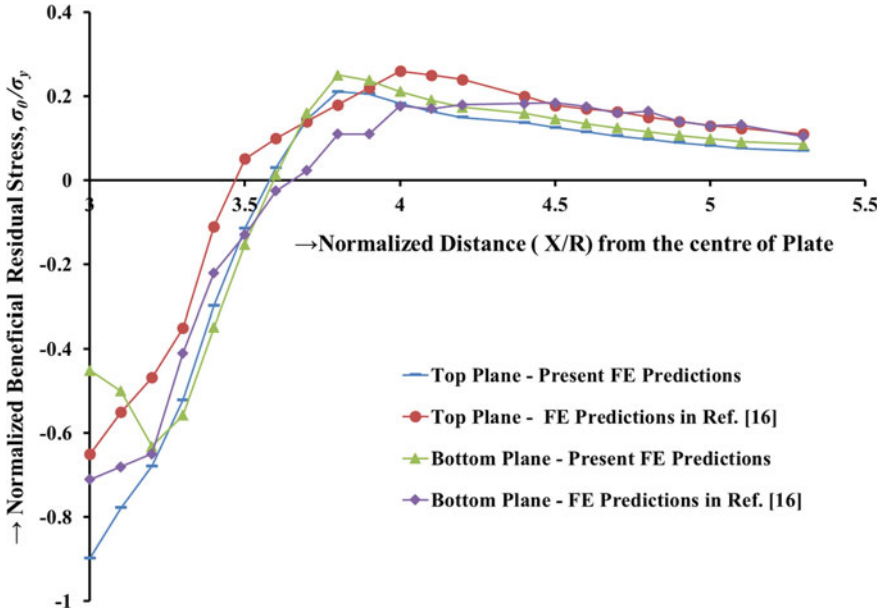

Fig. 6 Variation of normalized beneficial residual stresses over the normalized distance on hole centerline section

capable of realistically predicting through-thickness variations of cold expansion—induced beneficial residual stresses. Hence, the developed simplified FE simulation framework is reliably extended to simulate the cold expansion of elongated hole.

4.2 *Beneficial Residual Stresses Around Cold Expanded Elongated Hole*

The beneficial residual stress distributions predicted around cold expanded elongated hole is as shown in Fig. 7. It is clear from Fig. 7 that significant beneficial residual stresses are induced around the hole and along the thickness direction of critical locations, viz., semi-circular ends of elongated hole. These beneficial residual stresses are found to significantly vary throughout the thickness of elongated hole starting from the top plane to the bottom plane. Under remote fluctuating loads, sections HH^1 and VV^1 shown in Fig. 2 are found to be critical for fatigue failures around elongated hole. Hence, the variations of beneficial residual stresses on different planes (top, mid-thickness, and bottom) of critical sections (HH^1 and VV^1) are predicted and presented in Figs. 8 and 9. Also, the through-thickness variations of beneficial residual stress at two critical locations (H and V) on elongated hole boundary is predicted as shown in Fig. 10.

Along with the thickness of location 'H', the beneficial residual stresses vary from a minimum magnitude of 171 MPa (compressive) on bottom plane to 613 MPa (compressive) on a plane which is at a distance of 2.25 mm from top plane (Fig. 10).

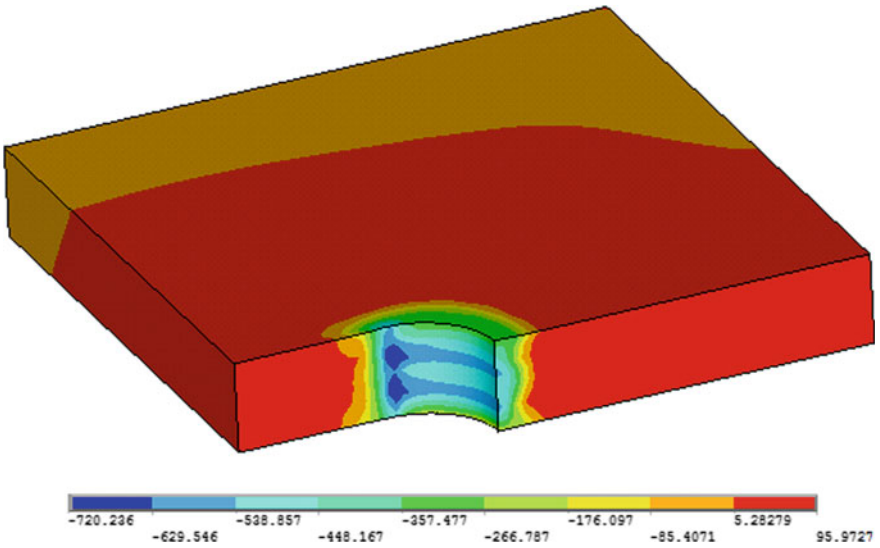

Fig. 7 Beneficial residual stress distribution around elongated hole

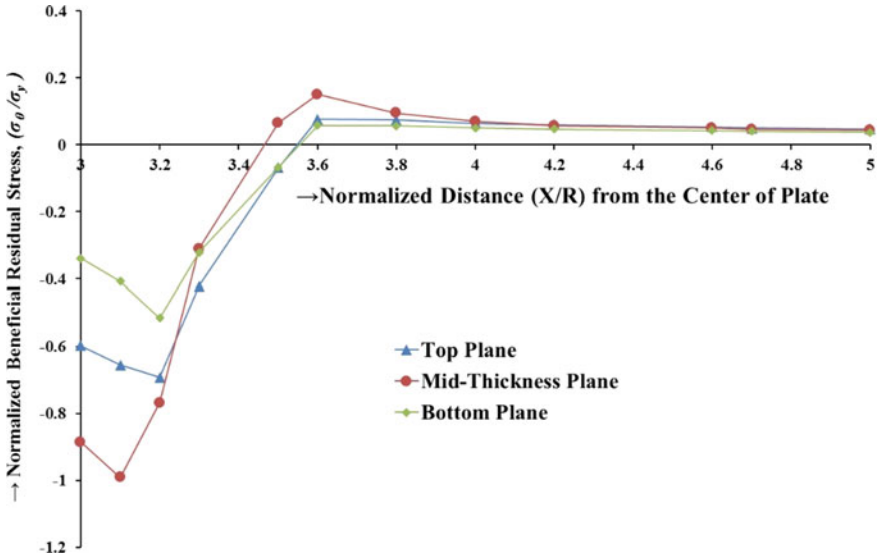

Fig. 8 Variation of normalized beneficial residual stresses over the normalized distance on centerline section HH^1 of elongated hole

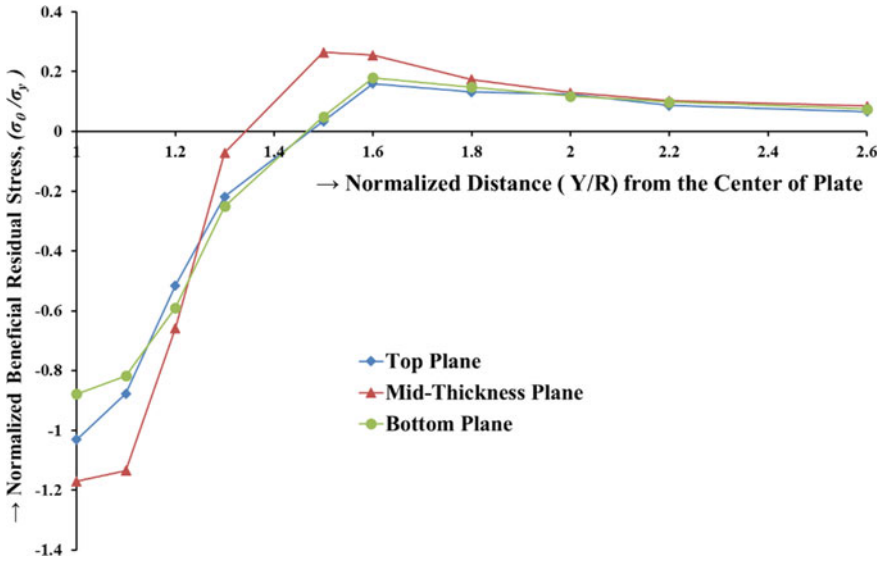

Fig. 9 Variation of normalized beneficial residual stresses over the normalized distance on section VV^1 of elongated hole

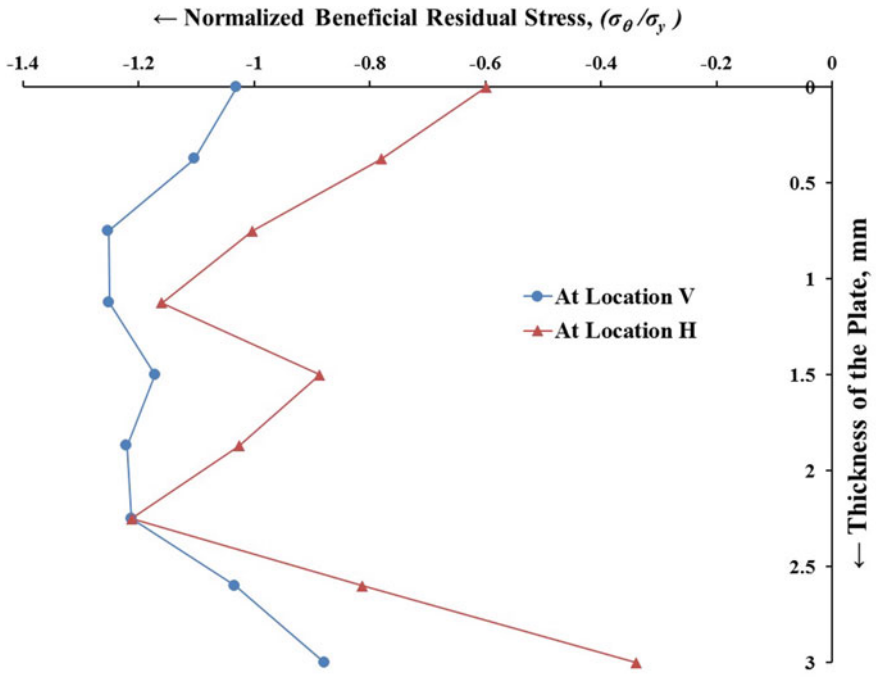

Fig. 10 Variation of beneficial residual stresses through the thickness of critical locations H and V of elongated hole

Similarly, along the thickness of location 'V', the beneficial residual stresses vary from a minimum magnitude of 444 MPa (compressive) on bottom plane to 633 MPa (compressive) on a plane which is at a distance of 0.75 mm from top plane (Fig. 10). In the region between elongated hole edge and edge of the plate, the magnitudes of beneficial residual stresses are found to be maximum at semi-circular end and gradually decays over the distance away from the semi-circular ends as observed from Figs. 8 and 9. On top, mid-thickness and bottom planes, the beneficial residual stresses remain compressive up to 1.25 mm distance from the elongated hole edge (H and V) as shown in Figs. 8 and 9. Beyond this region, equilibrating tensile residual stresses of small magnitudes are induced up to certain distance and further decays to negligible magnitude as observed in Figs. 7 and 8. Similar trend is observed for all the planes along the thickness direction. Due to the minimum magnitude of beneficial residual stress on bottom plane (Fig. 10), the locations on this bottom plane are the most probable locations for fatigue crack initiation/propagation. As observed from Figs. 7, 8, 9 and 10, the through-thickness variation of cold expansion—induced beneficial residual stresses are due to nonuniform expansion/recovery of the material and difference in material support conditions along the thickness direction.

Thus, the developed FE simulation framework is simple to implement and capable of adequately predict the cold expansion-induced beneficial residual stresses around

the hole and along with the thickness of elongated holes. The present predictions confirm the presence of significant beneficial residual stresses around the semi-circular ends and its thickness directions. As a result, the possibility of fatigue crack initiation/propagation around the semi-circular end locations is reduced thereby leading to appreciable fatigue life enhancement of elongated hole without adding extra material and modifying hole geometry.

5 Conclusions

- The simplified three-dimensional nonlinear FE simulation framework for realistically simulating the novel cold expansion method for elongated hole is developed
- The through-thickness variations of cold expansion-induced beneficial residual stresses around the elongated hole and along the thickness directions are predicted
- Induced beneficial residual stresses are found to significantly vary throughout the thickness of elongated hole owing to nature of cold expansion process
- Induced beneficial residual stresses reduce the tendency of fatigue crack initiation/propagation at the stress concentration locations (semi-circular ends) of elongated hole thereby leading to significant fatigue life enhancement
- The beneficial residual stress predictions from the present FE simulation can be further used to quantify the exact fatigue life enhancement benefit which can be achieved due to cold expansion.

Acknowledgements The authors acknowledge the support of M. S. Ramaiah University of Applied Sciences, Bengaluru-58 for carrying out this research work.

References

1. Heller M, Evans RL, Allan RB (1999) Cold expansion tests for plates containing elongated holes. Defense Science and Technology Organization Report No. DSTO-TN-0233
2. Weller S, McDonald M (2000) Stress analysis of the F-111 wing pivot fitting. Defense Science and Technology Organization Report No. DSTO-TN-0271
3. Das R, Jones R (2012) Extending the fatigue life of a fuel flow vent hole in an aircraft component using shape optimization. In: Proceedings of international conference on engineering optimization, Brazil
4. Kevin WC (1997) Strain surveys of FFVH#13 and stiffener run outs #2 in the F-111 WPF for a range of rework shapes. Defense Science and Technology Organization Report No. DSTO-TR-0567
5. Krishnapillai K, Jones R, Peng D (2009) Three-dimensional fatigue-based structural design optimization of fuel flow vent holes. J Eng Fail Anal 16:361–390
6. Allan RB, Heller M (1997) Stress analysis of an interference fit life extension option for a cold expanded elongated FFVH on the F-111 aircraft. Defense Science and Technology Organization Report No. DSTO-TR-0549

7. Wood HA, Engle Jr RM (1979) USAF damage tolerance design handbook: guidelines for the analysis and design of damage tolerant aircraft. Technical Report No. AFFDL-TR-79-3021
8. (2002) Aircraft structural integrity program general guidelines. Department of Defense Handbook, MIL-HDBK-1530A (USAF)
9. Ruffin AC (1993) Extending the fatigue life of aircraft engine components by hole cold expansion technology. J Eng Gas Turbines Power 115:165–171
10. Anil Kumar S, Mahendra Babu NC (2014) Numerical simulation of cold expansion of cut-out with semi-circular ends. In: Proceedings of international conference on advances in design and manufacturing 2014 (ICAD & M'14) organized by NIT-Trichy, pp 219–223. ISBN 978-93-84743-12-3
11. Babu NCM, Jagadish T, Ramachandra K, Sridhara SN (2008) A simplified 3-D finite element simulation of cold expansion of a circular hole to capture through thickness variation of residual stresses. J Eng Fail Anal 15:339–348
12. Karuppanan S, Hashim MH, Waheb AA (2013) Finite element simulation of residual stresses in cold-expanded plate. Asian J Sci Res. ISSN 1992-1454
13. Anil Kumar S, Mahendra Babu NC (2017) Effect of proximity hole on induced residual stresses during cold expansion of adjacent holes. J Mater Today Proc
14. Kim C, Kim D-J, Seok C-S, Yang W-H (2004) Finite element analysis of the residual stress by cold expansion method under the influence of adjacent holes. J Mater Process Technol 153–154:986–991
15. Papanikos P, Maguid SA (1999) Elasto-plastic finite-element analysis of the cold expansion of adjacent fastener holes. J Mater Technol 92–93:424–428
16. Papanikos P, Maguid SA (1998) Three-dimensional finite-element analysis of the cold expansion of adjacent holes. Int J Mech Sci 40:1019–1028

Effect of Module on Wear Reduction in High Contact Ratio Spur Gears Drive Through Optimized Fillet Stress

R. Ravivarman, K. Palaniradja and R. Prabhu Sekar

Abstract The current study intends to predict the wear obstruction of high contact ratio spur gears over optimized fillet stress between the wheel and pinion. As the fillet region of the wheel is considered to be the critical region with high stress concentration, it becomes essential to study the wear depth at this enhanced bending strength. The optimization of fillet stress is carried out through profile modification technique and the tooth wear of the gear drive is examined using contact analysis and analytical method by taking in the tooth load distribution at the contact points, fillet stress and strength during contact for various work cycles. This examination additionally investigates the impact of module over depletion of material from the tooth surface of the transmission system and lastly the outcomes are conferred that the reduced stress for the high contact ratio gear drive has enhanced wear resistance.

Keywords High contact ratio · Optimized · Module · Spur gear · Wear reduction

Nomenclature

E	Modulus of rigidity in GPa
F	Distribution of load in N
R	Radius of curvature in mm
X	Space between the contact and pitch point in mm
a	Semi contact width in mm

R. Ravivarman (✉) · K. Palaniradja
Department of Mechanical Engineering, Easwari Engineering College, Chennai, India
e-mail: varman92@gmail.com

K. Palaniradja
e-mail: palaniradja72@pec.edu

R. P. Sekar
Mechanical Engineering Department, Motilal Nehru National Institute of Technology, Allahabad, India
e-mail: rprabhusekar@mnnit.ac.in

B. N. Singh et al. (eds.), *Recent Advances in Theoretical, Applied, Computational and Experimental Mechanics*, Lecture Notes in Mechanical Engineering,
https://doi.org/10.1007/978-981-15-1189-9_20

h	Wear depth in mm
h_a	Addendum coefficient in mm
i	Gear ratio
k	Tooth thickness factor
m	Gear module in mm
p	Base pitch in mm
s	Sliding distance in mm
v	Sliding velocity in m/s
z	Teeth number

Symbols

α	Pressure angle in degree
θ	Angle of half tooth thickness at any engagement contact in degree
ν	Poisson's ratio
σ	Stress in MPa
ω	Angular velocity in rad/s

Subscripts

N	Normal in direction for the tooth
a	Addendum
b	Base circle
g	Wheel
i	Contact at any engagement
n	Meshing cycle
p	Pinion
o	Pitch circle
max	Maximum

Abbreviations

FE	Finite element
FHPDTC	First highest point of double tooth contact
FLPDTC	First lowest point of double tooth contact
HPTC	Highest point of tooth contact
LPTC	Lowest point of tooth contact
SHPDTC	Second highest point of double tooth contact
SLPDTC	Second lowest point of double tooth contact

1 Introduction

Nowadays power transmission drives demand for efficient load-carrying capacity under minimum wear, noise and vibration with compactness. This competitive scenario brings the high contact ratio gears into play as a swap for normal spur gear drives. Since high contact ratio gear drive gives the added advantage of increased contact ratio without the need for helical gears, which introduces thrust forces in the system. Bending of tooth and depletion of material from tooth surface is the significant reason for the major modes of failure which happen due to contact pressure and insufficient strength during the bending of tooth. This contact pressure and fillet stress is a significant parameter in disturbing the load-carrying ability of gear drives. In common inadequate contact, strength tends to failures like wear, surface pitting, and scoring.

In the accessible literature, numerous examinations have been done to predict the tooth wear of gear drives by changing the tooth profile. This variation in the tooth profile will cause changes in the tooth load distribution which will in turn lead to attrition of the tooth profile [1, 2]. Subsequently, it ends up vital to assess the wear profundity of the tooth profile during contact. Archard's [3] characterized a summed up equation for predicting the tooth wear during frictional sliding of the transmission system. The strength of the tooth profile during the bending in spur gear was studied and exploited by Andrews [4] using numerical analysis. The impact of load in sintered spur gear and the wear on the surface of the tooth was represented by Dhanasekaran and Gnanamoorthy in their study [5, 6]. Performance of a metallic involute spur gear drive was well predicted by Walton [7] under a dry and unlubricated condition and compared. Sivakumar et al. [8] directed an examination on the combat tracked vehicle(s), for enhancing the contact ratio of the transmission drive. The efficiency of non-standard normal contact ratio gears was obtained by Prabhu Sekar et al. [9] which aids the advantages of this improved bending strength drives. In all cases, just constrained investigation has been carried out on the removal of material from teeth surfaces of high contact ratio gear drive. In this work, an effort was carried out to predict the tooth wear depth by utilizing the method of altering the tooth thickness for different modules through finite element analysis.

2 Critical Contact Points of the Gear Teeth

In the course of power transmission, the full load (F_N) is shared by two consecutive teeth of the meshing spur gear for an instant of time (double pair contact regions—BC and DE) and for the remaining instant three teeth takes the full load (triple pair contacts regions—AB, CD and EF). Hence, it is important to get the critical contact point (Fig. 1) and its radial distance [10] which is given by Eqs. (1)–(6).

$$r_{\mathrm{HPTC}} = r_{\mathrm{ap}} \tag{1}$$

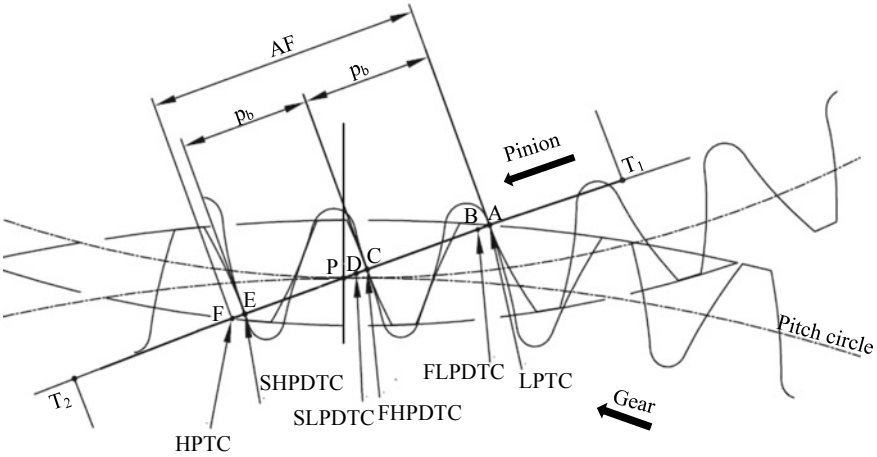

Fig. 1 Critical contact positions during meshing

$$r_{\text{SHPDTC}} = \sqrt{\left(\sqrt{r_{\text{ap}}^2 - r_{\text{bp}}^2} - AF + 2p_{\text{b}}\right)^2 + r_{\text{bp}}^2} \tag{2}$$

$$r_{\text{SLPDTC}} = \sqrt{\left(\sqrt{r_{\text{ap}}^2 - r_{\text{bp}}^2} - p_{\text{b}}\right)^2 + r_{\text{bp}}^2} \tag{3}$$

$$r_{\text{FHPDTC}} = \sqrt{\left(\sqrt{r_{\text{ap}}^2 - r_{\text{bp}}^2} - AF + p_{\text{b}}\right)^2 + r_{\text{bp}}^2} \tag{4}$$

$$r_{\text{FLPDTC}} = \sqrt{\left(\sqrt{r_{\text{ap}}^2 - r_{\text{bp}}^2} - 2p_{\text{b}}\right)^2 + r_{\text{bp}}^2} \tag{5}$$

$$r_{\text{LPTC}} = \sqrt{\left(\sqrt{r_{\text{ap}}^2 - r_{\text{bp}}^2} - AF\right)^2 + r_{\text{bp}}^2} \tag{6}$$

$$AF = \sqrt{r_{\text{ap}}^2 - r_{\text{bp}}^2} + \sqrt{r_{\text{ag}}^2 - r_{\text{bg}}^2} - a_0 \sin\ \alpha_0 \tag{7}$$

3 Methodology

3.1 FE Model of High Contact Ratio Transmission Drive

The fillet stress and contact pressure are assessed using FE analysis for which a code has been developed in Ansys Parametric Design Language (APDL). Bi-dimensional

five teeth model during contact (Fig. 2 and Table 1) with plain strain condition and four-noded quadrilateral elements (PLANE 42) with two degrees of freedom is assumed. CONTA172 (Contact) and TARGE169 (Target) is utilized for study from ANSYS. For this examination, the face width is taken uniform throughout the plane. Optimized edge length is found by performing a convergence study at the critical

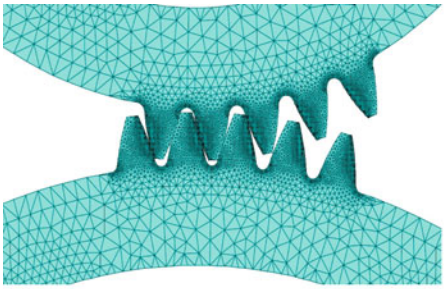

(a) Bi-Dimensional Model teeth during contact

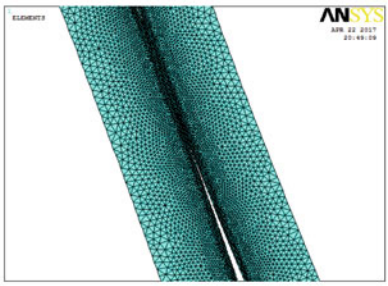

(b) Fine meshed region

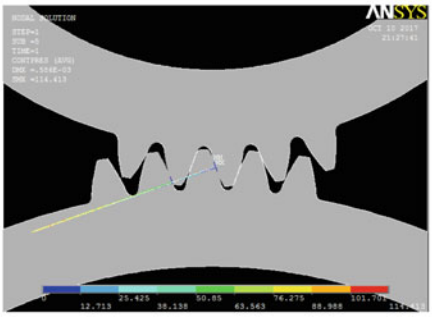

(b) Pressure distribution in contact point

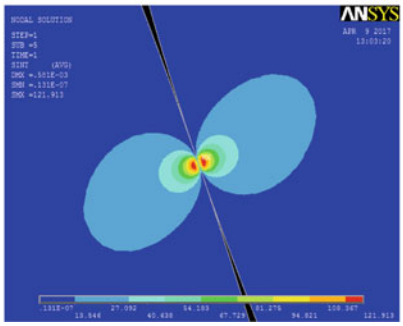

(b) Von Mises stress in contact point

Fig. 2 FE model of high contact ratio drive

Table 1 Input variables

Variables	Units	Symbols	Readings
Pressure angle	°	α_o	20°
Modulus of rigidity	GPa	E	210
Teeth number in pinion		z_p	50
Gear module	mm	m	1
Gear ratio		i	1.5
Addendum coefficient	mm	h_a	1.2
Poisson's ratio		ν	0.3
Input load	N	F_N	10
Input speed	rpm	N_p	500

regions of the gears. Rim portion of the gears is arrested in both the axis and the rim of the pinion is arrested only in the radial axis whereas in the other axis, the tangential force is applied in the rim.

3.2 *Prediction of Tooth Wear Depth*

Generalized equation by Anderson and Erikson [11] for calculating the tooth wear depth is specified as

$$h_{i,n} = h_{i,(n-1)} + J_{\mathrm{w}}(\sigma_{\mathrm{H}})_i \left(s_{\mathrm{p}}\right)_i \tag{8}$$

where

$J_{\mathrm{w}} = \frac{J}{H}$, wear coefficient—$5 \times 10^{-16}$ m^2/N [12]
h—wear depth

Sliding distance at any instant engagement point is by [12]

$$\left(s_{\mathrm{p}}\right)_i = 2a_i \left(\frac{\left(v_{\mathrm{p}}\right)_i - \left(v_{\mathrm{g}}\right)_i}{\left(v_{\mathrm{p}}\right)_i} \right) \tag{9}$$

Semi contact width (a_i) established during engagement along the contact path is specified as

$$a_i = \sqrt{\frac{4F_i}{\pi b} \frac{\frac{\left(1-\nu_{\mathrm{p}}^2\right)}{E_{\mathrm{p}}} + \frac{\left(1-\nu_{\mathrm{g}}^2\right)}{E_{\mathrm{g}}}}{\frac{1}{\left(R_{\mathrm{p}}\right)_i} + \frac{1}{\left(R_{\mathrm{g}}\right)_i}}} \tag{10}$$

Respective, peripheral velocity is known by

$$\left(v_{\mathrm{p}}\right)_i = \omega_{\mathrm{p}} \left(R_{\mathrm{p}}\right)_i \tag{11}$$

$$\left(v_{\mathrm{g}}\right)_i = \omega_{\mathrm{g}} \left(R_{\mathrm{g}}\right)_i \tag{12}$$

The radius of curvature at any instant engagement point is specified as [12].

$$\left(R_{\mathrm{p}}\right)_i = r_{\mathrm{op}} \sin \alpha_0 - X_i \tag{13}$$

$$\left(R_{\mathrm{g}}\right)_i = r_{\mathrm{og}} \sin \alpha_0 + X_i \tag{14}$$

Tooth profile layout with the coordinates is presented in Fig. 3. Equation (8) reveals the amount of wear depth after each working cycle. Totally 2000 working

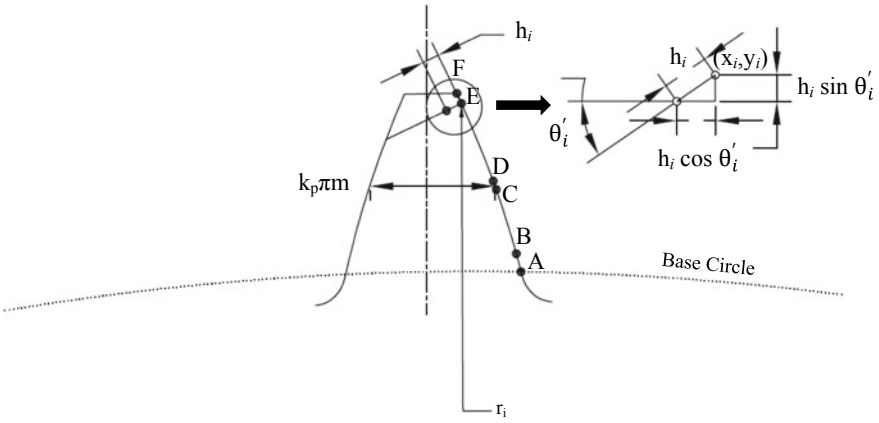

Fig. 3 Tooth layout with loading points

cycles is considered for the study in which the profile is updated periodically. Initial coordinates are specified as (x_i, y_i) and the worn out coordinates are mentioned as $\left(x_i', y_i'\right)$,

$$x_i' = x_i - h_i \cos\theta_i' \tag{15}$$

$$y_i' = y_i - h_i \sin\theta_i' \tag{16}$$

where

$$x_i = R_i \cos\theta_i$$
$$y_i = R_i \sin\theta_i$$

4 Optimization of Fillet Stress Through Profile Modification of Gear Tooth

In profile modification technique, the tooth thickness is modified along the reference line which is considered to be an effective technique in gear design as suggested by Prabhu Sekar and Muthuveerapan [13–15]. By varying the tooth thickness factor (k_p), the fillet stress of the pinion is optimized with respect to the gear. The tooth layout utilized for analysis and the critical points for the loading [10] in the wheel and pinion of high contact ratio gears engaged for finite element analysis are shown in Fig. 2. In this examination, the optimized fillet stress is accomplished between the gear drives by varying the thickness of the tooth at the pitch line. It is inferred that

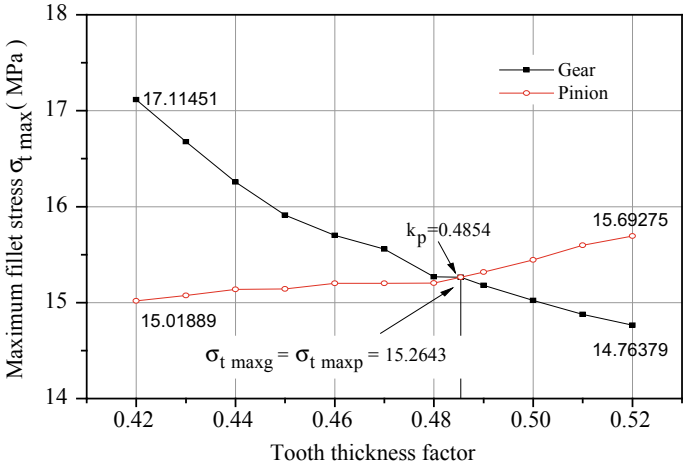

Fig. 4 Variation of fillet stress for tooth thickness

the unbalanced maximum fillet stresses begin to decrease with reduction in tooth thickness factor ($k_p = 0.42$) by which the required k_p for achieving the balanced fillet stress ($\sigma_{t\ max}$) decreases eventually. The optimum estimation point of tooth thickness factor (k_p) for attaining the balanced $\sigma_{t\ max}$ between the pinion and wheel is determined (Fig. 4). Maximum balanced stress at the fillet is achieved ($\sigma_{t\ maxp} = \sigma_{t\ maxg} = 15.269$ MPa) at $k_p = 0.4854$. Henceforth, the tooth load-carrying capacity of the spur gear drive is improved through the design modification suggested than the unbalanced one.

5 Effect of Module Over Wear Depth

The effect of module (m) on high contact ratio spur gear drive is examined for the increase of gear module ($m = 1$, 2 and 3) in optimized event. Along the contact path of instantaneous engagement points, the predicted values of load distribution of the gear drive, stress at the fillet region, contact pressure and wear depth are studied. While balancing the maximum bending stress for different module, the tooth thickness factor (k_p) is found to be constant because the ratio in which the size of the gear changes is also constant for increasing module. From Fig. 5b, it is evidenced a certain amount of decline in maximum balanced fillet stress for increasing module (Table 2) is observed as stated in Lewis equation where gear module is inversely proportional to fillet stress.

It is observed that the load share (Fig. 5a) is identical during the complete course of mesh cycle that is primarily because of the joint impact in constant bending moment arm and critical tooth thickness factor (k_p). As m increases, the contact pressure decreases during the total course of the work cycle due to the influence of the radius

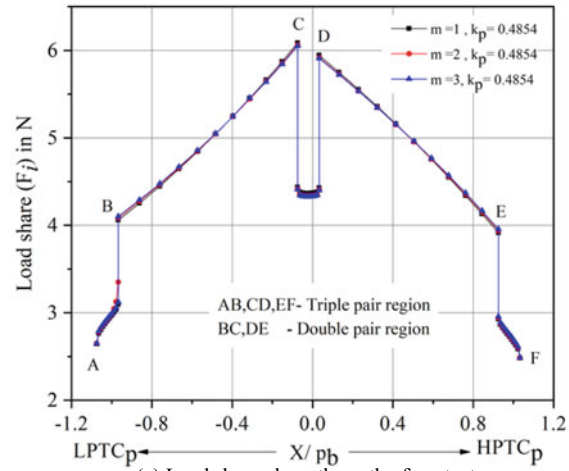

(a) Load share along the path of contact

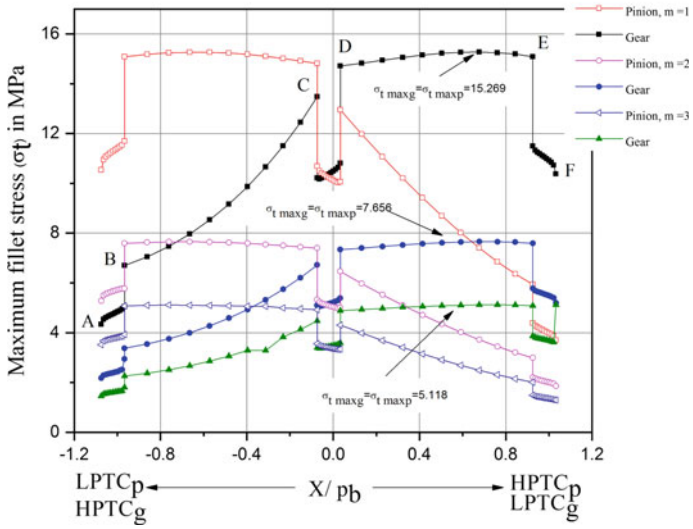

(b) $(\sigma_t)_{max}$ along the path of contact (for balanced stress)

Fig. 5 Effect of module on high contact ratio spur gear drive

of curvature (Fig. 5c). The accumulated wear depth reduces considerably along the contact path because of the reduced contact pressure and sliding distance. Thus, the material worn out from the pinion tooth surface is lower in the high contact ratio gear drive when the module increases (Fig. 5d).

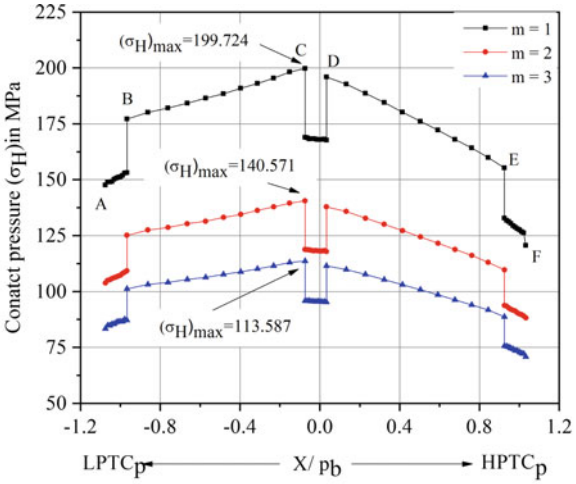

(c) Contact pressure (σ_H) along the path of contact

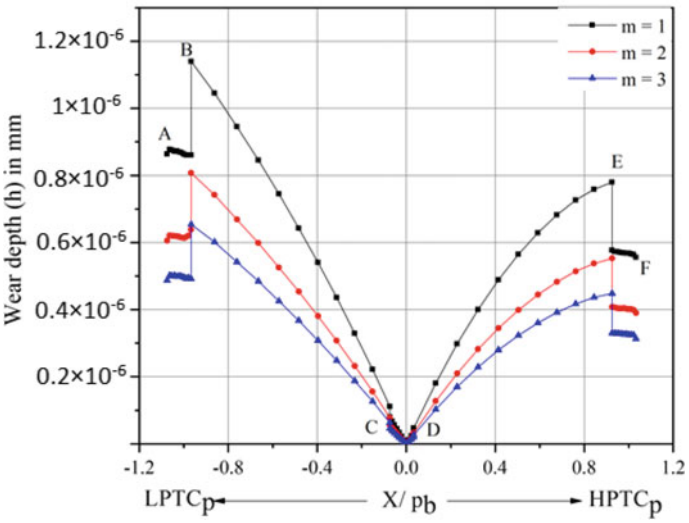

(d) Wear depth (h) along the path of contact

Fig. 5 (continued)

Table 2 Balanced fillet stresses for different modules

Module (m)	Balanced maximum fillet stress $(\sigma_t)_{max}$ MPa	Contact pressure $(\sigma_H)_{max}$ MPa
1	15.269	199.724
2	7.656	140.571
3	5.118	113.587

6 Conclusions

The maximum amount of material worn from the tooth surface on the high contact ratio spur gear drive (for optimized fillet stress) is assessed through the contact analysis and the subsequent conclusions have been brought down.

- In a transmission drive with a higher gear ratio, the bending strength of the wheel and pinion is not same which is optimized through profile modification.
- In increasing module, the balanced bending stress decreases since the critical tooth thickness of the teeth increases m number of times.
- There is a decrease in contact pressure observed during the complete course of the mesh cycle because of the increase in the radius of curvature.
- A high contact ratio gear drive with optimized stress in the fillet region has improved wear resistance for increasing gear module due to the influence of reduced contact pressure and fillet stress.

Acknowledgements Deepest gratitude of thanks to the INSPIRE Fellowship scheme of DST, Government of India for supporting with monetary assistance.

References

1. Tunalioglu MS (2011) A research of tooth profile damages in internal gears. Gazi University Institute of Science and Technology, Ankara, pp 1–5
2. Tunalioglu MS, Tuc B (2014) Theoretical and experimental investigation of wear in internal gears. Wear 309(1):208–215
3. Archard JF (1953) Contact of rubbing flat surfaces. J Appl Phys 24:981–988
4. Andrews JD (1991) A finite element analysis of bending stresses induced in external and internal involute spur gears. J Strain Anal 26(3):154–163
5. Dhanasekaran S, Gnanamoorthy R (2008) Gear tooth wear in sintered spur gears under dry running conditions. Wear 265(1):81–87
6. Imrek H, Düzcükoglu H (2007) Relation between wears and tooth width modification in spur gears. Wear 262:390–394
7. Walton D, Goodwin AJ (1998) The wear of unlubricated metallic spur gears. Wear 222:103–113
8. Sivakumar P, Gopinath K, Sundaresh S (2009) Performance evaluation of high-contact-ratio gearing for combat tracked vehicles—a case study. Proc Inst Mech Eng Part D J Automob Eng 224:631–643
9. Prabhu Sekar R, Geo VE, Jesu Martin L (2017) A mixed finite element and analytical method to predict load, mechanical power loss and improved efficiency in non-standard spur gear drives. J Eng Tribol Part J IMECHE (in press)
10. Thirumurugan R, Muthuveerappan G (2011) Critical loading points for maximum fillet and contact stresses in normal and high contact ratio spur gears based on load sharing ratio. Mech Based Des Struct Mach 39(1):118–141
11. Andersson S, Eriksson B (1990) Prediction of the sliding wear of spur gears. Proc NORDTRIB 90
12. Flodin A, Andersson S (1997) Simulation of mild wear in spur gears. Wear 207:16–23

13. Prabhu Sekar R, Muthuveerappan G (2014) A balanced maximum fillet stresses on normal contact ratio spur gears to improve the load carrying capacity through non-standard gears. Mech Based Des Struct Mach 43:150–163
14. Ravivarman R, Palaniradja K, Prabhu Sekar R (2018) Evolution of balanced root stress and tribological properties in high contact ratio spur gear drive. Mech Mach Theory 126:491–513
15. Ravivarman R, Palaniradja K, Prabhu Sekar R (2018) Influence of gear ratio on wear depth of nonstandard HCR spur gear drive with balanced fillet stress. Mater Today Proc 5:17350–17359

Force Estimation on a Clamped Plate Using a Deterministic–Stochastic Approach

Akash Shrivastava and Amiya R. Mohanty

Abstract Here, a model-based force estimation technique is presented for a clamped plate. The present technique uses a deterministic–stochastic technique to estimate unknown forces acting at known locations. This approach requires a modally reduced-order model and limited measurements of structural response to unknown forces. Numerical examples are presented for a clamped plate with different loading conditions. Gaussian noise is added in the response obtained from the full-order finite element model. The responses at unmeasured locations are predicted using system equivalent reduction expansion process (SEREP). The effects of the number of measurement and measurement noise level are shown. The results show that the proposed technique can successfully be used for force estimation of plate type structures.

Keywords Kalman filter · Force estimation · Finite element method · SEREP · Reduced-order model

1 Introduction

The forward and inverse problems are two important areas of research in structural dynamics. In the forward problem, the governing differential equations are solved to obtain structural responses for known forces and constraints. In the inverse problem approach, the excitation forces or structural parameters are obtained, which are difficult to measure directly. The regularization and statistical inversion [1] are two types of approaches to solving an inverse problem.

The most common engineering structures are plates, and their analysis is important in the fields of civil, mechanical, and aerospace engineering. The plate structures are often exposed to different loading environments. There are plenty of techniques

A. Shrivastava (✉) · A. R. Mohanty
Acoustics and Condition Monitoring Laboratory, Mechanical Engineering Department, Indian Institute of Technology, Kharagpur 721302, India
e-mail: shri.aka1990@gmail.com

A. R. Mohanty
e-mail: amohanty@mech.iitkgp.ernet.in

B. N. Singh et al. (eds.), *Recent Advances in Theoretical, Applied, Computational and Experimental Mechanics*, Lecture Notes in Mechanical Engineering,
https://doi.org/10.1007/978-981-15-1189-9_21

proposed by the researchers to solve a forward problem, e.g., obtaining strains, stresses for known forces. However, limited research work has been done in the field of the inverse problem. There are some deterministic kinds of solutions are proposed to solve inverse problems. In the last two decades, the deterministic–stochastic type approaches are proposed for unknown input estimation.

Here, a deterministic–stochastic type unknown force estimation technique is presented that uses a mathematical model of the system under consideration and system equivalent reduction expansion process (SEREP). Therefore, these techniques are now briefly reviewed.

To estimate unknown input, a Kalman filter-based technique is presented by Tuan et al. [2]. Later, this technique was applied for the estimation of external forces acting on beam [3] and plate [4] type structures. This algorithm consists of two parts, in the first part innovations and gains are calculated, and in the second part, the inputs are estimated using the recursive least-square algorithm. This technique requires a fading (or forgetting) factor 'γ' in the second step, which compromises between fast adaptive capability and loss of estimation accuracy and set to a value between 0 and 1. Later, a modification was presented for 'γ' using fuzzy logic inference [5]. In all the available literature of this technique, either single degree-of-freedom model, full-order finite element model [3], or experimentally identified model [4] are used. Finite element modeling is widely used to analyze engineering structures, e.g., plate. The full-order finite element model requires measurements of all the degrees-of-freedom. However, in a practical situation, only limited response measurements are available. Lourense et al. [6] presented an online unknown input estimation technique for force identification using limited output measurements, where modal parameters (natural frequency, modal damping) were used to form a mathematical model of the system. Recently, authors of the present paper have used a reduced-order model of the rotor system for unbalance [7] and strain estimation [8]. Authors of the present paper have also proposed a technique for force estimation in the clamped plate using reduced-order model [9] where the bandwidth of the force is limited by the number of modes considered in the system model and the number of modes depends upon the number of response measurements. To circumvent this issue the SEREP [10] method is used in the present work to obtain approximate responses at unmeasured locations and to increase the bandwidth of forces to be identified.

The aim of this work is to provide an efficient approach to estimate unknown inputs on a plate using reduced-order model. The paper is structured as follows. Section 2 consists of formulations that are used for force estimation. Numerical simulations are presented for a clamped steel plate in Sect. 3. In Sect. 4, the results and discussion are presented. Finally, conclusions are presented in Sect. 5.

2 Formulations

2.1 State-Space Modeling

The present technique uses state-space modeling of the system. The equation of motion of a linear dynamic system can be described by Eq. (1)

$$M\ddot{z}(t) + C\dot{z}(t) + Kz(t) = S_f f(t) \tag{1}$$

where M, C, and K are the mass, damping, and stiffness matrices, respectively. Matrix S_f is the force selection matrix, and $f(t)$ is the external force vector. The physical displacement, velocity, and acceleration are represented by $z(t)$, $\dot{z}(t)$ and $\ddot{z}(t)$, respectively.

Using coordinate transformation $z(t) = \Phi p(t)$ and premultiplying Φ^T in Eq. (1) we obtain [6]

$$\Phi^T M \Phi \ddot{p}(t) + \Phi^T C \Phi \dot{p}(t) + \Phi^T K \Phi p(t) = \Phi^T S_f f(t) \tag{2}$$

where matrix Φ contains modal vectors and $p(t)$ is the modal coordinates.

For mass-normalized eigenvectors Φ, following expression holds,

$$\Phi^T M \Phi = I,\ \Phi^T K \Phi = \Omega^2,\ \Phi^T C \Phi = \Gamma$$

where I represents unity matrix of appropriate dimension, Ω^2 is a diagonal matrix containing undamped eigenfrequencies ω_i, and the matrix Γ contains $2\varsigma_i\omega_i$ in its diagonal, ς_i represents ith modal damping ratio.

Now consider modal displacements and velocities as states, i.e. $x(t) = \left\{ p \ \dot{p} \right\}^T$, the state-space representation of Eq. (2) can be given as

$$\begin{aligned} \dot{x}(t) &= A_c x(t) + B_c f(t) \\ y(t) &= G_c x(t) \end{aligned} \tag{3}$$

where A_c, B_c, and G_c are state transition matrix, input influence matrix, and output matrix, respectively, and these matrices are defined as,

$$A_c = \begin{bmatrix} 0 & I \\ -\Omega^2 & -\Gamma \end{bmatrix}, \quad B_c = \begin{bmatrix} 0 \\ M^{-1} S_f \end{bmatrix}, \quad G_c = \begin{bmatrix} S_d \Phi & S_v \Phi \end{bmatrix}$$

Output vector $y(t)$ consists of displacements and/or velocities. Matrices S_d and S_v represent selection matrices for displacements and velocities, respectively. The discrete time equivalent of Eq. (3) can be written as

$$x_{n+1} = Ax_n + Bf_n$$

$$y_n = Gx_n \tag{4}$$

where n represents time-index. Matrices A, B, and G are the discrete time equivalent of matrices A_c, B_c, and G_c, respectively.

Use of the reduced-order model provides a two-fold advantage: it allows the use of available measurements for limited degrees-of-freedom and it reduces the computational time. A reduced-order model of the system is obtained by selecting the dominant modes that adequately describe the system's behavior. In this case, only a few mode shape vectors (Φ_r) and corresponding natural frequencies (Ω_r) are used in Eq. (3).

2.2 The Kalman Filter and Recursive Least-Square (KF-RLS) Based Input Estimation

The linear dynamic system with modeling and measurement errors can be described by following set of equations,

$$\begin{aligned} x_{n+1} &= Ax_n + Bf_n + w_n \\ y_n &= Gx_n + v_n \end{aligned} \tag{5}$$

where w_n and v_n are the random Gaussian noise vectors correspond to process and measurement noise with known covariance Q and R, respectively.

The KF-RLS based input force estimation technique is presented in Table 1, for detailed derivation refer the reader to Ref. [2]. The initial state and error estimates are assumed to be known. The innovation covariance $\mathrm{S}(n)$, Kalman gain $K_a(n)$, and innovation $\overline{Z}(n)$ are identified in the first step and used in the second step for the estimation of force, which is represented by $\widehat{F}(n)$.

3 Numerical Example

A clamped plate is considered here for the verification of the present approach. Finite element model of the plate is shown in Fig. 1, and Table 2 summarizes plate's properties. The Kirchhoff plate theory is used in the finite element modeling with a 4-noded quadrilateral finite element.

The following steps are followed in numerical simulations:

1. The displacement response is obtained using Eq. (4) for known transverse force acting at a particular location.
2. Noisy response is simulated by adding Gaussian random noise (y_{rand}), the added noise can be expressed as, $y_{\text{rand}} = N_{\text{L}} \times y_{\text{std}} \times r$, where N_{L} is the percentage

Table 1 Equations for input estimation based on KF-RLS algorithm [2]

Initialization
Initial state, $\hat{x}_0 = \mathrm{E}[x_0]$
Initial error covariance, $P_0^x = \mathrm{E}[(x - \hat{x}_0)^T]$
Simple Kalman filter
$\bar{x}(n/n-1) = A\bar{x}(n-1/n-1)$
$P(n/n-1) = AP(n-1/n-1)A^T + Q$
$S(n) = GP(n/n-1)G^T + R$
$K_a(n) = P(n/n-1)G^T S^{-1}(n)$
$P(n/n) = [I - K_a(n)G]P(n/n-1)$
$\overline{Z}(n) = y(n) - G\bar{x}(n/n-1)$
$\bar{x}(n/n) = \bar{x}(n/n-1) + K_a(n)\overline{Z}(n)$
Recursive least-square
$B_s(n) = G[AM_s(n-1) + I]B$
$M_s(n) = [I - K_a(n)C][AM_s(n-1) + I]$
$K_b(n) = \gamma^{-1} P_b(n-1)B_s^T(n)[B_s(n)\gamma^{-1} P_b(n-1)B_s^T(n) + S(n)]^{-1}$
$P_b(n) = [I - K_b(n)B_s(n)\gamma^{-1} P_b(n-1)]$
$\widehat{F}(n) = \widehat{F}(n-1) + K_b(n)[\overline{Z}(n) - B_s(n)\widehat{F}(n-1)]$

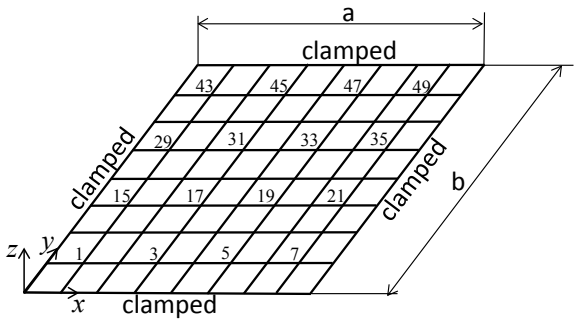

Fig. 1 Finite element model of a clamped plate with node numbering

Table 2 Material, physical, and modal properties of clamped steel plate

Length (a) (mm)	Width (b) (mm)	Thickness (mm)	Density (kg/m^3)	Young's modulus (GPa)	First four natural frequencies (Hz)
150	150	2.5	7800	210	954.6, 1940, 1940, 2793.2

noise level, y_{std} is the standard deviation of the exact response, and r is random sequences with zero mean and unit variance.

3. Force identification is performed using proposed approach.

The following parameters are selected in all the cases presented in next section: null initial conditions, sampling frequency is 20,000 Hz, fading factor $\gamma = 0.1$. Process noise is not considered and the measurement noise covariance R can be calculated as $(N_{\text{L}} \times y_{\text{std}})^2$.

The normalized mean square error between the true and estimated force has been used to quantify the estimation accuracy,

$$\text{Error}\,(\%) = 100 \times \frac{\sqrt{\sum_{i=1}^{N} (f(i) - \widehat{F}(i))^2}}{\sqrt{\sum_{i=1}^{N} f(i)^2}}$$

4 Results and Discussions

In the first example, three different measurement sets are used to estimate a low-velocity impact applied at node 17. First two modes are used to form reduced-order model, and the displacement responses with 5% measurements noise level are used. It is clear from Fig. 2 that the accuracy of estimated force is increased when more number of simulated responses is included in the output vector. Here, the simulated response means the response obtained by solving full-order finite element model, and the predicted response means the response obtained by expanding simulated response using SEREP method.

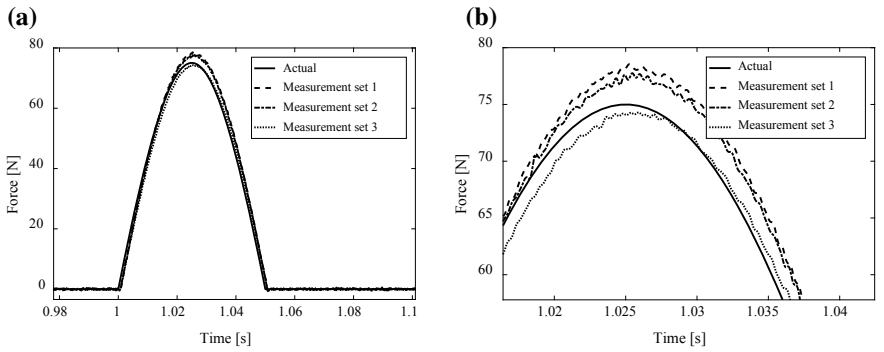

Fig. 2 **a** The plot of true and estimate impact force at node 17, **b** zoomed portion of (**a**) (details of measurement sets are given in Table 3)

Table 3 Normalized mean square error for three different measurement sets used to estimate low-velocity impact at node 17 (measurement noise level N_L is 5%)

Measurement sets	Node numbers	NMSE (%)	
		Simulated responses	Predicted responses using SEREP[a]
1	17,25	4.68	3.28
2	17, 25, 27, 33	3.82	6.95
3	17, 25, 27, 33, 24, 31	2.05	7.62

[a]Responses are predicted using simulated responses at node 17, 25, and first two modes

In Table 3, normalized mean square errors are presented for different cases where simulated, and predicted responses are used for force estimation. It can be observed that the error decreases when the number of simulated response is increased. But, when predicted responses from SEREP are used, the error is increased. This loss of accuracy is due to the error present in predicted responses. However, the percentage NMSE is below 10%, and only two simulated responses (at node 17 and 25) are used to form all the measurement sets. For the sampling frequency of 20,000 Hz, the estimated force convergences to the actual force within 450 time-steps. Effect of reduced-order modeling on converges and CPU time for different sampling frequencies is presented in Ref. [9].

In another example, random load acting at node 17 is estimated from predicted responses at nodes 17 and 25 using simulated responses at nodes 9 and 19. The simulated and predicted response at node 25 is shown in Fig. 3. It can be observed that the predicted response matches well with the simulated response. The actual and estimated force is shown in Fig. 4 for different measurement noise levels.

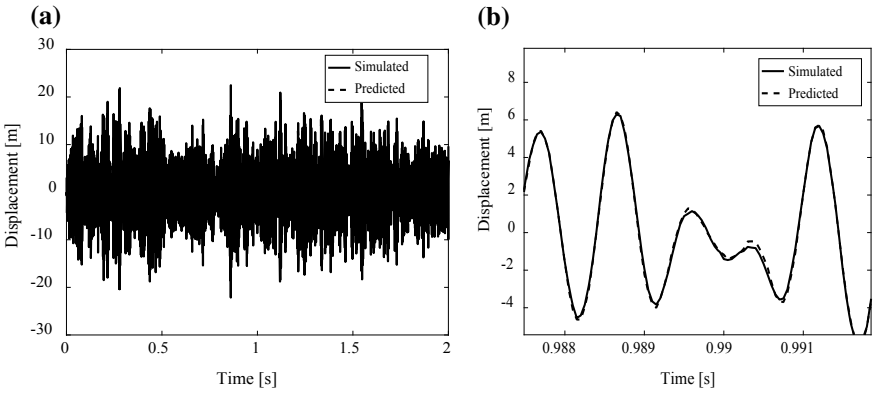

Fig. 3 **a** Time history and **b** details of simulated and predicted (using SEREP) displacement at node 25 due to a random load applied at node 17 (for prediction, response at nodes 9, 19, and first two modes are considered)

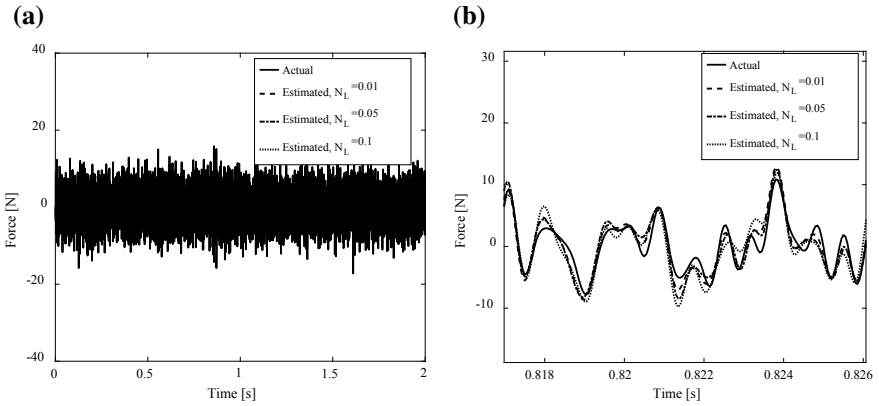

Fig. 4 **a** The plot of true and estimated random force at node 17, **b** zoomed portion of (**a**)

Now, a case of sinusoidal load is presented where a harmonic load of frequency 500 Hz is acting at node 17 and estimated using predicted responses at nodes 17 and 25. The predicted responses and estimated force are presented in Figs. 5 and 6, respectively. It can be seen that the estimated force follows well the actual force. In this case, the percentage NMSE errors are 4.45, 5.26, and 7.17 for measurement noise level of 1, 5, and 10%, respectively.

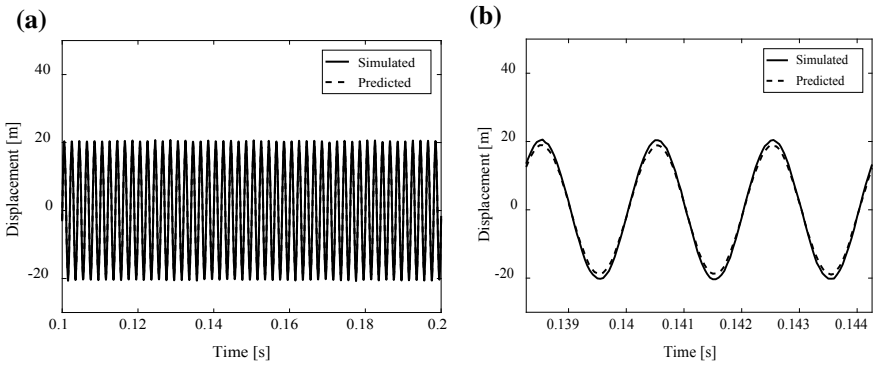

Fig. 5 **a** Time history and **b** details of simulated and predicted (using SEREP) displacement at node 25 due to a sinusoidal load applied at node 17 (for prediction, response at nodes 9, 19, and first two modes are considered)

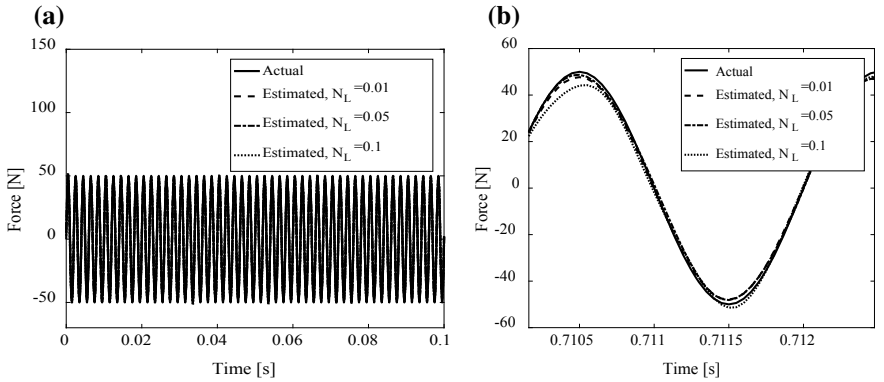

Fig. 6 **a** The plot of true and estimated sinusoidal force at node 17, **b** zoomed portion of (**a**)

5 Conclusions

In this paper, a Kalman filter-based input estimation technique is used for force identification on a clamped plate. Full-order finite element model is used in numerical simulations for response generation and the SEREP technique is used for response prediction. The proposed approach uses a reduced-order model of the dynamic system. The proposed approach has been verified for different types of loads and measurement noise levels.

The following conclusions can be drawn from the present study:

1. The Kalman filter and recursive least-square technique can be used to estimated external transverse forces acting on plate type structures. Based on the obtained results, it can be concluded that all kinds of loads can be estimated using the present approach.
2. The SEREP technique can be used to predict responses prior to force estimation, which can further reduce the number of response measurements. However, it is found that the use of predicted response in force estimation causes an increase in estimation error.

A force location identification technique is expected to combine with the present approach to make it more effective. As future work, the proposed approach can be verified experimentally.

References

1. Jari K, Somersalo E (2006) Statistical and computational inverse problems. Springer Science & Business Media
2. Tuan PC, Ji CC, Fong LW, Huang WT (1996) An input estimation approach to on-line two-dimensional inverse heat conduction problems. Numer Heat Tr A-Appl 29(3):345–363

3. Ma CK, Chang JM, Lin DC (2003) Input forces estimation of beam structures by an inverse method. J Sound Vib 259(2):387–407
4. Liu JJ, Ma CK, Kung IC, Lin DC (2000) Input force estimation of a cantilever plate by using a system identification technique. Comput Methods Appl Mech Eng 190(11):1309–1322
5. Lee MH, Chen TC (2010) Intelligent fuzzy weighted input estimation method for the input force on the plate structure. Struct Eng Mech 11(1):1
6. Lourens E, Papadimitriou C, Gillijns S, Reynders E, De Roeck G, Lombaert G (2012) Joint input-response estimation for structural systems based on reduced-order models and vibration data from a limited number of sensors. Mech Syst Signal Process 29:310–327
7. Shrivastava A, Mohanty AR (2017) Detection of unbalance in a rotor-bearing system using a deterministic-stochastic approach. 24th ICSV, London, UK
8. Shrivastava A, Mohanty AR, Pekpe K, Cassar J (2017) Estimation of strain in a rotating shaft using deterministic-stochastic approach. 1st ICEASSM Accra, Ghana
9. Shrivastava A, Mohanty AR (2019) Kalman filter-based force estimation in a clamped plate using reduced order model and noisy measurements. Inverse Prob Sci Eng 27(8):1–24
10. Baqersad J, Niezrecki C, Avitabile P (2015) Extracting full-field dynamic strain on a wind turbine rotor subjected to arbitrary excitations using 3D point tracking and a modal expansion technique. J Sound Vib 352:16–29

Dynamic Analysis of Composite Cylinders Using 3-D Degenerated Shell Elements

Pratik Tiwari, Dipak Kumar Maiti and Damodar Maity

Abstract This paper deals with the formulation of an 8-noded degenerated shell finite element for modeling and analysis of laminated composite shell structures. A MATLAB code has been developed based on the formulation to analyze the composite shell structures. The formulation is capable of solving both plate and shell structures. Use of degenerated shell elements allows the formulation to be used for any type of shells with various shapes and thickness ratios. The formulation is also capable of solving isotropic and laminated composite materials. The formulation developed has been validated with the results available in open literatures and software (ANSYS).

Keywords 8-noded elements · Degenerated shells · MATLAB · Laminated composite shell

1 Introduction

Shells with variable thickness have extensively been used in many fields such as aerospace, rocket, aviation, and submarine technology. Over the years much research has been conducted in attempts to produce precise, competent, and reliable shell elements. Various shell theories have been developed, over the years, based on the thickness of the shells.

Three separate classes of shell elements have been widely used for analyzing shell structures: flat elements, curved shell elements, and degenerated shell elements. Flat, plate-like elements which approximate the curved shell by a faceted surface, hence

P. Tiwari (✉) · D. K. Maiti
Department of Aerospace Engineering, IIT Kharagpur, Kharagpur, India
e-mail: pratik@iitkgp.ac.in

D. K. Maiti
e-mail: dkmaiti@aero.iitkgp.ernet.in

D. Maity
Department of Civil Engineering, IIT Kharagpur, Kharagpur, India
e-mail: dmaity@civil.iitkgp.ernet.in

B. N. Singh et al. (eds.), *Recent Advances in Theoretical, Applied, Computational and Experimental Mechanics*, Lecture Notes in Mechanical Engineering,
https://doi.org/10.1007/978-981-15-1189-9_22

sometimes called facet elements, show completely uncoupled behavior between in-plane stretching and bending. The coupling between in-plane stretching and bending only appears indirectly by linking adjacent elements through the nodal degrees of freedom. These elements are not preferred due to shortcomings such as the absence of curvature of the elements within the element. Also, slope discontinuity between neighboring plate elements can generate bending moments in the sections of structure where they do not exist. The interior of the individual elements will not have any coupling between bending effects and membrane effects due to curvature of shell. Curved shell elements are founded on several shell theories which are also quite popular. These elements have various limitations due to fact that the shell theories are not consistent with each other. Also, it is very difficult to find appropriate deformation idealizations where truly strain-free rigid body movements are allowed. The degenerated shell element is not based on any of the available shell theories and can be applied over a wide range of thicknesses and curvatures. The degenerate solid approach is used to develop this element, which is formulated on Reissner–Mindlin assumptions where, the shear deformation and rotary inertia effect of the shell is considered in the formulation and the 3D field is reduced to a 2D field in form of mid-surface nodal variables.

In the late sixties, Ahmad et al. [1] developed a Mindlin-type, degenerated, curved shell element which is quite competent as well as effortless. It can be used for any arbitrary shape and does not depend upon any specific shell theory. In order to eliminate shear and membrane locking, Zeinkiewicz et al. [2] improved the degenerated shell element developed by Ahmad et al. [1], by reducing the order of numerical integration. Huang & Hinton [3] presented a new nine node degenerated shell element formulation. To avoid locking phenomena, they proposed the assumed strain method where an enhanced interpolation of the transverse shear strains in the natural co-ordinate system is used. The nine-node degenerated shell element formulation developed by Huang and Hinton [3] was later extended by Jayashankar et al. [4] to conduct free vibration analysis of thick laminated composites. Because the degenerated shell element formulation works well for both thick and thin shells, nine-noded degenerated shell element was preferred over conventional solid elements for the modeling and analysis of laminated composite shell structures. Balamurugan and Narayanan [5] developed a nine-noded degenerate shell finite element model for the vibration and active vibration control of piezo-laminated composite plates and shells bonded with piezoelectric sensor and actuator layers.

Most of the research that has been done on degenerated shells is focused on the static analysis of structures such as dams, tanks, and dome, etc. Very less work is done on dynamic analysis using degenerated shells and fewer on the dynamic analysis of composite structures using degenerated shells. The main objective of this paper is to develop a MATLAB code for dynamic analysis of composite cylindrical shell using 3-D degenerated element which can accurately solve different types of shells and plates with both isotropic and composite materials.

2 Methodology

Some of the important aspects of the standard finite element scheme under plane strain platform are outlined in the following sub-sections.

2.1 3-D Degenerated Shell Element

In present study, we have considered an 8-noded degenerated shell element with natural coordinate system (ξ, η, ζ), which is defined by the element geometry and not by the element orientation in the global coordinate system. The natural elements are scaled such that the sides of the parent elements are defined by $\xi = \pm 1$, $\eta = \pm 1$ and $\zeta = \pm 1$. A 16-noded solid shell element and equivalent 8-noded degenerated shell element is shown in Fig 1.

Above element is similar to 8-noded serendipity element so we can use same shape function as the serendipity element.

$$\begin{aligned} N_1 &= \frac{(1-\xi)(1-\eta)(-\xi-\eta-1)}{4}; & N_5 &= \frac{(1+\xi)(1+\eta)(\xi+\eta-1)}{4}; \\ N_2 &= \frac{\left(1-\xi^2\right)(1-\eta)}{2}; & N_6 &= \frac{\left(1-\xi^2\right)(1+\eta)}{2}; \\ N_3 &= \frac{(1+\xi)(1-\eta)(\xi-\eta-1)}{4}; & N_7 &= \frac{(1-\xi)(1+\eta)(-\xi+\eta-1)}{4}; \\ N_4 &= \frac{(1+\xi)\left(1-\eta^2\right)}{2}; & N_8 &= \frac{(1-\xi)\left(1-\eta^2\right)}{2}; \end{aligned} \tag{1}$$

A point in the element can be represented as

$$\begin{Bmatrix} x \\ y \\ z \end{Bmatrix} = \sum N_i(\xi, \eta) \left[\begin{Bmatrix} x_i \\ y_i \\ z_i \end{Bmatrix} + \frac{\zeta}{2} V_{3i} \right] \tag{2}$$

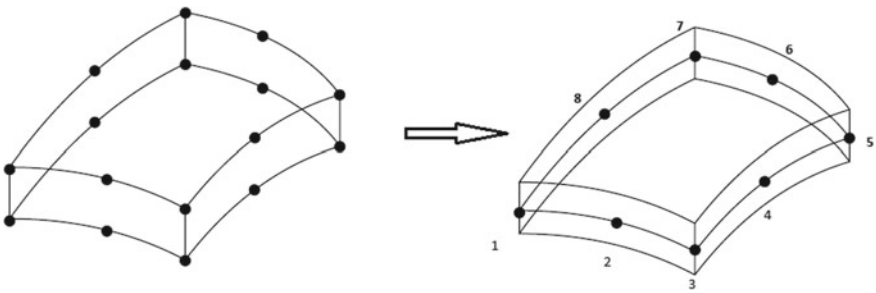

Fig. 1 A 16-noded solid shell element and equivalent 8-noded degenerated shell element

where,

$$\begin{Bmatrix} x_i \\ y_i \\ z_i \end{Bmatrix} = \frac{1}{2}\left[\begin{Bmatrix} x_i \\ y_i \\ z_i \end{Bmatrix}_{\text{top}} + \begin{Bmatrix} x_i \\ y_i \\ z_i \end{Bmatrix}_{\text{bottom}} \right] \quad \text{and} \quad V_{3i} = \begin{Bmatrix} x_i \\ y_i \\ z_i \end{Bmatrix}_{\text{top}} - \begin{Bmatrix} x_i \\ y_i \\ z_i \end{Bmatrix}_{\text{bottom}} \tag{3}$$

For thin structures, it is convenient to replace V_{3i} by a unit vector v_{3i}. Thus equation changes to

$$\begin{Bmatrix} x \\ y \\ z \end{Bmatrix} = \sum N_i(\xi, \eta)\left[\begin{Bmatrix} x_i \\ y_i \\ z_i \end{Bmatrix} + \frac{\zeta}{2} t_i v_{3i} \right] \tag{4}$$

where, t_i is the thickness of the shell at node i.

The displacement field, in the element, can be represented as

$$\begin{Bmatrix} u \\ v \\ w \end{Bmatrix} = \sum N_i(\xi, \eta)\left[\begin{Bmatrix} u_i \\ v_i \\ w_i \end{Bmatrix} + \frac{\zeta t_i}{2} [-v_{2i} \; v_{1i}] \begin{Bmatrix} \alpha \\ \beta \end{Bmatrix} \right] \tag{5}$$

where v_{2i}, v_{1i}, α and β are unit vectors in y and x directions and rotations in x and y directions respectively as shown in Fig. 2.

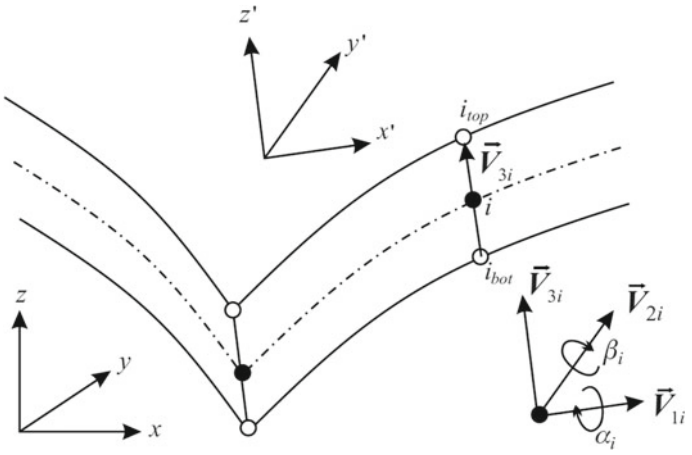

Fig. 2 Local and global coordinates of a middle surface shell element

2.2 Strain Definitions

Strain definitions are needed to find strain displacement matrix $[B]$. Since the elements have different coordinate system from global coordinates, we need strains in local coordinates by converting global strains to local strains.

$$\{\varepsilon'\} = \begin{Bmatrix} \varepsilon'_x \\ \varepsilon'_y \\ \gamma'_{xy} \\ \gamma'_{yz} \\ \gamma'_{xz} \end{Bmatrix} = \begin{Bmatrix} \frac{\partial u'}{\partial x'} \\ \frac{\partial v'}{\partial y'} \\ \frac{\partial u'}{\partial y'} + \frac{\partial v'}{\partial x'} \\ \frac{\partial v'}{\partial z'} + \frac{\partial w'}{\partial y'} \\ \frac{\partial u'}{\partial z'} + \frac{\partial w'}{\partial x'} \end{Bmatrix} \tag{6}$$

Also

$$\frac{\partial u'}{\partial x'} = \frac{\partial u'}{\partial x}\frac{\partial x}{\partial x'} + \frac{\partial u'}{\partial y}\frac{\partial y}{\partial x'} + \frac{\partial u'}{\partial z}\frac{\partial z}{\partial x'} \quad \text{and} \quad \frac{\partial u'}{\partial x} = \frac{\partial u}{\partial x}\frac{\partial u'}{\partial u} + \frac{\partial v}{\partial x}\frac{\partial u'}{\partial v} + \frac{\partial w}{\partial x}\frac{\partial u'}{\partial w}$$

where $\frac{\partial x}{\partial x'}, \frac{\partial y}{\partial x'}, \frac{\partial z}{\partial x'}, \frac{\partial x}{\partial y'}, \frac{\partial y}{\partial y'}, \ldots$. and $\frac{\partial u'}{\partial u}, \frac{\partial u'}{\partial v}, \frac{\partial u'}{\partial w}, \frac{\partial v'}{\partial u}, \frac{\partial v'}{\partial v}, \ldots$. are direction cosines between global and local coordinate system.

Solving Eq. (6) using Eq. (7), we get

$$\begin{Bmatrix} \varepsilon'_x \\ \varepsilon'_y \\ \gamma'_{xy} \\ \gamma'_{yz} \\ \gamma'_{xz} \end{Bmatrix} = \underbrace{\begin{bmatrix} l_x^2 & m_x^2 & n_x^2 & l_x m_x & m_x n_x & l_x n_x \\ l_y^2 & m_y^2 & n_y^2 & l_y m_y & m_y n_y & l_y n_y \\ 2l_x l_y & 2m_x m_y & 2n_x n_y & l_x m_y + l_y m_x & m_x n_y + m_y n_x & l_x n_y + l_y n_x \\ 2l_y l_z & 2m_y m_z & 2n_y n_z & l_y m_z + l_z m_y & m_y n_z + m_z n_y & l_y n_z + l_z n_y \\ 2l_x l_z & 2m_x m_z & 2n_x n_z & l_z m_x + l_x m_z & m_z n_x + m_x n_z & l_z n_x + l_x n_z \end{bmatrix}}_{[T]} \begin{Bmatrix} \varepsilon_x \\ \varepsilon_y \\ \varepsilon_z \\ \gamma_{xy} \\ \gamma_{yz} \\ \gamma_{xz} \end{Bmatrix} \tag{7}$$

Here $l_x, l_y, l_z, m_x, \ldots$ are the direction cosines which can be calculated using the Jacobian matrix of the element.

$$(n_x, n_y, n_z) = \left(\frac{dx}{d\xi}, \frac{dy}{d\xi}, \frac{dz}{d\xi}\right) \times \left(\frac{dx}{d\eta}, \frac{dy}{d\eta}, \frac{dz}{d\eta}\right) \tag{8}$$

$$(l_x, l_y, l_z) = \frac{(n_x, n_y, n_z)}{|(n_x, n_y, n_z)|} \tag{9}$$

$$(m_x, m_y, m_z) = (n_x, n_y, n_z) \times (l_x, l_y, l_z) \tag{10}$$

Global strains can be written as

$$\begin{Bmatrix} \varepsilon_x \\ \varepsilon_y \\ \varepsilon_z \\ \gamma_{xy} \\ \gamma_{yz} \\ \gamma_{xz} \end{Bmatrix} = \underbrace{\begin{bmatrix} \frac{\partial \xi}{\partial x} & \frac{\partial \eta}{\partial x} & \frac{\partial \zeta}{\partial x} & 0 & 0 & 0 & 0 & 0 & 0 \\ 0 & 0 & 0 & \frac{\partial \xi}{\partial y} & \frac{\partial \eta}{\partial y} & \frac{\partial \zeta}{\partial y} & 0 & 0 & 0 \\ 0 & 0 & 0 & 0 & 0 & 0 & \frac{\partial \xi}{\partial z} & \frac{\partial \eta}{\partial z} & \frac{\partial \zeta}{\partial z} \\ \frac{\partial \xi}{\partial y} & \frac{\partial \eta}{\partial y} & \frac{\partial \zeta}{\partial y} & \frac{\partial \xi}{\partial x} & \frac{\partial \eta}{\partial x} & \frac{\partial \zeta}{\partial x} & 0 & 0 & 0 \\ 0 & 0 & 0 & \frac{\partial \xi}{\partial z} & \frac{\partial \eta}{\partial z} & \frac{\partial \zeta}{\partial z} & \frac{\partial \xi}{\partial y} & \frac{\partial \eta}{\partial y} & \frac{\partial \zeta}{\partial y} \\ \frac{\partial \xi}{\partial z} & \frac{\partial \eta}{\partial z} & \frac{\partial \zeta}{\partial z} & 0 & 0 & 0 & \frac{\partial \xi}{\partial x} & \frac{\partial \eta}{\partial x} & \frac{\partial \zeta}{\partial x} \end{bmatrix}}_{[\text{Jac}]} \begin{Bmatrix} \frac{\partial u}{\partial \xi} \\ \frac{\partial u}{\partial \eta} \\ \frac{\partial u}{\partial \zeta} \\ \frac{\partial v}{\partial \xi} \\ \frac{\partial v}{\partial \eta} \\ \frac{\partial v}{\partial \zeta} \\ \frac{\partial w}{\partial \xi} \\ \frac{\partial w}{\partial \eta} \\ \frac{\partial w}{\partial \zeta} \end{Bmatrix} \tag{11}$$

where,

$$\begin{Bmatrix} \frac{\partial u}{\partial \xi} \\ \frac{\partial u}{\partial \eta} \\ \frac{\partial u}{\partial \zeta} \\ \frac{\partial v}{\partial \xi} \\ \frac{\partial v}{\partial \eta} \\ \frac{\partial v}{\partial \zeta} \\ \frac{\partial w}{\partial \xi} \\ \frac{\partial w}{\partial \eta} \\ \frac{\partial w}{\partial \zeta} \end{Bmatrix} = \sum_{i=1}^{8} \underbrace{\begin{bmatrix} \frac{\partial N_i}{\partial \xi} & 0 & 0 & -\frac{\partial N_i}{\partial \xi}\frac{\zeta t_i l_{2i}}{2} & \frac{\partial N_i}{\partial \xi}\frac{\zeta t_i l_{1i}}{2} \\ \frac{\partial N_i}{\partial \eta} & 0 & 0 & -\frac{\partial N_i}{\partial \eta}\frac{\zeta t_i l_{2i}}{2} & \frac{\partial N_i}{\partial \eta}\frac{\zeta t_i l_{1i}}{2} \\ 0 & 0 & 0 & -\frac{N_i t_i l_{2i}}{2} & \frac{N_i t_i l_{1i}}{2} \\ 0 & \frac{\partial N_i}{\partial \xi} & 0 & -\frac{\partial N_i}{\partial \xi}\frac{\zeta t_i m_{2i}}{2} & \frac{\partial N_i}{\partial \xi}\frac{\zeta t_i m_{1i}}{2} \\ 0 & \frac{\partial N_i}{\partial \eta} & 0 & -\frac{\partial N_i}{\partial \eta}\frac{\zeta t_i m_{2i}}{2} & \frac{\partial N_i}{\partial \eta}\frac{\zeta t_i m_{1i}}{2} \\ 0 & 0 & 0 & -\frac{N_i t_i m_{2i}}{2} & \frac{N_i t_i m_{1i}}{2} \\ 0 & 0 & \frac{\partial N_i}{\partial \xi} & -\frac{\partial N_i}{\partial \xi}\frac{\zeta t_i n_{2i}}{2} & \frac{\partial N_i}{\partial \xi}\frac{\zeta t_i n_{1i}}{2} \\ 0 & 0 & \frac{\partial N_i}{\partial \eta} & -\frac{\partial N_i}{\partial \eta}\frac{\zeta t_i n_{2i}}{2} & \frac{\partial N_i}{\partial \eta}\frac{\zeta t_i n_{1i}}{2} \\ 0 & 0 & 0 & -\frac{N_i t_i n_{2i}}{2} & \frac{N_i t_i n_{1i}}{2} \end{bmatrix}}_{[\partial N]} \begin{Bmatrix} u_i \\ v_i \\ w_i \\ \alpha_i \\ \beta_i \end{Bmatrix} \tag{12}$$

2.3 Strain Displacement Matrix

Strain displacement matrix $[B]$ can be defined as

$$[B] = [T][\text{Jac}][\partial N] \tag{13}$$

2.4 Stress Strain Relationship Matrix

Stress strain relationship matrix $[D]$ is considered in local coordinate system and taken as

$$[D] = \frac{E}{(1-\upsilon^2)} \begin{bmatrix} 1 & \upsilon & 0 & 0 & 0 \\ \upsilon & 1 & 0 & 0 & 0 \\ 0 & 0 & \frac{(1-\upsilon)}{2} & 0 & 0 \\ 0 & 0 & 0 & \frac{K_s(1-\upsilon)}{2} & 0 \\ 0 & 0 & 0 & 0 & \frac{K_s(1-\upsilon)}{2} \end{bmatrix} \tag{14}$$

where E, υ and K_s are modulus of elasticity, Poisson's ratio and shear correction factor for the given Isotropic material.

For orthotropic materials, the stress strain relationship matrix $[D]$ will be taken as

$$[D] = \frac{1}{1-\upsilon_{12}\upsilon_{21}} \begin{bmatrix} E_1 & \upsilon_{21}E_1 & 0 & 0 & 0 \\ \upsilon_{12}E_2 & E_2 & 0 & 0 & 0 \\ 0 & 0 & G_{12} & 0 & 0 \\ 0 & 0 & 0 & K_sG_{13} & 0 \\ 0 & 0 & 0 & 0 & K_sG_{23} \end{bmatrix} \tag{15}$$

2.5 Stiffness Matrix

Stiffness matrix $[K]$ can be expressed as

$$[K] = \iiint \left[B^T\right][D][B]|J|d\xi d\eta d\zeta \tag{16}$$

2.6 Mass Matrix

Mass matrix $[M]$ is expressed as

$$[M] = \iiint \rho N^T N|J|d\xi d\eta d\zeta \tag{17}$$

where ρ is the density of material. And

$$[N] = \sum_{i=1}^{8} \begin{bmatrix} N_i & 0 & 0 & -\frac{N_i t_i l_{2i}}{2} & \frac{N_i t_i l_{1i}}{2} \\ 0 & N_i & 0 & -\frac{N_i t_i m_{2i}}{2} & \frac{N_i t_i m_{1i}}{2} \\ 0 & 0 & N_i & -\frac{N_i t_i n_{2i}}{2} & \frac{N_i t_i n_{1i}}{2} \end{bmatrix} \tag{18}$$

2.7 Free Vibration

Free vibration equation of the structure, without damping, is given as

$$[M]\ddot{x} + [K]x = 0 \tag{19}$$

2.8 Numerical Integration

We have considered different Gauss points for bending and shear to avoid shear locking and to get more accurate results.

2.8.1 Isotropic Material

For Isotropic materials, we have taken 3 Gauss points each in ξ and η directions and two Gauss points in ζ direction in case of bending. For shear, we have taken 2 Gauss points each in ξ and η directions and one Gauss point in ζ direction.

2.8.2 Composite Material

Composite laminated shell elements require an independent quadrature for each lamina since the material property (stress-strain relationship matrix $[D]$) depends upon the fiber orientation. Thus if ζ_l and ζ_{l+1} define the thickness position of the lth layer, then

$$\zeta = \zeta_l + \frac{t_l}{t}\left(1 + \zeta'\right) \text{ and } d\zeta = \frac{t_l}{t} d\zeta' \tag{20}$$

where t_l is the layer thickness and $-1 \leq \zeta' \leq 1$ for $\zeta_l \leq \zeta \leq \zeta_{l+1}$.

For each lamina, we have taken 3 Gauss points each in ξ and η directions and two Gauss points in ζ direction in case of bending. For shear, we have taken 2 Gauss points each in ξ and η directions and one gauss point in ζ direction.

3 Results and Discussions

3.1 Convergence Study

3.1.1 Square Plate

A convergence study is performed in order to determine the required number of mesh division N_x (number of divisions in x-direction) $\times$ N_y (number of divisions in y-direction) at which the objective values converge. Thickness ratio (a/h) is assumed to be 5. The problem considered here is a cross ply (0/90/90/0) of square cross section and having simply supported boundary conditions which is defined as

$$v = w = \beta = 0 \text{ at } x = 0, a$$
$$u = w = \alpha = 0 \text{ at } y = 0, b$$

The elastic properties of the lamina with respect to the material axes has been taken as $E_1/E_2 = 10$, $G_{12} = G_{13} = 0.6\ E_2$, $G_{23} = 0.5\ E_2$, $\nu_{12} = 0.25$, and $\rho = 1$. Thickness ratio (a/h) is assumed to be 5.

Since it is clear form Table 1 that the program converges at 10 $\times$ 10, so we have taken mesh size as 10 $\times$ 10 for square plate.

3.1.2 Cylindrical Shell

A convergence study is performed in order to determine the required number of mesh division N_h (number of divisions in direction of height) $\times$ N_r (number of divisions in radial direction) at which the objective values converge. The problem considered here is an isotropic cylindrical shell having bottom side fixed which is defined as

$$u = v = w = \alpha = \beta = 0 \text{ at } z = 0$$

Table 1 Non-dimensional frequency parameter $\bar{\omega} = \omega a^2/h\sqrt{\rho/E_2}$ of a simply supported (SSSS) square cross ply (0/90/90/0) plate. $a/h = 5$

Mode no.	5 × 5	6 × 6	7 × 7	8 × 8	9 × 9	10 × 10	12 × 12	15 × 15
1	7.714	7.712	7.711	7.711	7.711	7.710	7.710	7.710
2	12.169	12.168	12.168	12.168	12.167	12.167	12.167	12.167
3	12.169	12.168	12.168	12.168	12.167	12.167	12.167	12.167
4	13.507	13.490	13.483	13.479	13.477	13.476	13.474	13.474

Table 2 Natural Frequency (Hz) of Isotropic cylindrical shell

Mode no.	Mesh size ($N_h \times N_r$)							
	8 × 80	8 × 85	8 × 90	8 × 100	9 × 100	8 × 110	8 × 120	8 × 150
1	147.81	147.52	147.29	146.99	146.96	146.81	146.80	146.80
2	148.97	148.67	148.45	148.15	148.11	147.96	147.91	147.89
3	183.61	182.72	182.04	181.13	181.10	180.57	180.50	180.44

The material properties have been taken as $E = 71$ GPa, $\nu = 0.33$, and $\rho = 2770$ kg/m^3. Height of tank is taken as 0.6 m, outer radius 0.15 m and thickness is taken as 1 mm.

From Table 2, it is clear that the program converges at 8 × 120, so we have taken mesh size as 8 × 120 for cylindrical shells.

3.2 Validation of Results

The results obtained from MATLAB code, created for solving free vibration of isotropic and laminated composite plates and shells, are compared with the results available in open literature and are in good agreement with the literature available in open source.

We have compared our result with the natural frequencies of composite plate and isotropic circular cylinder, available in literatures and result generated by ANSYS.

3.2.1 Composite Plate

The problem considered here is a cross ply (0/90/90/0) of square cross section and having simply supported boundary conditions. The elastic properties of the lamina with respect to the material axes has been taken as $E_1/E_2 = 10$, $G_{12} = G_{13} = 0.5\,E_2$, $G_{23} = 0.6\,E_2$, $\nu_{12} = 0.25$, and $\rho = 1$. Thickness ratio (a/h) is assumed to be 5.

As we can see from Table 3, the results obtained for composite plates from present formulation are in good agreement with the results available in open literature.

Table 3 Non-dimensional frequency parameter $\bar{\omega} = \omega a^2/h\sqrt{\rho/E_2}$ of a simply supported (SSSS) square cross ply (0/90/90/0). $a/h = 5$

	E_1/E_2 ratio			
	10	20	30	40
Exact [6, 7]	8.2982	9.5671	10.326	10.854
Liew et al. [8]	8.4298	9.6782	10.424	10.944
FSDT (present)	8.1974	9.7612	10.6894	11.3315
Degenerated (present)	7.985	9.4399	10.3628	11.016

Table 4 Natural frequency (Hz) of isotropic cylindrical shell

Frequency mode	1	2	3	4	6
Rawat [9]	146	175	242	263	381
ANSYS (present)	147.1	178.57	241.54	269.21	384.85
Degenerated (present)	146.8	180.56	242.46	272.99	385.31

3.2.2 Isotropic Cylindrical Shell

An Isotropic cylindrical shell of 0.6 m height, 0.15 m outer radius and 0.1 mm thickness is considered. We have assumed Aluminum as material with $E = 71$ GPa, $\upsilon = 0.33$ and density as 2770 kg/m^3. Bottom side of shell is assumed to be fixed and top is assumed to be free.

It is evident from Table 4 that the result obtained for isotropic cylindrical shell from present formulation are in good agreement with results available in open literature as well as the results obtained from software (ANSYS).

The formulation developed based on 3-D degenerated shell elements has been validated by comparing results obtained for composite plates and isotropic shells. The results are in good agreement with open literature and software. Thus we conclude that the formulation is correct and is able to produce accurate results.

3.3 Parametric Studies

We have considered a laminated composite cylindrical shell with varying no of lamina, ply angle, and thickness of shell.

Height of cylindrical shell is taken as 0.6 m, outer radius is taken as 0.15 m and this thickness of shell is taken as 1 mm. Material properties are considered as $E_1 =$ 45 GPa, $E_2 = 10$ GPa, $\upsilon_{12} = 0.3$, $G_{12} = 5$ GPa, $G_{23} = 4$ GPa, $G_{13} = 5$ GPa, and density is taken as 2000 kg/m^3 (Table 5).

Now we have increased the thickness of the shell to study its effect on natural frequency. Height of cylindrical shell is taken as 0.6 m, outer radius is taken as 0.15 m and this thickness of shell is taken as 2 mm. Material properties are considered as $E_1 = 45$ GPa, $E_2 = 10$ GPa, $\upsilon_{12} = 0.3$, $G_{12} = 5$ GPa, $G_{23} = 4$ GPa, $G_{13} = 5$ GPa, and density is taken as 2000 kg/m^3 (Table 6).

We have again increased the thickness of shell further. Height of cylindrical shell is taken as 0.6 m, outer radius is taken as 0.15 m and this thickness of shell is taken as 5 mm. Material properties are considered as $E_1 = 45$ GPa, $E_2 = 10$ GPa, $\upsilon_{12} =$ 0.3, $G_{12} = 5$ GPa, $G_{23} = 4$ GPa, $G_{13} = 5$ GPa, and density is taken as 2000 kg/m^3 (Table 7).

Table 5 Natural frequency (Hz) of composite cylindrical shell with thickness 1 mm

Frequency mode	0/90	0/90/0	0/90/90/0	0/90/0/90/0	0/90/0/90/0/90	0/45/0	0/45/45/0	0/45/90/45/0
1	91.57	103.70	108.97	104.11	101.10	92.08	92.88	100.83
2	91.76	104.08	109.40	104.54	101.57	92.47	93.34	101.36
3	91.82	144.28	144.20	139.38	121.65	119.40	121.73	141.56
4	92.18	144.48	144.40	139.60	121.90	121.50	124.11	141.84
5	129.44	147.05	159.26	152.16	158.59	141.38	141.56	144.39
6	129.45	150.37	163.54	155.86	163.01	141.60	141.82	148.18

Table 6 Natural frequency (Hz) of composite cylindrical shell with thickness 2 mm

Frequency mode	0/90	0/90/0	0/90/90/0	0/90/0/90/0	0/90/0/90/0/90	0/45/0	0/45/45/0	0/45/90/45/0
1	114.51	153.85	162.67	156.67	141.58	127.53	129.81	151.22
2	115.56	156.92	163.60	157.63	142.67	129.40	131.93	154.75
3	158.74	160.34	165.49	158.30	163.01	153.02	153.58	157.09
4	160.18	161.20	169.51	161.76	167.34	153.89	154.64	158.31
5	161.67	274.97	272.40	263.84	225.38	273.43	273.58	270.35
6	165.80	275.40	272.86	264.33	225.96	273.87	274.12	270.98

Table 7 Natural frequency (Hz) of composite cylindrical shell with thickness 5 mm

Frequency mode	0/90	0/90/0	0/90/90/0	0/90/0/90/0	0/90/0/90/0/90	0/45/0	0/45/45/0	0/45/90/45/0
1	173.68	192.14	201.08	193.25	188.91	171.32	173.32	189.40
2	178.81	193.99	203.79	195.47	192.40	172.09	174.39	191.73
3	212.16	340.55	351.20	340.01	292.99	306.07	312.02	347.61
4	215.20	343.38	353.60	342.53	295.91	311.61	319.16	350.71
5	358.08	353.60	356.32	347.76	357.27	350.14	350.50	353.93
6	360.22	355.83	359.34	350.60	360.10	352.38	353.21	362.94

From parametric study, it is evident that the natural frequency of composite shell is increasing as we increase the thickness of the shell, which is consistent with our understanding of composite shells. Other parameters such as fiber orientation and no of lamina are also varied to understand their impact on natural frequency.

4 Conclusion

In the present work, a finite element formulation has been created for the dynamic analysis of laminated composite shell using 8-noded 3-D degenerated shell element. Present formulation is capable of analysis both isotropic and laminated composite shells of arbitrary geometry. The results generated so far are in good agreement with the results available in open literature as well as with the software generated results.

4.1 Future Work

Presented work can be extended to material and geometric non-linearity.

This work can also be extended to formulate Functionally Graded Materials (FGM).

Present work can be coupled with fluid formulation to formulated Fluid-Structure Interaction.

References

1. Ahmad S, Irons BM, Zienkiewicz OC (1970) Analysis of thick and thin shell structures by curved finite elements. Int J Numer Meth Eng 2(3):419–451
2. Zienkiewicz OC, Taylor RL, Too JM (1971) Reduced integration technique in general analysis of plates and shells. Int J Numer Meth Eng 3(2):275–290
3. Huang HC, Hinton E (1986) A new nine node degenerated shell element with enhanced membrane and shear interpolation. Int J Numer Meth Eng 22(1):73–92
4. Jayasankar S, Mahesh S, Narayanan S, Padmanabhan C (2007) Dynamic analysis of layered composite shells using nine node degenerate shell elements. J Sound Vib 299(1–2):1–11
5. Balamurugan V, Narayanan S (2008) A piezolaminated composite degenerated shell finite element for active control of structures with distributed piezosensors and actuators. Smart Mater Struct 17(3):35031
6. Khdeir AA, Librescu L (1988) Analysis of symmetric cross-ply elastic plates using a higher-order theory, Part II: buckling and free vibration. Compos Struct 9:259–277
7. Reddy JN (1997) Mechanics of Laminated Composite Plates. Theory and Analysis. CRC Press, Boca Raton, FL

8. Liew KM, Huang YQ, Reddy JN (2003) Vibration analysis of symmetrically laminated plates based on FSDT using the moving least squares differential quadrature method. Comput Methods Appl Mech Eng 192(19):2203–2222
9. Rawat A, Matsagar V, Nagpal AK (2016) Finite element analysis of thin circular cylindrical shells. Proc Indian Natl Sci Acad 82(2):349–355

A New Hybrid Unified Particle Swarm Optimization Technique for Damage Assessment from Changes of Vibration Responses

Swarup K. Barman, Dipak Kumar Maiti and Damodar Maity

Abstract Unified particle swarm optimization (UPSO) and artificial bee colony (ABC) are two effective swarm based techniques to solve inverse damage detection problems. A hybrid algorithm of ABC and UPSO named UPSO_Scout has been proposed in the present paper. Comparisons among these three algorithms are demonstrated using three structural problems (beam, plane truss and space truss) considering natural frequencies and mode shapes as damage indicators. Proposed algorithm shows improved performance than UPSO and ABC for damage detection. Slow convergence speed of ABC reduces its effectiveness for larger problem. UPSO is sometimes prone to fall in local minima despite of its faster convergence speed. Efficacy of the proposed algorithm has also been examined in noisy environment.

Keywords ABC · UPSO · Frequency · Modeshapes · Damage detection · UPSO_Scout

1 Introduction

Structural health monitoring (SHM) has been turned into a significant area of study within the civil, mechanical and aerospace engineering research community in recent years. Damage identification at initial phases is a crucial part of structural health monitoring to evaluate the safety and to ward off the cataclysmic failure of the structure. A number of non-destructive tests are available to identify and quantify the damages. Among all the methods, damage identification using vibrational characteristics has become popular in recent years. Existence of damage changes the dynamic response

S. K. Barman (✉) · D. K. Maiti
Department of Aerospace Engineering, IIT Kharagpur, Kharagpur, India
e-mail: Swarup.jadavpur@gmail.com

D. K. Maiti
e-mail: dkmaiti@aero.iitkgp.ac.in

D. Maity
Department of Civil Engineering, IIT Kharagpur, Kharagpur, India
e-mail: dmaity@civil.iitkgp.ac.in

B. N. Singh et al. (eds.), *Recent Advances in Theoretical, Applied, Computational and Experimental Mechanics*, Lecture Notes in Mechanical Engineering,
https://doi.org/10.1007/978-981-15-1189-9_23

parameters (frequency, mode shapes, FRF, etc.) by altering the physical properties (mass, stiffness, damping, etc.) of the structures. Identification and quantification of damage can be carried out through investigating these changes in dynamic parameters. This is called inverse method for damage detection. Adams et al. [1], Cawley and Adams [2], Messina et al. [3] used change in natural frequency to detect damage in beams. Yang [4] used modal residual force criteria as damage indicator. Majumder et al. [5] used frequency change to detect damages in truss. Seyedpoor [6], Dinh-Cong et al. [7] used modal strain energy for damage detection for beam and truss. Mohan et al. [8] used frequency response function (FRF) to detect damage in beam and space frame. Kaveh and Zolghadr [9], Fei Kang et al. [10], Nanda et al. [11], Ding et al. [12], Nhamage et al. [13], Mishra et al. [14] , Barman et al. [15, 16], Kim et al. [17] used combined frequency and mode shapes data to quantify damage in different structures, as beam, plate, frame, truss etc. Another crucial attribute in inverse method of damage detection is to employ efficient optimization tool to save computational time and cost. Various soft computing tools such as particle swarm optimization (PSO) [6, 8], genetic algorithm (GA) [18], neural network (NN) [19], artificial bee colony (ABC) [12], ant colony optimization (ACO) [5], modified charge system search (CSS) [9], fuzzy cognitive map (FCM) [20], unified particle swarm optimization (UPSO) [11, 15, 16] antlion optimization (ALO) [14] etc. have been used by the researchers to solve the inverse problem commendably.

So, above literature review has given a clear idea about how metaheuristic techniques have been gaining popularity from last two–three decades in the field of damage detection of structures. However, no optimization techniques are full proof as each of them has their advantages and disadvantages in particular field of application. So, the researchers have been trying to make new robust hybrid algorithm by mixing two or more original algorithms as per the suitability of their particular field of applications. Hybrid algorithms show improved performance compared to the parent algorithms. So, keeping that in mind a new and effective optimization algorithm UPSO_Scout, which is a hybrid algorithm combining the features of ABC into UPSO has been proposed in the present study. Proposed algorithm has been used to solve inverse problem with an aim for detecting damages in the beam and truss of varying complexity. Natural frequencies and mode shapes are used as the diagnostic parameters. Performance of the proposed algorithm has also been scrutinized in case of noisy vibration data.

2 Mathematical Background

2.1 Finite Element Formulation

The finite element model for isotropic beam has been formulated using one-dimensional two noded element. Each node has two degrees of freedom (δ_y, θ_z) (Fig. 1a). Beam rigidity EI and cross-sectional area A are considered same through-

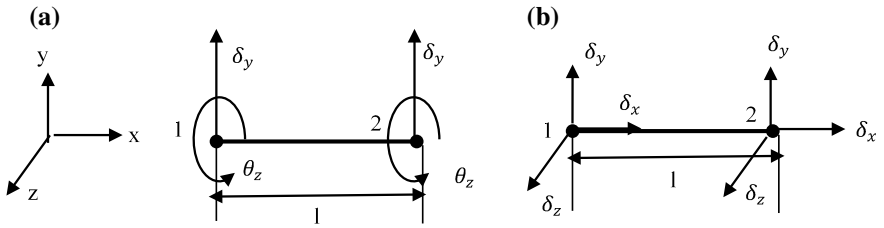

Fig. 1 **a** Beam element **b** Space truss element

out the length of the element. Element stiffness matrix and element mass matrix, respectively, are given by [21].

$$[K]_e = \frac{EI}{l^3}\begin{bmatrix} 12 & 6l & -12 & 6l \\ 6l & 4l^2 & -6l & 2l^2 \\ -12 & -6l & 12 & -6l \\ 6l & 2l^2 & -6l & 4l^2 \end{bmatrix} \quad [M]_e = \frac{\rho Al}{420}\begin{bmatrix} 156 & 22l & 54 & -13l \\ 22l & 4l^2 & 13l & -3l^2 \\ 54 & 13l & 156 & -22l \\ -13l & -3l^2 & -22l & 4l^2 \end{bmatrix}$$

Here, l is length of the element and ρ is mass density of the material. Finite element formulation of truss structures have been formulated using two-dimensional two noded truss element with two (δ_x, δ_y) and three $(\delta_x, \delta_y, \delta_z)$ degrees of freedom (Fig. 1b), respectively, for plane and space truss. Axial rigidity EA and cross-sectional area A are considered same throughout the length of the element. Element stiffness matrix and element mass matrix in element coordinate system, respectively, are given by [21].

$$[k]_e = \frac{EA}{l}\begin{bmatrix} 1 & -1 \\ -1 & 1 \end{bmatrix} \quad [m]_e = \frac{\rho Al}{6}\begin{bmatrix} 2 & 1 \\ 1 & 2 \end{bmatrix}$$

Here, l is length of the element and ρ is mass density of the material used. These matrices can be transformed into global coordinate system using the following equation, respectively.

$$[K]_e = [T]^T[k]_e[T] \quad [M]_e = [T]^T[m]_e[T]$$

where T is a transformation matrix. For plane truss

$$[T] = \begin{bmatrix} c & s & 0 & 0 \\ -s & c & 0 & 0 \\ 0 & 0 & c & s \\ 0 & 0 & -s & c \end{bmatrix}$$

Here, $c = \cos\alpha$, $s = \sin\alpha$. α is the inclination of the element axis with global X axis.

For space truss

$$[T] = \begin{bmatrix} m_1 & m_2 & m_3 & 0 & 0 & 0 \\ n_1 & n_2 & n_3 & 0 & 0 & 0 \\ p_1 & p_2 & p_3 & 0 & 0 & 0 \\ 0 & 0 & 0 & m_1 & m_2 & m_3 \\ 0 & 0 & 0 & n_1 & n_2 & n_3 \\ 0 & 0 & 0 & p_1 & p_2 & p_3 \end{bmatrix}$$

$\{m_1, n_1, p_1\}$ are the direction cosines of global X axis with respect to local x, y, z axis, respectively. Similarly $\{m_2, n_2, p_2\}$ and $\{m_3, n_3, p_3\}$ are the direction cosines of global Y and Z axis, respectively with respect to local x, y, z axis.

2.2 Damage Model

Only one damage parameter per structural element is considered as all the materials are considered isotropic. So, damaged stiffness matrix of an element can be written as

$$K_{\text{dam}} = (1 - \alpha) K_{\text{undam}}, \alpha \in [0, 1] \tag{1}$$

where K_{dam} and K_{undam} are damaged and undamaged element stiffness matrix, respectively. α is damage parameter.

2.3 Frequency and Mode Shapes Based Objective Function

The objective function considered here is given below, Nanda et al. [11]:

$$F(\%\text{damage in each element}) = \sqrt{\frac{1}{n}\sum_{i=1}^{i=n}\left(\left(\frac{f_i^m}{f_i^a}\right) - 1\right)^2} + \sum_{i=1}^{i=n}(1 - \text{MAC}_{ii}) \tag{2}$$

where

$$\text{MAC}_{ii} = \frac{\left|\varphi_{mi}^T \varphi_{ai}\right|^2}{\left(\varphi_{mi}^T \varphi_{mi}\right)\left(\varphi_{ai}^T \varphi_{ai}\right)} \tag{3}$$

Here, n stands for the number of modes, f and φ denote the frequency and corresponding mode shape, respectively. Suffix m and a stand for measured response

of damaged structures and computed response through FEM, respectively. MAC denotes the modal assurance criteria (MAC).

2.4 Frequency and mode shapes with noise

In practical measurement of vibration characteristics there may be possibility of error, which is characterized as noise in the measured data. Data with noise can be obtained from the noise free data using following expression mentioned by Mohan et al. [8].

$$H_n = H(1 + 2 * N_L(ranf - 0.5)) \tag{4}$$

Where, H_n and H are respectively with noise and noise free data; N_L is noise level (0.05 relates to 5 % noise level); is a random number between 0 and 1.

3 Optimization Algorithms

3.1 Unified Particle Swarm Optimization (UPSO)

Particle swarm optimization (PSO) was developed by Kennedy and Eberhart [22] as a stochastic optimization algorithm based on concepts and rules that govern socially organized populations in nature, such as bird flocks, fish schools and animal herds to search for food or to avoid predators. UPSO is a refinement of PSO and was first proposed by Parsopoulos and Vrahatis [23]. Basic steps involved in UPSO are as follows:

(i) Random initialization of swarm position and velocity: $x_{ij} \in [x_{\min}, x_{\max}]$, $v_{ij} \in [-v_{\max}, v_{\max}]$, $v_{\max} = 0.5 * (x_{\max} - x_{\min}), \forall i \in N, \forall j \in S$
(ii) Evaluate the swarm.
(iii) Cycle = 1.
(iv) **Repeat**.
(v) Calculate ***pb***: the best position ever visited by individual particle; ***gb***: the best position ever visited by all particles; ***lb***: best position ever visited by any of its neighbour.
(vi) **Update velocity**:

$$V_{ij}^{t+1} = \mu G_{ij}^{t+1} + (1 - \mu) L_{ij}^{t+1}, V_{ij}^{t+1} \in [-v_{\max}, v_{\max}] \tag{5}$$

Here,

$$G_{ij}^{t+1} = \chi\left[v_{ij}^{t} + c_1 r_1\left(pb_{ij} - x_{ij}^{t}\right) + c_2 r_2\left(gb_{ij} - x_{ij}^{t}\right)\right] \tag{6}$$

$$L_{ij}^{t+1} = \chi\left[v_{ij}^{t} + c_1 r_3\left(pb_{ij} - x_{ij}^{t}\right) + c_2 r_4\left(lb_{ij} - x_{ij}^{t}\right)\right] \tag{7}$$

$$\mu(t) = \exp\left(\frac{t\log(2.0)}{t_{\max}}\right) - 1 \tag{8}$$

Update position:

$$x_{ij}^{t+1} = x_{ij}^{t} + V_{ij}^{t+1},\ x_{ij}^{t+1} \in [x_{\min}, x_{\max}] \tag{9}$$

(vii) Evaluate the swarm and update $\boldsymbol{pb}$, $\boldsymbol{gb}$, $\boldsymbol{lb}$.
(viii) Memorize the best solution achieved so far.
(ix) Cycle = Cycle + 1.
(x) **Until** termination criteria.

where r_1, r_2, r_3 and r_4 are random number independent of each other between [0, 1]; c_1 and c_2 are cognitive and social parameter, respectively; χ is the constriction factor [24]. In the present study the termination criteria is when either the objective function assumes a predefined value or maximum iteration is reached. The UPSO parameter used in the present study are as follows: for better convergence $c_1 = c_2 = 2.05$; $\chi = 0.72984$.

3.2 *Artificial Bee Colony (ABC)*

Artificial bee colony (ABC) algorithm [25] simulates the behaviour pattern of a honey bee colony. Inside a bee hive, bees share information about food source with each other in the dancing area through waggle dance. In ABC algorithm, the position of a food source represents a possible solution to the optimization problem and the nectar amount of a food source corresponds to the quality (fitness) of the associated solution. The number of the employed bees or the onlooker bees is equal to the number of solutions in the population. The steps involved in ABC algorithm are

(i) Random initialization of population: $x_{ij} \in [x_{\min}, x_{\max}], \forall i \in SN, \forall j \in D$
(ii) Fitness evaluation.
(iii) Cycle = 1.
(iv) **Repeat**.
(v) Produce new solution for employed bees (Eq. 10) and evaluate them.

$$x_{ij}^{t+1} = x_{ij}^{t} + \text{rand}[-1, 1]\left(x_{ij}^{t} - x_{kj}^{t}\right) \tag{10}$$

$k \in \{1, 2 \ldots., SN\}$ and $j \in \{1, 2 \ldots., D\}$ are chosen randomly, but $k \neq i$.

(vi) Apply greedy selection process for employed bees.
(vii) Calculate probability p_i for each solution x_i:

$$p_i = \text{Fitness}_i / \sum_{n=1}^{SN} \text{Fitness}_n$$

(viii) Produce new solution for onlooker bees (Eq. 10) based on the probability and evaluate them.
(ix) Apply greedy selection process for onlooker bees.
(x) Determine the abandoned solution for the scout bee and if exists replace it with a randomly created solution:

$$x_{ij} = x_{\min} + \text{rand}[0, 1](x_{\max} - x_{\min}) \tag{11}$$

(xi) Memorize the best solution achieved so far.
(xii) Cycle = Cycle + 1.
(xiii) **Until** termination criteria.

In each cycle only one scout bee is allowed. In ABC, abandoned solution is decided through a parameter called 'limit'. So, if a particular solution within the population cannot be improved for a number of cycles equal to 'limit', that position is considered as abandoned. It can be considered from the following expression:

$$\text{limit} = SN * D \tag{12}$$

In the present study the termination criteria is when either the objective function assumes a predefined value or maximum iteration is reached.

3.3 Scout Unified Particle Swarm Optimization (UPSO_Scout)

In this section, a hybrid UPSO algorithm has been proposed by combining the scout bee phase of ABC algorithm with the existing UPSO algorithm to enhance its exploration property, and hence to enhance its performance for damage detection problems. The algorithm is named as scout unified particle swarm optimization (UPSO_Scout). The steps involved in this algorithm are mentioned below:

(i) Random initialization of swarm position and velocity: $x_{ij} \in [x_{\min}, x_{\max}]$, $v_{ij} \in [-v_{\max}, v_{\max}]$, $v_{\max} = 0.5 * (x_{\max} - x_{\min}), \forall i \in N, \forall j \in S$
(ii) Evaluate the swarm.
(iii) Cycle = 1.
(iv) **Repeat**.
(v) Calculate $\boldsymbol{pb}$, $\boldsymbol{gb}$, $\boldsymbol{lb}$.

(vi) Update velocity (Eq. 5) and position (Eq. 9).
(vii) Evaluate the swarm and update $\boldsymbol{pb}$, $\boldsymbol{gb}$, $\boldsymbol{lb}$.
(viii) Determine the abandoned particle and if exists, replace it with a new particle with a position (Eq. 11) and velocity (Eq. 13).

$$v_{ij} = \text{rand}[0, 1] * 2 * v_{\max} - v_{\max} \tag{13}$$

(ix) Memorize the best solution achieved so far.
(x) Cycle = Cycle + 1.
(xi) **Until** termination criteria.

Only one scout is allowed per cycle as mentioned in the case of ABC also. As in the case of ABC here also 'limit' is a very important parameter, which is problem specific.

4 Numerical Results

4.1 Problem Definition

A MATLAB based computer programming is developed for damage detection through finite element model updating. Efficiency of the proposed algorithm UPSO_Scout in comparison with ABC and UPSO is demonstrated for damage detection. All the computations have been performed using an Intel Core i5-4570 CPU 3.20 GHz processor with 8 GB of RAM on a 62 bit windows operating system. Three structural problem are considered for the study: (i) Isotropic cantilever beam [8] (Fig. 2a), (ii) 25 member plane truss [26] (Fig. 2b), (iii) 72 member space truss [9] (Fig. 2c). The material properties for each structure are mentioned in their respective figures. Frequencies and mode shapes are considered as damage indicator. At first natural frequencies of undamaged are validated against the results given in literature (Table 1). For brevity, only a limited number of modes have been included in the analysis. The number of modes should be enough so that the total effective modal mass of the model in any given direction is at least 80–90% of the actual mass of the structure [27, 28]. So, for all three structures more than 90% of the total mass can be incorporated in the analysis as cumulative effective modal mass by considering only first eight modes (Table 2). Thus, first eight modes are considered for damage detection purpose. Single and multiple element damage cases have been considered to demonstrate the effectiveness of the algorithms. Effectiveness of the three algorithms has been compared with respect to success rate and average convergence speed. Success rate is defined as the number of successful runs per 100 numerical runs. A particular numerical run for which the objective function has reached below a specified tolerance limit within the specified number of iterations, is termed as successful run. Specific parameters of the optimization algorithms for each structure have been mentioned in Table 3.

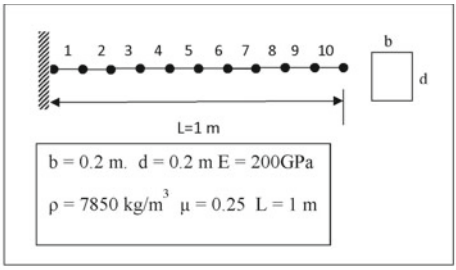

(a) Cantilever beam

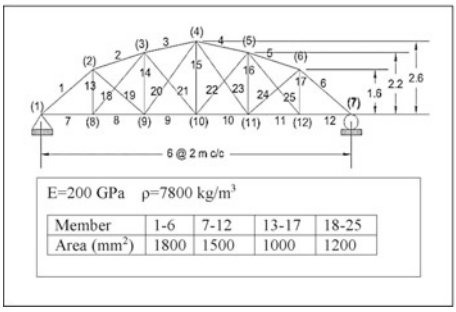

(b) 25 member plane truss

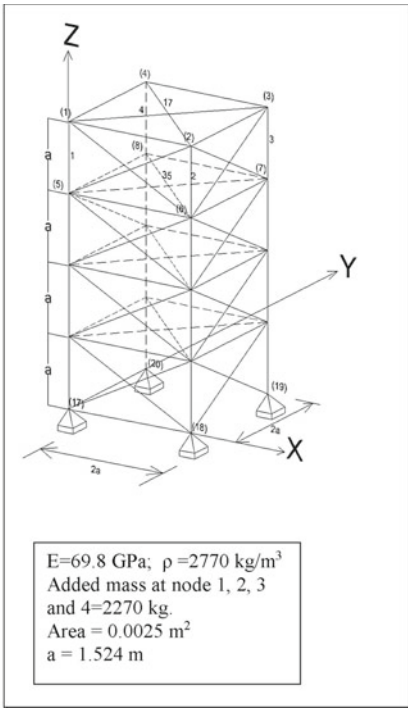

(c) 72 member space truss

Fig. 2 Details of the structures

4.2 Damage Detection Using Noise Free Data

The results obtained from the numerical study for the three structures have been presented here.

4.2.1 Isotropic Cantilever Beam

Damage has been modelled as percentage reduction in the bending stiffness for the particular element. Two damage cases are selected for demonstration of the algorithms and mentioned in Table 4. First eight natural frequencies of damaged structures are mentioned in Table 5. 100 numerical experiments are conducted for each damage case. Damage prediction for E1 and E2 damage cases by three algorithms are shown in Fig. 3a and b, respectively. All three algorithms are capable of detecting damages for both damage cases E1 and E2. A summary of all the numerical experiments conducted in the cantilever beam has been presented in Table 6. Mean number of function evaluation represents the average convergence speed. Among the three algorithms ABC has the lowest convergence speed (higher mean function evaluation)

Table 1 Natural frequencies of undamaged structures

Structure	Damage case	Natural frequency (Hz) for mode							
		1	2	3	4	5	6	7	8
Isotropic beam	Present	161.6	1015.7	2849.7	5593.0	9257.6	13844.0	19344.0	25703.5
	Mohan et al. [7]	163.1	1022.0	2862.3	5612.8	9293.0	13922.0	–	–
25 member plane truss	Present	30.34	68.95	96.31	181.71	223.24	275.54	321.55	352.08
72 member space truss	Present	6.02	6.05	10.48	18.35	25.47	25.49	26.61	38.11
	Kaveh and Zolghadr [8]	6.04	6.04	10.46	18.23	25.45	25.45	26.52	38.08

Table 2 Effective modal mass ratio of the cantilever beam

Structure	DOF	Effective modal mass ratio for mode number								Total
		1	2	3	4	5	6	7	8	
Isotropic beam	δ_y	0.613	0.187	0.063	0.031	0.018	0.011	0.007	0.004	0.936
	θ_z	0.971	0.025	0.003	0.001	0.000	0.000	0.000	0.000	1.000
25 member plane truss	δ_x	0.151	0.662	0.08	0.015	0.038	0.002	0.000	0.001	0.949
	δ_y	0.750	0.125	0.014	0.023	0.015	0.000	0.001	0.001	0.929
72 member space truss	δ_x	0.904	0.001	0.000	0.000	0.051	0.025	0.000	0.000	0.981
	δ_y	0.001	0.885	0.000	0.000	0.025	0.049	0.000	0.000	0.960
	δ_z	0.000	0.000	0.000	0.939	0.000	0.000	0.000	0.000	0.939

Table 3 Parameter setting for optimization algorithms

Optimization algorithm	Parameters	Isotropic beam	25 member plane truss	72 member space truss
UPSO	Swarm size	30	50	90
	Maximum iteration	500	1000	10,000
	Max. tol. limit	1E−05	1E−06	1E−07
ABC	Swarm size	30	50	90
	Maximum iteration	500	1000	10,000
	Abandonment limit	300	20	6480
	Max. tol. limit	1E−05	1E−06	1E−07
UPSO_Scout	Swarm size	30	50	90
	Maximum iteration	500	1000	10,000
	Abandonment limit	20	20	20
	Max. tol. limit	1E−05	1E−06	1E−07

Table 4 Details of damage cases

Damage case	Description
E1	5% in element 1
E2	20% in element 1 + 15% in element 4 + 10% in element 8

Table 5 Natural frequencies of damaged isotropic beam

Damage case	Natural frequency (Hz) for mode							
	1	2	3	4	5	6	7	8
E1	161.6	1015.7	2849.7	5593.0	9257.6	13844.0	19344.0	25703.5
E2	155	982.8	2746.3	5475.7	9045.5	13550.8	18931.7	25073.7

and UPSO has highest convergence speed. Convergence speed of UPSO_Scout is slightly lower than UPSO. However, success rate of UPSO_Scout is much higher (100%, 100%) for damage case (E1, E2) in comparison with the success rate of UPSO (84%, 90%) and ABC (46%, 0%). Also, in terms of computational time UPSO_Scout found to be least time consuming, while ABC is highest time consuming algorithm. So, UPSO_Scout has been found to be performed better in comparison with UPSO and ABC.

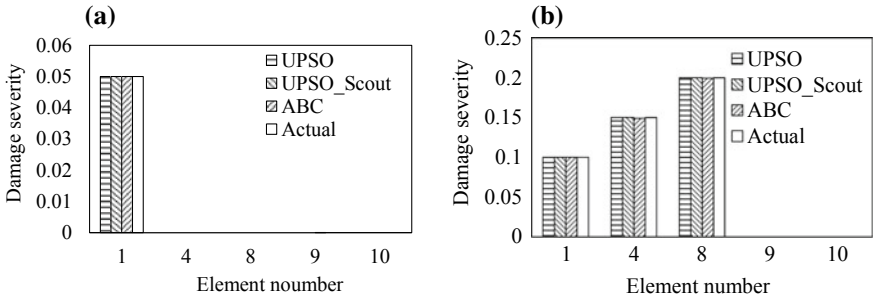

Fig. 3 Damage prediction by the algorithms: **a** damage case E1 **b** damage case E2

Table 6 Summary of damage detection for isotropic beam

Damage case	Optimization algorithm	Number of function evaluation		Success rate	Computational time (s)
		Mean	Standard deviation		
E1	UPSO	1151.07	288.27	84/100	612.26
	ABC	18824.35	4857.15	46/100	3945.91
	UPSO_Scout	**2280.73**	**2402.31**	**100/100**	414.67
E2	UPSO	3405.67	908.16	90/100	830.02
	ABC	–	–	0/100	4761.91
	UPSO_Scout	**4087.24**	**2145.66**	**100/100**	743.13

4.2.2 25 Member Plane Truss

In this case of 25 member plane truss, damage has been modelled as the percentage reduction in axial stiffness of the particular member. Two damage cases have been considered and mentioned in Table 7. First eight natural frequencies of damaged structures are mentioned in Table 8. 100 numerical experiments are conducted for each damage case. Damage prediction for E3 and E4 damage cases by UPSO and UPSO_Scout is shown in Fig. 4a and b, respectively. Comparison among the three algorithms can be performed from the summary of the experiments, presented in Table 9. ABC has failed to minimize the objective function and thus failed to detect the damage in both the cases. UPSO has slightly faster average convergence rate compared to UPSO_Scout for all the cases. However, the success rate of UPSO_Scout

Table 7 Details of damage cases

Damage case	Description
E3	5% in element 15
E4	20% in element 15 + 15% in element 20 + 10% in element 1

Table 8 Natural frequencies of damaged plane truss

Damage case	Natural frequency (Hz) for mode							
	1	2	3	4	5	6	7	8
E3	30.33	68.92	96.3	181.7	222.79	275.5	318.39	352.01
E4	30.22	68.5	94.51	181.15	218.6	272.62	306.42	347.95

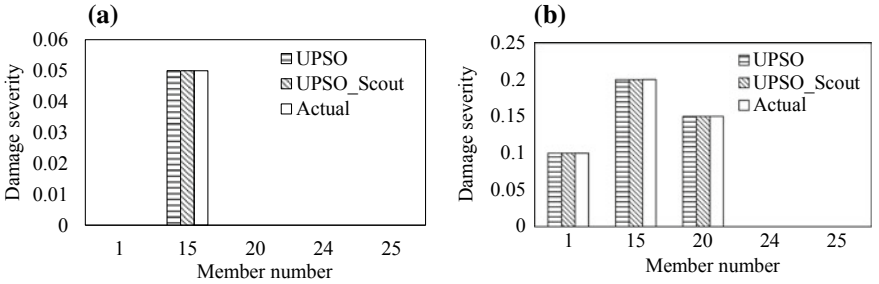

Fig. 4 Damage prediction by the algorithms: **a** damage case E3 **b** damage case E4

Table 9 Summary of damage detection for plane truss

Damage case	Optimization algorithm	Number of function evaluation		Success rate	Computational time (s)
		Mean	Standard deviation		
E3	UPSO	4418.82	750.95	85/100	14735.12
	ABC	–	–	0/100	131428.6
	UPSO_Scout	14402.48	5176.61	100/100	18854.16
E4	UPSO	16799.12	10234.35	57/100	40680.65
	ABC	–	–	0/100	131428.6
	UPSO_Scout	23681.58	7125.71	81/100	37547.45

is much higher (100%, 81%) for damage case (E3, E4) in comparison with the success rate of UPSO (85%, 57%) and ABC (0%, 0%). In case of E3 UPSO has taken least computational time, whereas, in case of E4 UPSO_Scout has taken least computational time. So, UPSO_Scout has been found to have superior performance in comparison with UPSO and ABC.

Table 10 Details of damage cases

Damage case	Description
E5	5% in element 17
E6	20% in element 17 + 15% in element 1 + 10% in element 35

Table 11 Natural frequencies of damaged space truss

Damage case	Natural frequency (Hz) for mode							
	1	2	3	4	5	6	7	8
E5	6.02	6.05	10.48	18.35	25.47	25.48	26.44	37.93
E6	6.02	6.04	10.48	18.26	25.06	25.47	25.82	37.13

4.2.3 72 Member Space Truss

In the case of 72 member space truss, damage has been modelled in similar manner as the plane truss. Two damage cases have been considered and mentioned in Table 10. First eight natural frequencies of damaged structures are mentioned in Table 11. 100 numerical experiments are conducted for each damage case. Damage prediction for E5 and E6 damage cases by UPSO and UPSO_Scout are shown in Fig. 5a, b. Performance of the three algorithms can be compared from the summary of the experiments, presented within Table 12. ABC has failed to detect the damage in both the cases. UPSO_scout has faster average convergence speed compared to UPSO for damage case E5. The difference in convergence speed between these two algorithms is not significant enough for damage case E6. However, success rate of UPSO_Scout is much higher (100%, 77%) for damage case (E5, E6) in comparison with the success rate of UPSO (86%, 19%) and ABC (0%, 0%). Again, UPSO_scout is found to be least time consuming for both the damage cases. Thus, UPSO_Scout has been found to have superior performance in comparison with UPSO and ABC.

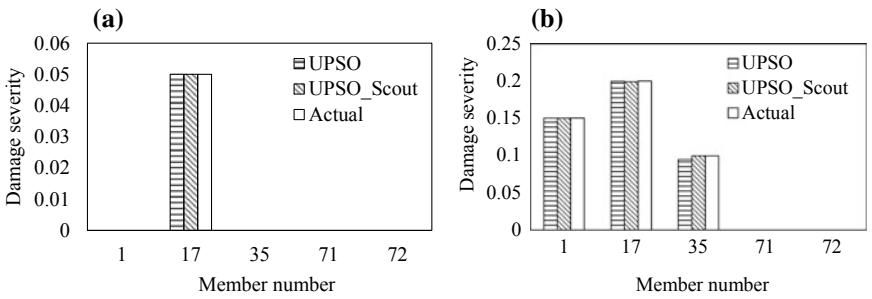

Fig. 5 Damage prediction by the algorithms: **a** damage case E5 **b** damage case E6

Table 12 Summary of damage detection for space truss

Damage case	Optimization algorithm	Number of function evaluation		Success rate	Computational time (s)
		Mean	Standard deviation		
E5	UPSO	331453.30	78558.17	86/100	1310792.26
	ABC	–	–	0/100	5544000.9
	UPSO_Scout	202288.00	40424.97	100/100	645073.96
E6	UPSO	466721.10	127478.80	19/100	2607481.1
	ABC	–	–	0/100	5544000.6
	UPSO_Scout	492086.80	197575.10	77/100	1868391.8

Table 13 Details of noise levels

Noise level	N1	N2	N5	N6	N7	N10
Noise in frequency (%)	0.1	0.2	0.5	0.6	0.7	1
Noise in mode shapes (%)	1	2	5	6	7	10

4.3 Damage Detection Using Noisy Data

The relative measurement error of frequency is about 1% and the mode shape is about 10% in practical cases [29]. To incorporate this error we have considered a range for different noise levels, where the noise for frequency is varying from 0 to 1% and the same for mode shapes is varying from 0 to 10%. The different noise levels are mentioned in Table 13. As from the previous section, it is clear that overall performance of UPSO_Scout is better than the other two; in this section only capability of the same is investigated for damage detection using noisy data. Figure 6 depicts the damage detection scenario using noisy data for six damage cases (E1–E6) considered before. For single element damage cases (E1, E3 and E5) where the amount of damage is very low (5%), the algorithm gives almost correct representation of damage up to noise level N2. But, for higher level of noise (N5, N10) the algorithm fails to differentiate between the change in vibrational parameter for noise and damage, as damage is very low and gives false representation of damage. Whereas the three element damage cases (E2, E4, E6) have comparatively higher magnitude of damage in the range of 10–20% and these cases have been investigated for noise cases starting from N5 and gradually for higher noise levels (N6, N7, N10). For these damage cases except E6 the algorithm has been able to detect damages almost accurately for noise level up to N7. At noise level N10 the algorithm detects the damage location correctly but failed to quantify the damages correctly. For E6 (Fig. 6f) the algorithm has been able to detect damages for noise level N1 but failed for noise level N2.

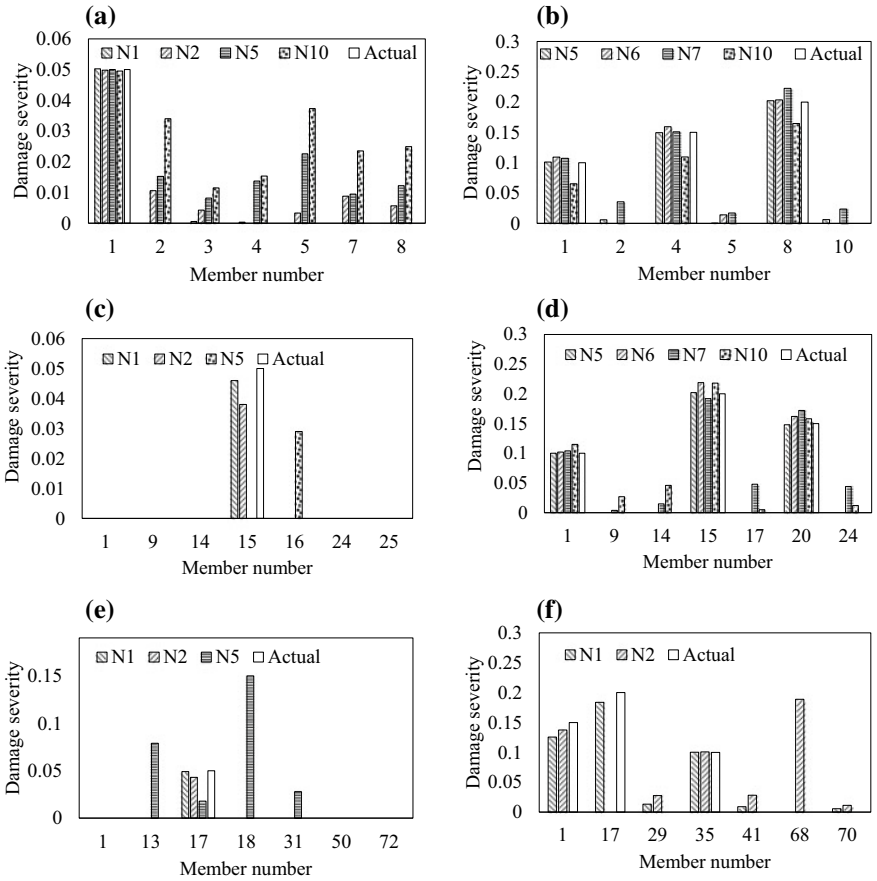

Fig. 6 Damage prediction by the UPSO_Scout in noisy environment : **a** damage case E1 **b** damage case E2 **c** damage case E3 **d** damage case E4 **e** damage case E5 **f** damage case E6

5 Conclusions

In the present study, the finite element formulation is developed for beam, plane and space trusses to find out natural frequencies and mode shapes for undamaged and damaged structures. The finite element-based computer code is developed in the MATLAB environment. Inverse algorithms based on UPSO, ABC and UPSO_Scout are developed to detect and quantify damages in such structures. The requirements of number of modes in damage detection have been decided based on cumulative effective modal mass for all three structures. The proposed algorithm is found to be more capable to recover from local minima without losing its convergence speed in comparison with UPSO and ABC. UPSO_Scout has produced more number of successful runs compared to UPSO and ABC. Thus, damage can be predicted correctly

with the help of UPSO_Scout even with a small number of numerical experiments, and overall computational efforts can be reduced significantly. Thus UPSO_Scout algorithm is found to be more reliable than UPSO and ABC to assess damages in structures. UPSO_Scout algorithm also performs satisfactorily in damage assessment in case of noisy environment.

Acknowledgements This research work is financially supported by ISRO (Indian Space Research Organisation) IIT Kharagpur cell. The authors are grateful to ISRO cell for their financial support to carry out the research work at Department of Aerospace Engineering, IIT, Kharagpur.

References

1. Adams RD, Cawley P, Pie CJ, Stone BJ (1978) A vibration technique for non-destructively assessing the integrity of structures. J Mech Eng Sci 20:93–100. https://doi.org/10.1243/JMES_JOUR_1978_020_016_02
2. Cawley P, Adams RD (1979) The location of defects in structures from measurements of natural frequencies. J Strain Anal Eng Des 14:49–57. https://doi.org/10.1243/03093247V142049
3. Messina A, Williams EJ, Contursi T (1998) Structural damage detection by a sensitivity and statistical-based method. J Sound Vib 216:791–808. https://doi.org/10.1006/jsvi.1998.1728
4. Yang QW (2009) A numerical technique for structural damage detection. Appl Math Comput 215:2775–2780. https://doi.org/10.1016/j.amc.2009.08.039
5. Majumdar A, Maiti DK, Maity D (2012) Damage assessment of truss structures from changes in natural frequencies using ant colony optimization. Appl Math Comput 218:9759–9772. https://doi.org/10.1016/j.amc.2012.03.031
6. Seyedpoor SM (2012) A two stage method for structural damage detection using a modal strain energy based index and particle swarm optimization. Int J Non Linear Mech 47:1–8. https://doi.org/10.1016/j.ijnonlinmec.2011.07.011
7. Dinh-Cong D, Vo-Duy T, Ho-Huu V, Nguyen-Thoi T (2019) Damage assessment in plate-like structures using a two-stage method based on modal strain energy change and Jaya algorithm. Inverse Probl Sci Eng 27:166–189. https://doi.org/10.1080/17415977.2018.1454445
8. Mohan SC, Maiti DK, Maity D (2013) Structural damage assessment using FRF employing particle swarm optimization. Appl Math Comput 219:10387–10400. https://doi.org/10.1016/j.amc.2013.04.016
9. Kaveh A, Zolghadr A (2015) An improved CSS for damage detection of truss structures using changes in natural frequencies and mode shapes. Adv Eng Softw 80:93–100. https://doi.org/10.1016/j.advengsoft.2014.09.010
10. Kang F, Li J, Xu Q (2012) Damage detection based on improved particle swarm optimization using vibration data. Appl Soft Comput 12:2329–2335. https://doi.org/10.1016/j.asoc.2012.03.050
11. Nanda B, Maity D, Maiti DK (2014) Modal parameter based inverse approach for structural joint damage assessment using unified particle swarm optimization. Appl Math Comput 242:407–422. https://doi.org/10.1016/j.amc.2014.05.115
12. Ding ZH, Huang M, Lu ZR (2016) Structural damage detection using artificial bee colony algorithm with hybrid search strategy. Swarm Evol Comput 28:1–13. https://doi.org/10.1016/j.swevo.2015.10.010
13. Nhamage IA, Lopez RH, Miguel LFF (2016) An improved hybrid optimization algorithm for vibration based-damage detection. Adv Eng Softw 93:47–64. https://doi.org/10.1016/j.advengsoft.2015.12.003

14. Mishra M, Barman SK, Maity D, Maiti DK (2019) Ant lion optimisation algorithm for structural damage detection using vibration data. J Civ Struct Heal Monit 9:117–136. https://doi.org/10.1007/s13349-018-0318-z
15. Barman SK, Maiti DK, Maity D (2016) A simple inverse technique to assess delamination in composite beam. In: Proceedings of the 61st congress of the indian society of theoretical and applied mechanics, VIT University Vellore, Tamil Nadu, India, 11–14 Dec, pp 1–8
16. Barman SK, Jebieshia TR, Tiwari P, Maiti DK, Maity D (2019) Two-stage inverse method to detect delamination in composite beam using vibration responses. AIAA J 57:1312–1322. https://doi.org/10.2514/1.J057471
17. Kim N Il, Kim S, Lee J (2019) Vibration-based damage detection of planar and space trusses using differential evolution algorithm. Appl Acoust 148:308–321. https://doi.org/10.1016/j.apacoust.2018.08.032
18. Maity D, Tripathy RR (2005) Damage assessment of structures from changes in natural frequencies using genetic algorithm. Struct Eng Mech 19:21–42. https://doi.org/10.12989/sem.2005.19.1.021
19. Zapico JL, González MP, Friswell MI, Taylor CA, Crewe AJ (2003) Finite element model updating of a small scale bridge. J Sound Vib 268:993–1012. https://doi.org/10.1016/S0022-460X(03)00409-7
20. Beena P, Ganguli R (2011) Structural damage detection using fuzzy cognitive maps and Hebbian learning. Appl Soft Comput 11:1014–1020. https://doi.org/10.1016/j.asoc.2010.01.023
21. Chandrupatla TR, Belegundu AD (2002) Introduction to finite elements in engineering. Prentice Hall, Upper Saddle River, New Jersey, USA
22. Kennedy J, Eberhart R (1995) Particle swarm optimization. In: Proceedings of IEEE international conference on neural networks, Piscataway, NJ, pp 1942–1948
23. Parsopoulos KE, Vrahatis MN (2005) Unified particle swarm optimization for solving constrained engineering optimization problems. In: Proceedings of the first international conference on advances in natural computation—Volume Part III. Springer, Berlin, Heidelberg, pp 582–591
24. Parsopoulos KE, Vrahatis MN (2010) Particle swarm optimization and intelligence
25. Karaboga D, Akay B (2009) A comparative study of artificial bee colony algorithm. Appl Math Comput 214:108–132. https://doi.org/10.1016/j.amc.2009.03.090
26. Esfandiari A, Bakhtiari-Nejad F, Rahai A (2013) Theoretical and experimental structural damage diagnosis method using natural frequencies through an improved sensitivity equation. Int J Mech Sci 70:79–89. https://doi.org/10.1016/j.ijmecsci.2013.02.006
27. Priestley MJN, Seible F, Calvi GM (1996) Seismic design and retrofit of bridges. Wiley, New York, USA
28. ASCE (2002) SEI/ASCE7-02: minimum design loads for buildings and other structures, SEI/ASCE 7. Reston, Virginia, USA
29. Hao H, Xia Y (2002) Vibration-based damage detection of structures by genetic algorithm. J Comput Civ Eng 16:222–229. https://doi.org/10.1061/(ASCE)0887-3801(2002)16:3(222)

Semi-active Control of a Three-Storey Building Structure

P. Chaudhuri, Damodar Maity and Dipak Kumar Maiti

Abstract This paper proposes two different semi-active control methods. Linear Quadratic Gaussian (LQG) controller is used as the first method for feedback control of the structure. The second method has used structural stabilization using pole placement and optimizing the response by pattern search genetic algorithm approach. Magnetorheological (MR) damper is attached to the structure to provide the required damping force. A clipped optimal control method is used to provide the required voltage to the MR damper to generate the desired control force to the structure.

Keywords Linear Gaussian quadratic controller · Feedback control · Genetic algorithm · Clipped optimal control

1 Introduction

Semi-active [1] control of a system has come to acceptance more than active and passive control systems in structural control nowadays. These systems have managed to possess the adaptability of active control systems along with their intrinsic stability as passive control systems. These systems can be operated using very low power. Different control methods [2] and optimization methods can be implemented easily with semi-active systems. This can further exceed the performance of that of active control systems.

Magnetorheological (MR) damper [3] is one semi-active device that seems to be particularly suitable for seismic protection. MR dampers [4, 5] are semi-active

P. Chaudhuri (✉) · D. Maity
Civil Engineering Department, IIT Kharagpur, Kharagpur, India
e-mail: payelce@gmail.com

D. Maity
e-mail: dmaity@civil.iitkgp.ernet.in

D. K. Maiti
Aerospace Engineering Department, IIT Kharagpur, Kharagpur, India
e-mail: dkmaiti@aero.iitkgp.ernet.in

B. N. Singh et al. (eds.), *Recent Advances in Theoretical, Applied, Computational and Experimental Mechanics*, Lecture Notes in Mechanical Engineering,
https://doi.org/10.1007/978-981-15-1189-9_24

devices. Therefore, they have very low power requirements and a controllable damping force. They can be made to achieve large force capacities as well. They also have a low sensitivity to temperature changes.

This study proposes two different semi-active control methods. The first method is Linear Quadratic Gaussian (LQG) controller used for semi-active feedback control of the structure. The second method involves structural stabilization using pole placement and adding compensatory gain and optimizing the response by pattern search genetic algorithm (GA) approach. Clipped optimal control strategy has been used to calculate the voltage required for MR damper to produce the desired control damping force to the structure.

2 Mathematical Formulation

A three-story shear building model has been taken up from Mahdi and Abdelhafid [6] and is shown in Fig. 1. A linear MR damper is attached to produce optimal control damper force from the required calculated voltage using clipped optimal controller. State space design of the model has been done to implement the proposed control designs. The controller $K_c(s)$ has been developed both by using LQG methods and genetic algorithms each. Block diagrams of this semi-active control system are shown in Figs. 1 and 2.

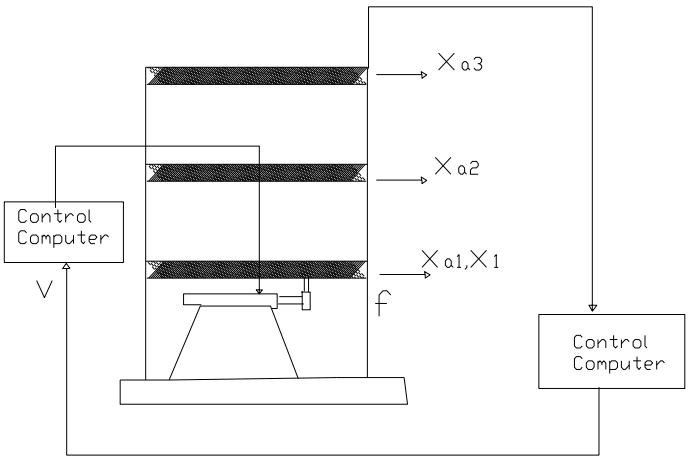

Fig. 1 A three story building control structure

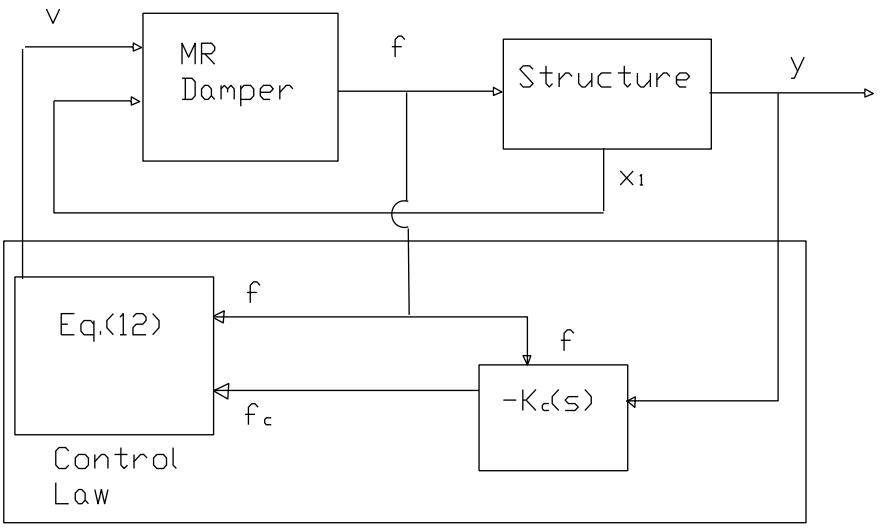

Fig. 2 Block diagram of feedback control

2.1 State Space Formulation

Considering a seismically excited structure, state space representation (Ogata, 5th Edition [7]) of a linear structure is written in Eqs. (1) and (2).

$$\dot{z} = Az + Bx \tag{1}$$

$$y = Cz + Dx \tag{2}$$

where z(.) is the "state vector", z(.) $\in R^n$;

y(.) is the "output vector", y(.) $\in R^q$;
x(.) is the "input (or control) vector", u(.) $\in R^p$;
A(.) is the "state (or structure) matrix", dim[A(.)] $= n \times n$,
B(.) is the "input matrix", dim[B(.)] $= n \times p$,
C(.) is the "output matrix", dim[C(.)] $= q \times n$,
D(.) is the feed-forward matrix
p is the number of inputs
q is the number of outputs
n are the number of state variables

The State space model has been prepared according to the Eqs. (1) and (2) are shown in Eq. (3).

$$A = \begin{bmatrix} -M^{-1}C & -M^{-1}K \\ E & 0 \end{bmatrix} B = \begin{bmatrix} -M^{-1}\Gamma & -E \\ 0 & 0 \end{bmatrix} C = [E] D = [0] \tag{3}$$

where [E] and [0] are identity and zeros matrices of suitable sizes. The vectors z and x can be written in Eq. (4)

$$z = \begin{bmatrix} \dot{u} \\ u \end{bmatrix} \text{and x} = \begin{bmatrix} f \\ \ddot{x}_g \end{bmatrix} \tag{4}$$

The structure is controllable up to four numbers of states out of six states. The control force required is produced by a single linear MR damper using clipped optimal control strategy.

2.2 Control Theory Implementation

A three degree of freedom seismically excited structure is assumed to be controlled with the control forces obtained from a single MR damper. The combined structure is considered to be linear and the equation of motion is written in Eq. (5).

$$M\ddot{u} + C\dot{u} + Ku = \Gamma f - M\Lambda\ddot{x}_g \tag{5}$$

where f is the controlled damper force, defined by Eqs. (6) and (7), $u = [\, u_1 \; u_2 \; u_3 \,]'$ are the floor displacements of the frame structure with respect to the ground.

The state space equation and output equations are modified in Eqs. (6) and (7).

$$\dot{z} = Az + Bf + G\ddot{x}_g \tag{6}$$

$$y = Cz + Df + v_{\mathrm{m}} \tag{7}$$

where $\ddot{x}_g$ is a unidirectional ground acceleration, f is the measured damper force provided by MR damper to the structure and z is the state vector. y is the measured output vector, and v is the noise vector provided to the structure.

2.3 Linear Quadratic Gaussian (LQG) Design

The controller $K_c(s)$ has been developed using LQG [8] methods which has been defined substantially. The major advantage of the LQG design is that it not only controls the output response of the controllable states to desirable values but also reduce the response of uncontrollable states. For a continuous-time linear structure, defined on $t \in [t_0, t_1]$, described by Eqs. (6) and (7) the state feedback law $u = -kx$ minimizes a quadratic cost function defined in Eq. (8).

$$J = x^T(t_1)F(t_1)x(t_1) + \int_{t_0}^{t_1} (x^T Qx + u^T Ru + 2x^T Nu)dt$$

$$N \geq 0,\ Q(t) \geq 0,\ R(t) \geq 0 \tag{8}$$

where E is the expected value. T is the final time. Using Matlab programs, the gain matrix K matrix has been computed by solving the algebraic Riccati equation.

2.4 Genetic Algorithm (GA)

It is a population based probabilistic search [10] and optimization technique [11]. A population [9] of initial solution of size N ($N = 100, 200, 300$) is generated at random in the beginning. The solutions are represented with number of strings [12]. A string is divided into a number of substrings equal to the number of design variables. The length of each substring can be calculated in Eq. (9).

$$l = \log_2\left(\frac{x_1^{\max} - x_1^{\min}}{\varepsilon}\right) \tag{9}$$

where l is the length of each sub-string; ϵ is the precision level; x_1^{max} and $x_1^{\min}$ are the maximum and minimum values of one design variable or substring. The fitness value of each full GA string is calculated from the substring values with the following relation given in Eq. (10).

$$x_1 = x_1^{\min} + \frac{x_1^{\max} - x_1^{\min}}{2^l - 1} \times D \tag{10}$$

where

x_1 is the real value of one sub-string;
D decoded value for the binary sub-string. The objective function is expressed as given in Eq. (11)

$$F(x_1, x_2, x_3) = f_i(X) \pm P_i \tag{11}$$

where $P_i = C\Sigma\varphi_{ik}(X)^2 =$ is the static penalty function for constraint optimization. Rank-based reproduction selection scheme is used to rank out the strings according to their fitness values [12]. Multiple point crossover scheme is used on each pair of strings. A bit-wise mutation scheme is developed to provide a local change in the current solution. One generation of a GA is completed after the population of strings is modified using the schemes. The whole procedure is repeated through a number

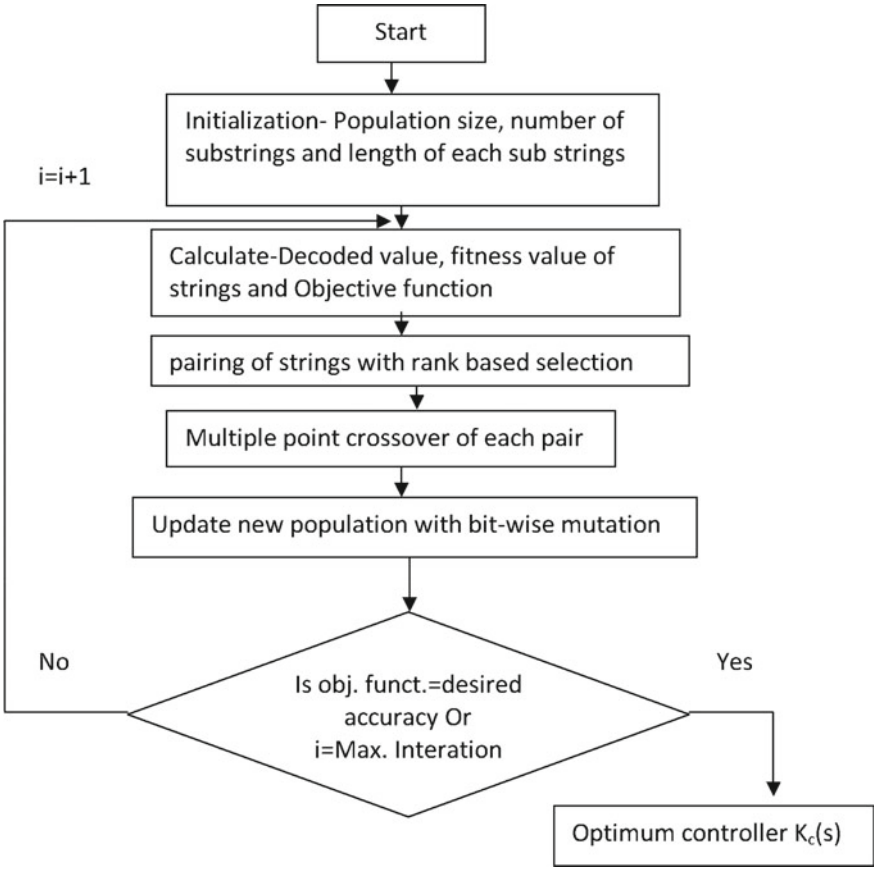

Fig. 3 A flowchart for genetic algorithm

of cycles until a termination criterion is satisfied that is either the objective function acquire a predefined value or maximum iteration is reached. A flowchart is shown in Fig. 3.

2.5 Clipped Optimal Controller

A type of clipped optimal controller [13] is introduced in this study. The controller $K_c(s)$ is designed both by LQG and GA each to estimate the desired control force, f_c (Eq. 12). y is the measured responses and f is the measured damper force. L is a Laplace transform.

$$f_c = L^{-1}\left[K_c(s)L\begin{bmatrix} y \\ f \end{bmatrix}\right] \tag{12}$$

This force f_c will be provided by the MR damper. Force generated by the MR damper can only be changed by changing the voltage applied to the MR damper. This desired voltage (Eq. 13) required for MR damper to produce the desired force f_c is supplied by the linear clipped optimal controller.

$$v = V_{\max} H\{(f_c - f)f\} \tag{13}$$

where $V_{\max}$ is the voltage required for the saturation of the magnetic field of the MR damper and H is the Heaviside step function and v is the voltage required. The controller algorithm of linear variation of the desired control force with the required voltage is shown in Fig. 4.

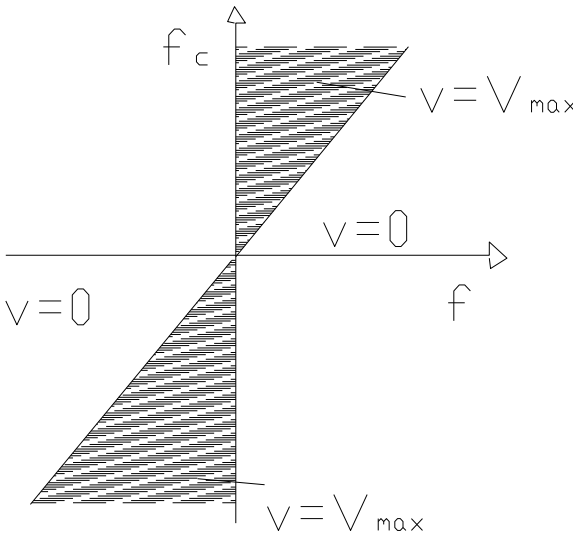

Fig. 4 A linear clipped optimal control algorithm

3 Results and Discussions

A three-storey frame model as shown in Fig. 1 spanning one bay in X direction and Z direction each is chosen for the present work. El-Centro (CA, USA) earthquake data (October, 1942) has been used as dynamic load to the structure. State space design of the model has been done to implement the proposed control design. The compensator gain has been suitably adjusted by adding a pole for a stable root locus diagram of the open-loop system. Suitable controllers from LQG design and genetic

Table 1 System Matrices of three-story building

Mass matrix, $[M]$	$M = \begin{bmatrix} 98.3 & 0 & 0 \\ 0 & 98.3 & 0 \\ 0 & 0 & 98.3 \end{bmatrix}$ kg
Stiffness matrix, $[K]$	$K = \begin{bmatrix} 12 & -6.84 & 0 \\ -6.84 & 13.7 & 6.84 \\ 0 & -6.84 & 6.84 \end{bmatrix} 10^5$ N/m
Damping matrix, $[C]$	$C = \begin{bmatrix} 175 & -50 & 0 \\ -50 & 100 & -50 \\ 0 & -50 & 50 \end{bmatrix}$ Ns/m
Location matrix of MR damper force	$\Gamma = [1\ 0\ 0]^T$
External force distribution matrix	$\Lambda = [1\ 1\ 1]^T$

algorithm are incorporated to control the dynamic response of the structure. An MR damper is attached to the model. The required control force has been calculated to produce optimum damper force using clipped optimal control method. The system matrices of the model are shown in Table 1.

The State space model has been prepared according to the Eq. (3). The structure is controllable up to four numbers of states out of six states.

Case 1. Step responses of the outputs in the uncontrolled model, LQG controlled, and GA controlled model are shown in Figs. 5, 6, and 7.

It can be clearly shown in the figures above that LQG design and GA control can reduce the responses to great extent. In GA controlled structure the step response can be smoothened out further to a steady state response with specific rise time and peak amplitude. It, therefore, reduces the noise generated in the structure and gives a steady state output.

Case 2. Dynamic responses of the outputs in the uncontrolled model, LQG controlled, and GA controlled model due to El-Centro (CA, USA) earthquake acceleration (October, 1942) are shown in Figs. 8, 9, and 10.

LQG controller and GA controller were used as a feedback controller to the structure to control the responses due to dynamic load. The required control force to be generated by the MR damper is regulated using the clipped optimal controller.

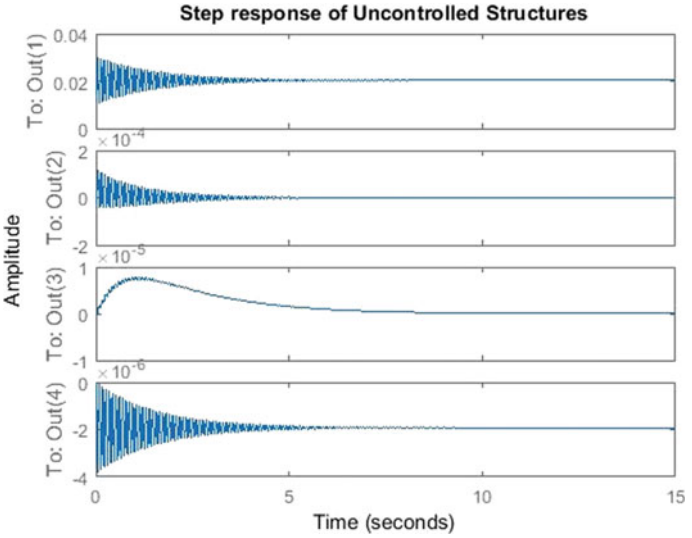

Fig. 5 Uncontrolled step response

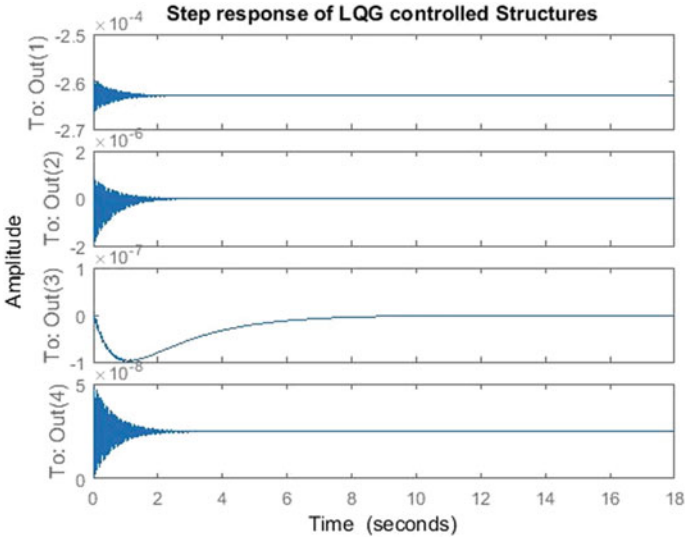

Fig. 6 LQG controlled step response

From figures it can be observed that LQG and GA control are both efficient in reducing the vibration response to a large extent.

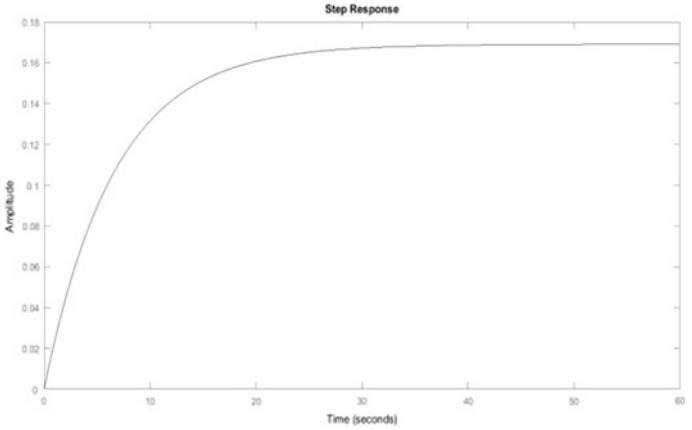

Fig. 7 GA controlled step response

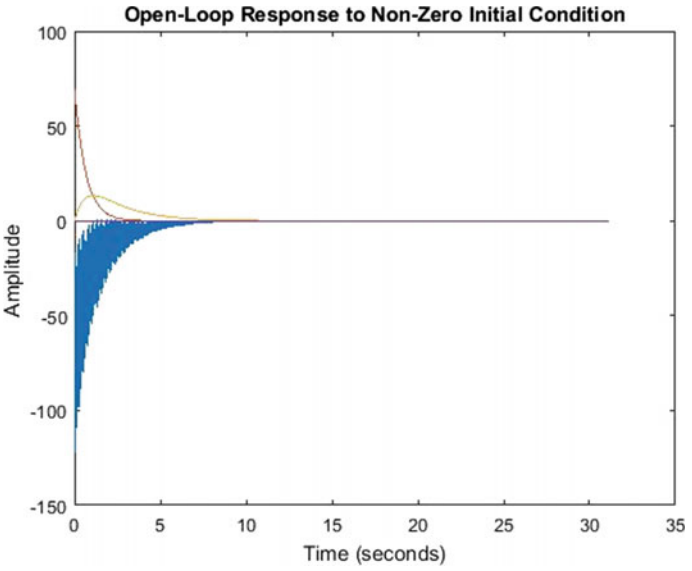

Fig. 8 Uncontrolled output response

Case 3. Horizontal displacements and Maximum displacement values of the floors due to earthquake in the uncontrolled, LQG designed, and GA optimized structure is shown in the Figs. 11 and 12.

It can be observed that horizontal displacements of floors have come to nil when the structure is controlled with semi-active control methods. Earthquake data of different magnitude and duration has been taken and a comparative study is done to

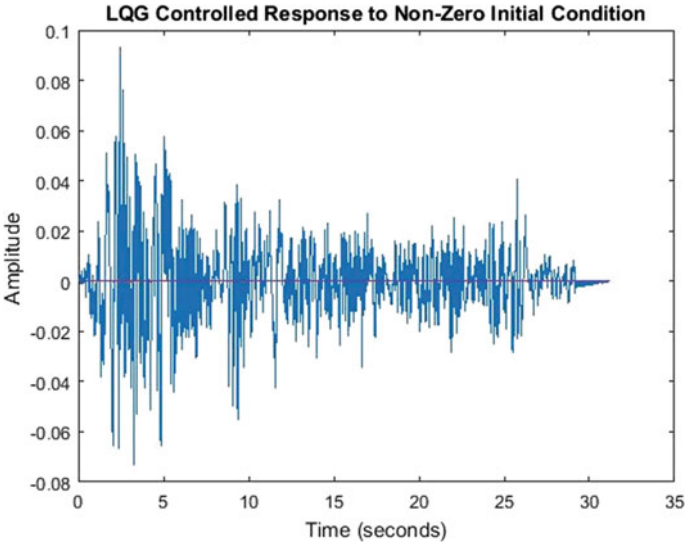

Fig. 9 LQG controlled output response

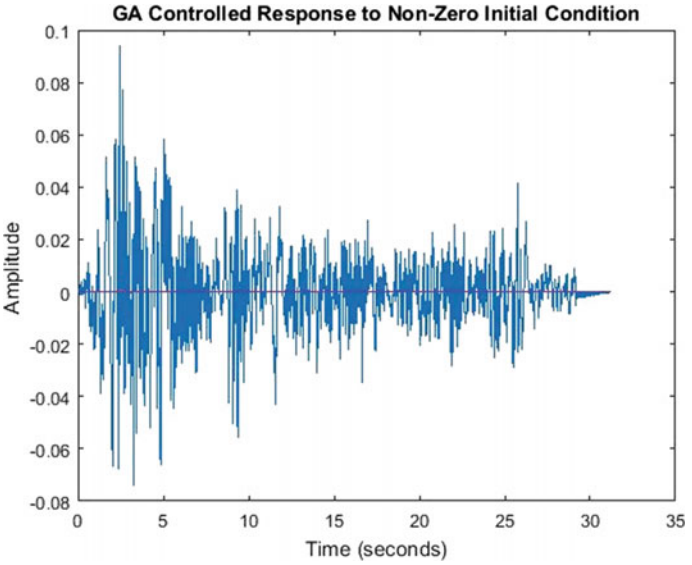

Fig. 10 GA controlled output response

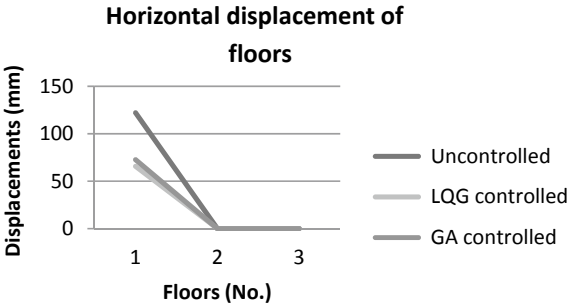

Fig. 11 Horizontal displacements in floors

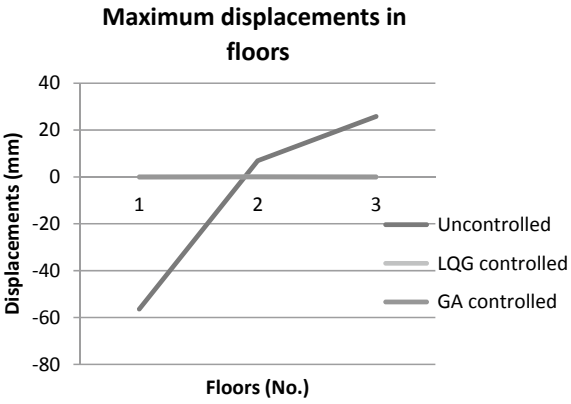

Fig. 12 Maximum displacements in floors

show the flexibility of both the methods. The root mean square value of displacements in each floor for all earthquake data has been tabulated in Table 2.

The efficiency of both the methods can be clearly observed in Table 2. The LQG controlled and GA controlled structures have shown a significant reduction in the displacement values for the structure.

Table 2 RMS value of the displacements

Earthquakes used	Maximum magnitude (mm/s^2)	Duration (s)	Root mean square displacement (mm)		
			Uncontrolled	LQG	GA
Elcentro NS	3.13	35	36.0087	0.0230	0.0233
Arizona NS	0.05	180	11	0.033	0.029
Fukushima EW	0.0037	120	10	0.011	0.010
Lomapreita	28.87	40	10.5	0.5	0.5

4 Conclusion

The controller is designed using both the conventional LQG method and genetic algorithm. These methods can show much flexibility to produce desirable range of outputs in different loading conditions. The clipped optimal controller has been used to get the optimized voltage required by MR damper to produce damper force. Suitable MR dampers can be placed to the structure and the responses can be studied. Both the methods have shown significant efficiency in reducing the seismic vibration of building. The proposed methods of controlling the structure itself can be implemented in higher storey space frame building.

References

1. Yi F, Dyke SJ, Caicedo JM, Carlson JD (2001) Experimental verification of multi-input seismic control strategies for smart dampers. J Eng Mech (ASCE) 127(11):1152–1164
2. Jansen LM, Dyke SJ (2000) Semiactive control strategies for MR dampers: comparative study. J Eng Mech (ASCE) 126(8):795–803
3. Park JM, Gang HG, Sohn JW (2015) Parametric study on damping force characteristics of MR damper with various inner magnetic core shapes. In: 22nd International congress on sound and Vibration, Florence, Italy, pp 1–2
4. Khan SA, Suresh A, Ramaiah NS (2014) Principles characteristics and applications of magneto rheological fluid damper in flow and shear mode. Procedia Mater Sci 6:1547–1556
5. Cha YJ, Zhang J, Agarwal AK, Dong B, Friedman A, Dyke SJ, Ricles J (2013) Comparative studies of semi-active control strategies for MR dampers: pure simulation and real-time hybrid tests. J Struct Eng (ASCE) 139(7):1237–1248
6. Mahdi A, Abdelhafid O (2015) Seismic response reduction using semi-active magneto-rheological dampers. Innov Constr
7. Ogata K (2009) Modern control engineering, 5th edn. Prentice Hall, pp 29–44, 645–688
8. Dyke SJ, Spencer BF Jr, Sain MK, Carlson JD (1996) Modeling and control of magnetorheological dampers for seismic response reduction. Smart Mater Struct 5(5):565–575
9. Pratihar DK (2014) Soft computing fundamentals and applications. Narosa Publishing House, pp 40–51, 87–89
10. Holland JH (1984) Adaptive control of ill-defined system. NATO Conf. Series (II Systems Science) Springer 16, pp 317–333
11. Jose K, Pratihar D (2016) Task allocation and collision-free path planning of centralized multi-robots system for industrial plant inspection using heuristic methods. Robot Auton Syst 80:2016. https://doi.org/10.1016/j.robot
12. Saxena P, Dixit A (2009) Software component retrieval using genetic algorithms. In: 2009 International Conference on Computer and Automation Engineering ICCAE, Bangkok, pp 151–155. https://doi.org/10.1109/iccae.2009.62
13. Dyke SJ, Spencer BF Jr, Sain MK, Carlson JD (1999) An experimental study of mr dampers for seismic protection. Smart Mater Struct 7(5):1–19

A Direction-Based Exponential Crossover Operator for Real-Coded Genetic Algorithm

Amit Kumar Das and Dilip Kumar Pratihar

Abstract In this paper, a new direction-based exponential crossover operator (DEX) for a real-coded genetic algorithm (RCGA) has been developed. Its name indicates that this newly designed DEX is influenced by the directional knowledge of the problem. This knowledge about a problem actually helps to decide the search direction of the algorithm in the variable space to move toward the globally optimum solution. Now, the task of collecting this data is quite tricky and may have several ways. However, we suggest one approach to obtain this knowledge during the evolution of solutions. Utilizing this prior knowledge during the crossover operation, the children solutions are created with a biasness of that search direction. This, in fact, makes the searching mechanism of an RCGA more efficient. To measure the performance of the DEX, ten classical benchmark test functions have been taken and the experiments are done using an RCGA with the proposed crossover operator, and the results are compared with another popular crossover operator, namely, simulated binary crossover (SBX).

Keywords Exponential crossover · Directional crossover · Genetic algorithm · Metaheuristic technique · Global optimization

1 Introduction

Optimization is the method of searching the best feasible candidate out of several potential solutions. In real-world applications, it deals with many nonlinear complex problems, which have one or more than one design variables and constraints. The purpose of optimizing a process or the design of a product is the reduction in various costs, such as material, rejection, and labor, or to increase the overall performance and profit [1]. Although traditional deterministic algorithms had been used for solving several optimization problems, these are not found to be suitable in case of solving large-scale problems with ill-conditioned or non-smoothed objective function.

A. K. Das · D. K. Pratihar (✉)
Indian Institute of Technology Kharagpur, Kharagpur 721302, India
e-mail: dkpra@mech.iitkgp.ernet.in

B. N. Singh et al. (eds.), *Recent Advances in Theoretical, Applied, Computational and Experimental Mechanics*, Lecture Notes in Mechanical Engineering,
https://doi.org/10.1007/978-981-15-1189-9_25

Therefore, researchers had copied the Mother Nature to obtain new ways to solve the problems and consequently, several nature-inspired optimization techniques have been designed and successfully implemented to solve a variety of problems. Among several bioinspired algorithms, Genetic algorithm [2] (GA), Particle swarm optimization [3] (PSO), Differential evolution [4] (DE), Ant colony optimization [5] (ACO), Bat algorithm [6] (BA), etc., are the most popular evolutionary optimization techniques available in the literature.

Genetic algorithm (GA) is one of the most robust stochastic algorithms used in different types of applications. It is very easy and straightforward to implement, able to handle a large variable space and very flexible in assigning the objective function and the constraints [7]. It works based on Darwin's principle of natural selection. It consists of three stochastic operators, such as selection, crossover, and mutation. In the selection scheme, better solutions (in terms of their fitness values) are given advantages for creating mating pools. During crossover, the properties of two mating parents are exchanged to obtain two new children solutions. After this operation, the solutions may find sudden changes while passing through the mutation operator, which helps the algorithm to overcome the problem of local optimum. Among these three main operators of a GA, the crossover scheme has a great role in searching for new solutions to reach the globally optimal point. Several attempts were made to design an efficient crossover operator of a GA. Wright [8] proposed a heuristic crossover operator, in which one child is created out of two parents and the child has a bias toward the better parent. Radcliffe [9] suggested a crossover operator, namely, flat crossover. In this type of recombination, one child solution is obtained randomly in between a pair of parents. Michalewicz [10] introduced an arithmetical crossover with two variants, such as uniform and nonuniform arithmetical crossover. Eshelman and Schaffer [11] developed a blend crossover operator (BLX-α), where the locations of the children solutions to be created by the parents, are calculated using the parameter α. The suggested standard value for α was equal to 0.5. Deb and Agrawal [12] proposed the simulated binary crossover (SBX), in which two offspring are generated from a pair of mating parents. It imitates the concept of a single-point crossover on binary strings in continuous space. Ono and Kobayashi [13] developed a unimodal normal distribution crossover operator (UNDX). In this scheme, two or more children solutions are generated from three parent solutions. To demonstrate the performance of the said operator, only three problems were solved, which might not be sufficient to conclude anything firmly. Tsutsui et al. [14] suggested a simplex crossover (SPX), where to create the offspring, three or more parents were used. From some numerical experiments, they inferred that SPX could give a better performance, where the objective function is multimodal and/or it has epistasis with a medium number of mating parents. Another operator, namely, parent-centric crossover (PCX) was developed by Deb et al. [15] for real parameter optimization and its performance was compared with the other popular crossover operator like SPX, UNDX, etc. However, it was tested on three problems only, which might not be sufficient enough to conclude anything significant. Utilizing the Laplace distribution to evaluate the location of the offspring solution, Deep and Thakur [16] proposed a new crossover operator, named Laplace crossover (LX). Apart from these,

Kuo and Lin [17] suggested a directed crossover for an RCGA. This recombination method was designed based on the reflection and expansion search mechanism of Nelder-Mead's simplex approach. Chuang et al. [18] developed a parallel-structured RCGA, in which a direction-based crossover (DBX) was proposed. From the various simulation results, it was observed that this method could yield good performance for multimodal and high-dimensional hybrid objective functions only.

It is to be noted that there are several crossover operators for the RCGA available in the literature of GA. However, the novel concept of deriving the most-favorable search direction and its application to yield new children solutions are missing in most of the crossover schemes. In this paper, we introduce a direction-based exponential crossover operator (DEX) for a real-coded genetic algorithm (RCGA), where two offspring are generated from a pair of mating parents using exponential functions and predetermined directional information of the decision variables. In the proposed DEX operator, most-promising directional information is used in an efficient way for creating the children solutions. Moreover, two probability terms, such as directional crossover probability (p_{cd}) and exploration probability (p_e) are introduced in the proposed DEX to preserve a superior balance between the exploitation and exploration of the search process and these are found to be the novelties of the present study. The remaining part of the text is arranged as follows: Sect. 2 describes the details of the proposed crossover operator, whereas the results and discussion are presented in Sect. 3. At the end, some conclusions are made in Sect. 4.

2 The Proposed DEX Operator

In this section, a novel crossover scheme is proposed, namely, direction-based exponential crossover (DEX). It uses exponential functions and predetermined information regarding the appropriate directions of the design variables to make the search process efficient. This operator has been designed in two stages:

- Getting directional knowledge of the design variables,
- Obtaining children solutions applying directional knowledge and exponential functions.

2.1 Getting Directional Knowledge of the Design Variables

The name of this crossover scheme clearly indicates that DEX is influenced by the directional knowledge of the problem. The collected information of the variables actually helps to decide the search direction of the algorithm in the variable space to move toward the globally optimal solution. Now, the task of obtaining this data is difficult and may have several ways for the same. Here, we propose one method to get this information during evolution.

At first, we have to calculate the average numerical value of the current population for each decision variable. This calculation is to be done for each generation. Now, for each variable, we have to make comparisons between the average value obtained in the current generation and that calculated in the previous generation. When the average value of a variable in the current generation is observed to be more compared to that of the previous generation, then the direction for that variable is considered as the positive in that generation. In another case, when the average value of a variable becomes less than that in the previous generation, the direction for the variable is taken as the negative in that particular generation. An example has been shown in Fig. 1 with a 2-D variable space. In this example, at $(T + 1)$th generation, the obtained directional information is positive for both the variables.

In this way, for every generation, except for the first and second ones, we can obtain the directional information for the design variables. For the second generation, the calculated average values of the variables are compared with the best solution available in that generation and in a similar way, the directional information is obtained. However, it is not required to derive the directional knowledge for the very first generation as there is no crossover taking place in that generation.

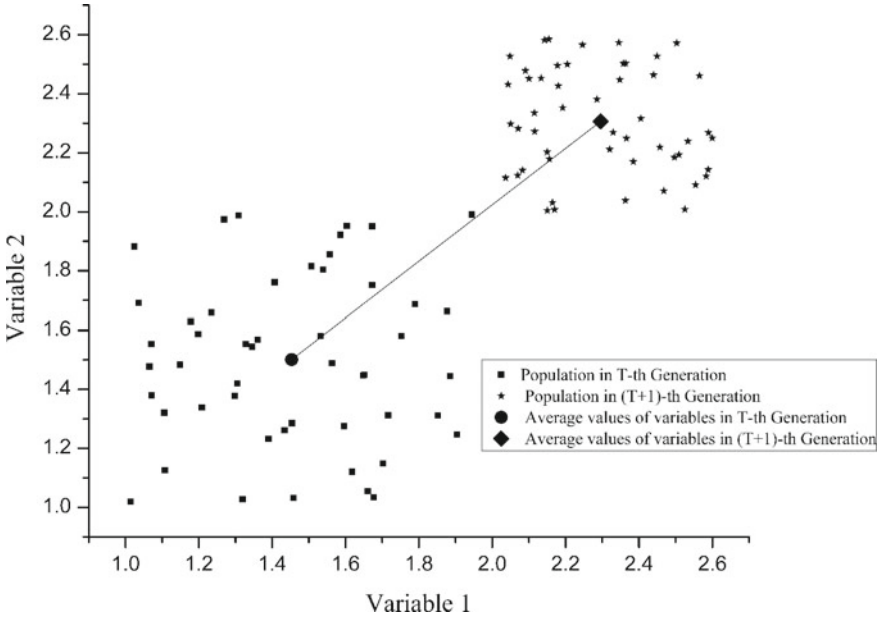

Fig. 1 In 2-D plane, the directional knowledge at $(T + 1)$th generation

2.2 Obtaining Children Solutions Applying the Directional Knowledge and Exponential Functions

Utilizing the obtained directional knowledge of the variables, the locations of the children solutions are controlled to a greater extent. However, there are other aspects which are also responsible for determining the positions of the offspring. A more detailed description of this scheme is given below in a few steps.

First step: Let us say, the population size of the solutions is taken as N. After the selection operation, $N/2$ pairs of mating solutions are created randomly from the N number of selected members. A mating pair participates in crossover, while the generated random value (ranging from 0 to 1) is observed to be either less than or equal to the crossover probability (p_c). Otherwise, the mating pair is not allowed to join in crossover.

Second step: After the first step, the recombination operator is applied variable-wise for the mating solutions, which are permitted to join in the crossover. Here, another probability, say variable-wise crossover probability (p_{cv}) is applied to decide whether the crossover is going to occur or not to a certain variable position. This concept of p_{cv} is implemented in a similar way to that of p_c as mentioned in first step.

Third step: The mating parents, which have passed through the said two steps and are allowed to join in the crossover, exchange their properties to yield children solutions according to the scheme described in this step. We consider a user-defined very small positive number, say ε. Depending on the value of ε, there may occur two scenarios, in which two different crossover schemes are adopted as follows:

- Scenario 1: Absolute difference between the two mating parents is more than ε

Between the two mating parents, let us take the smaller one as p_1 and the larger one as p_2. Then, a parameter, say val, is calculated using the Eq. (1):

$$\text{val} = 1 - 0.5^{\{e^{\frac{(p_2-p_1)}{(y_u-y_l)}}\}} \tag{1}$$

where y_u and y_l are the upper and lower boundaries of the decision parameters, respectively. Now, whenever the directional knowledge for a variable is found to be positive and a random number (varying from 0 to 1) is observed to be either less than or equal to a parameter, say directional crossover probability (p_{cd}), two children solutions (c_1 and c_2) are generated using the Eqs. (2) and (3).

$$c_1 = \text{val} \times (p_1 + p_2) + \alpha^r \times e^{(1-r)} \times (1 - \text{val}) \times (p_2 - p_1), \tag{2}$$

$$c_2 = (1 - \text{val}) \times (p_1 + p_2) - \alpha^{(1-r)} \times e^{(r-2.5\times r)} \times \text{val} \times (p_2 - p_1), \tag{3}$$

where α is the spread factor, which generally varies from 0 to 4, and r is a random number created in the range of (0,1). However, if the directional information of the

variable is seen to be positive and a random number (generated between 0 and 1) is found to be greater than the value of p_{cd}, the offspring c_1 and c_2 are created by the given two equations (Eqs. 4 and 5) as follows:

$$c_1 = \text{val} \times (p_1 + p_2) - \alpha^r \times e^{(1-r)} \times (1 - \text{val}) \times (p_2 - p_1), \tag{4}$$

$$c_2 = (1 - \text{val}) \times (p_1 + p_2) + \alpha^{(1-r)} \times e^{(r-2.5\times r)} \times \text{val} \times (p_2 - p_1). \tag{5}$$

In another case, where the directional information is found to be negative for a variable and a random value lying in the range of (0, 1), is found to be either less than or equal to the value of p_{cd}, the children solutions (c_1 and c_2) are yielded using the Eqs. (4) and (5). Similarly, generations of the offspring c_1 and c_2 are done by utilizing the Eqs. (2) and (3), respectively, when the directional information of the variable is obtained as negative and the value of p_{cd} is found to be less than a number randomly created in the range of 0–1.

- Scenario 2: Absolute difference between two mating parents is less than or equal to ε

In this case, a pair of mating pool is allowed to participate in the crossover only when a random number (varying from 0 to 1) is obtained as either less than or equal to a parameter, say exploration probability (p_e). If this condition is satisfied, that is, the two parents take part in the crossover, the children solutions are produced exactly in the same way as described in scenario 1, except the equation for deriving the parameter val (that is, Eq. 1). In this case, the parameter val is evaluated using the mathematical expression given in Eq. (6):

$$\text{val} = 1 - (0.5 \times E_r)^{\left\{\left(E_r^{(1-r)}\right)\times e^{\frac{(p_2-p_1)}{(y_u-y_l)}}\right\}} \tag{6}$$

where E_r is the exploration ratio and it takes a numerical value which is seen to be very near to 1, and r is a random number varying in the range of 0–1.

If a child solution is found to be greater than the upper limit of the variable (y_u) or less than the lower limit of the variable (y_l), then its value is taken as the value of y_u or y_l, respectively. These are called the variable limiting conditions.

Fourth step: This is the last step of the proposed scheme, where the newly generated offspring (c_1 and c_2) are recognized. If a random value (yielded between 0 and 1) is obtained as either less than or equal to 0.5, then c_2 and c_1 are considered as the first child and second child of the generated pair of solutions, respectively. In another case, c_1 and c_2 are recognized as the first child and second child of the yielded pair of solutions, respectively, if a random value, varying from 0 to 1, is found to be greater than 0.5. These defined conditions are denoted as children recognition conditions.

A pseudo-code of the proposed crossover operator is presented in Table 1.

Table 1 The pseudo-code of the DEX operator

Input: A mating pair ($Parent_1$ and $Parent_2$) with d number of decision variables, DEX parameters

Output: Generated children solutions ($Child_1$ and $Child_2$)

```
if rand ≤ p_c
    for i = 1 to d
        if rand ≤ p_cv
            p_1 ← mimimum between Parent_1(i) and Parent_2(i)
            p_2 ← maximum between Parent_1(i) and Parent_2(i)
            if abs(Parent_1(i) − Parent_2(i)) > ϵ
                val ← using Eq. (1)
                        if direction(i) is positive
                            if rand ≤ p_cd
                            c_1 and c_2 ← use Eq. (2) and Eq. (3)
                            else
                            c_1 and c_2 ← use Eq. (4) and Eq. (5)
                            endif
                        else
                            if rand ≤ p_cd
                            c_1 and c_2 ← use Eq. (4) and Eq. (5)
                            else
                            c_1 and c_2 ← use Eq. (2) and Eq. (3)
                            endif
                        endif
                Apply variable limiting conditions
                Apply children recognition conditions
            else
                if rand ≤ p_e
                    val ← using Eq. (6)
                    Obtain c_1 and c_2 similarly as line no. 8 to 22
                else
                    Child_1(i) = Parent_1(i)
                    Child_2(i) = Parent_2(i)
                endif
            endif
        else
            Child_1(i) = Parent_1(i)
            Child_2(i) = Parent_2(i)
        endif
    end of for loop
else
    Child_1(i) = Parent_1(i)
    Child_2(i) = Parent_2(i)
endif
```

3 Results and Discussion

To measure the performance of the newly designed crossover operator, we have taken ten classical benchmark test functions as given in Table 2. All the problems are assumed to have 30 dimensions (that is, $d = 30$). A real-coded genetic algorithm (RCGA) with DEX and polynomial mutation operator [19], has been run for 50 times for each of these test functions and the best solution obtained after each run has been captured. The best, worst, mean, median, and standard deviation of the obtained results are found out for each of these test functions. Similar experiments have been carried out with an RCGA equipped with simulated binary crossover and polynomial mutation operator.

Table 2 Ten benchmark test functions

Function	Mathematical formulae	Variable boundaries
F01: Sphere	$f(x) = \sum_{i=1}^{d} x_i^2$	$[-100, 100]^d$
F02: Sum of different powers	$f(x) = \sum_{i=1}^{d} \lvert x_i \rvert^{i+1}$	$[-100, 100]^d$
F03: rotated hyper-ellipsoid	$f(x) = \sum_{i=1}^{d} \sum_{j=1}^{i} x_j^2$	$[-65, 65]^d$
F04: Griewank	$f(x) = \frac{\sum_{i=1}^{d} x_i^2}{4000} - \prod_{i=1}^{d} \cos(x_i/\sqrt{i}) + 1$	$[-600, 600]^d$
F05: Trid	$f(x) = \sum_{i=1}^{d} (x_i - 1)^2 - \sum_{i=2}^{d} (x_i x_{i-1})$	$[-d^2, d^2]^d$
F06: Dixon-price	$f(x) = (x_1 - 1)^2 + \sum_{i=2}^{d} i(2x_i^2 - x_{i-1})^2$	$[-10, 10]^d$
F07: Powell	$f(x) = \sum_{i=1}^{d/4} [(x_{4i-3} + 10x_{4i-2})^2 + 5(x_{4i-1} - x_{4i})^2 + (x_{4i-2} - 2x_{4i-1})^4 + 10(x_{4i-3} + x_{4i})^4]$	$[-10, 10]^d$
F08: Alpine	$f(x) = \sum_{i=1}^{d} \lvert x_i \sin(x_i) + 0.1x_i \rvert$	$[-10, 10]^d$
F09: Bent ciger	$f(x) = x_1^2 + 10^6 \sum_{i=2}^{d} x_i^2$	$[-10, 10]^d$
F10: Schaffer F7	$f(x) = \frac{1}{d-1} \sum_{i=1}^{d-1} \left[\left(x_i^2 + x_{i-1}^2\right)^{0.25} + \left(x_i^2 + x_{i+1}^2\right)^{0.25} \sin^2\left(50\left(x_i^2 + x_{i+1}^2\right)^{0.1}\right) \right]$	$[-100, 100]^d$

Table 3 Selected special parameters' values of DEX operator

Parameter	Selected value
α	1.0
p_{cv}	0.8
p_{cd}	0.7
ε	1.0E−100
E_r	0.9999
p_e	Linearly decreasing from 0.5 to 0 over the generations

3.1 Parameters' Settings

To make a fair comparison, the common controlling parameters of both the algorithms, such as population size ($N = 60$), number of variables ($d = 30$), crossover probability ($p_c = 1.0$), mutation probability $\left(p_m = \frac{1}{d}\right)$, user-defined index parameter for polynomial mutation operator ($\eta_m = 10$), and maximum number of generations (max_gen = 500), have been kept the same. The user index parameter for SBX crossover operator (η_c) is taken as 2. Both the algorithms stop, if these are run for the maximum number of generation. Special parameters of the DEX operator, such as spread factor (α), variable wise crossover probability (p_{cv}), directional crossover probability (p_{cd}), small positive number (ε), exploration ratio (E_r), and exploration probability (p_e) are determined after several trial experiments and a set of suitable values of these parameters is selected to test the said ten benchmark functions. These chosen parameters' values are given in Table 3.

The obtained results are given in Table 4, where the best ones are marked in bold. In addition, the average number of function evaluations (f_{avg}) and average CPU time (in seconds) required in 50 runs to reach a particular accuracy of the objective function value (i.e., equal to 1 for F06 and 0.1 for others) for all the test functions are also provided in Table 4.

From the results, it is clear that RCGA with DEX operator is performing better than the RCGA with SBX operator for the ten benchmark functions. Moreover, it is observed that the proposed algorithm takes less CPU time to reach a particular accuracy of the objective function compared to that of the other. It might have happened due to the fact that the directional information derived from the problem itself has been utilized for creating the approximate children solutions in the RCGA with DEX operator. Moreover, the use of exploration probability (p_e) and exploration ratio (E_r) enhances the exploration capability of the RCGA, and this capability decreases over the generation maintaining a proper balance between the exploration and exploitation phenomena of the optimization algorithm.

Table 4 Results of benchmark test functions (F01–F10) using RCGA with DEX and SBX operators

Function		RCGA with DEX	RCGA with SBX	Function	RCGA with DEX	RCGA with SBX	Function	RCGA with DEX	RCGA with SBX
F01	Best	**4.059E−07**	9.673E−03	F02	**2.423E−10**	3.650E−04	F03	**3.249E−06**	4.474E−02
	Median	**3.743E−06**	4.259E−02		**3.674E−07**	2.939E−02		**2.400E−05**	2.382E−01
	Worst	**7.163E−04**	2.811E−01		**9.769E−05**	2.443E+00		**2.557E−03**	2.303E+00
	Mean	**2.332E−05**	5.391E−02		**7.351E−06**	1.524E−01		**1.250E−04**	3.141E−01
	SD	1.008E−04	4.186E−02		1.809E−05	3.835E−01		3.761E−04	3.323E−01
	f_{avg}	**1.341E+04**	2.486E+04		**2.060E+04**	2.819E+04		**1.622E+04**	3.902E+04
	t_{avg}	**4.469E−01**	7.342E−01		**7.607E−01**	9.722E−01		**5.520E−01**	1.222E+00
F04	Best	**5.849E−07**	1.954E−02	F05	**−3.855E+03**	−2.001E+03	F06	**6.666E−01**	6.852E−01
	Median	**2.017E−05**	9.949E−02		**−2.792E+02**	8.171E+03		**6.701E−01**	2.461E+00
	Worst	**3.927E−02**	1.108E+00		**8.166E+03**	3.892E+04		**4.417E+00**	5.845E+00
	Mean	**7.915E−03**	1.678E−01		**−3.219E+02**	9.562E+03		**1.024E+00**	2.738E+00
	SD	8.127E−03	2.386E−01		3.263E+03	9.041E+03		7.923E−01	1.381E+00
	f_{avg}	**1.456E+04**	2.638E+04		**3.041E+04**	1.249E+05		**2.869E+04**	2.590E+05
	t_{avg}	**4.910E−01**	8.184E−01		**9.598E−01**	3.653E+00		**9.488E−01**	7.053E+00
F07	Best	**1.535E−02**	4.278E−01	F08	**5.001E−06**	1.081E−03	F09	**3.077E−03**	4.954E+01
	Median	**9.045E−02**	1.746E+00		**1.309E−05**	4.885E−03		**2.232E−02**	2.545E+02
	Worst	**1.931E−01**	6.572E+00		**2.063E−04**	2.284E−02		**1.185E+00**	1.457E+03
	Mean	**9.065E−02**	2.088E+00		**2.468E−05**	6.394E−03		**7.151E−02**	3.584E+02
	SD	3.923E−02	1.214E+00		3.327E−05	5.084E−03		1.858E−01	2.993E+02
	f_{avg}	**2.813E+04**	9.369E+04		**6.773E+03**	1.182E+04		**2.809E+04**	5.393E+05
	t_{avg}	**9.445E−01**	2.939E+00		**2.319E−01**	3.628E−01		**8.834E−01**	1.314E+01

(continued)

Table 4 (continued)

Function		RCGA with DEX	RCGA with SBX	Function	RCGA with DEX	RCGA with SBX	Function	RCGA with DEX	RCGA with SBX
F10	Best	**3.577E−02**	2.351E−01						
	Median	**1.061E−01**	3.729E−01						
	Worst	**2.830E−01**	6.283E−01						
	Mean	**1.095E−01**	3.825E−01						
	SD	4.393E−02	9.138E−02						
	f_{avg}	**3.624E+04**	2.015E+05						
	t_{avg}	**1.767E+00**	8.617E+00						

4 Conclusion

In this study, a new direction-based exponential crossover (DEX) is proposed and described in detail. The proposed crossover operator is influenced by the directional information of the decision variables and this information is gathered from the problem using a newly developed method. This information helps to decide the locations of the children solutions and it makes the search process of the algorithm more efficient. Also, in the developed crossover operator, there is a method to inject more exploration capability into search process and this is reduced gradually over the generations, keeping a nice balance between the exploration and exploitation capabilities of an RCGA. The proposed DEX has been tested on the ten classical benchmark functions and the results are compared with that of the other crossover operator, such as simulated binary crossover (SBX). The obtained results clearly indicate that the proposed crossover operator outperforms the SBX operator for these test cases. The performance of the DEX will be tested in future for more number of test functions and real engineering optimization problems. Moreover, an effort will be taken to make the parameters of the DEX operator as self-adaptive or self-determinative, so that the user intervention may be avoided.

References

1. Mazhoud I, Hadj-Hamou K, Bigeon J, Joyeux P (2013) Particle swarm optimization for solving engineering problems: a new constraint-handling mechanism. Eng Appl Artif Intell 26(4):1263–1273
2. Davis L (1991) Handbook of genetic algorithms. Van Nostrand Reinhold, New York
3. Eberhart R, Kennedy J (1995) A new optimizer using particle swarm theory. In: The sixth international symposium on micro machine and human science (MHS'95), Japan, pp 39–43
4. Das S, Suganthan PN (2011) Differential evolution: a survey of the state-of-the-art. IEEE Trans Evol Comput 15(1):4–31
5. Dorigo M, Maniezzo V, Colorni A (1996) Ant system: optimization by a colony of cooperating agents. IEEE Trans Syst Man Cybern B Cybern 26(1):29–41
6. Yang X-S (2010) A new metaheuristic bat-inspired algorithm. In: González J, Pelta D, Cruz C, Terrazas G, Krasnogor N (eds) Nature inspired cooperative strategies for optimization (NICSO 2010), vol 284, Berlin, Heidelberg, pp. 65–74
7. Fahimnia B, Luong L, Marian R (2008) Optimization/simulation modeling of the integrated production-distribution plan: an innovative survey. WSEAS Trans Bus Econ 3(5):52–65
8. Wright AH (1991) Genetic algorithms for real parameter optimization. In: Rawlins GJE (ed) Foundations of genetic algorithms, vol 1, pp 205–218. doi:https://doi.org/10.1016/B978-0-08-050684-5.50016-1
9. Radcliffe NJ (1991) Equivalence class analysis of genetic algorithms. Complex Syst 2(5):183–205
10. Michalewicz Z (1992) Genetic algorithms + data structures = evolution programs. Springer-Verlag, New York
11. Eshelman LJ, Schaffer JD (1993) Real-coded genetic algorithms and interval-schemata. In: Proceedings of the workshop on foundation of genetic algorithms, Vail, CO, USA, pp 187–202
12. Deb K, Agrawal RB (1995) Simulated binary crossover for continuous search space. Complex Syst 9(2):115–148

13. Ono I, Kobayashi S (2003) A real-coded genetic algorithm for function optimization using unimodal normal distribution crossover. In: Ghosh A, Tsutsui S (eds) Advances in evolutionary computing. Natural Computing series, Berlin, Heidelberg
14. Tsutsui S, Yamamura M, Higuchi T (1999) Multi-parent recombination with simplex crossover in real-coded genetic algorithms. In: Banzhaf W, Daida J, Eiben A, Garzon M, Honavar V, Jakiela M, Smith R (eds) Proceedings of the Genetic and Evolutionary Computation Conference (GECCO-1 1999), pp 657–664
15. Deb K, Anand A, Joshi D (2002) A computationally efficient evolutionary algorithm for real-parameter evolution. Evol Comput J 10(4):371–395
16. Deep K, Thakur M (2007) A new crossover operator for real-coded genetic algorithms. Appl Math Comput 188:895–911
17. Kuo H-C, Lin C-H (2013) A directed genetic algorithm for global optimization. Appl Math Comput 219:7348–7364
18. Chuang Y-C, Chen C-T, Hwang C (2015) A real-coded genetic algorithm with a direction-based crossover operator. Inf Sci 305:320–348
19. Deb K, Goyal M (1996) A combined genetic adaptive search (GeneAS) for engineering design. Comput Sci Inform 26(4):30–45

Axial Deformation Characteristics of Graphene-Sonicated Vinyl Ester Nanocomposites Subjected to High Rate of Loading

B. Pramanik, P. R. Mantena and A. M. Rajendran

Abstract The mechanical characteristics of vinyl ester nanocomposites were investigated under a high rate of axial loading. The thermoset composites were sonicated with exfoliated graphite nanoplatelet (xGnP) and added with carboxyl-terminated butadiene nitrile (CTBN). High-strain rate axial tests were accomplished employing a split-Hopkinson pressure bar (SHPB) test-setup following a direct and a reverse impact method. Finite element analysis (FEA) and parametric optimization of the specimen geometry were performed using ANSYS Mechanical APDL®. Observing multi-surface fractures validated uniformity of stress distribution within the specimen gauge length. A laser occlusion expansion gauge (LOEG) technique was considered for measuring axial strain. The loading pulse within the transmitted bar was significantly low. Hence, an alternative approach (considering the pulse within the incident bar only) was applied for obtaining the stress–time history. A conventional SHPB setup provided a high rate of compressive deformation response. Both flow strength and energy absorbability of the participating material systems showed significantly lower under tension than under compression at a high rate. Nano-reinforcement marginally enhanced these mechanical characteristics for pristine vinyl ester under a high rate of tension. The material system responded detrimental under a high rate of compression.

Keywords High-strain rate tests · Axial deformation · Laser Occluding Expansion Gauge · Finite Element Analysis · Vinyl ester nanocomposites

B. Pramanik (✉)
Department of Mechanical Engineering, Montana Tech, Butte, MT 59701, USA
e-mail: bpramanik@mtech.edu

P. R. Mantena · A. M. Rajendran
Department of Mechanical Engineering, University of Mississippi, Oxford, MS 38677, USA

B. N. Singh et al. (eds.), *Recent Advances in Theoretical, Applied, Computational and Experimental Mechanics*, Lecture Notes in Mechanical Engineering,
https://doi.org/10.1007/978-981-15-1189-9_26

1 Introduction

Vinyl ester-based composites find applications in chemical storage tanks, pipelines, aerospace, automotive, wind energy, military, marine, and other fields of application. The extended molecular chain turns vinyl ester resin as a promising candidate in dynamic loading situations [1, 2]. Multiple researchers [3–8] attempted the inclusion of reinforcement in vinyl ester composites for improving the mechanical properties. This research incorporated graphite nanoplatelet with CTBN liquid rubber for improving the performance of this nanocomposite. The previous research [9–13], showed that the participant composite systems are rigid in stiffness but weak in strength, and demonstrated a brittle failure. It is evident that the tensile stress concentration initiates the failure of rigid and weak materials. Hence the investigation of the high strain-rate axial response of such materials requires serious consideration.

The split-Hopkinson pressure bar (SHPB) invented by Hopkinson [14] and improved by Davies [15] and Kolskey [16] is the most widely accepted laboratory test setup for obtaining the mechanical response at a high rate of loading. Harding et al. [17] first tailored this bar apparatus for performing the tensile tests at a high rate of loading. Many researchers [18–25] addressed the difficulties of producing a tensile pulse, optimizing the geometry of the tensile test specimen and the corresponding gripping system.

In this investigation, the dynamic characteristics of xGnP sonicated with CTBN added vinyl ester nanocomposites had been determined under a high rate of uniaxial tension and compression. First, a reverse-loading SHPB technique was employed to perform the dynamic axial test in tension. Dog bone-shaped specimen geometry of the tensile test was optimized based on finite element analysis of stress distribution within the specimen and fixture assembly using ANSYS Mechanical APDL®. During dynamic test event, high-speed photography showed the stress equilibrium and uniformity within the specimen gauge span. A noncontact laser occlusion technique [26] replaced the complex on-specimen stain gage technique for obtaining tensile strain. Finally, conventional compressive SHPB tests were performed. Both dynamic tensile and compressive strength and energy absorbability of the participant material system are reported and compared. The effects of xGnP sonication and CTBN inclusion on the dynamic response of vinyl ester composite system were evaluated.

2 Experimental Setup

This research exploited a traditional compression and a reverse impact-based tension SHPB apparatus. The reverse SHPB consists of a laser occluding expansion gage system for conducting high rate tensile tests on the participating composite specimens.

2.1 Material Description

DERAKANE 510A-40 [2] thermoset vinyl ester nanocomposites of 10 mm (0.4 in.) thick panels are tested for the high rate tensile and compressive characterization. The vinyl ester contains 38 weight % styrene, along with Butanone peroxide, N, N-Dimethylaniline, Cobalt Naphthenate, and 2–4-Pentanedione additives to improve fire retardancy, chemical resistance, and toughness. The pristine vinyl ester thermoset (VE) is sonicated [7, 12, 26] in two batches with each of 1.25 weight % (1.25xGnP+VE), and 2.5 weight % (2.5xGnP+VE) exfoliated graphite nanoplatelets respectively. The 10.0 weight % liquid CTBN rubber globules (1.25xGnP+CTBN+VE and 2.5xGnP+CTBN+VE) were added to one of the batches to improve the toughness of the composite material without decrementing the other mechanical properties, including glass transition temperature [5]. Drzal and Fukushima [7] described the processing technique of those composite systems.

2.2 Dynamic Tensile Test Setup

The tensile SHPB system as shown in Fig. 1 consists of a steel barrel having a steel hollow cylindrical striker bar. A compressed air vessel was connected with a solenoid switch valve to one end of the barrel. The striker was mounted on two Teflon rings for achieving frictionless sliding motion inside the barrel. The striker bar was propelled by the rapid release of air pressure from the compressed air vessel. The hollow cylindrical striker slides over the aluminum incident bar, inside the barrel and impacts the aluminum collar, mounted at the end of the incident bar, causing a tensile stress wave within the incident bar. A thin ring-shaped polyurea pulse shaper was used for producing a trapezoidal incident pulse. The SHPB bar system was retarded by a momentum bar, which was trapped against a block of putty-clay. The specimen was sandwiched between an incident bar and a transmission bar and was loaded with

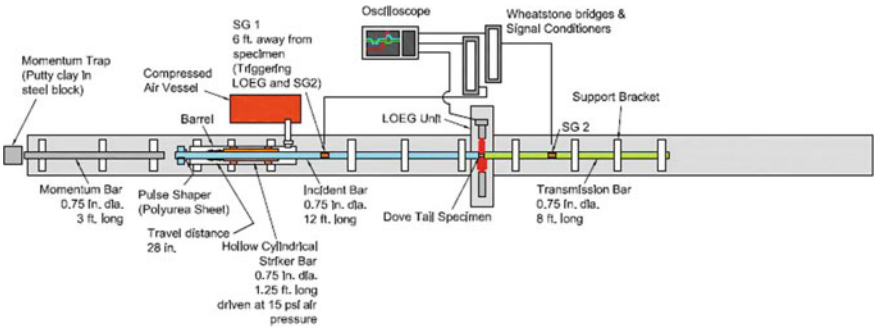

Fig. 1 SHPB set-up for direct tensile tests including LOEG device

tensile stress. A part of the incident wave was reflected back to the incident bar, and the other part was transmitted into the aluminum transmission bar.

Two batches of strain gauges were installed at a distance away from the specimen on the incidence and the transmission bars as the strain gauges can capture the commencement of the incident, reflected and transmitted pulses distinguishably. Each batch consisted of two gauges positioned on the transversely reverse sides of the bar and coupled in series network (Fig. 1). This arrangement eliminates the flexural influence of the bars and ensures uniaxial strain measurement. A digital oscilloscope was linked to each batch of the strain gauges, via a Wheatstone bridge circuit and a signal conditioner. The oscilloscope displayed the signal potential history over the entire test duration and stored in the database. Strain pulse response in SHPB bars at the strain gauge locations was applied in the 1-D wave equation and the tensile stress experienced by the test specimen was obtained.

2.3 Optimization of Specimen Geometry

A dog bone-shaped specimen and dovetail gripping mechanism [24] shown in Fig. 2a was adopted to reduce the wave dispersion, possibly caused due to complex specimen attachment configurations of previously attempted pinned [17], threaded [20], or cemented [23] fixtures. A plane-stress FEA was carried out to parametrically optimize the specimen geometry that prevented pre-mature failure of the specimen or the fixture due to undesirable stress concentrations, and also to ensure uniform stress distribution within the loading zone in the specimen.

The pulse width over time dictates the required least length of the loading zone within the specimen. The pulse needs to propagate back and forth within the specimen more than three times before yield or failure initiates. It ensures the internal stress equilibrium within the specimen. The wave speed in the specimen was estimated over quasi-static properties previously obtained [9] as per ASTM 638-08 [27].

The fundamental assumption for this FEA was the homogeneity of the material integrity in case of the load transfer. Only geometric influence of the components has been considered for this analysis. The FE model was constructed into two parts. One part was of the dog bone-shaped specimen, and the other part was of the dovetail end fixture. Figure 2b illustrates the load and the boundary condition considered in those models. The geometry was modeled using ANSYS Mechanical APDL® graphics tool and merged as an assembly (Fig. 2c). The models meshed with 10-noded elements (SOLID187 in ANSYS®) having quadratic displacement behavior is appropriate for modeling irregular meshes. Quarter symmetry of the geometry was considered to decrease the total number of nodes of the model. It allowed denser mesh and improved the accuracy of results.

The contact elements were modeled along the interface between the fixture and the specimen. The contact along the angular surfaces was defined with normal and tangential components. The contact elements follow a linear constitutive behavior

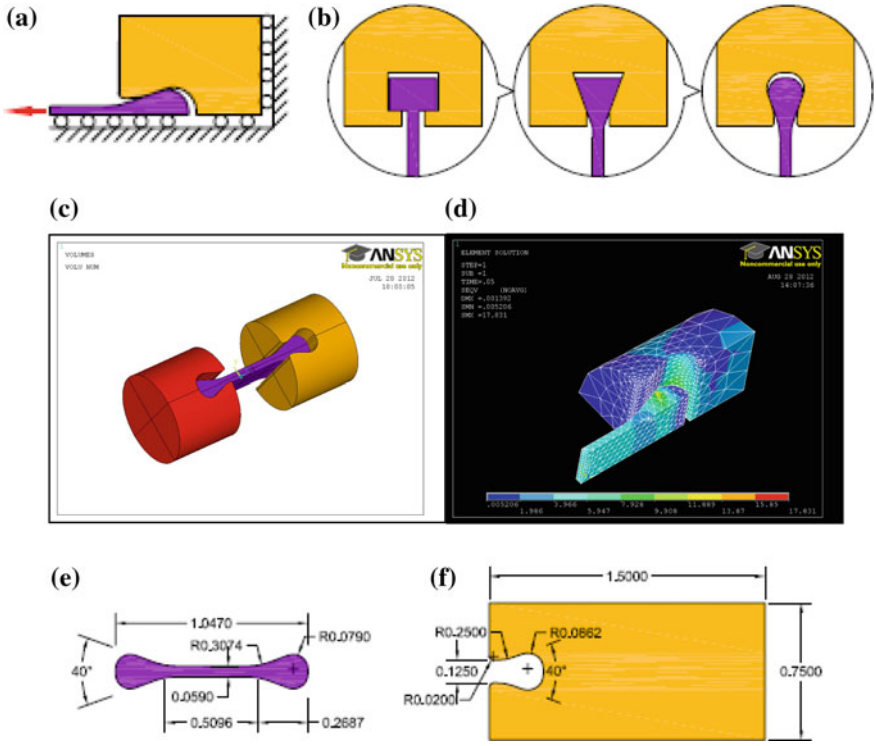

Fig. 2 **a** Development of direct tensile specimen geometry, **b** boundary condition applied in stress analysis of specimen and fixture assembly, **c** ANSYS model, **d** von-Mises stress distribution in ANSYS simulation, **e** specimen dimensions, and **f** fixture dimensions (all dimensions in inches)

normal to the surface. The aluminum fixture surface was chosen as the master surface. A stiffness-penalty method was considered for explaining the friction between the fixture and the specimen. Figure 2d shows a uniformly distributed tensile load applied at the end of the specimen. The end of the fixture was constrained from axial translation. The color-map of von Mises stress distribution for an imposed distributed load is shown in Fig. 2d. The von Mises stresses were distributed uniformly along the specimen gauge section and validated the optimization of the specimen (Fig. 2e) and fixture (Fig. 2f) geometry. A CNC machine, equipped with a carbide tipped tool, machined the optimized specimens for performing the test series.

2.4 Development of LOEG

A Laser Occluding Expansion Gauge, incorporated for measuring tensile strain response, worked through occluding a thin parallel laser sheet by either the specimen

fixture ends in case of direct dynamic loading, or the deforming specimen geometry in case of indirect dynamic loading [26]. This idea was adopted from the work of Ramesh and Narsimhan [28] on measuring radial strains in compression Kolsky bar experiment and the later work of Chen et al. [29] on dynamic tensile response of low strength brittle solid.

The LOEG consisted of a 635 nm wavelength laser system (©Coherent, Inc.). It included a single line projection head with 30° fan angle. It had two anti-reflector (MgF_2)-coated plano-convex cylindrical N-BK7 glass lenses of 25 mm diameter with 50 mm focal length (©Edmund Optics). It was equipped with an amplified, switchable gain, silicon PIN photodetector (©Thorlabs) having 1.5 MHz bandwidth at 4.25 MS/s sampling rate, and 0.2 mV noise, and 100 MHz. A 4-channel oscilloscope with 1.25 GS/s sampling rate (©Tektronix, Inc.) was included in this setup. It is to be noted that the same oscilloscope is used in SHPB system. The incident pulse (sensed at the incident bar strain-gauges) triggered the photodetector. The diode-laser unit generated 635 nm laser beam collimated (converted from a divergent beam to a parallel beam over an extended range of projection distance) with an elliptical cross section of 3.8 mm × 0.9 mm. It consisted of a single line projection head with 30° fan angle (the angular spread of the laser beam). The projection head consisted of Powell® glass lens which spreads the collimated laser beam and converts the elliptical projection into a 0.9 mm thick non-Gaussian line projection with almost uniform relative intensity along the fan angle. Line thickness was reduced to about 55 μm by the pre-focusing collimated laser beam at the target position on the specimen. The maximum power output was 5 mW. Black anodized aluminum housing held the entire laser unit. The plano-convex cylindrical lens used in this setup was made from a coated N-BK7 glass substrate. It developed a parallel laser sheet of 25 mm (~1 in.) width. The coating was of MgF_2 anti-reflectant (<1.75% per surface area in the wavelength within 400–700 nm). The light was detected through another similar plano-convex cylindrical lens arranged in a symmetrically opposite orientation. It converged the parallel sheet of light into a 9.8 mm diameter aperture of a photodiode light detector placed near the focal point of the laser sheet. The photodiode detector output was pre-amplified with a bandwidth of 1.5 MHz, and the output-voltage was proportional to the total amount of laser light entered into the photodetector including less than 1 mV noise level.

2.5 Stress Measurement—Tension

The incident pulse propagated along the incident bar, pulled the sample, reflected back a part of the incident pulse into the incident bar and the rest was transmitted to the transmission bar. In this test, the steel hollow cylindrical striker bar impacted the aluminum collar mounted at the end of the aluminum incident bar. Due to the striker collar impedance mismatch, the incident pulse exhibited extended restitution with gradually reducing amplitudes similar as described in [30]. Hence, the initial maximum amplitude portion of the incident pulse was used for SHPB analysis. The

candidate materials having low-impedance and low-dynamic tensile strength allowed only an insignificant part of the incident pulse propagated into the transmission bar. Since, the transmitted pulse was too weak to estimate stress, an alternative one-dimensional wave propagation analysis [31] was considered for estimating direct tensile stress (σ_{dt}) as shown in the following equation—

$$\sigma_{dt} = \frac{2A_s\rho_s C_s}{A_i\rho_i C_i + A_s\rho_s C_s}.\frac{A_i}{A_s}.E_i\varepsilon_i \tag{2}$$

where E is the elastic modulus; ε denotes the strain; A, is the cross-sectional area, ρ is the density, and C is the wave velocity for the incident bar (with a suffix, i) and the specimen (with a suffix, s).

2.6 Strain Measurement—Tension

The laser sheet, projected horizontally above the tensile test-specimen, was partially occluded by the ends of the specimen fixtures mounted on incident and transmission bars. In our experimental setup, the gap between the specimen holding fixture ends was almost equivalent to the specimen gage length. Hence, the tensile strain response was counted from the ratio ($\Delta V/V$) of the incremental change of potential along with specimen elongation to the initial potential within the grip ends holding the pristine test coupon.

A comparative study of the LOEG response was performed. A batch of strain gauges was installed on the dog bone-shaped coupon. The tensile strain history was obtained using LOEG and on-specimen strain gauges. A batch of two strain gauges was installed on opposite sides of the coupon and connected in a quarter-bridge circuit. The dynamic strain–time history response was plotted on an oscilloscope. The LOEG setup acquired a comparable strain data transferred to the same oscilloscope. It validated the applicability of the LOEG setup in tensile strain measurements.

2.7 Dynamic Compressive Test Setup

A traditional compression SHPB setup with aluminum bars was applied for obtaining the high rate compressive characteristics of the participant materials. The disk specimen geometry was considered for compression tests and loaded axially on the opposite faces. The compressive 1-D wave propagating through the specimen thickness was considered for computing the dynamic compressive stress and strain histories.

3 Experimental Results

The typical failure of an optimized dog bone specimen under a high rate of tension in SHPB apparatus has been studied. It showed multiple fractured surfaces on the post-test specimen. It indicates that the dynamic stress equilibrium was achieved before the fracture occurred. The instantaneous drop of stress indicated the onset of a crack within the specimen. The corresponding time of the visible first stress peak (representing the dynamic tensile strength) had been recorded as the time of crack initiation. The energy absorbability per unit specimen volume was obtained from the area-integral under the stress-versus-strain curve [32] until specimen failed.

3.1 Dynamic Tensile Response

Figure 3 summarizes the tensile response of vinyl ester composites containing xGnP and CTBN subjected at about 1000 s^{-1} strain-rate. All nano-reinforced specimens including the pristine vinyl ester showed brittle failure under a high rate of tension

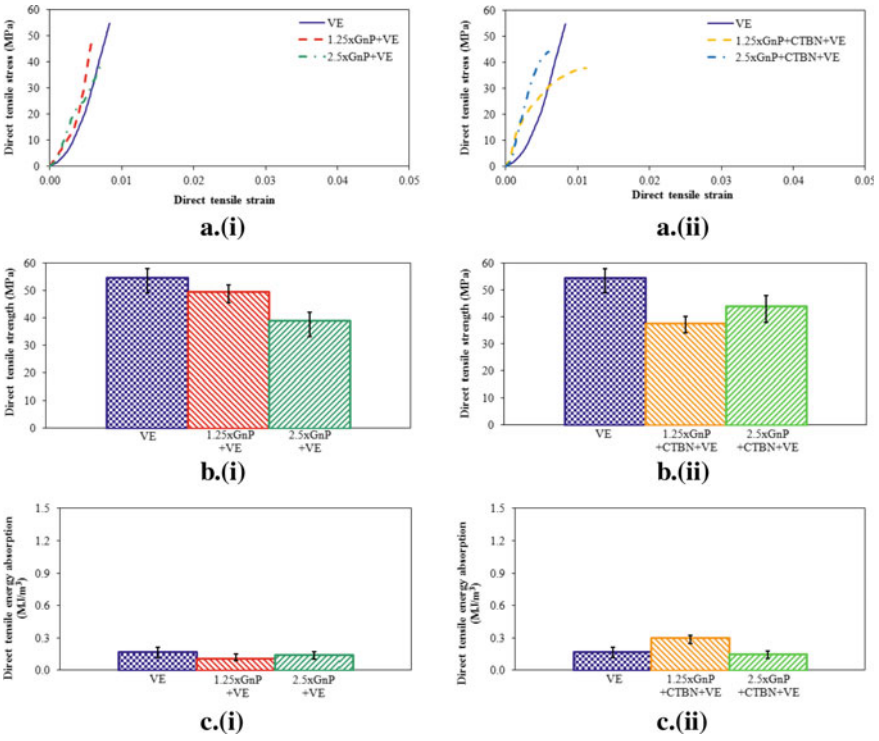

Fig. 3 Dynamic direct tensile response **a** typical constitutive response, **b** strength comparison, and **c** energy absorbability comparison for the composite system; (i) with graphite platelet, and (ii) with additional CTBN

(Fig. 3a). The tensile strength of pristine vinyl ester was decreased marginally with xGnP (Fig. 3b(i)). The inclusion of CTBN along with xGnP into the composite systems did not show significant improvement (Fig. 3b(ii)). The energy absorbability of pristine vinyl ester maintained almost similar response with xGnP (Fig. 3c(i)); however, this was minimally enhanced by further addition of CTBN to the xGnP in the composite systems (Fig. 3c(ii)).

3.2 Dynamic Compressive Response

Figure 4 shows dynamic compressive response of the candidate materials tested at similar strain rate of about 1000 s^{-1}. Figure 4b shows that compressive flow stress of pristine vinyl ester was decreased gradually by the inclusion of xGnP (Fig. 4b(i)), and even with CTBN (Fig. 4b(ii)). The energy absorbability (Fig. 4c) was decremented for xGnP (Fig. 4c(i)). The inclusion of CTBN could not enhance the energy absorbability

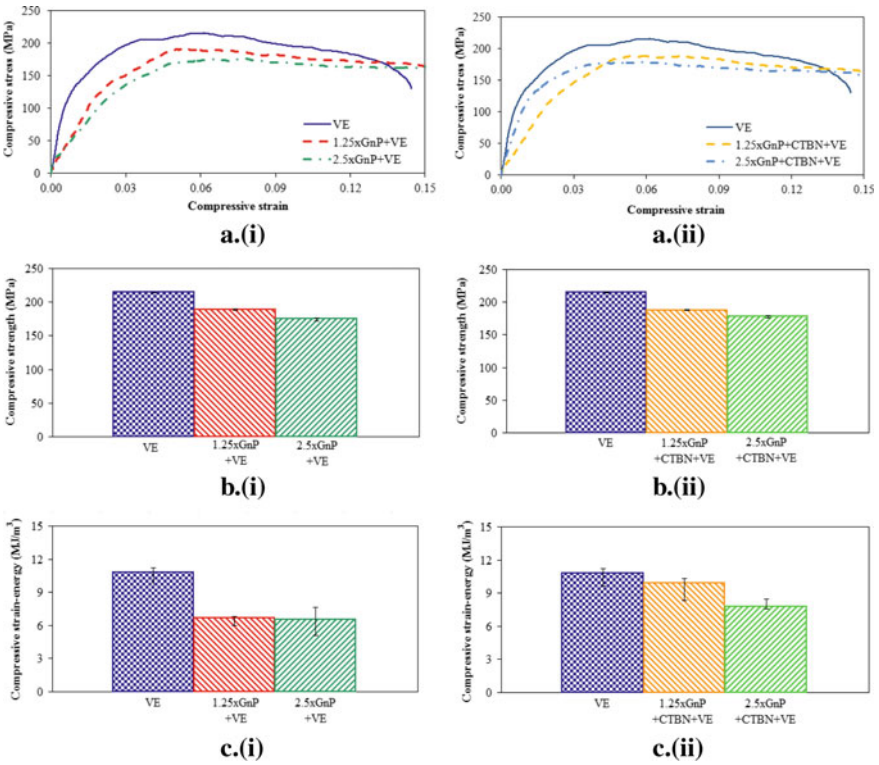

Fig. 4 Dynamic compressive response **a** typical constitutive response, **b** strength comparison, and **c** energy absorbability comparison for the composite system; (i) with graphite platelet, and (ii) with additional CTBN

(Fig. 4c(ii)) of pristine vinyl ester, nevertheless, a minimal increment (Fig. 4c(ii)) was observed (Fig. 4c(i)) upon comparing with that of the only xGnP added (without CTBN) composite systems.

3.3 Comparative Study of Dynamic Tensile and Compressive Responses

The constitutive materials within the composite system play an important role of transferring mechanical load. The anisotropic nature of load transfer is significant in composites due to the inherent differences of the bonding efficiency among constituents with the matrix along the loading directions. Tensile and compressive loads act mutually in opposite directions. Hence, the composite system responds differently for these counteracting loading systems. Comparative observation of Fig. 3 with Fig. 4 shows that the stress–strain characteristic of these candidate materials under high-rate tension varied considerably from its high-rate compression. The compressive strength (Fig. 4b) of the candidate materials was observed to be about 300% more than the tensile strength under high-rate of loading (Fig. 3b). The energy absorbability was also significantly higher (about 2000%) under dynamic compressive loading (Fig. 4c) than under dynamic tensile loading (Fig. 3c). It is evident that the vinyl ester-based nanocomposites are brittle at high strain rates. The nano-reinforcement and additional toughening are detrimental to the properties under dynamic compression. Still, the contribution of the inclusions showed minimal improvement in dynamic tension.

4 Conclusion

The significant features of the proposed techniques of the modified direct tensile test method described in this article—

- The SHPB reverse impact technique is implemented for the mechanical characterization of the candidate materials under a high rate of uniaxial tension.
- Due to the very low transmitted pulse signal, an alternative approach (using incident pulse and quasi-static properties of the candidate materials) is adopted for estimating stress–time history. The transmission bar may also be modified with a low impedance material and/or smaller cross-sectional area for obtaining true dynamic tensile stress.

The critical observations in this investigation regarding the effect of xGnP and CTBN on the axial response of vinyl ester composite system are—

- The pristine vinyl ester maintains almost the similar tensile strength with addition of xGnP and even with CTBN under quasi-static to high-strain rate tension.
- The energy absorbability of pristine vinyl ester is enhanced due to the presence of xGnP under dynamic tension.
- The high-rate of tensile response of the candidate materials varies significantly from the high-rate of compressive response.
- Reinforcing vinyl ester with xGnP and toughening with CTBN is found to be detrimental to the properties of candidate nanocomposites under dynamic compression, although a minimal improvement of these properties is observed in dynamic tension.

Acknowledgements The Office of Naval Research, Solid Mechanics Program (Dr. Y. D. S. Rajapakse, Program Manager) Grant No. N00014-7-1-1010; and US Army Research Office under the DOD-PIRT sub-contracted through North Carolina A & T University Grant No. 300223243A funded this research.

References

1. Shivakumar KN, Swaminathan G, Sharpe M (2006) Carbon vinyl ester composites for enahanced performance in marine applications. J Reinf Plast Compos 25(10):1101–1116. https://doi.org/10.1177/0731684406065194
2. Ashland Inc. (2008) DERAKANE 510A-40 Epoxy Vinyl Ester Resin. Technical Datasheet, Document 1775V2 F2, Language EN V1, Approved 2008-9-8, vol 201, pp 1–4
3. Yoshida A, Hishiyama Y, Inagaki M (1991) Exfoliated graphite from various intercalation compounds. Carbon 29(8):1227–1231. https://doi.org/10.1016/0008-6223(91)90040-P
4. Toshiaki E, Masatsugu S, Morinobu E (2003) Graphite intercalation compounds and applications. Oxford University Press Inc, New York
5. Fröhlich J, Thomann R, Mülhaupt R (2003) Toughened epoxy hybrid nanocomposites containing both an organophilic layered silicate filler and a compatibilized liquid rubber. Macromolecules 36(19):7205–7211. https://doi.org/10.1021/ma035004d
6. Fukushima H, Drzal LT (2004) Graphite nanoplatelets as reinforcement for polymers: structural and electrical properties. In: Proceedings of 17th international conference on American Society for composites
7. Drzal LT, Fukushima H (2006) Exfoliated graphite nanoplatelets (xGnP): a carbon nanotube alternative. The nanotechnology conference, Boston, 7–11 May 2006
8. Lu J, Do I, Drzal LT, Worden RM, Lee I (2008) Nanometal-decorated exfoliated graphite nanoplatelet based glucose biosensors with high sensitivity and fast response. ACS Nano 2(9):1825–1832. https://doi.org/10.1021/nn800244k
9. Magableh A (2010) Viscoelastic and shock response of nanoclay and graphite platelet reinforced vinyl ester nanocomposites. Dissertation, University of Mississippi
10. Mantena PR, Cheng AHD, Al-Ostaz A, Rajendran AM (2010) Blast and impact resistant composite structures for navy ships. In: Proceedings of marine composites and sandwich structures, 2010, Office of Naval Research—Solid Mechanics Program Review, Adelphi, MD, 27–29 Sept 2010

11. Pramanik B, Mantena PR (2011) Viscoelastic response of graphite platelet and CTBN reinforced vinyl ester nanocomposites. Mater Sci Appl 2(11):1667–1674. https://doi.org/10.4236/msa.2011.211222
12. Pramanik B, Mantena PR (2012) Energy absorption of nano-reinforced and sandwich composites in ballistic and low-velocity punch-shear. Open J Compos Mater 2(3):87–96. https://doi.org/10.4236/ojcm.2012.23010
13. Pramanik B, Tadepalli T, Mantena PR (2012) Surface fractal analysis for estimating the fracture energy absorption of nanoparticle reinforced composites. Materials 5(5):922–936. https://doi.org/10.3390/ma5050922
14. Hopkinson B (1914) A method of measuring the pressure produced in the detonation of high explosives or by the impact of bullets. Phil Trans R Soc Lond A 213:437–456. https://doi.org/10.1098/rsta.1914.0010
15. Davies RM (1948) A critical study of the Hopkinson pressure bar. Phil Trans R Soc Lond A 240(821):375–457. https://doi.org/10.1098/rsta.1948.0001
16. Kolsky H (1949) An investigation of the mechanical properties of materials at very high rates of strain. Proc Phys Soc B 62:676–700. https://doi.org/10.1088/0370-1301/62/11/302
17. Harding J, Wood EO, Campbell JD (1960) Tensile testing of materials at impact rates of strain. J Mech Eng Sci 2(2):88–96. https://doi.org/10.1243/JMES_JOUR_1960_002_016_02
18. Lindholm US, Yeakley LM (1968) High strain-rate testing: tension and compression. Exp Mech 8(1):1–9. https://doi.org/10.1007/BF02326244
19. Albertini C, Montagnani M (1974) Mechanical properties at high rates of strain. Institute of Physics, London
20. Nicholas T (1980) Tensile testing of materials at high rates of strain. Exp Mech 21(5):177–185. https://doi.org/10.1007/BF02326644
21. Rajendran AM, Bless SJ (1986) Determination of tensile flow stress beyond necking at very high strain rate. Exp Mech 26(4):319–323. https://doi.org/10.1007/BF02320146
22. Chen W, Lu F, Cheng M (2002) Tension and compression tests of two polymers under quasi-static and dynamic loading. Polym Test 21:113–121. https://doi.org/10.1016/S0142-9418(01)00055-1
23. Gilat A, Goldberg RK, Roberts GD (2005) Strain rate sensitivity of epoxy resin in tensile and shear loading. NASA/TM—2005-213595, 1–33
24. Owens AT, Tippur HV (2009) A tensile split Hopkinson bar for testing particulate polymer composites under elevated rates of loading. Exp Mech 47:799–811. https://doi.org/10.1007/s11340-008-9192-7
25. Chen R, Dai F, Lu L, Lu F, Xia K (2010) Determination of dynamic tensile properties for low strength brittle solids. Exp Appl Mech 6:321–326. https://doi.org/10.1007/978-1-4419-9792-0_53
26. Pramanik B, Mantena PR, Tadepalli T, Rajendran AM (2014) Indirect tensile characterization of graphite platelet reinforced vinyl ester nanocomposites at high-strain rate. Open J Compos Mater. https://doi.org/10.4236/ojcm.2014.44022
27. ASTM Standard D 638-08 (2008) Standard test method for tensile properties of plastics. ASTM International
28. Ramesh KT, Narsimhan S (1996) Finite deformations and the dynamic measurement of radial strains in compression kolsky bar experiments. Int J Solids Struct 33(25):3723–3738. https://doi.org/10.1016/0020-7683(95)00206-5
29. Chen R, Dai F, Qin J, Lu F (2013) Flattened brazilian disc method for determining the dynamic tensile stress-strain curve of low strength brittle solids. Exp Mech. https://doi.org/10.1007/s11340-013-9733-6
30. Song B, Connelly K, Korellis J, Lu WY, Antoun BR (2009) Improvements in kolsky-bar design for mechanical characterization of materials at high strain rates. Measr Sc Tech 20(11):115–701. https://doi.org/10.1088/0957-0233/20/11/115701

31. Chen W, Lu F, Zhou B (2000) A quartz-crystal embedded split hopkinson pressure bar for soft materials. Exp Mech 40(1):1–6. https://doi.org/10.1007/BF02327540
32. Yi F, Zhu Z, Zu F, Hu S, Yi P (2001) Strain rate effects on the compressive property and the energy-absorbing capacity of aluminum alloy foams. Mater Charact 47:417–422. https://doi.org/10.1016/s1044-5803(02)00194-8

State Estimation Using Filtering Methods Applied for Aircraft Landing Maneuver

P. S. Suresh, Niranjan K. Sura and K. Shankar

Abstract State estimation methods are the popular means of validating aerodynamic characteristics on maneuvering Aircraft. This work deals with adaptation of familiar filtering methods for Aircraft landing maneuvers, to estimate the aircraft touchdown states. The mathematical model for two-point landings (main wheel in contact with the ground and nose wheel airborne) consists of nonlinear flight mechanics equations representing Aircraft longitudinal dynamics. A nonlinear 6 DOF pilot in loop simulation model is used for the measurement of data generation that was mixed with process and measurement noises. These values are used for posterior state correction in the implementation of Kalman filter. With the state values just before the initiation of flare as initial conditions, filters such as Upper Diagonal factorized form of Adaptive Extended Kalman Filter (UDAEKF) and Unscented Kalman Filter (UKF) is implemented in Matlab environment. The estimated states and measured data are compared using performance metrics for vertical acceleration (Nz) which brings out the possibility of over quantification (3.5%) and under quantification (11.3%) at onset of touchdown having an impact on landing loads. As observed, the performance of UKF is two and half times faster than UDAEKF through superior state propagation.

Keywords State estimation · Kalman filters · Upper diagonal adaptive extended kalman filter · Unscented kalman filter · Pilot in loop simulation · Landing maneuver

P. S. Suresh (✉) · N. K. Sura
Aeronautical Development Agency (Min. of Defence, Govt. of India), P.B.No: 1718, Vimanapura Post, Bengaluru 560017, India
e-mail: pssuresh@jetmail.ada.gov.in

N. K. Sura
e-mail: nksura@nal.res.in

K. Shankar
Machine Design Section, Department of Mechanical Engineering, Indian Institute of Technology Madras, Chennai 600036, India
e-mail: skris@iitm.ac.in

B. N. Singh et al. (eds.), *Recent Advances in Theoretical, Applied, Computational and Experimental Mechanics*, Lecture Notes in Mechanical Engineering,
https://doi.org/10.1007/978-981-15-1189-9_27

1 Introduction

The vital phase of flight happens during landing, wherein "Abnormal Runway Contact" is cited as the primary reason for hard landing event [1]. During initial phase of design, specifications such as Military Specification (MIL), Joint Service Specification Guide (JSSG) are used for prediction of the landing loads on high performance aircraft [2, 3]. The landing gear and near attachment structures are sized according to the predicted loads for several ground maneuvering and landing cases.

The symmetric two-point (Main Landing Gears (MLG) touchdown and Nose Landing Gear (NLG) airborne) and three-point (Two MLG's and NLG touchdown) landings consists of states such as mass (m), vertical descent speed (h), pitch angle (θ), pitch rate (q), pitch acceleration ($\dot{q}$), true vertical (a_z) and longitudinal acceleration (a_x) that governs the impact loads on Aircraft [4]. The inertial measurement sensors measure the accelerations ($a_x \& a_z$) at the touchdown state, being prone usually with measurement issues such as noise, sensor bias and drift, location of sensor with respect to Aircraft Center of Gravity (CG), missing data, and so on. The rotary acceleration ($\dot{q}$) is a derived response from the rotational velocity which is prone to divergence due to integration time steps.

Aerodynamic parameter identification using state and parameter estimation method is the most common application followed by flight mechanics engineers, working on system identification domain [5, 6]. Several versions of Kalman filters are tried out against position, velocity tracking problem of size (2×2) observation equation [7]. This work explores the adaptation of popular nonlinear filtering algorithms on landing maneuver problems to determine the Aircraft touchdown states.

On the basis of first-order approximation of nonlinear dynamics, a well-known recursive state and parameter estimation called Extended Kalman Filter (EKF) is implemented in this work [8]. For landing dynamics, the filter is adapted with Upper diagonal (UD) form and adaptive tuning process using a fuzzy logic interface for state error covariance and process noise covariance matrices. These implementations will prevent state error covariance matrix to diverge and support the filter tuning process. Yet another algorithm implemented using Matlab, is on UKF which basically propagates finite set of points, called "sigma points", through nonlinear dynamics and by approximating the distribution (mean and covariance) through weighted sum and outer product of propagated sigma points [9].

A nonlinear 6 DOF flight mechanics module is coupled with the pilot in loop interface. This interface provides the pilot stick input during landing phase of Aircraft. Three sets of simulated landing cases were performed for measurement data generation with different flare techniques leading to low, nominal, and high sink rate velocity landing cases. Initially, the aircraft states during touchdown phase such as horizontal velocity (u), vertical velocity (w), pitch (θ), pitch rate (q), and altitude (h) are estimated and were compared with noisy simulated measurement data. The validity of the estimates is assessed by plotting the state error with bounds and comparing standard deviations. Then, the states such as vertical acceleration (a_z), pitch acceleration ($\dot{q}$), horizontal acceleration (a_x), and sink rate ($\dot{h}$) which has direct

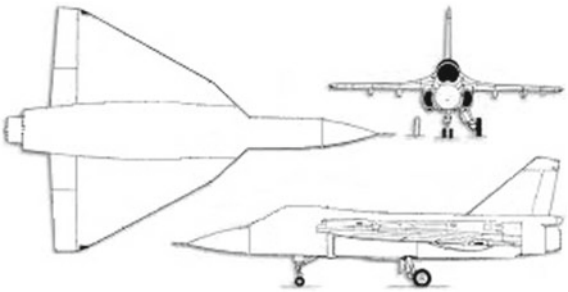

Fig. 1 Typical high performance aircraft

impact on landing loads, are obtained. The Aircraft state vector is augmented with aerodynamic parameters which were also estimated. These estimates can become an initial input for performing a multi-body dynamic simulation that can be used to predict landing impact loads.

The paper is ordered as follows: Sect. 2 describes the configuration of Aircraft and the equation of motion, Sect. 3 provides the implementation of nonlinear filters on landing maneuver, Sect. 4 provides the state estimation results for simulated landings, followed by discussion and conclusion.

2 Aircraft Dynamics: Longitudinal

2.1 Aircraft Configuration

A typical high performance Aircraft with four Elevons (Inboard and Outboard) and single vertical tail with Rudder is considered for the study as shown in Fig. 1. The Aircraft Elevons are at trailing edge for lateral (Roll) and longitudinal (Pitch) control, with a Rudder hinged to single vertical tail for directional (Yaw) control. The aircraft has a tricycle landing gear arrangement with Main landing gears (Starboard and Port side) symmetrically placed and positioned close to aircraft CG. The Nose landing gear is located forward of Main landing gear positioned at the front fuselage.

2.2 Flight Mechanics Equations

Three sets of first-order nonlinear differential equations such as translational velocities, angular velocities, and altitude angles are used for representation of Aircraft dynamics [10]. The aircraft is considered to be rigid body with XZ as plane of mirror symmetry. Greater emphasize for symmetrical landing events such as two point and three point landings are provided that are used to arrive the fatigue spectrum of aircraft. Equations for longitudinal dynamics of Aircraft states consist of variables as longitudinal velocity (u), vertical velocity (w), Altitude (h), pitch rate (q), and pitch angle (θ) pertinent to the body axis of aircraft as presented from Eqs. 1 to 5,

respectively.

$$\dot{u} = \left(\frac{\bar{q}s}{M}\right)C_x - qw - g\sin\theta + \left(\frac{T}{M}\right)\cos\epsilon \tag{1}$$

$$\dot{w} = \left(\frac{\bar{q}s}{M}\right)C_z + qu + g\cos\theta + \left(\frac{T}{M}\right)\sin\epsilon \tag{2}$$

$$\dot{q} = \left(\frac{\bar{q}s\bar{c}}{I_{yy}}\right)C_{my} \tag{3}$$

$$\dot{\theta} = q \tag{4}$$

$$\dot{h} = u\sin\theta - w\cos\theta \tag{5}$$

where

$$C_x = C_{x0} + C_{x_{uc}} + C_{x_{ge}} + C_{x\alpha^\alpha} + C_{x\delta^\delta}$$

$$C_z = C_{z0} + C_{z_{uc}} + C_{z_{ge}} + C_{z\alpha^\alpha} + C_{z\delta^\delta} + C_{z\left(\frac{qc}{2V}\right)}\left(\frac{qc}{2V}\right)$$

$$C_{my} = C_{my0} + C_{my_{uc}} + C_{my_{ge}} + C_{my\alpha^\alpha} + C_{my\delta^\delta} + C_{my\left(\frac{qc}{2V}\right)}\left(\frac{qc}{2V}\right)$$

With the state variables as $x = [u, w, q, \theta, h]$, $\bar{q}$ dynamic pressure, "s" wing surface area, "M" mass of the aircraft, $\left[C_x, C_z \& C_{my}\right]$ total drag, lift and moment coefficients, "g" acceleration due to gravity, "T" thrust characteristics, "ϵ" is the angle of inclination of engine to Fuselage Reference Line (FRL), "I_{yy}" is the pitch moment of inertia of aircraft. Aerodynamic parameters as augmented additional state variables:

$$x_a = \left[u, w, q, \theta, h, C_{x0}, C_{x\alpha}, C_{x\delta}, C_{z0}, C_{z\alpha}, C_{z\delta}, C_{z\left(\frac{qc}{2v}\right)}, C_{my0}, C_{my\alpha}, C_{my\delta}, C_{my\left(\frac{qc}{2v}\right)}\right]$$

$\left[0, \alpha, \delta, \frac{qc}{2v}, ge, uc\right]$ are the aerodynamic effects due to body, angle of attack, Elevon deflection, and nondimensional pitch rate. Two more effects such as ground and undercarriage extension are added to emulate the landing dynamics problem.

The observation equations consist of

$$u_m = u \tag{6}$$

$$w_m = w \tag{7}$$

$$q_m = q \tag{8}$$

$$\theta_m = \theta \tag{9}$$

$$h_m = h \tag{10}$$

$$a_{xm} = \left(\frac{\bar{q}s}{M}\right) C_x \tag{11}$$

$$a_{zm} = \left(\frac{\bar{q}s}{M}\right) C_z \tag{12}$$

$$\dot{q}_m = \left(\frac{\bar{q}s}{I_{yy}}\right) C_{my} \tag{13}$$

$$\dot{h}_m = u\sin\theta - w\cos\theta \tag{14}$$

which were estimated using the nonlinear filtering methods.

The subscript "m" on the left-hand side of observation equations denotes the measured quantities obtained from simulated/measured data. The motion before touchdown simulated using pilot in loop input wherein the vertical sink rate is reduced and horizontal range is increased to have a smooth landing.

3 Nonlinear Filtering Methods for Landing Maneuver

3.1 Upper Diagonal Adaptive Form of Extended Kalman Filter

The Aircraft dynamic system is represented as continuous state-space form with discrete measurement equations as

$$\dot{x}(t) = f[x(t), u(t), \Theta] + Fw(t), x(\mathrm{t}_0) = x_0 \tag{15}$$

$$y(t) = g[x(t), u(t), \Theta] \tag{16}$$

$$z(k) = y(k) + Gv(k) \tag{17}$$

$$where, k = 1 \ldots N$$

where f and h are in general nonlinear functions and Θ is the vector of unknown parameters; $x(t)$ is $n*1$ state vector; $u(t)$ is $p*1$ control input; z is $m*1$ measurement vector sampled at N discrete time steps with fixed sampling interval as Δt and k is the discrete-time index; $F\&G$ are the additive state and measurement noise matrices, which are considered to be time-invariant. The noise associated with mathematical

idealization of system, called process noise w is accounted as white Gaussian noise with zero mean and covariance matrix Q. The noise associated with the measurements such as calibration error and bias is represented as measurement noise v in Eq. 17 which is again a white Gaussian noise of zero mean and covariance matrix R.

The extended system consists of unknown parameter (Θ) as additional states in the form of the augmented (x_a) state vector [11].

$$x_a^T = \left[x^T \Theta^{\mathrm{T}}\right] \tag{18}$$

$$\dot{x}_a = f_a[x_a(t), u(t)] + F_a w_a(t) \tag{19}$$

$$y(t) = g_a[x_a(t), u(t)] \tag{20}$$

$$z(k) = y(k) + Gv(k) \tag{21}$$

where $k = 1 \ldots, N$.

For the augmented system, the EKF consist of prediction and an update step, with the usage of "tilde" ($\sim$) symbol and "hat" ($\wedge$) denote the predicted and corrected variables, respectively.

$$A_a(k) = \frac{\partial f_a}{\partial x_a}|_{x_a = \hat{x}_a(k-1)} \tag{22}$$

$$\emptyset_a = \exp[A_a \Delta t] \tag{23}$$

$$where\ \Delta t = t_{k-1} - t_k$$

$$H_a(k) = \frac{\partial g_a}{\partial x_a}|_{x_a = \hat{x}_a(k)} \tag{24}$$

where ϕ_a denotes discrete-time transition matrix, $A_a(k)$ denotes the linearized state matrix and $H_a(k)$ denotes the linearized measurement matrix.

The UDAEKF consists of two important steps namely (i) **Time propagation**: a priori states (represented by ~ tilde symbol) and state error covariance matrix predicted using a nonlinear mathematical model (ii) **Measurement update**: wherein with the available measurement data, the posteriori states (represented by ˆ hat symbol), and state error covariance matrix are updated using Kalman gain. The Upper diagonal (UD) form [12] and an adaptive tuning process using fuzzy logic interface [13] are detailed in the author's previous work [14] along with few flight data comparison. Although EKF is a widely used filtering strategy, the difficulty experienced while tuning the fuzzy-based covariance matrix for different sizes of observation equations and the well-known limitation of EKF that linearize all nonlinear model to enable linear filtering, had arisen the need for an alternative.

3.2 Unscented Kalman Filter (UKF)

The UKF classified under "sigma point filters" preserves the standard Kalman filter form which involves propagation of finite set of points, called sigma points, through the nonlinear dynamics and by approximating the distribution (mean and covariance) through a weighted sum and outer (cross) product [15].

In contrast to the first-order approximation used on EKF for covariance propagation, in the UKF, nonlinear dynamics are used without approximation, leading to better performance without the effort of computing Jacobian or Hessian matrix. It has been shown that UKF is equivalent to second-order EKF and for linear systems the behavior of Kalman filter, UKF, and EKF are identical [11]. Initially, $(2n_a + 1)$ sigma points are defined, where n_a, is the total number of states to be estimated, which include the basic system state, the aerodynamic parameters. Each sigma point consists of a vector, one of the sigma vectors is the expected value of the augmented state vector and the remaining $2n_a$ points are obtained from the columns of the matrix square root $\left(\pm\gamma P_k^a\right)$ for $k = 1, 2, \ldots n_a$ where P is the covariance matrix of the augmented state vector (x_a). Starting from setting of parameters as described below under UKF Parameters for weights of expected value and rest all sigma points are assigned using scale factors chosen appropriately pertinent to the problem. The next step is to initialize the state and covariance matrix and iterate through loop for apriori and posterior corrections.

UKF Parameters

$$sigmapoints : 2n_a + 1$$

$$where, n_a = n_x + n_q; n_x = no., of\ states, n_q = no., of\ parameters$$

$$\gamma = \alpha^2(n_a + k) - n_a$$

$$\lambda = \sqrt{n_a + \gamma}$$

$$W_o^m = \frac{\lambda}{(n_a + \lambda)}$$

$$W_o^c = \frac{\lambda}{(n_a + \lambda)} + \left(1 - \alpha^2 + \beta\right)$$

$$W_i^m = W_i^c = \frac{1}{2(n_a + \lambda)}, i = 1, 2, \ldots 2n_a$$

α determines the spread of sigma points around x_a (Range 0.001–1.000); κ secondary scaling parameter $(\kappa = 3 - n_a)$; β factor for prior knowledge of distribution of x_a (Optimum $\beta = 2$); W_0^m is the weight for mean of expected value; W_0^c is the

weight for covariance of expected value; W_i^m is the weight of mean of sigma points; W_0^c weight for covariance of sigma points.

Initialize state and covariance matrix as:

$$x_o^a = E\left[x_o^a\right] = E\left[x_o^T \Theta_O^T\right] \tag{25}$$

$$p_o^a = E\left[\left(x_o^a - \hat{x}_o^a\right)\left(x_o^a - \hat{x}_o^a\right)^T\right] = \begin{pmatrix} p_x^o & o \\ o & p_\Theta^o \end{pmatrix} \tag{26}$$

UKF Algorithm with apriori estimates, measurement update and posterior corrections steps is explained below as a flowchart along with equations

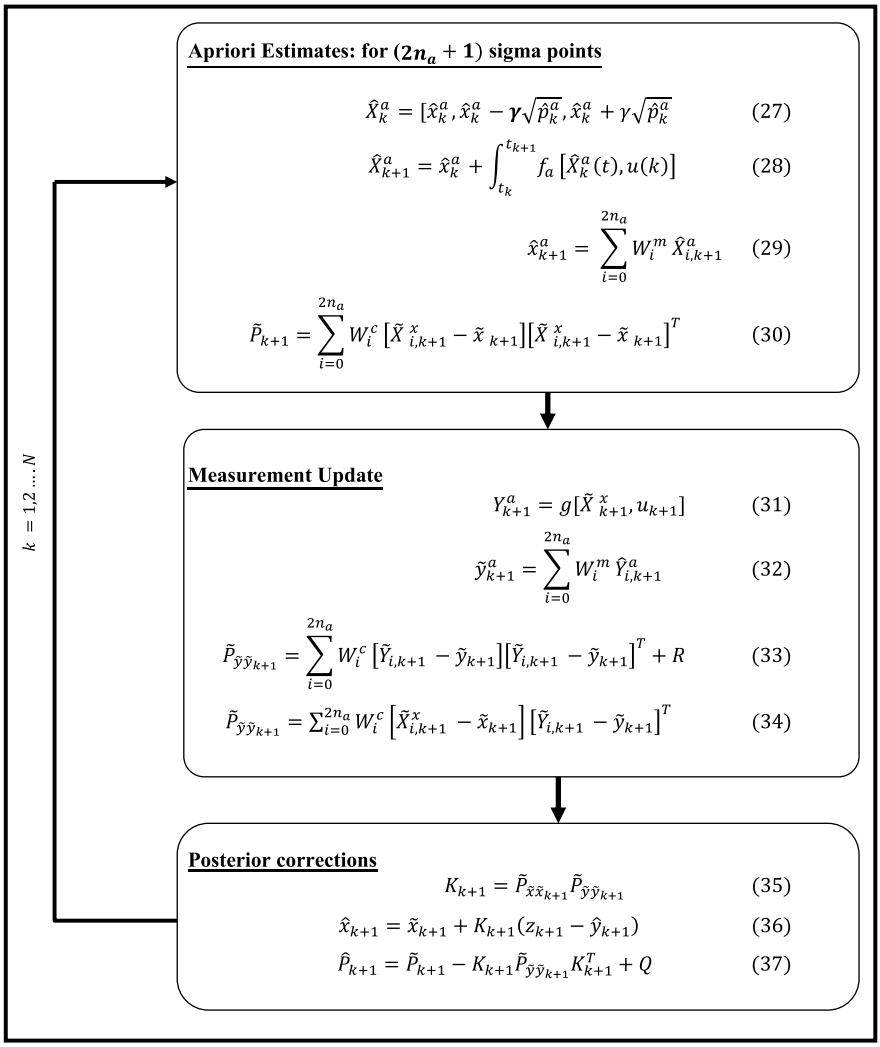

4 Results of Landing State Estimation Using UDAEKF and UKF

4.1 Aircraft States at the Instant of Touchdown

The initiation of flare maneuver at a height of ~50 ft above the ground level is taken as initial values for the augmented state (x_a) and considered to have a bias of 10% from the actual values. The measurement data obtained from the simulation is mixed with random process noise of $\sigma = 0.001$ on states to represent the uncertainty in math model and measurement noise of $SNR = 10$ is added to represent the uncertainty in measurement. These noise parameters are indicative of real measurement data obtained from several sensors on aircraft. The regular implementation of EKF suffers from the sensitivity to the initial values of the augmented state. The presence of adaptive tuning process (Fuzzy logic interface) in UDAEKF eases out the need for specifying a near about exact initial values. For the UKF, (2 × Number of states + 1) sigma points were created and appropriate scaling and tuning parameters were set.

Figure 2 presents the estimated states such as (u, w, θ, q, h) of the Aircraft during landing for case III of flared landing. The state estimates obtained from UDAEKF and UKF filtering methods are compared against the noisy measurement data obtained through 6 DOF simulation. The dot-dash line in *time* versus h subplot indicates the touchdown instance of Main Landing Gear (MLG). Inset in Fig. 2 shows the performance of the filters as state error bounds near touchdown time steps. The necessary and sufficient condition is satisfied by having the state errors within the

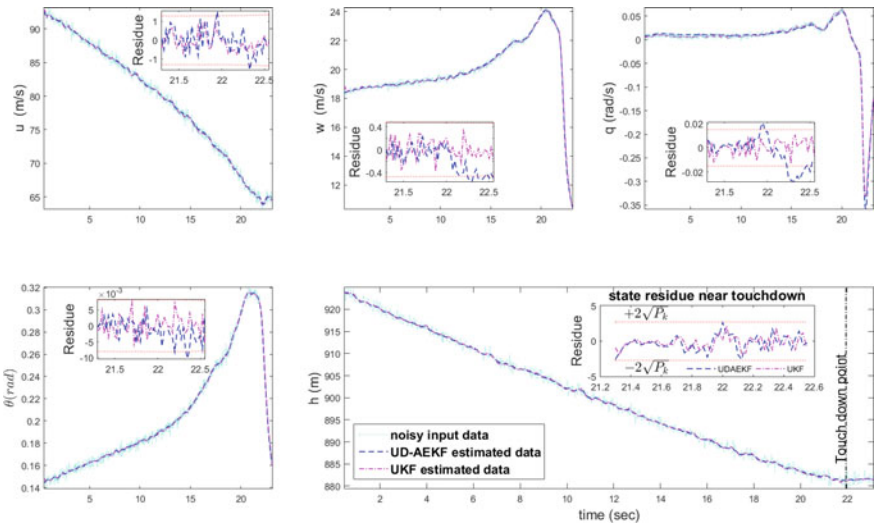

Fig. 2 Estimated Aircraft states and residues (inset) for case III of landing using UDAEKF and UKF algorithms for case III of flared landing

Table 1 Estimated states standard deviation at touchdown timestamp

Aircraft States	Case I of landing		Case II of landing		Case III of landing	
	UDAEKF	UKF	UDAEKF	UKF	UDAEKF	UKF
u (m/s)	0.3303	0.3200	0.2621	0.2362	0.2835	0.2763
w (m/s)	0.0643	0.0580	0.0523	0.05119	0.0553	0.0510
q (rad/s)	0.0005	0.0004	0.0014	0.0012	0.0014	0.00138
θ (rad)	0.00045	0.00047	0.0009	0.0008	0.000648	0.000523
h (m)	3.740	3.6530	2.965	2.632	3.185	3.132

bounds of $\pm 2\sqrt{P_k}$, where P_k is the state covariance matrix. Both these filters were able to predict the true states of the Aircraft near touchdown; with residues being minimal for UKF method as compared with UDAEKF. This is primarily due to the linear approximation of state equations and fuzzy adaptation of process noise covariance matrix for every time step in UDAEKF as against fair propagation of sigma points in UKF. Table 1 shows standard deviation for the states such as (u, w, θ, q, h) that are consistent and values being on the lower side for UKF. The computational time for UKF is two and half times faster as compared with UDAEKF that involves a fuzzy logic step.

4.2 Aircraft States that Dictate Landing Impact Loads

Three landing cases even though initiated at the same Point In The Sky (PITS), differ by execution of flare. For case I of flared landing, gentle flare leads to lower vertical acceleration a_z among all the three landing cases due to the incremental change of $\dot{h}$ and $\dot{q}$. For Case II of flared landing, the aircraft is flared at terminal phase. This has resulted in increased acceleration levels of $a_z \& \dot{h}$ and $\dot{q}$ at the time of touchdown.

$$\text{Root Mean Square Error (RMSE)} = \frac{1}{N}\sqrt{\sum_{k=1}^{t}\frac{\left(x_{ek} - x_p\right)^2}{n_y}}$$

where N is the number of time steps (t), $x_e \& x_p$ are the estimated aerodynamic parameters at each time step and actual aerodynamic parameters at the landing phase n_y is the number of aerodynamic parameters.

For the Case III of flared landing, an initial overshoot occurs due to the pitch stick input which was corrected by an abrupt flare just before touchdown, thereby leading to higher value of $a_z \& \dot{q}$, out of all the three landing cases. Figure 3 shows the acceleration levels at aircraft CG from the time of flare initiation to touchdown that dictates landing impact loads for higher sink rate observed in case III of landing. Figure 4 presents the aerodynamic parameter estimates using UDAEKF and UKF

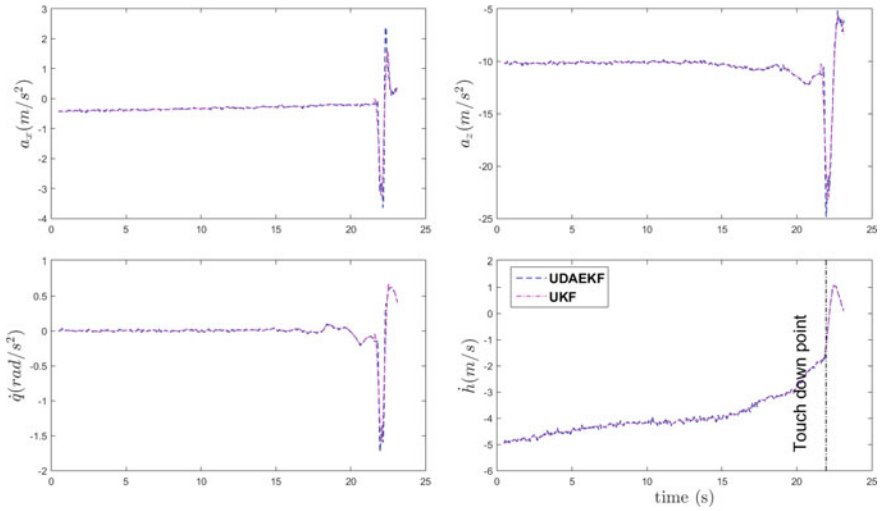

Fig. 3 Aircraft states estimates at touch down for case III of flared landing

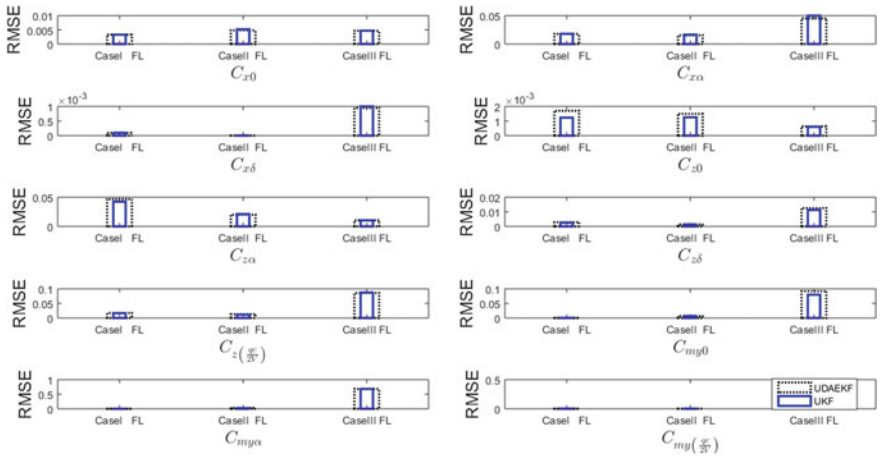

Fig. 4 Aerodynamic parameter estimates using UDAEKF and UKF

in the form of Root Mean Square Error (RMSE). The RMSE error is consistent in using these estimation methods.

Table 2 Aircraft states as PRSSE (%) at touch down time stamp for several flared landing cases

Aircraft states	Case I of landing		Case II of landing		Case III of landing	
	UDAEKF: PRSSE (%)	UKF: PRSSE (%)	UDAEKF: PRSSE (%)	UKF: PRSSE (%)	UDAEKF: PRSSE (%)	UKF: PRSSE (%)
Longitudinal acceleration (a_x)	(+) 1.8	(+) 0.9	(+) 7.0	(+) 3.9	(−) 8.3	(−) 6.4
Vertical acceleration (a_z)	(−) 14.1	(−) 11.3	(+) 3.3	(+) 3.2	(+) 4.3	(+) 3.5
Pitch acceleration ($\dot{q}$)	(−) 4.0	(−) 4.0	(+) 7.0	(+) 7.7	(+) 1.2	(+) 3.0
Vertical sink rate ($\dot{h}$)	(−) 2.8	(−) 3.4	(+) 4.1	(+) 3.6	(+) 5.7	(+) 6.2

PRSSE (%) $= \sqrt{\sum \frac{(x_m - x_e)\hat{}2}{x_m^2} * 100}$; Where x_m is the noisy input data and x_e is the estimated states from filtering methods. (+) indicates over quantified and (−) indicates under quantified measurements

4.3 Discussion

Table 2 presents the Aircraft state which governs the landing impact loads such as $a_x, a_z, \dot{q}, \dot{h}$ for all flared landing cases obtained using filtering methods. To quantify the error, a comparative metrics called Percentage Root Sum Square Error (PRSSE) is used. Greater emphasis is given to the estimates using UKF method as compared to UDAEKF since the residue and standard deviation are on the lower side. In Table 2 the (+) sign indicates that the measurement is over quantified and (−) sign indicates under quantified data.

The emphasis for aircraft true state estimation at touchdown is noticeable from the comparative data presented in Table 2. The results of vertical acceleration (a_z) are discussed in detail. The Case II and Case III of flared landing indicate that the measurement data of a_z are higher than the estimated by a maximum of 4.3% for UDAEKF and 3.5% for UKF. For Case I of flared landing, measurement data for a_z is lower than estimated by 14.1% for UDAEKF and 11.3% for UKF. The over quantification of vertical acceleration measurement data, during the event such as "hard landing", can lead to inevitable downtime of aircraft for thorough inspection [16]. On the other hand, the under quantification of measurement data leads to ignorance, causing higher nominal stresses that can lead to accumulation of cumulative fatigue damage.

5 Conclusion

An application of state estimation methods for landing maneuver problem is presented in this work, by using Upper Diagonal Adaptive Extended Kalman Filter (UDAEKF) and Unscented Kalman Filter (UKF) methods. Three sets of measurement data with different flare techniques were generated using a pilot in loop nonlinear 6 DOF simulation. The estimated aircraft states are found to be within the error bounds, which were compared against the noisy measurement data. Estimated aerodynamic parameters as augmented states are presented as Root Mean Square Error (RMSE) which is observed to be lower using UKF method. For the states that dictate the landing impact loads, a performance metric called 'Percentage Root Sum Square Error (PRSSE)' is used as an indicator to bring out the variation in measurement and estimated data. For Case II and Case III of flared landings, the vertical acceleration (a_z) measurement data is observed to be higher than the estimated by maximum PRSSE of 3.5%. For higher vertical descent rate landing, the inaccuracy in noisy measurement data, translate to inevitable downtime of Aircraft for thorough inspection. For Case I of landing, the measurement vertical acceleration (a_z) data is lower than the estimate with maximum PRSSE of 11.3%, which if ignored, results in higher nominal stresses leading to accelerated cumulative damage for the landing gear and its interface components. It is observed that the UDAEKF and UKF methods applied on landing maneuver problems are capable to determine the true aircraft states. Among these two methods, UKF performance is two and half times faster and observed to have better adaptation on aircraft states due to fair propagation of sigma points.

Acknowledgements The authors from Aeronautical Development Agency acknowledge "The Programme Director" for the facility provided to publish this work. Special thanks to Technology Director (Airframe) and Group Director (Loads, Airframe) for their technical support.

References

1. Lacagnina M (2004) Flight safety digest: avoiding hard landings. Tech Publ 23(8):249–250. Flight Safety Foundation
2. Airplane strength and rigidity: landing and ground loads, May 1960
3. Airplane strength and rigidity: ground loads for navy acquired airplanes, May 1987
4. Sartor P, Schmidt RK, Becker W, Worden K, Bond DA, Staszewski WJ (2010) Conceptual design of a hard landing indication system using flight parameter sensor simulation model. In: 27th international congress of the aeronautical science
5. Crassidis JL, Junkins JL (2012) Optimal estimation of dynamic systems, 2nd edn. CRC Press
6. Julier SJ, Uhlmann JK (1995) A new extension of Kalman filter to nonlinear systems. In: Proceedings of the American control conference, pp 1628–1632
7. Chen G, Chui CK (1991) A modified adaptive Kalman filter for real-time applications. IEEE Trans Aerosp Electron Syst 27(1):149–154
8. Mulder JA, Chu QP, Sridhar JK, Breeman JH, Laban M (2010) Non-linear aircraft flight path reconstruction review and new advances. Prog Aerosp Sci 35:673–726

9. Chowdhary G, Jategaonkar R (2010) Aerodynamic parameter estimation from flight data applying extended and unscented Kalman filter. Aerosp Sci Technol 14:106–117
10. Napolitano MR Aircraft Dynamics: from modeling to simulation. Wiley
11. Jategaonkar RV, Thielecke F (2000) Aircraft parameter estimation—a tool for development of aerodynamic databases. SaÅdhanaÅ 25(Part 2):119–135
12. Bierman GJ (1977) Factorization method for discrete sequential estimation. Academic Press, New York
13. Jetto L, Longhi S, Vitali D (1999) Localization of a wheeled mobile robot by sensor data fusion based on fuzzy logic adapted Kalman filter. Control Engg Pract 4:763–771
14. Suresh PS, Niranjan SK, Shankar K (2018) State estimation on landing maneuver on High performance Aircraft. J Inst Eng (India): Ser C, Aerosp Mech Eng. Springer, s40032-017-0428-0
15. Wan EA, van der Merwe R (2006) The unscented Kalman filter for nonlinear estimation. Center for Spoken Language and Understanding, OGI School of Science and Engineering. http://cslu.cse.ogi.edu/nsel/ukf/
16. Inspection process following high load events, Technical Report 05-01, Aerospace Industry Association, Sept 2012

Numerical Solution of Steady Incompressible Flow in a Lid-Driven Cavity Using Alternating Direction Implicit Method

Banamali Dalai and Manas Kumar Laha

Abstract The study of viscous flow in a lid-driven cavity is carried out using alternating direction implicit method. The conservation form of incompressible Navier–Stokes equation in stream function–vorticity form is solved using second-order accurate central difference scheme in a uniform finite-difference grid mesh. The numerical solution is obtained up to highest Reynolds number 32,500 from the lowest 0.00001 using the grid sizes 129 × 129, 257 × 257 and 513 × 513. Good agreement of the result is found with Erturk et al. (Int J Numer Methods Fluids 48:747–774, 2005) [1]. The study of flow properties in the form of velocity profiles, stream function and vorticity contour plots and location of primary and secondary eddies are carried out. The novelty of this study is that the magnitude of the vorticity value does not cross the theoretical limit −1.8859 (Burggraf 24:113–151, 1966 [2]).

Keywords Stream function–vorticity · Conservation · Incompressible · Reynolds number · ADI method

1 Introduction

The lid-driven cavity is a square cavity in which the vertical walls and lower horizontal wall are stationary. The top wall is allowed to move horizontally, and it is called the lid of the cavity. The non-dimensional length of the cavity is unity. Initially, the cavity is filled with fluid which is at rest. When the lid moves towards right with non-dimensional velocity unity, the fluid flow in the cavity sets up. The velocity of flow in the cavity becomes higher or lower depending upon the Reynolds number of

B. Dalai (✉)
Faculty, Centre for Advanced Post-Graduate Studies, Biju Pattnaik University of Technology Odisha, Rourkela, India
e-mail: banamali.2000@gmail.com

M. K. Laha
Faculty, Aerospace Engineering, Indian Institute of Technology Kharagpur, Kharagpur, West Bengal, India

B. N. Singh et al. (eds.), *Recent Advances in Theoretical, Applied, Computational and Experimental Mechanics*, Lecture Notes in Mechanical Engineering,
https://doi.org/10.1007/978-981-15-1189-9_28

the lid. The conserved incompressible Navier–Stokes equation in stream function–vorticity form is used for the solution of the flow patterns in the cavity. The general use of lid-driven cavity is in the manufacturing industry where one or more than one wall is allowed to move to produce different thicknesses and shapes of the steel or ceramic sheets. Some of the literatures regarding the lid-driven cavity flow at higher Reynolds numbers are presented below.

In the year 1966, Burggraf [2] started the study of flow in the lid-driven cavity using SOR techniques and became successful up to Reynolds number 400 using grid sizes 41 × 41 and 51 × 61. His attempts to solve for Reynolds number 1000 remain unsuccessful in the grids sizes 61 × 61. Later in the year 1982, Ghia et al. [3] studied the lid-driven cavity flow up to Reynolds number 10,000 using FAS-MG multigrid method in the grid sizes 129 × 129 and 257 × 257. Again in the year 2005, Erturk et al. [1] obtained the solution in the lid-driven cavity up to Reynolds number 20,000 using TDMA method in the grid sizes 401 × 401, 501 × 501 and 601 × 601. Erturk [4] solved the lid-driven cavity flow up to Reynolds number 21000 in the maximum grid size 1025 × 1025 in the year 2008. All the solutions obtained up to this point were second-order accurate. In the year 2009, Erturk and Gockol [5] obtained fourth-order accurate solution in the lid-driven cavity from the stream function–vorticity form of the Navier–Stokes equation using TDMA method up to maximum Reynolds number 21,000 in the grid sizes 401 × 401, 501 × 501 and 601 × 601.

From the literature, it is also observed that as the Reynolds number increases the vorticity strength at the centre of the primary eddy should not cross the theoretical limit −1.8859 as proposed by Burggraf [2] but this value is crossed by Ghia et al. [3] and Erturk et al. [1] within Reynolds number 10000. Here, it is observed that Ghia et al. [3] and Erturk et al.'s [1] solution was second-order accurate in space. In case of Erturk [4] even though the solution is second-order accurate in space the grid sizes were 1025 × 1025. That is the reason why the vorticity value at the centre of the primary eddy did not cross the limit −1.8859. In case of Erturk and Gockol [5], the solutions were fourth-order accurate in space resulting in the vorticity value at the centre of the primary eddy did not cross the theoretical limit. The main motivation is that since the alternating direction implicit method is second-order accurate in space and time; if the lid-driven cavity result is obtained using this method, it will be a point of observation whether the vorticity value at the centre of the primary eddy crosses the theoretical limit or not. So, the objective of this work is to find out the maximum possible Reynolds number solution in the lid-driven cavity flow using ADI two-step method and to test whether the vorticity strength at the centre of the primary eddy crosses the theoretical limit −1.8859 or not.

2 Formulation

The conservation form of incompressible Navier–Stokes equation is expressed as

$$\frac{\partial \omega}{\partial t} + \frac{\partial (u\omega)}{\partial x} + \frac{\partial (v\omega)}{\partial y} = \frac{1}{\mathrm{Re}}\left(\frac{\partial^2 \omega}{\partial x^2} + \frac{\partial^2 \omega}{\partial y^2}\right) \tag{1}$$

where u and v are the velocities in x- and y-directions, respectively; ω is the vorticity and Re is the Reynolds number of the flow. The Reynolds number for the flow is defined by $\mathrm{Re} = \frac{uL}{\nu}$. Here L is the length of the lid and ν is the kinematic viscosity of the fluid. The stream function (ψ) is coupled with vorticity by the equation as

$$\frac{\partial^2 \psi}{\partial x^2} + \frac{\partial^2 \psi}{\partial y^2} = -\omega \tag{2}$$

The boundary conditions for Eqs. (1) and (2) are

$$\begin{aligned} &\text{At } x = 0, 1 \text{ and } 0 \le y \le 1; \quad \psi = \frac{\partial \psi}{\partial x} = \frac{\partial \psi}{\partial y} = 0; \quad \text{At } y = 0 \text{ and } 0 \le x \le 1; \quad \psi = \frac{\partial \psi}{\partial x} = \frac{\partial \psi}{\partial y} = 0; \\ &\text{At } y = 1 \text{ and } 0 \le x \le 1; \quad \psi = \frac{\partial \psi}{\partial x} = 0 \text{ and } \frac{\partial \psi}{\partial y} = 1 \end{aligned} \tag{3}$$

Equation (1) is discretized using alternating direction implicit method which is second-order accurate in time and second-order accurate in space. The space derivative terms are discretized using central difference scheme in a finite-difference mesh.

After arrangement of the discretized equation at $n + 1/2$ time step:

$$\begin{aligned} &\left(c_x u_{ij+1}^{n+\frac{1}{2}} - d_x\right)\omega_{ij+1}^{n+\frac{1}{2}} + (1 + 2d_x)\omega_{ij}^{n+\frac{1}{2}} - \left(c_x u_{ij-1}^{n+\frac{1}{2}} + d_x\right)\omega_{ij-1}^{n+\frac{1}{2}} \\ &= \omega_{ij}^{n} + d_y\left(\omega_{i+1j}^{n} - 2\omega_{ij}^{n} + \omega_{i-1j}^{n}\right) - c_y\left((v\omega)_{i+1j}^{n} - (v\omega)_{i-1j}^{n}\right) \end{aligned} \tag{4}$$

where $c_x = \frac{\Delta t}{4\Delta x}$, $c_y = \frac{\Delta t}{4\Delta y}$, $d_x = \frac{\Delta t}{2\mathrm{Re}(\Delta x)^2}$, $d_y = \frac{\Delta t}{2\mathrm{Re}(\Delta y)^2}$, $(v\omega)_{i+1j}^{n} = v_{i+1j}^{n}\omega_{i+1j}^{n}$ and Δt, Δx and Δy are the time step, grid widths in x- and y-directions, respectively.

Similarly, after arrangement of the discretized equation at $n + 1$ time step:

$$\begin{aligned} &\left(c_y v_{i+1j}^{n+1} - d_y\right)\omega_{i+1j}^{n+1} + \left(1 + 2d_y\right)\omega_{ij}^{n+1} - \left(c_y v_{i-1j}^{n+1} + d_y\right)\omega_{i-1j}^{n+1} \\ &= \omega_{ij}^{n+\frac{1}{2}} + d_x\left(\omega_{ij+1}^{n+\frac{1}{2}} - 2\omega_{ij}^{n+\frac{1}{2}} + \omega_{ij-1}^{n+\frac{1}{2}}\right) - c_x\left((u\omega)_{ij+1}^{n+\frac{1}{2}} - (u\omega)_{ij-1}^{n+\frac{1}{2}}\right) \end{aligned} \tag{5}$$

Equation (2) is discretised using second-order accurate central difference scheme. Along the boundaries, the stream function values are obtained from Eq. (3) and the vorticity values are obtained from Eqs. (2) and (3) with application in the Taylor series formulation. Truncation error of the Taylor series formulation is third-order accurate. The solution to the discretized equations (Eqs. (4) and (5)) is obtained using

tridiagonal matrix algorithm at each time step. The convergence of the solution is obtained when the residues (LHS–RHS) of Eqs. (1) and (2) equals to 10^{-10}. The numerical solutions are obtained using the grid sizes 129×129, 257×257, 513×513 and 1025×1025.

The results obtained in the grid size 513×513 are validated with Erturk et al.'s [1] (grid size 601×601) result in the form of u- and v-velocity profiles along y- and x-directions, respectively, passing through the centre of the cavity as shown in Fig. 1. Good agreement of the result is obtained.

3 Results and Discussion

The solution of the discretized equation is obtained up to maximum Reynolds number 32,500 in the grid sizes 513×513, whereas using the grid sizes 1025×1025, the solution is obtained up to Reynolds number 22,500. The stream function contour plots (in Fig. 2) show that with increase of Reynolds number, the primary eddy grows in size and becomes circular in nature. The number of secondary eddies increases at the corners with increase of Reynolds number which can be seen from Fig. 2 and Table 3. In this study, maximum fifth level of secondary eddy is obtained at the right corner of the cavity at Reynolds number 32,500. The level of eddies can be distinguished from the sense of rotation. The sense of rotation of secondary eddies at consecutive levels is opposite to each other. The secondary eddy at the top position of the left vertical wall is observed between Reynolds number 1000 and 2500 which is denoted as TL1 in Table 3. Its size increases with increase of Reynolds number. The second level of secondary eddy (TL2) at that position is observed between Reynolds number 10,000 and 12,500 which are shown in Fig. 2. Henceforth with increase of Reynolds number, there is no development of more level of secondary eddies at that position which can be seen from Fig. 2 but the size of these eddies increases. In Table 3, BL1 represents the first level of secondary eddy at bottom left corner of the cavity and next level of eddies are denoted as BL2, BL3, BL4, etc. Similarly, BR1 represents the first level of secondary eddy at bottom right corner of the cavity and next level of eddies is represented by BR2, BR3, BR4, etc.

The vorticity contour plots in Fig. 3 show that with increase of Reynolds number, the central region of the primary eddy becomes constant vorticity region. The central portion of the cavity in Fig. 3 shows without any contours; those regions are represented by constant vorticity value. That constant vorticity region behaves like a solid core. Its radius increases with increase of Reynolds number as shown in Fig. 3. The increase in radius of constant vorticity core is confirmed from the velocity profiles (Fig. 1) in which the central profiles show linear in nature than the other regions. As the Reynolds number increases, the linear profile region becomes longer in the velocity profiles.

The vorticity value is represented by

$$\omega = \nabla \times \vec{V} \tag{6}$$

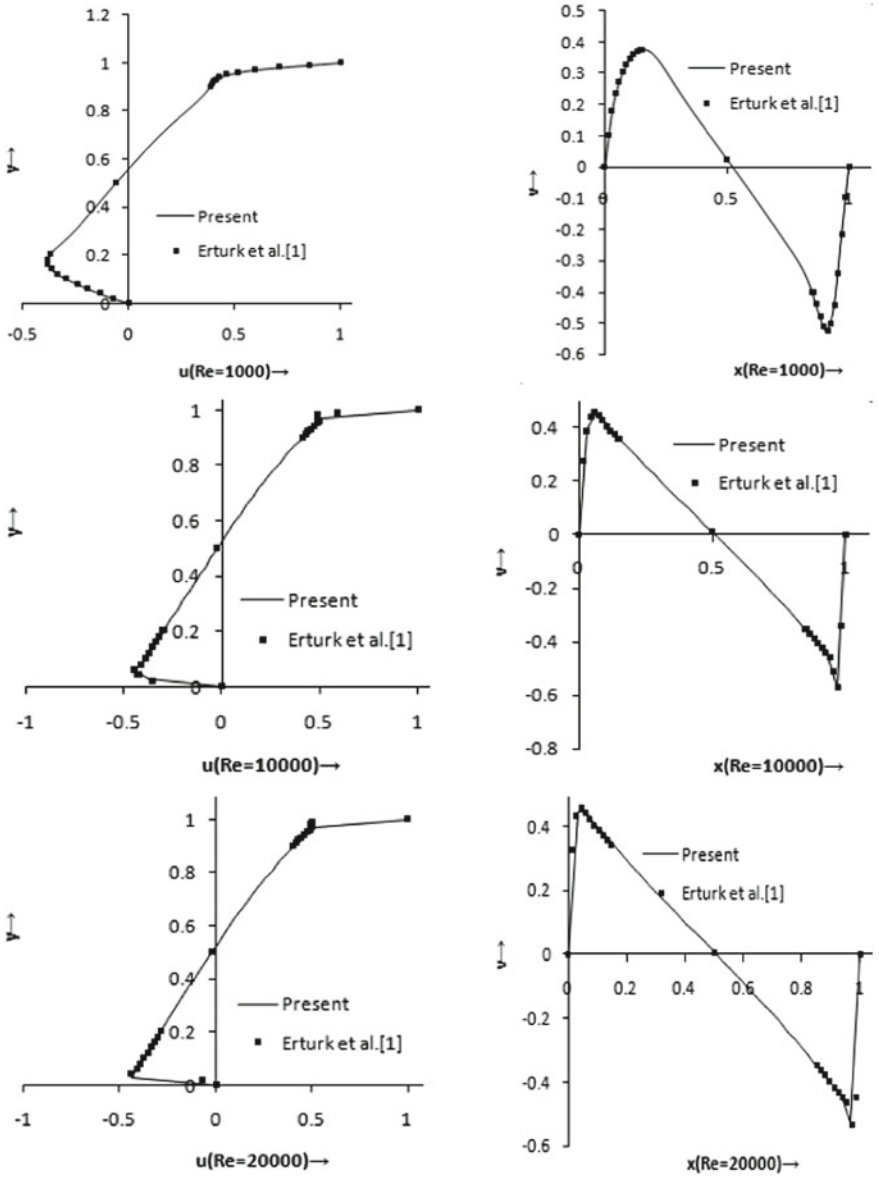

Fig. 1 Validation of *u*- and *v*-velocity profiles along *y*- and *x*-directions, respectively

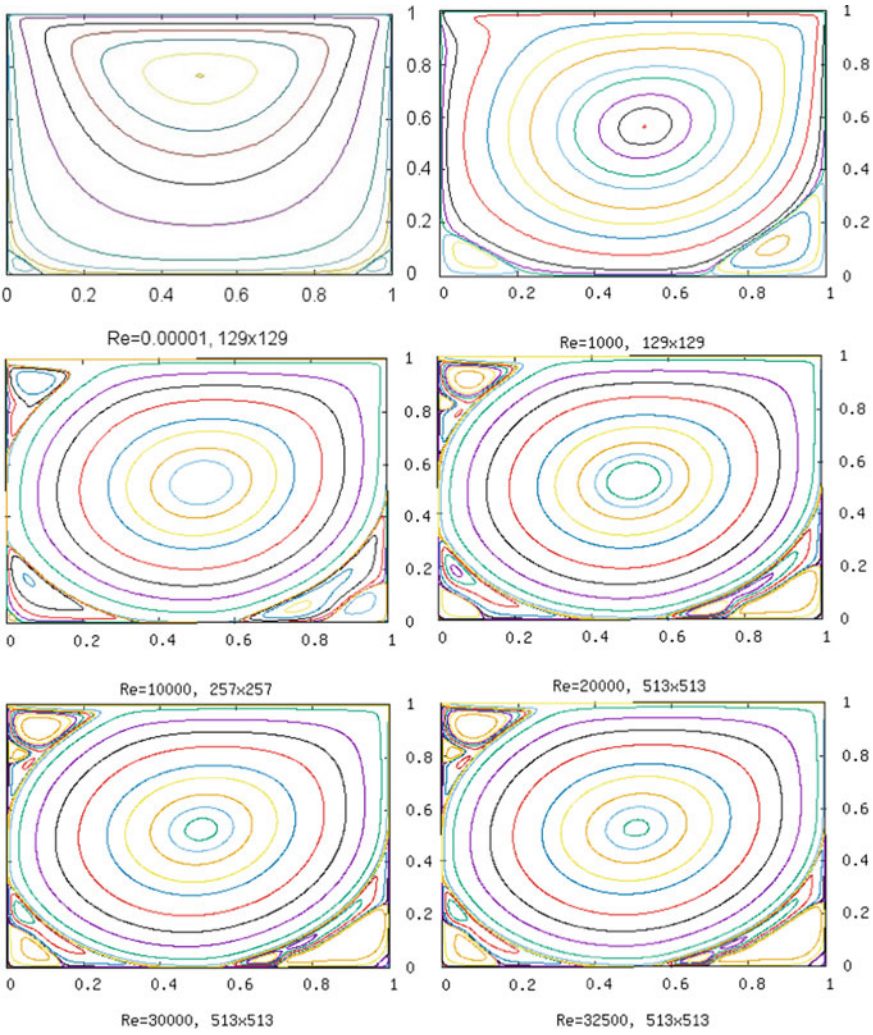

Fig. 2 Stream function contour plots at different Reynolds numbers

where $\vec{V} = u\hat{i} + v\hat{j}$ is the velocity of flow in the cavity. Expansion of Eq. (6) produces constant value at the central region of the cavity because the velocity gradients $\partial v / \partial x$ and $\partial u / \partial y$ are linear at the centre of the cavity. The vorticity values near the walls show large variation in comparison to the central region. This variation is due to the presence of more viscous flow region near the wall than that of central region. The viscous flow near the wall signifies the presence of boundary layer near the walls.

The location and strength of primary eddies at different Reynolds numbers are compared with Erturk et al. [1] in Table 1. It is observed that both results are found to match very well.

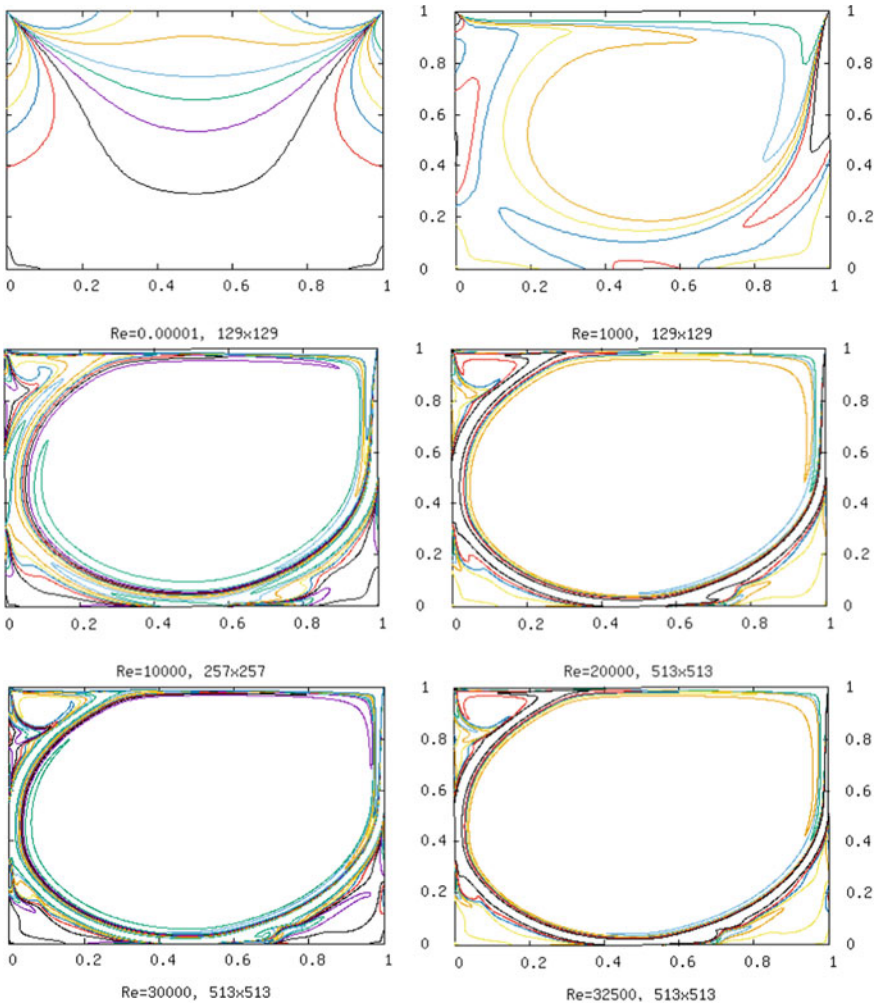

Fig. 3 Vorticity contour plots at different Reynolds numbers

Table 2 represents the magnitude of stream function and vorticity values at the centre of the primary eddy at different Reynolds numbers and various grid sizes. It is observed that the values are accurate up to two digits after decimal place in all grid sizes. This table shows that the values are independent of grid sizes.

Figure 4 shows the variation of vorticity value at the centre of the primary vortex at different Reynolds numbers. The magnitude of the vorticity value is also compared with the results published in the literature. Among the compared results, Erturk et al.'s [1] second-order accurate in the grid size 601 $\times$ 601, Erturk's [4] second-order accurate in the grid size 1025 $\times$ 1025 and Erturk and Gockol's [5] fourth-order accurate in the grid size 601 $\times$ 601 are compared with the present results in the grid

Table 1 Comparison of the location and strength at the centre of the primary eddy

Re	Grid	Location				Strength			
		Present		Erturk et al. [1]		Present		Erturk et al. [1]	
		x	y	x	y	ψ	ω	ψ	ω
1E−04	129 × 129	0.5000	0.7656	–	–	−0.1000	−3.2190	–	–
1000	513 × 513	0.5313	0.5645	0.5300	0.5650	−0.1188	−2.0664	−0.1189	−2.0655
5000	513 × 513	0.5313	0.5645	0.5150	0.5350	−0.1188	−2.0664	−0.1212	−1.9266
10,000	513 × 513	0.5117	0.5293	0.5117	0.5300	−0.1212	−1.9023	−0.1204	−1.8889
15,000	513 × 513	0.5098	0.5273	0.5100	0.5283	−0.1205	−1.8845	−0.1192	−1.8636
20,000	513 × 513	0.5098	0.5273	0.5100	0.5267	−0.1198	−1.8705	−0.1180	−1.8418
25,000	513 × 513	0.5078	0.5254	–	–	−0.1191	−1.8586	–	–
30,000	513 × 513	0.5078	0.5254	–	–	−0.1184	−1.8472	–	–
32,500	513 × 513	0.5078	0.5254	–	–	−0.1181	−1.8419	–	–

Table 2 The grid independence test at different Reynolds numbers

Re/Grid size	129 × 129		257 × 257		513 × 513		1025 × 1025	
	ψ	ω	ψ	ω	ψ	ω	ψ	ω
1000	−0.1175	−2.0458	−0.1186	−2.0622	−0.1188	−2.0664	−0.1189	−2.0674
5000	−0.1151	−1.8333	−0.1202	−1.9100	−0.1217	−1.9325	−0.12209	−1.9386
10,000	−0.1089	−1.7208	−0.1183	−1.8584	−0.1212	−1.9023	−0.12209	−1.9148
15,000	−0.1133	−1.6299	−0.1162	−1.8211	−0.1205	−1.8845	−0.1218	−1.9033
20,000	–	–	−0.1142	−1.7888	−0.1198	−1.8706	−0.1216	−1.8984

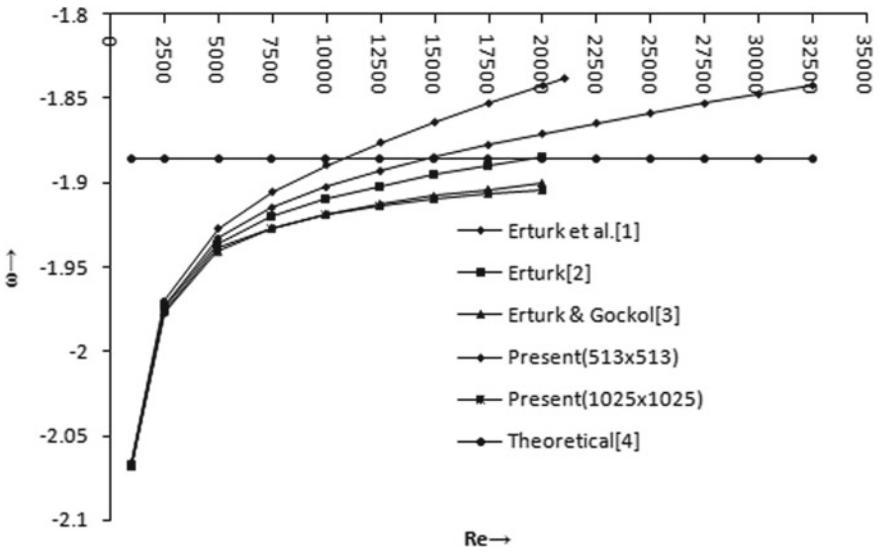

Fig. 4 Plot between the vorticity values at the centre of the primary eddy at different Reynolds numbers

sizes 513 × 513 and 1025 × 1025. The results in the present computation are possible up to Reynolds number 22,500 and 32,500 in the grid sizes 513 × 513 and 1025 × 1025, respectively. The present computed results up to Reynolds number 32,500 in the grid size 513 × 513 show better than the Erturk et al.'s [1] result in the grid size 601 × 601. The results up to Reynolds number 22,500 in the grid size 1025 × 1025 of present computation shows better than Erturk's [4] second-order accurate result in the grid size 1025 × 1025 because the vorticity values remain within the theoretical limit −1.8859 which was computed by the Burggraf [2] as shown in Fig. 4.

The study has been conducted up to maximum Reynolds number 32500 in the grid size 513 × 513 (Table 3). The flow at higher Reynolds number should achieve three-dimensional effect. Since the study is limited within two-dimensional effect, it is very difficult to predict three-dimensionality effect in this cavity study.

Table 3 Shows the location and strength of the secondary eddies at the corners of the cavity

Re/ Grid size	BL1		BR1		BL2		BR2		BL3		BR3		BR4	
	ψ	ω	ψ	ω	ψ	ω	ψ	ω	ψ	ω	ψ	ω	ψ	ω
	x	*y*	*x*	*y*	*x*	*y*	*x*	*y*	*x*	*y*	*x*	*y*	*x*	*y*
1000	2.334e-4	0.3562	1.732e-3	1.1141	-8.544e-3	-5.932e-8	-5.932e-8	-8.998e-3	8.826e-9	4.283e-3	8.646e-7	0.02999		
513	0.08398	0.0781	0.8633	0.1113	3.906e-3	5.859e-3	0.9922	0.0078	0.0059	0.0039	0.9844	0.0195		
5000	1.372e-3	1.4975	3.091e-3	3.091e-3	-7.671e-3	-1.004e-2	0.9922	-3.624e-2	1.049e-8	4.017e-3	1.744e-6	0.0449		
513	7.226e-2	0.1367	0.8027	2.7972	-7.671e-3	-1.004e-2	-1.524e-6	1.953e-2	0.0059	0.0039	0.9805	0.0215		
10000	1.607e-3	2.1436	3.224e-3	2.7972	-7.671e-3	-3.186e-2	-1.496e-4	-0.3133	5.09e-11	1.098e-3	6.509e-9	6.509e-9		
513	5.859e-2	0.1621	0.7734	3.8543	-3.186e-2	-3.186e-2	-1.496e-4	-0.3133	1.953e-3	1.953e-3	0.9961	3.906e-3		
15000	1.663e-3	2.5064	3.049e-3	5.1527	-2.252e-5	-0.14007	-3.624e-2	-0.4755	1.452e-9	1.743e-3	1.726e-8	5.436e-3		
513	5.273e-2	0.1719	0.7422	0.0488	0.0371	0.04297	0.04297	0.0898	1.953e-3	3.906e-3	0.9941	5.859e-3		
20000	1.614e-3	2.9735	2.859e-3	6.4940	-8.182e-5	-0.2505	-5.022e-4	-0.5818	4.261e-4	2.932e-3	3.964e-8	7.529e-3		
513	4.68e-2	0.1836	0.7188	0.0429	5.859e-2	5.468e-2	-0.25054	-0.5818	3.906e-3	3.906e-3	0.9922	7.813e-3		
25000	1.345e-3	3.4415	2.697e-3	7.7831	-6.357e-4	-0.6532	-6.357e-4	0.1191	6.826e-9	2.511e-3	1.601e-7	1.338e-2		
513	0.04297	0.1933	0.69727	0.0371	6.836e-2	-0.6532	-6.357e-4	-0.6532	3.906e-3	3.906e-3	0.9883	0.0195		

(continued)

Table 3 (continued)

30000	1.479e-3	3.9124	2.564e-3	8.9831	-1.779e-4	-0.35764	-7.609e-4	-0.6826	8.826e-9	4.283e-3	8.646e-7	0.02999		
513	0.03906	0.2031	0.06796	0.0332	0.072265	0.06055	0.92969	0.1231	0.0059	0.0039	0.9844	0.0195		
32500	1.446e-3	4.1611	2.506e-3	9.5568	-1.933e-4	-0.38611	-8.200e-4	-0.6974	1.049e-8	4.017e-3	1.744e-6	0.0449	-2.1e-10	-1.2e-3
513	0.0371	0.2070	0.67188	0.0313	0.076172	0.058594	0.929688	0.1250	0.0059	0.0039	0.9805	0.02148	0.9980	0.0019

Re	**2500**		**5000**		**10000**		**15000**		**20000**		**25000**		**32500**	
	ψ	**ω**	**ψ**	**ω**	**ψ**	**ω**	**ψ**	**ω**	**ψ**	**ω**	**ψ**	**ω**	**ψ**	**ω**
	x	**y**	**x**	**y**	**x**	**y**	**x**	**y**	**x**	**y**	**x**	**y**	**x**	**y**
TL1	3.452e-4	1.2955	1.448e-3	2.1010	2.619e-3	2.2828	3.27e-3	2.3843	3.716e-3	2.4612	1.338e-2	4.048e-3	4.433e-3	2.5846
	0.04297	0.8887	0.0625	0.9102	7.031e-2	0.9121	7.617e-3	0.9121	8.008e-2	0.9121	4.048e-3	2.5181	0.0859	0.9141
TL2							-1.907e-6	-0.2637	-7.42e-5	-0.9965	-1.35e-4	-1.2138	0.0313	0.8125
							7.81e-3	0.8300	2.539e-2	0.8184	0.0293	0.8144	0.03125	0.8105

4 Conclusion

The solution for the lid-driven cavity was obtained using alternating direction implicit method from Reynolds number 0.00001–32,500 in the grid sizes 513 × 513. The solution is obtained up to Reynolds number 22,500 in the grid size 1025 × 1025. The results obtained here are found to match very well with the literature. The vorticity value obtained in the grid size 1025 × 1025 remains within the theoretical limit of −1.8859 [5]. A remarkable result of appearance of fifth level of eddy is observed at the Reynolds number 32,500 in the grid size 513 × 513.

References

1. Erturk E, Corke TC, Gockol C (2005) Numerical solutions of 2-D steady incompressible driven cavity flow at higher Reynolds numbers. Int J Numer Methods Fluids 48:747–774
2. Burggraf OR (1966) Analytical and numerical studies of the structure of steady separated flows. J Fluid Mech 24:113–151
3. Ghia U, Ghia KN, Shin CT (1982) High re-solution for incompressible flow using the Navier-Stokes equations and a multigrid method. J Comp Phys 48:387–411
4. Erturk E (2009) Discussions on driven cavity flow. Int J Numer Methods Fluids 60:275–294
5. Erturk E, Gokcol C (2006) Fourth-order compact formulation of Navier-Stokes equations and driven cavity flow at high Reynolds numbers. Int J Numer Methods Fluids 50:421–436

Stagnation and Static Property Correlations for Equilibrium Flows

Shubham Maurya and Aravind Vaidyanathan

Abstract This paper presents an algorithm to determine the relationship between stagnation and static property for equilibrium flows. Results are presented for the combustion equilibrium of two different oxidizer–fuel combinations, namely, LOX/LH2 and MMH/N_2O_4. It is found that the ratio of stagnation to static properties depends on Mach number as well as initial mixture ratio and chamber pressure (stagnation pressure) of the reactants.

Keywords Combustion · Equilibrium flows · Gibbs free energy minimization · Element potential method

1 Introduction

The stagnation and static property relations for calorically perfect gases can be derived analytically [1]. Similarly, for thermally perfect gases where specific heat varies with temperature, the analytical derivation of relationship between stagnation and static properties has been worked out by Zebbiche [2]. Most of the previous studies considered a single non-dissociating gas. The aim of this work is the numerical development of stagnation–static property correlations for gaseous phase equilibrium flows where both specific heats and compositions vary with temperature.

Equilibrium flows are often encountered in rocket engines, where combustion products remain in equilibrium as they undergo expansion. The practical application of the study is hence linked to rocket engines and in particular liquid engines, which use a liquid fuel along with a liquid oxidizer.

S. Maurya · A. Vaidyanathan (✉)
Department of Aerospace Engineering, Indian Institute of Space Science and Technology, Thiruvananthapuram 695547, Kerala, India
e-mail: aravind7@iist.ac.in

S. Maurya
e-mail: shubham.maurya3@gmail.com

B. N. Singh et al. (eds.), *Recent Advances in Theoretical, Applied, Computational and Experimental Mechanics*, Lecture Notes in Mechanical Engineering,
https://doi.org/10.1007/978-981-15-1189-9_29

The method of analysis is based on the concept of Gibbs energy minimization which forms the basis for many equilibrium calculation algorithms as outlined in Refs. [3–5]. The number of simultaneous equations needed to be solved using Gibbs energy minimization technique is quite large which can be reduced further by incorporating the concept of Element potential method [6–8]. However, a comprehensive and systematic way of utilizing the results of equilibrium calculations for obtaining the ratio of stagnation to static properties does not exist in literature. Hence, in this study, we have developed a computational algorithm for establishing stagnation–static correlations for any oxidizer–fuel combination. The results for two cases, viz., LOX/LH2 and MMH/N_2O_4 fuel–oxidizer combinations, have been worked out and the effect of varying mixture ratio and chamber (stagnation) pressure has been studied.

2 Mathematical Formulation

For an isolated chemically reacting system consisting of "NS" species, the Gibbs energy is defined as [9]

$$G = \sum_{j=1}^{\mathrm{NS}} \left(\hat{G}_j^0 + RT\ln(x_j) + RT\ln\left(\frac{p}{p_{\mathrm{ref}}}\right)\right) n_j \tag{1}$$

where $\hat{G}_j^0$ is the standard molar Gibbs function of species "j"; n_j is the number of moles of species "j"; R is the universal gas constant equal to 8.314 J/mol K; x_j is the mole fraction of species "j"; "p" is the pressure; and p_{ref} is the reference pressure of 1 bar. The index "j" varies as 1, 2, …, NS. Application of mass balance for each element in the reacting system results in the following equation:

$$\sum_{j=1}^{\mathrm{NS}} a_{ij} n_j - b_i = 0 \tag{2}$$

where the index "i" varies as 1, 2, …, E (E being the total number of elements involved in the chemical reaction); a_{ij} denotes the number of atoms of element "i" in one molecule of the species "j"; and b_i denotes the total number of moles of element "i" in the mixture.

The equilibrium problem is basically related to the minimization of Gibbs energy subject to the constraint of mass conservation. Using method of Lagrange multipliers, a new function L is defined as

$$L(n_1, \ldots, n_{\mathrm{NS}}, \lambda_1, \ldots, \lambda_E) = \sum_{j=1}^{\mathrm{NS}} \left(\hat{G}_j^0 + RT \ln(x_j) + RT \ln\left(\frac{p}{p_{\mathrm{ref}}} \right) \right) n_j - \sum_{i=1}^{E} \lambda_i \left(\sum_{j=1}^{\mathrm{NS}} a_{ij} n_j - b_i \right) \tag{3}$$

where λ_i are Lagrange multipliers. At equilibrium, $\nabla L = 0$, leading to

$$\frac{\partial L}{\partial n_j} = \hat{G}_j^0 + RT \ln(x_j) + RT \ln\left(\frac{p}{p_{\mathrm{ref}}} \right) - \sum_{i=1}^{E} \lambda_i a_{ij} = 0 \tag{4}$$

and

$$\frac{\partial L}{\partial \lambda_i} = \sum_{j=1}^{\mathrm{NS}} a_{ij} n_j - b_i = 0 \tag{5}$$

Also, the following equation is valid at equilibrium:

$$\sum_{j=1}^{\mathrm{NS}} n_j - N_g = 0 \tag{6}$$

where N_g is the total number of moles of species at equilibrium.

Equations (4)–(6) constitute a system of simultaneous nonlinear equations with $n_1, n_2, \ldots, n_{\mathrm{NS}}, \lambda_1, \lambda_2, \ldots, \lambda_E$ and N_g as unknown variables. The number of unknowns is $\mathrm{NS} + E + 1$ which can only be found by solving $\mathrm{NS} + E + 1$ simultaneous nonlinear equations. The system of equations can be decoupled by invoking element potential method which involves algebraic manipulations as outlined in Ref. [8]. Equation (4) can be rewritten as

$$x_j \equiv \frac{n_j}{N_g} = \frac{p_{\mathrm{ref}}}{p} e^{\frac{-\hat{G}_j^0 + \sum_{i=1}^{E} \lambda_i a_{ij}}{RT}} \tag{7}$$

Because summation of mole fraction is unity, combining Eqs. (6) and (7) gives

$$\sum_{j=1}^{\mathrm{NS}} \frac{p_{\mathrm{ref}}}{p} e^{\frac{-\hat{G}_j^0 + \sum_{i=1}^{E} \lambda_i a_{ij}}{RT}} - 1 = 0 \tag{8}$$

Substituting Eq. (7) in Eq. (5) yields

$$\sum_{j=1}^{\mathrm{NS}} a_{ij} N_g \frac{p_{\mathrm{ref}}}{p} e^{\frac{-\hat{G}_j^0 + \sum_{i=1}^{E} \lambda_i a_{ij}}{RT}} - b_i = 0 \tag{9}$$

Both Eqs. (8) and (9) represent the final decoupled set of simultaneous nonlinear equations with unknowns $\lambda_1,\ \lambda_2, \ldots,\ \lambda_E$ and N_g. The number of simultaneous nonlinear equations to be solved is now reduced from NS + E + 1 to just E + 1. In order to determine mole fraction (or no. of moles) of each species, Eq. (7) is back substituted with $\lambda_1,\ \lambda_2, \ldots,\ \lambda_E$ and N_g.

In problems where equilibrium temperature is known, solution of Eqs. (8) and (9) yields the equilibrium composition. However, in most of the practical applications, equilibrium temperature needs to be determined and hence additional equations are required. This is achieved by following either of the two approaches, viz., (1) enthalpy balance or (2) entropy balance.

2.1 Enthalpy Balance

The enthalpy of reactants before combustion is equal to the summation of enthalpy of individual species present at equilibrium. Mathematically, this can be expressed as

$$\sum_{j=1}^{\mathrm{NS}} n_j \widehat{H}_j - H_{\mathrm{reactant}} = 0 \tag{10}$$

where $\widehat{H}_j$ is the molar enthalpy of jth species at temperature "T" and H_{reactant} is the enthalpy of oxidizer–fuel mixture before combustion.

2.2 Entropy Balance

The entropy of reactants is equal to the summation of entropy of individual species present at equilibrium. Mathematically, this condition is expressed as

$$\sum_{j=1}^{\mathrm{NS}} n_j \hat{S}_j - S_{\mathrm{reactant}} = 0 \tag{11}$$

where $\hat{S}_j$ is the molar entropy of jth species at temperature "T" and S_{reactant} is the entropy of oxidizer–fuel mixture before combustion.

$\hat{S}_j$ is evaluated as given in Ref. [5],

$$\hat{S}_j = \left(\hat{S}_j^0 - R\ln\left(x_j\right) - R\ln\left(\frac{p}{p_0}\right)\right) \tag{12}$$

where $\hat{S}_j^0$ is the standard molar entropy of jth species.

3 Methodology

The combustion equilibrium in liquid rocket engines is usually modeled by specifying the chamber/stagnation pressure (p_0) and enthalpy of reactants ($H_{\text{react.}}$) undergoing combustion in the thrust chamber. The fuel–oxidizer mixture is assumed to attain chemical equilibrium at constant pressure and under adiabatic conditions. The equilibrium temperature (T_0), compositions, entropy (S_0), etc., evaluated in the thrust chamber are termed as stagnation properties.

In the nozzle, combustion is modeled by assuming adiabatic and isentropic expansion of the products formed in thrust chamber. The equilibrium problem in the nozzle is solved by specifying equilibrium pressure "p" ($0 < p < p_0$) and entropy of mixture "S" ($S = S_0$). The equilibrium temperature (T), compositions, etc., obtained as solution, are labeled as static properties.

The speed of equilibrium mixture in the nozzle is then evaluated by energy balance as the expansion process is assumed to be adiabatic. This in turn is used to compute Mach number.

The algorithm flowchart is illustrated in Fig. 1. Each sequence of operation is separately explained as follows:

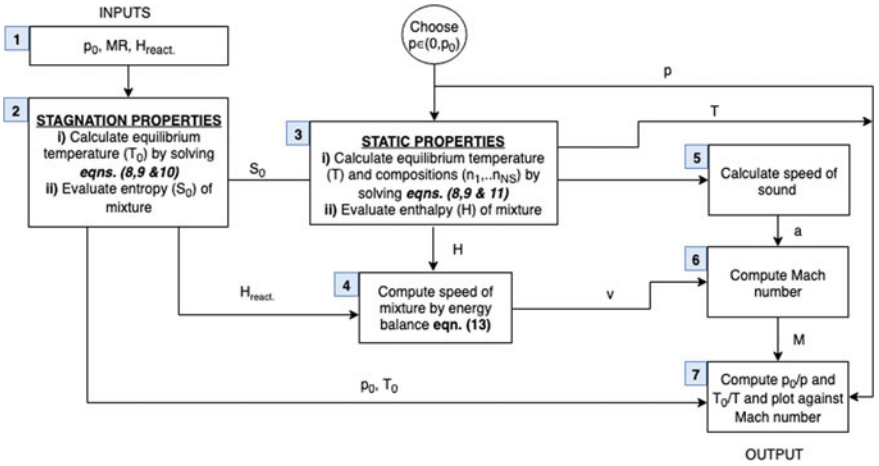

Fig. 1 Algorithm for determination of stagnation and static property correlations for equilibrium flows

3.1 Input Parameters

The input parameters such as chamber pressure, i.e., stagnation pressure (p_0), mixture ratio (MR), and enthalpy of reactants ($H_{\text{react.}}$), are specified by the user and fed into the next subroutine.

3.2 Evaluation of Stagnation Properties

This subroutine solves the equilibrium problem based on the stagnation conditions. Equations (8), (9), and (10) are solved to obtain the Lagrange multipliers ($\lambda_1, \lambda_2, \ldots, \lambda_E$), equilibrium temperature (T), and the total number of moles at equilibrium $\left(N_g\right)$. The equilibrium composition ($x_1, x_2, \ldots, x_{\text{NS}}$) is determined using Eq. (7). The entropy of the combustion products (S_0) is evaluated using Eq. (11) and its value is passed into next step.

3.3 Evaluation of Static Properties

Equations (8), (9), and (11) are solved for each value of pressure, and the corresponding equilibrium compositions are obtained from Eq. (7). The entropy remains fixed at S_0 throughout the run. The pressure at this step can be varied in the interval $(0, p_0)$ and corresponding to each value of pressure, a unique equilibrium solution is obtained. The equilibrium results for the chosen pressure value are input to next subroutines (see Fig. 1).

3.4 Calculation of Speed of Mixture

The enthalpies of the equilibrium mixture obtained in first and third steps (see Fig. 1) are used to compute the speed of equilibrium mixture. Noting that H_0 (also, $H_0 = H_{\text{react.}}$) denotes the stagnation enthalpy at chamber pressure (p_0), the enthalpy (H) of the equilibrium mixture at pressure "p" (where $p < p_0$) would be lesser than the stagnation enthalpy (H_0) in accordance with the principle of conservation of energy. The speed "v" of the equilibrium mixture is then expressed as

$$v = \sqrt{2 \times 1000 \times \left(\frac{H_0}{\text{MW}_0.N_{g,0}} - \frac{H}{\text{MW}.N_g} \right)} \tag{13}$$

where "MW" is the molecular weight (in g/mol) of equilibrium mixture, the subscript "0" denotes the stagnation condition and "1000" is the multiplication factor required for consistency of units. The speed is input to the next subroutine for computing the Mach number.

3.5 Calculation of Speed of Sound

The method of evaluation of speed of sound, "a", in a chemically reacting system at equilibrium is detailed in Ref. [5].

3.6 Computation of Mach Number

The Mach number ($M = v/a$) is calculated and stored for each value of pressure.

3.7 Computation of Stagnation to Static Properties' Ratios

The ratios of stagnation to static properties (i.e., p_0/p and T_0/T) are computed for a particular value of pressure. The pressure "p" is varied in the interval $(0,\ p_0)$ and the steps 3–7 are repeated. As a result, a mapping between pressure "p" and parameters $\left[p_0/\mathrm{p}\ ,\ T_0/T,\ M\right]$ is obtained.

4 Results and Discussion

The ratios of stagnation to static properties along with Mach numbers are computed at different chamber pressures and mixture ratios for LOX/LH2 and MMH/N_2O_4 fuel–oxidizer combinations. The results are presented separately for each case.

4.1 LOX/LH2

The LOX/LH2 combustion equilibrium is modeled with eight species, namely, H, H_2, H_2O, H_2O_2, HO_2, O, O_2, and OH. The ratio of stagnation to static properties versus Mach number is plotted in Fig. 2, such that the chamber (stagnation) pressure remains fixed at 10 MPa and mixture ratio (MR) takes discrete values of 2, 4, 6, 8, and 10.

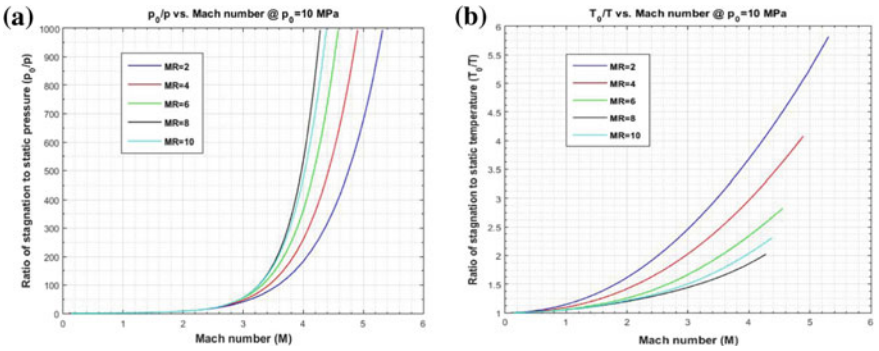

Fig. 2 Ratio of stagnation to static **a** pressure; **b** temperature versus Mach number at fixed chamber (stagnation) pressure of 10 MPa and varying mixture ratio for LOX/LH2 fuel–oxidizer combination

It is observed that both the stagnation to static ratios for pressure and temperature increase monotonically with Mach number—the same holds true for thermally and calorically perfect gases (where $T_0/T \propto M^2$ and $p_0/p \propto M^{\left(\frac{2\gamma}{\gamma-1}\right)}$). Also, the effect of varying mixture ratio on the stagnation to static ratios is clearly evident from the figures. In Fig. 2b, as mixture ratio increases, the T_0/T curve shifts down until the mixture ratio gets equal to 8, at which it approaches minimum (shown in black) and moves up thereafter. Since the value of stoichiometric mixture ratio for LOX/LH2 fuel combination is also 8 and it is known that equilibrium temperature attains maximum at stoichiometric mixture ratio, the ratio T_0/T attains minimum because of the denominator "T" attaining maximum.

The effect of varying chamber pressure at fixed mixture ratio is illustrated in Fig. 3. The mixture ratio is kept at 5, and chamber pressure varies from 1 to 10 MPa. The ratio T_0/T increases with increase in chamber (stagnation) pressure because with increase in chamber pressure, equilibrium temperature also increases but the extent by which T_0 increases outweighs the increase in T.

4.2 MMH/N_2O_4

The MMH/N_2O_4 combustion equilibrium is modeled with 11 species, namely, CO_2, N_2, H_2O, NO, O_2, CO, OH, H_2, O, H, and N. The ratios of stagnation to static pressure and temperature vs. Mach number are plotted in Figs. 4 and 5, respectively. The chamber pressure remains fixed at 1 MPa, and mixture ratio takes discrete values of 1, 2, 4, and 8.

The trends observed in Figs. 4 and 5 are similar to that for LOX/LH2 case. The effect of varying chamber pressure at a fixed mixture ratio is shown in Fig. 6. The mixture ratio is chosen as 2, and chamber pressure varies from 1 to 10 MPa. Again, similar trend as in LOX/LH2 case is being observed.

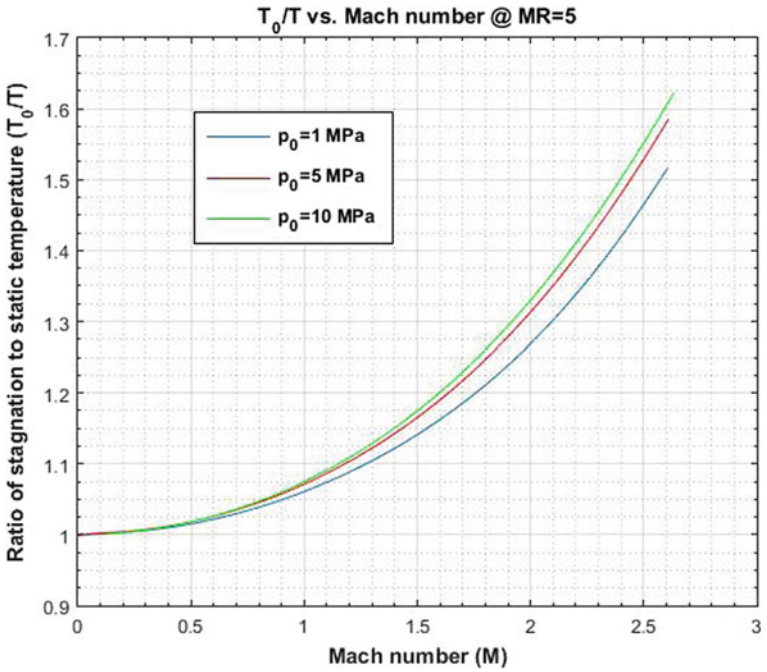

Fig. 3 Ratio of stagnation to static temperature versus Mach number at fixed mixture ratio (MR = 5) and varying chamber (stagnation) pressure for LOX/LH2 fuel–oxidizer combination

5 Conclusions

A method for determining stagnation and static property correlations for equilibrium flows is developed. Results are presented for combustion equilibrium of two oxidizer–fuel combinations, viz., LOX/LH2 and MMH/N_2O_4. The effect of variation in chamber pressure and mixture ratio upon stagnation to static property ratio is also studied. Unlike single non-dissociating calorically perfect gases where T_0/T and p_0/p depend on Mach number and specific heats ratio, in equilibrium flows, they depend on chamber pressure (stagnation conditions), mixture ratio, and Mach number. The intrinsic nature of equilibrium flows involves variation of specific heats and compositions with respect to temperature which in the present formulation are accounted by adjusting both chamber pressure and mixture ratio.

There are two limitations to the current study: first, the effect of number of species present at equilibrium upon the ratio of stagnation to static properties has not been studied; second, while formulating the methodology, the expansion process of equilibrium flow is assumed to be adiabatic and isentropic leading to an extra assumption of "isentropic flow" in the current definition of stagnation to static temperature, whereas the usual convention of defining stagnation temperature only assumes an adiabatic flow.

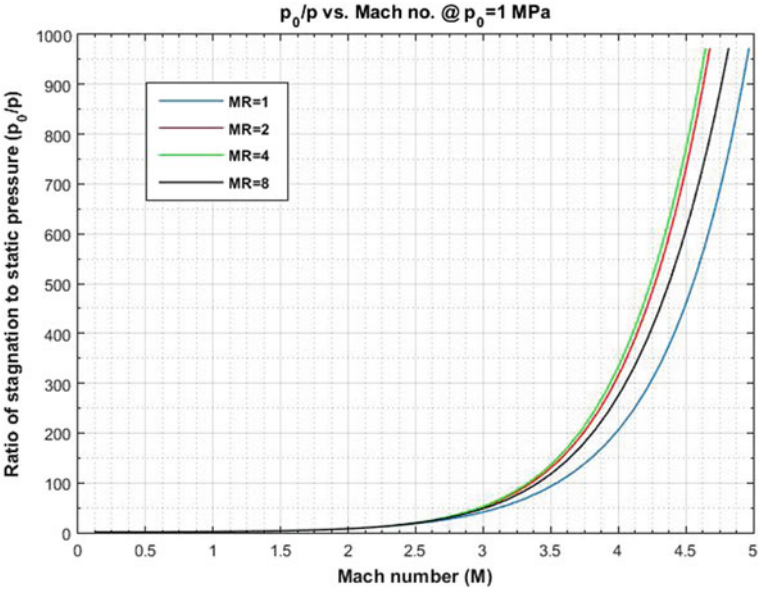

Fig. 4 Ratio of stagnation to static pressure versus Mach number at fixed chamber (stagnation) pressure of 1 MPa and varying mixture ratio for MMH/N_2O_4 fuel–oxidizer combination

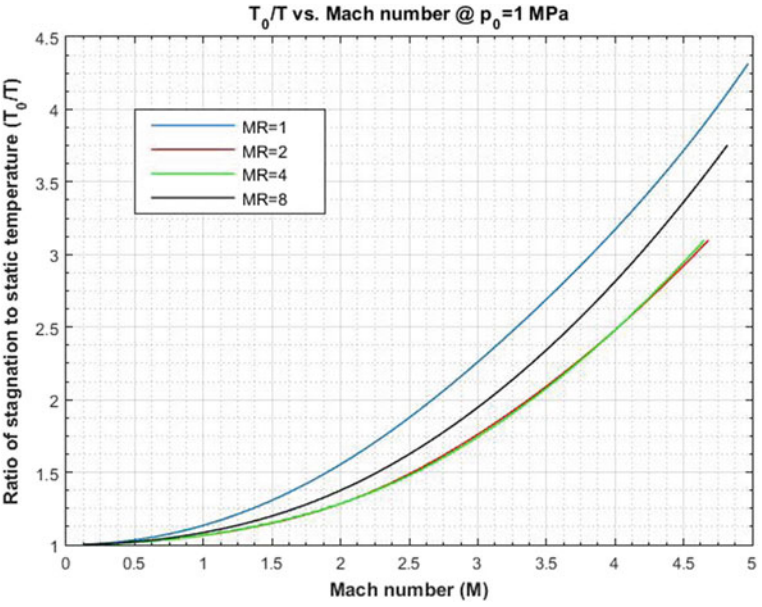

Fig. 5 Ratio of stagnation to static temperature versus Mach number at a fixed chamber (stagnation) pressure of 1 MPa and varying mixture ratio for MMH/N_2O_4 fuel–oxidizer combination

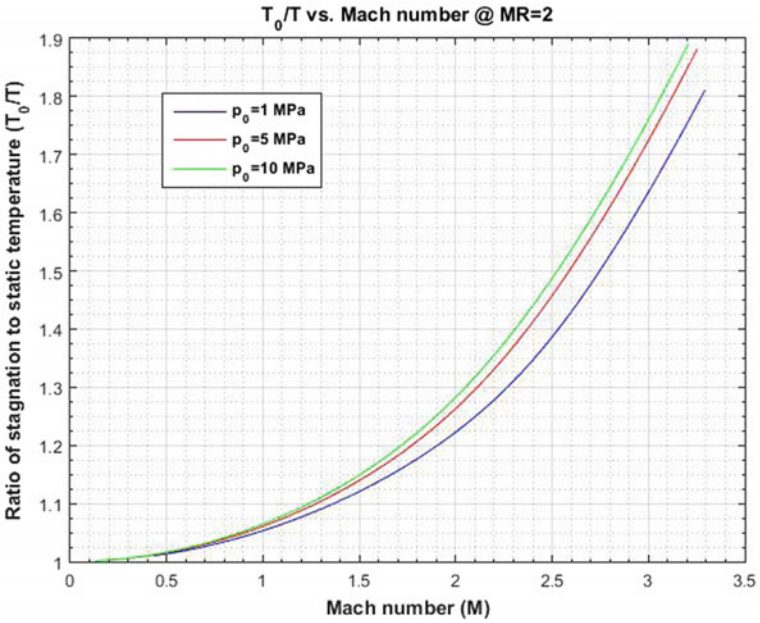

Fig. 6 Ratio of stagnation to static temperature versus Mach number at fixed mixture ratio (MR = 2) and varying chamber (stagnation) pressure for MMH/N_2O_4 fuel–oxidizer combination

Appendix: Worked Out Example

The stagnation and static properties for LOX/LH2 equilibrium mixture consisting of eight species, viz., H, H_2, H_2O, H_2O_2, HO_2, O, O_2, and OH are evaluated by following the steps aforementioned in Sect. 3. The detailed step-by-step procedure is given below:

Step-1: Input parameters

$p_0 = 10$ bar; MR $= 2$; $H_{\text{react.}} = -10{,}647$ J.

Note that number of species, NS $= 8$ and number of elements in the mixture, $E = 2$; Molecular weight of H_2 $\left(\text{MW}_{\text{H}_2}\right) = 2$ g/mol; Molecular weight of O_2 $\left(\text{MW}_{\text{O}_2}\right) = 32$ g/mol

Step-2: Evaluation of stagnation properties

Equation (8) results in

$$e^{\frac{-\widehat{G}^0_{\text{H}+\lambda_{\text{H}}}}{RT_0}} + e^{\frac{-\widehat{G}^0_{\text{H}_2}+2\lambda_{\text{H}}}{RT_0}} + e^{\frac{-\widehat{G}^0_{\text{H}_2\text{O}}+2\lambda_{\text{H}}+\lambda_{\text{O}}}{RT_0}} + e^{\frac{-\widehat{G}^0_{\text{H}_2\text{O}_2}+2\lambda_{\text{H}}+2\lambda_{\text{O}}}{RT_0}} + e^{\frac{-\widehat{G}^0_{\text{HO}_2}+\lambda_{\text{H}}+2\lambda_{\text{O}}}{RT_0}} + e^{\frac{-\widehat{G}^0_{\text{O}}+\lambda_{\text{O}}}{RT_0}} + e^{\frac{-\widehat{G}^0_{\text{O}_2}+2\lambda_{\text{O}}}{RT_0}} + e^{\frac{-\widehat{G}^0_{\text{OH}}+\lambda_{\text{H}}+\lambda_{\text{O}}}{RT_0}} - p_0 = 0 \tag{14}$$

Equation (9) results in

$$e^{\frac{-\widehat{G}^0_{\mathrm{H}+\lambda_\mathrm{H}}}{RT_0}} + 2e^{\frac{-\widehat{G}^0_{\mathrm{H}_2}+2\lambda_\mathrm{H}}{RT_0}} + 2e^{\frac{-\widehat{G}^0_{\mathrm{H}_2\mathrm{O}}+2\lambda_\mathrm{H}+\lambda_\mathrm{O}}{RT_0}} + 2e^{\frac{-\widehat{G}^0_{\mathrm{H}_2\mathrm{O}_2}+2\lambda_\mathrm{H}+2\lambda_\mathrm{O}}{RT_0}} + e^{\frac{-\widehat{G}^0_{\mathrm{HO}_2}+\lambda_\mathrm{H}+2\lambda_\mathrm{O}}{RT_0}} + e^{\frac{-\widehat{G}^0_{\mathrm{OH}+\lambda_\mathrm{H}+\lambda_\mathrm{O}}}{RT_0}} - 2\frac{p_0}{N_{g,0}} = 0 \tag{15}$$

and

$$e^{\frac{-\widehat{G}^0_{\mathrm{H}_2\mathrm{O}+2\lambda_\mathrm{H}+\lambda_\mathrm{O}}}{RT_0}} + 2e^{\frac{-\widehat{G}^0_{\mathrm{H}_2\mathrm{O}_2}+2\lambda_\mathrm{H}+2\lambda_\mathrm{O}}{RT_0}} + 2e^{\frac{-\widehat{G}^0_{\mathrm{HO}_2}+\lambda_\mathrm{H}+2\lambda_\mathrm{O}}{RT_0}} + e^{\frac{-\widehat{G}^0_{\mathrm{O}+\lambda_\mathrm{O}}}{RT_0}} + 2e^{\frac{-\widehat{G}^0_{\mathrm{O}_2}+2\lambda_\mathrm{O}}{RT_0}} + e^{\frac{-\widehat{G}^0_{\mathrm{OH}+\lambda_\mathrm{H}+\lambda_\mathrm{O}}}{RT_0}} - 2\frac{p_0}{N_{g,0}}\mathrm{MR}\frac{\mathrm{MW}_{\mathrm{H}_2}}{\mathrm{MW}_{\mathrm{O}_2}} = 0 \tag{16}$$

Equation (10) results in

$$\widehat{H}_\mathrm{H} e^{\frac{-\widehat{G}^0_{\mathrm{H}+\lambda_\mathrm{H}}}{RT_0}} + \widehat{H}_{\mathrm{H}_2} e^{\frac{-\widehat{G}^0_{\mathrm{H}_2}+2\lambda_\mathrm{H}}{RT_0}} + \widehat{H}_{\mathrm{H}_2\mathrm{O}} e^{\frac{-\widehat{G}^0_{\mathrm{H}_2\mathrm{O}}+2\lambda_\mathrm{H}+\lambda_\mathrm{O}}{RT_0}} + \widehat{H}_{\mathrm{H}_2\mathrm{O}_2} e^{\frac{-\widehat{G}^0_{\mathrm{H}_2\mathrm{O}_2}+2\lambda_\mathrm{H}+2\lambda_\mathrm{O}}{RT_0}} + \widehat{H}_{\mathrm{HO}_2} e^{\frac{-\widehat{G}^0_{\mathrm{HO}_2}+\lambda_\mathrm{H}+2\lambda_\mathrm{O}}{RT_0}} + \widehat{H}_\mathrm{O} e^{\frac{-\widehat{G}^0_{\mathrm{O}+\lambda_\mathrm{O}}}{RT_0}} + \widehat{H}_{\mathrm{O}_2} e^{\frac{-\widehat{G}^0_{\mathrm{O}_2}+2\lambda_\mathrm{O}}{RT_0}} + \widehat{H}_\mathrm{OH} e^{\frac{-\widehat{G}^0_{\mathrm{OH}+\lambda_\mathrm{H}+\lambda_\mathrm{O}}}{RT_0}} - \frac{p_0}{N_{g,0}} H_{\text{react.}} = 0 \tag{17}$$

Equations (14)–(17) are simultaneous nonlinear equations which can be solved iteratively by Newton's method as detailed in Ref. [5]. For each iteration, the standard molar Gibbs energy and molar enthalpy of respective species are evaluated at the value of temperature as existing in the particular iteration step by utilizing NASA Glenn thermodynamic database [10].

The solution of Eqs. (14)–(17) yields $T_0 = 1814.7$ K, $\lambda_H = -1.29 \times 10^5$ J/mol, $\lambda_O = -3.77 \times 10^5$ J/mol, and $N_{g,0} = 1.0018$ mol. These values are substituted into Eq. (7) to get the mole fraction of each species, viz., $x_\mathrm{H} = 0.0001$, $x_{\mathrm{H}_2} = 0.7451$, $x_{\mathrm{H}_2\mathrm{O}} = 0.2549$, $x_{\mathrm{H}_2\mathrm{O}_2} = 0$, $x_{\mathrm{HO}_2} = 0$, $x_\mathrm{O} = 0$, $x_{\mathrm{O}_2} = 0$, and $x_\mathrm{OH} = 0$.

The entropy of mixture (S_0) is calculated by using Eq. (11) where S_{reactant} is replaced with S_0.

$$S_0 = n_\mathrm{H}\hat{S}_\mathrm{H} + n_{\mathrm{H}_2}\hat{S}_{\mathrm{H}_2} + n_{\mathrm{H}_2\mathrm{O}}\hat{S}_{\mathrm{H}_2\mathrm{O}} + n_{\mathrm{H}_2\mathrm{O}_2}\hat{S}_{\mathrm{H}_2\mathrm{O}_2} + n_{\mathrm{HO}_2}\hat{S}_{\mathrm{HO}_2} + n_\mathrm{O}\hat{S}_\mathrm{O} + n_{\mathrm{O}_2}\hat{S}_{\mathrm{O}_2} + n_\mathrm{OH}\hat{S}_\mathrm{OH}$$

$\hat{S}_\mathrm{H}$, $\hat{S}_{\mathrm{H}_2}$, $\hat{S}_{\mathrm{H}_2\mathrm{O}}$, $\hat{S}_{\mathrm{H}_2\mathrm{O}_2}$, $\hat{S}_{\mathrm{HO}_2}$, $\hat{S}_\mathrm{O}$, $\hat{S}_{\mathrm{O}_2}$, and $\hat{S}_\mathrm{OH}$ are evaluated from Eq. (12) by extracting values of $\hat{S}^0_\mathrm{H}$, $\hat{S}^0_{\mathrm{H}_2}$, $\hat{S}^0_{\mathrm{H}_2\mathrm{O}}$, $\hat{S}^0_{\mathrm{H}_2\mathrm{O}_2}$, $\hat{S}^0_{\mathrm{HO}_2}$, $\hat{S}^0_\mathrm{O}$, $\hat{S}^0_{\mathrm{O}_2}$, and $\hat{S}^0_\mathrm{OH}$ at temperature "T_0" from thermodynamic database [10].

S_0 is then used in step-3.

Step-3: Evaluation of static properties

A particular value of pressure "p" such that $0 < p < p_0$ is chosen and the following equations are solved in a similar manner as in step-2.

Equation (8) results in

$$e^{\frac{-\widehat{G}^0_{H+\lambda_H}}{RT}} + e^{\frac{-\widehat{G}^0_{H_2+2\lambda_H}}{RT}} + e^{\frac{-\widehat{G}^0_{H_2O+2\lambda_H+\lambda_O}}{RT}} + e^{\frac{-\widehat{G}^0_{H_2O_2+2\lambda_H+2\lambda_O}}{RT}} + e^{\frac{-\widehat{G}^0_{HO_2+\lambda_H+2\lambda_O}}{RT}} + e^{\frac{-\widehat{G}^0_{O+\lambda_O}}{RT}} + e^{\frac{-\widehat{G}^0_{O_2+2\lambda_O}}{RT}} + e^{\frac{-\widehat{G}^0_{OH+\lambda_H+\lambda_O}}{RT}} - p = 0 \tag{18}$$

Equation (9) results in

$$e^{\frac{-\widehat{G}^0_{H+\lambda_H}}{RT}} + 2e^{\frac{-\widehat{G}^0_{H_2+2\lambda_H}}{RT}} + 2e^{\frac{-\widehat{G}^0_{H_2O+2\lambda_H+\lambda_O}}{RT}} + 2e^{\frac{-\widehat{G}^0_{H_2O_2+2\lambda_H+2\lambda_O}}{RT}} + e^{\frac{-\widehat{G}^0_{HO_2+\lambda_H+2\lambda_O}}{RT}} + e^{\frac{-\widehat{G}^0_{OH+\lambda_H+\lambda_O}}{RT}} - 2\frac{p}{N_g} = 0 \tag{19}$$

and

$$e^{\frac{-\widehat{G}^0_{H_2O+2\lambda_H+\lambda_O}}{RT}} + 2e^{\frac{-\widehat{G}^0_{H_2O_2+2\lambda_H+2\lambda_O}}{RT}} + 2e^{\frac{-\widehat{G}^0_{HO_2+\lambda_H+2\lambda_O}}{RT}} + e^{\frac{-\widehat{G}^0_{O+\lambda_O}}{RT}} + 2e^{\frac{-\widehat{G}^0_{O_2+2\lambda_O}}{RT}} + e^{\frac{-\widehat{G}^0_{OH+\lambda_H+\lambda_O}}{RT}} - 2\frac{p}{N_g}\mathrm{MR}\frac{\mathrm{MW}_{H_2}}{\mathrm{MW}_{O_2}} = 0 \tag{20}$$

Equation (11) results in

$$e^{\frac{-\widehat{G}^0_{H+\lambda_H}}{RT}}\left(\hat{S}^0_H - \frac{-\widehat{G}^0_H + \lambda_H}{T}\right) + e^{\frac{-\widehat{G}^0_{H_2+2\lambda_H}}{RT}}\left(\hat{S}^0_{H_2} - \frac{-\widehat{G}^0_{H_2} + 2\lambda_H}{T}\right) + e^{\frac{-\widehat{G}^0_{H_2O+2\lambda_H+\lambda_O}}{RT}}(\hat{S}^0_{H_2O}\frac{-\widehat{G}^0_{H_2O} + 2\lambda_H + \lambda_O}{T}) + e^{\frac{-\widehat{G}^0_{H_2O_2+2\lambda_H+2\lambda_O}}{RT}} (\hat{S}^0_{H_2O_2} - \frac{-\widehat{G}^0_{H_2O_2} + 2\lambda_H + 2\lambda_O}{T}) + e^{\frac{-\widehat{G}^0_{HO_2+\lambda_H+2\lambda_O}}{RT}}(\hat{S}^0_{HO_2} - \frac{-\widehat{G}^0_{HO_2} + \lambda_H + 2\lambda_O}{T}) + e^{\frac{-\widehat{G}^0_{O+\lambda_O}}{RT}}(\hat{S}^0_O - \frac{-\widehat{G}^0_O + \lambda_O}{T}) + e^{\frac{-\widehat{G}^0_{O_2+2\lambda_O}}{RT}}\left(\hat{S}^0_{O_2} - \frac{-\widehat{G}^0_{O_2} + 2\lambda_O}{T}\right) + e^{\frac{-\widehat{G}^0_{OH+\lambda_H+\lambda_O}}{RT}}\cdot\left(\hat{S}^0_{OH} - \frac{-\widehat{G}^0_{OH} + \lambda_H + \lambda_O}{T}\right) - \frac{p}{N_g}S_0 = 0 \tag{21}$$

For $p = 0.1$ bar, the solution of Eqs. (18)–(21) yields $T = 592.8$ K, $\lambda_H = -4.68 \times 10^4$ J/mol, $\lambda_O = -2.82 \times 10^5$ J/mol, and $N_g = 1$ mol.

The enthalpy of mixture (H) is calculated as

$$H = n_{\mathrm{H}}\widehat{H}_{\mathrm{H}} + n_{\mathrm{H_2}}\widehat{H}_{\mathrm{H_2}} + n_{\mathrm{H_2O}}\widehat{H}_{\mathrm{H_2O}} + n_{\mathrm{H_2O_2}}\widehat{H}_{\mathrm{H_2O_2}} + n_{\mathrm{HO_2}}\widehat{H}_{\mathrm{HO_2}} + n_{\mathrm{O}}\widehat{H}_{\mathrm{O}} + n_{\mathrm{O_2}}\widehat{H}_{\mathrm{O_2}} + n_{\mathrm{OH}}\widehat{H}_{\mathrm{OH}}$$

where $\widehat{H}_{\mathrm{H}}$, $\widehat{H}_{\mathrm{H_2}}$, $\widehat{H}_{\mathrm{H_2O}}$, $\widehat{H}_{\mathrm{H_2O_2}}$, $\widehat{H}_{\mathrm{HO_2}}$, $\widehat{H}_{\mathrm{O}}$, $\widehat{H}_{\mathrm{O_2}}$, and $\widehat{H}_{\mathrm{OH}}$ are evaluated at temperature "T" from thermodynamic database [10].

"H" is then used in Step-4.

Step-4 Calculation of speed of mixture

Values of H_0 ($H_0 = H_{\mathrm{react.}}$) and H are extracted from previous steps, and Eq. (13) is used to compute the speed of equilibrium mixture which is equal to 3704 m/s.

Step-5 Calculation of speed of sound

The results of Step-3 are utilized for obtaining speed of sound using the method detailed in Ref. [5]. The value of speed of sound (a) is calculated to be 1056.3 m/s.

Step-6 Computation of Mach number

Mach number is evaluated using $M = \frac{v}{a}$ and found to be $M = 3.5064$.

Step-7 Computation of stagnation to static property ratio

From step-2, stagnation properties are $p_0 = 10$ bar and $T_0 = 1814.7$ K.

From step-3, static properties are $p = 0.1$ bar and $T = 592.8$ K.

$p_0/p = 100$ and $T_0/T = 3.0612$ are the desired stagnation to static pressure and temperature ratios, respectively, at Mach 3.5064.

References

1. Anderson JD (2003) Modern compressible flow: with historical perspective. McGraw-Hill Education, New York
2. Zebbiche T (2011) Effect of stagnation temperature on supersonic flow parameters with application for air in nozzles. Thermodynamics—interaction studies—solids, liquids and gases (InTech, Rijeka)
3. Gautam R, Seider WD (1979) Computation of phase and chemical equilibrium: part I. Local and constrained minima in Gibbs free energy. Am Inst Chem Eng 25(6):991–999
4. Gordon S, McBride BJ (1994) Computer program of complex chemical equilibrium compositions and applications. NASA RP 1311, NASA Lewis Research Centre
5. Ponomarenko A (2014) RPA: tool for liquid propellant rocket engine analysis C++ implementation. Space Propulsion-2014, Cologne
6. Powell NH, Samar SF (1959) The use of element potential in analysis of chemical equilibrium. General Electric Company, New York

7. Reynolds WC (1986) The element potential method for chemical equilibrium analysis: implementation in the interactive program of STANJAN Version 3. Stanford University
8. Wang J et al (2009) Chemical equilibrium calculation of complex system based on element potential and its application. World congress on computer science and information engineering
9. Zucrow MJ, Hoffman JD (1977) Gas dynamics, vol 2. Wiley, New York
10. NASA Glenn Thermodynamic Database. https://www.grc.nasa.gov/WWW/CEAWeb/ceaThermoBuild.htm

CFD Simulation of Hypersonic Shock Tunnel Nozzle

Jigarkumar Sura

Abstract The design of a hypersonic nozzle for shock tunnel is of much importance as it plays a vital role in generating the required flow field. The computational simulation can help to understand the Mach number distribution inside the test section. This can help to design the mounting assembly for the model and to limit the dimension of the model. The flow field for an axisymmetric test section has been analysed using commercial software. The results revealed the variation of Mach number inside the test section and exit plane of the nozzle.

Keywords Shock tunnel · Nozzle flow · Hypersonics

1 Introduction

The hypersonic vehicles are considered as future means of fast transportation. The phenomena such as thick boundary layer, thin shock layer, viscous interaction, shock wave–boundary layer interaction and shock–shock interaction are present in hypersonic flow and cannot be ignored [1]. The hypersonic wind tunnel and hypersonic shock tunnel are major experimental facilities to study flow field inside and around the hypersonic vehicles. The hypersonic shock tunnel can simulate required surroundings for the vehicle with test duration of the order of millisecond. The high-speed flow is generated through reflection of the incident shock wave in the driven section of shock tube by sudden rupture of a diaphragm separating the driver and the driven section [2]. The axial Mach number distribution for ideal conditions can be estimated with one-dimensional isentropic flow equations [3]. But actual velocity direction is not parallel to axis at all radial locations due to three-dimensional effects [4]. Because of this, it is required to identify the useful region of the test section where velocity remains parallel to the axial direction.

J. Sura (✉)
Department of Aerospace Engineering, Amity School of Engineering & Technology, Amity University Mumbai, Panvel, Maharashtra, India
e-mail: jigar.sura@gmail.com

B. N. Singh et al. (eds.), *Recent Advances in Theoretical, Applied, Computational and Experimental Mechanics*, Lecture Notes in Mechanical Engineering,
https://doi.org/10.1007/978-981-15-1189-9_30

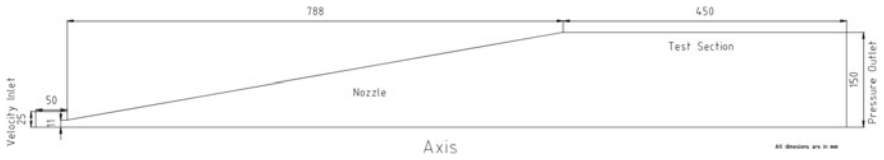

Fig. 1 Schematic of a hypersonic nozzle

Here, in this paper, an attempt has been made to identify the useful core region of a hypersonic shock tunnel test section using commercial simulation software Ansys. The inviscid simulation has been carried out. The diameter and length of the inlet (before throat) are 50 mm and 50 mm, respectively. The throat diameter is 22 mm, while exit diameter is 300 mm. The nozzle semi-cone angle is 10° and is designed for Mach 8 (Fig. 1). The stagnation pressure is 561 kPa, and stagnation temperature is 813 K [5].

2 Simulation Methodology

Computational fluid dynamics plays an important role to understand the internal and external flow field of the vehicle. Ansys is very useful commercial simulation software for this purpose. With the application of appropriate grid size and boundary conditions, one can obtain results which can be used for design and development of the hypersonic vehicle. The 2D geometry was created with SI units. As the nozzle is a simple axisymmetric geometry, the structured grid could be easily generated using Ansys workbench grid generator. The grid independence test is required to be carried out before accepting the results of the simulation. In current work, the number of grid points was varied along axial and radial directions. When the results were independent of the grid points, further analysis was carried out. Figure 2 shows the Mach number variation along axial direction of the shock tunnel nozzle. It can be seen that there is no significant variation in Mach number for the current grid points. Similarly, the grid points were also varied in radial direction.

Appropriate boundary conditions were applied to the simulation. The velocity inlet (subsonic—1 m/s) and pressure outlet (0 Pa) were inlet and outlet boundary conditions, respectively. The surfaces of the nozzle and test section were classified as wall boundary condition. The analysis was carried out for steady state only.

The simulation results are required to be independent of the mesh/grid size to be acceptable for any analysis. Therefore, the grid independence tests were carried out. Different x (axial)- and y (radial)-direction cell sizes were chosen, and the results were superimposed. Figure 3 shows the grid independency test for axial direction grid size. The number of cells in each section was kept at 130, and the results were found to be independent of size. Similarly, 50 cells were able to provide acceptable grid-independent results for radial direction. Default discretization scheme was used for solution in which the flow equations are solved using the second-order scheme.

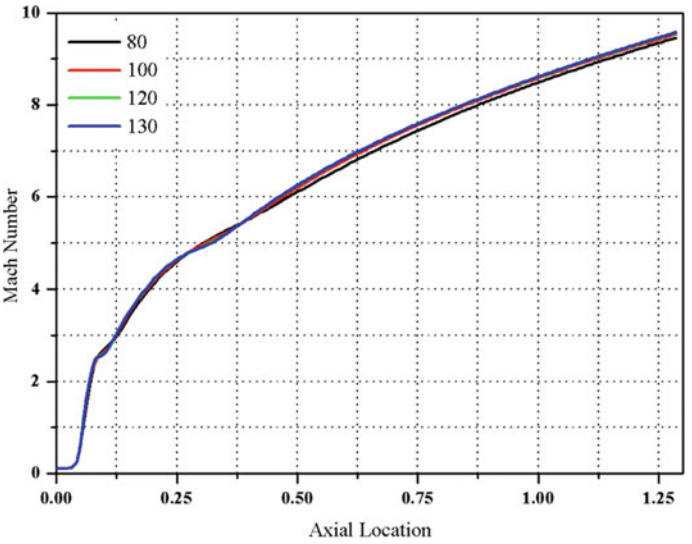

Fig. 2 Grid independency test for axial direction

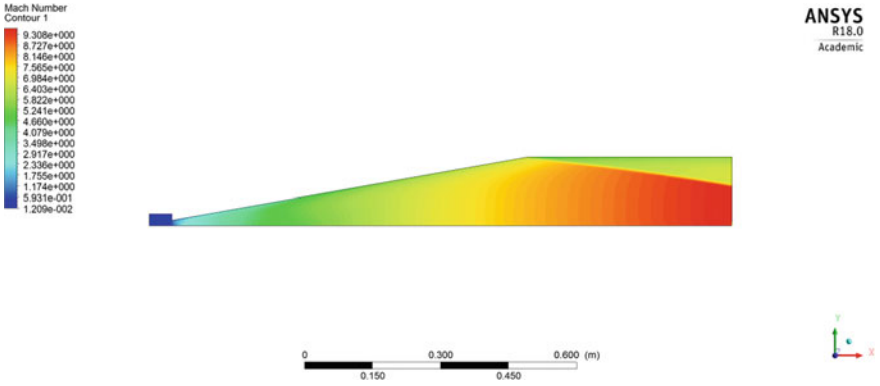

Fig. 3 Mach number contour plot

The convergence criteria for various parameters were set to 1E−6 and the solution converged to that limit. The implicit Advection Upstream Splitting Method (AUSM) was used for simulations, which was good for capturing shocks in fluid flow. After the simulation was completed, the mass flux imbalance was checked. It was found that there was no significant mass accumulation inside the computational domain. Hence, the converged solution could be used for further analysis.

3 Results and Discussion

The simulation results provided insight into the flow field of hypersonic shock tunnel nozzle. The inviscid flow field has been analysed using commercially available simulation software Ansys. The grid independency tests have been carried out.

The contour plot provides information about the variation of properties such as pressure, temperature and Mach number. Figure 3 shows the contour plot for Mach number. It can be seen that the flow field inside the test section is not uniform. There is a variation of Mach number in both axial and radial directions. The oblique shock wave beginning from exit of the nozzle extending into test section is also visible. This can be attributed to the flow turning into itself because of beginning of the constant diameter test section. The strength of this shock wave depends on the nozzle divergence angle. This shock wave defines the dimensions of the models that can be put inside the test section. If the shock wave hits any of the surfaces of the model, then the flow field downstream from the impingement location will be affected. Also, the shock boundary layer interaction will alter the flow field and the experimental data will be erroneous.

The results show the notable variation of Mach number in radial direction at the exit of the nozzle. For comparison, the plots for radial distribution of Mach number in test section at five equally spaced locations (0 mm, 112.5 mm, 225 mm, 337.5 mm and 450 mm from test section inlet) including test section entry and exit have been given in Fig. 4. The x-axis shows the Mach number, while y-axis shows the distance from centreline. It can be seen that at the entrance of the test section (first from the left in Fig. 4), the flow Mach number is 8 which is the design Mach number.

The Mach number reduces when one goes away from the axis of the nozzle. This is because of three-dimensional effects due to nozzle divergence angle. It can also be seen that the change in Mach number is gradual, and available core region is only up to 0.1 m from centreline above which the Mach number variation is significant.

The second plot from left in Fig. 4 also shows that there is sudden change in Mach number at 0.13 m radial location. And that change is visible in remaining figures (third, fourth and fifth from left) also but distance from axis is reducing. This is attributed to shock wave generated at the beginning of the test section. It can also be seen in Fig. 4 that the axial Mach number increases in flow direction inside the test section.

The test section of the hypersonic shock tunnel is kept at almost zero pressure. This helps to start the nozzle flow without any back pressure effect. Also, the volume of the dump tank is kept very large so that throughout the tunnel operation, the back pressure effect does not affect the nozzle performance. This leads to the underexpanded nozzle as the expansion is not complete till nozzle exit plane. Therefore, the flow further expands into the test section. This is the reason why the axial Mach number increases inside the test section. For a given area ratio, the Mach number at the exit of the nozzle is fixed. So, usually the experiments are carried out at design Mach number only. But looking at the underexpansion of the flow, it is thought that the change in mounting

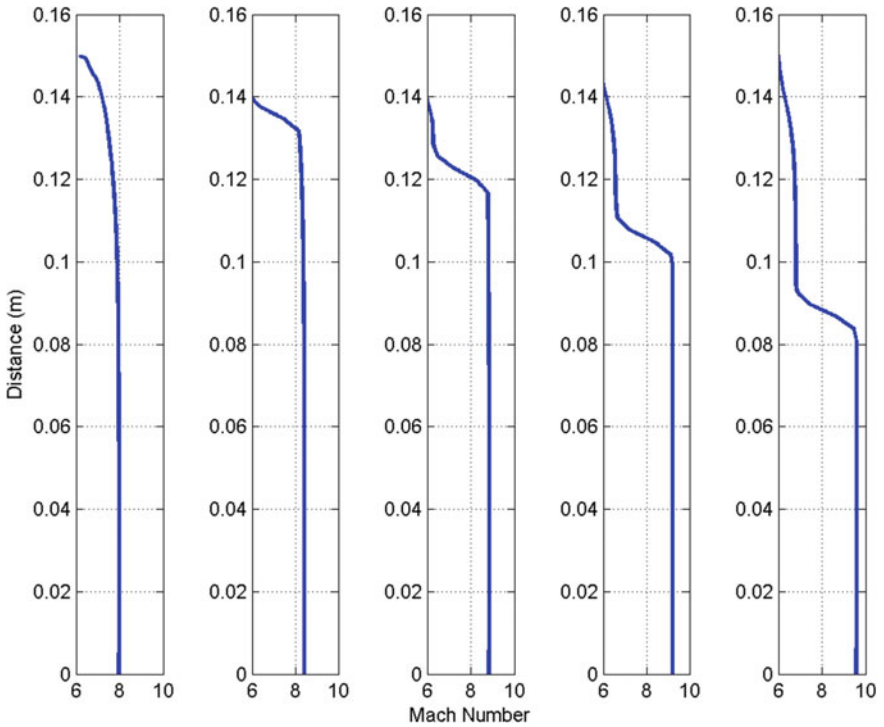

Fig. 4 Mach number variation in test section

location for the model can help to carry out experiments at different higher Mach numbers.

The oblique shock wave from the test section entrance plane limits the useful core available for experiments. Not only the model cross section should be sufficiently smaller than the core area (160 mm diameter in current case), but also the length of the model should not be in the downstream of the oblique shock. This limits the length of the model for experiments. Based on Mach number distribution, the available core region can be identified. This core region will have most uniform free streamflow.

4 Conclusion

The flow-through hypersonic nozzle of the simple shock tunnel has been analysed. The results from the simulation provided the information about the core area to mount model without any external disturbances. Also, the fixed Mach number nozzle can be used for higher Mach number with appropriate changes in model dimension.

References

1. Anderson JD (1989) Hypersonic and high temperature gas dynamics. McGraw-Hill, New York
2. Martin WA (1958) A review of shock tubes and shock tunnels. CONVAIR, San Diego
3. Rathakrishnan E (2012) Gas dynamics. PHI Limited
4. Crown JC, Heybey WH (1950) Supersonic nozzle design. Project NOL 159, April
5. Trivedi SD (2013) Development and validation of a force balance for a lifting model in an ultra short duration hypersonic test facility. Ph.D. thesis

A DNS Study of Bulk Flow Characteristics of a Transient Diabatic Plume that Simulates Cloud Flow

Samrat Rao, G. R. Vybhav, P. Prasanth, S. M. Deshpande and R. Narasimha

1 Introduction

Clouds are complex systems, and interaction among a wide range of scales makes the cloud parameterization problem "deadlocked" [1]. The Intergovernmental Panel on Climate Change (IPCC) has identified clouds as one of the most urgent and difficult problems needing attention, as the absence of a sufficiently successful model to capture the actual dynamics of the cloud leads to significant biases (depending on the model chosen) in climate predictions [2]. For the Indian monsoons, on which about a half of the country's agriculture is dependent, a significantly better parameterization of clouds could help in improving rainfall predictions [3].

The major problem in modeling a cloud lies in the lack of our understanding of how a cumulus cloud interacts with the surroundings. Earlier cloud fluid-dynamical models based on steady-state plumes, thermals, and bubbles [4, 5] turned out to be unsuccessful as the experiments did not incorporate an adequate model for describing the effects of latent heat release on condensation of water vapor into liquid water. Also, the transient nature of cumulus clouds has to be taken into account. Narasimha [6] and Diwan et al. [7] incorporated these two parameters and demonstrated that a transient diabatic plume (TDP) provides an appropriate fluid-dynamical model for cumulus cloud flow. Meanwhile, large-eddy simulations (LES) of cumulus

S. Rao (✉)
Department of Mechanical Engineering, IIT Jammu, Jammu, Jammu and Kashmir, India
e-mail: samrat.rao@gmail.com

G. R. Vybhav · S. M. Deshpande · R. Narasimha
Engineering Mechanics Unit, Jawaharlal Nehru Center for Advanced Scientific Research, Bangalore 560064, India

P. Prasanth
Michigan Technological University, Michigan, USA

B. N. Singh et al. (eds.), *Recent Advances in Theoretical, Applied, Computational and Experimental Mechanics*, Lecture Notes in Mechanical Engineering,
https://doi.org/10.1007/978-981-15-1189-9_31

convection [8] are gaining more attention in the recent past for their use in super-parameterization schemes. In contrast to LES, our approach to model the cloud flow as a TDP and solve it by employing a high-resolution direct numerical simulation (DNS) technique has an emphasis on improving the fundamental understanding of entrainment/detrainment and mixing mechanisms in free turbulent shear flows including clouds.

2 Governing Equation and Computational Details

The numerical technique involves the simulation of the TDP by solving the 3D Boussinesq approximations of the Navier–Stokes equations of mass, momentum, and energy balance [9]. The equations solved are

$$\text{Continuity} : \nabla \cdot u = 0 \tag{1}$$

$$\text{Momentum} : \frac{\partial u}{\partial t} + (u \cdot \nabla)u = \frac{-1}{\rho_0}\nabla P + \upsilon \nabla^2 u + \beta \Delta T \boldsymbol{g} \tag{2}$$

$$\text{Energy} : \frac{\partial (\Delta T)}{\partial t} + (u \cdot \nabla)\Delta T = \kappa \nabla^2 (\Delta T) + \frac{J(t)}{\rho_0 C_P} H(\boldsymbol{x}, t) \tag{3}$$

$$\text{Vorticity} : \frac{\partial \omega}{\partial t} + (u \cdot \nabla \omega) - (\omega \cdot \nabla)u - \upsilon \nabla^2 \omega = \beta \boldsymbol{g} \times \nabla T \tag{4}$$

where u is the velocity vector, $\Delta T = T(\boldsymbol{x}, t) - T_0$ is the temperature differential of the plume fluid to the ambient T_0, P is the pressure, ρ_0 is the ambient density, υ is the kinematic viscosity, κ is the thermal diffusivity, β is the coefficient of thermal expansion of the cloud fluid, g is the acceleration due to gravity ($\boldsymbol{g} = -\boldsymbol{g}\hat{z}$, $\hat{z}$ is the unit vector along the vertical axis), $J(t)$ is the heat added per unit volume per unit time, and $H(x, t)$ is the distribution function which determines the special region in which heat is released at time t. The density of the TDP fluid is $\rho(x, t) = \rho_0(1 - \beta \Delta T)$. ω is the vorticity vector. $\beta \boldsymbol{g} \times \nabla T$ is the baroclinic torque.

Except for a hot circular patch at the bottom wall at $z = 0$ (Fig. 1), the temperature boundary conditions are Neumann. Pressure boundary conditions are also Neumann at all walls. Velocity boundary conditions at the wall demand no-slip and impenetrability at the surface. The normal derivatives of all the variables are set to zero at the top. Equations 1–3 are non-dimensionalized using the bottom hot patch diameter d_0, velocity $w_0 = \sqrt{\boldsymbol{g}\beta d_0 \Delta T_0}$, and the temperature differential ΔT_0 at $z = 0$. Three nondimensional numbers relevant to the problem are

$$\text{Reynolds number, Re} = \frac{w_0 d_0}{\upsilon}$$

$$\text{Prandtl number, Pr} = \frac{\upsilon}{\kappa}$$

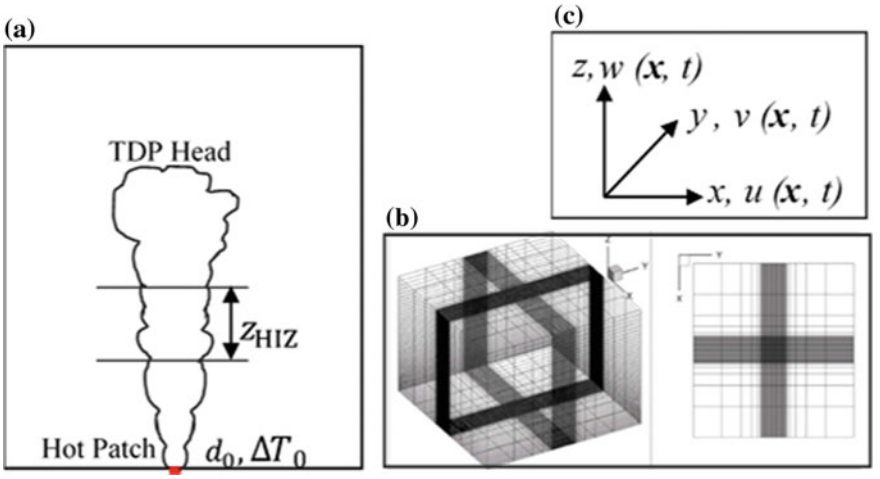

Fig. 1 **a** Flow schematic. **b** Nonuniform mesh grid. **c** Coordinate system convention

$$\text{Heat release number, G} = \frac{J}{\rho C_P} \frac{d_0}{w_0 \Delta T_0}$$

The third parameter G plays a key role in the flow development as discussed by Bhat and Narasimha [10]. The numerical technique employed is discussed by Prasanth [11]. A finite-volume technique with staggered grid arrangement has been used. In the first sub-step, the momentum equation is solved for the velocity components without taking the pressure term into account. This velocity field is non-divergent. In the subsequent sub-step, the pressure Poisson equation is obtained by taking the divergence of what ought to have been a non-divergent velocity field. The pressure so obtained (using the HYPRE library, [12]) is used to get the final non-divergent velocity field. This corrected velocity field is then used as the initial condition for the next time step. This two-step procedure is continued till the simulation is completed.

The 360 TF supercomputer (Ananta) at CSIR-4PI, Bangalore, has been used for the simulations. The total number of grids in the computational domain is $\approx$1.6 billion. The number of processors used is 3375, which required a total wall time of $\approx$16 days. The grid shown in Fig. 1b is a nonuniform Cartesian grid with higher spatial resolution in the region where the TDP evolves. The time span of the flow is 90 flow units where each flow unit (FU) is defined as d_0/w_0.

3 Results and Discussion

3.1 Transient Diabatic Plume (TDP) Flow Configuration

The flow schematic along with the coordinate system used in the simulation is shown in Fig. 1, and Table 1 gives the details of the simulation.

In a TDP, the off-source heat addition which mimics the latent heat release due to condensation of water vapor to liquid water in a cloud is simulated by dynamically matching the nondimensional heat release number G (defined in Sect. 2). For the present simulation, off-source heat is added over $10 \leq z \leq 15$ and we call this the heat injection zone (HIZ hereafter). The HIZ is equally divided into five subzones, and varying amounts of heat are injected into each subzone (see Fig. 2). The amount of heat injected into the HIZ may be specified by the heat release number G ($\boldsymbol{x}$, t), where G can be a function of space or time or both space and time (Fig. 2). In shallow cumulus clouds, G is ~0.1–0.5 [13], where in the present simulation G varies in the range of 0.04 to a maximum value of 0.35. The heating profile chosen to get a cloud with a tall tower and cauliflower head is shown in Fig. 2.

3.2 Bulk Parameters of the Flow

As this is for the first time that the results on a fully resolved DNS study on a TDP are being presented, it is not possible to compare it with any other study. Our objective here is to demonstrate the effect of off-source heat addition on bulk parameters like axial velocity (w), temperature (ΔT), equivalent diameter ($d||eq$), and mass flux

Table 1 Simulation details, where Pr is Prandtl number and Re is Reynolds number (see Sect. 2)

Simulation	Domain size (x, y, z)	Grid size	Time step	Pr	Re
TDP-1	(50, 50, 40)	(1007, 1007, 1577)	0.003 $t \leq 63$ FU	1	2000
			0.001 $t > 63$ FU		

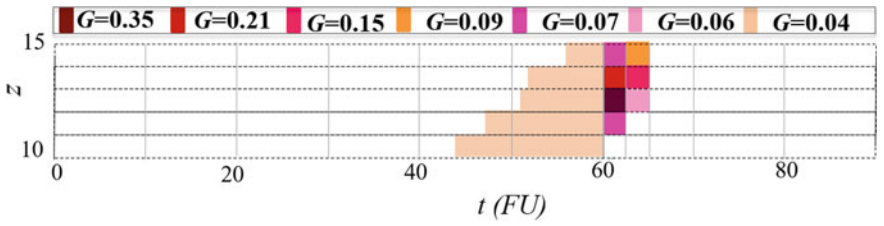

Fig. 2 History of the heating profile used in the present simulation. Time is nondimensionalized using w_0 and d_0. Heating starts at 43 FU and ends at 63 FU

(Q) (the latter two to be defined below). Ensemble averaging is required to obtain the average quantities in a transient flow. This demands that the simulations in the present study be repeated several times with different initial perturbations. However, results are available only from a single realization, but azimuthal averaging helps in obtaining approximate mean values of flow parameters.

3.3 *Evolution of TDP*

The characteristic feature of a turbulent shear flow is the stochastic nature of the vorticity field. Hence, the total vorticity modulus $|\omega|$, defined in Fig. 3, is an appropriate variable for visualizing the evolution of TDP, and for determining boundaries between turbulent flow and nonturbulent flow. The evolution of $|\omega|$ in the TDP through $t = 63$, 68, and 72 FU is shown in Fig. 3a–c. From the figures, it can be seen that the flow has an advancing cap or flattened thermal (cauliflower head) followed by a trailing plume (stem). The figures also show the flow width ceases to grow in any significant way with height, except in the plume head which is contrasting with a starting plume where the flow width increases with height [14]. Comparing Fig. 3a, c shows that even though maximum heat is injected between $t = 60$–63 FU, it takes at least a few FUs for the $|\omega|$ to feel the effect of off-source heat addition [7]. For analyzing the bulk parameters mentioned in Sect. 3.2, TDP flow at $t = 72$, which

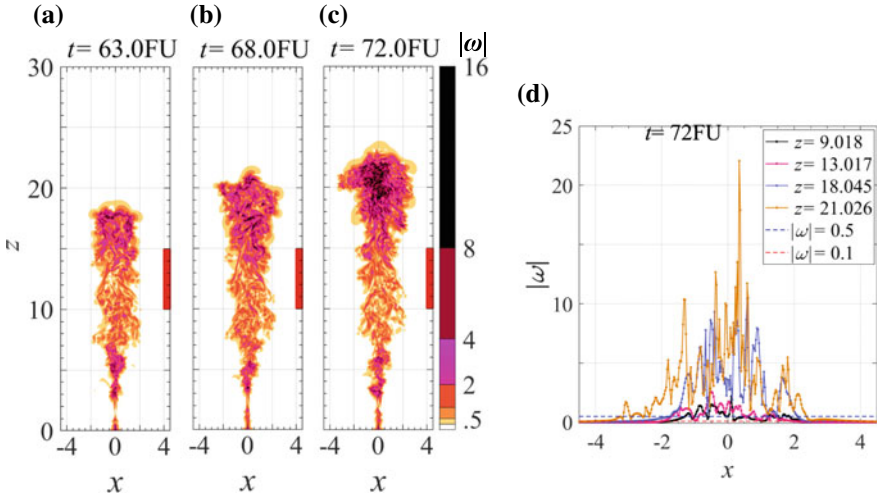

Fig. 3 **a–c** Evolution of $|\boldsymbol{\omega}|$ ($\equiv \left|\left(\omega_x^2 + \omega_y^2 + \omega_z^2\right)^{\frac{1}{2}}\right|$, the total vorticity modulus) in the TDP at different instants of time in the axial section (x-z plane, $y = 0$). The red strip in $10 \leq z \leq 15$ represents the heat injection zone. $|\boldsymbol{\omega}|$ is nondimensionalized by w_0 and d_0. Figure 3d shows the variation of $|\boldsymbol{\omega}|$ at $t = 72$FU with radial distance for selected heights z

has developed to a tall tower (stem) with a cauliflower head (cap), is chosen as an appropriate candidate for further analysis.

Figure 3d is plotted to demonstrate the effect of heating on vorticity distribution for four selected values for z. It can be seen by comparing $z = 9.018$ and $z = 21.026$ that $|\omega|$ goes up by an order of magnitude in the latter case. The reason for such a dramatic increase in $|\omega|$ may be attributed to the baroclinic torque $\beta \boldsymbol{g} \times \nabla T$ [9], which is a source for vorticity generation.

3.4 Axial (Vertical) Velocity ($\overline{w}$)

Instantaneous axial velocity distribution across the diametral sections (x-y plane) of the TDP at $t = 72$ FU is shown in Fig. 4 on the same scale as that shown in Fig. 4d. Addition of off-source heating increases the axial velocity by ~2–4 times: this can be seen by comparing the plume before (Fig. 4a) and plume after (Fig. 4c, d) heating. Another striking feature of the velocity field in Figs. 4c, d (more pronounced in the latter) is the presence of sinking velocities within and beyond the edges of plume head.

Radial distributions of azimuthally averaged axial velocity ($\overline{w}$) are plotted in Fig. 5a. It is seen that $\overline{w}$ increases with height indicating that flow is accelerating. It shows that centerline velocity increases continually, in contrast to the decay observed in the classical plume ($\overline{w}_c \sim z^{-1/3}$).

3.5 Temperature ($\overline{T}$)

Radial distributions of azimuthally averaged temperature are plotted in Fig. 5b. It can be seen from Fig. 5b that due to off-source heat addition, $\overline{T}$ decay in TDP above $z > 10$ is much less than in the classical plume ($\overline{T}_c \sim z^{-5/3}$). Buoyancy flux is a conserved variable in classical plume. However, in a TDP buoyancy flux increases (not shown here) due to the increase in ∇T and w. The dramatic increase in the vorticity (Fig. 4d) is the result of the increase in ∇T and the accompanying baroclinic torque (Eq. 4), as found in the temporal simulations of a cloud flow in a periodic box by Basu and Narasimha [9].

3.6 Equivalent Diameter (d_{eq})

It is the average diameter of the plume at a given height. It is defined as the diameter of the circular area of same magnitude as covered by the $|\boldsymbol{\omega}|_{\text{thr}}$ edge or boundary of the TDP at that height,

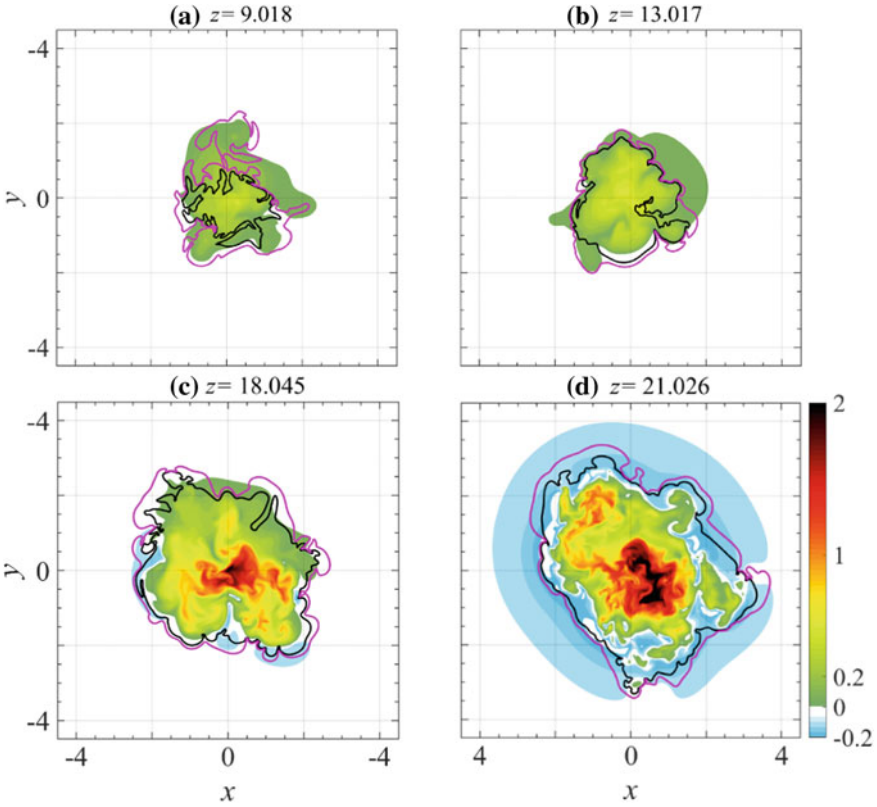

Fig. 4 Contour plot showing diametral section (x-y plane) of instantaneous vertical velocity, w at different heights at $t = 72$ FU. w is nondimensionalized using exit velocity at hot patch $w_0 = \sqrt{g\beta d_0 \Delta T_0}$. Superimposed pink ($|\boldsymbol{\omega}| = 0.25$) and black ($|\boldsymbol{\omega}| = 0.5$) curves represent the magnitude of total vorticity $|\boldsymbol{\omega}|$ on the boundary. The inner boundary (black curve) separates turbulent flow from nonturbulent flow (T\NT interface), based on the data shown in Fig. 3d. Outer boundary (pink curve) separates rotational and irrotational flow. $|\boldsymbol{\omega}|$ is nondimensionalized using w_0/d_0. **a** the w distribution below HIZ, **b** middle of HIZ, **c** above the HIZ in the cylindrical stem, and **d** above the HIZ in the plume head part

$$d_{eq} = \frac{2}{\sqrt{\pi}} \sqrt{\sum_{i,j=1,1}^{|\boldsymbol{\omega}|_{i,j} \geq |\boldsymbol{\omega}|_{\text{thr}}} \Delta x_{i,j} \Delta y_{i,j}}, \tag{3.2}$$

where $\Delta x_{i,j}$, $\Delta y_{i,j}$ represent grid size in x- and y-directions, respectively.

Figure 6b shows the equivalent diameter d_{eq} of TDP at $t = 72$ FU.

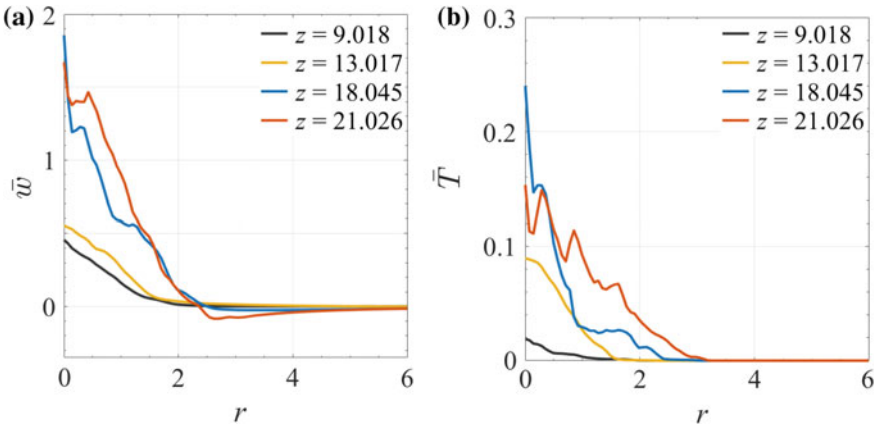

Fig. 5 **a** Azimuthally averaged distributions of vertical velocity $\overline{w}$ (**a**) and azimuthal averaged temperature $\overline{T}$ (**b**). Curves are plotted for different heights at $t = 72$ FU. Velocity is nondimensionalized by $w_0 = \sqrt{g\beta d_0 \Delta T_0}$, temperature by ΔT_0 and r *by* d_0. Black, yellow, blue, and orange lines represent the $\overline{w}$ distribution, respectively, below HIZ, inside HIZ, inside the cylindrical stem above HIZ, and plume head part above HIZ

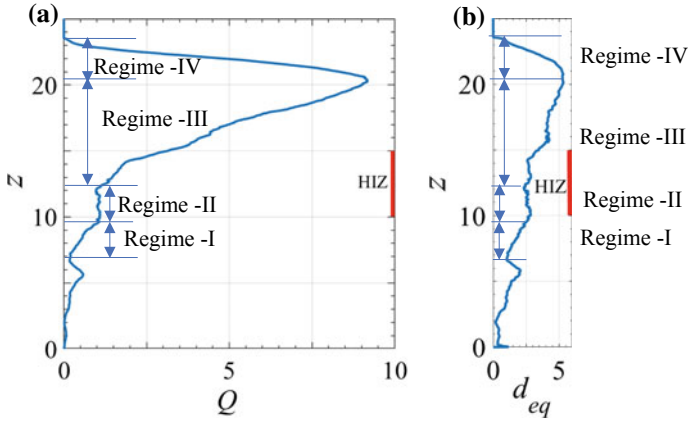

Fig. 6 Axial variation of **a** turbulent mass flux (Q) and **b** equivalent (turbulent) diameter (d_{eq}) both at $t = 72$ FU. Q and d_{eq} are nondimensionalized by w_0 and d_0, respectively. $|\boldsymbol{\omega}| = 0.5$ is used as the threshold to define the T\NT interface

3.7 Mass Flux (Q)

The quantity central to understanding the growth of TDP is entrainment. Entrainment/detrainment is a process by which the TDP fluid and ambient fluid mix with each other. Entrainment is the inflow of ambient fluid to TDP, while detrainment is the flow of TDP fluid out to the ambient. Entrainment is quantified through the

rate of change of mass flux with height. The axial variation of the mass flux is often obtained from an arbitrary choice of radial location on the mean velocity distribution but is here defined as

$$Q = \sum_{i,j=1,1}^{|\boldsymbol{\omega}|_{i,j} \geq |\boldsymbol{\omega}|_{thr}} w_{i,j} \Delta x_{i,j} \Delta y_{i,j}, \text{ where } |\boldsymbol{\omega}|_{thr} = 0.5.$$

It must be noted that this mass flux is obtained by integrating the axial velocity in the horizontal plane (x-y) from plume axis ($r = 0$) to $r = |\boldsymbol{\omega}|_{thr}$ at the relevant azimuthal angle (Fig. 4). A more detailed justification of such thresholds based on $|\boldsymbol{\omega}|$ will be found in Prasanth et al. [15]. The Q value so reported here adds up to the true turbulent mass flux. While computing Q no assumption is made on the axial velocity profile or on azimuthal symmetry. Figure 6a shows the variation of Q with axial distance and is broadly consistent with the results of Diwan et al. [7]. In regime-I, the flow is still a classical plume and Q increases linearly with height. Regime-II is in the HIZ where the increase in velocity over that in regime-II is only slightly higher than in regime-I (yellow curve in Fig. 5a), however, the flow width is nearly constant, and hence the Q hardly increases. Q goes up by a decade in regime-III and rapidly falls to zero in regime-IV. The reason for the former is that the flow begins to experience the effect of heat, as a result w goes up, resulting in more entrainment. In the later stages, even though w goes up there are sinking velocities near the edges which contribute to negative mass flux (Figs. 4d, 5a), resulting in appreciable detrainment. This behavior is in striking contrast to that in a classical self-preserving plume, where the mass flux increases with height at a constant rate.

4 Conclusions

This paper describes a fully resolved study of a transient diabatic plume (TDP). We have simulated a first-order minimalistic model of a cumulus cloud flow by incorporating a dynamically matched off-source heat addition. The results show that the addition of off-source heating makes the evolution of a transient diabatic plume strikingly different from that of a classical plume. It causes the flow to accelerate and enhances fluctuating vorticity above HIZ by an order of magnitude through the action of the baroclinic torque. We have presented here the true turbulent mass flux in TDP at one time instant. The results on the bulk parameters discussed above are broadly consistent with the previous studies on diabatic jets and plumes [7, 11].

A more detailed analysis of DNS results for the TDP and comparison with the results of experiments on TDP and LES results on clouds might help in understanding some of the more important factors that govern entrainment/detrainment and mixing in clouds.

References

1. Randall DA (2013) Beyond deadlock. Geophys Res Lett 40:5970–5976
2. Shaw RA (2003) Particle-turbulence interactions in atmospheric clouds. Annu Rev Fluid Mech 35:183–227
3. Kumar B, Bera S, Prabha TV, Grabowski WW (2017) Cloud-edge mixing: direct numerical simulation and observations in Indian Monsoon clouds. J Adv Model Earth Syst 9:332–353
4. Morton BR, Taylor GI, Turner JS (1956) Turbulent gravitational convection from maintained and instantaneous sources. Proc Roy Soc Lond Ser A Math Phys Sci, 234
5. Scorer R (1957) Experiments on convection of isolated masses of buoyant fluid. J Fluid Mech 2(6):583–594
6. Narasimha R (2012) cumulus clouds and convective boundary layers: a tropical perspective on two turbulent shear flows. J Turbul 13:1–25
7. Diwan SS, Prasanth P, Sreenivas KR, Deshpande SM, Narasimha R (2014) Cumulus-type flows in the laboratory and on the computer: simulating cloud form, evolution and large-scale structures. Bull Amer Meteor Soc 94(10):1541–1548
8. Grabowski WW (2016) Towards global large eddy simulation: super-parameterization revisited. J Meteorol Soc Jpn 94(4):327–344
9. Basu A, Narasimha R (1999) Direct numerical simulation of turbulent flows with cloud-like off-source heating. J Fluid Mech 385:199–228. https://doi.org/10.1017/S0022112099004280
10. Bhat GS, Narasimha R (1996) A volumetrically heated jet: large-eddy structure and entrainment characteristics. J Fluid Mech 325:303–330
11. Prasanth P (2013) Direct numerical simulations of a transient diabatic plume. MSc thesis, JNCASR, Bangalore
12. Falgout RD, Yang UM (2002) Hypre: a library of high-performance preconditioners, pp 632–641. Springer Berlin Heidelberg
13. Venkatakrishnan L, Bhat GS, Narasimha R (1999) Experiments on a plume with off-source heating: implications for cloud fluid dynamics. J Geophy Res 104:14271–14281
14. Turner JS (1962) The 'starting plume' in neutral surroundings. J Fluid Mech 13(3):356–368
15. Prasanth P, Sachin YS, Narasimha R (2019) A DNS study of entrainment in an axisymmetric turbulent jet as an episodic process (Submitted)

Transverse-Only Vibrations of a Rigid Square Cylinder

Subhankar Sen

Abstract Undamped transverse-only Vortex-Induced Vibration (VIV) of a rigid square cylinder is investigated numerically at a Reynolds number of 250. A stabilized space-time finite-element formulation is employed to discretize the governing equations of fluid motion in two dimensions. The reduced speed is varied from 3.5 to 9.5. For the entire range of reduced speed, synchronization between cylinder oscillations and vortex shedding is 1:1. The response consists of initial and lower branches. Two kinks are present in the response curve; the first one appears at a reduced speed of 4.7 and indicates the onset of lock-in.

Keywords Free transverse vibrations · Square cylinder · Surface pressure · Asymmetric wake mode · Kink

1 Introduction

The free or vortex-induced vibration of a rigid obstacle immersed in a moving viscous fluid is one in which the motions of fluid and solid are coupled, i.e., they influence each other. In other words, feedback between the fluid and solid is two-sided. In contrast, for controlled or forced vibrations, the motion of the rigid body governs the fluid motion in the neighborhood of the body, but the fluid, in turn, cannot deliver any influence on the motion of its solid counterpart. Thus, feedback between the two media is one-sided.

In the last two decades, study of the vibration characteristics of isolated square/rectangular section cylinders has received much attention just next to those of the circular cylinders. Some studies [1] explored the effects of rotation of the upstream square cylinder on flow in a two-cylinder system. Sen and Mittal [2–4] reported several aspects of free vibrations of a square cylinder in the Reynolds number, Re range of 50–250. They investigated the existence of various resonance branches, their dependence on oscillator mass ratio, types of wake modes, and also proposed

S. Sen (✉)
Department of Mechanical Engineering, IIT (ISM) Dhanbad, Dhanbad, India
e-mail: subhankars@gmail.com

B. N. Singh et al. (eds.), *Recent Advances in Theoretical, Applied, Computational and Experimental Mechanics*, Lecture Notes in Mechanical Engineering,
https://doi.org/10.1007/978-981-15-1189-9_32

an empirical formula yielding the lowest value of Re or reduced speed for galloping to occur. Sen and Mittal [4] also listed the total number of kinks (in characteristic curves) or transition regimes and provided possible explanations for the absence of asymmetric wake modes. Jaiman et al. [5] showed that galloping does not occur in a freely vibrating square cylinder once the sharp corners are smoothed out. He et al. [6] numerically explored the single and two-degrees-of-freedom VIV of a square cylinder and also studied the effects of mass ratio in brief.

In the earlier studies by us [2–5], the Reynolds number was coupled to the reduced speed, U^* (defined in Sect. 2) by an empirical formula. This imposed dependency resulted in reduction in the number of controlling parameters by one. In the current set of computations, the reduced speed is varied independent of Re. A fundamental study concerning free vibrations of a rigid square cylinder at low Reynolds number is still unavailable in the literature. This forms the motivation of the current work. Direct numerical simulations of the governing differential equations are performed at $\mathrm{Re} = 250$ assuming the flow to remain two-dimensional since vibrations delay all the transitions [7].

2 Methodology

The governing differential equations for the coupled fluid-rigid body system include the continuity equation as well as those of motion of fluid and cylinder. The equations of motion are derived from Newton's second law; these are the Navier–Stokes equations for fluid medium and a second-order ODE for the solid medium, respectively. In strong form, the governing momentum and continuity equations for incompressible fluid flow are expressed as

$$\rho\left(\frac{\partial u}{\partial t} + \boldsymbol{u}.\nabla\boldsymbol{u} - \boldsymbol{f}\right) = \nabla.\sigma \tag{1}$$

$$\nabla.\boldsymbol{u} = 0. \tag{2}$$

In vector Eqs. 1 and 2, t, ρ, $\boldsymbol{u}$ $(= u, v)$, $\boldsymbol{f}$, and σ, respectively, stand for the time, density of the fluid, velocity vector for flow, body force vector per unit volume, and stress tensor. The contribution from body force is not considered in the present work. In context of the present problem, the flow domain in which the oscillator resides is of rectangular shape. Free-stream inlet $(u = U, v = 0)$, stress-free exit and slip lateral boundaries define the boundary conditions for the rectangular domain. At the fluid–solid interface, no-slip on velocity is considered. A solenoidal or divergence-free velocity field is used as initial condition for the above system of PDEs.

For undamped translations of the square oscillator across the flow, Newton's second law of motion reduces to

$$\frac{\mathrm{d}^2 Y}{\mathrm{d}t^2} + (2\pi F_{\mathrm{N}})^2 Y = C_{\mathrm{l}}/2m^* \tag{3}$$

where Y is the displacement of the oscillator measured from its initial (0, 0) location. Here, $F_{\mathrm{N}} = (f_{\mathrm{n}}D)/U$ is the reduced or normalized natural frequency of the oscillator, C_{l} is the instantaneous lift force, and m^* denotes the mass ratio of the oscillator. Mass ratio or relative density of the oscillator signifies the ratio of the mass of the oscillator and mass of the displaced fluid per unit length. The dimensional natural frequency is denoted by the symbol f_{n}. The reciprocal of reduced natural frequency is known as the reduced speed. For the ODE corresponding to Eq. 3, the initial condition is $Y = 0$ and $\frac{\mathrm{d}Y}{\mathrm{d}t} = 0$ at $t = 0$. However, this initial condition is used only for the lowest value of reduced speed, i.e., $U^* = 3.5$. For other U^*, the solutions for Y and its first derivative at the nearest U^* are considered as the initial conditions.

A stabilized space-time finite-element formulation [8, 9] accommodating equal order bilinear interpolation for velocity and pressure is used for discretization of the conservation equations of mass and linear momentum in two dimensions. A rigid square cylinder of edge length D resides in a rectangular computational domain. In the absence of viscous damping, the cylinder executes free transverse-only vibrations. The mass ratio of the cylinder is 10. A blockage of 5% is used for all the calculations. For a Reynolds number of 250 based on the edge length of the cylinder, the reduced speed is varied from 3.5 to 9.5. Motion of the cylinder is depicted relative to a fixed or inertial frame of reference, the origin (0, 0) of which coincides with the center of the cylinder when it is stationary.

A multi-block, non-uniform, and structured finite-element mesh containing 24,149 nodes and 23,780 bilinear quadrilateral elements has been used for the computations. The mesh is composed of five component blocks—a central block and four rectangular blocks surrounding the central block. The central block accommodates the cylinder. The mesh is reconstructed at each time step. During the reconstruction, the central block remains undeformed (but it moves), while the other blocks deform due to movement of the central block along with the cylinder. A detailed discussion of the finite-element mesh is available in Sen and Mittal [2].

Table 1 establishes mesh insensitivity of the computed results. The free transverse vibrations of a square cylinder of $m^* = 10$ at zero incidence are computed on two

Table 1 Flow past a freely vibrating (transverse-only) rigid square cylinder $m^* = 10$ at $\mathrm{Re} = 250$ and $U^* = 15$: details of meshes M1 and M2

Mesh	Nodes	Elements	$Y_{\max}/D$	Mean C_{d}	C_{lrms}
M1	24,149	23,780	0.6772	2.0686	0.8627
M2	47,800	47,280	0.6697	2.0703	0.8645

Also listed are the values of maximum response and fluid forces obtained from these meshes

Table 2 Flow past a freely vibrating rigid square cylinder of $m^* = 3$ at Re $= 100$ and $U^* = 5$: comparison of the predicted maximum transverse response with those reported by Zhao et al. [1]

Studies	Y_{max}/D
Zhao et al. [1]	0.3500
Present	0.3231

For both cases, the blockage equals 0.025 and the cylinder executes simultaneous in-line and transverse translations

meshes M1 and M2 at Re $= 250$ and a much higher U^* of 15. At such high U^*, the cylinder executes galloping motion (not discussed in this paper). As apparent from this table, the resolution of mesh M2 is about two times the resolution of M1. Columns four through six of Table 1 ascertain that the characteristic vibration (maximum cross-stream displacement, Y_{max}) and flow quantities (mean drag and r.m.s. lift) do not exhibit any noteworthy deviation when obtained from meshes M1 and M2. Mesh M1, therefore, is considered for all computations in this work.

For two-degrees-of-freedom translations of an $m^* = 3$ square cylinder at Re $=$ 100 and $U^* = 5$, Table 2 compares the predicted maximum transverse response with the one obtained by Zhao et al. [1] via finite-element computations. For both cases, a blockage of 0.025 is considered. The closeness of the peak response values establishes the accuracy of the predicted results.

3 Results and Discussion

The variation of Y_{max}, pressure recovery at cylinder base, and drag on the cylinder are presented as a function of reduced speed. Some flow features are also discussed for a representative U^* of 4.6 belonging to the initial branch of response. For a pair of fixed square cylinders at incidence and in tandem arrangement, [10] studied the flow topology.

3.1 Cylinder Response

Figure 1 illustrates the transverse response–reduced speed relationship over the U^* range of 3.5–9.5. In this range, the cylinder executes pure vortex-induced vibration (VIV) and an 1:1 synchronization between vortex shedding and cylinder oscillation is observed. As U^* is progressively increased, two kinks are identified in the response curve. The first kink appears at $U^* = 4.7$ and the second one at $U^* = 5.1$. The first kink marks the onset of lock-in, while the second one is characteristic to transition from initial to lower resonance branch and a phase shift between lift and response by about 180°. A contrasting and new observation associated with the response curve is that a fall as opposed to a rise (as observed earlier in [2–5]) in Y is seen at the U^*

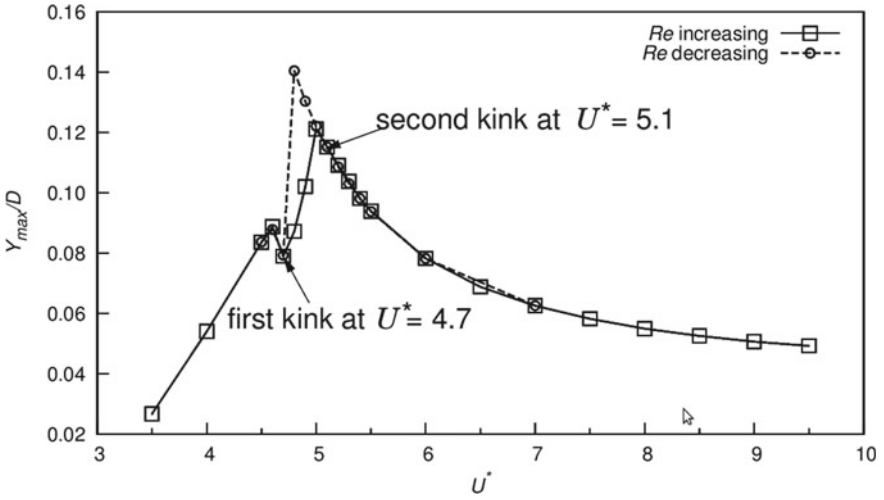

Fig. 1 Undamped free transverse vibrations of a rigid square cylinder $m^* = 10$ at Re $= 250$: variation of the normalized maximum transverse displacement with reduced speed

marking the transition from initial to lower branch of response. The response attains the maximum value of $0.12D$ at $U^* = 5$ in the initial branch.

3.2 Recovery of Surface Pressure

The relationship between pressure recovery at cylinder base and reduced speed is shown in Fig. 2. Pressure recovery is the difference between the time-mean forward stagnation pressure, C_{p0}, and time-mean base pressure, C_{pb}. A lower value of (C_{p0}-C_{pb}) indicates higher recovery of pressure and vice versa. A higher recovery implies delayed separation of boundary layer, narrow wake, and low drag. The minimum pressure recovery occurs at $U^* = 5.1$ marking the onset of lock-in.

3.3 Variation of Drag

The drag, C_d, of a cylinder is closely linked to the degree of pressure recovery at the base of the cylinder. The drag curve shown in Fig. 3 bears close resemblance with the pressure recovery curve. It can be seen that drag is low in the initial branch when recovery is more and the largest value of drag is obtained at the onset of lower branch, i.e., at $U^* = 5.1$ where pressure recovery is also minimum.

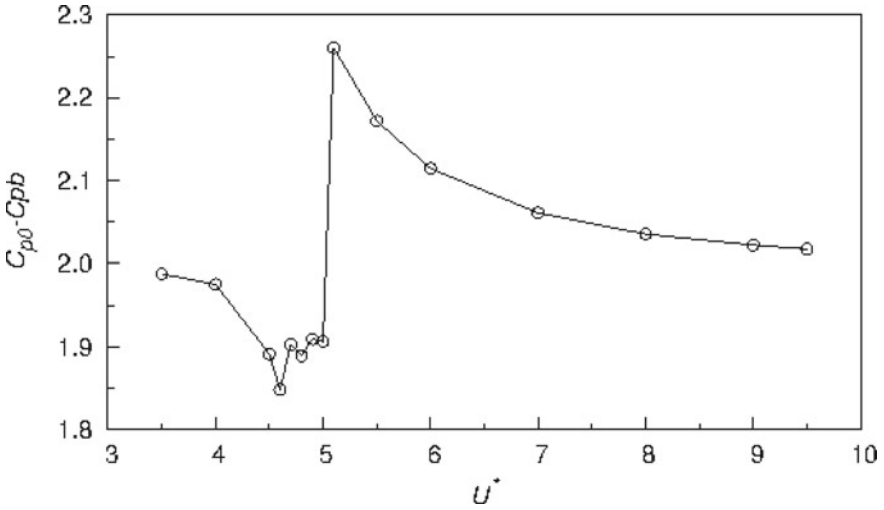

Fig. 2 Undamped free transverse vibrations of a rigid square cylinder $m^* = 10$ at Re = 250: variation of pressure recovery, C_{p0}-C_{pb} with reduced speed

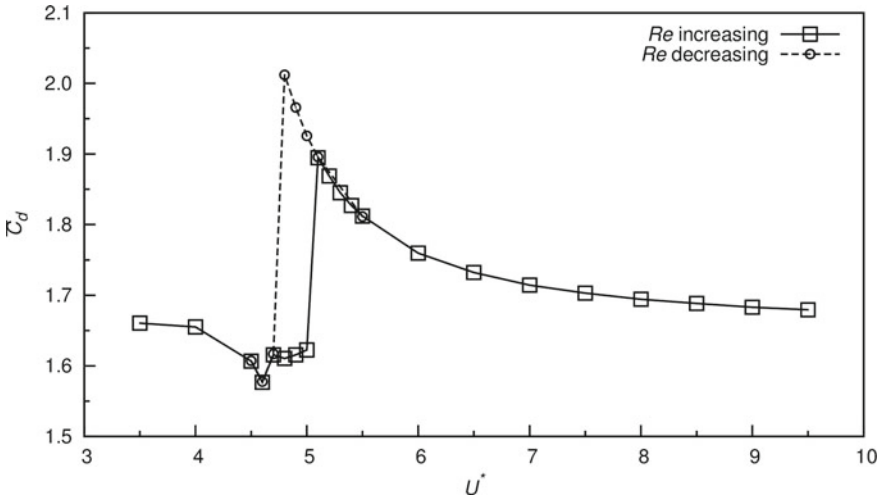

Fig. 3 Undamped free transverse vibrations of a rigid square cylinder $m^* = 10$ at Re = 250: variation of mean drag with U^*

3.4 Flow Features for U* = 4.6

Figure 4 plots the drag-lift Lissajous diagram at $U^* = 4.6$. The presence of multiple curves of similar profiles ensures that the flow is quasi-periodic at this reduced speed. The phase plot is asymmetric about the zero-lift line. This implies that mean lift is

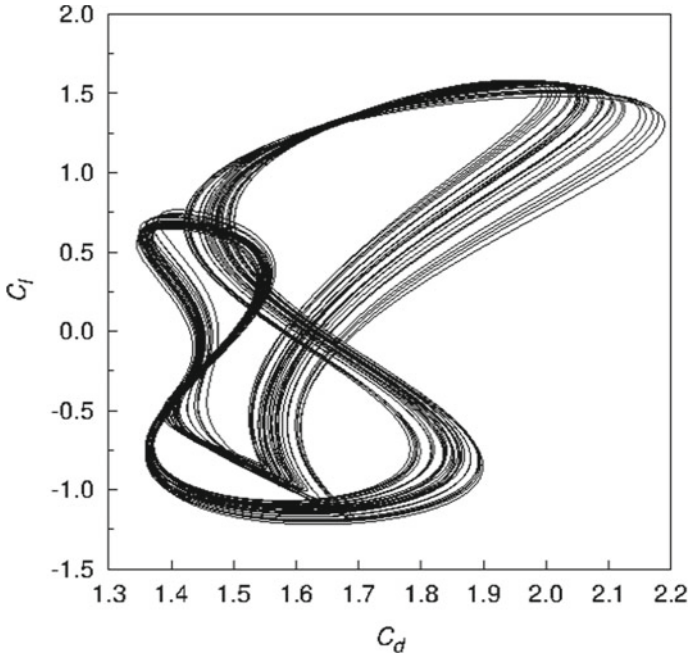

Fig. 4 Undamped free transverse vibrations of a rigid square cylinder $m^* = 10$ at Re = 250: drag-lift phase diagram at $U^* = 4.6$

nonzero. From this, it can be concluded that time-averaged pressure distribution between the stagnation points along the upper and lower halves of the cylinder must not be identical. Only under this circumstance, an unbalanced lift can be generated per lift/shedding cycle. The obvious outcome is that the vortex shedding must be biased or asymmetric. Thus, even though the synchronization is 1:1, the wake vortex mode cannot be 2S and it must be an asymmetric mode.

For $U^* = 4.6$, the mean surface pressure, C_p, on the square is shown in Fig. 5. The maximum pressure is attained at the forward stagnation point B and pressure is minimum at locations very close to the corners *A* and *C*. The pressure is mostly negative; it is positive over a very narrow region surrounding the forward stagnation point B. Following the discussion in the previous paragraph, the mean pressure along lower half BCDE differs from mean pressure along upper half EFAB. This asymmetry is the origin of the asymmetric vortex shedding and nonzero mean lift at $U^* = 4.6$.

For viscous fluid flow at low Re, the value of forward stagnation pressure coefficient (pressure at point *B* in Fig. 5) exceeds the value of unity obtained from the potential flow theory. In potential flow past a circular cylinder, the effects due to fluid viscosity or Reynolds number are absent and unique solutions for C_p exist at the forward stagnation point or elsewhere on the cylinder surface. When viscous effects are strong, i.e., Re is low or diffusion mode of transport is more powerful than the convection mode, the flow velocity is low in the vicinity of the cylinder.

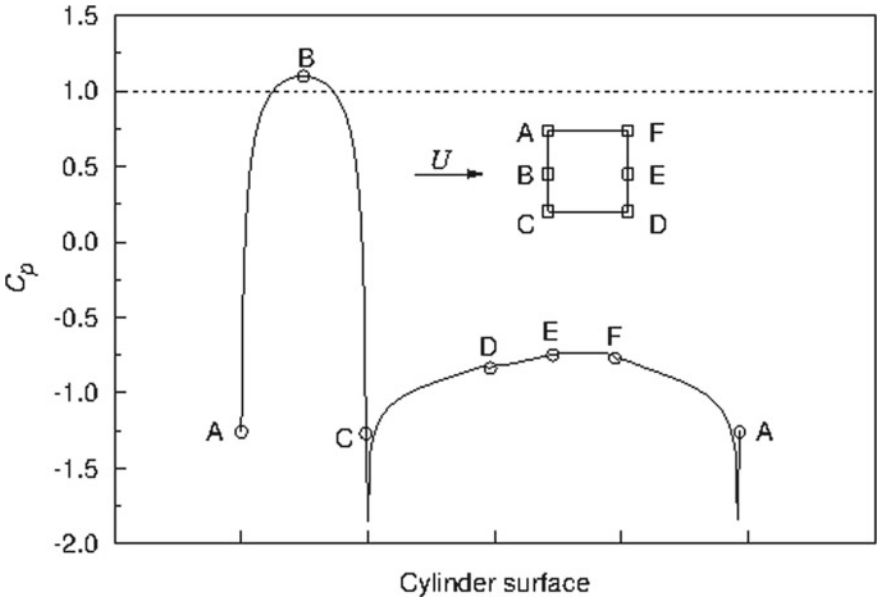

Fig. 5 Undamped free transverse vibrations of a rigid square cylinder $m^* = 10$ at Re $= 250$: time-averaged surface pressure on the cylinder at $U^* = 4.6$

This explains the value of higher C_p at low Re at point B. As Re increases, convection turns stronger, flow velocity increases, and C_p drops and approaches the value predicted by the potential flow theory.

In terms of instantaneous vorticity, Fig. 6 depicts the wake structures at $U^* = 4.6$. By a detailed analysis of vortex shedding in a complete oscillation cycle, it is found that vortex shedding for the quasi-periodic $U^* = 4.6$ case is one-sided. The wake structures repeat in every two oscillation cycles. In the first cycle, two weak vortices of same sign (CCW) are shed from the lower portion of the cylinder. In the next cycle, the asymmetric $P + S$ shedding pattern is observed. To the best of the author's knowledge, wake modes involving successive shedding of like sign vortices are not discussed in the literature. Also, the identification of $P + S$ mode for a freely vibrating square cylinder is being reported perhaps for the first time. The newly identified one-sided mode is introduced by the symbol S_1S_2. This symbol suggests shedding of two like-signed (here, positive) vortices S_1 and S_2 (marked in Fig. 6) instead of two opposite-signed vortices seen in an oscillation/shedding cycle of antisymmetric or Karman shedding.

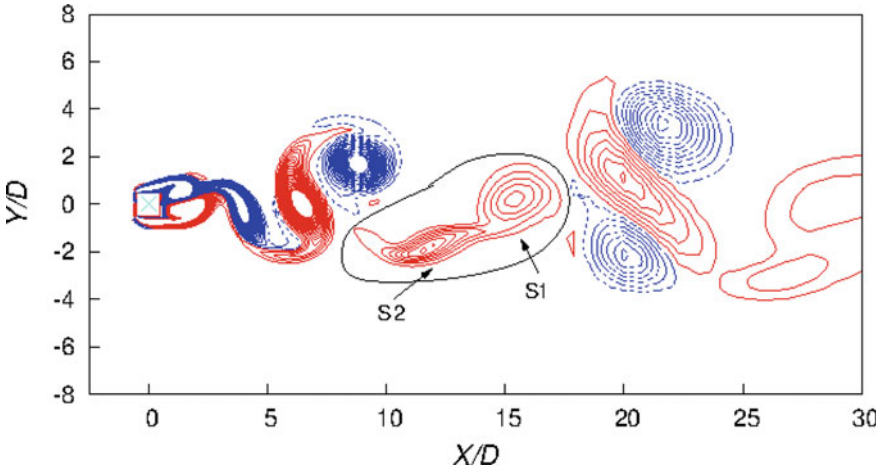

Fig. 6 Instantaneous vorticity field at $U^* = 4.6$ showing the one-sided S_1 and S_2 vortices. The cross symbol (x) marks the origin of the inertial (fixed) frame of reference

4 Conclusions

The free transverse vibration of a rigid square cylinder of mass ratio 10 is investigated numerically at Re = 250. The motion is purely VIV and devoid of galloping for the U^* range of 3.5–9.5. For the first time, existence of asymmetric wake modes is noted for a square cylinder executing 1:1 VIV. A new wake mode corresponding to one-sided shedding is identified. This newly identified mode is denoted by the symbol S_1S_2 where two vortices of same sign are shed from each oscillation cycle.

References

1. Zhao M, Cheng L, Zhou T (2013) Numerical simulation of vortex-induced vibration of a square cylinder at low Reynolds number. Phys Fluids 25:023603-1–023603-25
2. Sen S, Mittal S (2011) Free vibration of a square cylinder at low Reynolds numbers. J Fluids Struct 27:875–884
3. Sen S, Mittal S (2015) Effect of mass ratio on free vibrations of a square cylinder at low Reynolds numbers. J Fluids Struct 54:661–678
4. Sen S, Mittal S (2016) Free vibrations of a square cylinder of varying mass ratios. Proc Eng 144:34–42
5. Jaiman RK, Sen S, Gurugubelli PS (2015) A fully implicit combined field scheme for freely vibrating square cylinders with sharp and rounded corners. Comput Fluids 112:1–18
6. He T, Zhou D, Bao Y (2012) Combined interface boundary condition method for fluid-rigid body interaction. Comput Methods Appl Mech Eng 223–224:81–102
7. Leontini JS, Thompson MC, Hourigan K (2007) Three-dimensional transition in the wake of a transversely oscillating cylinder. J Fluid Mech 577:79–104

8. Tezduyar TE, Behr M, Liou J (1992) A new strategy for finite element computations involving moving boundaries and interfaces-the DSD/ST procedure: I. The concept and the preliminary numerical tests. Comput Methods Appl Mech Eng 94:339–351
9. Tezduyar TE, Behr M, Mittal S, Liou J (1992) A new strategy for finite element computations involving moving boundaries and interfaces-the DSD/ST procedure: II. Computation of free-surface flows, two-liquid flows, and flows with drifting cylinders. Comput Methods Appl Mech Eng 94:353–371
10. Dash SM, Lee T-S (2012) Impulsively started flow topology around tandem arrangement of two square cylinder at incidence. Int J Mod Phys Conf Ser 19:100–108

Steady Flow Past Two Square Cylinders in Tandem

Deepak Kumar, Kumar Sourav and Subhankar Sen

Abstract In the present work, two-dimensional, incompressible steady flow around a pair of identical square cylinders in tandem arrangement is studied numerically using stabilized finite-element formulation. Reynolds number (Re), based on free stream speed and cross-flow width of the cylinder, is fixed at 40. The spacing ratio (*S/D*) is the ratio of distance between the center of cylinders to the cross-flow dimension of the cylinder which is varied from 2 to 10. Three distinct flow patterns are identified for the given range of *S/D*. With increase in *S/D*, the wake interaction between both the cylinders weakens and both cylinders form separate closed wakes for *S/D* $\geq$ 6. Interestingly, a weak recirculation zone other than the closed wake structure of both the cylinders is found near the forward stagnation point of downstream cylinder in the gap region. This recirculation zone disappears with a marginal change in the spacing ratio. As *S/D* is increased further, both upstream and downstream cylinders behave as an isolated cylinder.

Keywords Tandem square cylinders · Steady flow · Flow regimes · Recirculation zone

1 Introduction

Despite being simple in geometry, due to its vast applicability and abundance of flow physics, flow over a circular cylinder has been the most explored problem in the field of bluff body flow. A detailed review for the same can be found in Zadravkovich [1], Sumner [2], and many more. The knowledge of aerodynamic forces on the structure and subsequent changes in flow field is very important before designing any structure experiencing fluid–structure interaction. These structures may include from tube bundles of heat exchangers, wires in the transmission line, floating platforms in oversea, pipelines near seabed, chimney stacks skyscrapers, and many more. Presence of another bluff structure in the vicinity makes the analysis even

D. Kumar (✉) · K. Sourav · S. Sen
IIT (ISM), Dhanbad 826004, Jharkhand, India
e-mail: deepakkmr799@gmail.com

B. N. Singh et al. (eds.), *Recent Advances in Theoretical, Applied, Computational and Experimental Mechanics*, Lecture Notes in Mechanical Engineering,
https://doi.org/10.1007/978-981-15-1189-9_33

more challenging. Two or more than two cylinders can be arranged in three possible arrangements, namely, tandem, side-by-side, and staggered [1]. Depending upon the closeness of two circular cylinders and interaction of vortices of one cylinder with the other, Zadravkovich [3] defined three different regimes of flow. (i) The proximity interference regime (cylinders are adjacent to each other), (ii) wake interference regime (rear cylinder is in the wake of the front cylinder), and (iii) no-interference regime (cylinders are far from each other and are not affected by the presence of the other). Patil et al. [4] conducted numerical experiments on two circular cylinders placed in tandem arrangement. They studied the effect of varying shear parameter, spacing ratio, and Reynolds number on flow separation and aerodynamic forces. Singha and Sinhamahapatra [5] reported steady and unsteady flow past two circular cylinders for varying Re and *S/D*. They found the flow to be fully steady irrespective of the spacing ratio for Re = 40. However, as the Re is increased to a value of 70, the flow progressively switches from steady to unsteady as the spacing ratio advances from 0.2 to 4.

As compared to circular cylinder, the square counterpart is relatively less explored. Flow past a pair of identical square cylinders at low Re has been studied numerically by Sohankar [6]. He investigated the effect of spacing ratio for selected values of Re and found a critical spacing ratio beyond which the fluid forces increased considerably. He also presented the effect of Reynolds number for a fixed spacing of $S/D = 4$. Based on the study, Sohankar [6] found three major regimes, namely, single-slender body regime, reattach regime, and co-shedding regime. Later, Shyam and Chhabra [7] conducted numerical experiments to depict the effect of Prandtl number on in-line cylinders of square cross section and immersed in power-law fluid for Re range 1–40. *S/D* is varied from 2 to 6. Ehsan et al. [8] investigated steady and unsteady flow over a pair of square cylinders in in-line arrangements for Re range 1–200 and for shear parameter varying from 0.5 to 1.8. They found that the onset of separation from the leading edge occurs early for shear-thinning fluid and is delayed for shear thickening fluid. Most of the numerical and experimental studies on flow around pair of square cylinders are confined to high Re flow. The flow regimes in all the reported literature are defined for unsteady flow based on the patterns of shedding of vortices from the upstream and downstream cylinders. Therefore, the obvious questions which come to the mind are: Can we identify different regimes of flow in the absence of vortex shedding from the cylinders, i.e., when the flow is steady? What will be the criterion for defining the regimes? The lack of literature for low Re flow past two square cylinders in tandem arrangement in steady flow regime and the above-unanswered questions motivated us to explore the problem further. Therefore, in the present investigation, our objective is to identify the flow structure formed by varying *S/D* of two identical square cylinders at a Re = 40. An attempt to understand the effect of spacing on the streamlines variation, in-line velocity distribution on the wake centerline in the gap region and the corresponding effect on wake structure is also made. Structure of the remaining paper is as follows: Governing equations are discussed in Sect. 2. Section 3 describes the problem setup and mesh information. Validation study and grid independence test are discussed in Sect. 4. Results are presented in Sect. 5. The first Sect. 5.1 in Sect. 5 describe overall flow. Critical

flow region is separately discussed in 5.2 followed by discussions on wake length reattachment point.

2 Governing Equations

The motion of incompressible fluid in steady flow is governed by Eqs. 1 and 2 listed below:

$$\rho(u.\nabla u - f) - \nabla\sigma = 0 \tag{1}$$

$$\nabla u = 0 \tag{2}$$

Here, $\boldsymbol{u}$ vector is the velocity of the fluid, $\boldsymbol{f}$ is body force, and $\boldsymbol{\sigma}$ represents the Cauchy stress tensor. Since the flow is advection dominated, therefore the contribution of body force is not considered in the computations. The stress tensor consists of isotropic and deviatoric parts:

$$\sigma = -pI + T, \quad T = 2\mu\varepsilon(u), \varepsilon(u) = 1/2\left((\nabla u) + (\nabla u)^{\mathrm{T}}\right) \tag{3}$$

Here, p is the pressure, I is the identity matrix, μ is the dynamic viscosity of the medium, and ε is the strain rate.

3 Problem Description and Finite-Element Mesh

Figure 1 shows the schematic of the problem. The rectangular box represents the flow domain. Two identical square cylinders whose centers are separated by a spacing S are fixed in the domain. The inlet and exit of the domain are provided with free stream and stress-free boundary conditions, respectively. Cylinder surfaces are no-slip surfaces. The sidewalls are free-slip walls. A collocated, multi-block, structured, nonuniform finite-element mesh consisting of 94,391 nodes and 93,440 elements for $S/D = 2$ is shown in Fig. 2a. The mesh consists of total ten blocks. This arrangement allows to control the resolution of the mesh locally. The cylinders are placed in two central mesh blocks. The enlarged view of central block consisting of upstream cylinder is shown in Fig. 2b. The other blocks adjacent to the central blocks are stitched with the central blocks. The origin of Cartesian coordinate system is located at the geometric center of upstream cylinder. The distance of inlet and exit walls from the origin of the coordinate system is 30D and 95D, respectively. Both the upper and lower walls are placed at a distance of 25D from the origin, thus offering a blockage (B, ratio of cross-stream dimension of the cylinder to the total cross-stream width of the domain) of 2%.

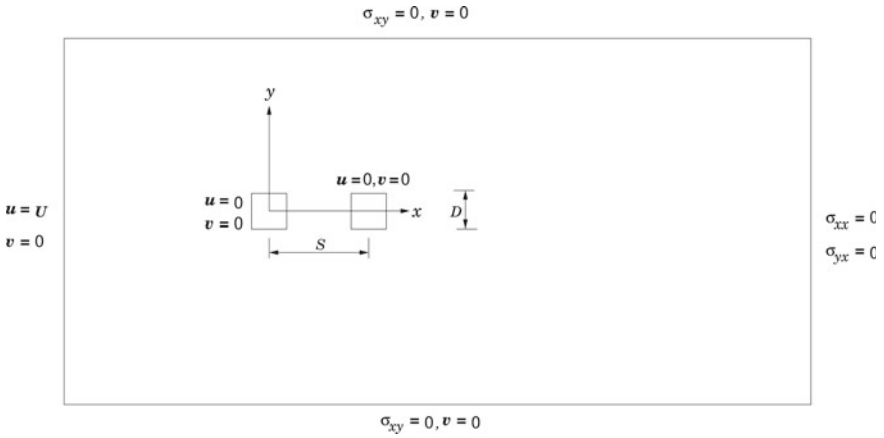

Fig. 1 Sketch of the problem statement and associated boundary conditions for steady flow past a pair of identical square cylinder in tandem arrangement

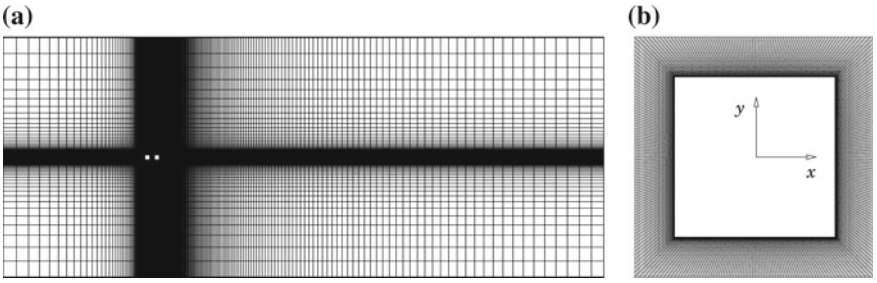

Fig. 2 **a** The finite-element mesh consisting of two identical square cylinders for $S/D = 2$. **b** Enlarged view of the central mesh block consisting the upstream cylinder. The two orthogonal arrows represent the coordinate system

4 Validation of the Numerical Model and Grid Independence Test

The results reported by Sharman et al. [9] for a pair of circular cylinders and Bao et al. [10] for two square cylinders in tandem are compared with the results of present computation to establish the accuracy of the numerical model used (see Table 1). Unsteady computations are carried out at Re = 100 and for a spacing ratio of $S/D =$ 4 and 5 two identical circular and square cylinders, respectively. Table 2 lists the grid independence test for the present computations. Two grids M1 and M2 have been tested and based on the results obtained, mesh M1 is chosen for all the computations in the present work.

Table 1 Unsteady flow past a pair of identical circular and square cylinder at Re = 100. The comparison of aerodynamic coefficients as reported by Sharman et al. [9] and Bao et al. [10] with the present computations

Geometry	Study	*S/D*	Blockage	Upstream cylinder		Downstream cylinder	
				$C_{D\,AVG}$	$C_{L\,RMS}$	$C_{D\,AVG}$	$C_{L\,RMS}$
Circle	Sharman et al. [9]	4	0.02	1.2756	0.3028	0.7033	0.9869
Circle	Present	4	0.02	1.2602	0.3019	0.7007	0.9700
Square	Bao et al. [10]	5	0.02	1.4260	0.2890	1.0990	1.2110
Square	Present	5	0.02	1.3910	0.2901	1.0956	1.2060

Table 2 Steady flow past a pair of identical square cylinder at Re = 40 and for $B = 0.02$. Grid independence test for $S/D = 6$

Mesh	Nodes	Elements	Upstream cylinder		Downstream cylinder	
			C_{Dp}	C_{Dv}	C_{Dp}	C_{Dv}
M1	98,577	97,600	1.32156	0.27975	0.22733	0.17848
M2	200,063	198,620	1.33518	0.26598	0.23106	0.17575

5 Results

The results of steady flow around two bluff obstacles of square cross section are presented for a fixed Re value of 40 and for *S/D* ranging between 2 and 10. The equations governing the flow are discretized using stabilized finite-element formation.

5.1 The Flow

Flow patterns in terms of streamline contours for spacing ratio range considered are shown in Fig. 3. As apparent from Fig. 2a, b, for low *S/D* (= 2 and 4), wake of the upstream cylinder reattaches on the downstream cylinder. Initially, the classical

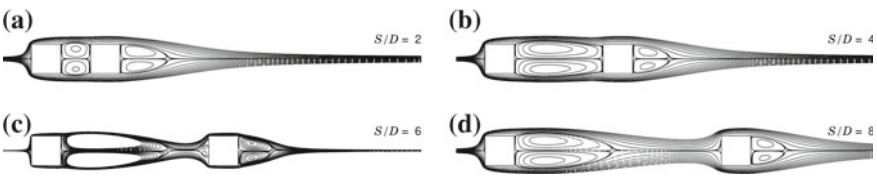

Fig. 3 Flow past a pair of square cylinders in tandem at Re = 40: streamline plots for *S/D* = **a** 2, **b** 4, **c** 6, and **d** 8

closed wake structure is observed only behind downstream cylinder up to $S/D = 4$. $S/D = 6$ (Fig. 2c) is found to be a critical spacing ratio where the reattachment of separated shear layers on the rear cylinder ceases and the classical close wake appears for the first time behind both the cylinders. Here, it is interesting to note that a pair of weak antisymmetric rotating eddies is also generated near the forward stagnation point of the downstream cylinder. With further increase of spacing ratio, both cylinders behave like two distinct isolated (negligible effect of the presence of other bluff object) cylinder. Thus, three distinct flow regimes are identified, namely, precritical ($S/D < 6$), critical ($S/D = 6$), and postcritical ($S/D > 6$).

5.2 *Flow Characteristic in the Critical Regime*

To understand the changes in the flow structure near the critical regime (i.e., when a closed wake is observed for upstream cylinder in the gap region), computations are carried out at intermediate spacing ratio values between $S/D = 4$ and $S/D = 6$. The variation is shown with respect to streamline contours in Fig. 4. As apparent from Fig. 4a, at $S/D = 5.5$, the wake of upstream cylinder shows a tendency to detach from downstream cylinder, thereby making a very narrow structure near the frontal edge of downstream cylinder. As the spacing ration approaches six (i.e., the critical value), a completely closed wake structure of the upstream cylinder is observed in the gap region for the first time. Interestingly, another weak yet observable counterrotating recirculation zone above and below the wake centerline also appears adjacent to the wake of upstream cylinder and frontal edge of downstream cylinder. This is caused by the flow reversal in this zone. To understand the flow direction in the gap region, the variation of in-line component of the velocity is plotted with in-line spacing for $S/D = 6$. Figure 5 clearly depicts the reversal of flow as the in-line component of flow velocity changes its sign from positive to negative near the frontal edge. The first negative u-velocity region represents the wake of upstream cylinder.

The effect of spacing ratio on the flow structure is presented via variation of wake length in Fig. 6a. While the upstream cylinder shows a monotonic decrease in the wake length after its evolution at $S/D = 6$, the wake length of the downstream cylinder initially decreases up to $S/D = 6$ and then increases gradually. Figure 6b presents the distribution of surface vorticity on the downstream cylinder. The intersection of vorticity curve with zero line represents either the separation or reattachment points.

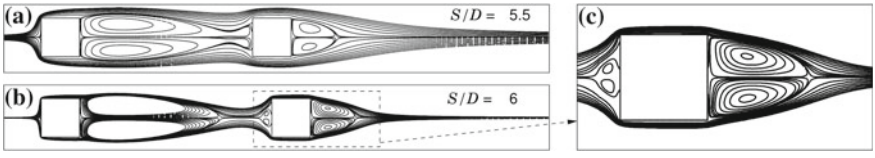

Fig. 4 Streamline plots for $S/D =$ **a** 5.5, **b** 6, and **c** enlarged view of downstream cylinder. A weak recirculation zone near can be clearly observed near the frontal edge of downstream cylinder

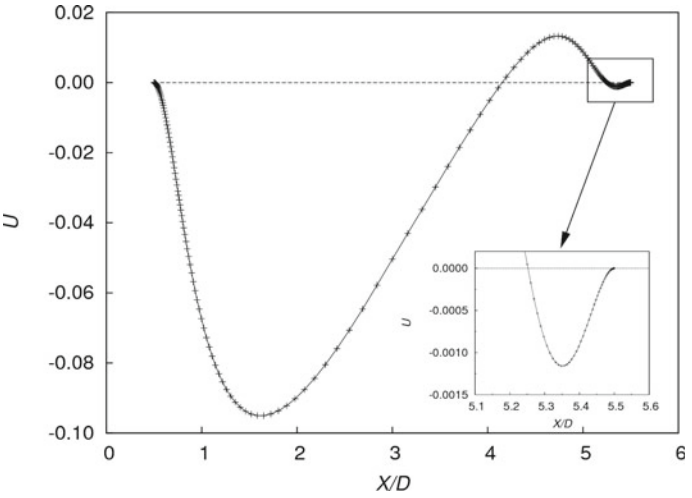

Fig. 5 Steady flow past two identical square cylinders at Re = 40 and *S/D* = 6. Variation of in-line velocity component (u) in the gap region. The inset shows enlarged view of the variation of u-x near the frontal edge of downstream cylinder

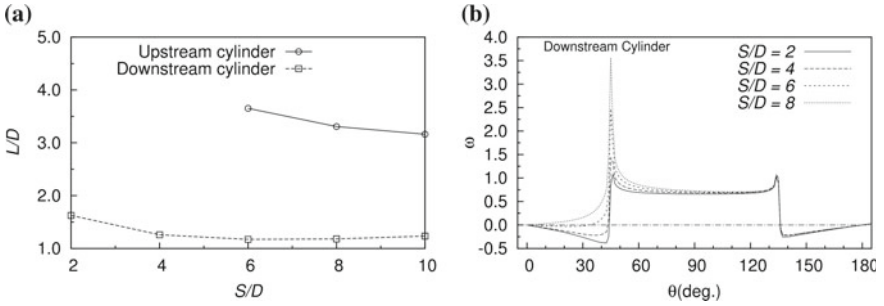

Fig. 6 The variation of **a** length of the wake of both the cylinders and **b** surface vorticity distribution around the downstream cylinder as a function of *S/D*. The angular position 0° and 180° represents the forward stagnation point and base points (moving in counterclockwise direction) of the square cylinder, respectively

It is worth noting that for *S/D* = 2 through 6, when the wake of the upstream cylinder has interaction with its downstream counterpart, the reattachment point is not fixed and it gradually move toward forward stagnation point (on the leading edge).

6 Conclusions

Flow past a pair of square cylinder in tandem arrangement is investigated numerically for a fixed Re of 40 and *S/D* ranging between 2 and 10. Based on the flow patterns observed, three distinct flow regimes are identified, namely, precritical, critical, and postcritical regimes. In precritical regime (*S/D* = 2–4), the separated shear layer from first cylinder reattaches on the rear cylinder. A closed steady wake behind the downstream cylinder is observed for all condition considered. At a critical spacing ratio (*S/D* = 6), reattachment ceases and a classical closed wake appears for the first time behind the upstream cylinder. In the critical regime, a recirculation zone near the forward stagnation point is also created. As *S/D* increases from 2 to 6, the reattachment point on the downstream cylinder shifts (from the corners on the leading edge) toward the forward stagnation point. In the postcritical regime, the interaction between the cylinders weakens and they tend to behave as isolated cylinders. While the wake length (measured from the base to the wake stagnation point) of the upstream cylinder decreases monotonically, the wake length of the rear cylinder decreases first up to critical *S/D* and then again starts increasing slowly.

References

1. Zdravkovich MM (1977) Review of flow interference between two circular cylinders in various arrangements. ASME J Fluids Eng 99:618–633
2. Sumner D (2010) Two circular cylinders in cross-flow: a review. J Fluids Struct 26(6):849–899
3. Zdravkovich MM (1985) Flow induced oscillations of two interfering circular cylinders. J Sound Vib 101(4):511–521
4. Patil RC, Bharti RP, Chhabra RP (2008) Steady flow of power law fluids over a pair of cylinders in tandem arrangement. Ind Eng Chem Res 47(5):1660–1683
5. Singha S, Sinhamahapatra KP (2010) High-resolution numerical simulation of low Reynolds number incompressible flow about two cylinders in tandem. J Fluids Eng 132(1):011101
6. Sohankar A (2012) A numerical investigation of the flow over a pair of identical square cylinders in a tandem arrangement. Int J Numer Methods Fluids 70(10):1244–1257
7. Shyam R, Chhabra RP (2013) Effect of Prandtl number on heat transfer from tandem square cylinders immersed in power-law fluids in the low Reynolds number regime. Int J Heat Mass Transf 57(2):742–755
8. Ehsan I, Mohammad S, Reza NM, Ali J, Tashnizi ES (2013) Power-law fluid flow passing two square cylinders in tandem arrangement. J Fluids Eng 135(6):061101
9. Sharman B, Lien FS, Davidson L, Norberg C (2005) Numerical predictions of low Reynolds number flows over two tandem circular cylinders. Int J Numer Methods Fluids 47:423–447.
10. Bao Y, Wu Q, Zhou D (2012) Numerical investigation of flow around an inline square cylinder array with different spacing ratios. Comput Fluids 55:118–131

A Robust and Accurate Convective-Pressure-Split Approximate Riemann Solver for Computation of Compressible High Speed Flows

Sangeeth Simon and J. C. Mandal

Abstract The Harten-Lax-van Leer (HLL) based Convective-Pressure-Split (CPS) approximate Riemann solver (HLL-CPS) is a popular upwind scheme designed to discretize the Euler system of equations that governs compressible high speed flows. However, the HLL-CPS scheme is known to possess two major drawbacks: high numerical dissipation on shear waves and susceptibility to numerical shock instability. In this paper, we demonstrate that the accuracy of the shear waves can be recovered by directly employing an HLLC-type anti-diffusive term in the discretized pressure system of the HLL-CPS scheme. We show that the resulting scheme, termed HLLC-CPS, can be made shock stable by selectively controlling this anti-diffusive term in the vicinity of a numerical shock front using a pressure-ratio based control parameter. Numerical results show the efficacy of the proposed scheme.

Keywords Euler equations · Convective-pressure split · Numerical shock instability · Riemann solvers · Contact and shear preserving

1 Introduction

Computation of high-speed compressible flows, governed by the Euler system of equations, continues to be a major challenge in the field of Computational Fluid Dynamics. Complexities arise inaccurately and robustly resolving the genuinely nonlinear waves like the shock wave and expansion fans, the linearly degenerate waves like the contact wave and shear wave and the mutual interactions between these wavefields. Over the past several decades, various upwind schemes have been developed to address this challenge. The two major categories of these schemes are the Flux Vector Splitting (FVS) schemes and the Flux Difference Splitting (FDS)

S. Simon · J. C. Mandal (✉)
Department of Aerospace Engineering, IIT Bombay, Mumbai 400076, India
e-mail: mandal@aero.iitb.ac.in

S. Simon
e-mail: sangeethsimon2@gmail.com

B. N. Singh et al. (eds.), *Recent Advances in Theoretical, Applied, Computational and Experimental Mechanics*, Lecture Notes in Mechanical Engineering,
https://doi.org/10.1007/978-981-15-1189-9_34

schemes. While the FVS schemes work by decomposing the total Euler flux vector at an interface into an upwind and downwind contribution based on local wavespeeds, the FDS schemes seek the solution of a Riemann problem to estimate the numerical flux at an interface. The most cost-effective implementation of the FDS schemes is the approximate Riemann solvers and the most popular of them include the Roe scheme [1], the HLL scheme [2], the HLLC scheme [3] etc. Although the superior accuracy has rendered these schemes more popular than the FVS schemes over the years, they still lack the inherent robustness of the FVS schemes against the phenomenon of numerical shock instability [4].

A particular scheme that represents a combination of the philosophy of the FVS and the FDS schemes, yet remains distinct from each of them, is the AUSM scheme of Liou et al. [5]. The AUSM scheme is notable for pioneering the philosophy of Convective-Pressure Splitting (CPS) by arguing that since the Euler equations comprise of separable convective and pressure systems with distinct physics of propagation, it is meaningful to decompose it accordingly and discretize these components independently. The AUSM scheme rivaled most of the approximate Riemann solvers in its accuracy while closely retaining the robustness of the FVS schemes in shock-capturing. The philosophy of CPS that was put forward by this scheme had subsequently inspired several other schemes [6–8]. Most of these schemes used a one-sided differencing for the convective component and a Mach number or velocity-based polynomial approximations for the pressure component.

Recently, Mandal et al. [9] proposed an interesting CPS based approximate Riemann solver called the HLL-CPS scheme. In this scheme, the Euler flux is first decomposed into its respective convective and pressure systems based on either AUSM-type or Zha-Bilgen-type [6] splitting. The resulting convective system was governed by a single linear wave and the pressure system was governed by two nonlinear waves and a stationary contact wave. While the convective system is upwinded based on locally averaged fluid velocity, the pressure system is subjected to HLL-type discretization inspired by the AUFS scheme of Sun et al. [10]. The contact ability was introduced explicitly by replacing the density jumps appearing in the numerical dissipation of the pressure system to pressure jumps using an isentropic condition. The individually discretized convective and pressure systems are then coupled to each other using the slowest and fastest wavespeeds that occur as the solution of the local Riemann problem. The HLL-CPS scheme was shown to be as accurate as the HLLC scheme at least on several inviscid problems. It also inherited several appealing features like positivity, entropy satisfaction without explicit entropy fixes and flux differentiability from the HLL scheme. Further, all versions of the scheme were shown to avoid numerical shock instability on selected problems. The HLL-CPS formulation has been shown to work effectively even on the Toro-Vazquez-type flux splitting [11] and has been easily extended to its genuinely multidimensional version [12], which clearly demonstrates the versatility of the method. However, recent studies reveal that the HLL-CPS scheme has two major drawbacks. Firstly, the numerical dissipation tuning employed to resolve stationary contacts adversely affected the capability of the scheme to resolve shear waves [13]. Secondly, our

experience shows that the HLL-CPS may succumb to numerical shock instability on certain problems.

To alleviate these shortcomings, in this work, we propose a new low diffusion approximate Riemann solver based on the CPS philosophy. Although we reuse the framework made available by the HLL-CPS scheme, the proposed scheme differs from it specifically in the discretization of the pressure system. In particular, we show that full accuracy on the linearly degenerate wavefields can be recovered by simply introducing an HLLC-type anti-diffusive term into the formulation. Further, we demonstrate that the proposed scheme could be made robust against numerical shock instability by simply controlling this anti-diffusive term in the vicinity of a numerical shock front.

2 Formulation

The governing equations for x-directional-split inviscid compressible flow can be expressed in their conservative form as,

$$\frac{\partial \mathbf{U}}{\partial t} + \frac{\partial \mathbf{F}(\mathbf{U})}{\partial x} = 0 \tag{1}$$

where $\mathbf{U}$ and $\mathbf{F}(\mathbf{U})$ are the vector of local conserved variables and grid normal fluxes at any interfaces given respectively as $\mathbf{U} = [\rho, \rho u, \rho v, \rho E]^T$ and $\mathbf{F}(\mathbf{U}) = \left[\rho u, \rho u^2 + p, \rho uv, (\rho E + p)u\right]^T$. In these expressions, ρ, u, v, p and E stands, respectively, for density, normal velocity, tangential velocity, pressure, and specific total energy. The system of equations are closed through the equation of state. In the above expression the grid tangent fluxes are neglected in a finite volume discretization because they do not contribute to the flux across an interface. A semi discretized form of Eq. (1) that uses a conventional Finite Volume based two-state approximate Riemann solver on a two-dimensional quadrilateral mesh with a cell element i of area $|\Omega_i|$ can be written as,

$$\frac{d\mathbf{U}_i}{dt} = -\frac{1}{|\Omega|_i} \sum_{k=1}^{4} [\mathbf{F}_{\text{Riemann}}(\mathbf{U_L}, \mathbf{U_R})] \Delta s_k \tag{2}$$

where $\mathbf{U_L}, \mathbf{U_R}$ indicates the initial conditions of a local Riemann problem across kth interface of cell i and $\mathbf{F}_{\text{Riemann}}$ is the Riemann flux operator at any interface with face length Δs_k. In this work we use the Zha-Bilgen type flux splitting strategy [6] to split the total Euler flux vector into its convective ($\mathbf{F^C}$) and pressure ($\mathbf{F^P}$) systems as,

$$\mathbf{F} = \mathbf{F^C} + \mathbf{F^P}$$

where,

$$\mathbf{F^C} = u \begin{pmatrix} \rho \\ \rho u \\ \rho v \\ E \end{pmatrix} \qquad \mathbf{F^P} = \begin{pmatrix} 0 \\ p \\ 0 \\ pu \end{pmatrix} \tag{3}$$

For the proposed scheme, the convective part is discretized using a simple local average velocity based upwinding similar to [9].

$$\mathbf{F}^C = M_k \begin{pmatrix} \rho \\ \rho u \\ \rho v \\ E \end{pmatrix}_k a_k \tag{4}$$

$$k = \begin{cases} L & \text{if } \bar{u} \geq 0 \\ R & \text{if } \bar{u} < 0 \end{cases} \tag{5}$$

where the local average velocity $\bar{u} = \dfrac{u_L + u_R}{2}$

$$M_k = \begin{cases} \dfrac{\bar{u}}{\bar{u} - S_L} & \text{if } \bar{u} \geq 0 \\ \dfrac{\bar{u}}{\bar{u} - S_R} & \text{if } \bar{u} < 0 \end{cases} \tag{6}$$

and

$$a_k = \begin{cases} u_L - S_L & \text{if } \bar{u} \geq 0 \\ u_R - S_R & \text{if } \bar{u} < 0 \end{cases} \tag{7}$$

The $S_L = \min(0, u_L - a_L, \tilde{u} - \tilde{a})$ and $S_R = \max(0, u_R + a_R, \tilde{u} + \tilde{a})$ are the wavespeeds. The pressure part can be discretized using the two-wave HLL Riemann solver as in [9],

$$\mathbf{F^P} = \frac{S_R \mathbf{F_L^P} - S_L \mathbf{F_R^P} + S_R S_L (\mathbf{U_R} - \mathbf{U_L})}{S_R - S_L} \tag{8}$$

Now, instead of tuning the term $(\mathbf{U_R} - \mathbf{U_L})$ to recover accuracy on linearly degenerate waves like contact waves and shear waves as advocated in the HLL-CPS scheme, we simply add an HLLC-type anti-diffusive term to the pressure discretization. Hence, we write,

$$\mathbf{F^P} = \frac{S_R \mathbf{F_L^P} - S_L \mathbf{F_R^P} + S_R S_L (\mathbf{U_R} - \mathbf{U_L})}{S_R - S_L} + \omega \mathbf{A_{HLLC}} \tag{9}$$

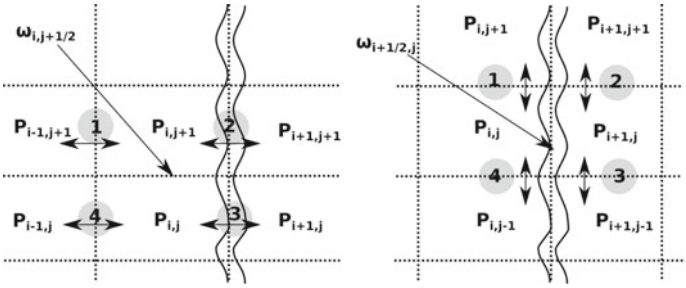

(a) Stencil for $\omega_{i,j+1/2}$ **(b)** Stencil for $\omega_{i+1/2,j}$

Fig. 1 Stencils for evaluation of the anti-diffusion control parameter ω. **a** On horizontal interfaces. **b** On vertical interfaces

where the anti-diffusion term $\mathbf{A_{HLLC}}$ can be written as,

$$\mathbf{A_{HLLC}} = \begin{cases} S_L(\mathbf{U_{*L}}^{HLLC} - \mathbf{U}_*^{HLL}), & \text{if } S_L \leq 0 \leq S_M \\ S_R(\mathbf{U_{*R}}^{HLLC} - \mathbf{U}_*^{HLL}), & \text{if } S_M \leq 0 \leq S_R \end{cases} \tag{10}$$

where, S_M is the estimated speed of the contact and shear wave and can be obtained as suggested in [14]. Since this anti-diffusive term is responsible for triggering shock instability [15], a pressure-ratio based control parameter ω is introduced in order to control this term in the vicinity of strong normal shocks. The control parameter ω is given as,

$$\omega_{i,j+1/2} = \min_k(f_k), \quad k = 1...4 \tag{11}$$

The term f_k denotes a pressure-ratio based function that uses a predefined stencil around a particular interface as shown in Fig. 1a. At any interface k, f_k is defined as,

$$f_k = \min\left(\frac{p_R}{p_L}, \frac{p_L}{p_R}\right)_k^5 \tag{12}$$

We term the resulting scheme as HLLC-CPS-Z (**Z**ha-Bilgen split). We note that an HLLC-CPS-A and an HLLC-CPS-T can also be constructed in similar fashion by starting, respectively, with the AUSM-type or the Toro-Vazquez-type flux splittings although we choose not to discuss them presently. In the next section, we test the HLLC-CPS-Z scheme for its accuracy on linearly degenerate waves and robustness against numerical shock instability.

3 Results and Discussions

3.1 Subsonic Laminar Flow Over a Flat Plate

A $M = 0.1$ laminar flow over a flat plate is used as a test case to demonstrate the capability of the proposed HLLC-CPS-Z scheme to satisfactorily resolve a shear dominated viscous flow. The domain is divided into 31×33 Cartesian cells with fifteen cells retained in the boundary layer. Viscous fluxes are discretized using simple averaging. The CFL number is taken to be 0.7. In Fig. 2, we plot the normalized longitudinal velocity profiles ($\frac{u}{u_\infty}$) against the Blasius parameter $\eta = y\sqrt{u_\infty/\mu L}$. It can be clearly seen that HLLC-CPS-Z scheme has a marked improvement over the HLL-CPS-Z scheme in capturing the boundary layer.

3.2 Two-Dimensional Supersonic Shear Flow

This problem investigates the inviscid contact capturing ability of a given scheme by simulating a fluid system consisting of two different density fluids sliding over each other at different speeds [16]. The top fluid is chosen to have conditions $(\rho, p, M)_{\text{top}} = (1, 1, 2)$ while the bottom fluid is chosen to have conditions $(\rho, p, M)_{\text{bottom}} = (10, 1, 1.1)$. The domain of 1.0×1.0 is coarsely discretized using 10×10 cells. The simulation is run for 1000 iterations using a CFL number of 1.0. All simulations are plain first-order accurate. Figure 3 shows a comparison of the density variation along y-location at the center of the domain. The plot clearly shows that while the HLL-CPS-Z scheme diffuses the interface to an unacceptable level, the proposed HLLC-CPS-Z scheme is able to retain it exactly.

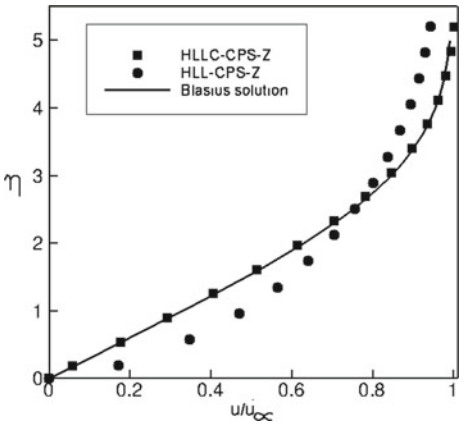

Fig. 2 Comparison of velocity profiles computed by the HLL-CPS-Z scheme and the proposed HLLC-CPS-Z scheme for a $M = 0.1$ laminar flow over a flat plate

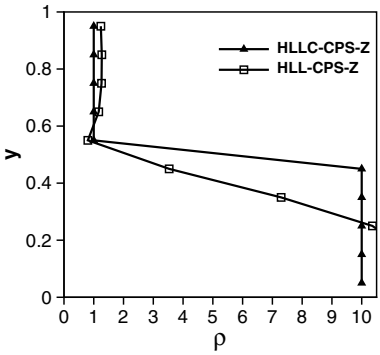

Fig. 3 Variation of density along the *y*-direction at the center of the domain in the two-dimensional supersonic shear flow

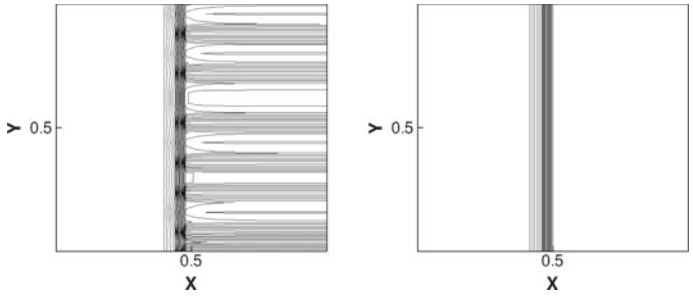

(a) HLL-CPS-Z **(b)** HLLC-CPS-Z

Fig. 4 Results for $M = 7$ standing shock instability problem

3.3 Standing Shock Instability

This simple test case evaluates the ability of a numerical scheme to compute an isolated normal shock front without allowing random perturbations to grow and distort the initial shock structure or produce contaminated post-shock values [17]. A normal shock of strength $M = 7$ is located in the middle of an unit-dimensional domain divided into 26×26 Cartesian cells. The CFL number is 0.5. First-order solution is sought. Figure 4 shows thirty density contour lines equally spanning values from 1.0 to 7.4 for this experiment at t = 50 units. From the figure, it is evident that HLL-CPS-Z scheme produces this variant of shock instability while the HLLC-CPS-Z scheme is completely free of this.

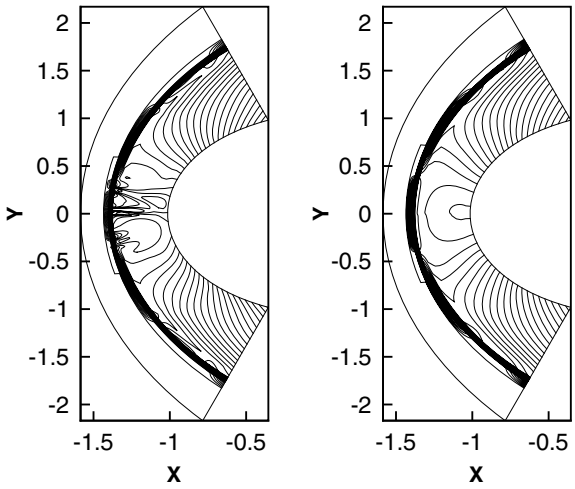

(a) HLL-CPS-Z **(b)** HLLC-CPS-Z

Fig. 5 Results for $M = 20$ supersonic flow over a blunt body problem

3.4 Supersonic Flow Over Bluntbody

This problem investigates the susceptibility of the numerical scheme to produce the dreaded "Carbuncle" phenomenon. A unit-dimensional cylinder is placed in a $M = 20$ inviscid flow with free stream conditions chosen as $(\rho, u, v, p) = (1.4, 20.0, 0.0, 1.0)$. The computational mesh consists of 320×40 body-fitted structured quadrilateral cells in circumferential and radial directions, respectively. To trigger the instability, the centerline grid is perturbed to the order of 10^{-3}. The CFL number for the computation is taken to be 0.5 and First-order simulation is run for 20,000 iterations. The results showing twenty density contours equally spanning value from 1.4 to 8.5 are shown in Fig. 5. The contours clearly show the presence of instability in the HLL-CPS-Z scheme while the HLLC-CPS-Z scheme is completely free of it.

4 Conclusions

In this paper we propose a novel approximate Riemann solver called the HLLC-CPS-Z scheme for robust and accurate computation of high speed flows. The proposed scheme is primarily based on the Convective-Pressure split (CPS) strategy wherein the total Euler flux is split into a convective and pressure systems. The resulting convective and pressure systems are discretized similar to the HLL-CPS scheme [9]. However, for resolving contact and shear waves accurately, we introduce an HLLC-type anti-diffusive term to the pressure system in contrast to the numerical dissipation tuning employed by the HLL-CPS scheme. This anti-diffusive term

is also selectively controlled near strong shocks using a pressure-ratio-based control parameter to prevent the occurrence of numerical shock instability. Numerical results demonstrate that the HLLC-CPS-Z scheme possesses superior accuracy on linearly degenerate waves while displaying high robustness against numerical shock instability.

References

1. Roe P (1981) Approximate Riemann solvers, parameter vectors, and difference schemes. J Comput Phys 43:357–372
2. Harten A, Lax PD, van Leer B (1983) On upstream differencing and Godunov-type schemes for hyperbolic conservation laws. SIAM Rev 25:35–61
3. Toro EF, Spruce M, Speares W (1994) Restoration of the contact surface in the HLL-Riemann solver. Shock Waves 4:25–34
4. Pandolfi M, DâAmbrosio D (2001) Numerical instabilities in upwind methods: analysis and cures for the carbuncle phenomenon. J Comput Phys 166:271–301
5. Liou MS, Steffen CJ (1993) A new flux splitting scheme. J Comput Phys 107:23–39
6. Zha G-C, Bilgen E (1993) Numerical solutions of Euler equations by using a new flux vector splitting scheme. Int J Numer Methods Fluids 144:115–144
7. Liou MS (2010) The evolution of AUSM schemes. Def Sci J 60(6):606–613
8. Shima E, Kitamura K (2011) Parameter-free simple low dissipation AUSM-family scheme for all speeds. AIAA J 49(8):1690–1709
9. Mandal J, Panwar V (2012) Robust HLL-type riemann solver capable of resolving contact discontinuity. Comput Fluids 63:148–164
10. Sun M, Takayama K (2003) An artificially upstream flux vector splitting scheme for the euler equations. J Comput Phys 189(1):305–329
11. Xie WJ, Hua L, Sha P, Tian ZY (2015) On the accuracy and robustness of a new flux splitting method. Acta Phys Sin 64
12. Mandal J, Sharma V (2015) A genuinely multidimensional convective pressure flux split Riemann solver for Euler equations. J Comput Phys 297:669–688
13. Kitamura K A further survey of shock capturing methods on hypersonic heating issues. 21st AIAA computational fluid dynamics conference, San Diego, CA, pp 1–21
14. Batten P, Clarke N, Lambert C, Causon DM (1997) On the choice of wavespeeds for the HLLC riemann solver. SIAM J Sci Comput 18:1553–1570 Nov.
15. Simon S, Mandal J (2018) A cure for numerical shock instability in HLLC Riemann solver using antidiffusion control. J Comput Phys 174:144–166
16. Wada Y, Liou M-S (1997) An accurate and robust flux splitting scheme for shock and contact discontinuities. SIAM J Sci Comput 18:633–657
17. Dumbser M, Moschetta JM, Gressier J (2004) A matrix stability analysis of the Carbuncle phenomenon. J Comput Phys 197:647–670

Numerical Investigation of Flow Through a Rotating, Annular, Variable-Area Duct

Palak Saini, Sagar Saroha, Shrish Shukla and Sawan S. Sinha

Abstract We perform computational fluid dynamic simulations of a compressible fluid through a rotating annular variable-area duct. The objective of this study is to understand the influence of rotation on flow separation and development of vortical structures inside the duct. We solve steady Navier–Stokes equations over the domain with respect to a frame attached to the rotating duct itself. In this frame, influence of rotation on the flow field is captured by adding a rotation-dependent body force (centrifugal force). An approximately defined Froude number (ratio of inertial to body forces) is used as a simulation parameter to identify and understand the role of rotation on flow dynamics. As body force increases, the Froude number decreases. The findings of this study are employed to explain the low-load behavior of steam in power plant turbines.

Keywords Separated flow · Nozzle flow · Rotating duct

1 Introduction

With the increasing use of renewable sources of energy and their time-varying energy output, grid demand for steam-power plants is becoming increasingly more variable [1]. This poses a severe constraint on conventional power plants to operate frequently and over prolonged duration at small fractions of the design output power (the so-called low-load operation).

Stator and rotor blades of a steam turbine are designed to work under favorable pressure gradient fields. Low-load operation of turbine involves a low throughput mass flow rate. However, angular velocity of the rotor has to be maintained constant to match the grid frequency. Under such conditions, the flow field inside a turbine rotor is found to be associated with a complex vortical structure around the rotor

P. Saini (✉)
Department of Aerospace Engineering, PEC University of Technology, Chandigarh 160012, India
e-mail: palaksaini.beaero14@pec.edu.in

S. Saroha · S. Shukla · S. S. Sinha
Department of Applied Mechanics, Indian Institute of Technology Delhi, New Delhi 110016, India

B. N. Singh et al. (eds.), *Recent Advances in Theoretical, Applied, Computational and Experimental Mechanics*, Lecture Notes in Mechanical Engineering,
https://doi.org/10.1007/978-981-15-1189-9_35

blades. Vigorous action of viscous heating within these vortical zones leads to high temperature which can be detrimental for blade material and can cause severe damage to the turbine. Thus, for safe and economically viable operations of modern steam turbines at low-load conditions, it is imperative to investigate and understand the origin and the behavior of the vortical structures that develop under low-load conditions inside a turbine rotor.

Probably the work of Ref. [2] is the first published report in open literature on low-load behavior of steam turbines. Subsequently, several other experimental studies have been reported on the subject. Reference [3] performed a series of experiments on single- as well as multi-stage steam turbines and demonstrated the occurrence of vortices under low-load conditions. Reference [4] performed detailed measurements of the flow field inside low-pressure steam turbine. Reference [5] conducted measurements on a four-stage model air turbine and confirmed the presence of vortices and associated recirculation zones. Recently Ref. [6] has conducted measurements of the flow field in a 7-stage model high-pressure (HP) steam turbine blading in order to develop better understanding of part and low-load operation of HP steam turbines.

In recent years, several researchers have also attempted to numerically simulate low-load behavior of steam turbines. References [7, 8] employed a finite element (FE) procedure to numerically simulate the steam flow in the meridional plane of a turbine cylinder. They further simulated several cases with mass flow rate as low as 20% of the design value and demonstrated good agreement of their results with the corresponding experimental measurements. Reference [9] proposed a through-flow code based on the primary variable method and reached up to 6.1% of design mass flow rate. Reference [10] presented a full three-dimensional computational fluid dynamic (CFD) analysis of a two-stage low-pressure steam turbine. Reference [11] performed simulations of a four-stage model air turbine during low-load operation. Reference [1] performed an extensive three-dimensional CFD study employing Reynolds-Averaged Navier–Stokes (RANS) equations in conjugation with several turbulence models, and specifically studied temperature field under low-load conditions.

Indeed, these studies have provided convincing evidence of the existence of complex vortical structures and associated pressure and temperature fields around turbine rotor blades under low-load conditions. However, the studies have been restricted to some specific turbine designs, and not much attention has been paid to the reasons behind the origin of these vortices. The focus of these studies has been primarily on identifying and visualizing the vortical patterns. Since it is further desirable (i) to have a more clear understanding of the origin of these vortices and (ii) to predict the flow behavior in response to more generalized changes in the geometry of flow passage and the boundary conditions, further research efforts in the form of fundamental studies can prove to be quite useful. Such is the objective of this work.

From a computational point of view, a full three-dimensional CFD simulation which accounts for all details of the rotor blade geometry would be the ideal platform to study and understand the vortical structures in a turbine operating at low-load conditions. However, setting up such simulations is extremely expensive and time consuming. To avoid huge demands in terms of time and resource, and yet make a

useful computational attempt to understand the behavior of steam under low-load conditions, we employ a simplified computational domain. Admittedly, this approach lacks the description of finer details but can be expected to account for the most important and fundamental aspects that characterize the low-load flow inside a turbine rotor.

We model the flow domain inside a turbine rotor as a variable-area annular duct. Flow behavior is studied with respect to a frame attached to the rotor itself. With respect to this frame, fluid particles experience a radially outward centrifugal force, which in our computational setup is represented by a body-force function. This simplified computational domain is conducive for performing simple parametric investigations with parameters such as body-force magnitude, diverging angle of the duct, inlet-to-exit area ratio, mass flow rate, etc. In this paper, we focus specifically on how the magnitude of body force (which characterizes low-load behavior of steam turbines, more on this in next section) affects the generation of vortical structures in the flow field.

Several CFD studies have been previously performed across variable-area duct of various shapes and boundary conditions. Reference [12] conducted a numerical investigation on one over-expanded condition. Reference [13] conducted a numerical study to capture the effect of throat contouring on nonaxisymmetric 2D convergent–divergent nozzles. Hamed et al. performed extensive numerical investigations to study the flow field in over expanded two-dimensional converging–diverging (CD) nozzles. Reference [14] conducted studies with different over-expanded pressure ratios. Later, Ref. [15] compared the thrust predictions with different turbulence models. Reference [16] also conducted a numerical investigation to predict flow fields in vented and unvented supersonic exhaust nozzles for different operating conditions. Reference [17] used a CFD-based optimization system to maximize performance of bell-shaped rocket nozzles. Reference [18] altered the geometry in the post contraction region of a nozzle to investigate how the exit flow characteristics change. Reference [19] investigated gas flows in micro-nozzles under both slip and no-slip boundary conditions. Reference [20] performed numerical simulations on under-expanded sonic jets issuing from nozzles having different inlet geometries.

Numerous computational investigations have been performed on the effect of divergence angle on the flow field in two-dimensional axisymmetric models as well [21, 22]. Reference [23] investigated the effect of nozzle pressure ratio. Reference [24] studied the influence of inlet Mach number, whereas Ref. [25] investigated the influence of the geometry of nozzle. While all these studies have contributed significantly to our understanding of compressible flow through nozzle, one aspect of nozzle flow that has not been addressed adequately is the influence of rotor body force on the nozzle. Thus, the presented work not only has the potential to help us understand the behavior of flow in a practical problem of interest (turbines under low-load conditions) discussed earlier, it also contributes directly to the otherwise continuing pursuit of better understanding of flow through a variable-area duct in the presence of body force. To the best of authors' knowledge, influence of a radially varying body force on an annular variable-area nozzle has not been studied. The presented work attempts to address this subject.

This paper is organized into five sections. In Sect. 2 we describe the flow domain considered in this work and justify how despite its simplicity, the domain still retains the fundamental aspects of the actual flow through a steam turbine rotor under low-load conditions. In Sect. 3 we present the governing equations. This is followed by Sect. 4 which contains the results and discussions.

Section 5 presents major conclusions of the study.

2 Computational Domain

Figure 1 shows a schematic diagram of our computational domain. It is an 8 m long annular duct. As one moves downstream, the radius of inner wall first increases for 0.5 m, and then remains constant throughout the length of the duct. The radius of the outer wall in the first part of the duct decreases making it a converging passage. Downstream of the minimum cross-sectional area, radius of the outer wall increases for 2 m. Subsequently in the third part, the cross-sectional area remains constant. A two-dimensional axisymmetric geometry of fluid domain is created using Geometry Workbench of ANSYS ^{R}. The axis boundary condition is used at the centerline of the flow domain to reduce the computational time. All boundaries of the annulus are defined as adiabatic no-slip walls. The inlet boundary condition is set as mass flow inlet. A pressure-outlet boundary condition is assigned to the outlet boundary.

The computational grid is generated using the ANSYS ^{R} Meshing module. In this work we perform simulations using several grids. These grids differ in terms of number of elements. Computational domain is meshed using quadrilateral elements with map scheme. Table 1 summarizes the details of the simulations performed in this study. The optimal refinement of the computational grids is examined to ensure that the solution is independent of the mesh element count. Uniform node count in the cross stream direction led to denser grid in the region near the throat. For simulations 1–4, a grid with 2.3 * 10^4 elements was employed. For simulation 5, grid with

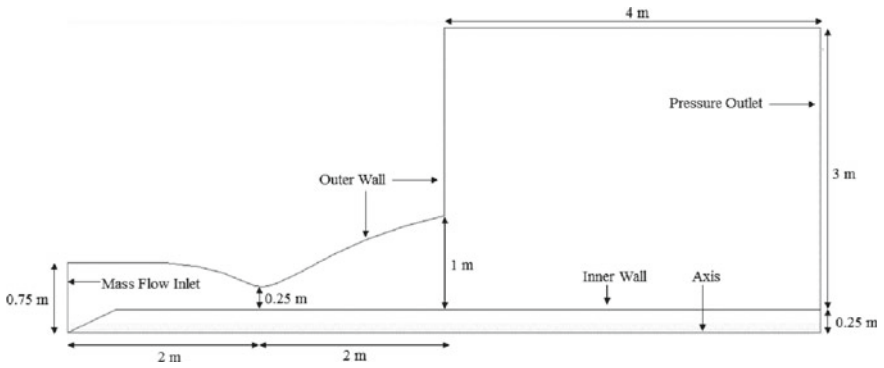

Fig. 1 Geometry of the computational domain and the related boundary conditions

Table 1 Details of simulations

Simulation	1	2	3	4	5
Froude number (F)	∞	0.47	0.21	0.16	∞

9.4 * 10^4 elements was employed. Results of simulations 1 and 5 are studied for performing a grid convergence study. Grids 2–4 are used to perform study on the influence of body force on nozzle flow.

3 Equations

The governing equations of the flow field under consideration are the continuity, radial, and axial momentum equations along with the energy and state equations of a perfect gas. These equations are written with radial (r) and axial (x) coordinates as the independent variables:

$$\frac{\partial(\rho v_x)}{\partial x} + \frac{\partial(\rho v_r)}{\partial r} + \frac{\rho v_r}{\partial r} = 0 \tag{1}$$

$$\frac{1}{r}\frac{\partial}{\partial x}(r\rho v_x v_x) + \frac{1}{r}\frac{\partial}{\partial r}(r\rho v_r v_x) = -\frac{\partial p}{\partial x} + \frac{1}{r}\frac{\partial}{\partial x}\left[r\mu\left(2\frac{\partial v_x}{\partial x} - \frac{2}{3}(\nabla \cdot V)\right)\right] + \frac{1}{r}\frac{\partial}{\partial r}\left[r\mu\left(\frac{\partial v_x}{\partial r} + \frac{\partial v_r}{\partial x}\right)\right] \tag{2}$$

$$\frac{1}{r}\frac{\partial}{\partial r}(r\rho v_r v_r) + \frac{1}{r}\frac{\partial}{\partial x}(r\rho v_r v_x) = -\frac{\partial p}{\partial r} + \frac{1}{r}\frac{\partial}{\partial r}\left[r\mu\left(2\frac{\partial v_r}{\partial x} - \frac{2}{3}(\nabla \cdot V)\right)\right] + \frac{1}{r}\frac{\partial}{\partial x}\left[r\mu\left(\frac{\partial v_x}{\partial r} + \frac{\partial v_r}{\partial x}\right)\right] - \frac{2}{3}\mu\frac{v_r}{r^2} + \frac{2}{3}\frac{\mu}{r}(\nabla \cdot V) + Cr \tag{3}$$

$$\frac{1}{r}\frac{\partial}{\partial r}\left[r\left(\rho C_v T v_r + \rho_r v_r - v_r\left[2\mu\frac{\partial v_r}{\partial r} + \frac{2}{3}\mu\left(\frac{1}{r}\frac{\partial(r v_r)}{\partial r} + \frac{\partial v_x}{\partial x}\right)\right] - v_x\mu\left(\frac{\partial v_x}{\partial r} + \frac{\partial v_r}{\partial x}\right) - k\frac{\partial T}{\partial r}\right)\right] + \frac{\partial}{\partial x}\left[\left(\rho C_v T v_x + \rho_x v_x - v_x\left[2\mu\frac{\partial v_x}{\partial x} + \frac{2}{3}\mu\left(\frac{1}{r}\frac{\partial(r v_r)}{\partial r} + \frac{\partial v_x}{\partial x}\right)\right] - v_r\mu\left(\frac{\partial v_x}{\partial r} + \frac{\partial v_r}{\partial x}\right) - k\frac{\partial T}{\partial x}\right)\right] = 0 \tag{4}$$

$$\rho = \frac{P}{RT} \tag{5}$$

The symbols p, ρ, T represent pressure, density, and temperature of the fluid, respectively. v_x and v_r are the axial and radial components of velocity, respectively. Fluid is taken to be an ideal gas with a specific heat ratio of 1.4 and gas constant R as 287 J/kg-K. The last term in the radial momentum Eq. (3) is the body force per unit volume. The body force is taken to be proportional to the radius with C being a constant for a simulation. This form of the radial force accurately captures the variation of centrifugal acceleration experienced by fluid particles passing through a turbine. Since the governing equations are written with respect to the rotor frame, the body force appears as a pseudo force.

The outward radial direction of the force represents the rotating effect of the annular duct on the flow. In continuum mechanics, the Froude number is a dimensionless number defined as the ratio of the flow inertia to the external field. Froude number will play a significant role whenever there is a significant body force. In this case the Froude number appears because of the centripetal force. In accordance with the computational setup of this work, Froude number (F) of the flow can be defined using various geometric and boundary parameters in the following manner:

$$F = \frac{\dot{m}}{A\sqrt{\rho LC\sqrt{A}}} \tag{6}$$

where $\dot{m}$ is the mass flow rate through the duct, L is the inlet radius, A is the inlet area, ρ is the density at the inlet, and C is the coefficient of body force per unit volume. The quantity C actually represents the magnitude of angular velocity of the rotor. With Froude number being inversely proportional to the coefficient C, an increase in the value of C results into a decrease in Froude number and equivalently an increase in the influence of body force on flow dynamics. The limiting case of C being zero (no body force) implies an infinite value of Froude number. Similarly, relevant geometrical and boundary parameters can be used to define a representative Reynolds number as well:

$$\mathrm{Re} = \frac{\dot{m}L}{A\mu} \tag{7}$$

Low-load operation of steam turbines involves mass flow rates which are small fractions of the design mass flow rate while the rotation rate of the rotor remains the same as that at designed condition. With the derived expression for the Froude number (6), it is clear that the low-load flow through a steam turbine can be characterized by low values of Froude number itself. Thus to systematically understand low-load behavior of flow through turbines, in this work, we perform several simulations with varying Froude number. A summary of these simulations is presented in Table 1.

The commercial software ANSYS ^{R} FLUENT is used to obtain the numerical solution to the two-dimensional compressible Navier–Stokes equations, in general, curvilinear coordinates (x, r). Rest of the flow modeling details have been taken from a previous study done at IIT Delhi [26, 27]. Three convergence criteria were used to ensure that the results were accurate. First, the convergence criteria for all residuals were set to 10^{-6}. In addition to this, the net mass flux was monitored to ensure that there was no imbalance. Finally, primary variables (velocity, density and pressure) were monitored through the iterations at inlet and exit to ensure that they reached a steady value.

4 Results and Discussion

Our study is based on several simulations performed with Froude number as parameter. Description of these simulations is provided in Table 1. All these simulations are performed with identical mass flow rates (25 kg/s) specified at the inlet of the nozzle. Reynolds number in each simulation is 1.7×10^5.

Before employing our results to understand the underlying physics, we have subjected all our results to extensive grid convergence studies. Here, we present comparisons for zero-force case (Simulation 1 and 5) only. Case 1 and Case 5 are identical in all aspects except the grid. Case 5 simulation is performed with a grid element size that is smaller than that of Case 1. In Figs. 2 and 3 we present streamlines and pressure contours from Case 1 and 5 simulations. Close agreement is seen between results of the two simulations. Based on our convergence studies, we deem the mesh size with 2.3×10^5 elements adequate for our study. All the remaining results in this paper have been obtained with this finer mesh. In the following sections, we first study the general flow characteristics with zero body force. Subsequently, the influence of varying Froude number on the flow is studied.

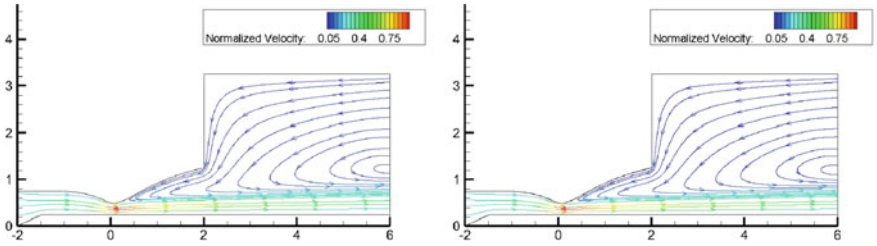

Fig. 2 Streamlines colored by normalized velocity magnitude

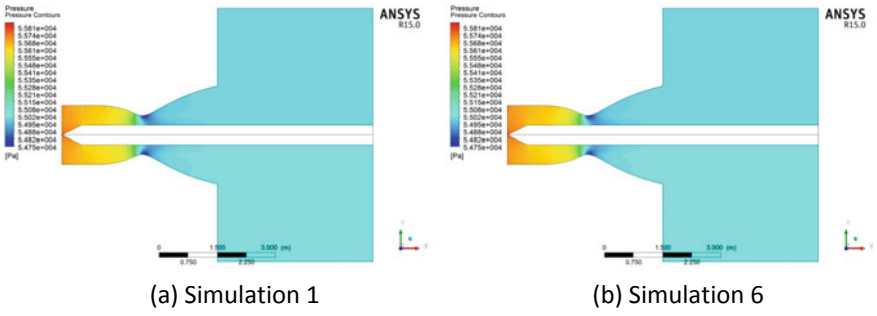

Fig. 3 Pressure contours

4.1 General Flow Characteristics with Zero Body Force

In simulation case 1 which represents our baseline case without any body force, the flow accelerates in the converging portion, remains subsonic at the throat and subsequently decelerates in the diverging portion. Further, in the diverging section of the nozzle, the primary flow separates from the outer nozzle wall and forms a recirculation zone. However, the primary flow remains attached to the inner wall throughout the flow domain and maintains a predominantly axial direction.

Significant variations in pressure are only shown by the primary flow in the variable-area part of the duct. In the constant area duct pressure is almost the same as that in the ambience. At the outlet boundary of the flow domain, backflow occurs. A recirculation zone with very low velocities is formed here. The recirculating flow enters at farther radial locations (near the exit wall) and joins the primary flow stream at smaller radial locations. With this simulation as our base case study, in the next section we discuss how this flow is influenced by varying Froude number.

4.2 Influence of Varying Body Force

In Fig. 4a, c, e, we present streamlines from simulations 2, 3, and 4. We observe that as the Froude number increases the streamlines patterns in the diverging and constant area sections of the domain become increasingly different as compared to simulation 1 (Figs. 2 and 3). The most prominent difference between simulation 1 on one hand and simulations 2, 3, and 4 on the other hand is the detachment of flow from the inner wall. Further, these detached streamlines undergo a steep turn in radially outward direction. The detachment and the subsequent radial turn are associated with the formation of a large recirculation zone in the constant area duct. In this recirculation zone, the flow enters the nozzle from ambience near the inner wall and tends to exit back into the ambience near the outer walls of the nozzle.

Increasing the body force further (Simulations 3 and 4) detachment at the inner wall happens at an earlier upstream location, and the size of the recirculation bubble existing downstream becomes larger. Note that the backflow direction in simulation cases 2, 3, and 4 has completely reversed as compared to Case 1. The backflow enters the outlet at smaller radial locations and exits to ambience at farther radial locations.

In Fig. 4b, d, f, we present pressure contour plots from simulations 2, 3, and 4. On application of body force, we see that the pressure decreases slightly in the converging part and then increases while passing through the divergent section. As the magnitude of body force is increased, the pressure change associated with the flow through the variable area part of the duct looks insignificant, when compared with the large pressure variations seen as one moves radially outward in the constant area duct. The pressure variations propagate to farther radial locations. Unlike our base case, the pressure does not stay constant in the constant area duct. It shows lower values near the annulus and increases as one moves farther away from the axis. Due to

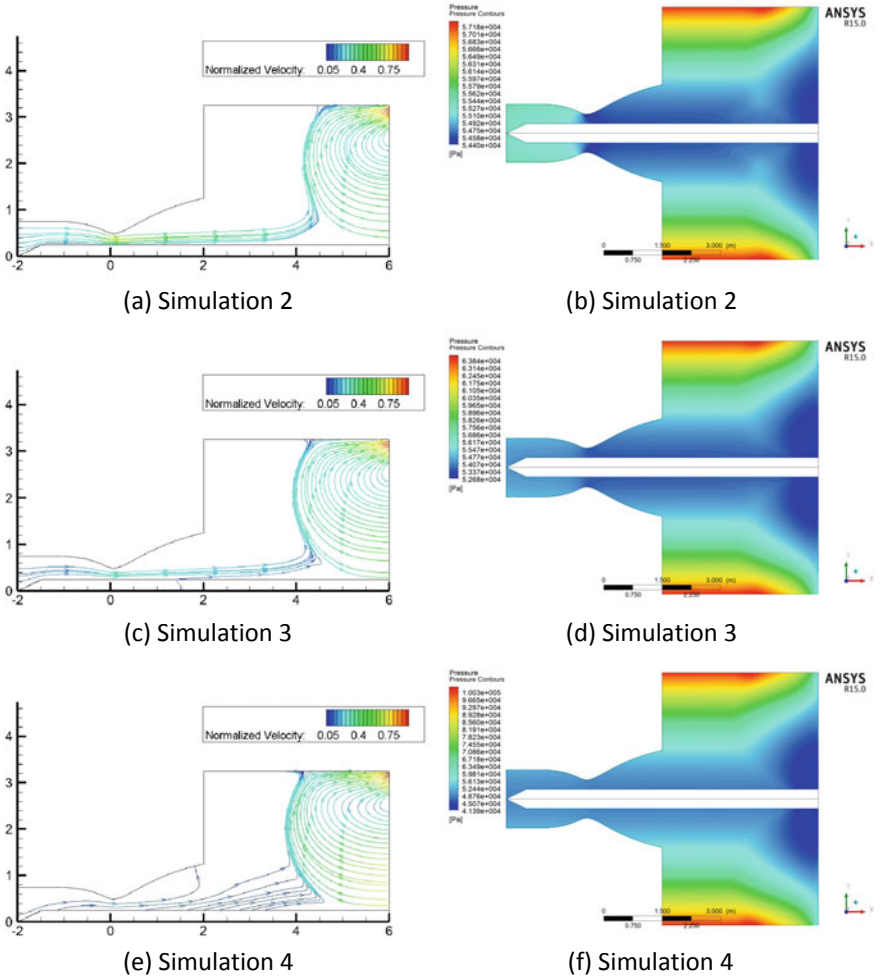

Fig. 4 Streamlines colored by normalized velocity magnitude (**a**, **c**, **e**) and pressure contours (**b**, **d**, **f**) for simulations 2, 3, and 4

the deflection induced by larger body force, the fluid tends to move radially outward. The acceleration of the flow in a direction away from the axis causes the pressure to drop in the vicinity of the annulus. The obstruction offered by the wall stagnates the flow, thus explaining the reason for the higher pressures observed near the outer walls.

In summary, our results clearly show that the Froude number has profound effects on the flow pattern inside an annular nozzle. As the Froude number decreases, the flow characteristics start following a trend. In successive simulations, as the magnitude of body force increases (i) the primary flow shows a clear tendency to separate from the inner annulus wall, (ii) the separation point at the inner wall moves upstream,

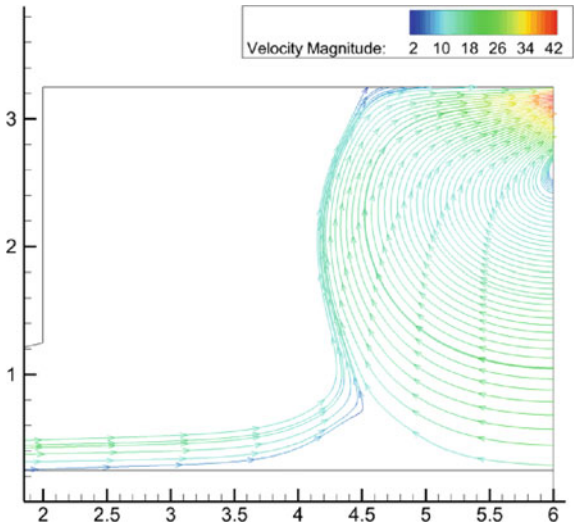

Fig. 5 Zoomed in view of streamlines near the outlet boundary

(iii) the tendency of the primary flow to turn radially outward becomes stronger, (iv) magnitude of velocity in the recirculation zone becomes larger and (iv) pressure near the outer annulus wall becomes larger.

These observed changes in the flow field can be explained as follows. As the Froude number decreases, a fluid particle is subjected to more intense radial acceleration, which in turn leads to the development of substantial radial velocity in the diverging/constant area section of the nozzle. This substantial radial velocity makes the flow detach from the inner nozzle wall creating a recirculation zone near the inner wall wherein flow enters the nozzle from outlet ambiance. As the primary flow in the diverging and constant area section of the nozzle is forced to become radial over the bulk of the nozzle cross section, it can now exit the nozzle axially only through a thin annular area adjacent to the outer wall of the nozzle (see Fig. 5). This behavior of the primary flow is akin to what has been observed in full three-dimensional CFD simulations and experiments performed on steam turbines (Fig. 11 of Ref. [1]). Thus the study presented in this paper seems to provide a plausible explanation of the steam behavior in turbines under severe low-load conditions.

5 Conclusions

We perform a computational fluid dynamics-based study to investigate the influence of a radial body force on the flow through an annular duct with a converging, diverging, and constant area parts. The body force is taken to be proportional to radial location so that it correctly represents the centrifugal acceleration experienced by a fluid particle when the flow is observed with respect to a reference frame fixed

to the rotor. The motivation behind choosing such a canonical domain is to isolate, identify, and understand the influence of a radially-dependent body force on the flow pattern through a variable-area duct. This study in turn is expected to aid in explaining the flow behavior in steam turbines working under severe low-load conditions, which is indeed characterized as a low-Froude number flow. Our simulations show that as the magnitude of body force increases, the pattern of streamlines gets substantially modified in the diverging and the constant area parts of the nozzle. The presence of a radially outward body force induces severe separation tendency near the inner nozzle wall. This behavior is in stark contrast to the separation induced by high-divergence angle, which happens at the outer wall of ducts. We find that in our simulations streamlines turn radially outward leading to the formation of a large recirculation zone near the exit of the constant area section. As the strength of body force increases, the separation from the inner walls occurs further upstream and the size of the recirculation zone increases. This behavior is akin to the flow pattern observed in experiments on steam turbine rotors and also in full three-dimensional CFD simulations of the flow over the exact rotor geometry. Thus, despite having employed a relatively simple flow domain, the study seems to successfully isolate and identify the essential body force influences which are responsible for the development of flow separation and a massive recirculation zone near the rotor exit of steam turbines operating under low-load conditions. The authors believe that the results of this study make a strong case for the viability of further employing the presented flow domain to perform detailed studies of the influence of other parameters like duct divergence angle, viscosity, etc. on rotating annular flows. These parameters will be the subjects of our future work.

References

1. Sigg R, Heinz C, Casey MV et al (2009) Numerical and experimental investigation of a low-pressure steam turbine during windage. Proc Inst Mech Eng, Part A: J Power Energy 223:697708
2. Lagun VP, Simoyu L, Frumin YZ et al (1971) Distinguishing features of operation of lpc last stages at low loads and under no-load conditions. Therm Eng 18(2):30
3. Evers H (1985) Flow patterns during windage operation of a single stage and multi stage model turbine
4. Schmidt D, Reiss W (1999) Steady and unsteady flow measurements in the last stages of lp steam turbines, vol 1, p 723734
5. Kang G, Seume JR, Gndogdu Y et al. (2005) Development of a measuring technique for the investigation of windage phenomena in a four-stage air turbine vol 1, p 3136
6. Binner M, Seume JR (2014) Flow patterns in high pressure steam turbines during low-load operation. J Turbomach 136(6)
7. Petrovic M, Reiss W (1995) Through-flow calculation in axial flow turbines at part load and low load. Vdi Berichte 1185:309309
8. Petrovic M, Riess W (1997) Off-design flow analysis of low-pressure steam turbines. Proc Inst Mech Eng, Part A: J Power Energy 211:215224
9. Liu B, Chen S, Martin HF (2000) A primary variable throughflow code and its application to last stage reverse flow in lp steam turbine, p 2326

10. Lampart P, Puzyrewski R (2006) On the importance of adaptive control in extraction/condensing turbines. In: ASME turbo expo 2006: power for land, sea, and air. American Society of Mechanical Engineers, pp 893–901
11. Herzog N, Binner M, Seume J et al (2007) Verification of low-flow conditions in a multi-stage turbine. In: ASME turbo expo 2007: power for land, sea, and air. American Society of Mechanical Engineers, pp 563–574
12. Shieh C (1988) Navier-stokes solutions of transonic nozzle flow with shock-induced flow separations. In: 1st national fluid dynamics conference
13. Zha G-C, Bilgen E (1992) Effect of throat contouring on two-dimensional converging-diverging nozzles using urs method. In: AIAA Applied Aerodynamics Conference, 10 th, Palo Alto, CA, Technical Papers. Pt. 1, 22(24)
14. Hamed A, Vogiatzis C (1995) Assessment of turbulence models in overexpanded 2d-cd nozzle flow simulations. In: 31st joint propulsion conference and exhibit
15. Hamed A, Vogiatzis C, Hamed A et al (1997) Three dimensional flow computations and thrust predictions in 2dcd overexpanded nozzles. In: 35th aerospace sciences meeting and exhibit
16. Hamed A, Yeuan J, Liang T et al (1998) 3-d navier-stokes simulation of turbulent after-body/nozzle flows. In: 36th AIAA aerospace sciences meeting and exhibit, p 964
17. Shebalin J-P, Tiwari S (2001) Noz-op-2d—a cfd-based optimization system for axially symmetric rocket nozzles. In: 39th aerospace sciences meeting and exhibit
18. Yu Y, Shademan M, Barron RM et al (2012) Cfd study of effects of geometry variations on flow in a nozzle. Eng Appl Comput Fluid Mech 6(3):412425
19. Lin CX, Gadepalli VVV (2009) A computational study of gas flow in a de-laval micronozzle at different throat diameters. Int J Numer Meth Fluids 59(11):12031216
20. Menon N, Skews B (2009) Effect of nozzle inlet geometry on underexpanded supersonic jet characteristics. Shock Waves 955960
21. Pandey KM, Singh AP (2010) Cfd analysis of conical nozzle for mach 3 at various angles of divergence with fluent software. Int J Chem Eng Appl IJCEA 179185
22. Biju Kuttan P, Sajesh M (2013) Optimization of divergent angle of a rocket engine nozzle using computational fluid dynamics. Int J Eng Sci (IJES) 2(2):196207
23. Ekanayake S, Gear JA, Ding Y (2010) Flow simulation of a two dimensional rectangular supersonic convergent divergent nozzle. ANZIAMJ J 51:377
24. Alam MA, Setoguchi T (2012) Effect of inflow conditions on under-expanded supersonic jets. Int J Eng Appl Sci (IJEAS) 4(1):1730
25. Li D, Xia G, Merkle CL (2003) Analysis of real fluid flows in converging diverging nozzles. AIAA Paper 4132
26. Shukla S, Mishra R, Sinha SS et al (2016) Numerical investigation of flow through steam turbines using the mixing plane method. Int Congr Comput Mech Simul 6:323–326
27. Shukla S, Mishra R, Sinha SS et al (2016) Influence of thermal boundary conditions on initiation of compressor mode in steam turbines. In: Proceedings of the 6th international and 43rd national conference on fluid mechanics and fluid power

Development of M–DSMC Numerical Algorithm for Hypersonic Flows

G. Malaikannan and Rakesh Kumar

Abstract This paper demonstrates the newly developed particle method in the Direct Simulation Monte Carlo (DSMC) framework, and we refer to it as the Maxwellian–DSMC (M–DSMC) method. The M–DSMC solver is utilized for various fluid flow problems with different length scales varied from continuum to transitional regime. The hypersonic flow of argon over a cylinder simulation is carried out using M–DSMC and the same simulation results are compared with the regular DSMC method. The present work shows that the M–DSMC results are quite a good match with the DSMC results. The computational cost is significantly reduced by using M–DSMC method and the same is compared with regular DSMC method.

1 Introduction

In the present work, computational models and associated numerical methods are developed to focus on minimization of the computational cost by instigating effective and robust algorithm. The same aspect has motivated us to develop a simplified DSMC method, which works more efficiently than the regular DSMC method, and is within acceptable limits of accuracy. To this end, there have been some earlier works, which attempted to extend the DSMC method to continuum regime. In these works, researchers had either restricted the number of collisions, or relaxed cell size, time step restrictions, which are typically followed in the regular DSMC method. Breuer et al. [1] utilized the CFL [2, 3] number and artificial viscosity [1] in their work to extend the DSMC method into continuum regime. Lengrand et al. [4] used approximate method to the regular DSMC method, which employs limited number of collisions in a cell for expanding plume flows.

G. Malaikannan (✉)
Department of Aerospace Engineering, SRM Institute of Science and Technology, Chennai, India
e-mail: malaikannan.g@ktr.srmuniv.ac.in; malaikag@srmist.edu.in

R. Kumar
Department of Aerospace Engineering, Indian Institute of Technology Kanpur, Kanpur, India
e-mail: rkm@iitk.ac.in

B. N. Singh et al. (eds.), *Recent Advances in Theoretical, Applied, Computational and Experimental Mechanics*, Lecture Notes in Mechanical Engineering,
https://doi.org/10.1007/978-981-15-1189-9_36

Similar to Lengrand et al. [4], Bartel et al. [5] also used an approximate scheme for the DSMC method to simulate high-density flows through nozzle. Lengrand et al. [4] and Bartel et al. [5] used the collision limiter technique to extend the DSMC method in the continuum regime for expanding flows through nozzle. There have been some works focusing on extending the applicability range of the DSMC method to higher density flows. Pullin [6] developed Equilibrium Particle Simulation Method (EPSM) for compressible inviscid ideal gas flows. Recently, Titov and Levin [7] used the eDSMC method to simulate high-pressure flows, which is also based on the collision limiter scheme.

In order to extend the range of applicability of DSMC approach to higher density near-equilibrium flows, in the present work, we have developed a new approximate method in the DSMC framework, and we refer to it as the Maxwellian–DSMC (M–DSMC) method, which is analogous to the EPSM method [6]. M–DSMC is capable of solving flows ranging from continuum to rarefied regime.

2 Maxwellian–DSMC Approach

The M–DSMC is similar to the regular DSMC [8, 9] method, except the collision modeling part. In contrast to the binary collision modeling of dilute gas flows in the conventional DSMC setup, the collisional modeling is completely done away with in the M–DSMC framework. Instead, the simulated particles are assigned properties sampled from the Maxwellian distribution at the local temperature. It is expected that the simplified calculation procedure for collisions would result in huge savings in the computational cost. The calculation procedure of the M–DSMC method is discussed below.

Particle velocities are averaged over each cell at each time step. The instantaneous particle velocity data in each cell is first averaged out to calculate bulk velocity using Eq. 1.

$$\begin{aligned} u_x &= \frac{\overline{C_x}}{N_c} \\ u_y &= \frac{\overline{C_y}}{N_c} \\ u_z &= \frac{\overline{C_z}}{N_c} \end{aligned} \tag{1}$$

where C_x, C_y, and C_z are the components of particle velocity in x-, y-, and z-directions at a given time; u_x, u_y, *and* u_z are the components of bulk velocity; and *Nc* is the total number of particles in a particular cell at each time step.

On the other hand, the translation kinetic temperature is computed by referring to the equipartition theorem, given as follows:

$$\frac{3}{2}k_B T_{trans} = \frac{1}{2}m\left[\overline{c_x^2} + \overline{c_y^2} + \overline{c_z^2}\right] \tag{2}$$

where T_{trans} is the translational temperature, c_i is the random translational velocity component in the ith direction, and k_B is the Boltzmann constant. Equation 2 can now be rephrased as follows:

$$T_{trans} = m\frac{\left(\overline{C_x^2} - u_x^2\right) + \left(\overline{C_y^2} - u_y^2\right) + \left(\overline{C_z^2} - u_z^2\right)}{3k_B} \tag{3}$$

Thermal velocities are sampled from the Maxwellian distribution at translational temperature, calculated using most probable speed of molecules and random numbers as follows:

$$\begin{aligned} c_x &= \cos(2\pi R_1)\sqrt{-\ln(R_2)} \cdot c_{mps} \\ c_y &= \sin(2\pi R_1)\sqrt{-\ln(R_2)} \cdot c_{mps} \\ c_z &= \cos(2\pi R_3)\sqrt{-\ln(R_4)} \cdot c_{mps} \end{aligned} \tag{4}$$

where, c_x, c_y, and c_z are the thermal velocity components in the x-, y-, and z-directions, R_1, R_2, R_3, *and* R_4 are random numbers, c_{mps} is the most probable speed. Later, particle velocities are obtained by using corresponding thermal velocities and the bulk velocity. The local cell-based most probable speed, c_{mps}, is calculated from the known translational temperature and is given by the following equation:

$$c_{mps} = \sqrt{\frac{2k_B T_{trans}}{m}} \tag{5}$$

The particle velocity components are then obtained as follows:

$$\begin{aligned} C_x &= c_x + u_x \\ C_y &= c_y + u_y \\ C_z &= c_z + u_z \end{aligned} \tag{6}$$

3 Results and Discussion

To validate the M–DSMC numerical algorithm, we have simulated one of the classical fluid flow problems. Hypersonic flow of argon over a cylinder is simulated at two different freestream conditions, and the results are compared with the regular DSMC method. The diagrammatic view of the problem is illustrated in Fig. 1. The freestream parameters for both cases are given in Table 1. Noteworthy is the fact that the two

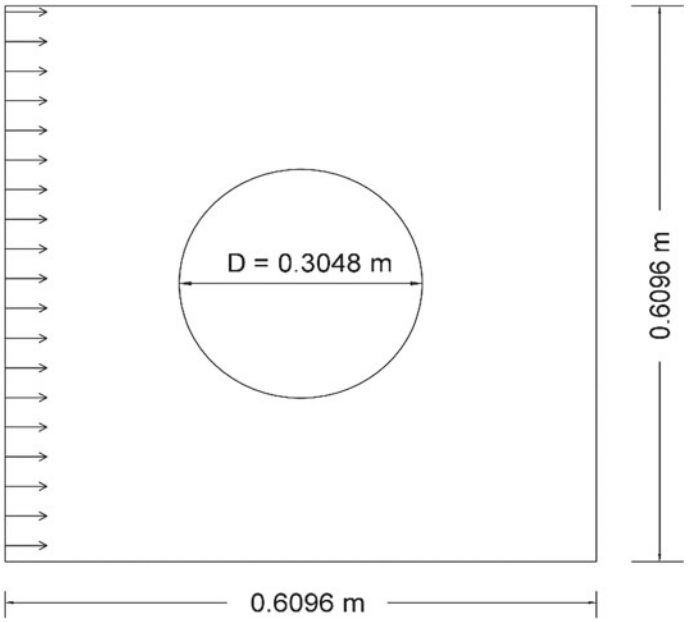

Fig. 1 Schematic diagram of flow of argon at Mach 10 over a cylinder

Table 1 Freestream parameters for hypersonic flow over a cylinder

Freestream parameters	Freestream values (Case-I)	Freestream values (Case-II)
Gas	Argon	Argon
Temperature	200 K	200 K
Number density	4.247E+21 m^{-3}	4.247E+20 m^{-3}
Knudsen number	0.001	0.01
Mach number	10	10
Velocity of gas	2634.5542 m/s	2634.5542 m/s

cases differ only in terms of number density or Knudsen number (based on cylinder diameter). The time step, cell size, and other numerical parameters are set as per the DSMC procedures, and they remain the same for both M–DSMC and DSMC approaches. In both cases, simulation for first 25,000 time steps was done till the system reached steady state, beyond which sampling was done for another 40,000 time steps to give a similar level of statistical error (<3%). The detailed investigation is carried out for both flow and surface properties of the cylinder.

3.1 Flow Properties Variation

Flow properties are obtained for hypersonic flow over a cylinder using M–DSMC at two different global Knudsen numbers (based on the cylinder diameter), and are compared with the in-house DSMC solver. Contour plot of x-component of velocity and temperature are given in Fig. 2, whereas Fig. 3 shows the same properties at a Knudsen number of 0.01, based on cylinder diameter. M–DSMC method is found to clearly capture the strong detached shock and the wake region. The variation of x-component of velocity and temperature across the domain compares well between

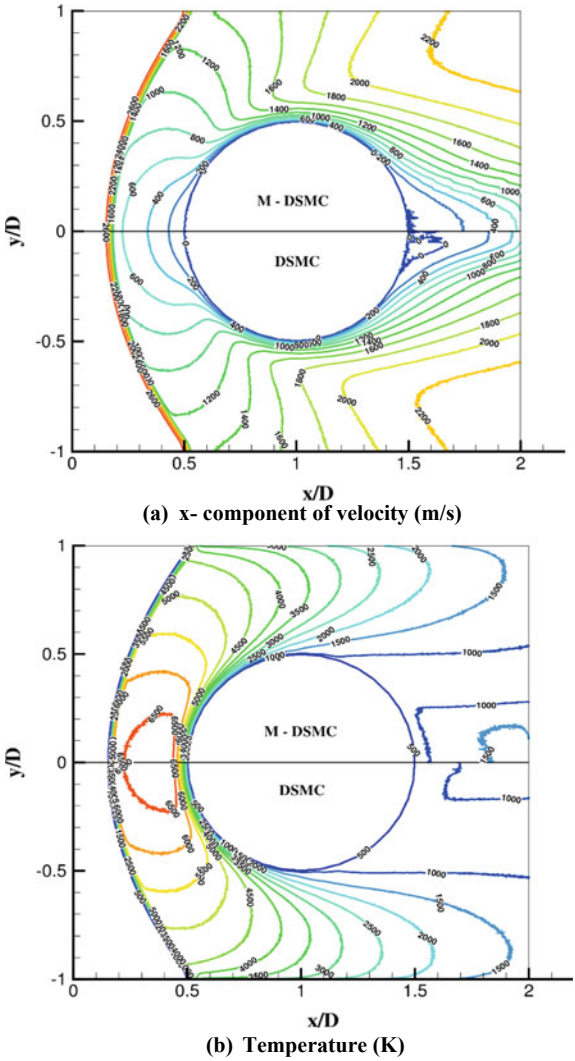

Fig. 2 Comparison of x-component of velocity and temperature contour of DSMC and M–DSMC for flow over a cylinder at a Knudsen number of 0.001

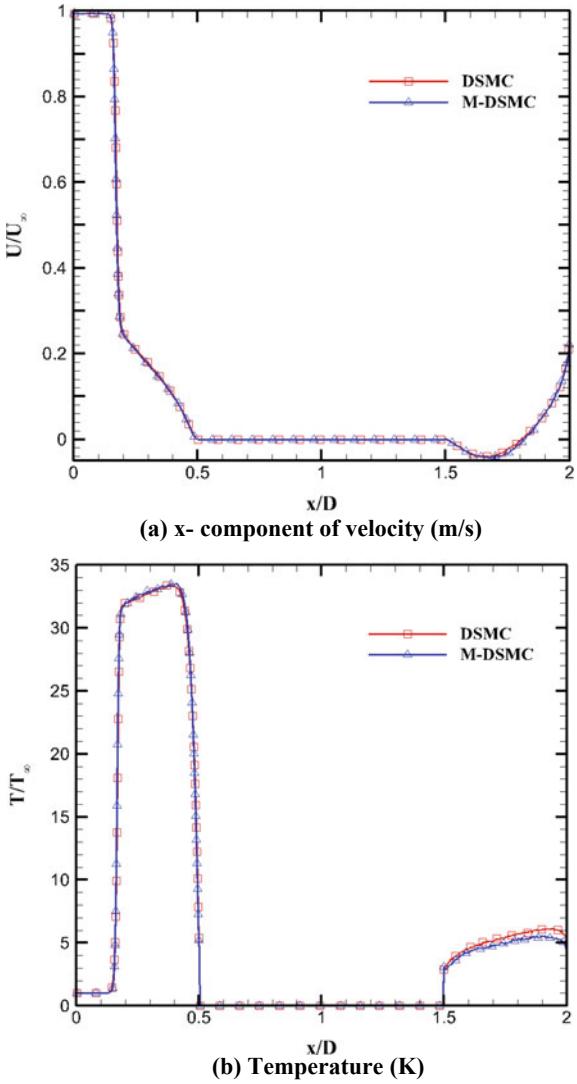

Fig. 3 Comparison of x-component of velocity and temperature contour of DSMC and M–DSMC for flow over a cylinder at a Knudsen number of 0.01

DSMC and M–DSMC methods for both cases. Small deviations can be seen in the wake region, particularly for a Knudsen number of 0.01. This is understandable as the local degree of rarefaction in the wake region is quite large as compared to that shown by the global Knudsen numbers for these cases. Linear plot of x-component of velocity and temperature along the stagnation streamline are given in Fig. 4 for the first test case with a Knudsen number of 0.001. On the other hand, Fig. 5 shows the same properties along the stagnation streamline for the second test case with a Knudsen number of 0.01. From Figs. 4 and 5, it is distinctly visible that M–DSMC results are quite good match with the regular DSMC method. Small deviations can

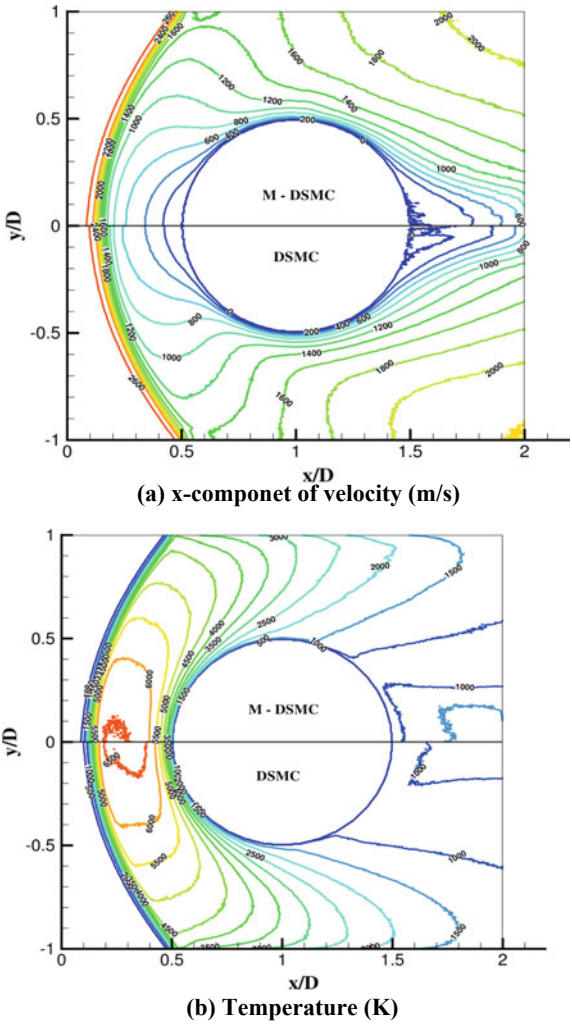

Fig. 4 Comparison of x-component of velocity and temperature along the stagnation streamline for flow over a cylinder at a Knudsen number of 0.001

be noticed in the wake region, which is the zone of large rarefaction, however, shock is found to be well captured.

3.2 Surface Properties Variation

Similar to flow properties, the surface properties such as heat flux and pressure coefficient are obtained using the M–DSMC approach and the results are compared with regular DSMC method for the two case studies.

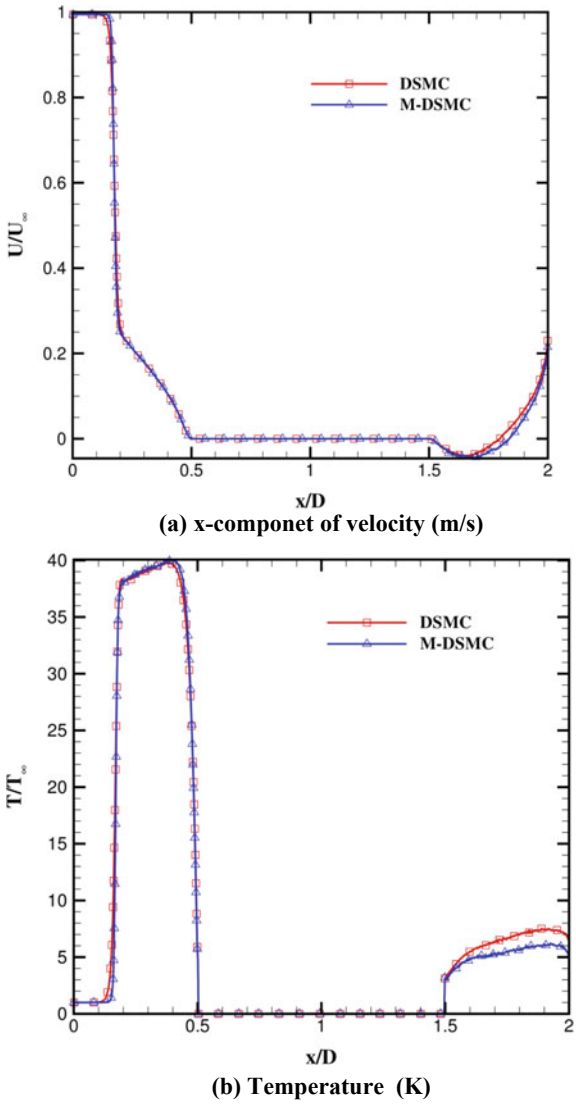

Fig. 5 Comparison of x-component of velocity and temperature along the stagnation streamline for flow over cylinder at a Knudsen number of 0.01

$$C_H = \frac{q}{\frac{1}{2}\rho_\infty U_\infty^3} \tag{7}$$

Heat flux along the surface of the cylinder is normalized and is given as follows, where q is the convective heat flux and ρ_∞ and U_∞ are the freestream density and velocity, respectively.

Figure 6 shows the variation of surface heat flux along the length of the cylinder for the two cases. From Fig. 6a, it is distinctly visible that normalized heat flux

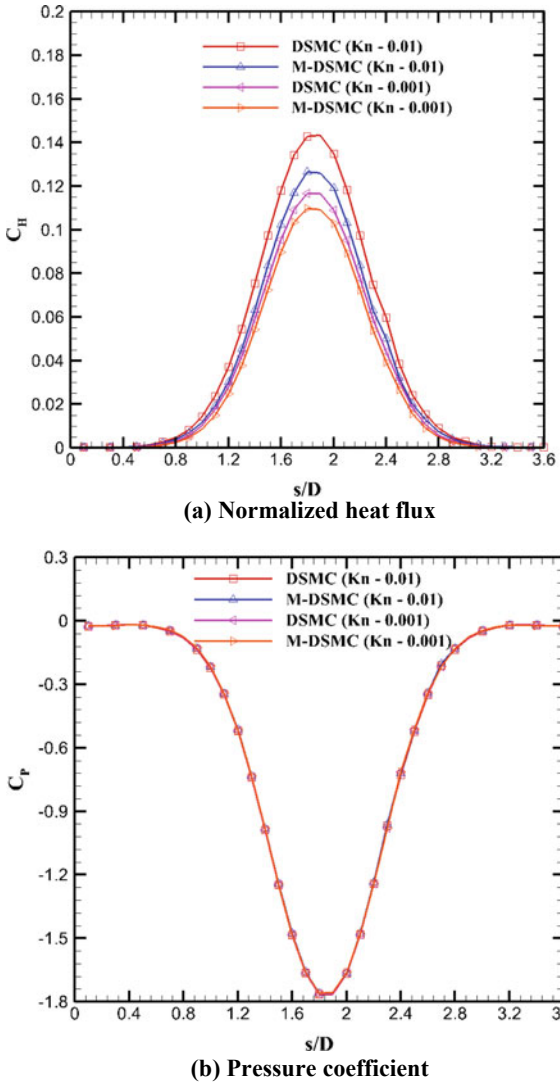

Fig. 6 Normalized surface properties along the surface of the cylinder for two case studies

variation along the surface of the cylinder obtained from M–DSMC approach shows same trend as that obtained from DSMC. There is a maximum deviation of ~15% from the DSMC results at a Knudsen number of 0.01 (based on cylinder diameter), whereas the deviation for a Knudsen number of 0.001 is less than 10%. Noteworthy is the fact that actual local degree of rarefaction is much more than as shown by the global Knudsen numbers. Thus, it can be said that the M–DSMC approach works quite well for near-continuum to semi-rarefied flow regime.

Similarly, differential pressure is normalized to the dynamic pressure and given as the pressure coefficient, CP. The normalized pressure coefficient is given as follows:

Table 2 Comparison of computational cost of each method for hypersonic flow over a cylinder for Knudsen number of 0.001

Parameter	DSMC	M–DSMC
CPU time (hours)	203	103
Number of cells	640,000	640,000
Number of particles	2,797,968	2,798,111

Table 3 Comparison of computational cost of each method for hypersonic flow over a cylinder for Knudsen number of 0.01

Parameter	DSMC	M–DSMC
CPU time (hours)	224	126
Number of cells	640,000	640,000
Number of particles	3,042,676	3,056,466

$$C_P = \frac{P - P_\infty}{\frac{1}{2}\rho_\infty U_\infty^2} \tag{7}$$

where P is the static pressure and P_∞ is the freestream pressure.

Pressure coefficient is shown in Fig. 6b. From Fig. 6b, the classical trend is observed along the surface of the cylinder. The pressure coefficient varies from 0 to −1.8, and agrees very well with the DSMC results for both cases.

3.3 Numerical Expenditures for Both M–DSMC and DSMC Method

In this section computational cost is estimated individually by M–DSMC and DSMC method. All the simulations are carried out using Intel Xeon E5-2670 v2 processors. The computational cost for each method and corresponding parameters are tabulated in Table 2 for simulation of flow over a cylinder at a Knudsen number of 0.001. Similarly, Table 3 gives the computational cost for the two methods at a Knudsen number of 0.01. The M–DSMC scheme shows almost 50% computationally cost-effective than the regular DSMC method. From this work, it could be demonstrated that M–DSMC solver is computationally much more prominent than the regular DSMC method and the results are almost parallel to the DSMC method for monatomic gas flows in semi-rarefied to rarefied flow regime.

4 Conclusions

We developed a simplified DSMC scheme, referred to as the M–DSMC method, in which the collision modeling is simplified such that all particles in a cell are assigned

velocities sampled from Maxwellian at local instantaneous cell temperature. The M–DSMC numerical scheme was tried for rarefied flow of argon over a cylinder at Mach 10 at two different Knudsen numbers. M–DSMC results were found to be in good agreement with the DSMC solver. Small deviations were found in the wake region of the cylinder for the temperature profile. Pressure coefficient was found to have a very good agreement with regular DSMC method. The heat flux coefficient showed ~15% deviation from the regular DSMC method for higher Knudsen number case. In general, the M–DSMC method was found to be more accurate and efficient at lower Knudsen number or in the near-continuum regime. M–DSMC solver was found to be computationally much more efficient than the regular DSMC method, which can be used to get quick results for near-continuum to semi-rarefied flow problems, and used in preliminary design procedures of a system.

References

1. Breuer K, Piekos E, Gonzales D (1995) DSMC simulations of continuum flows. In: 30th thermophysics conference, p 2088
2. Courant R, Friedrichs K, Lewy H (1928) On the partial differential equations of mathematical physics. Math Ann 100(1):32–74
3. Courant R, Friedrichs KO (1948) Supersonic flow and shock waves. In: Applied mathematical sciences, vol 12
4. Lengrand J-C, Raffin M, Allegre J (1981) Monte-Carlo simulation method applied to jet-wall inter-actions under continuum flow conditions. Rarefied Gas Dyn 994–1006
5. Bartel TJ, Sterk TM, Payne J, Preppernau B (1994) DSMC simulation of nozzle expansion flow fields. In: 6th AIAA and ASME, joint thermophysics and heat transfer conference. Colorado Springs, CO
6. Pullin D (1980) Direct simulation methods for compressible inviscid ideal-gas flow. J Comput Phys 34(2):231–244
7. Titov EV, Levin DA (2007) Extension of the DSMC method to high pressure flows. Int J Comput Fluid Dyn 21(9–10):351–368
8. Chinnapan AK, Malaikannan G, Kumar R (2017) Insights into flow and heat transfer aspects of hypersonic rarefied flow over a blunt body with aerospike using direct simulation Monte-Carlo approach. Aerosp Sci Technol 66:119–128
9. Malaikannan G, Kumar R (2017) Hybrid particle-particle numerical algorithm for high speed non-equilibrium flows. Comput Fluids 152:24–39

Fluid–Structure Interaction Dynamics of a Flexible Foil in Low Reynolds Number Flows

Chandan Bose, Sunetra Sarkar and Sayan Gupta

Abstract The present paper numerically investigates the aerodynamic characteristics of a chord-wise flexible filament-like structure subjected to a fluctuating inflow in terms of the wake of a rigid cylinder situated upstream in the low Reynolds number regime ($RE_D = 500$, where D is the diameter of the cylinder). The numerical simulations are performed with a strongly coupled partitioned fluid–structure interaction (FSI) solver based on finite volume approach. An incompressible Navier–Stokes solver is used to capture the unsteady viscous flow features and the flexible structural model is considered to be nonlinear and elastic. The foil is fixed at its leading edge, and the structural properties (mass ratio (μ), flexural rigidity (EI), etc.) are chosen appropriately to have a comparable fluid and structural inertia with dominant FSI effects to significantly augment the aerodynamic loads. It can be seen that the chord-wise flexibility of the wing manifests a passive pitching achieving greater propulsive efficiency. The deflection envelope reflects the fundamental bending modes of the structure. The interactions between the wake of the rigid cylinder and the flexible structure are investigated with the help of vorticity contours as well as Lagrangian coherent structures to have a clear understanding of the vortex-induced FSI dynamics. Moreover, the aerodynamic forces generated by the flexible foil are compared with that of a rigid stationary foil of same length and subjected to similar upstream flow fluctuations. It is observed that the chord-wise flexibility enhances the lift and thrust generation remarkably compared to the rigid foil.

Keywords Fluid–structure interaction · Chord-wise flexibility · Passive pitching · Strongly coupled FSI solver · Low Reynolds number flows

C. Bose · S. Gupta
Department of Applied Mechanics, Indian Institute of Technology Madras, Chennai 600036, India
e-mail: cb.ju.1991@gmail.com

S. Gupta
e-mail: gupta.sayan@gmail.com

S. Sarkar (✉)
Department of Aerospace Engineering, Indian Institute of Technology Madras, Chennai 600036, India
e-mail: sunetra.sarkar@gmail.com

B. N. Singh et al. (eds.), *Recent Advances in Theoretical, Applied, Computational and Experimental Mechanics*, Lecture Notes in Mechanical Engineering,
https://doi.org/10.1007/978-981-15-1189-9_37

1 Introduction

Research into design and development of bio-inspired futuristic devices like Micro Aerial Vehicles (MAVs) or Autonomous Underwater Vehicles (AUVs) has recently gained an impetus due to the necessity for futuristic surveillance tools. A crucial feature in investigating the behavior of these systems is to gain clear understanding of the underlying fluid mechanics behind flapping-wing/fin propulsion [1–3]. The inspiration for the design of MAVs/AUVs comes from the natural bio-propulsion systems like insect flight or swimming of fishes. Both insect wings and fish fins are very flexible structures that undergo significant deformation due to the interactions with the surrounding fluid flow during their locomotion. Furthermore, the fluid viscosity and the flexibility of the structure play a key role in generation of propulsive and maneuvering forces as the body inertia is comparable to the fluid inertia. Hence, the intricacy of the fluid–body interactions of flexible foils/filaments in the surrounding flow has become a central problem over the past two decades. A comprehensive survey of existing literature in this regard can be found in the review paper by Shelley and Zhang [4].

On the other hand, passive flexibility of wings/fins is seen to play a pivotal role in boosting their aerodynamic and hydrodynamic performance. The role of passive flexibility in propulsion has been studied experimentally in the literature in terms of the dynamics of a flag or a filament. Taneda [5] was the first to explore the flapping dynamics of a flag through wind tunnel experiments. Zhang et al. [6] revisited the problem by performing soap film experiments. A variety of flapping modes ("stretched straight" (SS), coherent flapping) with different flapping frequencies were reported by them. The "SS" mode was accompanied by a von Kármán wake, whereas the coherent flapping mode showed an undulating vortex street having mostly same-sense fine-scale vortices which can be attributed to the Kelvin–Helmholtz instability of the shear layer vortex street. They also reported bistability and hysteresis behavior between different flapping modes. Moreover, a transition to irregular flapping was observed with the increase in the length scale or the flow velocity. The other important experimental works include Shelley et al. [7] and Elloy et al. [8].

However, the experimental studies are limited in the parametric space. Therefore, we have to rely on numerical simulations to get better insights into the essential features of the FSI dynamics with respect to the key parameters such as mass ratio, bending rigidity, and Reynolds number. Due to prohibitive computational cost of full-fidelity FSI simulations, some of the numerical studies have considered the surrounding fluid to be inviscid while modeling the structure as an elastic continuum [9, 10]. Alben et al. [10] modeled a fin as an elastic continuum, and the flow was modeled by the inviscid potential theory with some empirical modification to incorporate the effects of viscous drag. However, the applicability of the model was limited especially at low Reynolds numbers. On the other hand, some works relied on lower order structural models such as flexibly mounted rigid components coupled with fluid [11, 12]. Notably, the FSI behavior of such systems is much different from that of a fully elastic continuum. With the increase in the computational resources in recent days,

viscous simulation of a flexible filament has been carried out in a few studies [13–16]. Some of the very recent numerical simulations of self-propelled flapping system [17–19] showed that the flexibility can enhance the propulsive performance which is also in accord with the experimental observations [20, 21]. However, most of the abovementioned studies have been performed in uniform flow condition. The effect of flow fluctuations onto the FSI dynamics of a flexible filament has not received much attention except in a few recent studies [22–24].

Therefore, the primary focus of this study is to unravel the physics associated with the FSI behavior of such systems subjected to a fluctuating flow field in the low Reynolds number regime, relevant for natural locomotion. The corresponding coupled systems are phenomenologically rich in dynamics due to complex FSI. This paper aims to numerically investigate the FSI behavior of these systems by considering complexities that include the flexibility of the structure and the viscous flows in the low Reynolds number regime. The flow topology over the flexible structure is investigated along with its different vibrating modes during the passive flapping motion. The remainder of the paper consists of the following sections: Sect. 2 discusses the computational methodology. The deflection envelope of the flexible filament, the vortex interactions as well as the generation of aerodynamic forces have been discussed in Sect. 3. The salient outcomes of this study are summarized in Sect. 4.

2 Computational Framework

Dynamics of a flexible filament subjected to a fluctuating inflow is investigated using a strongly coupled FSI framework [25, 26] consisting of an incompressible Navier–Stokes solver coupled with a nonlinear elastic structural model. The flow governing equation (incompressible N-S equation) can be cast into Arbitrary Lagrangian–Eulerian (ALE) form [27] as

$$\nabla \cdot u = 0,$$
$$\frac{\partial u}{\partial t} + \left[\left(u - u^m\right) \cdot \nabla\right] u = -\frac{\nabla p}{\rho_f} + \nu \nabla^2 u.$$

Here, u is the flow velocity, u^m is the grid point velocity, p is the pressure, ρ_f is the fluid density, ν is the kinematic viscosity, and ∇ is the gradient operator. The details of the flow solver can be found in [25, 26]. The flexible filament is modeled as a solid continuum. The equation for conservation of linear momentum is given by

$$\frac{\partial}{\partial t} \int \rho_s v dV = \oint n \cdot \sigma d\Gamma + \int \rho_s b dV,$$

where V is the volume of the foil, bounded by the surface Γ with unit normal n, v is the velocity vector, σ is the Cauchy stress tensor, ρ_s is the density of the material of the structure, and b is the body force per unit mass. Assuming large strain, the material behavior of the filament can be modeled using Kirchhoff–St. Venant hyper-elasticity theory. The linear momentum equation can therefore be written in terms of Piola–Kirchhoff stress tensor S as

$$\sigma = \frac{1}{J} F \cdot S \cdot F^T,$$

where $F = I + \nabla w$ is the deformation gradient, I is the second-order identity tensor, and w is the deformation vector. A large strain elastic stress analysis solver based on Lagrangian displacement formulation [28] is used to solve the structural governing equations. A strong coupling methodology [28], illustrated through the flowchart shown in Fig. 1, is adopted in this study using a quasi-Newton coupling algorithm with an approximation for the inverse of the residual's Jacobian matrix from a least-square model (abbreviated as IQN-ILS). The present FSI solver is well validated with the existing literature [29]. A rectangular computational domain (see Fig. 2a)

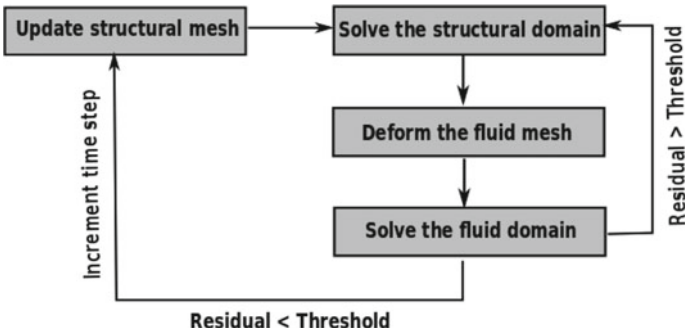

Fig. 1 Strong coupling algorithm

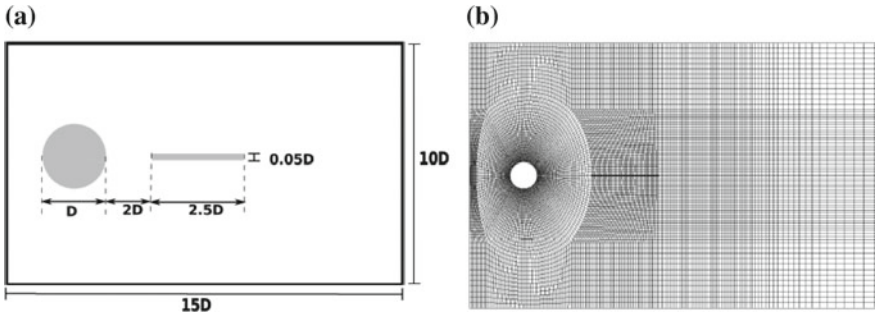

Fig. 2 **a** Computational domain, **b** structured mesh

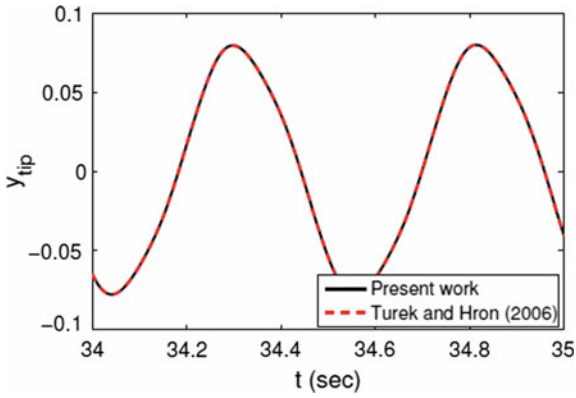

Fig. 3 Validation study of the FSI solver

has been discretized using structured grids. The mesh (Fig. 2b), having 89,052 grid points, has been chosen after a grid convergence study. Standard boundary conditions are applied: a zero pressure gradient and a constant free stream at the inlet; a zero velocity gradient and atmospheric pressure condition at the outlet; no-slip and zero-normal pressure gradient condition on the horizontal walls and traction boundary condition on the flexible flapper.

The FSI solver has been quantitatively validated in the present study with the benchmark case of a flexible splitter plate attached with a rigid cylinder given by Turek and Hron [30]. The parameters corresponding to "FSI2" case presented in [30] have been considered for the benchmark validation. It can be clearly seen from Fig. 3 that vertical tip displacement time history of the flexible plate shows an excellent match with the results presented by Turek and Hron [30] in the self-sustained periodic oscillatory state.

The present computations are performed in the following parametric space: Reynolds number $(RE_D) = 500$, mass ratio $\left(\mu = \rho_s/\rho_f\right) = 1$, nondimensional Young's modulus $\left(\bar{E} = E/\rho_f u_\infty^2\right) = 5600$, and nondimensional length $(\bar{l} = l/D) = 2.5$. Here, ρ_s and ρ_f are the solid and fluid density, respectively, E is the dimensional Young's modulus of the structure, l and D are the length of the filament and diameter of the cylinder, respectively, and u_∞ is the uniform velocity at the inlet.

3 Results and Discussions

The present work focuses on the role of chord-wise flexibility of a filament in enhancing the aerodynamic loads in comparison to a rigid foil subjected to a flow fluctuation in terms of the wake of a rigid stationary cylinder. Figure 4 presents the vorticity contour past the rigid foil at $t = 10$ s. It is observed that the interaction of shear layers separated from the rigid cylinder is delayed due to the presence of the rigid foil; the immediate formation of the von Kármán vortex street is inhibited which

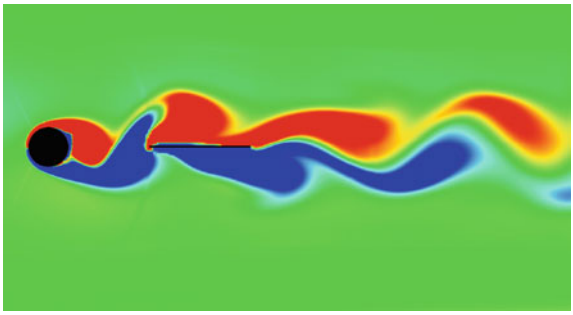

Fig. 4 Vorticity contour behind a rigid filament in the wake of a rigid cylinder

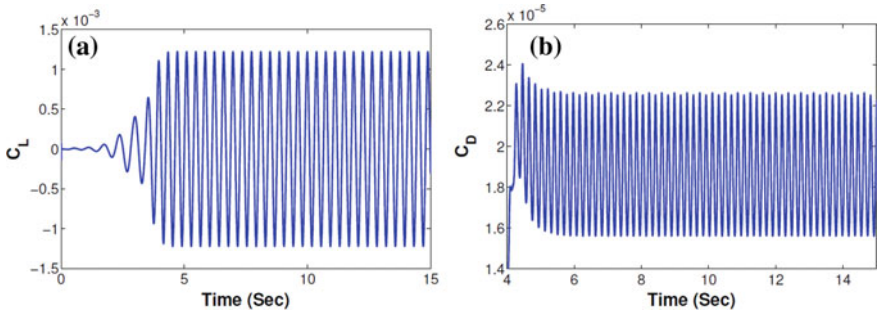

Fig. 5 **a** Lift coefficient and **b** drag coefficient time histories

eventually occurs in longer time. Figures 5a and 5b show the time history of the lift coefficient (C_L) and drag coefficient (C_D), respectively. Since the rigid foil is placed symmetrically at zero angle of attack in the fluctuating flow field, C_L has a zero mean and C_D has a very small mean value in the order of 10^{-5}.

Thereafter, the FSI dynamics of a flexible filament with same length and similar inflow condition has been simulated. The filament is kept fixed at its leading edge. In this low Reynolds number regime, the filament exhibits a passive pitching in terms of its different natural bending modes. The deflection envelope and the time history of the tip displacement have been plotted in Figs. 6a and 6b, respectively. At $RE_D = 500$, the shear layers past a rigid cylinder roll up and consequently vortex cores are formed evolving with time, thus gaining more strength. Subsequently, the vortex cores convect over the structure, acting as a periodic forcing and subsequently shed in the downstream forming a vortex street of alternate shedding vortices. It is observed that the first mode shape is initially triggered when the vortex cores start convecting over it. However, it attains a mixed-mode vibration between the first and second mode shapes once the vortices impinge on it and start shedding from the trailing edge. Figures 6c and 6d present the C_L and C_D time histories for the flexible filament. It can be evidently seen that the aerodynamic loads have been significantly increased in this case with a high maximum C_L value along with a high mean C_D (negative)

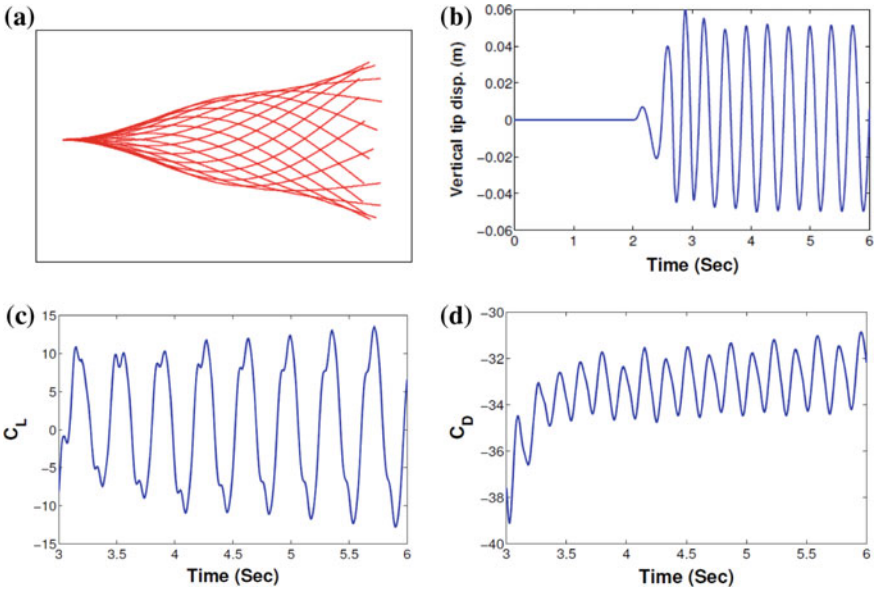

Fig. 6 FSI dynamics of a chord-wise flexible filament: **a** deflection envelope, **b** tip deflection time history, **c** lift coefficient, and **b** drag coefficient time histories

value. It can be noted that the fluid–body interaction results in a symmetric wake that results in zero-mean lift. Besides, it produces significant thrust on the structure desirable for efficient propulsion.

The impingement of the vortex core on the flexible filament causes it to bend in different modes depending on the location of impingement and the Strouhal frequency of the fluctuating flow. The vortex–filament interactions and evolution of the trailing edge flow topology have been investigated by the vorticity contours at different time instances as shown in Fig. 7a. To get more insight into the vortex interaction, the Lagrangian coherent structures (LCS) are presented in the near field along with the vorticity contours (Fig. 7b). LCSs are obtained by plotting the backward finite-time Lyapunov exponents (FTLE) of the velocity field which clearly show how the impingement of the vortex cores cause the filament to bend in different modes augmenting the propulsive efficiency.

To understand the fluid–body interactions in more detail, the flow physics is analyzed through a sequence of vortex contour snapshots at different time instances, see Fig. 8. At $t = 2.68$ s, a large clockwise vortex core "4" (generated as the primary wake vortex of the cylinder in the previous cycle) is seen to be convecting over the elastic structure along with a small weak counterclockwise vortex "3" at the leading edge. Besides, two opposite sense vortices "1" and "2" are seen to be formed through rolling up of the separated shear layers from the cylinder. Clockwise vortex "4" gradually moves forward and impinges on the structure at the tip bending it downward. At the same time, the counter clockwise vortex "2" impinges in the middle

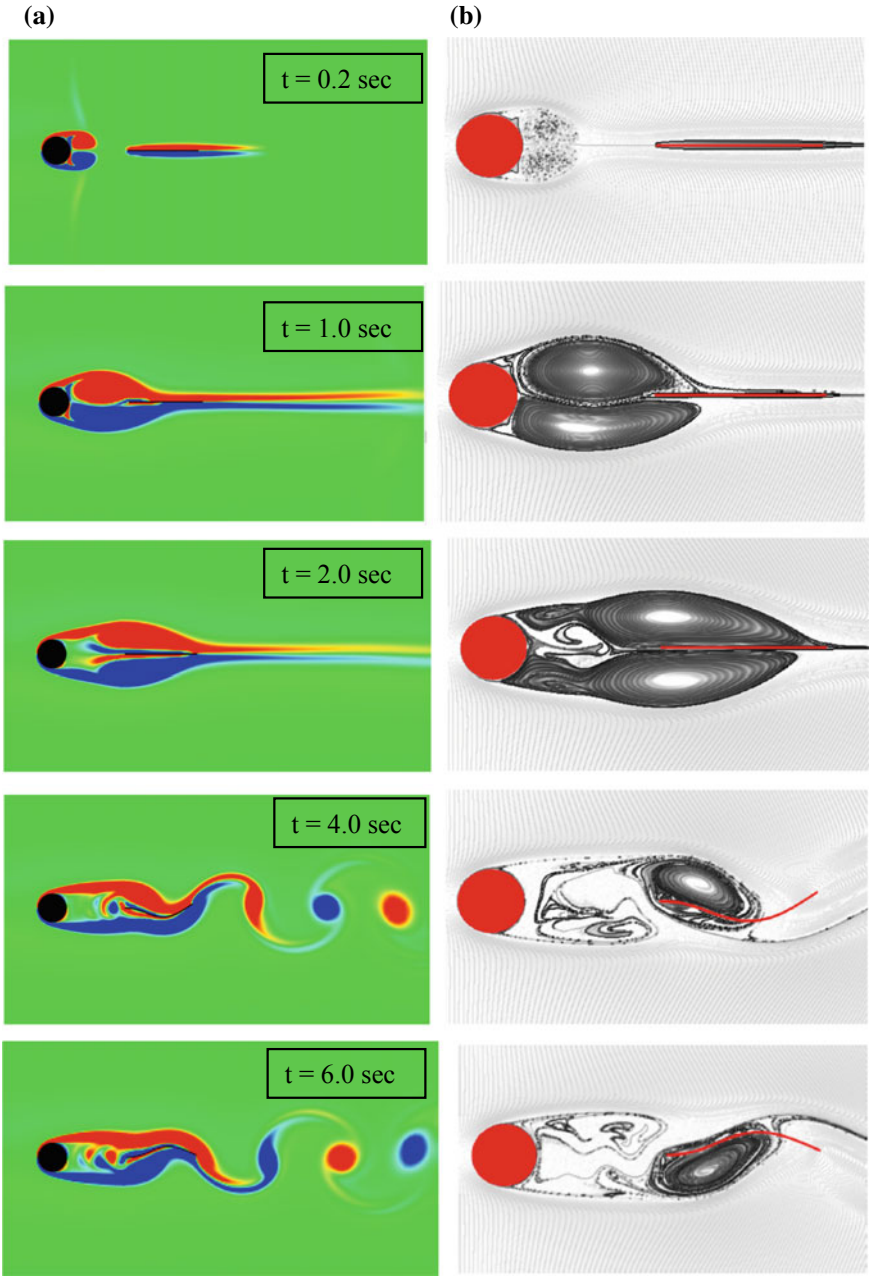

Fig. 7 **a** The instantaneous vorticity field and **b** the corresponding LCS (bFTLE ridges)

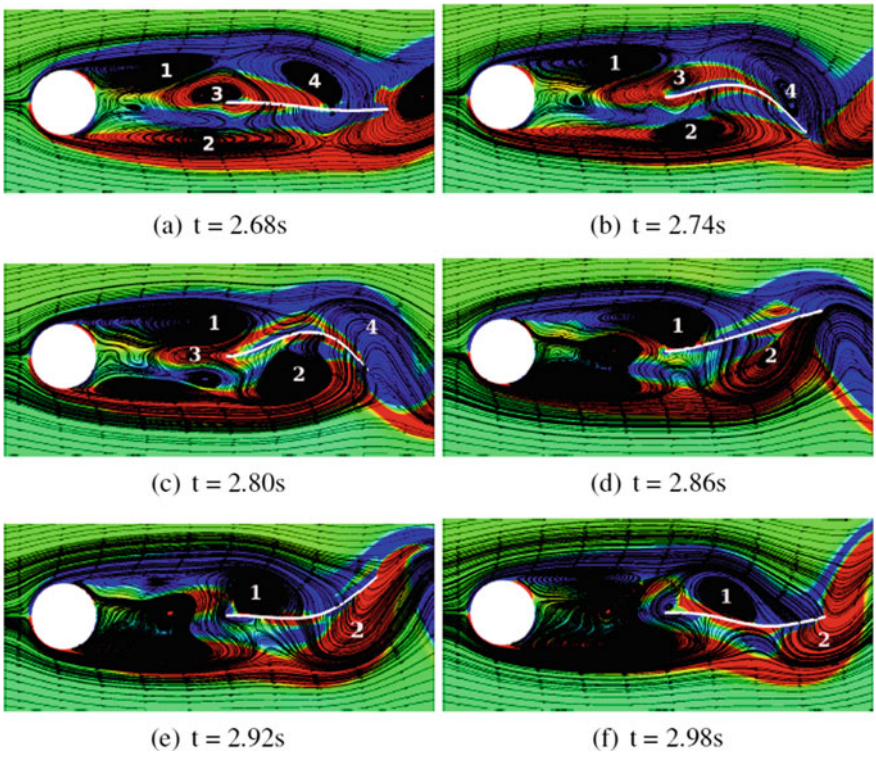

Fig. 8 Change of mode shapes due to vortex impingement on the flexible filament

of the structure making it bend in its second mode shape; see Fig. 8c. Thereafter, the vortex "4" sheds downstream and becomes a part of the vortex street, while the vortex "2" convects over the structure and reaches to the tip. On the other hand, newly formed clockwise vortex "1" deforms the weaker counterclockwise vortex "3" and comes near the leading edge of the structure. As a result, the flapper again bends upward in the first mode shape at $t = 2{:}86$ s (see Fig. 8d); thus, a mixed-mode oscillation is observed. These interactions take place periodically in the subsequent cycles.

In case of a shorter flapper ($\bar{l} = 1$), it appears to oscillate predominantly in its first natural mode shape; see Fig. 9a. This can be attributed to the fact that the wake vortices impinge at the tip of the structure, thus making it bend in the upward and downward directions periodically in its first natural mode. However, it attains a mixed-mode vibration for $\bar{l} = 2.5$ as the length of the flapper becomes greater than the formation length of the wake vortices; see Fig. 9b. As a result, the vortices impinge in the middle of the longer elastic structure leading to a periodic mixed-mode oscillation.

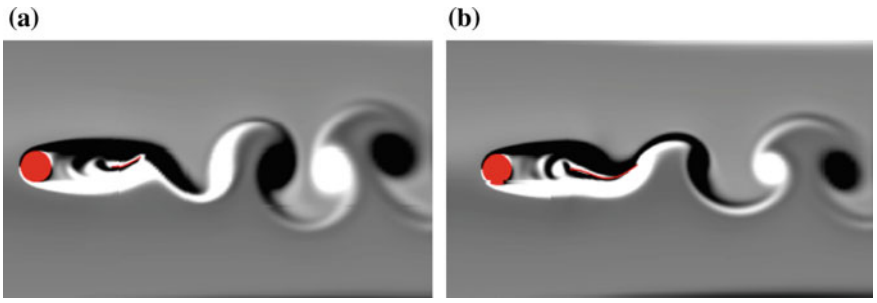

Fig. 9 **a** First mode oscillation ($\bar{l} = 1$); **b** mixed-mode oscillation ($\bar{l} = 2.5$)

4 Concluding Remarks

The flow-induced dynamics of a chord-wise flexible filament, fixed at its leading edge, in a viscous fluctuating inflow has been simulated using a strongly coupled FSI solver at a low Reynolds number. The periodically fluctuating inflow is generated as the wake of a rigid stationary cylinder situated upstream of the filament. Initially, the filament starts to exhibit oscillations with small deformation and subsequently asymptotes to a steady periodic oscillation having higher deformation. The periodic impingement of the wake vortices into the flexible filament causes it to bend in different modes resulting in a passive pitching mechanism. The filament starts to bend in its first fundamental mode and transitions into mixed-mode oscillations involving first and second mode shapes at longer times. The aerodynamic load generation due to the FSI dynamics of the passively flapping filament is found to be enhanced significantly as compared to the rigid filament. The effect of various bending modes of the structure on the propulsive efficiency is considered a possible future work.

References

1. Shyy W, Aono H, Chimakurthi SK, Trizila, Kang CK, Cesnik CES, Liu H (2010) Recent progress in flapping wing aerodynamics and aeroelasticity. Prog Aerosp Sci 46:284–327
2. Platzer MF, Jones KD, Young J, Lai JS (2008) Flapping wing aerodynamics: progress and challenges. AIAA J 46:2136–2149
3. Triantafyllou MS, Techet AH, Hover FS (2004) Review of experimental work in biomimetic foils. IEEE J Oceanic Eng 29:585–594
4. Shelley MJ, Zhang J (2011) Flapping and bending bodies interacting with fluid flows. Annu Rev Fluid Mech 43:449–465
5. Taneda S (1968) Waving motions of flags. J Phys Soc Jpn 24:392–401
6. Zhang J, Childress S, Libchaber A, Shelley M (2000) Flexible filaments in a flowing soap film as a model for one-dimensional flags in a two-dimensional wind. Nature 408:835–839
7. Shelley M, Vandenberghe N, Zhang J (2005) Heavy flags undergo spontaneous oscillations in flowing water. Phys Rev Lett 94:094302
8. Eloy C, Lagrange R, Souilliez C, Schouveiler L (2008) Aeroelastic instability of cantilevered flexible plates in uniform flow. J Fluid Mech 611:97–106

9. Alben S (2008) Optimal flexibility of a flapping appendage in an inviscid fluid. J Fluid Mech 614:355–380
10. Alben S, Witt C, Baker TV, Anderson E, Lauder GV (2012) Dynamics of freely swimming flexible foils. Phys Fluids 24:051901
11. Spagnolie SE, Moret L, Shelley MJ, Zhang J (2010) Surprising behaviors in flapping locomotion with passive pitching. Phys Fluids 22:041903
12. Zhang X, Ni S, Wang S, He G (2009) Effects of geometric shape on the hydrodynamics of a self-propelled flapping foil. Phys Fluids 21:103302
13. Zhu L (2007) Viscous flow past a flexible fibre tethered at its centre point: vortex shedding. J Fluid Mech 587:217–234
14. Huang W-X, Shin SJ, Sung HJ (2007) Simulation of flexible filaments in a uniform flow by the immersed boundary method. J Comput Phys 226:2206–2228
15. Zhu L (2009) Interaction of two tandem deformable bodies in a viscous incompressible flow. J Fluid Mech 635:455–475
16. Olivier M, Dumas G (2016) A parametric investigation of the propulsion of 2d chordwise flexible flapping wings at low Reynolds number using numerical simulations. J Fluids Struct 63:210–237
17. Lee J, Lee S (2013) Fluid–structure interaction for the propulsive velocity of a flapping flexible plate at low Reynolds number. Comput Fluids 71:348–374
18. Yeh PD, Alexeev A (2014) Free swimming of an elastic plate plunging at low Reynolds number. Phys Fluids 26:053604
19. Tang C, Lu X (2015) Propulsive performance of two-and three-dimensional flapping flexible plates. Theor Appl Mech Lett 5:9–12
20. Heathcote S, Gursul I (2007) Flexible flapping airfoil propulsion at low Reynolds numbers. AIAA J 45:1066–1079
21. Cleaver D, Calderon D, Wang Z, Gursul I (2016) Lift enhancement through flexibility of plunging wings at low Reynolds numbers. J Fluids Struct 64:27–45
22. Jia L-B, Yin X-Z (2009) Response modes of a flexible filament in the wake of a cylinder in a flowing soap film. Phys Fluids 21:101704
23. Zhu L (2014) Numerical investigation of the dynamics of a flexible filament in the wake of cylinder. Adv Appl Math Mech 6:478–493
24. Kundu A, Soti AK, Bhardwaj R, Thompson MC (2017) The response of an elastic splitter plate attached to a cylinder to laminar pulsatile flow. J Fluids Struct 68:423–443
25. Kumar SK, Bose C, Ali SF, Sarkar S, Gupta S (2017) Investigation on a vortex induced vibration based energy harvester. Appl Phys Lett 111(24):243903
26. Bose C, Kumar SK, Sarkar S, Gupta S (2019) Interaction of a flexible splitter plate with vortex shedding past a rigid circular cylinder. Recent Adv Struct Eng 2:841–852
27. Ferziger JH, Peric M, Leonard A, Computational methods for fluid dynamics (1997)
28. Cardiff P, Tukovic Z, Jasak H, Ivankovic A (2016) A block-coupled finite volume methodology for linear elasticity and unstructured meshes. Comput Struct 175:100–122
29. Tukovic Z, Cardiff P, Karac A, Jasak H, Ivankovic A (2014) OpenFOAM library for fluid structure interaction. In: 9th OpenFOAM workshop. Zagreb, Croatia
30. Turek S, Hron J (2006) Proposal for numerical benchmarking of fluid-structure interaction between an elastic object and laminar incompressible flow. In: Fluid-structure interaction. Springer, Berlin, Heidelberg, pp 371–385